

# THERMOCHEMICAL MODELS OF OCEANIC UPPER MANTLE

By  
Christopher J. Grose

A THESIS SUBMITTED TO MACQUARIE UNIVERSITY  
FOR THE DEGREE OF DOCTOR OF PHILOSOPHY  
DEPARTMENT OF EARTH AND PLANETARY SCIENCES

AUSTRALIAN RESEARCH COUNCIL CENTRE OF EXCELLENCE FOR  
CORE TO CRUST FLUID SYSTEMS (CCFS) AND GEMOC

OCTOBER 2015





# Acknowledgements

This thesis would not have been possible without the support, wisdom, and advice of so many. Anne Hofmeister was very kind to provide many preprints of her work, clarifications of her ideas, and discussions on the nature of heat transport phenomena in silicates. I am grateful to Derrick Hasterok for discussions and clarifications regarding seafloor heat flow measurements. Thanks to John Hillier for providing his database of filtered global seafloor topography and comments on statistical analysis of seafloor topography. Also, thanks to Paul Asimow, Derrick Hasterok, and Jean-Claude Mareschal for providing many thoughtful comments on the submitted draft of this thesis.

Many aspects of my work and thought processes have benefited from exchanges with Jun Korenaga, Dan McKenzie, and Yaoling Niu. Norm Pearson, John Adam, and Bill Griffin have all been kind, enthusiastic, and very helpful in our discussions on matters of geochemistry and petrology. My submitted and published manuscripts, on which some of the chapters of this thesis are based, have benefited from detailed comments and reviews by Norm Sleep, Dietmar Müller, Laurent Husson, Jeroen van Hunen, Rocco Malerisi, and many more anonymous reviewers.

Thanks to Joe Meert, who inspired me with his consideration and patience in my scientific infancy. The encouragement and mentorship of Jeff Ryan during my undergraduate years will never be forgotten.

Thanks to Beñat Oliveira Bravo for helping me think about problems in mathematics, as well as being a good friend and helping with the construction of this thesis. Special thanks to Juan Carlos Afonso for taking me on as his student. Your encouragement, criticism, and keen scientific insight have been indispensable to this young scientist. Thanks to my Sherry, for bearing with me. Most of all, I wish to thank my family, whom I have endlessly missed over these last few years. Mom, Dad, Ryan, Josh, and Kristin, I dedicate this thesis to your love and your patience.





# List of Publications

- **Chapter 2.** Grose, C. J., *Properties of Oceanic Lithosphere: Revised Plate Cooling Model Predictions*. Earth and Planetary Science Letters. **333-334**, 250-264 (2012).  
Thesis Author Contributions: Concept (100%); Data collection (n/a); Analysis (95%); Writing (100%).
- **Chapter 3.** Grose, C. J., and J. C. Afonso, *Comprehensive Plate Models for the Thermal Evolution of Oceanic Lithosphere*. Geophysics, Geochemistry, Geosystems. **14, I9**, 3751-3778 (2013).  
Thesis Author Contributions: Concept (95%); Data collection (n/a); Analysis (95%); Writing (95%).
- **Chapter 4.** Grose, C. J., and J. C. Afonso, *The Hydrothermal Power of Oceanic Lithosphere*. Solid Earth. **vol.**, pages (2015).  
Thesis Author Contributions: Concept (95%); Data collection (n/a); Analysis (95%); Writing (95%).
- **Chapter 5.** Grose, C. J., and J. C. Afonso, *Modeling Microchemical Disequilibria During OIB Source Melting*. (submitted).  
Thesis Author Contributions: Concept (90%); Data collection (n/a); Analysis (90%); Writing (95%).
- Shan, B., J. C. Afonso, Y. Yang, C. J. Grose, Y. Zheng, X. Siong, and L. Zhou, *The Thermochemical Structure of the Lithosphere and Upper Mantle Beneath South China: Results from Multiobservable Probabilistic Inversion*. Journal of Geophysical Research: Solid Earth. **119**, 8417-8441 (2015).  
Thesis Author Contributions: Concept (5%); Data collection (0%); Analysis (5%); Writing (25%).

The chapters of this thesis are based on the above published and submitted papers, with the incorporation of some textual modifications to accommodate connectivity among chapters as well as to update some discussions in earlier publications in light of the findings of later work. Note that my contributions to the work of Shan et al. (2015) are not represented as a chapter here.



# Declaration

I certify that the work in this thesis entitled, "Thermochemical Models of Oceanic Upper Mantle" has not previously been submitted for a degree, nor has it been submitted as a partial requirement for a degree to any other university or institution other than Macquarie University.

I also certify that this thesis is an original piece of research and has been written by me. Any help and assistance that I have received in my research work and the preparation of the thesis itself has been properly acknowledged.

In addition, I certify that all data, information sources and literature used are indicated in the thesis.

Christopher J. Grose  
Student ID: 42712122  
Date: June 16, 2016



# Abstract

The thermal state of the oceanic upper mantle is reassessed by developing new progressively more sophisticated models of the thermal evolution of oceanic lithosphere. Model Properties are constrained by experimental mineral physics data for the thermal properties of the mantle, statistical analyses of the major geophysical observables (topography and surface heat flow), and sensitivity analyses of physical parameters. Predictions of geothermal structure, plate thickness, subsidence rates, and net seafloor heat flow are discussed. Sensitivity analyses demonstrate that physically simple plate cooling models cannot fit geophysical observations unless thermal expansivity is substantially lower than experimental estimates for forsterite. More physically complete models resolve improved fits to geophysical observations with less artificial adjustments in physical properties. The inclusion of an insulating oceanic crust is found to significantly impact the cooling behavior of oceanic lithosphere. To estimate the total amount of heat vented to the oceans by ventilated hydrothermal circulation, we integrate the deficit between modeled and measured heat flow over young seafloor. A model with insulating oceanic crust predicts a loss of about 6.6 TW and the fraction of heat extracted on ridge axes is about 50% of the total. Lastly, the thermal structure of oceanic lithosphere is linked to the chemistry of Ocean Island Basalts (OIB) via the 'LID effect'. We developed a two-dimensional numerical model of multi-phase coarsening, diffusive trace element partitioning, and near-fractional melting. The model is applied to the generation of melts in the OIB source, and results are compared to observed correlations in La/Sm and Sm/Yb with seafloor age. Using the model we explain Rare-Earth element (REE) systematics in Global OIB, constrain the LAB temperature to be approximately 1225° C, suggest that experimental partition coefficients may be a few tens of percent away from appropriate effective values in OIB melting, suggest that the mean grain radius in the OIB source is on the order of 2.5-5 mm, demonstrate that the OIB source is in a state of extreme disequilibrium, show that the REE composition of the bulk OIB source is both heavily enriched and similar to the MORB source, and we show that the potential temperature of the OIB source is likely < 1400°C.



# Contents

<b>Acknowledgements</b>	<b>iii</b>
<b>List of Publications</b>	<b>v</b>
<b>Abstract</b>	<b>ix</b>
<b>List of Figures</b>	<b>xv</b>
<b>List of Tables</b>	<b>xxxiii</b>
<b>1 Introduction</b>	<b>1</b>
<b>2 Properties of Oceanic Lithosphere: Revised Plate Cooling Model Predictions</b>	<b>3</b>
2.1 INTRODUCTION . . . . .	3
2.2 METHODS AND FORMALISMS . . . . .	5
2.2.1 Heat transport modeling . . . . .	5
2.2.2 Effective heat transport properties . . . . .	6
2.2.3 Effective versus Apparent Values . . . . .	6
2.2.4 Isostatic formalism and seafloor subsidence . . . . .	7
2.2.5 Treatment of variable thermal expansivity . . . . .	8
2.2.6 Net seafloor heat flow . . . . .	9
2.2.7 Sensitivity analysis and fitting experiments . . . . .	9
2.3 RESULTS . . . . .	10
2.3.1 Sensitivity analysis . . . . .	10
2.3.2 Fitting experiments . . . . .	11
2.4 DISCUSSION . . . . .	12
2.4.1 Properties of best fit plate models . . . . .	12
2.4.2 On slow cooling estimates . . . . .	13
2.4.3 Low apparent thermal expansivity . . . . .	14
2.4.4 Thermal diffusivity . . . . .	15
2.4.5 Adjustable treatment of dependent parameters . . . . .	15
2.4.6 Mantle potential temperature . . . . .	17
2.4.7 Constraints provided by topography and heat flow . . . . .	17
2.4.8 Treatment of old-age topography, regional behaviors, and the problem of 'flattening' . . . . .	17

2.4.9	Small-scale convection, plate thickness, and the geoid . . . . .	18
2.5	CONCLUSIONS . . . . .	20
<b>3</b>	<b>Comprehensive Plate Models for the Thermal Evolution of Oceanic Lithosphere</b>	<b>33</b>
3.1	INTRODUCTION . . . . .	33
3.2	METHODS AND ANALYSES . . . . .	34
3.2.1	Heat transport modeling . . . . .	34
3.2.2	Compressibility, thermal expansion, and bulk density . . . . .	35
3.2.3	Heat transport properties . . . . .	36
3.2.4	Decompression melting and the initial geotherm . . . . .	37
3.2.5	Seafloor topography . . . . .	38
3.2.6	Fitting analysis . . . . .	38
3.2.7	Net seafloor heat flux . . . . .	40
3.3	RESULTS AND DISCUSSION . . . . .	41
3.3.1	Best fit properties from fitting experiments . . . . .	41
3.3.2	Preferred reference models . . . . .	43
3.3.3	Seafloor heat flux . . . . .	43
3.3.4	Net seafloor heat flow: A new low estimate . . . . .	45
3.3.5	Seafloor topography . . . . .	46
3.3.6	Thermal structure and the seismogenic zone . . . . .	47
3.3.7	Mantle potential temperature and melting models . . . . .	47
3.3.8	Hydrothermal circulation and the young geotherm . . . . .	48
3.3.9	Properties of oceanic crust . . . . .	49
3.3.10	Thermal expansivity adjustment: Thermoviscoelastic behavior of the lithosphere . . . . .	50
3.3.11	Thermal expansivity adjustment: Petrology . . . . .	51
3.4	CONCLUSIONS . . . . .	51
<b>4</b>	<b>The Hydrothermal Power of Oceanic Lithosphere</b>	<b>79</b>
4.1	INTRODUCTION . . . . .	79
4.2	Methods . . . . .	81
4.2.1	The Power Deficit . . . . .	81
4.2.2	Statistical Analysis . . . . .	82
4.2.3	Reference Models for Seafloor Heat Flow . . . . .	83
4.2.4	Spatial Power Distribution . . . . .	85
4.3	Results and Discussion . . . . .	85
4.3.1	The Net Power Deficit . . . . .	86
4.3.2	Spatial Distribution of the Power Deficit . . . . .	87
4.4	Heat Flow Constrained by Topography . . . . .	88
4.4.1	The subsidence rate . . . . .	90
4.4.2	Note on Old-Age Topography and Seafloor Flattening . . . . .	91
4.5	Constraints from the Thermal Budget of Crustal Cooling . . . . .	92
4.6	Constraints from High-Resolution Heat Flow Surveys . . . . .	93
4.6.1	Heat Flow at High-Resolution Sites . . . . .	93



4.6.2	Comparison of Surveys and Models . . . . .	95
4.6.3	Summary of High-Resolution Sites . . . . .	97
4.7	CONCLUSIONS . . . . .	98
4.8	ACKNOWLEDGEMENTS . . . . .	101
<b>5</b>	<b>Microchemical Disequilibria in OIB Source Melting</b>	<b>111</b>
5.1	INTRODUCTION . . . . .	111
5.2	The LID effect and OIB Compositions . . . . .	112
5.3	Modeling Mantle Melting: New Horizons . . . . .	114
5.4	Microstructural Simulation . . . . .	115
5.4.1	Large Energy Stencil . . . . .	117
5.4.2	Forward Scheme . . . . .	117
5.4.3	Accelerated Coarsening . . . . .	118
5.5	The Equilibrium Assemblage and Restite Composition . . . . .	118
5.5.1	Melt fraction and Restite Composition Model . . . . .	119
5.6	Phase Transformations . . . . .	119
5.7	Diffusive Partitioning . . . . .	123
5.7.1	Comparison to non-equilibrium thermodynamics . . . . .	123
5.7.2	2D near-fractional melting . . . . .	124
5.7.3	Mass conservation during melt production . . . . .	124
5.7.4	Conservation equations for two-phase compaction . . . . .	126
5.8	Model Summary . . . . .	127
5.9	Partition Coefficients . . . . .	128
5.10	Diffusion Coefficients . . . . .	128
5.11	Multi-Phase Grain Growth . . . . .	129
5.12	Petrology and Microstructural Evolution . . . . .	130
5.12.1	Exsolution Lamellae . . . . .	133
5.13	Model Grain Size Distributions . . . . .	133
5.14	Microchemical Disequilibria . . . . .	135
5.14.1	Lanthanum . . . . .	136
5.14.2	Samarium . . . . .	136
5.14.3	Ytterbium . . . . .	137
5.15	Melt Concentrations of Default Model . . . . .	137
5.15.1	OIB source temperature is not high . . . . .	139
5.15.2	Default models fail to fit Sm/Yb . . . . .	139
5.15.3	A minor observation . . . . .	140
5.16	Analysis of Some Model Sensitivities . . . . .	141
5.16.1	Choice of partition coefficient database . . . . .	141
5.16.2	Residual melt fraction . . . . .	141
5.16.3	Extent of hydrous melting . . . . .	141
5.16.4	Disequilibrium kinematics . . . . .	141
5.17	Partition Coefficient Sensitivity . . . . .	147
5.17.1	Analysis of partition coefficient sensitivity . . . . .	148
5.17.2	Results of partition coefficient sensitivity . . . . .	149

5.18	LAB Temperature . . . . .	151
5.19	REE Composition of the OIB Source . . . . .	152
5.19.1	Compositional similarity of MORB and OIB sources . . . . .	152
5.19.2	REE concentration of primitive mantle . . . . .	153
5.20	The Chemical Step and Major Element Systematics . . . . .	154
5.21	Isotopic Variations . . . . .	155
5.22	Viability of Thermal Plumes . . . . .	157
5.23	Some Caveats and Future Efforts . . . . .	158
5.23.1	Microstructural evolution . . . . .	158
5.23.2	Major element non-equilibrium thermodynamics . . . . .	159
5.23.3	The 3D versus 2D polycrystal . . . . .	160
5.23.4	Diffusion rates in melt . . . . .	161
5.23.5	Open-system melting and melt migration dynamics . . . . .	162
5.23.6	Melting lithologies . . . . .	163
5.24	CONCLUSIONS . . . . .	164

**References****243**

# List of Figures

2.1	The distribution of seafloor area over age as predicted by the analytical models from Stein et al. (1995) and Jaupart et al. (2007) and our analysis using global area-age grids from Müller et al. (2008). Analytical models appear as straight lines while the global analysis is given in 0.1 Ma bins. . . . .	23
2.2	(a) The relationship between effective thermal diffusivity and the 'mineral physics subsidence rate' (see Section 2.3.1). Predictions for mantle temperature of $1340 \pm 60^\circ \text{C}$ are highlighted. Vertical bars indicate the thermal diffusivity predicted for various $H$ values. The box symbols and dashed curve indicate the thermal diffusivity predicted when the thermal expansivity is $3.0 \times 10^{-5} \text{K}^{-1}$ for different temperatures. (b) Relationship between effective thermal diffusivity and the expansivity reduction ratio. (c) Relationship between effective thermal diffusivity and net seafloor heat flux. Mineral physics subsidence rates and expansivity reduction ratios are indicated. The black dashed and thick solid curves are the net seafloor heat flux predictions for a $1500^\circ \text{C}$ mantle temperature when the area-age seafloor distribution is that from Jaupart et al. (2007) and Stein et al. (1995), respectively. The $\sim 31.5 \pm 1.3 \text{ TW}$ range is highlighted is the range for good fit plate models determined through our fitting analysis. (d) The percent increase in seafloor heat flux for plate models having properties from panel (c). Solid lines are constant diffusivity predictions and dashed lines are PH06 model predictions. Reference models L1, R1, and RT1 are indicated. . . . .	24

- 2.3 Results of fitting experiments for constant thermal diffusivity models (first column), PH06 models (second column), and PH06-R models (third column). Panels (a)-(c) show colored curves indicating the best fitting thermal diffusivity as a function of plate thickness for different mantle temperatures. The goodness of fit varies with plate thickness as indicated by solid 'isofitness' lines and circles labeled with their corresponding  $R^2$  values. The thick dashed line is the line of best fit and the thick solid blue line indicates the best fits to topography alone. The unadjusted effective thermal diffusivity as a function of mantle temperature is also shown for PH06 (3b) and PH06-R (3c) models, and reference models L1, R1 and RT1 are indicated. Predictions for  $T_m = 1350 \pm 50^\circ\text{C}$  and  $R^2 > 0.99$  are highlighted. Panels (d)-(f) show the subsidence of joint fits against the topography from Hillier (2010). The open boxes indicate neglected points in the polynomial fit (thin dashed curve) to Hillier (2010), the highlighted area is the range for parameterizations with  $R^2 > 0.99$ , and the thick blue curve is the best fit to topography. Panels (g)-(i) show the same models as above, except heat flow predictions are represented against the heat flow data from Hasterok et al. (2011). The thick dashed line is the polynomial fit to Hasterok's data in the boxed range. The arrows point in the direction the best fit model predictions tend to go when the plate thickness is decreased (compare to panels (a)-(c)). This figure continues on the next page. . . . . 26
- 2.4 Results of fitting experiments for constant thermal diffusivity models (first column), PH06 models (second column), and PH06-R models (third column). Panels (a)-(c) are comparable to Figures 2.3a-c, showing the  $R^2$  fields for the case of  $T_m = 1400^\circ\text{C}$  and with a line of best fitting thermal diffusivity as a function of mantle temperature. The diamonds show the overall best fit models and the dashed ellipsoids are isofitness lines where  $R^2 = 0.99$  for mantle temperatures  $1300\text{--}1500^\circ\text{C}$ . For comparison, in panels (b)-(c) the 0.99 isofitness ellipsoid for  $T_m = 1400^\circ\text{C}$  constant thermal diffusivity models is indicated. Panels (d)-(f) show the  $R^2$  field in an alpha composite over the net seafloor heat flux, and Panels (g)-(i) show the  $R^2$  field in an alpha composite over the thermal expansivity reduction factor,  $H$ . This figure continues on the next page. . . . . 28
- 2.5 Thermal diffusivity and specific heat (in units of  $\text{kJ kg}^{-1} \text{K}^{-1}$ ; from Berman and Aranovich, 1996) of isotropic  $\sim\text{Fo}_{90}\text{Fa}_{10}$  as a function of temperature with the thermal conductivity artificially scaled by the factor  $F$ . The dashed curves are the lattice diffusivity only from Pertermann and Hofmeister (2006) and the solid curves are the lattice diffusivity with a radiative contribution to conductivity (Hofmeister, 2005). The open (lattice only) and solid (lattice + radiative) circles indicate the effective thermal diffusivity of each transport model when the initial half-space cooling temperature is  $1300^\circ\text{C}$  (blue) and  $1500^\circ\text{C}$  (red). . . . . 29

- 2.6 This figure shows 'difference geotherms', or the  $\Delta T(z, t)$  of a case model (columns) minus a reference model (rows). The properties of models in panels (a)-(d) are as given in Table 2.1. The  $D_E$  analog models in panels (e)-(f) have all the same properties as case models L1 and R1, respectively, excepting that constant heat transport properties are used. The large temperature differences found near the base of the plate are due to different plate thicknesses and mantle temperature. The difference in ambient mantle temperature  $\Delta T_m$  is given for each model comparison. Note that contours are defined by  $10^\circ\text{C}$  intervals, so their thickness is an indicator of thermal gradients (in  $\Delta T$ ), in addition to their spacing. . . . . 30
- 2.7 This figure shows the  $R^2$  fields of constant thermal diffusivity models for the fit to heat flow (for  $T_m = 1400^\circ\text{C}$ ) and seafloor topography (no dependence on  $T_m$ ). The  $R^2$  field for the fit to topography overlays the  $R^2$  field for heat flow in an alpha composite. The colored curves indicate the best fit thermal diffusivity as a function of plate thickness for mantle temperature between  $1300$  to  $1500^\circ\text{C}$  (comparable to the curves for joint fits in Fig. 2.3a), and the dashed ellipsoids indicate where  $R^2=0.99$ , and diamonds indicating the best fit for the given mantle temperature. The two black curves show the best fit to depth (thick dashed) and the fit to depth corresponding to the best joint fit (thin dashed,  $R^2 \sim 0.995$ ). . . . . 31
- 2.8 Geoid slope of thermal models predicted using the one-dimensional Haxby and Turcotte (1978) model against fracture zone data from Sandwell and Schubert (1982), Cazenave et al. (1983), Driscoll and Parsons (1988), and Freedman and Parsons (1990). Two solid black lines are simple plate solutions from Driscoll and Parsons (1988) and the dashed red line is model RT1. . . . . 32
- 3.1 Flow chart depicting the steps in model development, calculation of properties, and fitting analyses (with links to some relevant equations and figures) in this work. . . . . 59
- 3.2 Boundary and initial conditions for two-dimensional ( $100 \times 45.5$  km) thermal models. (a) The temperature in the region outlined in white dashes varies with depth but remains over horizontal distance. The distance between the surface and the top of the axial boundary condition is 1.4 km. All material around this space advects at a constant rate away from the ridge axis. Additional boundary conditions are explained in the text. For ages  $\leq 0.2$  Ma and mantle with  $T < 800^\circ\text{C}$ ,  $\text{Nu}=10$  for models with axial hydrothermal convection. (b) Closer inspection of ridge axis environment. (c) Panel showing the large-scale thermal evolution of oceanic lithosphere. After the two-dimensional model in panel A reaches steady-state, the geotherm at  $t=2.0$  Ma is imported into a one-dimensional model and calculated to 170 Ma. . . . . 60

- 3.3 One-dimensional convergence test calculations in our models using properties of G13R. Finite difference spacing was varied from 25 m to 1000 m. Numeric error is calculated by normalizing predicted surface heat flux against the predictions of the high resolution model (25 m vertical spacing). An important assumption in our analysis is that, for purposes of speed of calculation in these tests, G13R was reconfigured to be one-dimensional everywhere, although we expect the difference to be small. The dashed line is the expected error in our two-dimensional 'comprehensive' models, and the blue line is the expected error in our one-dimensional models. . . . . 61
- 3.4 This figure illustrates the consequences of using a different spreading rate for model G13R. Model G13R developed in the manuscript assumes a half-spreading rate of 50 mm yr<sup>-1</sup>. The curves in each panel represent the same predictions, except the left panels show the full intensity of heat flow, right panels focus on the off-axis heat flow, top panels depict the variation with age, and the bottom figures depict the variation with distance from the ridge axis. In addition, we have assumed in our analysis that the age where axial hydrothermal circulation ceases is 0.2 Ma or 10 km from the ridge axis. However, it is not completely clear whether how to treat the cutoff age or distance when the spreading rate is varied. Although it seems most realistic to use a cutoff age instead of distance, we also report calculations with the distance held constant, for completeness. . . . . 62
- 3.5 Temperature-dependence of thermal properties used in this work. Thermal diffusivity  $D$  (mm<sup>2</sup> s<sup>-1</sup>) of ~Fo<sup>90</sup> olivine, augite, and An<sub>65</sub> plagioclase; density  $\rho$  ( $\times 10^3$  kg m<sup>-3</sup>) of mantle and crust; thermal expansivity  $\alpha$  (dimensionless  $\times 10^{-5}$ ) of forsterite (mantle) and ocean crust; specific heat  $C_p$  (kJ kg<sup>-1</sup> K<sup>-1</sup>) of mantle and ocean crust; and the radiative contribution to effective thermal conductivity  $k_{rad}$  (W m<sup>-2</sup>) for a grain size of 1 cm. Mineral physics coefficients and references are given in Table 3.1. . . . . 63
- 3.6 Lattice thermal conductivity adjustment factor  $F_k$  versus the thermal expansivity adjustment factor  $F_\alpha$  for best-fitting models as a function of plate thickness and mantle potential temperature. Panels (a)-(g) show results for each 'simple' model type indicated in the panel caption and shown in Fig. 3.9. The type of data shown by each line is described in panel (a). "BF" is the line indicating best-fitting models. Panel (h) is an illustration describing the implications of different values of  $F_k$  and  $F_\alpha$ . Adjustment factors  $> 1$  indicate that the experimental value is too low and values  $< 1$  indicate the experimental value is too high to explain geophysical observations. Panel (i) shows a summary of all best joint fit models, including comprehensive models (dashed lines) that retain radiative thermal conductivity (see Fig. 3.7). . . . 64

3.7	Same representation as in Fig. 3.10 for 2D 'comprehensive' models with hydrothermal circulation ( $Nu=10$ ). Top panels show models with a high radiative contribution to thermal conductivity, bottom panels show models with no radiative thermal conductivity, left panels show models with no oceanic crust and right panels show models with oceanic crust. See Fig. 3.3 for the same figure describing results of models with no hydrothermal circulation ( $Nu=1$ ). Panels (b) and (d) show models G13R and G13L, respectively. . . . .	65
3.8	Same illustrations as in Fig. 3.11, except results for models without hydrothermal circulation are shown. . . . .	66
3.9	Thermal conductivity adjustment factor of best-fitting comprehensive models as a function of mantle potential temperature. The grey highlighted region indicates bounds for models with insulating oceanic crust with and without radiative thermal conductivity. Solid lines include radiative transport, dashed lines have no radiative transport, thick lines include insulating oceanic crust, and thin lines have no crust. The violet boxed area indicate the mantle potential temperatures where best-fitting models can be found which do not require adjustments to lattice thermal conductivity (that is, one can adjust the radiative contribution without changing lattice thermal conductivity). Compare to Fig. 3.7. . . . .	67
3.10	Properties of models G13R and G13L at $T_p = 1300^\circ\text{C}$ . Colors show the misfit for depth (a,d), misfit for heat flow (b,e), and thermal expansivity adjustment factor $F_\alpha$ (c,f) as a function of the thermal conductivity adjustment $F_k$ versus plate thickness $L$ . The shading is an 'alpha transparency' of the joint misfit in $F_k$ versus $L$ . This means that the field of joint misfit is everywhere black with transparency changing with magnitude, and this is overlain on the other fields in color (Fig. 3.19). The diamond is the point of minimum joint misfit (for $T_p = 1300^\circ\text{C}$ ) and the dotted line shows where joint misfit $M^J=0.3$ . See Fig. 3.19 for more about the construction of this figure. . . . .	68
3.11	(a) Comparison of measured seafloor heat flow with predictions of comprehensive models, GDH1 (Stein and Stein, 1992), and global heat flow as a function of age. (b) Ratio of observed heat flow against predictions of GDH1 as a function of $t^{1/2}$ . The grey and black thin lines with markers are 1st, 2nd (median) and 3rd quartiles for sediment uncorrected heat flow, and the thick violet line is the median sediment corrected heat flow from Hasterok (2013). The boxed markers are the heat flow points used in our calculation of misfit to heat flow. The orange boxes with error bars are median heat flow and interquartile distributions for specific sites of well resolved heat flow from Hasterok (2013). . . . .	69
3.12	Predictions and observations of seafloor topography and subsidence. (a) Seafloor topography of our best-fitting 2D comprehensive models compared with model GDH1 (Stein and Stein, 1992) and 0.1 Myr binned mean global depth with $1\sigma$ standard deviation from Hillier (2010). The orange boxes are the 1.0 Myr bins used in our formal analysis of misfit. (b) Close-up of model predictions on ridge flanks. . . . .	70

- 3.13 Thermal structure of our model G13R as compared to PS77 and GDH1. Colors indicate the difference between models with the mantle potential temperature of G13R varied between 1300 and 1400°C. Lines are isotherms for G13R. Dots are intraplate earthquake hypocenters from McKenzie et al. (2005) and Geli and Sclater (2008). . . . . 71
- 3.14 Thickness of oceanic crust predicted from the melting model of Asimow et al. (2001) by integrating the melt column from infinite depth to Moho depth. Predictions for mantle temperature 1300-1450°C are shown (color), solid lines assume that all melt produced is incorporated into the crust and dashed lines assume that the first 3% of melt resides remains unextracted. The highlighted area indicates the range for most normal oceanic crust ( $6.5 \pm 1.5$  km) which can be compared to our assumption that oceanic crust is always 7 km thick. 72
- 3.15 Geotherms for comprehensive models at 5.5 km (0.11 Ma) and 10 km (0.2 Ma) from the ridge axis. The lines for our models show predictions for models with a potential temperature of 1300°C and the highlighted regions outline the predictions for 1450°C. The thick black lines with circle markers give geotherms on either side of the East Pacific Rise from seismic tomography by Dunn et al. (2000). Models with no axial hydrothermal circulation ( $Nu=1$ ) significantly overestimate temperature at depth while models with  $Nu=10$  show good agreement. The best-fitting models have both hydrothermal circulation and crustal insulation. The case of  $t=0.11$  Ma is compared with model predictions of Cochran and Buck (2001), Cherkaoui et al. (2003), MacLennan et al. (2005), and Spinelli and Harris (2011). Cochran and Buck's geotherm is actually for 0.1 Ma. . . . . 73
- 3.16 Predictions of forsterite density for our study compared to the self-consistent thermodynamic approach of Xu et al. (2008) as calculated using PerpleX (Connolly, 2009). (a) Density as a function of pressure at 270 K and 1900 K. (b) Ratio of volume compression predicted by the thermodynamic model over our approximation. (c) Density as a function of temperature at 0.1 GPa and 10 GPa. The open circles are volume measurements from Bouhifd et al. (1996) assuming  $\rho_0=3230 \text{ kg m}^{-3}$  at 270 K (this reference density is used to match the reference density in the PerpleX calculation). (d) Ratio of volume expansion predicted by Xu et al. (2008) over our EOS as a function of temperature at 0.1 GPa and 10 GPa. Both models predict the same compression at 270 K (Fig. 3.18a-b). The difference in predictions at temperature are similar at 0.1 GPa and 10 GPa (Fig. 3.18c-d). These observations indicate that most of the difference between these predictions is simply due to our use of a linear temperature-dependent thermal expansivity versus the thermal pressure formulation of Xu et al. (2008). . . . . 74



- 3.17 Radiative thermal conductivity in olivine, applied in our modeling analysis to the entire lithosphere. (a) Predictions of Eq. 3.8 using the crystallographic assumptions of Hofmeister (2005), although we have evaluated  $\sim\text{Fo}_{90}\text{Fa}_{10}$  spectra continuously with temperature using a cubic interpolation scheme. (b) Prediction of Eq. 3.17 (Appendix A), our approximation of Hofmeister's (2005) model. (c) Difference of Eq. 3.8 and 3.17. The parameter space where the difference is less than  $\pm 0.25 \text{ W m}^{-1} \text{ K}^{-1}$  is white, overestimates are colored using the same scale as in Fig. 3.5a-b, and underpredicted values are purple. The fit is good for  $T < 3000 \text{ K}$  except for a region at high temperature and grain-size where Hofmeister's (2005) model predicts that  $k_{\text{rad}} \rightarrow 0$ . This feature could be accounted for with an additional term in Eq. 3.17, but we ignore it since our models only experience  $T < 1900 \text{ K}$ . . . . . 75
- 3.18 (a) Melt mass fraction predicted by the melting models of Asimow et al. (2001), McKenzie and Bickle (1988), and Herzberg and O'Hara (2002). Data points are graphically approximated from Asimow et al. (2001), which we have used to derive our fit (Appendix B). (b) Geotherms for potential temperatures between  $1300\text{-}1500^\circ\text{C}$  using the melting models of Asimow et al. (2001) and McKenzie and Bickle (1988), and an adiabatic gradient of  $0.5^\circ\text{C km}^{-1}$ . . . . 76
- 3.19 This figure is an attempt at illustrating the use of an alpha composite to construct Fig. 3.10. The joint misfit  $M_J$  uses a partial transparency to illustrate magnitude, whereas the misfit to topography  $M_T$  simply uses color. . . . . 77
- 4.1 Cartoon showing the relationship between hydrothermal circulation patterns in the crust and resulting heat flow measured at the surface. Ventilation results in a net reduction in seafloor heat flux (sub-conductive heat flow), and vigorous hydrothermal circulation without ventilation results in a higher measured heat flux (super-conductive heat flow). The black squiggly lines indicate conductive heat transport and the blue convection lines indicate hydrothermal flow patterns. The sites of recharge and discharge are located at basement highs in these examples. . . . . 103
- 4.2 (a) Cumulative distribution functions of heat flow (shown by color) for 1 Ma bins to 100 Ma compared to the three thermal plate models used in this study. (b) Cumulative distribution functions of heat flow in 1 Ma bins between 1 and 100 Ma. . . . . 103

- 4.3 Probability density functions of the heat flow deficit determined from Monte-Carlo analysis for models (a) H13 (Hasterok 2013a), (b) GH, and (c) GHC (Grose and Afonso, 2013; Chapter 3). The red PDF (left panels) represents numerical integration only within the first 1 Ma bin (near-axial power deficit), and the blue PDF is the heat flow deficit integrated to 60 Ma (Net Power Deficit). The filled circles, triangles, and squares indicate the mode, median, and mean of the PDF's. The white filled circles with error bars indicate the mode and half-maximum bounds for the 1 Ma (near-axial power deficit) and 60 Ma (net power deficit) PDF's. The red, green, and blue bars above the graphs (left panels) indicate the fraction of active, flank, and passive advective power, respectively. Hasterok's (2013b) "unfiltered" estimate is indicated in panel (a). The right-side panels show the mean, median, mode, and half-maximum uncertainty of the power deficit as a function of age for each model. 104
- 4.4 Boundary and initial conditions for model GH and GHC. The temperature in the region outlined in white dashes varies with depth but remains constant over horizontal distance. The distance between the surface and the top of the axial boundary condition is 1.4 km. All material around this space migrates at a constant rate away from the ridge axis. The top figure shows the boundary conditions of the 2D part of the model (0-2 Ma), and the bottom figure shows the conditions of the 1D part of the model (2-170 Ma). After figure 2 in Grose and Afonso (2013). . . . . 105
- 4.5 Predicted heat flow (a) and heat flow diminution rate (b) for models H13, GH, and GHC as a function of age compared with global and site-specific data. The site-specific data-points are discussed in the text. The global sediment filtered and unfiltered data shown here are from Hasterok (2013b). The highlighted region is the uncertainty ( $1\sigma$ ) of the sediment-filtered global dataset. Note that the misfit between models GHC and the data occurs because Grose and Afonso (2013) fitted model GHC to heat flow data which did not include a correction for continuous sedimentation. . . . . 106
- 4.6 (a) Subsidence rates for models GH and GHC (Grose and Afonso, 2013), the classical model GDH1 (Stein and Stein, 1992), and the new plate heat-flow constrained plate model of Hasterok (2013b), compared with subsidence rates estimated from the global depth dataset of Hillier (2010). Red-yellow colors correspond to small sliding windows and blue-violet colors correspond to large sliding windows over which subsidence rates are determined using a least-squares fit. The small discontinuities around 20 Ma for GHD1 and H13 are due to the imperfect fit of their author's respective equations for seafloor depth. (b) Comparison of model predictions of model GHC, GC, and G. Models GC and G have not been used to calculate hydrothermal power loss but are included here to clarify the role of hydrothermal circulation and crustal insulation on seafloor subsidence. . . . . 107

4.7	Predictions and observations of seafloor topography and subsidence on ridge flanks. (a) Seafloor topography of our models compared with model GDH1 (Stein and Stein, 1992), 0.1 Ma binned global 'normal' depth data with $1\sigma$ standard deviation from Hillier (2010), and EPR ridge depth data from Cochran and Buck (2001). (b) Close-up on the model predictions and observed topography on ridge flanks. In addition, the bottom left corner shows an additional cause of ridge elevation due to the buoyancy of melt beneath the ridge based on two models of seismic tomography from Dunn et al. (2000). For ages $<0.2 \text{ Ma}^{1/2}$ there is no subsidence in our models since energy transfer is supported by latent heat release. Figrue modified after Grose and Afonso (2013). . . . .	108
4.8	Sediment thickness and heat flow for the Costa Rica Rift. (a) Sediment thickness map constructed from a bicubic spline of seismic reflection profiles (dotted line, where dots are datapoints; Swift et al., 1998). Open circles are sites of heat flow measurement. (b) Heat flow map constructed from a bicubic spline of measurements (black dots). (c) Non-normalized Probability density functions (PDF) of heat flow. The red PDF is from the bicubic spline in panel (b), whereas the black line is the PDF using only measurements. . . . .	109
4.9	Predicted seafloor heat flow for model GHC with varied crust thickness and parameters affecting hydrothermal circulation are varied, compared to measured heat flow (mean, median, mode, and half-maximum bounds) for the Costa Rica Rift (Fig. 4.8). The black line is model GHC with oceanic crust varied between 0 and 10 km. The black dashed line is the same model, except hydrothermal circulation is not allowed to occur below the insulating layer. The red line is model GHC with the thickness of oceanic crust varied and no hydrothermal circulation on the ridge axis. All predictions are for 5.9 Ma seafloor. . . . .	110
5.1	Illustration of the oceanic lithosphere cooling and thickening with distance and age from the ridge axis. Isotherms are to scale based on the model developed in Chapter 3 for $T_p = 1300^\circ\text{C}$ . Also shown are plume-like conduits which ascend in the mantle until interrupted by mechanical interaction with the base of the lithosphere (LAB). The three small images illustrate examples of microstructure and microchemistry which our melting model predicts to exist in the ascending OIB source. . . . .	173
5.2	Graphs of OIB geochemical data for La/Sm and Sm/Yb (with no normalizations) from Humphreys and Niu (2009) on the left, compared to our reconstructions using the same chemical data with our estimates of seafloor age. The grey areas are standard deviations from Humphreys and Niu's (2009) dataset. . . . .	174
5.3	Difference in ages using the distance to ocean ridges estimate in Humphreys and Niu (2009) compared to our estimates using the global database of Müller et al. (2008). . . . .	175

5.4	La/Sm and Sm/Yb systematics as a function of the final depth of melting. In the top figures the final depth of melting is based on the 1300°C isotherm from the model we developed in Chapter 3 (for $T_p = 1300^\circ\text{C}$ ). The bottom figures are the same, except using the 1100°C isotherm. The green bar highlights the region where the step-like feature occurs in the data, which we associate with the dry solidus. . . . .	176
5.5	Equilibrium batch melting (left) and near-fractional melting (right) models using our thermodynamically constrained equilibrium restite assemblage ( $T_p = 1300^\circ\text{C}$ ) and partition coefficient databases of Adam and Green (2006) as dashed lines, and Salters et al. (2002) as solid lines. The red lines are predictions of La/Sm and black lines are for Sm/Yb. Near-fractional melting models use Salters et al. (2002) database only. Results for 20 near-fractional melting models are shown with the amount of residual melt varied between 0.05 and 1.0%. The depths at which wet melting and dry melting occur in our models are indicated. . . . .	177
5.6	Restite phase equilibria for $T_p = 1400 \pm 100^\circ\text{C}$ as a function of total melt fraction (left panels) and depth (right panels) calculated as described in Sec. 5.5. The grey highlighted regions are modal abundances of abyssal peridotites as a function of melt fraction from Niu (2004). . . . .	178
5.7	The same presentation as in Fig. 5.6, except that here are shown the non-equilibrium modal abundances as a function of depth in typical models. . . .	179
5.8	Adjustment of concentrations for flux determination across phase boundaries. For each calculation of flux between neighboring elements (or nodes), the neighbor with the lower partition coefficient has its concentration multiplied by the factor $\delta K$ , while the concentration of the other node is unchanged. In the case illustrated here, since the apparent concentration of Node 1 is greater than Node 2, a flux will occur in the direction of Node 2. . . . .	180
5.9	Total melt fraction for dry fertile peridotite as a function of pressure. The dots are predictions of Herzberg (2004) and the lines are our 'fits'. The large misfit for some temperatures is due to our attempt to fit a single function to all of the data. It is not clear to us if the changes in the slope of melt production observed in the experiments is real or if our approximation does not capture complex variations in the melting process. . . . .	181
5.10	Chemical diffusivities as a function of temperature used in this study. Note that mineral diffusivities are taken from the literature, but melt diffusivity is estimated. See Table 5.24 for diffusion coefficient parameters. . . . .	182
5.11	Results of coarsening experiments shown in terms of the coarsening exponent $1/n$ as it changes over time (or Monte-Carlo step). See text for discussion. . .	183
5.12	A dense survey of coarsening exponents fitted to the predictions of our Potts models as a function of model noise (or temperature), $K_T$ . . . . .	184

5.13	Results of a typical model with default properties ( $v_z=1$ m yr <sup>-1</sup> , $G_r=1$ , $T_p = 1300^\circ\text{C}$ , $\phi_r=0.05\%$ ). The top panels (row 1) show the microstructure with colors corresponding to phases as labeled in the first panel. The labeling of individual crystals shown in panel C1 and D1 are for the purposes of discussion in the text. The remaining panels in Rows 2-6 show microchemical predictions with concentrations given relative to bulk source concentration (i.e., the average concentrations found in column 1). . . . .	185
5.14	Same visualization as in Fig. 5.13, except that the mantle potential temperature $T_p = 1500^\circ\text{C}$ is used. . . . .	186
5.15	Probability density functions for the grain size in the OIB source as a function of depth for mineral modes olivine, orthopyroxene, clinopyroxene, and garnet. All results here are for our default model where the model domain size is 1 cm <sup>2</sup> . . . . .	187
5.16	Predicted La/Sm (left) and Sm/Yb (right) as a function of final melting depth in our default models with $T_p$ varied between 1300 and 1500°C. The top figures show model results normalized to bulk source concentration. Bottom figures show the same models with source concentration adjusted to best fit the data (black dots). The colored open circles and squares are the depth of dry melting and garnet transition, respectively. . . . .	188
5.17	Predicted La, Sm, and Yb concentrations in erupted OIB, normalized to bulk source concentration, in our default models with $T_p$ varied between 1300 and 1500°C. Horizontal bars are ranges of possible thick-plate OIB concentration, the horizontal black line are OIB concentrations from Sun and McDonough (1989), and pink horizontal lines are our estimates of thick-plate OIB from the GEOROC database. . . . .	189
5.18	Comparison of the input model total melt fraction as a function of depth (black) with the non-equilibrium output model result (colored lines) for mantle potential temperatures between 1300 and 1500°C . . . . .	190
5.19	Predicted La/Sm and Sm/Yb, normalized to bulk source concentration, for default models with $T_p = 1300 - 1500^\circ\text{C}$ , as a function of garnet fraction (top panels) and total melt fraction (bottom panels). The color of lines corresponds to potential temperatures indicated in the scale. . . . .	191
5.20	Depiction of the difference in predicted La/Sm and Sm/Yb, normalized to bulk source concentration, for models with different parameters controlling the depth and extent of melting occurring between the dry and wet solidi. . . . .	192
5.21	Illustration of a moving average of the empirical data for La/Sm and Sm/Yb as a function of the final depth of melting for different choices of LAB temperature. Depths of final melting increase with the choice of higher LAB temperature since the higher temperature isotherms occur at greater depth for any given seafloor age. . . . .	193
5.22	Predicted cumulative melt La/Sm and Sm/Yb (left panel) and La, Sm, and Yb (right panel) as a function of final melting depth for a default model and choice of partition coefficient databases from either Salters et al. (2002, black lines) or Adam and Green (2010, red lines). . . . .	194

5.23	Elemental concentrations (ppm) of La (high concentration lines), Sm (medium concentration lines), and Yb (low concentration lines) as a function of final melting depth. The different curves for each element, characterized by colors red to blue, indicate predictions with residual melt fraction changed from 0.1% (blue) to 1.0% (red). . . . .	195
5.24	Misfit of default models to observed OIB La/Sm (left panel) and Sm/Yb (right panel) as a function of residual melt fraction and the mantle potential temperature of the source. . . . .	196
5.25	Sensitivity analysis of our models to changes in diffusion rates. The diffusivity factor is a scaling factor multiplied by the diffusivities of all phases to obtain higher or lower case diffusivities. Concentrations for La/Sm, Sm/Yb, La, Sm, and Yb, all normalized to bulk source concentration are shown. The top panels show the cumulative melt concentrations as a function of final melting depth. The bottom panels show lines of cumulative melt concentrations for a constant depth as a function of the varied diffusivity factor. The colors of the lines on the top panels correspond to slices in the bottom panel, and vice versa. These results have been slightly smoothed. The black curve in the top panels is the default model of this work, for comparison. . . . .	197
5.26	Sensitivity analysis of our model results of cumulative melt concentration to changes in the grain size (or grain size factor). The presentation of the model results is the same as in fig. 5.25. Models with low grain size are closer to equilibrium, and models with greater grain size are farther from equilibrium, compared to the default model (black lines). . . . .	198
5.27	Model predictions of cumulative melt composition for models in which the ascent rate is varied between $0.025 \text{ m yr}^{-1}$ and $1.0 \text{ m yr}^{-1}$ . All other parameters are those in our default model, represented by the thick black lines. The top figures show melt composition as a function of final melting depth and the bottom figures show isobaric compositions for models in the range of ascent rates. The color bar in the top figures correspond to the curves in the bottom figures, and vice versa. . . . .	199
5.28	Density functions for La/Sm, Sm/Yb, La, Sm, and Yb in MORB from the database of Gale et al. (2013). Absolute values are in ppm. Horizontal highlighted bars are the HMB from our analysis of best fitting models in our tests of sensitivity to partition coefficients. The vertical position of these bars is meaningless. The large dots on the curves for ratios and elemental concentrations indicate the means of each distribution function. . . . .	200

5.29	Results of our analysis of our model sensitivity to joint variation in the ascent rate and grain size factor. Top panels show the misfits to La/Sm and Sm/Yb, and the corresponding $T_{LAB}$ for each fit. The remaining figures show predictions of bulk source concentrations (second row), Mid-Ocean Ridge Island Basalt (MORIB) concentrations (third row), and thick-plate OIB concentrations (fourth row) corresponding to the fit to La/Sm and Sm/Yb. The predictions of La, Sm(La/Sm), and [La/Sm] indicate predictions from the fit to La/Sm, whereas Sm(Sm/Yb), Yb, and [Sm/Yb] are obtained from the fit to Sm/Yb. . . . .	201
5.30	Comparison of the empirical data (black diamonds with white borders), our bins to which we fit models (white connected diamonds with black borders), and the predictions of all models in Fig. 5.29. The top figures show data and model results for La/Sm, and the bottom figures show data and models for Sm/Yb. The curves in the left panels are colored according to their misfit, whereas the curves in the right panels are colored according to the $T_{LAB}$ of each model. The data in the bottom plots has used $T_{LAB} = 1225^\circ \text{C}$ , and in the top plots have used $T_{LAB} = 1275^\circ \text{C}$ . In addition, the pink data on the left hand side of each figure shows a density function for La/Sm and Sm/Yb in MORB from the data of Gale et al. (2013). . . . .	202
5.31	Probability density fields constructed from the predicted model properties in Fig. 5.29. The horizontal scales in each of these figures is the misfit $m$ . Values of La, Sm, and Yb for bulk source (bsrc), thick-plate OIB (oib), and Mid-Ocean Ridge Island Basalt (morib) concentrations are in units of ppm. Values of $T_{LAB}$ are in units of $^\circ\text{C}$ . . . . .	203
5.32	Predicted cumulative melt concentrations of La/Sm (left panel) and Sm/Yb (right panel) as a function of depth (in km), for 20 runs of our default model. Repeated model runs show variation about a mean. The thick red line is the mean of the models shown. . . . .	204
5.33	Predicted misfit to La/Sm for models in which the partition coefficients of Sm and La in cpx and garnet are varied. The position of our default model is indicated in the second row, second column panel. See text for discussion. . .	205
5.34	Predicted misfit to Sm/Yb for models in which the partition coefficients of Yb and Sm in cpx and garnet are varied. The position of our default model is indicated in the second row, second column panel. See text for discussion. . . . .	206
5.35	Best fitting LAB temperature for each model in Fig. 5.33. The position of our default model is indicated in the second row, second column panel. The black contours are corresponding values of misfit from Fig. 5.33. See text for discussion. . . . .	207
5.36	Best fitting LAB temperature for each model in Fig. 5.34. The position of our default model is indicated in the second row, second column panel. The black contours are corresponding values of misfit from Fig. 5.34. See text for discussion. . . . .	208

5.37	Predicted absolute La concentration in the OIB source obtained from the fit to La/Sm and an estimate of Sm concentration in thick-plate OIB. The position of our default model is indicated in the second row, second column panel. The black contours are corresponding values of misfit from Fig. 5.33. See text for discussion. . . . .	209
5.38	Predicted absolute Sm concentration in the OIB source obtained from the fit to La/Sm and an estimate of Sm concentration in thick-plate OIB. The position of our default model is indicated in the second row, second column panel. The black contours are corresponding values of misfit from Fig. 5.33. Note that all of these models have different source concentrations while predicting that Sm in thick plate OIB = 10 ppm. . . . .	210
5.39	Predicted absolute Sm concentration in the OIB source obtained from the fit to Sm/Yb and an estimate of Sm concentration in thick-plate OIB. The position of our default model is indicated in the second row, second column panel. The black contours are corresponding values of misfit from Fig. 5.34. Note that all of these models have different source concentrations while predicting that Sm in thick plate OIB = 10 ppm. . . . .	211
5.40	Predicted absolute Yb concentration in the OIB source obtained from the fit to Sm/Yb and an estimate of Sm concentration in thick-plate OIB. The position of our default model is indicated in the second row, second column panel. The black contours are corresponding values of misfit from Fig. 5.34. . . . .	212
5.41	Predicted La/Sm concentration in the OIB source obtained from the fit to La/Sm. The position of our default model is indicated in the second row, second column panel. The black contours are corresponding values of misfit from Fig. 5.33. . . . .	213
5.42	Predicted Sm/Yb concentration in the OIB source obtained from the fit to Sm/Yb. The position of our default model is indicated in the second row, second column panel. The black contours are corresponding values of misfit from Fig. 5.34. . . . .	214
5.43	Predicted absolute La concentration in thick-plate OIB (approximated by eruptions on seafloor age of 64 Ma) obtained from the fit to La/Sm and an estimate of Sm concentration in thick-plate OIB. The position of our default model is indicated in the second row, second column panel. The black contours are corresponding values of misfit from Fig. 5.33. . . . .	215
5.44	Predicted absolute Yb concentration in thick-plate OIB (approximated by eruptions on seafloor age of 64 Ma) obtained from the fit to Sm/Yb and an estimate of Sm concentration in thick-plate OIB. The position of our default model is indicated in the second row, second column panel. The black contours are corresponding values of misfit from Fig. 5.34. . . . .	216
5.45	Predicted La/Sm concentration in thick-plate OIB (approximated by eruptions on seafloor age of 64 Ma) obtained from the fit to La/Sm. The position of our default model is indicated in the second row, second column panel. The black contours are corresponding values of misfit from Fig. 5.33. . . . .	217



5.46	Predicted Sm/Yb concentration in thick-plate OIB (approximated by eruptions on seafloor age of 64 Ma) obtained from the fit to Sm/Yb. The position of our default model is indicated in the second row, second column panel. The black contours are corresponding values of misfit from Fig. 5.34. . . . .	218
5.47	Predicted absolute La concentration over ridge axes (approximated by eruptions on seafloor age of 1 Ma) obtained from the fit to La/Sm and an estimate of Sm concentration in thick-plate OIB. The position of our default model is indicated in the second row, second column panel. The black contours are corresponding values of misfit from Fig. 5.33. . . . .	219
5.48	Predicted absolute Sm concentration over ridge axes (approximated by eruptions on seafloor age of 1 Ma) obtained from the fit to La/Sm and an estimate of Sm concentration in thick-plate OIB. The position of our default model is indicated in the second row, second column panel. The black contours are corresponding values of misfit from Fig. 5.33. . . . .	220
5.49	Predicted absolute Sm concentration over ridge axes (approximated by eruptions on seafloor age of 1 Ma) obtained from the fit to Sm/Yb and an estimate of Sm concentration in thick-plate OIB. The position of our default model is indicated in the second row, second column panel. The black contours are corresponding values of misfit from Fig. 5.34. . . . .	221
5.50	Predicted absolute Yb concentration over ridge axes (approximated by eruptions on seafloor age of 1 Ma) obtained from the fit to Sm/Yb and an estimate of Sm concentration in thick-plate OIB. The position of our default model is indicated in the second row, second column panel. The black contours are corresponding values of misfit from Fig. 5.34. . . . .	222
5.51	Predicted La/Sm concentration over ridge axes (approximated by eruptions on seafloor age of 1 Ma) obtained from the fit to La/Sm. The position of our default model is indicated in the second row, second column panel. The black contours are corresponding values of misfit from Fig. 5.33. . . . .	223
5.52	Predicted Sm/Yb concentration over ridge axes (approximated by eruptions on seafloor age of 1 Ma) obtained from the fit to Sm/Yb. The position of our default model is indicated in the second row, second column panel. The black contours are corresponding values of misfit from Fig. 5.33. . . . .	224
5.53	Comparison of the empirical data (black diamonds with white borders), our bins to which we fit models (white connected diamonds with black borders), and the predictions of all models from our sensitivity analysis of partition coefficients (Fig. 5.33-5.36). The top figures show data and model results for La/Sm, and the bottom figures show data and models for Sm/Yb. The curves in the left panels are colored according to their misfit, whereas the curves in the right panels are colored according to the $T_{LAB}$ of each model. The data in the bottom plots has used $T_{LAB} = 1225^\circ \text{C}$ , and in the top plots have used $T_{LAB} = 1275^\circ \text{C}$ . In addition, the pink data on the left hand side of each figure shows a density function for La/Sm and Sm/Yb in MORB from the data of Gale et al. (2013). . . . .	225

5.54	Predictions of cumulative melt concentration, as in Fig. 5.53, except all combinations of $Z_{La,cpx}$ and $Z_{La,grt}$ are shown, corresponding to the panels in Fig. 5.33. Curves are colored according to the misfit of each model. . . . .	226
5.55	Predictions of cumulative melt concentration, as in Fig. 5.53, except all combinations of $Z_{La,cpx}$ and $Z_{La,grt}$ are shown, corresponding to the panels in Fig. 5.33. Curves are colored according to the LAB temperatures of each model. .	227
5.56	Predictions of cumulative melt concentration, as in Fig. 5.53, except all combinations of $Z_{Sm,cpx}$ and $Z_{Sm,grt}$ are shown, corresponding to the panels in Fig. 5.34. Curves are colored according to the misfit of each model. . . . .	228
5.57	redictions of cumulative melt concentration, as in Fig. 5.53, except all combinations of $Z_{Sm,cpx}$ and $Z_{Sm,grt}$ are shown, corresponding to the panels in Fig. 5.34. Curves are colored according to the LAB temperatures of each model. .	229
5.58	Probability density fields constructed from the predicted model properties in Fig. (5.33 and Fig. 5.34). The horizontal scales in each of these figures is the misfit $m$ . Values of La, Sm, and Yb for bulk source (bsrc), thick-plate OIB (oib), and Mid-Ocean Ridge Island Basalt (morib) concentrations are in units of ppm. Values of $T_{LAB}$ are in units of °C. The means and half-maximum bounds of the data for misfit $< 0.05$ are tabulated in Table 5.24. . . . .	230
5.59	The empirical Sm/Yb data (normalized to Chondrite) from Humphreys and Niu (2009) with islands, and some island groups, labeled. . . . .	231
5.60	Major element systematics for oxides corrected to Mg-number 0.72 by Humphreys and Niu (2009) and Niu (2011). Values are given in wt. %. Error bars are $1\sigma$ standard deviations of the intra-islandic dataset. Green symbols indicate islands associated with classical hotspots (Fig. 5.59) and red values indicate all other islands. . . . .	232
5.61	Continued from previous panels. . . . .	233
5.62	Absolute values of La, Sm, Yb, and ratios La/Sm and Sm/Yb of all OIB sources considered in this work. Data from Humphreys and Niu (2009). Error bars are $1\sigma$ standard deviations of the intra-islandic dataset. Green symbols indicate islands associated with classical hotspots (Fig. 5.59) and red values indicate all other islands. . . . .	234
5.63	Isotopic ratios for all islands in the dataset of Niu (2011). Error bars are $1\sigma$ standard deviations of the intra-islandic dataset. The pink density function projecting to the left of each panel represents values observed in MORB from Gale et al. (2013). Green symbols indicate islands associated with classical hotspots (Fig. 5.59) and red values indicate all other islands. . . . .	235
5.64	Three-dimensional microstructures produced from our 3D Potts models. a) model without melt present, b) model with 5% melt. Green is olivine, grey is opx, blue is cpx, red is garnet, and white is melt. . . . .	236
5.65	Compositions of phases at equilibrium as a function of pressure, calculated as described in Sec. 5.5. . . . .	236
5.66	Benchmark of model resolution, here results are shown for 250 finite difference nodes. See Appendix 5.C.1 for discussion. . . . .	237

---

5.67	Benchmark of model resolution, here results are shown for 100 finite difference nodes. See Appendix 5.C.1 for discussion. . . . .	238
5.68	Benchmark of model resolution, here results are shown for 50 finite difference nodes. See Appendix 5.C.1 for discussion. . . . .	239
5.69	Sm/Yb predicted by models with different grid sizes. See Appendix 5.C.2 for discussion. . . . .	240
5.70	Benchmark of mass conservation in a typical model. See Appendix 5.C.3 for discussion. . . . .	241



# List of Tables

2.1	Tabulated properties for models L1, R1, and RT1 (this work) along with those for former reference models GDH1 (Stein and Stein, 1992) and PS77 (Parsons and Sclater, 1977). Model RT1 is the preferred model of this work . . . . .	21
2.2	Tabulated properties for constant heat transport, PH06 and PH06-R models with different mantle temperatures. Bounds indicate values where joint fit $R^2 > 0.99$ . . . . .	22
3.1	Mineral physics coefficients for crust and mantle . . . . .	56
3.2	Properties of best joint fitting models <sup>a</sup> . . . . .	57
3.3	Symbols for variables in this work . . . . .	58
4.1	*SS94 - Stein and Stein (1994), P94 - Pelayo et al. (1994), M03 - Mottl (2003), SH11C - Conduction-only model of Spinelli and Harris (2011), SH11H - Hydrothermally corrected conduction model of Spinelli and Harris (2011), H13U - Hasterok (2013b) using his unfiltered heat flow database, H13SF - Hasterok (2013b) using his sediment-filtered heat flow database. **Based on Spinelli and Harris's (2011) assertion that hydrothermal circulation does not change total hydrothermal power. ***Estimated based on inspection of figures in Hasterok (2013b). . . . .	102
5.1	Partition coefficients used in this study. . . . .	170
5.2	Chemical diffusivity coefficients used in this study. . . . .	170
5.3	Properties obtained from inversions with variable partition coefficients. Note that while these values are precise, the HMB are not indicators of accuracy. Precise values are obtained due to the assumption that $Sm_{oib}=10$ ppm is exact, whereas it actually has a standard deviation of $\sim 20\%$ (Fig. 5.62) . . . . .	171
5.4	Comparison of previous estimates of the REE compositions of Depleted MORB Mantle (DMM) and Primitive Mantle (PM) with our calculations using OIB source composition as a proxy to the composition of a uniform depleted mantle reservoir. . . . .	172



# 1

## Introduction

This research collection attempts to further our understanding of the properties, structure, and behavior of the oceanic lithosphere and upper mantle. While the history of research into these problems extends back to the inception of the seafloor spreading hypothesis, it seems that only the basic groundwork of this understanding has been well established. After evaluating the basic structure of viable models for the oceanic lithosphere, we attempt to systematically improve our understanding of some of the more detailed aspects of the geophysical observations and the material properties which characterize the oceanic upper mantle. Consequently, our models and analyses progress from relatively simple mathematical descriptions to more sophisticated accounts of the physics and chemistry of the upper mantle.

The primary objectives of this thesis are (a) to develop new models of the thermal evolution of oceanic lithosphere which optimally fit geophysical observations as well as experimental constraints on material properties, (b) evaluate the major geophysical implications of these models for the behavior of the Earth, and (c) to link the geophysical structure of oceanic lithosphere to the geochemistry of oceanic basalts via the 'LID effect'. The elaborate constraints on the thermal state of oceanic lithosphere resulting from our analyses will prove important to establishing links between the chemistry of oceanic basalts and the structure of oceanic lithosphere.

In Chapter 2, I develop a relatively simple 1D plate model of the thermal evolution of oceanic lithosphere using experimentally constrained functions for the temperature-dependent thermal conductivity and thermal expansivity of olivine. By fitting models to global datasets for seafloor depth and heat flow I make predictions of various important properties of the Earth (e.g., plate thickness, mantle potential temperature, and net seafloor heat flux) as well as the effective properties of the cooling lithosphere (e.g., thermal diffusivity and thermal expansivity). Here, I arrive at the conclusion that while simple thermal plate models can represent the first-order properties of the mantle, the large adjustment in thermal expansivity needed to fit the models to the data demonstrates that it is not possible to link material

properties and geophysical observables using simple theories of lithospheric evolution.

Chapter 3 builds on the conclusions of the previous chapter. As simple models of the thermal evolution of oceanic lithosphere can only fit the data with large adjustments to material properties, I develop more physically comprehensive models of lithospheric evolution. In addition to temperature-dependent properties, I include contributions from 2D heat transport, hydrothermal circulation, insulating oceanic crust, pressure-dependence, and a mantle melting contribution to temperature (via latent heat). As in our previous model investigation, I fit the resulting models to global seafloor topography and heat flow data. The resulting models feature improved fits to young-age seafloor topography and, most importantly, do so with significantly less adjustments to material properties. The predictions of plate thickness, thermal expansivity, net seafloor heat flux, and the temperature at the base of the seismogenic zone are discussed.

In Chapter 4, I calculate the extent of hydrothermal extraction of heat from oceanic lithosphere based on the models obtained in the previous chapter. Because heat flow is low in proximity to ridge axes, I predict that the hydrothermal heat flux is much lower than that predicted by conventional models. In addition, most of this heat is mined on ridge axes, such that ambient diffusive hydrothermal circulation off ridge axes is relatively low.

Finally, in Chapter 5, I explore the possibility of constraining the properties of oceanic upper mantle by explaining the contribution of the so-called LID effect on the chemistry of Ocean Island Basalts (OIB). By developing a new sophisticated melting model which takes into account the details of microstructural and microchemical evolution in the source of these lavas, I am both able to explain the OIB data with the LID effect using our thermal model from Chapter 3, as well as draw a series of important conclusions regarding the extent of chemical disequilibria during melting, the temperature of the (thermo-mechanical) lithosphere-asthenosphere boundary, the composition and temperature of the source, and the apparent compositional similarity between the sources of OIB and Mid-Ocean Ridge Basalts.



# 2

## Properties of Oceanic Lithosphere: Revised Plate Cooling Model Predictions

### 2.1 INTRODUCTION

As seafloor is created at ocean ridges and gradually migrates away, heat is conducted through the seafloor and the underlying lithospheric mantle cools, contracts, and thickens. The thermal gradient near the surface and the subsidence associated with contraction and loading (primarily by seawater) are two key geophysical observables used to constrain models of the thermal evolution of oceanic lithosphere. Unfortunately, constraining models of the oceanic lithosphere is made difficult by complicated and incomplete views of the geophysical observables, properties of mantle materials, and the thermomechanical behavior of the upper mantle. These complications have caused the problem of explaining geophysical observations with increasingly sophisticated geodynamic models to persist for more than 45 years (McKenzie, 1967; Sclater and Francheteau, 1970; Davis and Lister, 1974; Parsons and Sclater, 1977; Heestand and Crough, 1981; Stein and Stein, 1992; Doin and Fleitout, 1996; Honda and Yuen, 2004; McKenzie, 2005; Goutorbe, 2010). Seafloor topography is generally regarded as the best constraint as the subsidence of young age seafloor is in strong agreement with the simple half-space cooling models, but the 'flattening' behavior of old age ( $>80$  Ma) seafloor has been an arduous problem for the analysis of thermal structure since the sources of divergence from simple half-space cooling are not certain (Sclater and Francheteau, 1970; Heestand and Crough, 1981; Doin and Fleitout, 1996; Zlotnik, et al. 2008; Sleep, 2011a;b). On the other hand, for young ages ( $<50$  Ma) the seafloor heat flux is known to be complicated by the effects of hydrothermal circulation, causing a systematic underprediction of heat flow through the lithosphere (Davis and Elderfield, 2004), while global heat flow is quite well behaved at old age (Stein and Stein, 1992; Hasterok et al., 2011). As such, constraints from seafloor topography are best for young ages and more suspect for old ages,

while constraints from seafloor heat flux are largely uncertain for young ages but good for old ages. In evaluating the relationship between models and geophysical observations, it is important to consider this confidence contrast in fitting analysis. In particular, the fitness is usually allowed to vary at all ages as long as the overall fit to the observations is good. Fitting procedures employed here avoid this caveat.

While the seafloor subsidence rate is known to have significant regional variation (Marty and Cazenave, 1989), it is generally thought that these variations are integrable such that the average behavior of the seafloor can be properly related to the 'normal' evolution of oceanic lithosphere as resolved in regional and global databases (Korenaga and Korenaga, 2008). The normal seafloor subsidence rate of oceanic lithosphere has conventionally been determined using data for the North Pacific and North Atlantic (Parsons and Sclater, 1977; Stein and Stein, 1992; Carlson and Johnson, 1994) for which  $\sim 350 \text{ m Ma}^{-1/2}$  has been estimated. While many other analyses of seafloor subsidence exist in the literature, this estimate seems to have been made popular as the analyses by Parsons and Sclater (1977) and Stein and Stein (1992) were accompanied by the determination of important benchmark reference cooling models. Indeed, other early investigators have provided lower estimates (Heestand and Crough, 1981; Schroeder, 1984), and more recently it has been shown that analyses both of the Pacific plate and of global data indicate that the normal subsidence rate is closer to  $320 \text{ m Ma}^{-1/2}$  (Hillier and Watts, 2005; Zhong et al., 2007; Crosby et al., 2006; McKenzie and Crosby, 2009; Korenaga and Korenaga, 2008; Hillier, 2010).

Although the examination of variable mineral physics properties in thermal models of oceanic lithosphere is not new (eg. Denlinger, 1992; Doin and Fleitout, 1996; Hearn et al., 1997) it has recently become routine to include variable thermal properties in the cooling problem using numerical techniques (eg. Honda and Yuen, 2001; 2004; McKenzie et al., 2005; Korenaga and Korenaga, 2008; Goutorbe, 2010; Hasterok, 2010). Ultimately, this modeling research will continue in this direction to involve increasingly more sophisticated views of the dynamical state of the lithosphere (eg. Korenaga, 2007b; Zlotnik et al., 2008; Afonso et al., 2008), petrological structure (eg. Afonso et al., 2007; Afonso and Schutt, 2012), and heat transport properties (eg. Hofmeister, 2005; Hofmeister, 2007; Pertermann and Hofmeister, 2006; Whittington et al., 2009), and other sources of complexity.

The purpose of this chapter is to present a new assessment of the basic cooling oceanic lithosphere problem using temperature-dependent heat transport properties and thermal expansivity. We use the experimental specific heat (Berman and Aranovich, 1996) and thermal expansivity (Bouhifd et al., 1996) for olivine as used in many recent cooling model analyses, along with experimental temperature-dependent lattice thermal diffusivity of olivine from Pertermann and Hofmeister (2006) and a radiative component is taken from Hofmeister (2005). Building on past interests in the effective or average properties of the lithosphere when variable properties are used (eg. Doin and Fleitout, 1996; Afonso et al., 2005; Korenaga, 2007a), we introduce formalisms for the determination of the effective properties of the lithosphere. Moreover, it is important to acknowledge uncertainty and controversy surrounding the accuracy of experimental mineral physics properties as well as the extent to which experimental properties can be applied to the simplified conditions of the cooling lithosphere problem. For example, while we employ Pertermann and Hofmeisters (2006) olivine thermal diffusivity, more than 40% of upper mantle volume consists of other phases,

and there is some controversy regarding the accuracy of the various methods of measuring thermal conductivity at temperature (Hofmeister, 2007; 2009; Beck et al., 2009). Experiments determining the thermal expansivity of olivine also have significant variation and the existing data are of uncertain quality (Afonso et al., 2005; Korenaga, 2007a). Other uncertainties will also be discussed. Accordingly, we treat the thermal conductivity and thermal expansivity as simultaneously temperature-dependent and adjustable properties.

This approach to fitting analysis, in addition to new constraints and treatments of the geophysical observables, resolves excellent fits to observations. However, the effective thermal diffusivity and the apparent thermal expansivity are significantly different from previous reference models with either constant or variable transport properties. We also show that a model with unadjusted heat transport properties can provide excellent fits while also being in agreement with evidence of plate thickness from seismic tomography and of mantle potential temperature. On the other hand, all model parameterizations indicate that the apparent thermal expansivity of the oceanic lithosphere is lower than determined by experiments on forsterite.

## 2.2 METHODS AND FORMALISMS

### 2.2.1 Heat transport modeling

Thermal structure is predicted by numerically solving (explicit forward finite difference model) the one-dimensional conduction equation

$$\rho C_p \frac{\partial T}{\partial t} = \frac{\partial}{\partial z} \left( k \frac{\partial T}{\partial z} \right), \quad (2.1)$$

where  $k$  is the thermal conductivity,  $\rho$  is the density,  $C_p$  is the isobaric specific heat,  $T$  is temperature,  $t$  is time, and  $z$  is vertical distance. All models are non-deforming approximations (constant spacing irrespective of temperature), and horizontal conduction is ignored since its impact on thermal structure is known to rapidly become negligible over time (Sleep, 1975; Honda and Yuen, 2004; McKenzie et al., 2005). The initial condition is a mantle column of constant temperature, the surface temperature remains a constant 0°C and the lower plate boundary remains at the initial mantle temperature.

A rigorous fitting analysis is performed for three model types: constant heat transport property models, PH06 models, and PH06-R models. In constant heat transport models the transport properties  $\rho$ ,  $C_p$ , and  $k$  are constants. In PH06 models we use the temperature-dependent lattice thermal diffusivity of  $\sim \text{Fo}_{90}\text{Fa}_{10}$  from Pertermann and Hofmeister (2006), specific heat from Berman and Aranovich (1996), and thermal expansivity of forsterite from Bouhifd (1996). PH06-R models use the same properties as PH06 models in addition to a radiative contribution to conductivity using the model of Hofmeister (2005) with a 10 mm grain size. This grain size was chosen as it predicts the highest increase in effective thermal diffusivity against lattice only (PH06) models ( $\sim 15\%$  increase). Later (Chapter 5), we will run models of microstructural and microchemical evolution in the source of Ocean Island basalts. Due to the dependence of melt chemistry on grain size, we will show that OIB chemistry is consistent with such a grain size, although it may also be lower. The maximum

thickness of the numerical model is 325 km and models use 1 km spacing in  $z$ . Note that models with constant heat transport properties will also be analyzed a posteriori using variable thermal expansivity, but for the sake of thermal modeling the density is constant.

### 2.2.2 Effective heat transport properties

Investigating the predictions of various parameterizations requires an assessment of their effective properties, the most important of which is the effective thermal diffusivity,  $D_E$ , which can be determined from the geotherm. The effective thermal diffusivity is found as the diffusivity for which the difference of the integrated change in temperature between a variable diffusivity model and its effective (constant) diffusivity model is zero as

$$\int_0^\infty (T_C - T_V) dz = 0, \quad (2.2)$$

where  $T_C$  and  $T_V$  are temperatures of the constant and variable diffusivity models, respectively. Also, from the effective thermal diffusivity and the surface heat flux one can also obtain the effective thermal conductivity  $k_E$  and effective volume heat capacity,  $[\rho C_p]_E$ , as

$$k_E = \frac{\sqrt{\pi D_E t}}{T_m - T_0} q_{sf}, \quad (2.3)$$

and

$$[\rho C_p]_E = \frac{k_E}{D_E} = \frac{q_{sf}}{T_m - T_0} \sqrt{\frac{\pi t}{D_E}}, \quad (2.4)$$

where  $T_m$  is mantle temperature,  $T_0$  is the surface temperature, and  $q_{sf} = kdT/dz|_{z=0}$  is the surface heat flux. Although the thermal conductivity is always temperature dependent, we also treat it as an adjustable parameter by multiplying by some factor  $F$  such that an 'apparent' thermal diffusivity  $D_A$  (subscript  $A$  indicates 'apparent' values) can be related to the 'effective' thermal diffusivity as  $D_A = F D_E$ , and since we assume that  $[\rho C_p]_E = [\rho C_p]_A$  is always true, the apparent coefficient for conductivity is  $k_A = F k_E$ .

### 2.2.3 Effective versus Apparent Values

The difference between effective and apparent values is primarily of heuristic interest. The idea is that one can introduce known mineral physics properties into a model for which results can be analyzed for the determination of that models effective properties. However, inasmuch as the model is an incomplete treatment of reality and that the properties have various degrees of uncertainty, there will remain an unaccounted source which will change the 'true' effective value of the system. If additional sources are negligible and model properties are accurately constrained, the effective value from the model will be equal to the apparent value, else the modeled value will differ by a fractional amount ( $F$  and  $H$  for thermal diffusivity and thermal expansivity, respectively).

### 2.2.4 Isostatic formalism and seafloor subsidence

Seafloor topography satisfies the balance equation

$$\int_0^L \rho(z, 0) dz = \int_0^w \rho(z, t) dz + \int_w^L \rho(z, t) dz, \quad (2.5)$$

where  $\rho$  is density,  $w$  is the surface of the lithosphere, and  $L$  is the depth of compensation. When the material between ridge height and seafloor depth is only seawater of constant density, Eq. 2.5 can be given as

$$\rho_a L = \rho_w w + \rho_L (L - w), \quad (2.6)$$

where  $\rho_a$  is the density of asthenosphere,  $\rho_w$  is the density of seawater, and  $\rho_L$  is the average density of the mantle between the depths  $w(t)$  and  $L$ . Eq. 2.6 may be rearranged to give the seafloor depth above the ridge axis,

$$w = \frac{\rho_a - \rho_L}{\rho_w - \rho_L} L. \quad (2.7)$$

The mean density of the mantle column,  $\rho_L$ , can be found as

$$\rho_L = \rho_a + \frac{\rho_a}{L - w} \int_0^L \left(1 - \frac{\rho_a}{\rho}\right) dz. \quad (2.8)$$

Substituting Eq. 2.8 into the numerator of Eq. 2.7 and taking the limit

$$\lim_{L \rightarrow \infty} (\rho_a - \rho_L) L = -\rho_a \int_0^\infty \left(1 - \frac{\rho_a}{\rho}\right) dz, \quad (2.9)$$

and as  $\rho_L \rightarrow \rho_a$  in the limit, Eq. 2.7 can be rewritten simply as

$$w = \frac{\rho_a}{\rho_a - \rho_w} \int_0^\infty \left(1 - \frac{\rho_a}{\rho}\right) dz. \quad (2.10)$$

It is worth noting that the isostatic term,  $\rho_a/(\rho_a - \rho_w)$ , depends on the mantle temperature, and in our models is about 1.51 for  $T_m=1350^\circ\text{C}$  and  $\rho_w=1065 \text{ kg m}^{-3}$ . The above derivation shows that  $\rho_a$  is the initial mantle density ( $\rho_a \sim 3150 \text{ kg m}^{-3}$ , with dependence on temperature only) and not the reference density ( $\rho_0 \sim 3300 \text{ kg m}^{-3}$ ) occasionally used in reference models.

Also, for half-space cooling models a well known solution for the subsidence rate,  $b$ , with the temperature dependent properties is (Turcotte and Schubert, 2002)

$$b = \frac{w}{\sqrt{t}} = 2\rho_a \alpha_{AC} \frac{T_m - T_0}{\rho_a - \rho_w} \sqrt{\frac{D_A}{\pi}}, \quad (2.11)$$

where  $\alpha_{AC}$  is the apparent volumetric coefficient of thermal expansion of the mantle column introduced next.

### 2.2.5 Treatment of variable thermal expansivity

When there occurs a temperature change,  $\Delta T = T - T_0$ , the effective coefficient of thermal expansion with temperature dependence only is

$$\alpha_E = \frac{1}{\delta T} \int_{T_0}^T \alpha(T) dT \quad (2.12)$$

Analogous to the treatment of the thermal diffusivity, the apparent coefficient of thermal expansion may be given simply as

$$\alpha_A = H \alpha_E \quad (2.13)$$

so that the factor  $H$  quantifies the contribution of the additional unknown sources of density change and the error in  $\alpha(T)$ . One may also describe an effective coefficient of thermal expansion for a volume,  $V$ , with an arbitrary (initial and final) temperature distribution as

$$\alpha_{EV} = \int_V \int_{T_0}^T \alpha(T) dT dV / \int_V \delta T dV \quad (2.14)$$

and the apparent coefficient for a body of arbitrary temperature distribution is from Eq. 2.13 and 2.14,

$$\alpha_{AV} = \int_V H \int_{T_0}^T \alpha(T) dT dV / \int_V \delta T dV, \quad (2.15)$$

which for a cooling problem (initial  $\rho = \rho_a$ ) is also

$$\alpha_{AV} = \int_V \left( 1 - \frac{\rho_a}{\rho} \right) dV / \int_V \delta T dV, \quad (2.16)$$

where the density is

$$\rho = \rho_0 \left( 1 - H \int_{T_0}^T \alpha(T) dT \right). \quad (2.17)$$

Since our volume is the mantle column, the apparent coefficient of thermal expansion is

$$\alpha_{AC} = H \int_0^L \int_{T_0}^T \alpha(T) dT dz / \int_0^L \delta T dz = \int_0^L \left( 1 - \frac{\rho_a}{\rho} \right) dz / \int_0^L \delta T dz. \quad (2.18)$$

where  $H$  is placed outside of the integral because it is treated as constant with depth (and age), and

$$\alpha_{EC} = \alpha_{AC} / H. \quad (2.19)$$

The case where  $\alpha_{AC} = \alpha_{EC}$ , or  $H=1.0$ , is equivalent to the assumption that contraction is instantaneous, occurs in the vertical direction only (fluid thermal isostasy approximation), additional mineral modes do not change the coefficient, and that no special phenomena such as phase changes or thermal stresses contribute to density.

Note that Eq. 2.17 is only solved while assuming  $H=1.0$  during thermal modeling analysis since the source of nonzero  $H$  is undetermined and unlikely to significantly affect transport properties. Instead,  $H$  is adjusted *a posteriori* as a procedure in fitting analysis (Section

2.2.7). Furthermore, it should be noted that this treatment assumes that the cause of  $H \neq 1.0$  originates from processes in the lithosphere as we assume that  $H=1.0$  in the determination of  $\rho_a$  as applied in the isostatic treatment (Eq. 2.10-2.11). Nevertheless, if  $H \neq 1.0$  is due to different properties of the mantle assemblage the error in the isostatic solution is small compared to the more important impact on contraction.

### 2.2.6 Net seafloor heat flow

The net seafloor heat flow,  $Q_{sf}$ , is the sum of the surface heat flux over the total seafloor area. When transport properties have no dependence on depth or time this may be predicted as

$$Q_{sf} = [\rho C_p]_E (T_m - T_0) \sqrt{\frac{D_A}{\pi}} A_t + \int_A q_b dA, \quad (2.20)$$

where  $q_b$  is some additional heat flux,  $A$  is the seafloor area and  $A_t$  is the 'time-weighted' seafloor area given as

$$A_t = \int_A \frac{dA}{\sqrt{t}} = \sum_{t=0}^{t_m/\delta t} \frac{A(\delta t)}{\sqrt{t}}, \quad (2.21)$$

where  $A(\delta t)$  is the seafloor area of a time interval  $\delta t$ , and  $t_m$  is the maximum time ( $\sim 180$  Ma). We may also replace the uncertain thermal diffusivity with the observed subsidence rate by arranging Eq. 2.11 and 2.20 to give

$$Q_{sf} = b_o [\rho C_p]_E \frac{\rho_a - \rho_w}{2\rho_a \alpha_{AC}} A_t + \int_A q_b dA, \quad (2.22)$$

where  $b_o$  is the observed subsidence rate and  $\alpha_{AC}$  is the apparent thermal expansivity.

The seafloor area-age distribution is usually described using a linear function in time of the form  $dA/dt = C(1 - t/t_m)$  where  $C$  is the seafloor area creation rate. Stein et al. (1995) used  $C = 3.45 \times 10^6 \text{ km}^2 \text{ yr}^{-1}$  and  $t_m=180$  Ma, and more recently Jaupart et al. (2007) argued that  $C = 3.34 \times 10^6 \text{ km}^2 \text{ yr}^{-1}$  is more accurate. However, the actual seafloor area-age distribution is only roughly linear (Fig. 2.1). We use the global gridded seafloor age database from Müller et al. (2008) in 0.1 Ma bins, ensuring that the roughness of the area-age distribution is properly accounted for.

### 2.2.7 Sensitivity analysis and fitting experiments

In the fits to seafloor topography the 1 My binned global bathymetric data from Hillier (2010) is used, which uses a boot-strap resampling analysis method first employed to seafloor topography by Korenaga and Korenaga (2008). We further remove elevated data points over old age seafloor and fit the polynomial,  $h = a + bt + ct^2 + dt^3$  (depth in km), to the remaining data with the coefficients;  $a=2.860$ ,  $b=0.14131407$ ,  $c=0.0449484$ ,  $d=-0.00320261$ . Thermal model predictions are explored with the parameter ranges  $T_m=1400\pm 100^\circ\text{C}$ ,  $D=0.9\pm 0.5 \text{ mm}^2 \text{ s}^{-1}$ , and  $L=120\pm 50 \text{ km}$ .

The first step in fitting is to adjust the 'normal' subsidence rate of each thermal model (for any thermal diffusivity and mantle temperature) to match that observed by Hillier (2010).

This is done by changing the apparent thermal expansivity in each model by the factor  $H$  until the average subsidence rate of the model matches the average subsidence rate from the polynomial fit to the same age range. This subsidence rate is about  $321 \text{ m My}^{-1/2}$  for the age range 0-64 Ma. The  $R^2$  value for the fit to depth is then determined for all model parameterizations. This fitting procedure is a special test of the plate model as it demands that young-age subsidence always fits that inferred from observations and misfit is associated with the impact of the plate boundary condition.

The fit to seafloor heat flow uses the sediment corrected seafloor heat flow database from Hasterok et al. (2011), although data younger than 100 Ma and older than 165 Ma is ignored. Younger data are neglected as they systematically trend away from the predictions of plate models (Hasterok, et al., 2011), and older  $>165$  Ma data are neglected as there is an anomalously abrupt jump in the data. The remaining data is approximated by the polynomial  $q_{sf} = a + bt + ct^2$  ( $\text{mW m}^{-2}$ ) with coefficients  $a=92.998$ ,  $b=-0.507324$ , and  $c=0.00150612$ .  $R^2$  values for the age range 100-165 Ma were obtained for all models. The joint fit to depth and heat flow for a given parameterization is represented by the average  $R^2$  value for the fit to depth and heat flow.

## 2.3 RESULTS

### 2.3.1 Sensitivity analysis

Modeled subsidence rates as a function of thermal diffusivity are graphed in Fig. 2.2a for the experimental coefficient of thermal expansion and mantle temperature between  $1200^\circ\text{C}$  to  $1500^\circ\text{C}$ . Taking the observed seafloor subsidence rate,  $b_o$ , to be  $320 \text{ m My}^{-1/2}$ , if there is no reduction in the effective coefficient of thermal expansion (i.e.,  $H=1.0$ ), the effective thermal diffusivity predicted is about  $0.43 \pm 0.05 \text{ mm}^2 \text{ s}^{-1}$  for the 'nominal' mantle temperature range  $1340 \pm 60^\circ\text{C}$  petrochemically constrained by Herzberg et al. (2007). On the other hand, if  $H < 1.0$  then the thermal diffusivity which fits observed seafloor subsidence will be higher. This effect of reducing the apparent thermal expansion coefficient on predictions is illustrated by vertical lines in Fig. 2.2a, which identify various values of  $H$  corresponding to the (approximately) observed subsidence rate of  $320 \text{ m Ma}^{-1/2}$ . For example, a mineral physics subsidence rate of  $400 \text{ m Ma}^{-1/2}$  requires a 20% reduction ( $H=0.8$ ) in the thermal expansivity to fit observations. This relationship is also shown in Fig. 2.2b for  $H$  as low as 0.5. The thermal diffusivity usually used in reference cooling models of about  $0.8 \text{ mm}^2 \text{ s}^{-1}$  predicts  $H=0.73 \pm 0.04$ , for  $T_m=1340 \pm 60^\circ\text{C}$ . The dashed curves in Fig. 2.2a and 2.2b indicate the predictions for  $b_o=320 \text{ m My}^{-1/2}$  and an apparent coefficient of thermal expansion of  $3.0 \times 10^{-5} \text{ K}^{-1}$ , showing that the effective expansion coefficient from mineral physics ( $\alpha_E \sim 3.8 \times 10^{-5} \text{ K}^{-1}$ ) predicts that the subsidence rate is about 25-30% higher than  $3.0 \times 10^{-5} \text{ K}^{-1}$ .

Model predictions of net seafloor heat flux,  $Q_{sf}$ , are shown in Fig. 2.2c. The low thermal diffusivity predicted using  $H=1.0$  corresponds to  $Q_{sf}=19.4 \pm 0.2 \text{ TW}$ , about 40% lower than the conventional estimate of 31-32 TW (Pollack et al., 1993; Stein et al., 1995). Reproducing the conventional estimate requires about a 40% lower thermal expansivity and a thermal diffusivity on the order of  $0.9\text{-}1.3 \text{ mm}^2 \text{ s}^{-1}$ . Using  $H=0.8$ , which is about that suggested by



thermoviscoelastic modeling of the oceanic lithosphere (Pollack, 1980; Korenaga, 2007a), the apparent coefficient becomes about  $3.0 \times 10^{-5} \text{ K}^{-1}$ . While this expansion coefficient is close to that used by model GDH1 (Stein and Stein, 1992; Table 2.1 in this work), the thermal diffusivity is still only around  $0.69 \pm 0.06 \text{ mm}^2 \text{ s}^{-1}$  and predicted heat flow is only about 24.7 TW.

The predictions of net seafloor heat flow shown in Fig. 2.2c apply to half-space models only ( $q_b=0$  in Eq. 2.20 and 2.22). Fig. 2.2d shows the increase in the net seafloor heat flux due to the lower boundary condition for plate thicknesses between 80 and 125 km for constant thermal diffusivity models and PH06 models. Unless the thermal diffusivity is high and the oceanic plate is thin the added heat flow is no more than a few percent, and PH06 models require an even thinner plate to increase surface heat flux as much as constant thermal diffusivity models.

### 2.3.2 Fitting experiments

Results of fitting experiments are shown in Fig. 2.3 and 2.4. Fig. 2.3a-c show the best fitting apparent thermal diffusivity as a function of plate thickness for mantle temperatures between 1300 and 1500°C for constant thermal diffusivity, PH06 models, and PH06-R models, respectively. As the plate thickness changes the goodness of fit also changes. The best fitting properties are indicated with diamonds and a thick dashed line, lines of equal fitness are drawn at 0.01 intervals, and the space where  $R^2 > 0.99$  is highlighted. Different mantle temperatures can achieve essentially equal best joint fit  $R^2$  of about 0.996-0.998 for all model types. The black boxes connected by a thick solid line in Fig. 2.3b and 2.3c indicate the effective thermal diffusivity of the transport model for different mantle temperatures when the thermal conductivity is not changed ( $F=1.0$ ). Fig. 2.3d-f show predicted subsidence against the topography of Hillier (2010) and a polynomial approximation. Each topographic curve represents a subsidence model with different goodness of fit and can be represented by the properties of any point along an isofitness line in Fig. 2.3a-c. The shaded space shows predictions for models with  $R^2 > 0.99$  and the thick dashed line is the best fit model. Fig. 2.3g-i show the same model results for the heat flow against the data of Hasterok et al. (2011) and our polynomial approximation of their data.

Fig. 2.4a-c show the joint fit  $R^2$  fields for 1400°C models with constant transport properties, PH06 models, and PH06-R models, respectively. The regions where  $R^2 > 0.99$  are indicated by a dashed ellipsoid and diamonds indicate the best fit models. Figures below show the predicted net seafloor heat flux,  $Q_{sf}$  (Fig. 2.4d-f), and the thermal expansivity reduction ratio,  $H$  (Fig. 2.4g-i), for the parameter space with the  $R^2$  field overlaying the predictions in an alpha composite. Supplementary Figures (see published documents in the online version of this Chapter at Elsevier as Grose (2012)) A-C show the same determinations as in Fig. 2.4 for mantle temperatures between 1300 and 1500°C. Results for models with mantle temperature lower than 1300°C are not reported as the apparent thermal diffusivity of good fit models becomes extremely high.

In general, the best fitting models are characterized by exceptionally high apparent thermal diffusivity and a relatively thick plate. The difference between predictions of PH06 and constant diffusivity models is about a 15-20 km thinner plate, 5% higher  $H$ , and about 5%

lower effective thermal diffusivity for PH06 models. PH06-R models predict only about a 5 km thinner plate than constant diffusivity models while other properties are about the same as for PH06 models (Fig. 2.4). Predicted net seafloor heat flux for best fit models is about 31.5 TW not only between constant and variable diffusivity models (Fig. 2.4), but for different mantle temperatures (see Supplementary Figures in online version of this Chapter (Grose, 2012)). The parameter ranges of good fit models are tabulated in Tables 2.1 and 2.5.

Three specific parameterizations have been identified as useful benchmark reference models: L1, R1, and RT1. Models L1 and R1 are the best joint fit PH06 and PH06-R models, respectively, both with unadjusted heat transport properties (Fig. 2.3). While both models are best joint fits ( $R^2 > 0.997$ ), model L1 is characterized by a lower thermal diffusivity, higher mantle temperature, and thinner plate than R1. The high mantle temperature and the absence of a radiative component in model L1, suggests that this model is less realistic. An additional parameterization, model RT1, was identified after surveying the results of fitting analysis and evidence of plate thickness from seismic tomography. Although the joint fit for model RT1 is not the best ( $R^2 \sim 0.99$ ), the fit to topography alone is significantly improved ( $R^2 \sim 1.0$ ) at little cost to heat flow given the scatter in heat flow data. The poor fit to heat flow ( $R^2 \sim 0.98$ ) is an caveat of the technique of fitting to polynomial approximations, which does not account for contrasts in the variance between topographic and heat flow datasets (Fig. 2.3). RT1 uses unadjusted heat transport properties, a thicker plate, and mantle temperature is around the acceptable window (Table 2.1).

## 2.4 DISCUSSION

### 2.4.1 Properties of best fit plate models

Although the predictions of our best fit models are in excellent agreement with observations, the associated model properties are quite different from previous reference cooling models. Conventional reference models use a thermal diffusivity of about  $0.8 \text{ mm}^2 \text{ s}^{-1}$  (Sclater and Francheteau, 1970; Parsons and Sclater, 1977; Stein and Stein, 1992), and it can be demonstrated that the effective thermal diffusivities of some previous models with variable transport properties (Honda and Yuen, 2001; 2004; McKenzie et al., 2005; Goutorbe, 2010) are only slightly higher ( $\sim 0.9 \text{ mm}^2 \text{ s}^{-1}$ ). Modeling results indicate that  $0.8 \text{ mm}^2 \text{ s}^{-1}$  is too low to fit observations unless mantle temperature is  $> 1500^\circ\text{C}$ , and  $0.9 \text{ mm}^2 \text{ s}^{-1}$  still requires about  $1450^\circ\text{C}$  mantle temperature to provide a good joint fit (Fig. 2.3b,c). Furthermore, the apparent thermal diffusivity range predicted for nominal mantle temperature ( $1340 \pm 60^\circ\text{C}$ ) is  $1.15 \pm 0.11 \text{ mm}^2 \text{ s}^{-1}$  for best fit variable transport models (Fig. 2.3b,c). Even the low end of this ranges is about 30% higher than the conventional reference values and 15% higher than prior models with variable transport properties.

The principal difference between predictions of constant and variable transport models is in the thermal structure of the plate and the corresponding impact on plate thickness (Honda and Yuen, 2004; McKenzie et al., 2005; Goutorbe, 2010). The steady-state geotherm of constant diffusivity plate models is linear when there is no internal heating. On the other hand, the lattice thermal diffusivity decreases with temperature (Fig. 2.5) such that conduction of

heat near the surface is faster than at depth, steepening the geotherm and cooling the plate beyond the predictions of constant diffusivity models (Fig. 2.6). Since a thermal plate of a given thickness is colder for variable transport models, this means that the plate thickness must be lower than a constant diffusivity analog ( $D_{const} = D_A$ ) to predict the same old age seafloor topography. This is why the plate thickness predictions of PH06 models are 15-20 km thinner than constant diffusivity models (Fig. 2.3 and 2.4; Table 2.5). Moreover, the amount of steepening in the geotherm is roughly controlled by the difference between thermal diffusivity at low and high temperature. Including a large radiative contribution lowers this difference and so the steady-state geotherm is closer to the predictions of constant diffusivity models (Fig. 2.6e,f), and the predicted plate thickness of best fit PH06-R models are about half-way between constant diffusivity and PH06 models (Fig. 2.3; Table 2.5). Also, the plate thicknesses for all best fit models are higher than previous modeling studies (Honda and Yuen, 2004; McKenzie et al., 2005; Goutorbe, 2010), probably due to differences in fitting procedures, geophysical data used, and transport properties (Fig. 2.5).

Furthermore, combining the influence of variable heat transport properties, differences in mantle temperature, and differences in plate thickness can cause differences in temperature among reference models on the order of 100-400°C (Fig. 2.6a-2.6d). Fig. 2.6a-2.6d shows temperature difference isotherms of the two reference models of this work (L1 and R1) against the thermal structure of GDH1 and PS77. Since model L1 has a different plate thickness from PS77 (Fig. 2.6a) and R1 has a different plate thickness to GDH1 (Fig. 2.6d), when compared these models have large temperature differences near the base of the thinner plate model which can exacerbate already significant differences in ambient mantle temperature, particularly against GDH1. On the other hand, reference model PS77 is only slightly warmer than R1 (Fig. 2.6b). These differences should be important for the interpretation and use of seismic tomography as a constraint on thermal structure (Goutorbe, 2010). However, resolving relative velocity heterogeneity has generated conflicting results on its own (Ritzwoller, et al. 2004; Maggi, et al. 2006; Priestly and McKenzie, 2006) and the further inference of absolute temperature involves additional assumptions about poorly known properties of attenuation, composition, and thermoelasticity (Afonso et al., 2008; Goutorbe, 2010).

## 2.4.2 On slow cooling estimates

It may seem surprising that a mineral physics estimate of net seafloor heat flow with unadjusted thermal expansivity is as low as  $19.4 \pm 0.2$  TW for half-space models (Fig. 2.2), but such a low estimate is not entirely new. Wei and Sandwell (2006) investigated variations in seafloor subsidence using global depth and age grids to infer heat flux for Cenozoic seafloor and the Earth. Using this method along with cooling models with unadjusted experimental thermal expansivity, they find that Cenozoic heat flux is about 19 TW, which is consistent with net seafloor heat flux of about 28 TW, only a few terawatts lower than conventional estimates (Pollack, 1993; Stein et al., 1995) and our new reference models (Fig. 2.4; Table 2.1 and 2.5). However, following from Doin and Fleitout (1996) it was assumed that there exists an unaccounted heat flux of about  $35 \text{ mW m}^{-2}$  exiting the oceanic lithosphere which adds about 10 TW to seafloor power. This means that the associated thermal model is not

a half-space or plate model and that their analysis of seafloor topography actually predicts a net seafloor heat flux of about 18 TW and a global heat flux close to 30 TW. A plate model with such low surface heat flux cannot match geophysical observations. An alternative solution to this inconsistency is to suppose that the apparent thermal expansivity of the lithosphere is lower than indicated by experiments on forsterite.

### 2.4.3 Low apparent thermal expansivity

Goutorbe (2010) performed a joint inversion of topography, heat flow, and seismically inferred mantle temperature and found that a plate model requires about a 30% lower thermal expansivity ( $H=0.7$ ) to fit observations, in some agreement with our predictions. However, Goutorbe (2010) believed that this possibility should be dismissed because such a reduction is beyond that predicted from thermoviscoelastic modeling of oceanic lithosphere (about 15-20% for realistic rheology; Pollack, 1980; Korenaga, 2007a). The role of thermoviscoelastic behavior in the determination of density in cooling mantle is interesting because it shows that a solution to the problem of cooling and the relationship between lithospheric density and temperature is not simply a matter of experimentally constraining mineral physics properties as inputs in simple mathematical models and testing model outputs against observations. In a thickening thermoelastic or thermoviscoelastic plate, the apparent coefficient of thermal expansion is reduced by the accumulation of thermal stress in low temperature mantle and potentially cracking the lithosphere, which may in turn lead to infilling by foreign materials (eg. seawater) and deep mantle serpentinization. The basics of this behavior in oceanic lithosphere have been a subject of study at least since Turcotte (1974), and its importance for the thermal expansion coefficient was detailed by Pollack (1980) and has been recently explored with numerical models of varying complexity by Korenaga (2007a,b). Nevertheless, there are a number of other possible contributors to a lower apparent coefficient of thermal expansion: i) forsterite expansivity data from Bouhifd et al. (1996) may be inaccurate, ii) pressure dependence may be important, or iii) forsterite may be an inaccurate approximation of the mantle mineral assemblage.

Although we cannot dismiss inaccuracy, note that the effective expansion coefficient from this dataset is lower than other reports for olivine (see compilations in: Bouhifd et al., 1996; Korenaga, 2007a; Li et al., 2007), so the use of other estimates will require even greater reductions to fit geophysical observations. Pressure dependence is generally thought to be unimportant for cooling models (McKenzie et al., 2005; Korenaga and Korenaga, 2008), although pressure should impact the apparent coefficient by at least a few percent (Afonso et al., 2005). Doin and Fleitout (1996) and Hasterok (2010) studied models with pressure dependent thermal expansion, both contending that while pressure dependence is important for local density, its role for the depth integrated consequences of cooling (mainly topography) are not important. On the other hand, Doin and Fleitout (1996) compared results of pressure-temperature dependent models against models using average values, so their analysis does not evaluate whether or not dependence on pressure itself is important.

That additional modes in the mantle mineral assemblage significantly change the effective thermal expansivity is probable (Afonso et al., 2005). Korenaga (2007a) argue that expansivity should be approximated well by pure forsterite and that the major uncertainties

are coefficients for orthopyroxene and fayalite. However, in addition, garnet has a lower thermal expansivity by on the order of 25% (Thieblot et al., 1998) and the elastic weakness of pyroxenes should result in a greater sensitivity to pressure. These phase contributions may be important for cooling of lithosphere at depths below where melt extraction is important ( $>1$  GPa).

Alternatively, the plate model cannot be used to describe the thermal evolution of oceanic lithosphere, as argued by Goutorbe (2010).

#### 2.4.4 Thermal diffusivity

The uncertainties in the thermal expansion coefficient are also largely translatable to the treatment of heat transport properties. Although the volume heat capacity is relatively well constrained and varies significantly only with composition (Berman and Aranovich, 1996), the thermal conductivity in silicates is a measure of phonon propagation through and between crystal lattices such that a number of properties in addition to composition control the conductivity (eg. Pertermann and Hofmeister, 2006; Hofmeister, 2006; Whittington et al., 2009). Also, the lattice diffusivity used here from Pertermann and Hofmeister (2006) is an isotropic approximation (geometric mean of three crystallographic orientations), and each crystallographic orientation is significantly different. As such, lattice preferred orientation, which is thought to be strong in oceanic lithosphere (Becker et al., 2006) may significantly lower the effective thermal diffusivity of the mantle column (Hearn et al., 1997; Tommasi et al., 2001). The lattice thermal diffusivity also has a dependence on pressure which is significant (Hofmeister, 2007), although it is unlikely to substantially impact the effective value. Furthermore, although we have incorporated radiative transport in PH06-R transport models using the radiative model from Hofmeister (2005), this radiative model is strictly applicable only to olivine and the strong dependence on grain size and other dependences on compositional properties controlling radiative behavior may need to be considered in greater detail (Hofmeister, 2005; 2007; Hofmeister and Yuen, 2007). Moreover, in light of disagreements regarding the accuracy of various measurement techniques of thermal conductivity and diffusivity at temperature (eg. Hofmeister, 2007; 2009; Beck et al., 2009), some consensus from the mineral physics community on the reliability of available data is ultimately desired.

While the uncertainties are real, fitting experiments indicate that the apparent thermal diffusivity may not be much different from the predictions of olivine as a lower thermal diffusivity will tend to require a prohibitively high mantle temperature (Fig. 2.3).

#### 2.4.5 Adjustable treatment of dependent parameters

Latent uncertainties are the cause for the treatment of the thermal diffusivity and the thermal expansivity as both free and temperature-dependent parameters. This treatment turns out to be more important for thermal expansion than diffusion as the effective thermal expansion coefficient from mineral physics turns out to be much higher than acceptable for all good-fitting plate model parameterizations, whereas good parameterizations can be resolved without adjusting heat transport properties (Fig. 2.3). As such, parameterization

of the thermal expansivity was necessary, whereas good fits could have been found without changing heat transport properties.

Most recent investigations into the consequences of variable thermal conductivity on lithospheric cooling (Honda and Yuen, 2001; 2004; McKenzie et al., 2005; Goutorbe, 2010) have used the theoretical conductivity model of Hofmeister (1999) which is composed of freely adjustable terms to fit experimental data. Honda and Yuen (2001; 2004) took advantage of this adjustable formulation and incorporated sensitivity analysis of the conductivity in their fits to depth and heat flow. On the other hand, McKenzie et al. (2005) and Goutorbe (2010) do not treat the conductivity as adjustable. However, the case of McKenzie et al. (2005) is notable as while they did not present the results of formal fitting and sensitivity analysis and did not treat any mineral physics term as adjustable, their model is apparently in agreement with geophysical observations. This is a significant deviation from our observation that one must at least lower the thermal expansion coefficient to fit observations.

Using the transport properties from McKenzie et al. (2005) and  $T_m=1315^\circ\text{C}$ , the effective thermal diffusivity is about  $0.9 \text{ mm}^2 \text{ s}^{-1}$  and Fig. 2.2a shows that the predicted subsidence rate of this model is about  $455 \text{ m My}^{-1/2}$ . Normally this model would require about a 20-30% lower coefficient of thermal expansion to fit observed subsidence, but McKenzie et al. (2005) were able to fit observations with no mineral physics adjustments. The nature of the disagreement is not entirely clear, although it seems that modeling techniques, the isostatic formulation and reference properties, and the initial mantle geotherm systematically increase our own predictions against theirs. In particular, the approximation of the role of isentropic melting on the initial geotherm can be significant, and this may account for a large fraction of the differences in our analysis (see next section).

Moreover, the enthalpy of melting lay among a number of other complexities of the same type which may be important. In particular, the properties of the lithosphere may be time dependent. Indeed, Korenaga (2007a) has already shown that the effective thermal expansivity may change rapidly over young lithosphere due to thermoviscoelastic effects. Similarly, petrological variations with depth arise due to melt depletion and extracted melt is incorporated in the crust (Afonso and Schutt, 2012). Variations in transport properties of these different materials may result in time dependence of the effective thermal diffusivity. The impact of such heterogeneities on the properties of the lithosphere is a primary subject of our next two chapters (3-4). However, it is notable that observed subsidence (Fig. 2.3) is strongly linear in  $t^{1/2}$  with only small systematic deviation at young ( $<5 \text{ Ma}$ ) ages, which may only support a weak signal from such characteristics. Such signals are much stronger when the crustal thickness is higher (Chapter 3-4), and such phenomena may be important in the interpretation of global variations in regional subsidence rate (Marty and Cazenave, 1989) and seafloor heat flow (Hasterok, 2010; Chapter 4), but our analysis can only clarify normal seafloor. It should be clear that our current results are intended as benchmarks for simple isothermal mantle plate models with temperature-dependent properties. A principal observation that we have established is that the simple plate models developed since the tectonics revolution only succeed to first-order. In chapter 3, we will show that more physically comprehensive models of the thermal evolution of oceanic lithosphere achieve agreement with the data without large *ad hoc* changes to input parameters.

### 2.4.6 Mantle potential temperature

McKenzie et al. (2005) argued that a potential temperature of  $1315^{\circ}\text{C}$  was most appropriate based on predictions of crustal thickness from the melt production model of McKenzie and Bickle (1988). For oceanic crust with a thickness of  $6\pm 1$  km, McKenzie and Bickle's (1988) melting model predicts that mantle potential temperature is about  $1300\pm 20^{\circ}\text{C}$  (Brown and White, 1994). Higher temperatures systematically elevate crustal thickness. Alternatively, the equilibrium thermodynamic model, MELTS (Ghiorso and Sack, 1995; Asimow et al., 2001), predicts higher mantle temperature for passive isentropic decompression melting at around  $1375\pm 30^{\circ}\text{C}$  for normal oceanic crust. Although both predictions do not disagree with geochemical estimates by Herzberg et al. (2007), MELTS is in better accord with our numerical observations, so we contend that models with mantle potential temperature on the order of  $1400^{\circ}\text{C}$  may not be unrealistic. Moreover, this large difference in the melt productivity predictions between models indicates that although McKenzie et al. (2005) include this component in their thermal calculations, the impact on thermal structure involves significant uncertainty and may have been overestimated.

### 2.4.7 Constraints provided by topography and heat flow

Both heat flow and topography are sensitive to thermal diffusivity, mantle temperature, and plate thickness, but the topography has an additional sensitivity to thermal expansivity. Because the apparent thermal expansivity can be freely adjusted in our analysis to compensate for the relative values of the apparent thermal diffusivity and the mantle temperature, the surface heat flux constrains plate cooling models much more tightly than topography. Fig. 2.7 shows the  $R^2$  field for topography in an alpha composite (shaded transparency) overlaying the  $R^2$  field for heat flow (colored). The  $R^2$  field for heat flow depends on the mantle temperature, whereas the  $R^2$  field for topography is the same for all mantle temperatures. For a given plate thickness and mantle temperature, the fit to heat flow requires a tightly constrained thermal diffusivity, whereas the topography can fit a large thermal diffusivity range as the thermal expansivity is adjusted to yield the best possible fit. This feature of analysis is notable because the observation of seafloor 'flattening' is usually given greater attention as an indicator of plate behavior due to its more dramatic effect on observations; up to 103 meter surface displacements (from the linear subsidence in  $t^{1/2}$  trend) compared to a  $\sim 6$   $\text{mW m}^{-2}$  difference in heat flow.

### 2.4.8 Treatment of old-age topography, regional behaviors, and the problem of 'flattening'

We have studied plate models in part for conservative reasons, and in part because the plate model appears to be the best fitting mathematical idealization of the processes thought to cause subsidence and eventual 'flattening' of topography and heat flow. However, the precise relationship between elevated heat flow and topography at old age and the phenomenology of cooling oceanic lithosphere remains controversial (Parsons and Sclater, 1977; Marty and Cazenave, 1989; Carlson and Johnson, 1994; Calcagno and Cazenave, 1994; Hillier and

Watts, 2005; Crosby et al., 2006; Zhong et al., 2007; Crosby and McKenzie, 2009; Korenaga and Korenaga, 2008; Hillier, 2010).

Marty and Cazenave (1989) showed that regional subsidence rates are in good agreement with normal half-space behavior (linear subsidence in  $t^{1/2}$ ) until a deflection occurs between 65 and 100 Ma, although some Atlantic regions may be consistent with half-space behavior to much larger ages. Interestingly, in their analysis only Pacific seafloor apparently exhibits the type of asymptotic flattening expected from plate models. Nearly all of the remaining global seafloor show linear subsidence until terminus or a departure uncharacteristic of plate models occurs, such as a dramatic sign change in the subsidence rate. Crosby and McKenzie (2006) argue that an abrupt sign change in subsidence can be explained by an initially large detachment of basal lithosphere at the onset of small-scale convection as observed in early numerical small-scale convection experiments (Houseman and McKenzie, 1982), but recent small-scale convection studies with realistic flow laws appear to be in better agreement with the more gradual deflection of plate models (Zlotnik et al., 2008; Afonso, et al. 2008). On the other hand, how small-scale convection impacts surface topography depends on rheology and on the isostatic treatment of density variations near the base of the lithosphere (Afonso, et al. 2008). Moreover, old age Atlantic seafloor is not easily compared to the Pacific basin because the low velocity plate is covered by thick sediments almost everywhere (Divins, 2011), and most old age seafloor is in close proximity to (or may be part of) passive continental margins (Mooney, et al. 1998). The former implies that there may be an important role for sediment insulation effects in thermal evolution (eg. Hutnak and Fisher, 2007) and proximity to passive margins means that any 'flattening' signal may be related to crustal thickening, although the analysis of seafloor along Atlantic margins by Winterbourne et al. (2009) indicated that large discrepancies between these basins may be accounted for.

Consistent with Crosby et al. (2006), our treatment of observed topography (i.e., removal of elevated points at old age; Fig. 2.3) supposes that the 'bulge' in global data around 100-130 Ma is not a feature explained by plate models, but that older bathymetry may be properly related to the plate model as it may not be affected by the same processes responsible for the bulge. Hillier and Watts (2005) showed that after filtering out anomalous seafloor on various scales in the North Pacific, the bulge is effectively removed and topography appears to be in strong agreement with plate-like flattening. However, as noted above, the data reductions from Marty and Cazenave (1989) seem to suggest that Pacific seafloor may be the only region where such an analysis would be successful, so applying this treatment to global data may be presumptuous. Normally this would have been problematic for the present study of plate models, as we have used results of global topographic analyses (Korenaga and Korenaga, 2008; Hillier, 2010), but it turns out that the 'flattening' observed in global topography is not appreciably different from flattening in the Pacific basin as evaluated by Hillier and Watts (2005). This is probably due to the rejection of 'anomalous' old-age seafloor in the Atlantic which is already sparse.

#### 2.4.9 Small-scale convection, plate thickness, and the geoid

Observations of geoid slope over seafloor age inferred from geoid offsets along fracture zones have been used to constrain plate models (Sandwell and Schubert, 1982; Cazenave et al.,



1983; Driscoll and Parsons, 1988; Freedman and Parsons, 1990), although we have not considered it since even pronounced features in geoid-slope are poorly understood. Although the data exhibits a high variance, in general most fracture zone geoid slope data show a high at young ages followed by a rapid decrease, an abrupt increase around 30 Ma, and finally a decrease to about the value found around 20 Ma at old age (Fig. 2.8). The usual interpretation of this structure is that the young ( $<30$  Ma) lithosphere behaves as a thin ( $\sim 60$  km) plate and abruptly transitions to behaving like a nominally thick ( $\sim 90$  km) plate (see above references). However, if elevated geoid slope at young ( $<20$  Ma) ages is explained by long-wavelength signals associated with proximity to ridges, or a complexity in cooling model properties leading to age dependent transport properties or thermal expansivity, then the classical interpretation may no longer be valid. In this case, one could use a thick plate or a half-space having a normal geoid slope of around  $10 \text{ cm Ma}^{-1}$ , and consider deviations anomalous. A plot of geoid slope predicted by the current model RT1 (Fig. 2.8) using the one-dimensional geoid model of Haxby and Turcotte (1978) shows elevated slope inconsistent with the data and this interpretation, but again the source of misfit remains unclear for any structure in the data beyond zero order.

Moreover, the classical explanation is problematic because there is no additional convincing evidence for plate behavior or shallow convection at young ages (Crosby and McKenzie, 2009). Simulations by Zlotnik et al. (2008) and Afonso et al. (2008) indicate that small scale convection develops when the effective viscosity drops below  $\sim 10^{20} \text{ Pa s}$  and the thickness of low viscosity lithosphere is great enough to promote instability (usually where age is  $>50$  Ma). Experimental flow laws for olivine (Korenaga and Karato, 2008) indicate that this viscosity may only occur when the wet dislocation creep regime is activated, otherwise the grain size must be small for the effective viscosity to be this low in the diffusion creep regime. Additionally, if dislocation creep is responsible for small-scale convection this may agree with the observation that plate behavior is most apparent over the fast-moving Pacific plate as the stress dependence of dislocation creep will allow low viscosities to be reached in the presence of strong basal tractions, which are also known to result in more vigorous three-dimensional convective behaviors (van Hunen et al., 2003; Sleep, 2011a;b). As such, low-order structure in geoid slope cannot yet be explained.

These interpretations are also consistent with the hypothesis that any boundary layer behavior of the oceanic lithosphere is best approximated by a relatively thick plate. Moreover, this 'thick plate' interpretation seems to be in good accord with limited tomographic evidence for a thin plate. The surface wave tomography from Ritzwoller et al. (2004) indicated that there may be a strong reheating signal around 70-100 My, suggesting an average plate thickness on the order of 100-120 km, but this is an exception to previous surface wave studies (Forsyth, 1977; Zhang and Lay, 1999), and more recent surface wave tomography studies (Maggi et al. 2006; Priestly and McKenzie, 2006) show evidence of largely monotonic thickening of cool oceanic lithosphere which extends down to about 130-150 km beneath old Pacific seafloor. This is in good agreement with the high end of our results for constant heat transport and PH06-R models, and best fits to topography (eg. model RT1) are associated with thick plates precisely in this range (Fig. 2.3a,c).

## 2.5 CONCLUSIONS

A new sensitivity and fitting analysis of plate cooling models to seafloor topography and heat flow indicates that the effective properties of oceanic lithosphere may need to be reevaluated, or that additional phenomena beyond the conditions of simple mineral physics plate models are important. All good fitting parameterizations predict that, a) the apparent thermal expansivity is about 35-40% lower than for forsterite, b) effective thermal diffusivity is about  $1.1 \pm 0.1 \text{ mm}^2 \text{ s}^{-1}$ , c) net seafloor heat flux is  $31.5 \pm 1.3 \text{ TW}$ , d) and plate thickness is about  $125 \pm 15 \text{ km}$ .

Two reference models (R1 and RT1) are resolved which do not require adjustments to heat transport properties to fit observations, include a large radiative contribution to conductivity, and agree with evidence of mantle temperature. Model R1 provides the best joint fit to depth and heat flow with a thick plate (125 km) and modest mantle temperature ( $1360^\circ\text{C}$ ), whereas model RT1 biases the fit to topography with a thicker plate (135 km) and higher mantle temperature ( $1400^\circ\text{C}$ ), although scatter in the data shows that the fit to heat flow remains good.

	Model:	L1	R1	RT1	GDH1	PS77
$D_A$ (mm <sup>2</sup> s <sup>-1</sup> )	Apparent thermal diffusivity	0.96	1.113	1.106	0.804	0.804
$C_p$ (kJ kg <sup>-1</sup> K <sup>-1</sup> )	Isobaric specific heat	–	–	–	1.172	1.172
$F$	Lattice diffusivity reduction ratio	1.0	1.0	1.0	–	–
$(\rho C_p)_E$ (kJ m <sup>-3</sup> K <sup>-1</sup> )	Effective vol. heat capacity	3.94	3.94	3.94	3.9	3.9
$k_E$ (W m <sup>-1</sup> K <sup>-1</sup> )	Effective thermal conductivity	3.78	4.39	4.36	3.14	3.14
$L$ (km)	Plate thickness	105.7	123.6	134.9	95	125
$T_m$ (°C)	Mantle temperature	1446	1358	1402	1450	1333
$\alpha_{EM}$ ( $\times 10^{-5}$ K <sup>-1</sup> )	Effective thermal expansivity	3.85	3.82	3.84	3.89 <sup>a</sup>	3.82 <sup>a</sup>
$\alpha_A$ ( $\times 10^{-5}$ K <sup>-1</sup> )	Apparent thermal expansivity	2.39	2.39	2.29	3.1	3.28
$H$	Expansivity reduction ratio	0.621	0.625	0.596	0.8	0.86
$\rho_0$ (kg m <sup>-3</sup> )	Mantle density ( $T=0^\circ\text{C}$ )	3300	3300	3300	3330	3330
$\rho_w$ (kg m <sup>-3</sup> )	Deep seawater density	1065	1065	1065	1000	1000
$b$ (m My <sup>-1/2</sup> )	Normal subsidence rate	321	321	321	365	355
$R$ (km)	Ridge height	2.675	2.675	2.675	2.6	2.5
$Q_{sf}$ (TW)	Net seafloor heat flux	31.4	31.5	32.4	29.1 <sup>b</sup>	26.4 <sup>b</sup>

<sup>a</sup> Effective thermal expansivity when the experimental values from Bouhifd et al. (1996) are applied. The values given by the original authors are thus the apparent values,  $\alpha_A$ , which differ from the effective values from mineral physics,  $\alpha_{EC}$ , by the factor  $H$  as given.

<sup>b</sup> Net seafloor heat flux as determined with the area-age distribution from Müller et al. (2008).

TABLE 2.1: Tabulated properties for models L1, R1, and RT1 (this work) along with those for former reference models GDH1 (Stein and Stein, 1992) and PS77 (Parsons and Sclater, 1977). Model RT1 is the preferred model of this work

Model:		Constant heat transport properties				
$D_A$ (mm <sup>2</sup> s <sup>-1</sup> )	Apparent thermal diffusivity	1.26 ± 0.08	1.17 ± 0.08	1.08 ± 0.08	1.01 ± 0.08	0.95 ± 0.07
$C_p$ (kJ kg <sup>-1</sup> K <sup>-1</sup> )	Isobaric specific heat	1.172	1.172	1.172	1.172	1.172
$F$	Lattice diffusivity reduction ratio	–	–	–	–	–
$(\rho C_p)_E$ (kJ m <sup>-3</sup> K <sup>-1</sup> )	Effective vol. heat capacity	3.87	3.87	3.87	3.87	3.87
$k_E$ (W m <sup>-1</sup> K <sup>-1</sup> )	Effective thermal conductivity	4.88 ± 0.31	4.53 ± 0.31	4.18 ± 0.31	3.91 ± 0.31	3.68 ± 0.27
$L$ (km)	Plate thickness	137 ± 16	133 ± 16	128 ± 16	123 ± 15	120 ± 14
$T_m$ (°C)	Mantle temperature	<b>1300</b>	<b>1350</b>	<b>1400</b>	<b>1450</b>	<b>1500</b>
$\alpha_{EM}$ (× 10 <sup>-5</sup> K <sup>-1</sup> )	Effective thermal expansivity	3.8	3.83	3.86	3.89	3.92
$\alpha_A$ (× 10 <sup>-5</sup> K <sup>-1</sup> )	Apparent thermal expansivity	2.35 ± 0.11	2.37 ± 0.11	2.35 ± 0.12	2.33 ± 0.12	2.35 ± 0.12
$H$	Expansivity reduction ratio	0.62 ± 0.03	0.62 ± 0.03	0.61 ± 0.03	0.6 ± 0.03	0.6 ± 0.03
$\rho_0$ (kg m <sup>-3</sup> )	Mantle density ( $T=0$ °C)	3300	3300	3300	3300	3300
$\rho_w$ (kg m <sup>-3</sup> )	Deep seawater density	1065	1065	1065	1065	1065
$b$ (m My <sup>-1/2</sup> )	Normal subsidence rate	321	321	321	321	321
$R$ (km)	Ridge height	2.675	2.675	2.675	2.675	2.675
$Q_{sf}$ (TW)	Net seafloor heat flux	31.5 ± 1.0	31.5 ± 1.0	31.5 ± 1.0	31.4 ± 1.0	31.6 ± 1.0
Model:		PH06				
$D_A$ (mm <sup>2</sup> s <sup>-1</sup> )	Apparent thermal diffusivity	1.21 ± 0.11	1.12 ± 0.1	1.04 ± 0.09	0.96 ± 0.08	0.9 ± 0.08
$C_p$ (kJ kg <sup>-1</sup> K <sup>-1</sup> )	Isobaric specific heat	–	–	–	–	–
$F$	Lattice diffusivity reduction ratio	1.28 ± 0.12	1.18 ± 0.11	1.09 ± 0.1	0.99 ± 0.08	0.91 ± 0.08
$(\rho C_p)_E$ (kJ m <sup>-3</sup> K <sup>-1</sup> )	Effective vol. heat capacity	3.92	3.93	3.94	3.95	3.96
$k_A$ (W m <sup>-1</sup> K <sup>-1</sup> )	Apparent thermal conductivity	4.74 ± 0.43	4.4 ± 0.4	4.1 ± 0.36	3.8 ± 0.32	3.56 ± 0.32
$L$ (km)	Plate thickness	120 ± 18	116 ± 17	111 ± 16	107 ± 16	104 ± 15
$T_m$ (°C)	Mantle temperature	<b>1300</b>	<b>1350</b>	<b>1400</b>	<b>1450</b>	<b>1500</b>
$\alpha_{EC}$ (× 10 <sup>-5</sup> K <sup>-1</sup> )	Effective thermal expansivity	3.76	3.79	3.82	3.85	3.88
$\alpha_{AC}$ (× 10 <sup>-5</sup> K <sup>-1</sup> )	Apparent thermal expansivity	2.41 ± 0.15	2.42 ± 0.15	2.41 ± 0.15	2.42 ± 0.16	2.41 ± 0.16
$H$	Expansivity reduction ratio	0.64 ± 0.04	0.64 ± 0.04	0.63 ± 0.04	0.63 ± 0.04	0.62 ± 0.04
$\rho_0$ (kg m <sup>-3</sup> )	Mantle density ( $T=0$ °C)	3300	3300	3300	3300	3300
$\rho_w$ (kg m <sup>-3</sup> )	Deep seawater density	1065	1065	1065	1065	1065
$b$ (m My <sup>-1/2</sup> )	Normal subsidence rate	321	321	321	321	321
$r$ (km)	Ridge height	2.675	2.675	2.675	2.675	2.675
$Q_{sf}$ (TW)	Net seafloor heat flux	31.4 ± 1.2	31.4 ± 1.2	31.4 ± 1.2	31.4 ± 1.2	31.5 ± 1.1
Model:		PH06-R				
$D_A$ (mm <sup>2</sup> s <sup>-1</sup> )	Apparent thermal diffusivity	1.21 ± 0.1	1.11 ± 0.09	1.04 ± 0.08	0.97 ± 0.07	0.9 ± 0.06
$C_p$ (kJ kg <sup>-1</sup> K <sup>-1</sup> )	Isobaric specific heat	–	–	–	–	–
$F$	Lattice diffusivity reduction ratio	1.09 ± 0.1	1.0 ± 0.09	0.93 ± 0.08	0.86 ± 0.07	0.8 ± 0.07
$(\rho C_p)_E$ (kJ m <sup>-3</sup> K <sup>-1</sup> )	Effective vol. heat capacity	3.94	3.95	3.96	3.97	3.98
$k_E$ (W m <sup>-1</sup> K <sup>-1</sup> )	Effective thermal conductivity	4.77 ± 0.4	4.39 ± 0.36	4.12 ± 0.32	3.85 ± 0.28	3.58 ± 0.24
$L$ (km)	Plate thickness	130 ± 17	125 ± 15	121 ± 14	118 ± 14	114 ± 12
$T_m$ (°C)	Mantle temperature	<b>1300</b>	<b>1350</b>	<b>1400</b>	<b>1450</b>	<b>1500</b>
$\alpha_{EC}$ (× 10 <sup>-5</sup> K <sup>-1</sup> )	Effective thermal expansivity	3.79	3.82	3.85	3.88	3.91
$\alpha_{AC}$ (× 10 <sup>-5</sup> K <sup>-1</sup> )	Apparent thermal expansivity	2.43 ± 0.15	2.44 ± 0.15	2.43 ± 0.15	2.44 ± 0.14	2.43 ± 0.13
$H$	Expansivity reduction ratio	0.64 ± 0.04	0.64 ± 0.04	0.63 ± 0.03	0.63 ± 0.03	0.62 ± 0.03
$\rho_0$ (kg m <sup>-3</sup> )	Mantle density ( $T=0$ °C)	3300	3300	3300	3300	3300
$\rho_w$ (kg m <sup>-3</sup> )	Deep seawater density	1065	1065	1065	1065	1065
$b$ (m My <sup>-1/2</sup> )	Normal subsidence rate	321	321	321	321	321
$r$ (km)	Ridge height	2.675	2.675	2.675	2.675	2.675
$Q_{sf}$ (TW)	Net seafloor heat flux	31.4 ± 1.1	31.5 ± 1.0	31.5 ± 1.0	31.6 ± 1.0	31.6 ± 1.0

TABLE 2.2: Tabulated properties for constant heat transport, PH06 and PH06-R models with different mantle temperatures. Bounds indicate values where joint fit  $R^2 > 0.99$

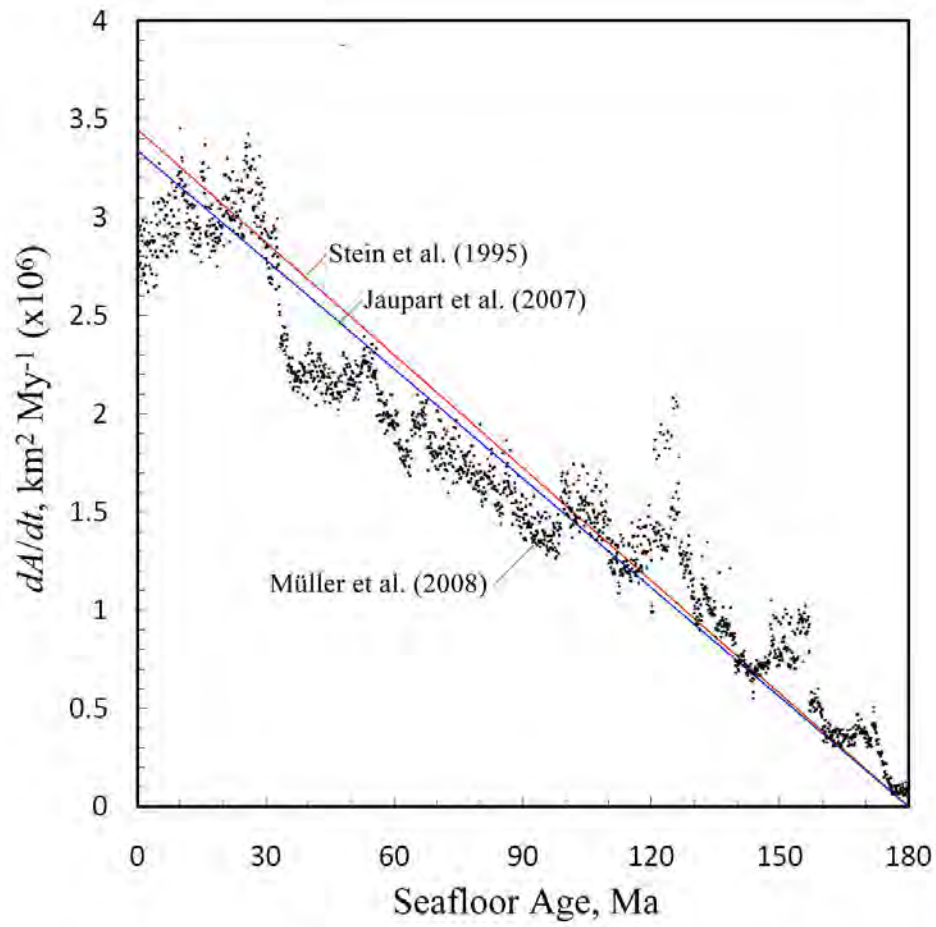


FIGURE 2.1: The distribution of seafloor area over age as predicted by the analytical models from Stein et al. (1995) and Jaupart et al. (2007) and our analysis using global area-age grids from Müller et al. (2008). Analytical models appear as straight lines while the global analysis is given in 0.1 Ma bins.

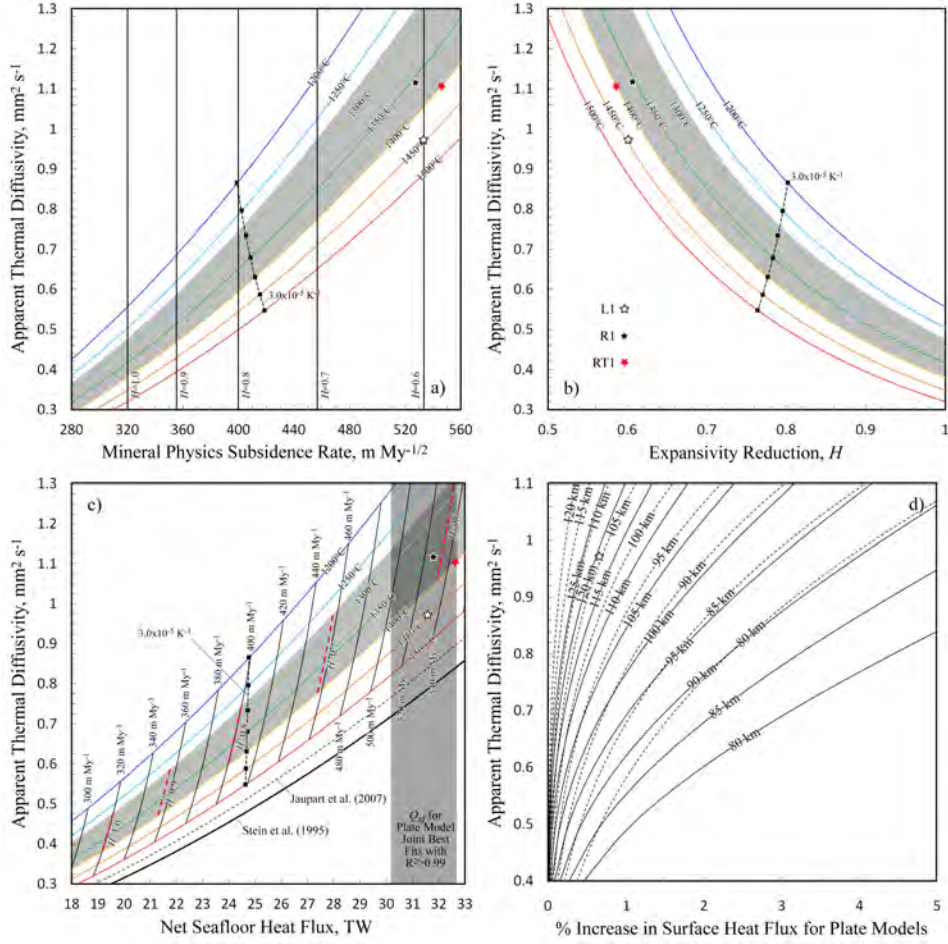
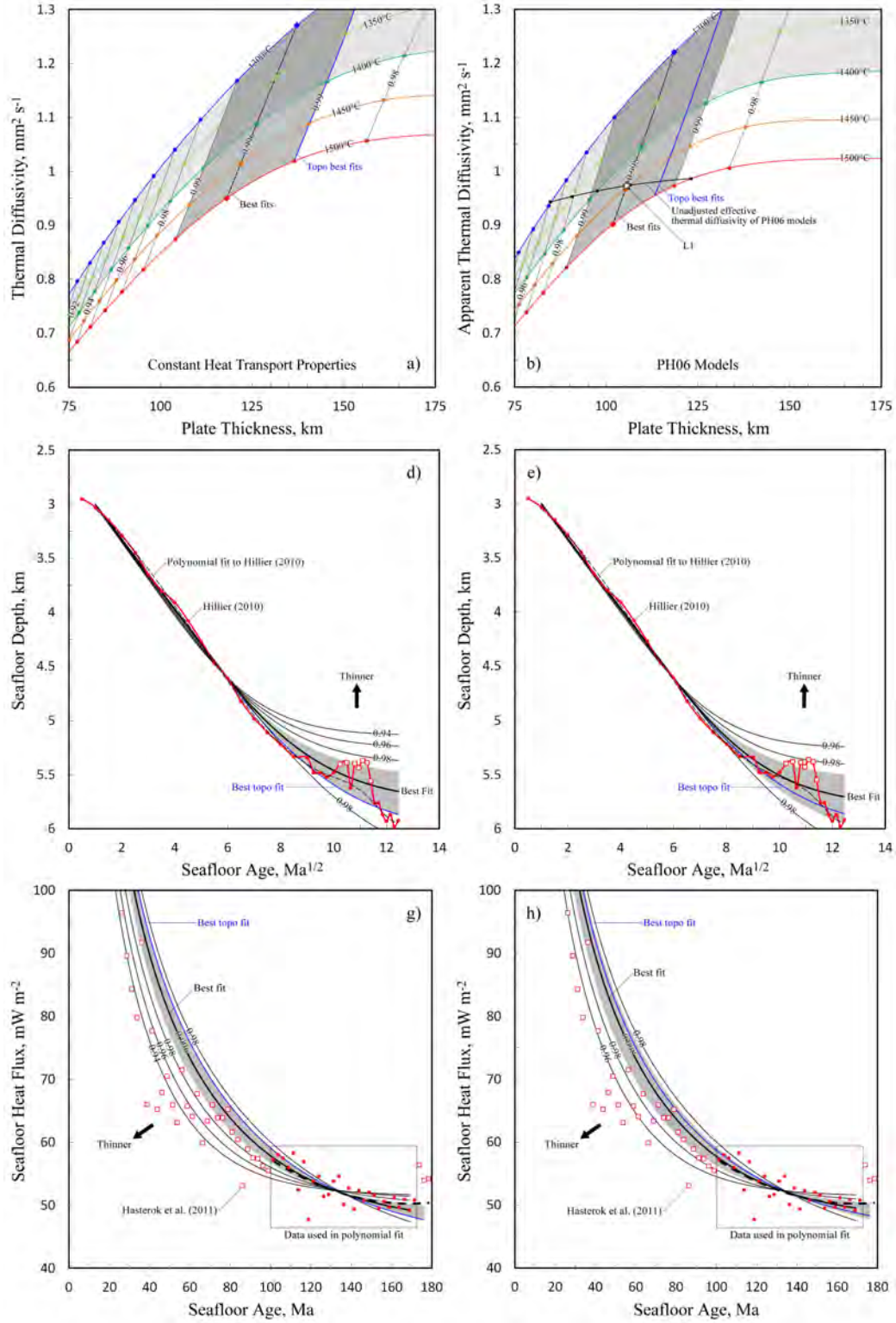


FIGURE 2.2: (a) The relationship between effective thermal diffusivity and the 'mineral physics subsidence rate' (see Section 2.3.1). Predictions for mantle temperature of  $1340 \pm 60^\circ \text{C}$  are highlighted. Vertical bars indicate the thermal diffusivity predicted for various  $H$  values. The box symbols and dashed curve indicate the thermal diffusivity predicted when the thermal expansivity is  $3.0 \times 10^{-5} \text{ K}^{-1}$  for different temperatures. (b) Relationship between effective thermal diffusivity and the expansivity reduction ratio. (c) Relationship between effective thermal diffusivity and net seafloor heat flux. Mineral physics subsidence rates and expansivity reduction ratios are indicated. The black dashed and thick solid curves are the net seafloor heat flux predictions for a  $1500^\circ \text{C}$  mantle temperature when the area-age seafloor distribution is that from Jaupart et al. (2007) and Stein et al. (1995), respectively. The  $\sim 31.5 \pm 1.3 \text{ TW}$  range is highlighted is the range for good fit plate models determined through our fitting analysis. (d) The percent increase in seafloor heat flux for plate models having properties from panel (c). Solid lines are constant diffusivity predictions and dashed lines are PH06 model predictions. Reference models L1, R1, and RT1 are indicated.





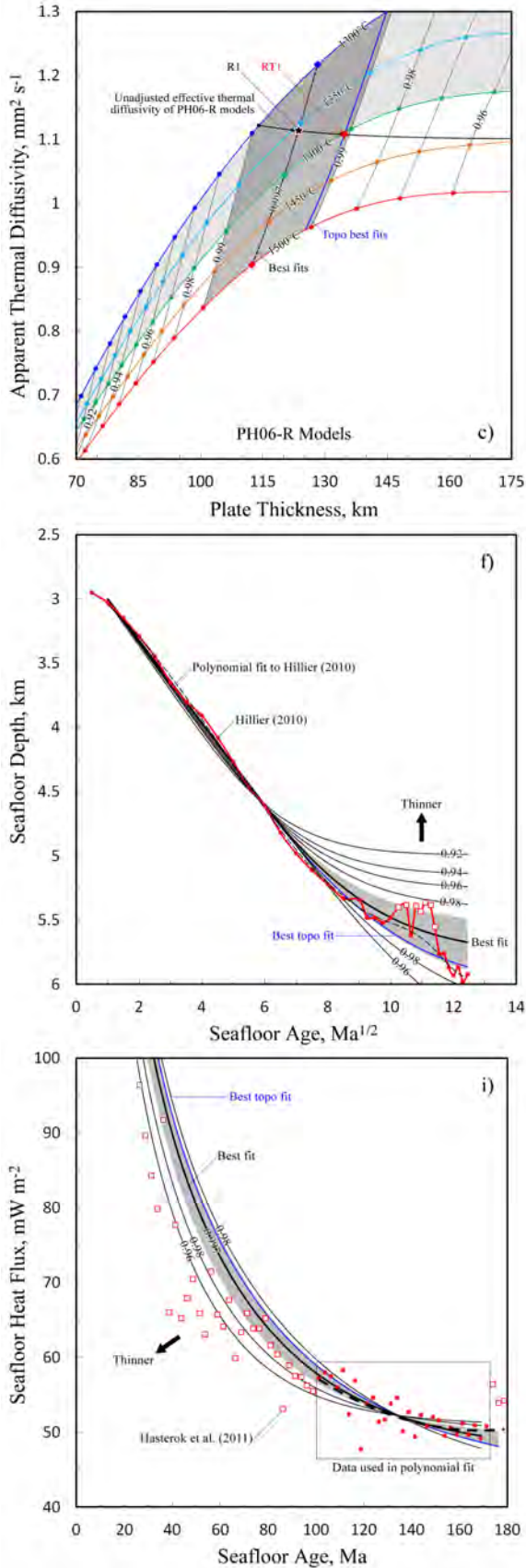
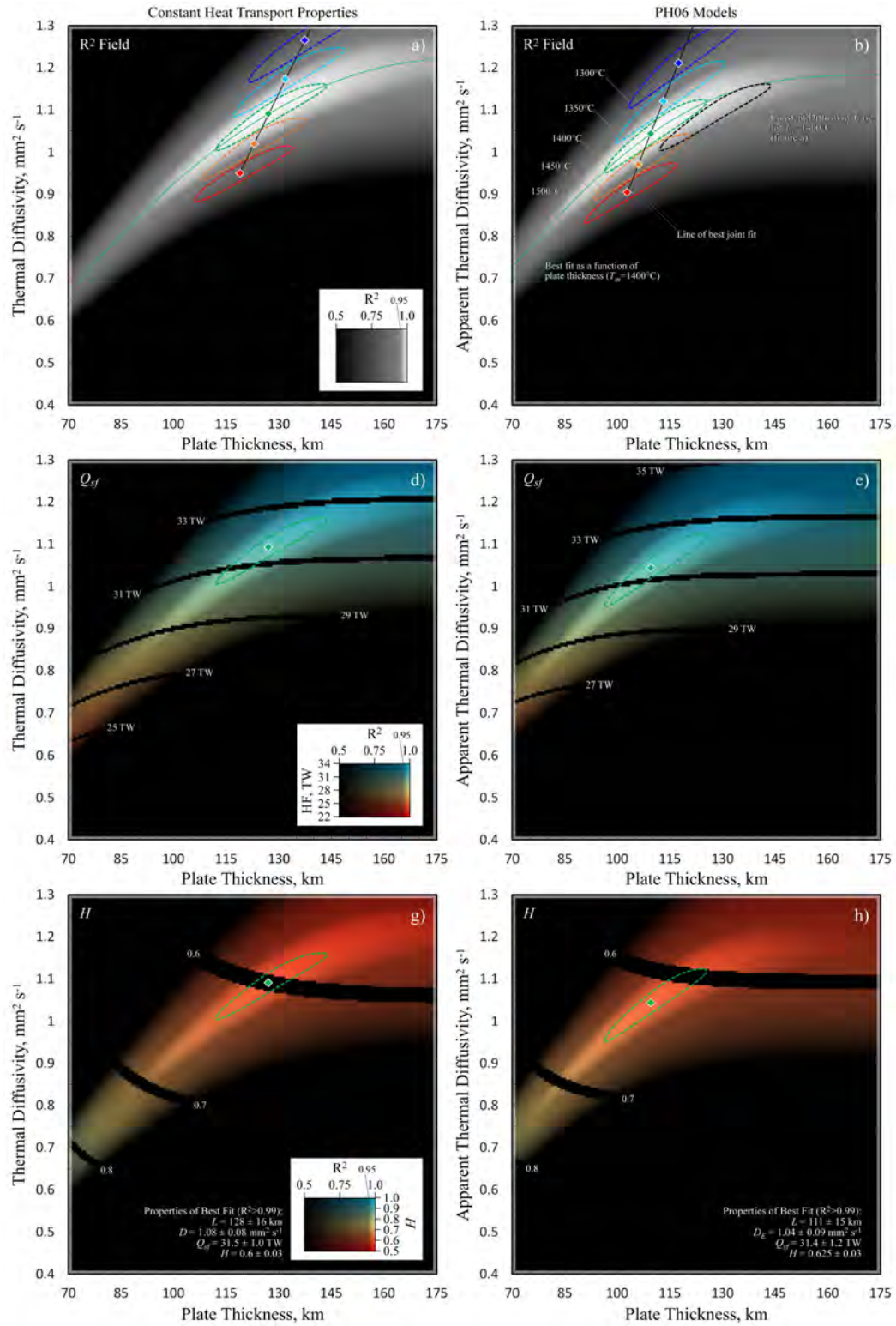


FIGURE 2.3: Results of fitting experiments for constant thermal diffusivity models (first column), PH06 models (second column), and PH06-R models (third column). Panels (a)-(c) show colored curves indicating the best fitting thermal diffusivity as a function of plate thickness for different mantle temperatures. The goodness of fit varies with plate thickness as indicated by solid 'isofitness' lines and circles labeled with their corresponding  $R^2$  values. The thick dashed line is the line of best fit and the thick solid blue line indicates the best fits to topography alone. The unadjusted effective thermal diffusivity as a function of mantle temperature is also shown for PH06 (3b) and PH06-R (3c) models, and reference models L1, R1 and RT1 are indicated. Predictions for  $T_m = 1350 \pm 50^\circ\text{C}$  and  $R^2 > 0.99$  are highlighted. Panels (d)-(f) show the subsidence of joint fits against the topography from Hillier (2010). The open boxes indicate neglected points in the polynomial fit (thin dashed curve) to Hillier (2010), the highlighted area is the range for parameterizations with  $R^2 > 0.99$ , and the thick blue curve is the best fit to topography. Panels (g)-(i) show the same models as above, except heat flow predictions are represented against the heat flow data from Hasterok et al. (2011). The thick dashed line is the polynomial fit to Hasterok's data in the boxed range. The arrows point in the direction the best fit model predictions tend to go when the plate thickness is decreased (compare to panels (a)-(c)). This figure continues on the next page.





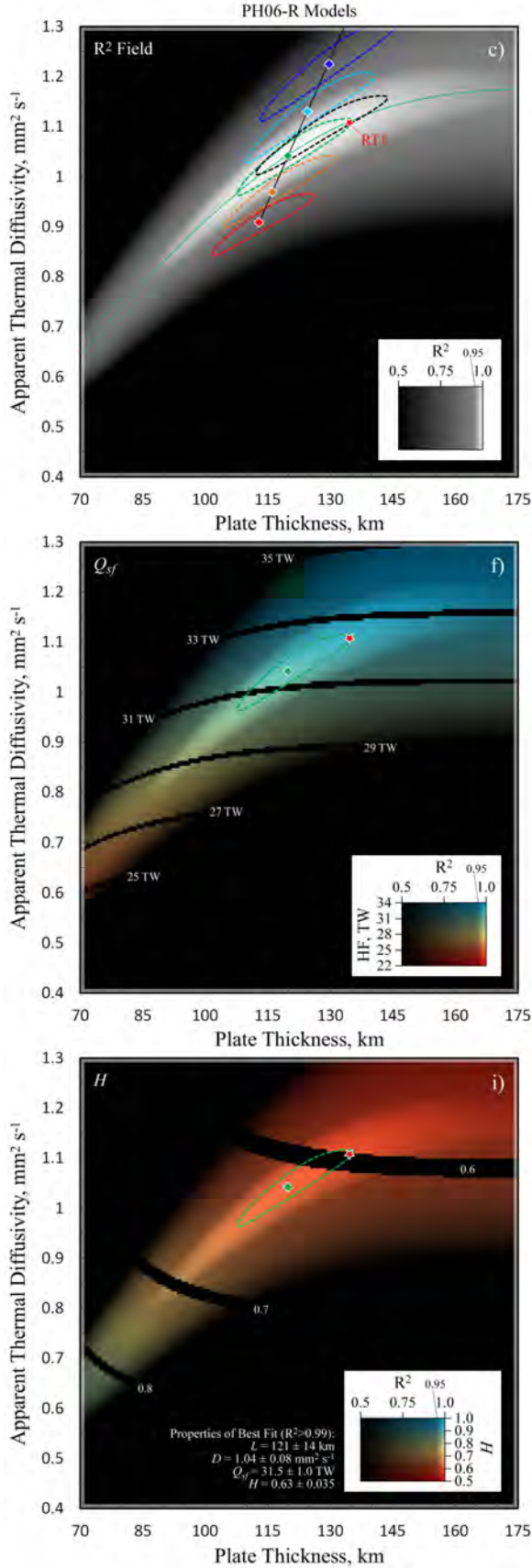


FIGURE 2.4: Results of fitting experiments for constant thermal diffusivity models (first column), PH06 models (second column), and PH06-R models (third column). Panels (a)-(c) are comparable to Figures 2.3a-c, showing the  $R^2$  fields for the case of  $T_m = 1400^\circ\text{C}$  and with a line of best fitting thermal diffusivity as a function of mantle temperature. The diamonds show the overall best fit models and the dashed ellipsoids are isofitness lines where  $R^2 = 0.99$  for mantle temperatures  $1300\text{--}1500^\circ\text{C}$ . For comparison, in panels (b)-(c) the  $0.99$  isofitness ellipsoid for  $T_m = 1400^\circ\text{C}$  constant thermal diffusivity models is indicated. Panels (d)-(f) show the  $R^2$  field in an alpha composite over the net seafloor heat flux, and Panels (g)-(i) show the  $R^2$  field in an alpha composite over the thermal expansivity reduction factor,  $H$ . This figure continues on the next page.

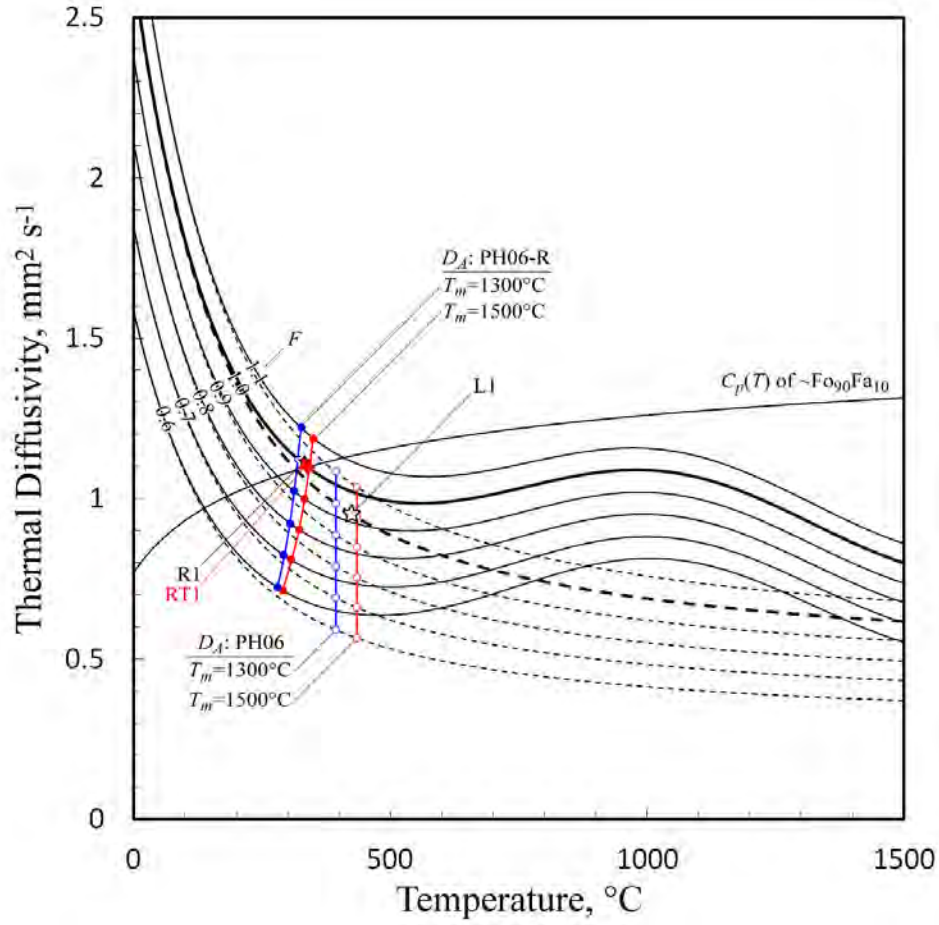


FIGURE 2.5: Thermal diffusivity and specific heat (in units of  $\text{kJ kg}^{-1} \text{K}^{-1}$ ; from Berman and Aranovich, 1996) of isotropic  $\sim\text{Fo}_{90}\text{Fa}_{10}$  as a function of temperature with the thermal conductivity artificially scaled by the factor  $F$ . The dashed curves are the lattice diffusivity only from Pertermann and Hofmeister (2006) and the solid curves are the lattice diffusivity with a radiative contribution to conductivity (Hofmeister, 2005). The open (lattice only) and solid (lattice + radiative) circles indicate the effective thermal diffusivity of each transport model when the initial half-space cooling temperature is  $1300^\circ\text{C}$  (blue) and  $1500^\circ\text{C}$  (red).

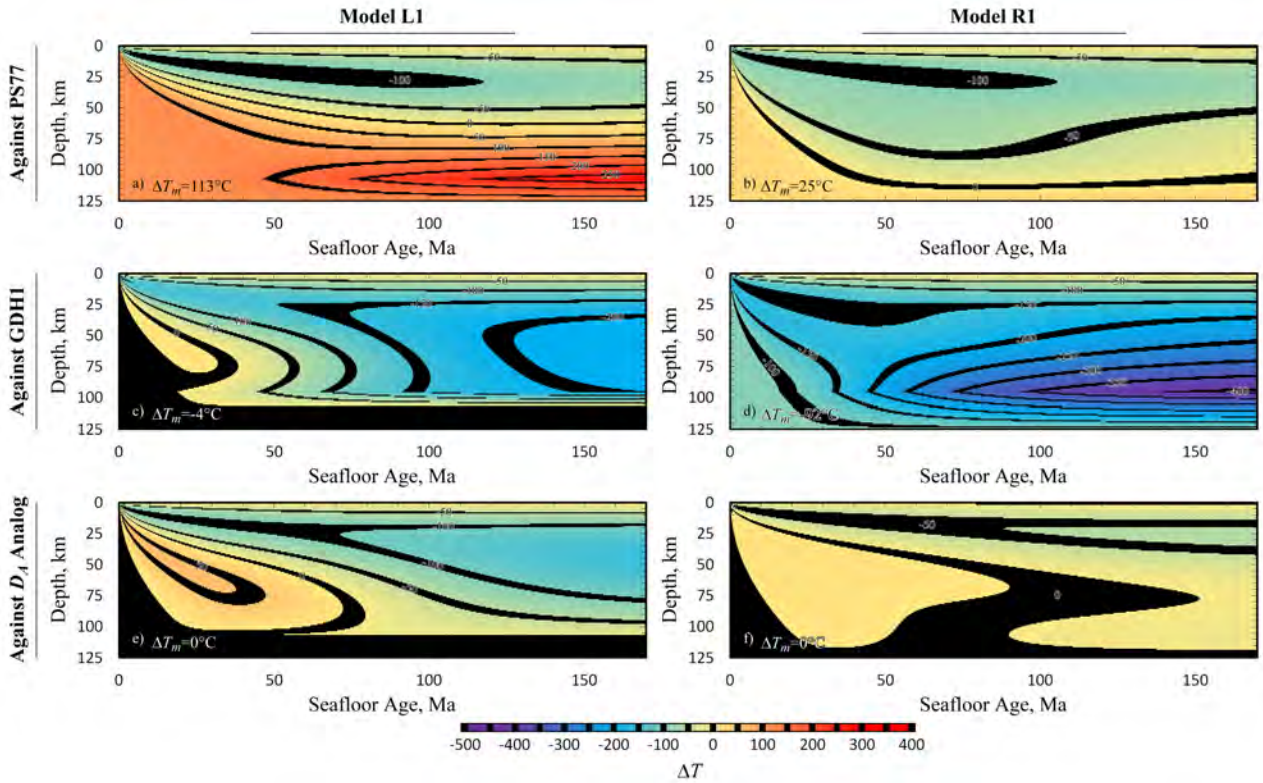


FIGURE 2.6: This figure shows 'difference geotherms', or the  $\Delta T(z, t)$  of a case model (columns) minus a reference model (rows). The properties of models in panels (a)-(d) are as given in Table 2.1. The  $D_E$  analog models in panels (e)-(f) have all the same properties as case models L1 and R1, respectively, excepting that constant heat transport properties are used. The large temperature differences found near the base of the plate are due to different plate thicknesses and mantle temperature. The difference in ambient mantle temperature  $\Delta T_m$  is given for each model comparison. Note that contours are defined by  $10^\circ\text{C}$  intervals, so their thickness is an indicator of thermal gradients (in  $\Delta T$ ), in addition to their spacing.



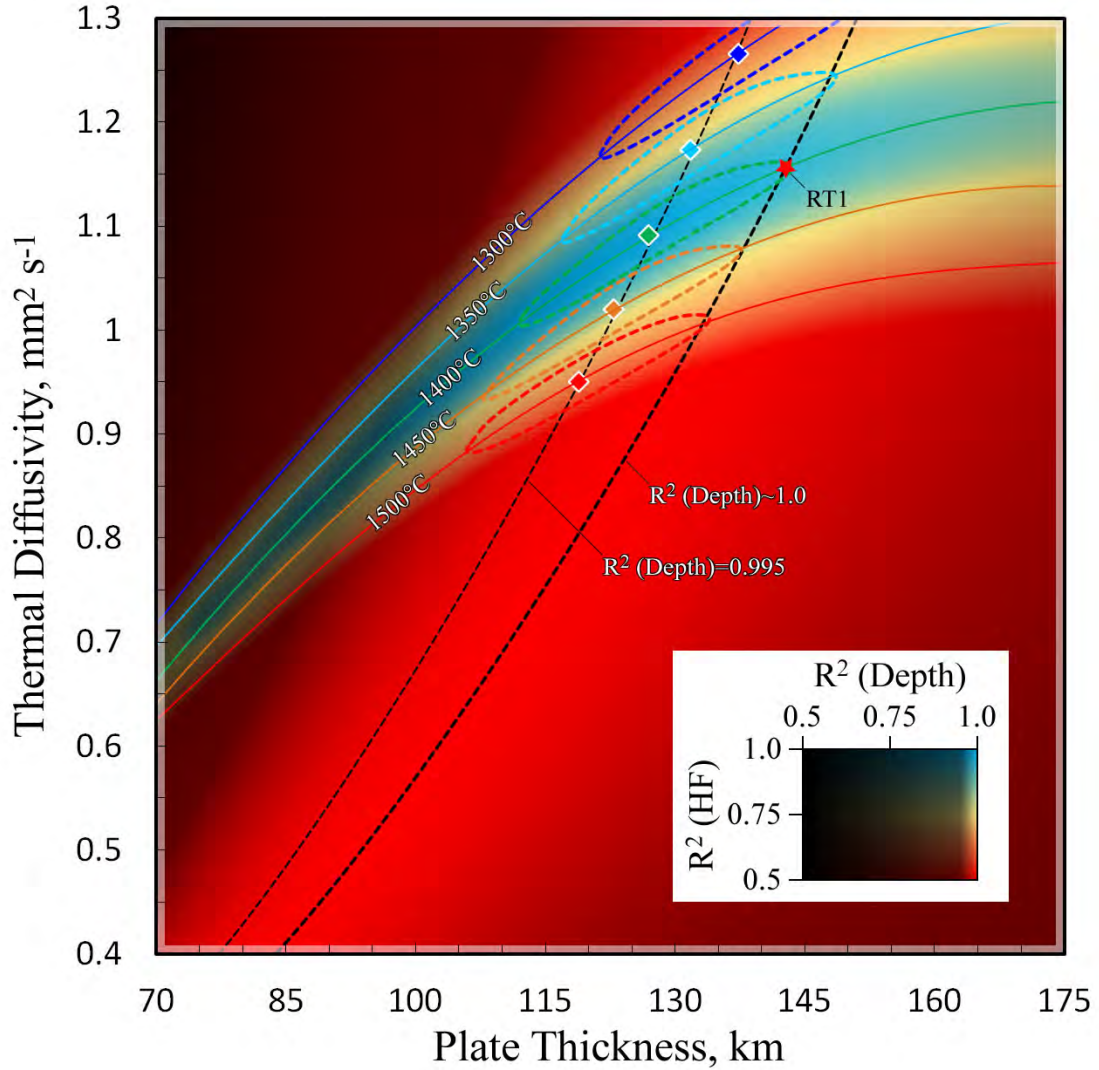


FIGURE 2.7: This figure shows the  $R^2$  fields of constant thermal diffusivity models for the fit to heat flow (for  $T_m = 1400^\circ\text{C}$ ) and seafloor topography (no dependence on  $T_m$ ). The  $R^2$  field for the fit to topography overlays the  $R^2$  field for heat flow in an alpha composite. The colored curves indicate the best fit thermal diffusivity as a function of plate thickness for mantle temperature between  $1300$  to  $1500^\circ\text{C}$  (comparable to the curves for joint fits in Fig. 2.3a), and the dashed ellipsoids indicate where  $R^2=0.99$ , and diamonds indicating the best fit for the given mantle temperature. The two black curves show the best fit to depth (thick dashed) and the fit to depth corresponding to the best joint fit (thin dashed,  $R^2 \sim 0.995$ ).

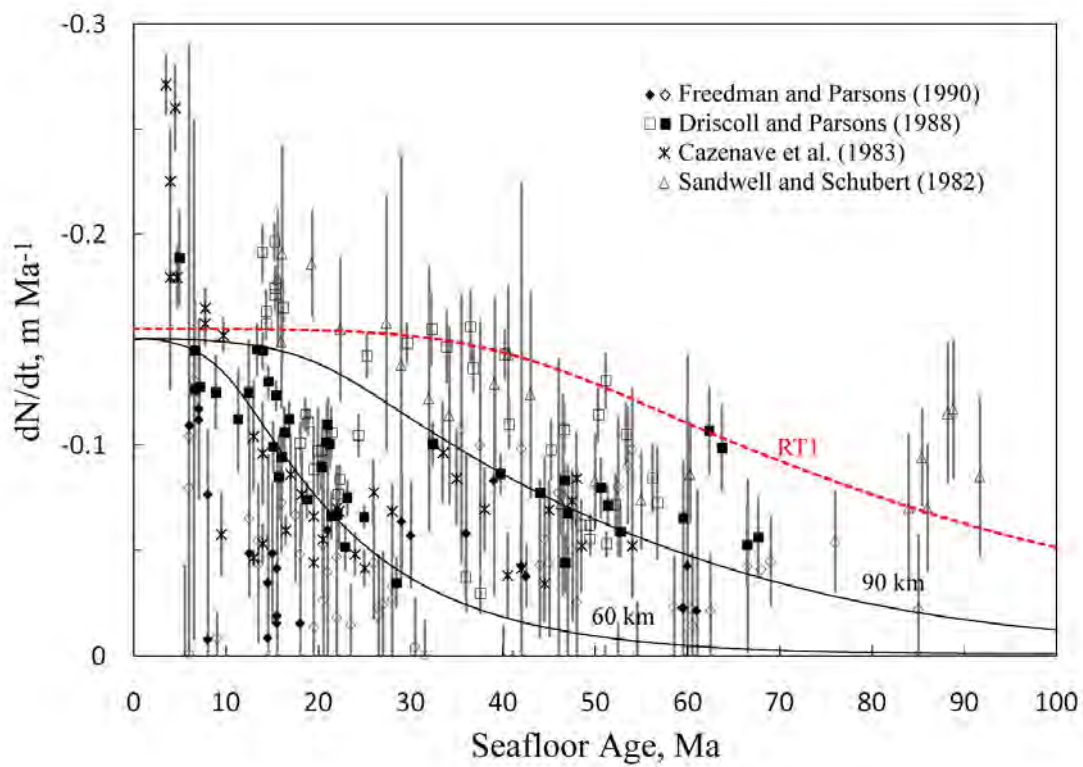


FIGURE 2.8: Geoid slope of thermal models predicted using the one-dimensional Haxby and Turcotte (1978) model against fracture zone data from Sandwell and Schubert (1982), Cazenave et al. (1983), Driscoll and Parsons (1988), and Freedman and Parsons (1990). Two solid black lines are simple plate solutions from Driscoll and Parsons (1988) and the dashed red line is model RT1.

# 3

## Comprehensive Plate Models for the Thermal Evolution of Oceanic Lithosphere

### 3.1 INTRODUCTION

Linking geophysical observations to the state of the oceanic lithosphere is primarily a task of modeling, and although the cooling of oceanic lithosphere is thought to be a simple process, constraining thermal models is complicated by incomplete views of geophysical observations, properties of mantle materials, and the complex thermomechanical behavior of the upper mantle. These complications have resulted in most efforts focusing on simple thermal models which do not incorporate details that unnecessarily obscure the fundamental behavior of oceanic lithosphere, such as variable heat transport properties (Davis and Lister, 1974). Such investigations of constant-property models are abundant and have succeeded in informing the fundamental behavior of oceanic lithosphere (e.g. McKenzie, 1967; Sclater and Francheteau, 1970; Davis and Lister, 1974; Parsons and Sclater, 1977; Heestand and Crough, 1981; Stein and Stein, 1992; Carlson and Johnson, 1994; Hillier and Watts, 2005; Hasterok, 2013). Attempts to further constrain models with mineral physics data are not new (e.g. Denlinger, 1992; Doin and Fleitout, 1996; Hearn et al., 1997; Honda and Yuen, 2004; McKenzie et al., 2005; Afonso et al., 2007; 2008a;b; Goutorbe, 2010; Grose, 2012; Chapter 2), but have been limited by the availability of high quality data (Korenaga, 2007a). For instance, some of these models use the theoretical thermal conductivity model of Hofmeister (1999) to describe temperature-dependence, which is superseded by more recent experimental work on major mantle minerals (e.g. Hofmeister, 2005; Pertermann and Hofmeister, 2006; Hofmeister and Pertermann, 2008; Branlund and Hofmeister, 2012). The modeling study of our previous chapter employed recent experimental mineral physics properties for olivine in thermal plate models and found that while excellent fits to seafloor topography and heat flow can be found without changing heat transport properties, the thermal expansivity must

be reduced by about 40% from the experimental value for forsterite. The need for such a large artificial modification demonstrates that such simple models are incomplete.

The purpose of this chapter is to develop a more complete model of the oceanic lithosphere by testing the consequences of incorporating improved heat transport properties and boundary conditions in thermal models of oceanic lithosphere. In addition to updated temperature-dependent thermal properties, we investigate pressure-dependent thermal properties, latent heat of melting beneath ridges, two-dimensional heat transport with appropriate ridge-axis boundary conditions, low values for thermal properties of oceanic crust, and vigorous hydrothermal circulation near ridge axes. In the following sections, we characterize the conditions and properties of our thermal plate models and describe the fitting techniques employed to constrain models with observed seafloor topography and surface heat flow. We discuss results focusing on i) the properties of best-fitting models, ii) tests of the importance of various second-order properties in cooling models, iii) the fits to seafloor heat flow and topography, and iv) discuss implications for net seafloor heat flux, thermal structure of the lithosphere, thermoviscoelastic behavior of the lithosphere, and petrology of the upper mantle.

## 3.2 METHODS AND ANALYSES

### 3.2.1 Heat transport modeling

Thermal structure is obtained numerically by solving the 1D conduction equation

$$\rho C_p \frac{\partial T}{\partial t} = \frac{\partial}{\partial z} \left( k \frac{\partial T}{\partial z} \right), \quad (3.1)$$

and the 2D conduction-advection equation

$$\rho C_p \left( \frac{\partial T}{\partial t} + u \frac{\partial T}{\partial x} \right) = \frac{\partial}{\partial x} \left( k \frac{\partial T}{\partial x} \right) + \frac{\partial}{\partial z} \left( k \frac{\partial T}{\partial z} \right), \quad (3.2)$$

where  $k$  is the thermal conductivity,  $\rho$  is the density,  $C_p$  is the isobaric specific heat,  $T$  is temperature,  $t$  is time,  $u$  is the horizontal velocity of the plate (half-spreading rate), and  $x$  and  $z$  are the horizontal and vertical Cartesian coordinates, respectively. We solve two classes of forward finite difference models (Fig. 3.1): "simple" models, which solve Eq. 3.1 for 170 Ma (3-point stencil), and 'comprehensive' models, which solve Eq. 3.2 (5-point stencil) close to the ridge ( $< 2$  Ma or  $x=100$  km) and then solves Eq. 3.1 for an additional 168 Ma.

All models are non-deforming, meaning that finite-difference spacing does not change with temperature. The vertical resolution used to solve Eq. 3.1 is 1 km, whereas vertical and horizontal resolutions for Eq. 3.2 are 0.14 km and 1 km, respectively. The surface boundary is kept at 0°C and there is a lower isothermal boundary condition at a depth  $L$ , also known as the plate thickness. For vertical boundary conditions in 2D models, the ridge axis is reflecting and the boundary at 2 Ma is transmitting (Fig. 3.2). Beneath the ridge there is a region which is set to have a time-independent temperature distribution. The heat flux along the boundaries of this region effectively simulates the release of latent heat



during magma solidification and/or convective processes beneath the ridge (e.g. MacLennan, 2008). The dimensions of this region (white dashed line in Fig. 3.2a-b) are based on the seismic tomography experiment over the East Pacific Rise (9°30N) by Dunn et al. (2000). Everywhere outside this region the temperature field is allowed to conductively cool and migrate away from the ridge axis.

The timestep is kept sufficiently small to guarantee numerical stability and accuracy in all models. Convergence and resolution tests indicate that the numerical error in our thermal models is less than  $\sim 1\%$  (Fig. 3.3). In addition, while we assume  $u=50 \text{ mm yr}^{-1}$  for all models discussed in this work, predictions from models with different spreading rates were also computed and are shown in Fig. 3.4.

In some 2D models, we also model hydrothermal heat transport using a scaling of the lattice thermal conductivity (e.g. Cochran and Buck, 2001). The thermal conductivity scaling we adopt is  $k = k_l \text{Nu} + k_{rad}$  where  $k_l$  is the experimental lattice thermal conductivity, Nu is the "Nusselt" number and  $k_{rad}$  is the radiative conductivity which is unaffected by convective transport. As shown in Fig. 3.2, this conductivity scaling is allowed to occur in lithosphere where  $T < 800^\circ\text{C}$  for ages  $t < 0.2 \text{ Ma}$ , otherwise Nu=1 (no convective transport). We have chosen to only test Nu=10 for brevity, and since our early tests showed that it is close to the amount required to fit ridge flank topography.

### 3.2.2 Compressibility, thermal expansion, and bulk density

Isothermal compression is estimated with the third-order Birch-Murnaghan Equation of State (EOS)

$$P = K_0 \frac{3}{2} \left[ \left( \frac{V_0}{V} \right)_T^{\frac{7}{3}} - \left( \frac{V_0}{V} \right)_T^{\frac{5}{3}} \right] \left\{ 1 + \frac{3}{4} (K'_T - 4) \left[ \left( \frac{V_0}{V} \right)_T^{\frac{2}{3}} - 1 \right] \right\}, \quad (3.3)$$

where  $P$  is pressure,  $K_0$  the bulk modulus at  $P=0$ ,  $(V_0/V)_T$  is the isothermal volume change, and  $K'_T$  the pressure derivative of the isothermal bulk modulus. The corresponding isothermal density is

$$\rho(P) = \rho_0 \left( \frac{V_0}{V} \right)_T. \quad (3.4)$$

The next step is to evaluate the contribution of temperature using a pressure-dependent thermal expansivity. The pressure-dependence of the thermal expansivity  $\alpha$  is controlled by the Anderson-Grneisen parameter  $\delta_T$ , which also depends on the pressure (Anderson, 1967). We use the form (Anderson et al., 1992; Anderson and Isaak, 1993; Kumar and Bedi, 1998)

$$\frac{\alpha(P, T)}{\alpha(T)} = \left( \frac{V_0}{V} \right)_T \exp \left\{ (\delta_T + 1) \left[ \left( \frac{V_0}{V} \right)_T^{-1} - 1 \right] \right\}. \quad (3.5)$$

Thus, our thermal EOS can be given as

$$\rho(P, T) = \rho(P) \left( 1 - \frac{\alpha(P, T)}{\alpha(T)} \int_{T_0}^T \alpha(T) dT \right). \quad (3.6)$$

Moduli used are consistent with  $\sim\text{Fo90}$ :  $K_0=130 \text{ GPa}$ ,  $K'_T=4.8$ , and  $\delta_T=6$  (Anderson, 1974; Anderson and Isaak, 1995; Raynard and Price, 1990). Since the pressure effect in the

oceanic crust is small, we use the above moduli for Fo<sub>90</sub> to compute isothermal compression in both crust and mantle. Thermal expansivity is described using the linear form  $\alpha(T) = \alpha_0 + \alpha_1 T$  for all phases involved. For estimating thermal expansivity in the mantle, we use the data from Bouhifd et al. (1996) for Fo<sub>90</sub>, with a reference density  $\rho_0 = 3300 \text{ kg m}^{-3}$ . For the oceanic crust, thermal expansivity corresponds to that of a 15/20/39/26 Forsterite/Diopside/Anorthite/Albite assemblage, with reference density  $\rho_0 = 2950 \text{ kg m}^{-3}$ . All mineral physics parameters are given in Table 3.1 and temperature-dependent properties are depicted in Fig. 3.5. We note that predictions of bulk density from Eqs. 3-6 and from the thermodynamically-consistent formulation of Xu et al. (2008) differ by  $<10 \text{ kg m}^{-3}$  at pressures  $<10 \text{ GPa}$  (Fig. 3.16).

### 3.2.3 Heat transport properties

#### Lattice thermal conductivity and specific heat

Conductive heat transport in the Earth occurs via lattice vibrations and diffusive radiation. To describe the lattice thermal conductivity in our thermal models we rely on experiments measuring thermal diffusivity  $D(T)$  and specific heat  $C_p(T)$  on major mantle minerals at temperature. Thermal conductivity may then be calculated as  $k = D\rho C_p$ . While thermal diffusivity of minerals have been described using various functions in the literature (Hofmeister et al., 2007), we have used the general form

$$D(T) = a + b \exp(-cT) + d \exp(-eT), \quad (3.7)$$

where  $T$  is in Celsius. This expression provides excellent fits to a wide variety of recently acquired data and predicts a constant value at high-temperature as expected for electrical insulators. Tabulated coefficients are given in Table 3.1. Conductivity and specific heat in the mantle is assumed to be that of pure olivine ( $\sim\text{Fo}_{90}$ ). For the crust, however, the variable availability of high-quality mineral physics data for different properties forces us to have mineralogically-inconsistent assemblages for conductivity and specific heat (and density). While our crustal assemblage always has phase abundances of 15/20/65 Olivine/Clinopyroxene/Plagioclase, the actual mineralogy (or phase composition) used to estimate thermal expansivity, thermal conductivity, and specific heat is slightly different (Table 3.1).

Comparing the thermal diffusivity of augite, olivine, and plagioclase (Fig. 3.5) shows that the properties of the crust relative to the mantle are controlled by plagioclase. We have used  $D(T)$  of near end-member anorthite (5% albite) to describe plagioclase, but a dense survey of thermal diffusivity for Ab-An solid-solutions shows that  $D(T)$  of higher albite plagioclase is not significantly greater unless plagioclase is  $> 70\%$  albite. In addition, the roles of basaltic glass, sediment cover, pore water, and hydrothermal alteration contribute additional uncertainties to the properties of oceanic crust. Nevertheless, due to the strong effect of plagioclase on heat transport properties, our study should be able to explore the basic contribution of insulating oceanic crust on the thermal evolution of oceanic lithosphere.

For scalar thermal properties ( $C_p$ ,  $\rho$ ,  $\alpha$ ), we use an arithmetic mean mixing rule. On the other hand, we use a geometric mean to describe composite thermal conductivity (e.g. Aichlmayr and Kulacki, 2006). We expect the geometric mean to be an appropriate estimate

for a rock with randomly distributed minerals since it is mid-way between arithmetic and harmonic means which are appropriate for perfectly layered media with foliation parallel and perpendicular to the direction of conduction, respectively. In addition, although olivine and pyroxenes contain strong conductivity anisotropy with crystallographic orientation, and this may be important in the upper mantle (Hearn et al., 1997; Tommasi et al., 2001), we assume an isotropic conductivity tensor by employing a geometric mean among orientations. The pressure-dependence of the lattice conductivity is small in the upper mantle but is also much simpler than other contributions to thermal behavior, reasonably approximated as  $d\ln(k)/dP \sim 5\% \text{ GPa}^{-1}$  (Hofmeister, 2007).

### Radiative thermal conductivity

The radiative conductivity is a complicated function of temperature, composition, grain size, and optical properties of crystals (Shankland et al., 1979; Hofmeister, 2005). Hofmeister (2005) used near-infrared spectra to model diffusive radiation in  $\sim\text{Fo}_{90}$  olivine and estimated the dependence of radiative conductivity on temperature and grain size. Hofmeister’s (2005) equation for diffusive radiation with concentration dependence may be written as

$$k_{rad} = \pi h d c^2 n^2 \frac{8}{3} \int_0^\infty \phi \frac{1 - \exp(-dA)}{1 + dA} \nu^3 \frac{\partial}{\partial T} \left[ \exp\left(\frac{h c \nu}{k_b T}\right) - 1 \right]^{-1} d\nu \quad (3.8)$$

where  $h$  is Planck’s constant,  $d$  is grain size,  $c$  is velocity of light,  $n$  is the index of refraction,  $A$  is an absorption coefficient,  $\nu$  is light frequency,  $T$  is temperature, and  $k_b$  is Boltzman’s constant. Hofmeister (2005) used a summation notation to denote frequencies over which the integral is resolved, which we denote in Eq. 3.8 by the parameter  $\phi$  which is a discontinuous function of  $\nu$  equal to unity or zero. Radiative heat transport in our thermal models uses a single fitted equation to approximate Eq. 3.8 which is accurate to  $\pm 0.25 \text{ W m}^{-1} \text{ K}^{-1}$  (see Appendix 3.A and Fig. 3.17).

We use the above approximation of  $k_{rad}$  for both the mantle and crust. In reality, it is likely that  $k_{rad}$  will vary significantly with petrology (e.g. mantle versus crust, or spinel-versus garnet-bearing mantle; Schatz and Simmons, 1972). However, the lack of an effective medium theory for radiative heat transport in composite mineral assemblages and the need for high-temperature spectra for minerals precludes significantly more detail at this point. Spectra for olivine is all that is available at present (Hofmeister, 2005). Such details may ultimately be important, but our analysis is only meant to be a basic test of the importance of the presence or absence of radiative transport.

### 3.2.4 Decompression melting and the initial geotherm

Melt production beneath ridges is important for at least two reasons: i) melting extracts latent heat from the internal energy, causing a decrease in mantle temperature relative to a simple adiabatic process, and ii) melt migrates to the surface and is incorporated into the oceanic crust, resulting in a constraint on mantle temperature by observing crustal thickness. In our thermal models, we use an approximation of the melting model of Asimow et al. (2001). We treat their isentropic batch melting paths (melt fraction as a function of

pressure for some potential temperature) as known and use a constant heat of fusion ( $335 \text{ kJ kg}^{-1}$ ) to calculate initial geotherms (i.e. temperature profile at  $t=0$ ; see Appendix 3.B and Fig. 3.18).

Note that while we explicitly account for temperature changes from the latent heat of fusion, we do not model release of latent heat on solidification beneath the ridge, nor do we model the process of advective heat transport associated with melt migration. Instead, our 2D models implicitly consider the release of latent heat and advective transport by maintaining a time-independent temperature distribution in a region beneath the ridge (see Sec. 3.2.1 and Fig. 3.2b).

In addition, we assume that the crustal thickness is 7 km everywhere, regardless of mantle temperature. This means that our model should be expected to represent the average behavior of 'normal' oceanic lithosphere and cannot necessarily represent regional observations.

### 3.2.5 Seafloor topography

Seafloor topography is predicted using the isostatic formula (Appendix 3.C)

$$b(t)\sqrt{t} = w(t) - r = F_\alpha \frac{\rho_b}{\rho_b - \rho_{wa}(t)} \int_0^\infty \left( 1 - \frac{\rho_a(z)}{\rho(z,t)} \right) dz, \quad (3.9)$$

where  $b(t)$  is the age-dependent subsidence rate,  $w(t)$  is the seafloor depth,  $r$  is the ridge depth,  $\rho_b$  is the mean density of the initial mantle column ( $\rho_b \sim 3200 \text{ kg m}^{-3}$ ),  $\rho_a(z)$  is the density of the initial mantle column,  $\rho_{wa}(t)$  is the mean density of the seawater column,  $\rho(z,t)$  is mantle density, and  $F_\alpha$  is an adjustment to thermal expansivity used in fitting (Sec. 3.2.6).

Due to the simple pressure-dependence of seawater we treat the seawater density as age-dependent. The density of seawater at seafloor depth can be given as  $\rho_w(P) = 1028(1 + P/2.2)$ , where  $P$  is pressure (in GPa), or approximately  $\rho_w(t) = 1028 + 4.8w(t)$ , where  $w$  is the seafloor depth (km), so the mean density of the water column participating in isostasy (i.e., between ridge height and seafloor depth) is  $\rho_{wa}(t) = 1028 + 2.4[w(t) + r]$ .

### 3.2.6 Fitting analysis

#### Approach

We reproduce the constant property and temperature-dependent models (developed in Chapter 2) with age-dependent seawater density and further investigate possible contributions of additional properties such as decompression melting, pressure-dependences, realistic axial boundary conditions, thermal properties of the crust, and axial hydrothermal circulation. To understand the relative importance of these properties we study a set of "simple" models which sequentially add each new property (Fig. 3.1). We then focus on two-dimensional "comprehensive models" (so-called as they include most of the properties independently analyzed in the "simple" models) which illustrate the interrelationships between axial hydrothermal circulation, radiative conductivity, and crustal insulation (Fig. 3.1).

The primary goal of our fitting analysis is to isolate realistic models, for all model types which best-fit global seafloor topography and heat flow. The most important aspect of our analysis is that we treat experimental properties as adjustable. This treatment of adjustable properties may be explained as follows: An experimental value  $X$  of a thermal property (e.g.  $k$ ,  $\alpha$ ) may be related to the apparent value  $A$  by an adjustment factor  $F = A/X$  so that  $F$  is a measure of artificial modification of the experimental value required to fit observations. For example, assume that the 'observed' seafloor subsidence rate is  $350 \text{ m Ma}^{-1/2}$ . If a particular cooling model using experimental thermal properties predicts a subsidence rate of  $465 \text{ m Ma}^{-1/2}$ , this model may be made to fit geophysical observations if the thermal expansivity is reduced by 25%, corresponding to  $F_\alpha = 0.75$ . This artificial adjustment may be physically associated with inaccuracy or incompleteness in our model, such as an inappropriate mineral assemblage or contribution from some physical process which acts to change the effective properties of the system. An important assumption in our analysis is that  $F$  is a global constant over all ages and lithospheric depth for each model. As such, each model parameterization is characterized by a single value,  $F_\alpha = \alpha_A/\alpha_X$  for thermal expansivity and  $F_k = k_A/k_X$  for thermal conductivity.

### Non-adjusted properties

Many of the properties in our models are not treated as adjustable such as the pressure-dependence of seawater density, reference densities of mantle and crust, specific heat, pressure-dependence of density and thermal expansivity, mantle adiabat, latent heat of melting, extent of melting, hydrothermal circulation (Nusselt number), mineralogy of oceanic crust, and radiative heat transport. However, the above properties are explored in 15 model types by adding or removing their respective effects (Fig. 3.1; Sec. 3.3.1).

### Method

Our fitting analysis consists of two parts (Fig. 3.1). In the first part, we adjust all models to best fit observed topography of seafloor younger than 64 Ma by adjusting the thermal expansivity. This is done with a least squares fit on 1 Myr bins of mean depth equally weighted in time. The fit  $s_f$  may be given by

$$s_f = \sum_{t=0}^{64 \text{ Ma}} [w_{mod}(t) - w_{obs}(t)]^2, \quad (3.10)$$

where  $w_{obs}(t)$  is the observed seafloor depth (using the database of Hillier (2010)) and

$$w_{mod}(t) = r + F_\alpha \frac{\rho_b}{\rho_b - \rho_{wa}(t)} \int_0^\infty \left(1 - \frac{\rho_a(z)}{\rho(z, t)}\right) dz \quad (3.11)$$

is the modeled depth. Both  $F_\alpha$  and  $r$  are varied until  $s_f$  is minimized. We find the best-fitting thermal expansivity adjustment  $F_\alpha$  for models in the parameter ranges  $F_k = 0.9 \pm 0.5$ ,  $L = 120 \pm 50 \text{ km}$ , and  $T_p = 1375 \pm 75^\circ\text{C}$ . The model sampling is 0.1 in  $F_k$ , 5 km in  $L$ ,  $50^\circ\text{C}$  in  $T_p$ , and a bicubic interpolation of fitted model properties ( $F_k$ ,  $F_\alpha$ ,  $L$ ,  $r$ ) is used to explore continuous predictions throughout these ranges.

In the second part, we assess the misfit to old-age heat flow and old-age topography of all the above models. Model misfit to topography is given by

$$M_h = \sqrt{\frac{1}{N} \sum_{i=1}^N \left( \frac{h_{mod} - h_{obs}}{2\sigma} \right)^2}, \quad (3.12)$$

where  $N$  is the number of age bins,  $h_{mod}$  is the predicted depth,  $h_{obs}$  is the observed mean depth, and  $\sigma$  is the standard deviation of depth in each individual bin. For the fit to heat flow, we follow Hasterok (2013) in using interquartile ranges and median heat flow to assess misfit since means and standard deviations are inflated by outliers. Misfit to heat flow is taken as

$$M_q = \sqrt{\frac{1}{N} \sum_{i=1}^N \left( 1.349 \frac{q_{mod} - q_{obs}}{IQR} \right)^2}, \quad (3.13)$$

where  $q_{mod}$  is modeled heat flow,  $q_{obs}$  is observed median heat flow, and IQR is the interquartile range. The joint misfit to depth and heat flow is

$$M_J = \sqrt{\frac{M_h^2 + M_q^2}{2}} \quad (3.14)$$

Depth and heat flow are equally weighted since we have no a priori reasons to weigh them differently, and unequal weighting does not significantly change properties of best joint fit models.

The depth database is taken from Hillier (2010) which follows the filtering analysis of Korenaga and Korenaga (2008), and the heat flow database is that of Hasterok (2013) without thermal rebound correction for sedimentation. The misfit to topography is evaluated for ages 134-156 Ma and misfit to heat flow is found over 90-168 Ma. This range for topography was chosen since global data over the age range 100-134 Ma data appears to be elevated by some anomalous processes unrepresentative of plate model evolution (Hillier and Watts, 2005), and after 156 Ma 'normal' seafloor becomes scarce. The range chosen for heat flow is based on an attempt to avoid using data 'contaminated' by hydrothermal circulation. This is because hydrothermal circulation is known to vent heat to the oceans at topographic highs and outcrops, reducing estimates of mean heat flow from measurements scattered over sedimented areas. Such processes are important over ages less than about 50 Ma (e.g. Von Herzen, 2004), although there is evidence for continued circulation in oceanic crust older than 80 Ma (e.g. Fisher and Von Herzen, 2005). Therefore we begin sampling at 90 Ma. While the heat flow data extend to  $\sim 178$  Ma, we end the range at 168 Ma as an attempt to avoid an apparent increase in heat flow in the oldest data (Hasterok et al., 2011). However, we ultimately found that neglecting or preserving  $>168$  Ma data did not significantly influence our fits.

### 3.2.7 Net seafloor heat flux

The net seafloor heat flux  $Q_{sf}$  is the sum of surface heat flux over the total seafloor area:

$$Q_{sf} = \int_0^t q_{sf} \frac{dA}{dt} dt \quad (3.15)$$

where  $A$  is seafloor area. The net seafloor heat flux is calculated using the empirical area-age grid of Müller et al. (2008) discretized in intervals of 0.02 Myr to a maximum of 180 Ma. The age spacing is small in order to capture the rapid variations in  $q_{sf}$  at young age.

### 3.3 RESULTS AND DISCUSSION

#### 3.3.1 Best fit properties from fitting experiments

Results of fitting experiments for one-dimensional "simple" model types are shown in Fig. 3.6a-g. Two-dimensional "comprehensive" models with hydrothermal circulation ( $Nu=10$ ) are shown in Fig. 3.7. Two-dimensional models without hydrothermal circulation are given in Fig. 3.8 since basin-scale fitness does not change significantly with or without hydrothermal circulation. For each mantle potential temperature the best-fitting models for different plate thicknesses are represented by a curve in parameter-space (lattice thermal conductivity adjustment  $F_k$  versus thermal expansivity adjustment  $F_\alpha$ ). Models with thicker plates tend to require higher thermal conductivity and lower thermal expansivity to fit geophysical data. Also, for a given mantle potential temperature and different plate thicknesses the misfit varies. Lines of equal misfit are shown in intervals of 0.05. Tabulated predictions for best-fitting models are given in Table 3.2. For best joint fitting models, the misfit to heat flow is  $\sim 0.34$ , the fit to topography is  $\sim 0.07$ , and the joint misfit is  $\sim 0.24$ . While these misfits are surprisingly consistent for all model types, the properties of each model are significantly different (Table 3.2). A summary of properties ( $F_k$  versus  $F_\alpha$ ) predicted by best-fitting models for each model type from Fig. 3.6a-g and Fig. 3.7 is shown in Fig. 3.6i.

#### Constant property and temperature-dependent models

As expected, our simplest models (constant thermal diffusivity, PH06, and R1; Fig. 3.6a-c) are in close agreement with our previous study (Chapter 2). When the thermal diffusivity is constant (Fig. 3.6a), the best-fitting plate models require very high thermal diffusivity (on the order of  $1.05\text{--}1.3 \text{ mm}^2 \text{ s}^{-1}$ ), plate thicknesses of 135–150 km and thermal expansivity about 35–40% lower than experimental predictions ( $F_\alpha \sim 0.63$ ). Adding temperature-dependent lattice thermal conductivity of olivine (Fig. 3.6b), best-fitting models predict thinner plates (110–125 km) with slightly higher thermal expansivity ( $F_\alpha \sim 0.66$ ), and the adjustment to lattice thermal conductivity is  $F_k \sim 1.1 \pm 0.1$ . Adding a high radiative contribution to thermal conductivity (Fig. 3.6c) does not change thermal expansivity, but best-fitting models have thicker plates (also see Chapter 2) and  $F_k$  is reduced to  $0.95 \pm 0.1$ . The lower lattice conductivity adjustment is essentially a consequence of 'making room' for the radiative contribution; with or without radiative transport, the effective thermal conductivity of best-fitting models is similar, but the lattice contribution must decrease to compensate for radiative transport.

#### Depth and pressure-dependent properties

Models introducing depth and pressure-dependent properties are shown in Fig. 3.6d-g. Each of these models have temperature-dependent lattice conductivity and radiative transport

and successively add the properties noted in the figure panels. Pressure-dependence of the density and thermal expansivity (model PA) increases  $F_\alpha$  by about 8% to  $\sim 0.71$  with little change to  $F_k$  (Fig. 3.6d). Similarly, pressure-dependence of the thermal conductivity (model PAK) decreases  $F_k$  by about 8% with little change to  $F_\alpha$  (Fig. 3.6e). Next the effect of the adiabat (model PAKA) is an  $\sim 8\%$  decrease in thermal conductivity,  $\sim 3\%$  increase in thermal expansivity and a thinner plate (Fig. 3.6f). Lastly, the effect of melting on the initial geotherm (model PAKAM) is shown to have a surprisingly minor effect (Fig. 3.6g): thermal conductivity remains unchanged while the thermal expansivity has a minor ( $<4\%$ ) increase, depending on mantle potential temperature.

Overall, the net result of including the above depth and pressure-dependent properties (compare model R1 with PAKAM) is that  $F_k$  decreases by about 20% from  $0.96 \pm 0.12$  to  $0.77 \pm 0.07$ , and  $F_\alpha$  increases by about 15% from  $\sim 0.66$  to  $\sim 0.77$ .

### Two-dimensional comprehensive models: importance of oceanic crust

Fig. 3.7 shows results of our "comprehensive" models, all of which have two-dimensional heat transport and boundary conditions representing an axial partial melt column near the ridge (Fig. 3.2) in addition to the basic temperature- and pressure-dependent properties discussed above (Fig. 3.5). The models in Fig. 3.7 show results with a 7 km oceanic crust (right panels), without oceanic crust (left panels), with radiative transport (top panels), and without radiative transport (bottom panels). Predictions of these models with no hydrothermal circulation ( $Nu=1$ ) are not much different ( $F_\alpha$  is a few percent lower when  $Nu=1$ ), and are provided in Fig. 3.8.

Comparing model RN10 (Fig. 3.7a) and PAKAM (Fig. 3.6g) shows that adding realistic axial boundary conditions, two-dimensional heat conduction, and hydrothermal circulation barely changes the need to adjust mineral physics properties. This is because these three properties are only important in close proximity to ridge axes, and so do not significantly impact geophysical observations over basin scales. On the other hand, comparison of model RN10 (Fig. 3.7a) and RN10C (Fig. 3.7b) shows that the thermal properties of oceanic crust increase  $F_\alpha$  of best joint fit models by about 10% and  $F_k$  increases by 10%. Compared to other thermal properties, the effect of oceanic crust is the most important influence on thermal properties, especially  $F_\alpha$  (Fig. 3.6i).

### On the remaining disparity between mineral physics and geophysical observations

From the above analysis, we cannot arrive at a good fitting model which allows less than  $\sim 15\%$  reduction in thermal expansivity from mineral physics. However, comparing oceanic crust models with radiative transport (Fig. 3.7b) to models without radiative transport (Fig. 3.7d) shows that because of the uncertainty in the radiative contribution, models can be derived which do not require any adjustment to the lattice thermal conductivity. In Fig. 3.9 we examine  $F_k$  as a function of mantle potential temperature for models with and without insulating crust and radiative conductivity. If  $T_p$  is less than  $\sim 1370^\circ\text{C}$ , best-fitting models with  $F_k=1.0$  are possible (see violet colored box). For  $T_p \sim 1370^\circ\text{C}$  the best-fitting model with  $F_k=1.0$  predicts that there is no radiative contribution to conductivity. Lower mantle



temperature predicts greater radiative transport, with about 60% of the maximum radiative contribution at  $T_p \sim 1300^\circ\text{C}$ . Using Hofmeister's (2005) diffusive radiation model for olivine (Eq. 3.8), this is consistent with a mantle grain size of  $\sim 3$  mm. For  $T_p > 1370^\circ\text{C}$ , all best-fitting models require some reduction in thermal conductivity to fit geophysical observations. Such a disparity may be caused by conditions which can lower thermal conductivity such as additional mineral modes in the lithosphere or thermal anisotropy in olivine (Tommasi et al., 2001). Nevertheless, the above analysis suggests that olivine may be a reasonable approximation of heat transport properties in the upper mantle.

### 3.3.2 Preferred reference models

We choose two preferred models (G13L and G13R), which include both axial hydrothermal circulation and crustal insulation, on the basis of model completeness and success in fitting models to seafloor topography without the need for excessive adjustments to mineral physics properties. The main difference between these two models is that G13L does not have radiative transport, whereas G13R does. This choice reflects the current limitation in determining the importance of radiation in a robust way. Because of the complexity of our models, we do not provide simple analytic approximations of geophysical predictions. Instead, we include (as a digital supplement to this thesis) Excel files showing preferred model outputs for i) the basin-scale thermal structure of the oceanic lithosphere, ii) higher resolution thermal structure near the ridge axis, and iii) predicted seafloor topography and heat flow.

The results of fitting analysis for these models are shown in Fig. 3.10. These figures depict the misfit to topography (Fig. 3.10a,d), misfit to heat flow (Fig. 3.10b,e), and the thermal expansivity adjustment factor (Fig. 3.10c,f) as functions of the thermal conductivity adjustment factor versus plate thickness for  $T_p = 1300^\circ\text{C}$ . All of the models in the domain ( $F_k$  versus  $L$ ) have been optimized (minimum misfit) for  $F_\alpha$ , but the misfit still varies as a function of  $F_k$  and  $L$ . The minimum misfit represents the best-fitting model for each of these model types at  $T_p = 1300^\circ\text{C}$ . On top of these maps we superimpose, in an alpha transparency (the field of joint misfit is black with transparency as a function of misfit), the joint misfit  $M_J$ . Properties such as the thermal conductivity and plate thickness predicted by these two models are significantly different (Table 3.2), but both models exhibit similar fits to geophysical observations. In fact, the fit to geophysical observations among all of our best joint fitting models does not seem to change among all model types (Table 3.2). On the other hand, models G13L and G13R provide improved fits to small-scale features in seafloor topography (discussed in Sec. 3.3.5), and  $F_\alpha$  is closer to 1.0.

### 3.3.3 Seafloor heat flux

Predictions of heat flow for comprehensive models are compared to the classic model GDH1 (Stein and Stein, 1992), global median heat flow, and 'site specific' heat flow in Fig. 3.11. Because the differences in predictions for different mantle potential temperatures are negligible (since each  $T_p$  is combined with different values of  $F_k$  and  $F_\alpha$  to fit geophysical observations), we show only one curve for each model type. Global median heat flow from Hasterok (2013) is shown with and without his correction for thermal rebound from sedimentation. We chose

to use the uncorrected heat flow as Hasterok's (2013) global sediment correction is based on a simple analytic thermal rebound model which is expected to be reasonable for average seafloor only (Hasterok et al., 2011). As such, it is unclear if the very oldest data ( $>145$  Ma, where corrected heat flow begins to significantly increase from uncorrected measurements; Fig. 3.11) accurately represents lithospheric cooling. Reference model H13, the heat-flow-only optimized plate model from Hasterok (2013), closely follows GDH1 until old age where it closely fits the sediment corrected database (Fig. 3.11b). All of our models closely fit the uncorrected heat flow (Fig. 3.11) and, incidentally, our preferred models which include oceanic crust, better fit the sediment corrected heat flow over ages 25-65 Ma (data unused in our fitting analysis).

If, instead, the sediment-corrected heat flow is used in the joint fit analysis, resulting models have similar plate thickness and misfit, but  $\sim 5\%$  lower  $F_\alpha$ ,  $\sim 5\%$  higher  $F_k$ , and about 5% higher  $Q_{sf}$ . Clearly, the choice of database has some pertinence. Although basic thermal corrections from the effect of sedimentation are routine (e.g. Von Herzen and Uyeda, 1963; Hutchison, 1985; Davis et al., 1999), future numerical modeling work may be desirable to clarify the details of sediment corrections to global heat flow.

The interesting characteristic of our comprehensive models is that the heat flow variation with age is poorly represented by a simple  $gt^{-1/2}$  law, where  $g$  is a rate of heat flow diminution over time, even for young ages. Models with or without radiative transport do not predict significantly different observations, so only the presence or absence of hydrothermal circulation and oceanic crust are important for interpretation. Models with no oceanic crust or hydrothermal circulation predict the same heat flow as GDH1 near zero-age but heat flow gradually increases against GDH1 with age before returning to GDH1 at old age. Models with hydrothermal circulation show significantly high heat flow over ridge axes ( $<0.2$  Ma), after which heat flow drops far below predictions of GDH1, followed by a gradual rebound toward predictions of models without hydrothermal circulation. Conductive rebound takes about 15 Myr (Fig. 3.11). Among models with hydrothermal circulation, the off axis heat flow is up to 60% lower than GDH1 if there is no oceanic crust, and up to 75% lower than GDH1 if there is oceanic crust. Also, while the rebound toward conductive values occurs over the same timescale with or without oceanic crust, the insulation effect of oceanic crust results in an additional depression of young age heat flow. Models with oceanic crust and hydrothermal circulation are lower than GDH1 until  $\sim 30$  Ma, whereas hydrothermal circulation predicts lower heat flow for only  $<10$  Ma (Fig. 3.11b). The effect of oceanic crust alone is about 30% lower heat flow than GDH1 near ridge axes. Because the time-scale of 'rebound' is significantly longer for oceanic crust than for hydrothermal circulation, and because some of the heat flow deficit from hydrothermal circulation is offset by high axial heat flux from hydrothermal circulation, the effect of oceanic crust is significantly more important for net lithospheric cooling. Nevertheless, both contributions compound to predict low seafloor heat flux at young age.

Clearly, an important question is whether or not there is evidence that lithospheric heat flow 'bends' towards lower crustal values in proximity to ridge axes. Global seafloor heat flow is known to be systematically depressed by ventilated hydrothermal circulation processes at young age, even when filtered for sediment cover (e.g. Schlater, 2004; Hasterok, 2010; Hasterok et al., 2011). In an attempt to constrain heat flow through young ( $>25$  Ma) oceanic

lithosphere, Hasterok et al. (2011) and Hasterok (2013) surveyed data published for specific sites where environmental conditions indicate that heat loss due to ventilated hydrothermal circulation is minimized. They recognized that sites well resolved for conductive signals happen to be in much better agreement with GDH1 than the global data (Fig. 3.11). Interestingly, the variation among these site-specific data appears to show a trend of heat flow in proximity to ridges decreasing against the predictions of GDH1, similar to that predicted by our preferred models (Fig. 3.11b). The site-specific data are in remarkably good agreement with our comprehensive models N10 and RN10, which have axial hydrothermal circulation and no crust, although some points remain high. The data are consistently about 5-10% higher than the predictions of our preferred reference models G13L and G13R. If our preferred models better represent lithospheric cooling, it must be that these site-specific data are anomalously elevated by about 5-10% against normal lithospheric heat loss. Further inspection is beyond the scope of this study, but two possible factors may include a) the need to further examine field measurements to possibly reveal a lower heat flow interpretation or b) recognizing some sites as characterizing anomalously elevated lithospheric heat flow.

Alternatively, our preferred models may inaccurately represent the properties of the lithosphere. For instance, our use of  $Nu=10$  may be too high, our crude temperature-dependent Nusselt number scaling may itself be a poor representation of axial circulation, or the oceanic crust may not be as insulating as in our models (Sec. 3.3.9).

### 3.3.4 Net seafloor heat flow: A new low estimate

Net seafloor heat flux  $Q_{sf}$  calculated for each of our best-fitting models is tabulated in Table 3.2. Conventional analyses of plate cooling models with basic thermal properties (no dependence on depth) predict  $Q_{sf} \sim 32 \pm 2$  TW (e.g. Davies, 1980; Stein et al., 1995; Pollack et al., 1993; Jaupart et al., 2007; Davies and Davies, 2010; Hasterok et al., 2011), although it is known that using empirical estimates of the seafloor area-age distribution can yield estimates less than 30 TW (e.g. Davies and Davies, 2010; Hasterok, 2013). Our analysis of models with constant or temperature-dependent properties (models CST, PH06, and R1) and an empirical area-age distribution estimates  $\sim 31.5$  TW (Table 3.2). Although there is some variation, the consistency of these estimates of oceanic heat flow, regardless of plate thickness, thermal conductivity, or mantle potential temperature, is a consequence of the fit to heat flow. A plate model with simple thermal properties that fits heat flow at old age will constrain heat flow at young age also. This may be best demonstrated by Hasterok's (2013) analysis, in which he showed that even if the fit to seafloor depth is ignored, the resulting predictions for seafloor heat flow do not change significantly, even with the degrees of freedom offered by plate thickness and mantle temperature.

On the other hand, depth-dependent thermal properties results in an important change. Since the effective thermal properties are different between young and old lithosphere, there will be some relative difference in predicted heat flow over young seafloor. This occurs because we use old-age heat flow to fit models, while heat flow over young lithosphere is unconstrained. We have tested predictions of models with and without the following properties: pressure-dependent thermal expansivity, pressure-dependent thermal conductivity, mantle adiabat, and latent heat of melting. Each of these properties tend to reduce  $Q_{sf}$ ,

with a net reduction of about 1.5 TW (Table 3.2). Comparing model RN1 to PAKAM (Table 3.2) shows that adding two-dimensional conduction near the ridge does not significantly change  $Q_{sf}$ . The impact of oceanic crust is by far the most important contribution, reducing  $Q_{sf}$  by about 3 TW (compare model RN1C to RN1). Adding hydrothermal circulation (model RN10) increases  $Q_{sf}$  by about 0.5-1 TW. However, when hydrothermal circulation is included with oceanic crust, the effect of hydrothermal circulation on  $Q_{sf}$  appears removed and both models have similar estimates (compare model RN10C and RN1C). This is because the lattice conductivity of oceanic crust is much lower than olivine, resulting in a lower hydrothermal flux from our Nusselt number approximation (Sec. 3.2.3).

Overall, our preferred models (G13R and G13L) predict a net seafloor heat flux of about 27 TW (Table 3.2), about 4.5 TW lower than models with constant thermal properties, and 10-25% lower than conventional estimates. Whether or not such a low estimate is corroborated by future research depends primarily on three uncertainties: i) uncertainty in the actual heat transport properties of oceanic crust, ii) the detailed nature of active and passive regimes of hydrothermal circulation, and iii) accurate estimates of lithospheric heat flow from seafloor measurements.

### 3.3.5 Seafloor topography

Model predictions of seafloor topography are shown in Fig. 3.12 against 0.1 Myr bins of mean global seafloor depth from Hillier (2010). The overall fits for all models are excellent. The major disagreement occurs at old age where the data around 100-130 Ma are significantly elevated against plate model predictions. Following Crosby et al. (2006) and our previous investigation (Chapter 2) we have discarded this data in fitting as the elevation appears to reflect an anomalous history. The coverage of remaining data used in the formal analysis of misfit appears small, but should be sufficient if a) the plate model is a reasonable geodynamic approximation of oceanic lithosphere and b) discarding the 'anomalous' 100-130 Ma data is justified. Hillier and Watts (2005) showed that this anomalous feature can be almost completely removed in the North Pacific by filtering out anomalous seafloor on various scales (seamounts, plateaus, etc.), and remaining data clearly exhibited plate-like flattening. Accordingly, our analysis relies on the assumption that the depth of the oldest (>135 Ma) seafloor is an appropriate constraint on plate thickness.

Although our examination surface heat flow showed substantial age-dependence, such a large complementary variation is not apparent in seafloor topography. Instead, the age-dependence manifests itself as a perturbation over young ages (<5 Ma) which in terms of absolute depth is of small magnitude. Models without oceanic crust or hydrothermal circulation have the usual roughly linear subsidence in  $t^{1/2}$ . Models with hydrothermal circulation have a high axial subsidence rate until cessation of circulation, followed by a low ridge flank subsidence rate which gradually increases over 0-5 Ma (Fig. 3.12b). Models with oceanic crust and no hydrothermal circulation have a deep ridge axis and a modestly increasing subsidence rate over time. Our preferred models have both features (deep ridge axis and increasing subsidence rate). Although the standard deviation of the means (about  $\pm 350$  m) is much larger than the predicted differences in depth between our preferred and simpler models (<250 m), the fit of our preferred models to global means for ages <4 Ma is

remarkable (Fig. 3.12b). Both the axial rise and low subsidence rate of ridge flanks appear to be well represented in global data. The fit of model G13R to normal seafloor depth would be difficult to improve for any age.

### 3.3.6 Thermal structure and the seismogenic zone

The thermal structure of the lithosphere predicted by model G13R is compared to classical models PS77 (Parsons and Sclater, 1977) and GDH1 (Stein and Stein, 1992) in Fig. 3.13 by depicting the difference in temperature between these models over depth and age. As the mantle temperature is  $1333^{\circ}\text{C}$  for PS77 and  $1450^{\circ}\text{C}$  for GDH1, our model G13R is most similar to PS77 when  $T_p \sim 1300^{\circ}\text{C}$  and to GDH1 when  $T_p \sim 1400^{\circ}\text{C}$ . However, as a consequence of temperature and depth dependent thermal properties and boundary conditions, thermal structure varies substantially in different regions of G13R compared to these classical models. Because our models have complicated P-T dependent properties, it is difficult to compare our predictions of thermal structure against predictions of conventional constant-property models in a straightforward way, but several features are worth attention. The most important feature is that the upper lithosphere of G13R is hotter than PS77 and GDH1 by  $100\text{--}200^{\circ}\text{C}$  (especially at young ages), depending on  $T_p$ . This may be contrasted with some previous predictions that upper lithosphere is actually colder than these models by  $100\text{--}150^{\circ}\text{C}$  when only temperature-dependent properties are considered (Honda and Yuen, 2004; McKenzie et al., 2005; Goutorbe, 2010; Chapter 2). Our prediction of relatively warm upper lithosphere is caused by the insulating properties of oceanic crust. Because this insulation effect diminishes with age as the oceanic crust becomes thinner relative to the thickness of the cooling lithospheric column, this relative excess in temperature diminishes slightly with age (Fig. 3.13). Nevertheless, even G13R at  $T_p = 1300^{\circ}\text{C}$  remains warmer than GDH1 around mocho depths at old age while predicting about  $400^{\circ}\text{C}$  colder temperature near the base of the plate (Fig. 3.13). Compared to PS77 our model tends to be warm everywhere except near the base of the lithosphere for young ages.

McKenzie et al. (2005) investigated a model of oceanic lithosphere with temperature-dependent properties and showed that most oceanic intra-plate earthquakes occur at depths where temperature is less than  $600^{\circ}\text{C}$ . Therefore, our observation that upper lithosphere is significantly warmer than predicted by temperature-dependent models carries nontrivial implications for the rheology of the lithosphere. We have superimposed the earthquake database from McKenzie et al. (2005) with modifications by Geli and Sclater (2008) in Fig. 3.13. Depending on the choice of mantle potential temperature, our models predict that the base of the seismogenic zone is closer to the  $700\text{--}800^{\circ}\text{C}$  isotherm than to the  $600^{\circ}\text{C}$  isotherm.

### 3.3.7 Mantle potential temperature and melting models

We have investigated predictions for mantle potential temperatures between  $1300$  and  $1450^{\circ}\text{C}$ , roughly the range predicted by geochemistry and petrology of ocean ridge volcanics (Herzberg et al., 2007; Herzberg and Asimow, 2008; Putirka, 2008; Lee et al., 2009). Large regional variations in seafloor depth at ocean ridges suggest that the temperature of ambient upper mantle may vary (Marty and Cazenave, 1989), but since we constrain lithospheric models

using global seafloor data the mean depth should correspond to a mean mantle temperature. An inherent limitation of our investigation is the simplifying assumption that topographic variations related to upper mantle temperature heterogeneities are randomly rather than systematically distributed in time. For instance, some deepening (shallowing) with age may be related to gradually decreasing (increasing) temperature (Korenaga and Korenaga, 2008). On the other hand, we note that the lack of any significant age dependence of the thickness of oceanic crust (McClain and Atallah, 1986; Chen, 1992; Brown and White, 1994) suggests that thermal heterogeneities are in fact randomly distributed. Nevertheless, since we cannot map these heterogeneities in time we operate under the assumption that any systematic distribution is negligible.

One approach to constrain mantle temperature is to use the relationship between melt productivity and the thickness of oceanic crust (McKenzie, 1984). From a melt model describing the melt mass fraction  $M$  as a function of pressure or depth, the thickness of oceanic crust  $L_c$  can be estimated as

$$L_c = \frac{1}{\rho_c} \int_{\infty}^{L_c} \rho_a M_e dz, \quad (3.16)$$

where  $\rho_c$  is the mean density of oceanic crust and  $M_e = M - M_r \leq 0$  is the extracted melt mass fraction, or the total melted mass  $M$  minus a residual melt fraction,  $M_r$ . Given a known mean thickness of oceanic crust, the mantle potential temperature can be constrained. Fig. 3.14 shows the predicted thickness of oceanic crust for the melting model of Asimow et al. (2001) which we used to estimate the temperature change due to the latent heat of melting in our thermal models (Fig. 3.18). The potential temperature that agrees with the observed thickness of oceanic crust is about 1400°C.

The difficulty with this approach is that existing melting models predict widely varying extents of melting for the same mantle temperature (e.g. McKenzie and Bickle, 1988; Langmuir et al., 1992; Asimow et al., 2001; Herzberg, 2004). It is notable that the model of Asimow et al. (2001), which we have used here, appears to have one of the lowest total productivities (Fig. 3.18). This means that the choice of a different model with greater melt productivity would predict  $T_p < 1400^\circ\text{C}$  for the observed crustal thickness. Furthermore, water and chromium contents are known to impact melt productivity (Asimow et al., 2001), the amount of residual melt is poorly known, and the above relationship may be an underestimate if active flow beneath spreading centers generates additional melt (e.g. Langmuir et al., 1992).

Later (Chapter 5), based on geochemical modeling and observations, as well as the use of the melting model of Herzberg (2004), we will show that the source of OIB volcanism is consistent with  $T_p < 1400^\circ\text{C}$ . Consequently, it is likely that ambient mantle is this temperature or lower.

### 3.3.8 Hydrothermal circulation and the young geotherm

An additional *a posteriori* constraint we consider is a tomographic inversion for temperature over a segment of the East Pacific Rise by Dunn et al. (2000), which was also the basis for our initial and boundary conditions (Fig. 3.2). In Fig. 3.15 we compare geotherms for

off-axis lithosphere at 0.11 and 0.2 Ma from some of our comprehensive models together with the estimates of Dunn et al. (2000). The fit at 0.11 Ma is shown compared to model geotherms from Cochran and Buck (2001), Cherkaoui et al. (2003), MacLennan et al. (2005), and Spinelli and Harris (2011). While these previous models yield significantly lower temperatures compared to those estimated by Dunn et al. (2000), our models with hydrothermal circulation are in much better agreement with the seismically-derived geotherm. This is partly due to the high Nusselt numbers used in these previous studies ( $Nu \sim 20$ , whereas  $Nu = 10$  is used here). The fact that our models are consistent with seismic evidence of ridge thermal structure and topography suggests a strong relationship between active hydrothermal power and ridge flank topography. We expect that this relationship may be extended by correlating regional variations in hydrothermal power and topography. In addition, this consistency suggests that short wavelength (in time) bins of seafloor topography can be used to constrain thermal models well within their standard deviation.

### 3.3.9 Properties of oceanic crust

The insulation effect of oceanic crust occurs because the lattice thermal conductivity of the crust is low, in our analysis caused by the abundance of plagioclase (Fig. 3.5). An obvious concern is whether or not a higher-order description of the heat transport properties of oceanic crust will reveal differences from our somewhat crude crustal mineralogy (and this may also apply to the mantle assemblage). It is first worth noting that experimental uncertainty reported for thermal diffusivity measurements from laser-flash experiments is about 2% (Branlund and Hofmeister, 2012). Also, a limitation of our study is that we have assumed that plagioclase is 95% anorthite, whereas oceanic crust is closer to 60% anorthite (e.g. Hertogen et al., 2002). Thermal conductivity of anorthite is significantly lower than albite, but Branlund and Hofmeister's (2012) relatively dense survey of Ab-An solid-solutions shows that thermal conductivity of  $An_{60}$  is not significantly higher than  $An_{95}$ . Moreover, the true effective lattice thermal conductivity of oceanic crust may be even lower than our models because silicate glasses (e.g. basalts) have very low conductivity on the order of  $\sim 0.6 \text{ mm}^2 \text{ s}^{-1}$  at low temperature (Hofmeister et al., 2009), pore water has a diffusivity of about  $0.1 \text{ mm}^2 \text{ s}^{-1}$ , and hydrothermal alteration will tend to lower rock thermal conductivity (e.g. Seipold and Schilling, 2003; Hofmeister et al., 2006; Osako et al., 2010). In addition, sediment cover will insulate the oceanic crust by preventing fluid exchange with oceans and by its very low thermal conductivity from high porosity (e.g. Hasterok et al. 2011). On the other hand, the effective thermal conductivity of the crust will increase in response to the circulation of hydrothermal fluids. In our models, we only include axial hydrothermal circulation, but it is known that off-axis ventilated hydrothermal circulation occurs in the upper crust over long time-scales. For example, Spinelli and Harris (2011) included a near-surface aquifer as a proxy to modeling ventilated hydrothermal circulation. The importance of including approximations of off-axis hydrothermal circulation in models is not entirely clear, but the timescales of convergence in predicted surface heat flow for conductive and hydrothermal models observed in our models versus those in of Spinelli and Harris (2011) seems to indicate that it does not significantly impact lithospheric heat flow.

Nevertheless, the form of our experiments is designed to partially compensate for some

of these uncertainties. While the true properties of the system are much more complicated than we have studied, we allowed the properties to vary about their experimental values. Our analysis cannot constrain the individual uncertainties of manifold free variables, but we have shown that agreement between thermal models, mineral physics, and geophysical observations appears to improve when models are more physically comprehensive.

### 3.3.10 Thermal expansivity adjustment: Thermoviscoelastic behavior of the lithosphere

The approximations of heat transport properties in our best models are probably reasonable since significant changes to heat transport properties from true lithospheric petrology are not expected, but the thermomechanical behavior and petrology of the upper mantle is likely to substantially complicate models of the density of the lithosphere. Unlike thermal conductivity, all of our models show that our mineral physics estimates of thermal contraction in the crust and mantle are too high to describe the lithosphere, although our new observations are more realistic than we previously found (Chapter 2). As we previously observed, our simplest models (Fig. 3.6a-c) indicated that the true effective thermal expansivity of the lithosphere is on the order of 35-40% lower than forsterite. On the other hand, our new preferred reference models indicate that the effective thermal expansivity of the lithosphere is a more realistic  $\sim 15\%$  lower than our model consisting of an olivine mantle and 15/20/65 Ol/Cpx/Plg oceanic crust (Fig. 3.7b,d).

A deficit of  $\sim 15\%$  is in good agreement with some thermoviscoelastic models of cooling oceanic lithosphere which predict that thermal contraction is resisted by thermal stresses (Pollack, 1980; Korenaga, 2007a). However, the role of thermoelastic stresses on density changes in cooling oceanic lithosphere remains unclear due to uncertainties regarding how to treat tectonic boundary conditions and brittle cracking. Korenaga (2007b) has attempted a step in this direction by performing finite element modeling of a cooling thermoviscoelastic lithosphere, although he assumed that horizontal displacements are focused on vertical cracks of an imposed spacing and that boundary conditions hold that no deformations are concentrated along normal faults and no other form of tectonic shortening takes place (e.g. Kumar and Gordon, 2009). Moreover, Korenaga (2007b) predict that thermoelastic stresses are everywhere tensional, contradicting many previous models showing thermal stresses both in compression and tension (Sandwell, 1986; Parmentier and Haxby, 1986; Haxby and Parmentier, 1988; Denlinger and Savage, 1989; Kusznir et al., 1991). In addition, Korenaga (2007a) has estimated the role of brittle failure by assuming that horizontal displacements of the lithosphere along cracks will create space to be replaced by seawater. Although noting that this may lead to hydration, Korenaga (2007a) considers the effect of hydration to be about the same as infill by seawater. It is difficult to confirm this assumption as while the densities of hydration minerals are well understood, perhaps the critical parameter is the volume expansion from the phase change, which has proven difficult to constrain (e.g. Thayer, 1966; Hostetler et al., 1966; Page, 1967; O'Hanley, 1992; Evans, 2004). There may also be the possibility that cracking can penetrate sufficient depth to allow the infiltration of melts into cracks (e.g. Sandwell et al., 1995; Lynch, 1999; Forsyth et al., 2006), in which case the density of the lithosphere might be well described by the conventional assumption



that all contraction occurs in the vertical. Lastly, we note that Korenaga (2007a) estimated a substantial age-dependence of what we have called the thermal expansivity adjustment, whereas we have assumed it to be constant in time for all models.

### 3.3.11 Thermal expansivity adjustment: Petrology

As noted above, more complicated thermotectonic deformation regimes than those represented by conventional thermoviscoelastic models may be able to dissipate thermoelastic stresses easily, meaning that the observed deficit between experimental thermal expansivity and that predicted by geophysical observations may originate elsewhere. Another probable source of this disparity is that our simple olivine mantle and Ol/Cpx/Plg oceanic crust is an inaccurate mineral physics approximation of the lithosphere. The additional petrological counterpart may be of two kinds: i) either our assemblage is a poor representation such that additional modes reduce thermal expansivity or ii) petrological heterogeneities related to thermodynamic stability and major phase transitions result in systematic age-dependent variations in mantle mineral abundances. In the second case a component of contraction or expansion arises as a secondary effect of large temperature changes during cooling: contractions and expansions arise from the changing abundances of minerals of different densities. This idea of a petrological contribution to density of the lithosphere is not new (Sclater and Francheteau, 1970; Forsyth and Press, 1971; Ito, 1974; Bottinga and Steinmetz, 1979; Wood and Yuen, 1983; Afonso, et al. 2007), but efforts to link petrological heterogeneity of the lithosphere to observed seafloor topography has not yielded exemplary results, and the success of simpler models in the explanation of seafloor topography appears to have resulted in shelving this problem. The recent introduction of robust thermodynamic models to attack problems of lithospheric geodynamics (e.g. Connolly, 2005; 2009; Stixrude and Lithgow-Bertelloni, 2005; Kaus et al., 2005; Afonso et al., 2007; Afonso et al., 2008a;b; Zlotnik et al., 2008; Simon and Podladchikov, 2008; Nikolaeva et al., 2008; Afonso and Zlotnik, 2011) should allow us to revisit the problem of linking petrological structure of oceanic lithosphere to geophysical observations.

## 3.4 CONCLUSIONS

We have developed a suite of new thermal plate models which investigate the contributions of temperature-pressure dependent thermal properties using updated mineral physics, axial hydrothermal circulation, and oceanic crust. By treating mineral physics properties as adjustable, all model types are able to achieve good fits to geophysical observations for any mantle potential temperature. However, in agreement with the findings of our previous chapter, we find that the simplest model types (e.g. temperature-dependent thermal properties only) require substantial adjustment to thermal expansivity ( $\sim 35\%$  reduction) to achieve good joint fits. On the other hand, new models which add pressure-dependent properties, hydrothermal circulation, and insulating oceanic crust achieve good fits with only minor adjustment to mineral physics thermal expansivity ( $\sim 15\%$  reduction). In addition, our preferred models predicts a plate thickness of about  $123 \pm 5$  km when the radiative contribution to thermal conductivity is high and  $109 \pm 6$  km if it is negligible (for  $T_p = 1375 \pm 75^\circ\text{C}$ ).

Moreover, our models provide significantly improved fits to seismic inversions for thermal structure over ridge axes.

A principal observation of our investigation is that the insulating properties of the oceanic crust is a significant second-order contributor to the cooling behavior of oceanic lithosphere and markedly influences predictions of geophysical observations. The impact on seafloor topography is a decreasing subsidence rate in proximity to ridge axes. Although this deviation from linear subsidence in  $t^{1/2}$  is apparent only over very young lithosphere ( $<5$  Ma), when axial hydrothermal circulation is also included subsidence is in excellent agreement with global data. Predictions of seafloor heat flow by our preferred models is more consequential. Models with oceanic crust and hydrothermal circulation predict surface heat flow up to 75% lower than GDH1 for young seafloor ( $<35$  Ma) while maintaining excellent fit with older data. This strongly reduced heat flow results in a low net seafloor heat flow of about 27 TW, or 10-25% lower than conventional estimates. Finally, an additional consequence of crustal insulation is that the base of the seismogenic zone in oceanic lithosphere corresponds to an isotherm on the order of 700-800°C, higher than predicted with simple temperature-dependent models.

## APPENDICES

### 3.A Radiative conductivity

Because a solution to Eq. 3.8 is not easily obtained Hofmeister (2005) found fitted equations for three ranges of grain size. We have preferred to use a single equation to describe the dependence on temperature and grain size, arriving at the following form:

$$k_{rad}(T, d) = A \exp\left(-\frac{(T - T_A)^2}{2x_A^2}\right) + B \exp\left(-\frac{(T - T_B)^2}{2x_B^2}\right), \quad (3.17)$$

Where  $A$ ,  $B$ ,  $T_A$ ,  $T_B$ ,  $x_A$ , and  $x_B$  are all functions of grain size as:

$$A = 1.8[1 - \exp(-d^{1.3}/0.15)] - [1 - \exp(-d^{0.5}/5)],$$

$$B = 11.7 \exp(-d/0.159) + 6 \exp(-d^3/10),$$

$$T_A = 490 + 1850 \exp(-d^{0.315}/0.825) + 875 \exp(-d/0.18),$$

$$T_B = 2700 + 9000 \exp(-d^{0.5}/0.205),$$

$$x_A = 167.5 + 505 \exp(-d^{0.5}/0.85),$$

and

$$x_B = 465 + 1700 \exp(-d^{0.94}/0.175),$$

where  $d$  is grain size in cm. Predicted radiative conductivity values from Hofmeister's (2005) model are shown in Fig. 3.17 together with predictions from our approximation (Eq. 3.17), and the respective differences between the two formulas.

### 3.B Melting

The results of the melting model by Asimow et al. (2001) have been approximated by fitting to melt fraction isopleths for batch melting without  $\text{Cr}_2\text{O}_3$  for  $T_p = 1400 \pm 100^\circ\text{C}$ . The function giving melt mass fraction is

$$M = a_1 a_2 + (1 - a_1) a_3 + a_4, \quad (3.18)$$

where

$$\begin{aligned} a_1 &= \exp(-P^a/b), \\ a_2 &= 0.00032T_p - 0.165 + cP, \\ a_3 &= 0.45 + dP, \\ a_4 &= f \exp(-Pe), \end{aligned}$$

and where  $P$  is pressure in GPa and

$$\begin{aligned} a &= 0.01T_p - 9 \\ b &= 1.7451 \times 10^{-23} \exp(0.0395798T_p) \\ c &= -0.000002871T_p^2 + 0.0088T_p - 6.8517 \\ d &= -0.00000011429T_p^2 + 0.000397T_p - 0.34794 \\ e &= 0.02T_p + 34 \\ f &= 0.000002542857T_p^2 - 0.006626T_p + 4.31749 \end{aligned}$$

where  $T_p$  is the mantle potential temperature in Celsius.

Fig. 3.18a shows the melt fraction predicted for the above model as a function of pressure and mantle temperature. Fig. 3.18b shows initial geotherms and the corresponding changes in mantle temperature due to extraction of latent heat. For comparison, we also show predicted melt fractions from the melting models of McKenzie and Bickle (1988) and a model based on near-fractional melting experiments on fertile peridotite by Herzberg (2004).

### 3.C Isostasy

Seafloor topography satisfies the balance equation

$$\int_0^L \rho(z, 0) dz = \int_0^w \rho(z, t) dz + \int_w^L \rho(z, t) dz, \quad (3.19)$$

where  $\rho$  is density,  $w$  is the surface of the lithosphere, and  $L$  is the depth of compensation. When the material between ridge height and seafloor depth is only seawater of constant density, Eq. 3.19 can be given as

$$\rho_b L = \rho_w w + \rho_L (L - w), \quad (3.20)$$

where  $\rho_b$  is the average density of asthenosphere,  $\rho_w$  is the density of seawater, and  $\rho_L$  is the average density of the mantle between the depths  $w(t)$  and  $L$ . Eq. 3.20 may be rearranged to give the seafloor depth below the ridge,

$$w = \frac{\rho_b - \rho_L}{\rho_w - \rho_L} L. \quad (3.21)$$

The mean density of the mantle column,  $\rho_L$ , must be consistent with vertical isostatic displacements. Consider a depth of compensation  $L$ . Prior to the isostatic adjustment from the seawater load no mass is displaced across the compensation depth. Afterwards, mass is displaced below a loaded column of lithosphere to a depth

$$L_M = L + w - \epsilon_L, \quad (3.22)$$

where  $\epsilon_L$  is the vertically integrated contraction of the mantle

$$\epsilon_L = \int_0^\infty \left(1 - \frac{\rho_a}{\rho}\right) dz = \int_0^\infty \left(1 - \frac{\rho(t_0)}{\rho(t)}\right) dz. \quad (3.23)$$

where  $\rho_a$  is the density of the asthenosphere. We may express  $\epsilon_L$  in terms of the contraction of an initial column of average density  $\rho_b$  as

$$\rho_L(t) = \rho_b \frac{L}{L_M(t) - w(t)}, \quad (3.24)$$

such that the initial column of density  $\rho_a$  and height  $L$  has the surface displacement  $0 \rightarrow w(t)$  and a basement displacement of  $L \rightarrow L_M(t)$  at time  $t$ . This is equivalent to

$$\rho_L(t) = \rho_b \frac{L}{L - \epsilon_L(t)}, \quad (3.25)$$

which may also be given as

$$\rho_L(t) = \rho_b \left(1 + \frac{\epsilon_L(t)}{L - \epsilon_L(t)}\right) = \rho_b + \rho_b \frac{\epsilon_L(t)}{L - \epsilon_L(t)}. \quad (3.26)$$

Incorporation into the algebraic form of the balance equation (Eq. 3.21) requires the following clarification:

$$w(t) = \frac{\rho_b - \rho_L(t)}{\rho_w - \rho_L(t)} L_M(t). \quad (3.27)$$

We may give the rearrangement

$$(\rho_b - \rho_L) L_M(t) = -\rho_b \frac{\epsilon_L L + \epsilon_L w - \epsilon_L^2}{L - \epsilon_L}, \quad (3.28)$$

which has the limit

$$\lim_{L \rightarrow \infty} -\rho_b \frac{\epsilon_L L + \epsilon_L w - \epsilon_L^2}{L - \epsilon_L} = -\rho_b \frac{\epsilon_L L}{L} = -\rho_b \epsilon_L, \quad (3.29)$$

and as

$$\rho_w - \rho_L = \rho_w - \rho_b \left( 1 + \frac{\epsilon_L}{L - \epsilon_L} \right), \quad (3.30)$$

the limit of the denominator (Eq. 3.27) is

$$\lim_{L \rightarrow \infty} (\rho_w - \rho_L) = \rho_w - \rho_b, \quad (3.31)$$

such that

$$w(t) = \lim_{L \rightarrow \infty} \frac{\rho_b - \rho_L(t)}{\rho_w - \rho_L(t)} L_M(t) = -\frac{\rho_b}{\rho_w - \rho_b} \int_0^\infty \left( 1 - \frac{\rho_a}{\rho} \right) dz = \frac{\rho_b}{\rho_b - \rho_w} \int_0^\infty \left( 1 - \frac{\rho_a}{\rho} \right) dz. \quad (3.32)$$

Mineral Physics Coefficients for Crust and Mantle: Thermal Expansivity<sup>a</sup>

Mineral	$\alpha_0 (\times 10^{-5})$	$\alpha_1 (\times 10^{-8})$	Mode % Crust	Mode % Mantle	Basis
Fo	2.832	0.758	15	100	<i>Bouhifd et al. [1996]</i>
Di	2.1	1.75	20	0	<i>Saxena et al. [1993];</i> <i>Isaak et al. [2006]</i>
An	0.87	0.9	39	0	<i>Tribaudino et al. [2010]</i>
Ab	1.75	1.95	26	0	<i>Tribaudino et al. [2010]</i>
Crust	1.639	1.322	—	—	Arithmetic mean of modes

<sup>a</sup>Fo = Forsterite, Di = Diopside, Au = Augite, An = Anorthite, Ab = Albite.Mineral Physics Coefficients for Crust and Mantle: Specific Heat<sup>a</sup>

Mineral	$C_p(T)$	Mode % Crust	Mode % Mantle	Basis
Fo <sub>90</sub> Fa <sub>10</sub>	$1.6108 - 12.4788T^{-0.5} - 1728477T^{-3}$	15	100	<i>Berman and Aranovich [1996]</i>
Di	$2.1715 - 0.0004555T + 1133.2T^{-2} - 22.2716T^{-0.5} + 0.000000129972$	20	0	<i>Robie and Hemingway [1995]</i>
An	$1.85757 - 0.0003324T - 5061T^{-2} - 16.4946T^{-0.5} + 0.000000150572$	65	0	<i>Robie and Hemingway [1995]</i>

<sup>a</sup>Fo = Forsterite, Di = Diopside, Au = Augite, An = Anorthite, Ab = Albite.Mineral Physics Coefficients for Crust and Mantle: Thermal Diffusivity<sup>a</sup>

Mineral	$a$	$b$	$c$	$d$	$e$	Mode % Crust	Mode % Mantle	Basis
Fo <sub>90</sub> Fa <sub>10</sub>	0.565	0.67	590	1.4	135	15	100	"Mantle olivine," <i>Pertermann and Hofmeister [2006]</i> ; Isotropic
Au	0.59	1.03	386	0.928	125	20	0	"Augite," <i>Hofmeister and Pertermann [2008]</i> ; Isotropic
An <sub>95</sub> Ab <sub>5</sub>	0.36	0.4	300	—	—	65	0	95% Anorthite "FMA", <i>Branlund and Hofmeister [2012]</i> ; Isotropic
Crust	0.432	0.44	380	0.305	145	—	—	Geometric mean of modes

<sup>a</sup>Fo = Forsterite, Di = Diopside, Au = Augite, An = Anorthite, Ab = Albite.

TABLE 3.1: Mineral physics coefficients for crust and mantle

Model Name	$T_p$ (°C)	$d$ (cm)	$Nu$ (–)	$L_c$ (km)	$dT/dz$ (°C)	$F_k$ (–)	$F_\alpha$ (–)	$L$ (km)	$Q_{sf}$ (TW)	$M_q$ (–)	$M_h$ (–)	$M_J$ (–)	$r$ (km)
<i>Simple Models</i>													
CST <sup>b,c</sup>	1300	0	1	0	0	1.29	0.63	148.5	31.6	0.336	0.079	0.244	2.59
CST <sup>b,c</sup>	1350	0	1	0	0	1.21	0.62	144.5	31.6	0.339	0.071	0.245	2.591
CST <sup>b,c</sup>	1400	0	1	0	0	1.12	0.62	139	31.5	0.343	0.073	0.248	2.592
CST <sup>b,c</sup>	1450	0	1	0	0	1.05	0.61	134.5	31.6	0.352	0.08	0.255	2.592
PH06 <sup>b,d</sup>	1300	0	1	0	0	1.21	0.67	124.5	31.4	0.332	0.072	0.24	2.603
PH06 <sup>b,d</sup>	1350	0	1	0	0	1.13	0.66	119.5	31.3	0.337	0.075	0.244	2.6
PH06 <sup>b,d</sup>	1400	0	1	0	0	1.05	0.66	114.5	31.4	0.343	0.084	0.25	2.599
PH06 <sup>b,d</sup>	1450	0	1	0	0	0.99	0.65	111.5	31.5	0.331	0.08	0.241	2.601
R1 <sup>b</sup>	1300	1	1	0	0	1.07	0.67	137	31.6	0.337	0.079	0.245	2.595
R1 <sup>b</sup>	1350	1	1	0	0	0.99	0.66	133	31.6	0.336	0.077	0.244	2.599
R1 <sup>b</sup>	1400	1	1	0	0	0.91	0.66	128	31.5	0.336	0.077	0.244	2.596
R1 <sup>b</sup>	1450	1	1	0	0	0.84	0.65	123.5	31.5	0.347	0.077	0.251	2.6
PA	1300	1	1	0	0	1.05	0.73	137.5	31.3	0.345	0.077	0.25	2.543
PA	1350	1	1	0	0	0.97	0.72	133.5	31.5	0.344	0.076	0.249	2.543
PA	1400	1	1	0	0	0.89	0.71	129.5	31.5	0.339	0.071	0.245	2.552
PA	1450	1	1	0	0	0.82	0.71	124	31.3	0.343	0.074	0.248	2.546
PAK	1300	1	1	0	0	0.97	0.74	139	30.9	0.34	0.073	0.246	2.555
PAK	1350	1	1	0	0	0.90	0.73	134.5	30.9	0.335	0.07	0.242	2.554
PAK	1400	1	1	0	0	0.82	0.73	128	30.7	0.339	0.078	0.246	2.555
PAK	1450	1	1	0	0	0.77	0.71	126.5	31.2	0.347	0.074	0.251	2.557
PAKA	1300	1	1	0	0.5	0.89	0.76	134.5	30.4	0.332	0.07	0.24	2.562
PAKA	1350	1	1	0	0.5	0.82	0.76	128	30.1	0.336	0.077	0.244	2.558
PAKA	1400	1	1	0	0.5	0.77	0.74	126.5	30.7	0.346	0.075	0.25	2.563
PAKA	1450	1	1	0	0.5	0.71	0.73	120.5	30.4	0.333	0.073	0.241	2.565
PAKAM <sup>c</sup>	1300	1	1	0	0.5	0.89	0.77	134.5	30	0.331	0.07	0.239	2.58
PAKAM <sup>c</sup>	1350	1	1	0	0.5	0.82	0.77	128	29.7	0.336	0.074	0.243	2.584
PAKAM <sup>c</sup>	1400	1	1	0	0.5	0.78	0.75	127	30.1	0.341	0.076	0.247	2.588
PAKAM <sup>c</sup>	1450	1	1	0	0.5	0.72	0.76	121	29.6	0.335	0.071	0.242	2.576
<i>Comprehensive 2-D Models</i>													
RN1C	1300	1	1	7	0.5	0.95	0.84	127.5	27	0.341	0.076	0.247	2.784
RN1C	1350	1	1	7	0.5	0.89	0.83	125	26.9	0.326	0.071	0.236	2.788
RN1C	1400	1	1	7	0.5	0.82	0.84	119	26.9	0.336	0.073	0.243	2.781
RN1C	1450	1	1	7	0.5	0.79	0.83	118.5	26.9	0.328	0.076	0.238	2.776
RN1	1300	1	1	0	0.5	0.88	0.77	135.5	29.6	0.337	0.069	0.243	2.621
RN1	1350	1	1	0	0.5	0.81	0.78	128.5	29.7	0.332	0.072	0.24	2.621
RN1	1400	1	1	0	0.5	0.76	0.76	126.5	29.5	0.35	0.077	0.253	2.631
RN1	1450	1	1	0	0.5	0.71	0.76	121.5	29.6	0.331	0.073	0.24	2.625
RN10	1300	1	10	0	0.5	0.89	0.78	135	30.6	0.335	0.069	0.242	2.588
RN10	1350	1	10	0	0.5	0.81	0.76	129	30.4	0.333	0.072	0.241	2.588
RN10	1400	1	10	0	0.5	0.77	0.77	126	30.1	0.348	0.074	0.252	2.601
RN10	1450	1	10	0	0.5	0.71	0.77	121	30.1	0.331	0.073	0.239	2.594
N1C	1300	0	1	7	0.5	1.08	0.83	115	26.7	0.329	0.072	0.238	2.833
N1C	1350	0	1	7	0.5	1.01	0.83	110	26.7	0.327	0.072	0.237	2.837
N1C	1400	0	1	7	0.5	0.97	0.83	107	26.5	0.335	0.081	0.244	2.836
N1C	1450	0	1	7	0.5	0.91	0.84	103	26.5	0.325	0.081	0.237	2.826
N1	1300	0	1	0	0.5	1	0.77	121	29.7	0.328	0.071	0.237	2.634
N1	1350	0	1	0	0.5	0.94	0.77	115.5	29.6	0.35	0.079	0.254	2.637
N1	1400	0	1	0	0.5	0.9	0.76	113.5	29.5	0.328	0.075	0.238	2.642
N1	1450	0	1	0	0.5	0.85	0.77	108.5	29.4	0.355	0.085	0.258	2.632
N10	1300	0	10	0	0.5	1	0.78	120.5	30.8	0.327	0.07	0.236	2.587
N10	1350	0	10	0	0.5	0.94	0.78	115	30.6	0.349	0.081	0.253	2.589
N10	1400	0	10	0	0.5	0.9	0.78	113	30.4	0.326	0.078	0.237	2.593
N10	1450	0	10	0	0.5	0.85	0.78	108.5	30.2	0.354	0.083	0.257	2.583
<i>Preferred Models</i>													
RN10C (G13R)	1300	1	10	7	0.5	0.95	0.85	127	27.2	0.34	0.076	0.247	2.758
RN10C (G13R)	1350	1	10	7	0.5	0.89	0.84	124.5	27.2	0.325	0.071	0.235	2.763
RN10C (G13R)	1400	1	10	7	0.5	0.83	0.85	119	27.2	0.336	0.076	0.243	2.757
RN10C (G13R)	1450	1	10	7	0.5	0.79	0.84	118.5	27.1	0.327	0.076	0.237	2.755
N10C (G13L)	1300	0	10	7	0.5	1.08	0.85	115	27.2	0.327	0.072	0.237	2.787
N10C (G13L)	1350	0	10	7	0.5	1.02	0.85	110	27.1	0.327	0.075	0.237	2.789
N10C (G13L)	1400	0	10	7	0.5	0.97	0.85	106	26.8	0.336	0.089	0.246	2.787
N10C (G13L)	1450	0	10	7	0.5	0.92	0.86	103	26.6	0.325	0.083	0.237	2.782

<sup>a</sup>The various parameters are described in the text and in Table 3.3. Among the tabulated parameters the input parameters are:  $T_p$ ,  $d$ ,  $Nu$ ,  $L_c$ ,  $dT/dz$ ;  $L$ ; Output parameters are:  $Q_{sf}$ ,  $M_q$ ,  $M_h$ , and  $M_J$ , and fitted parameters are:  $F_k$ ,  $F_\alpha$ ,  $L$ , and  $r_T$ .

<sup>b</sup>Models comparable to *Grose* [2012].

<sup>c</sup>All thermal properties are constants. Note, however, that we use thermal expansivity of forsterite [Bouhifd *et al.*, 1996] for purposes of calculating  $F_\alpha$  for constant property models.

<sup>d</sup>Model properties somewhat comparable to *Goutorbe* [2010].

<sup>e</sup>Model properties somewhat comparable to *McKenzie et al.* [2005].

TABLE 3.2: Properties of best joint fitting models<sup>a</sup>



Parameter	Meaning	Units
$\alpha$	Thermal expansivity	Dim
$b$	Seafloor subsidence rate	m Ma <sup>1/2</sup>
$C_p$	Specific heat	kJ kg <sup>-1</sup> K <sup>-1</sup>
$d$	Grain size	cm
$D$	Thermal diffusivity	mm <sup>2</sup> s <sup>-1</sup>
$F$	Adjustment factor for some property	Dim
$F_\alpha$	Thermal expansivity adjustment factor	Dim
$F_k$	(Lattice) thermal conductivity adjustment factor	Dim
$h_{mod}$	Modeled seafloor depth	km
$h_{obs}$	“Observed” mean seafloor depth in an age bin	km
IQR	Interquartile range	Dim
$k$	Thermal conductivity	W m <sup>-1</sup> K <sup>-1</sup>
$k_{rad}$	Radiative thermal conductivity	W m <sup>-1</sup> K <sup>-1</sup>
$K'_T$	Pressure derivative of bulk modulus	GPa
$K_0$	Bulk modulus at P=0	GPa
$L$	Plate thickness	km
$L_c$	Oceanic crust thickness	km
$M_J$	Joint misfit	Dim
$M_h$	Misfit to seafloor topography	Dim
$M_q$	Misfit to seafloor heat flow	Dim
$M_e$	Extracted melt mass fraction	Dim
$Nu$	Nusselt number	Dim
$P$	Pressure	GPa
$q_{mod}$	Modeled heat flux	mW m <sup>-2</sup>
$q_{obs}$	“Observed” median heat flux in an age bin	mW m <sup>-2</sup>
$q_{sf}$	Seafloor heat flux	mW m <sup>-2</sup>
$Q_{sf}$	Net seafloor heat flux	TW
$r$	Ridge height	km
$\rho$	Density	kg m <sup>-3</sup>
$\rho_0$	Reference density at standard $TP$	kg m <sup>-3</sup>
$\rho_a$	Density below ridge	kg m <sup>-3</sup>
$\rho_b$	Mean density of ridge mantle column	kg m <sup>-3</sup>
$\rho_c$	Mean density of oceanic crust at standard $TP$	kg m <sup>-3</sup>
$\rho_w$	Seawater density	kg m <sup>-3</sup>
$\rho_{wa}$	Average density of seawater column below ridge height	kg m <sup>-3</sup>
$s_f$	Least squares fit to <64 Ma seafloor topography	Dim
$T$	Temperature	°C
$T_p$	Mantle potential temperature	°C
$u$	Half-spreading rate	mm yr <sup>-1</sup>
$V$	Volume	m <sup>3</sup>
$V_0$	Reference volume at standard $TP$	m <sup>3</sup>
$w$	Seafloor depth	km
$w_{mod}$	Modeled seafloor depth	km
$w_{obs}$	“Observed” mean seafloor depth in age bin	km

TABLE 3.3: Symbols for variables in this work



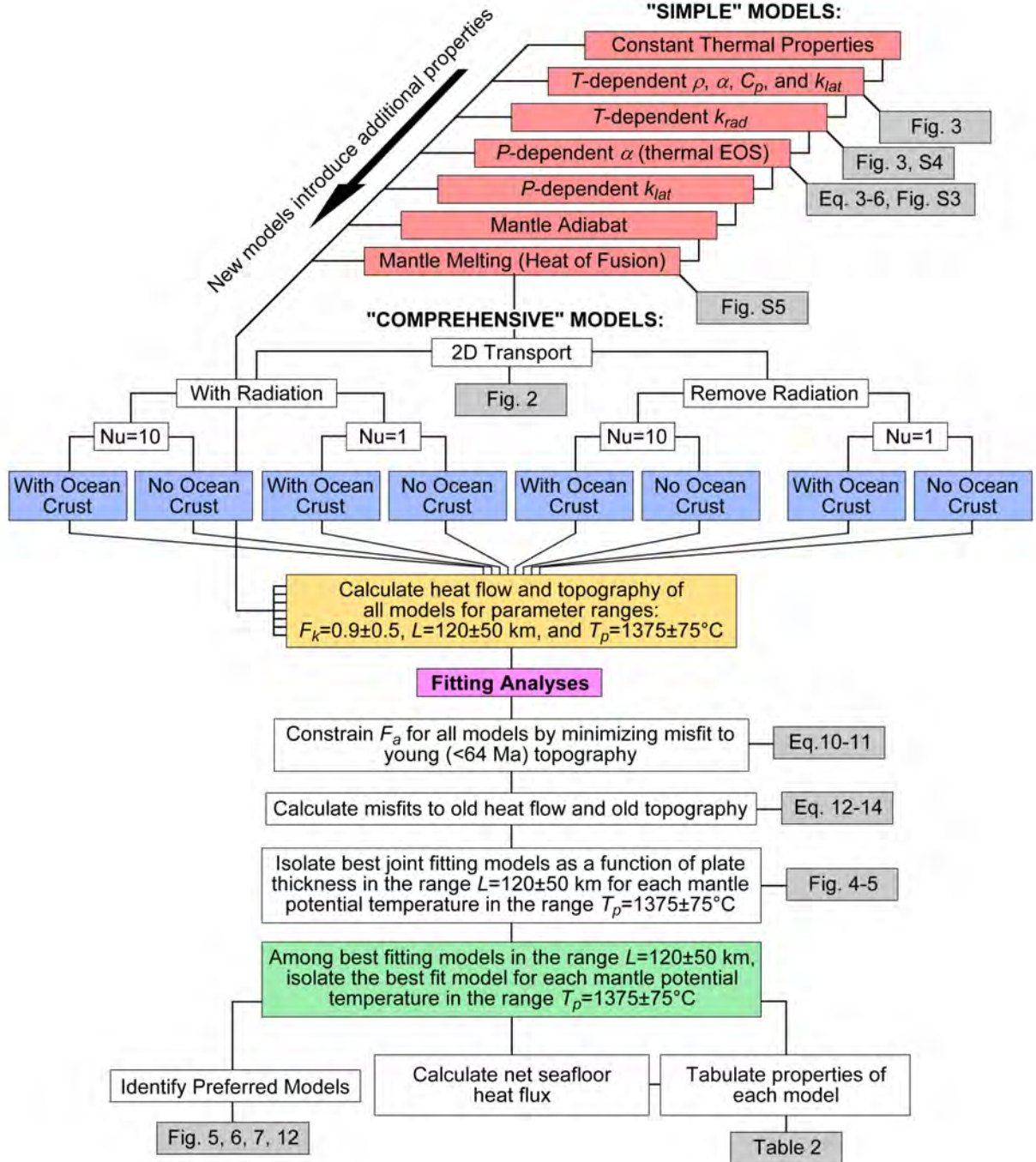


FIGURE 3.1: Flow chart depicting the steps in model development, calculation of properties, and fitting analyses (with links to some relevant equations and figures) in this work.

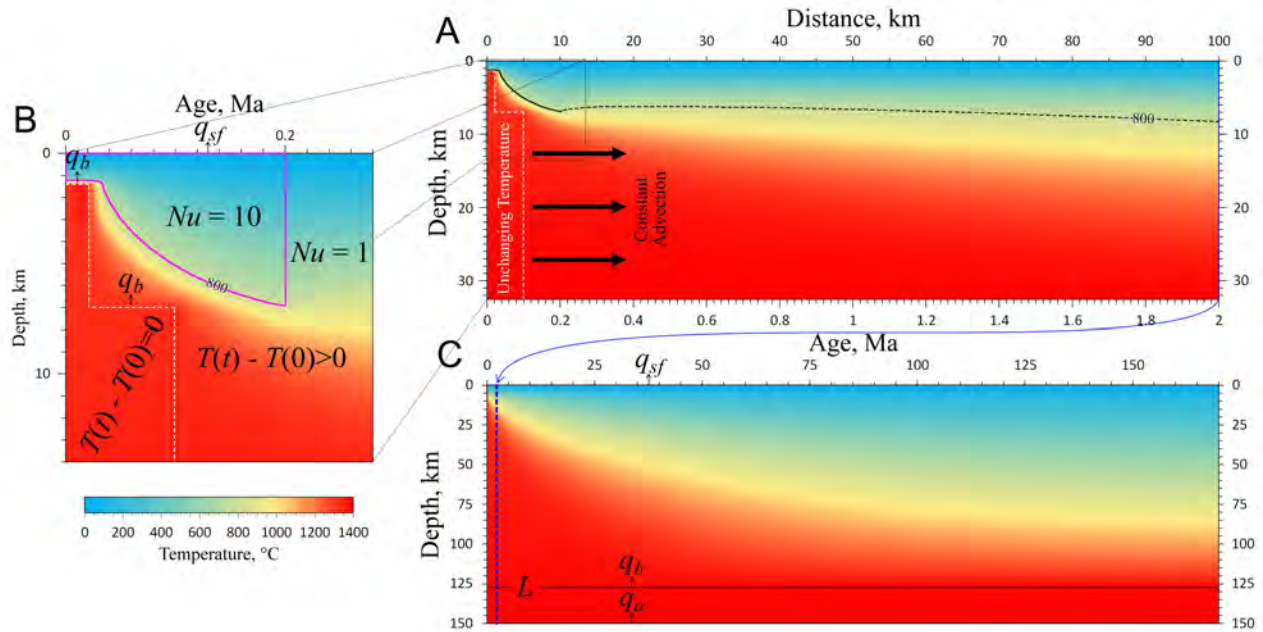


FIGURE 3.2: Boundary and initial conditions for two-dimensional ( $100 \times 45.5$  km) thermal models. (a) The temperature in the region outlined in white dashes varies with depth but remains over horizontal distance. The distance between the surface and the top of the axial boundary condition is 1.4 km. All material around this space advects at a constant rate away from the ridge axis. Additional boundary conditions are explained in the text. For ages  $\leq 0.2$  Ma and mantle with  $T < 800^\circ\text{C}$ ,  $Nu=10$  for models with axial hydrothermal convection. (b) Closer inspection of ridge axis environment. (c) Panel showing the large-scale thermal evolution of oceanic lithosphere. After the two-dimensional model in panel A reaches steady-state, the geotherm at  $t=2.0$  Ma is imported into a one-dimensional model and calculated to 170 Ma.

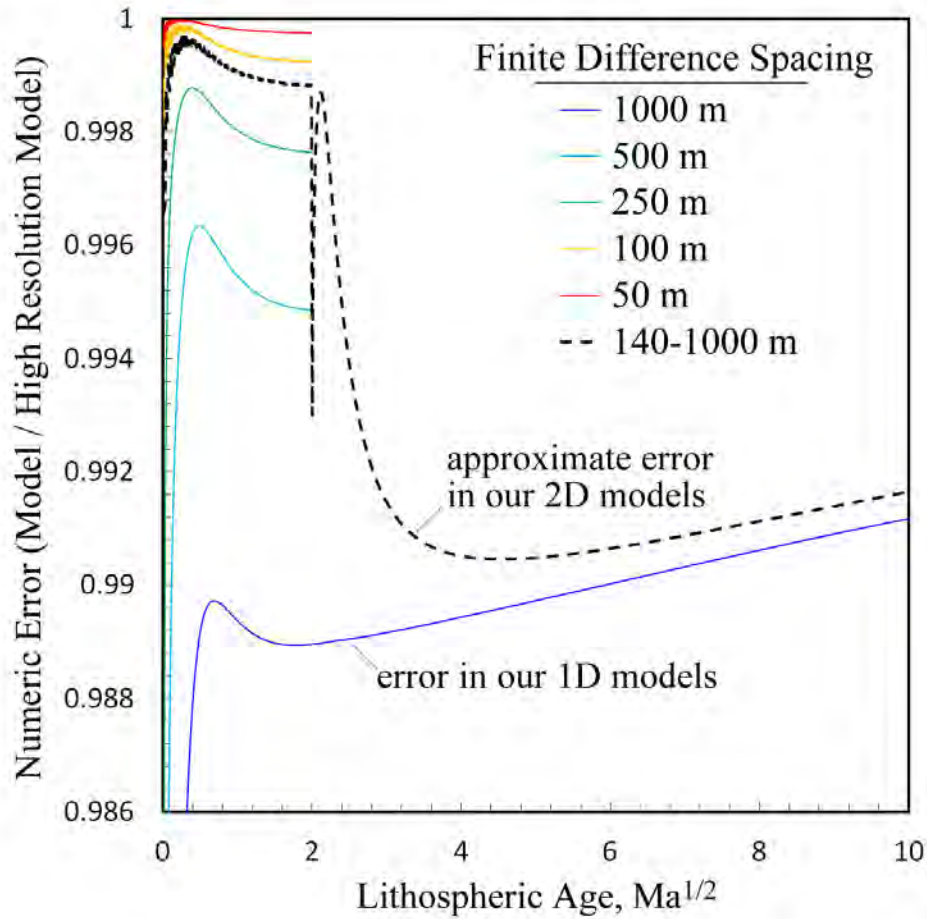


FIGURE 3.3: One-dimensional convergence test calculations in our models using properties of G13R. Finite difference spacing was varied from 25 m to 1000 m. Numeric error is calculated by normalizing predicted surface heat flux against the predictions of the high resolution model (25 m vertical spacing). An important assumption in our analysis is that, for purposes of speed of calculation in these tests, G13R was reconfigured to be one-dimensional everywhere, although we expect the difference to be small. The dashed line is the expected error in our two-dimensional 'comprehensive' models, and the blue line is the expected error in our one-dimensional models.

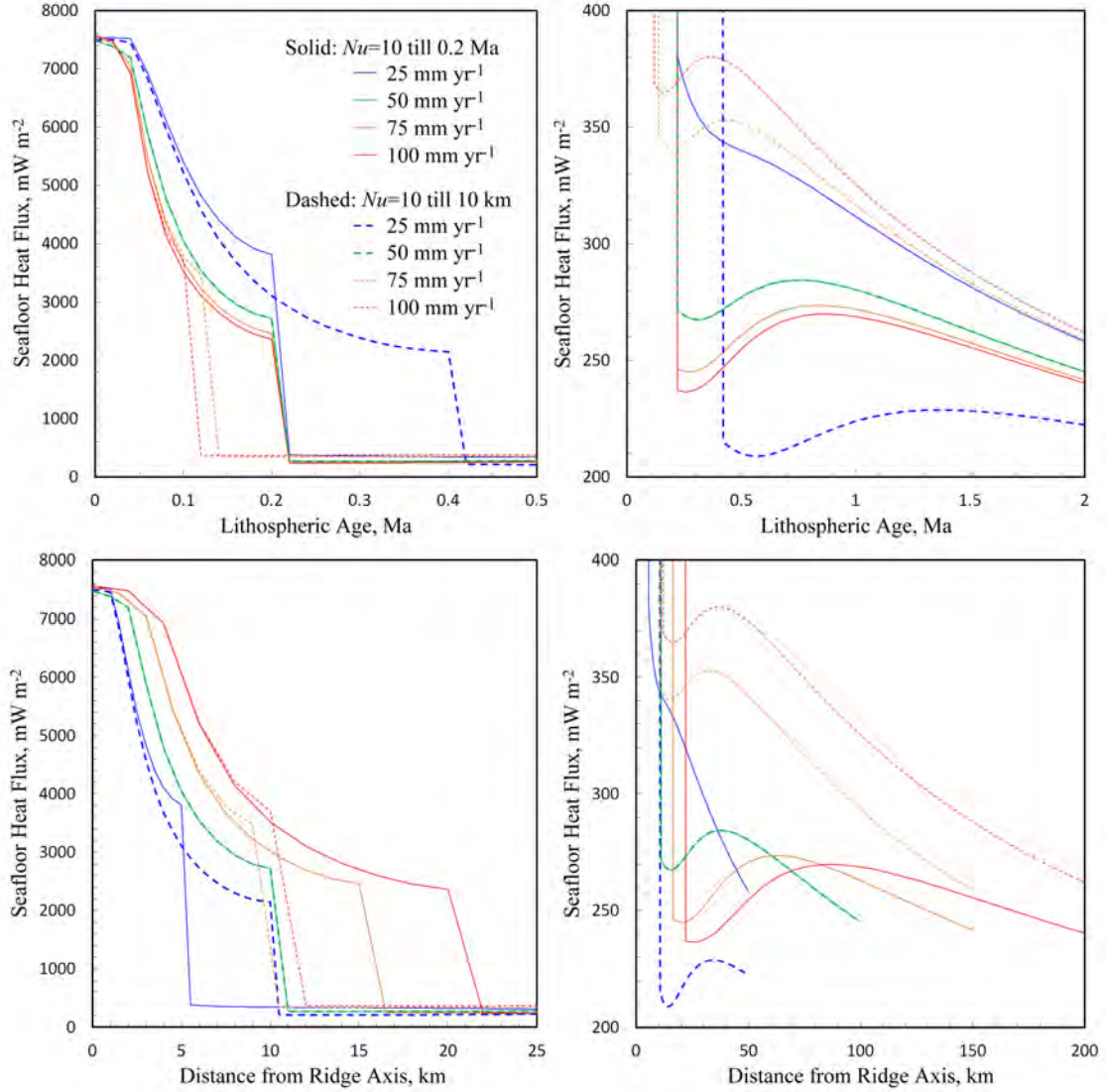


FIGURE 3.4: This figure illustrates the consequences of using a different spreading rate for model G13R. Model G13R developed in the manuscript assumes a half-spreading rate of  $50 \text{ mm yr}^{-1}$ . The curves in each panel represent the same predictions, except the left panels show the full intensity of heat flow, right panels focus on the off-axis heat flow, top panels depict the variation with age, and the bottom figures depict the variation with distance from the ridge axis. In addition, we have assumed in our analysis that the age where axial hydrothermal circulation ceases is 0.2 Ma or 10 km from the ridge axis. However, it is not completely clear whether how to treat the cutoff age or distance when the spreading rate is varied. Although it seems most realistic to use a cutoff age instead of distance, we also report calculations with the distance held constant, for completeness.



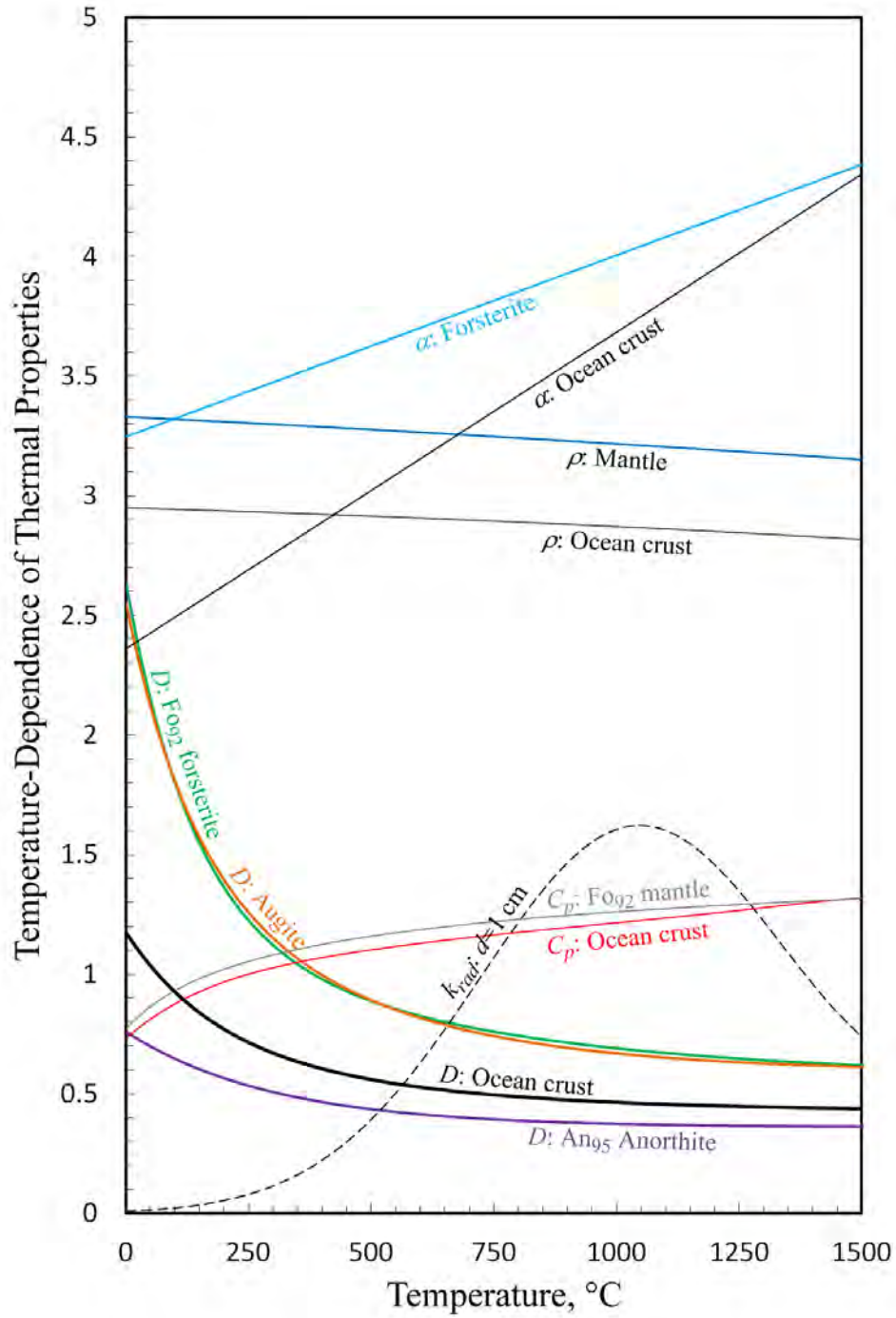


FIGURE 3.5: Temperature-dependence of thermal properties used in this work. Thermal diffusivity  $D$  ( $\text{mm}^2 \text{s}^{-1}$ ) of  $\sim\text{Fo}^{90}$  olivine, augite, and  $\text{An}_{65}$  plagioclase; density  $\rho$  ( $\times 10^3 \text{ kg m}^{-3}$ ) of mantle and crust; thermal expansivity  $\alpha$  (dimensionless  $\times 10^{-5}$ ) of forsterite (mantle) and ocean crust; specific heat  $C_p$  ( $\text{kJ kg}^{-1} \text{K}^{-1}$ ) of mantle and ocean crust; and the radiative contribution to effective thermal conductivity  $k_{rad}$  ( $\text{W m}^{-2}$ ) for a grain size of 1 cm. Mineral physics coefficients and references are given in Table 3.1.

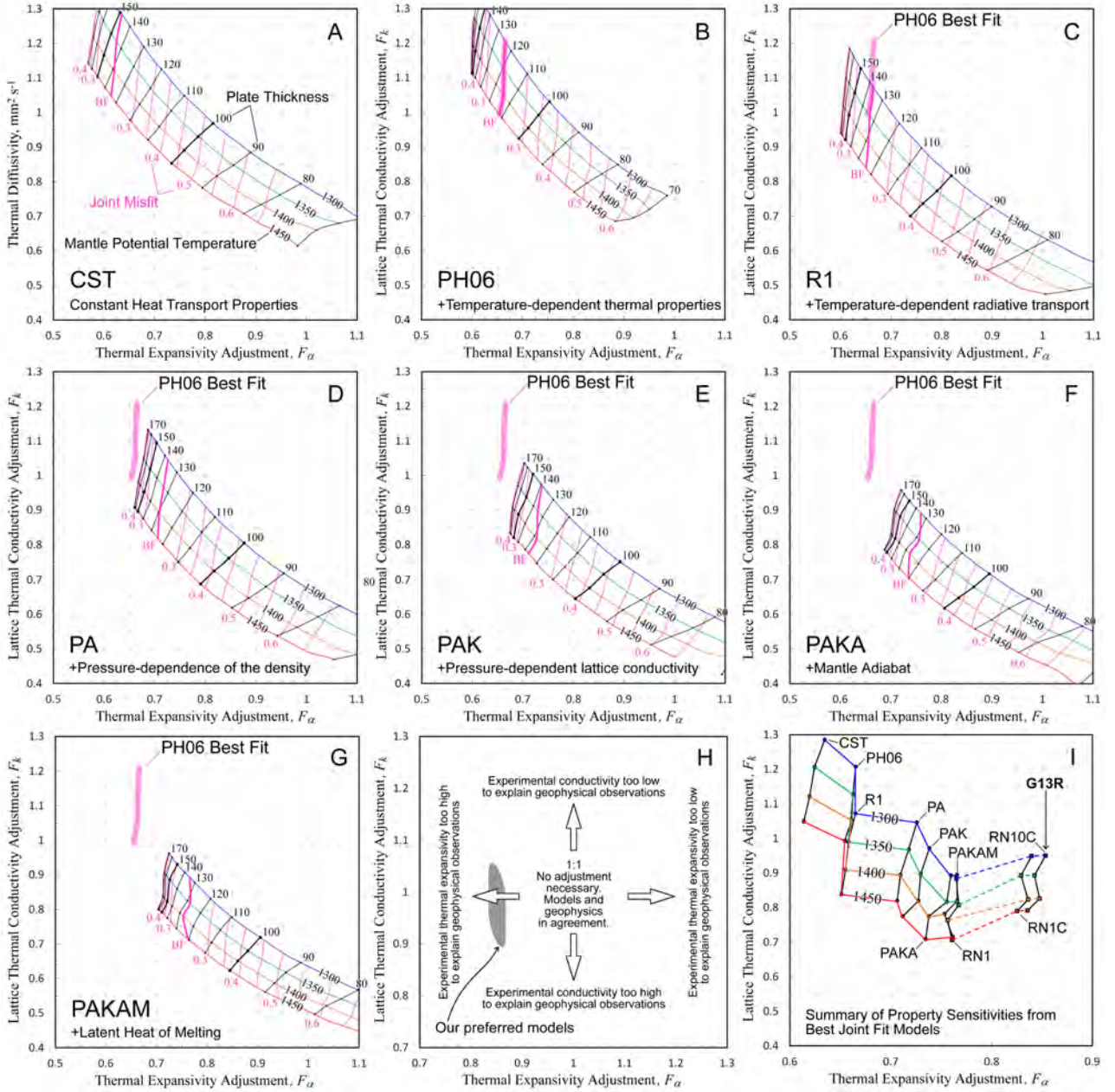


FIGURE 3.6: Lattice thermal conductivity adjustment factor  $F_k$  versus the thermal expansivity adjustment factor  $F_\alpha$  for best-fitting models as a function of plate thickness and mantle potential temperature. Panels (a)-(g) show results for each 'simple' model type indicated in the panel caption and shown in Fig. 3.9. The type of data shown by each line is described in panel (a). "BF" is the line indicating best-fitting models. Panel (h) is an illustration describing the implications of different values of  $F_k$  and  $F_\alpha$ . Adjustment factors  $> 1$  indicate that the experimental value is too low and values  $< 1$  indicate the experimental value is too high to explain geophysical observations. Panel (i) shows a summary of all best joint fit models, including comprehensive models (dashed lines) that retain radiative thermal conductivity (see Fig. 3.7).

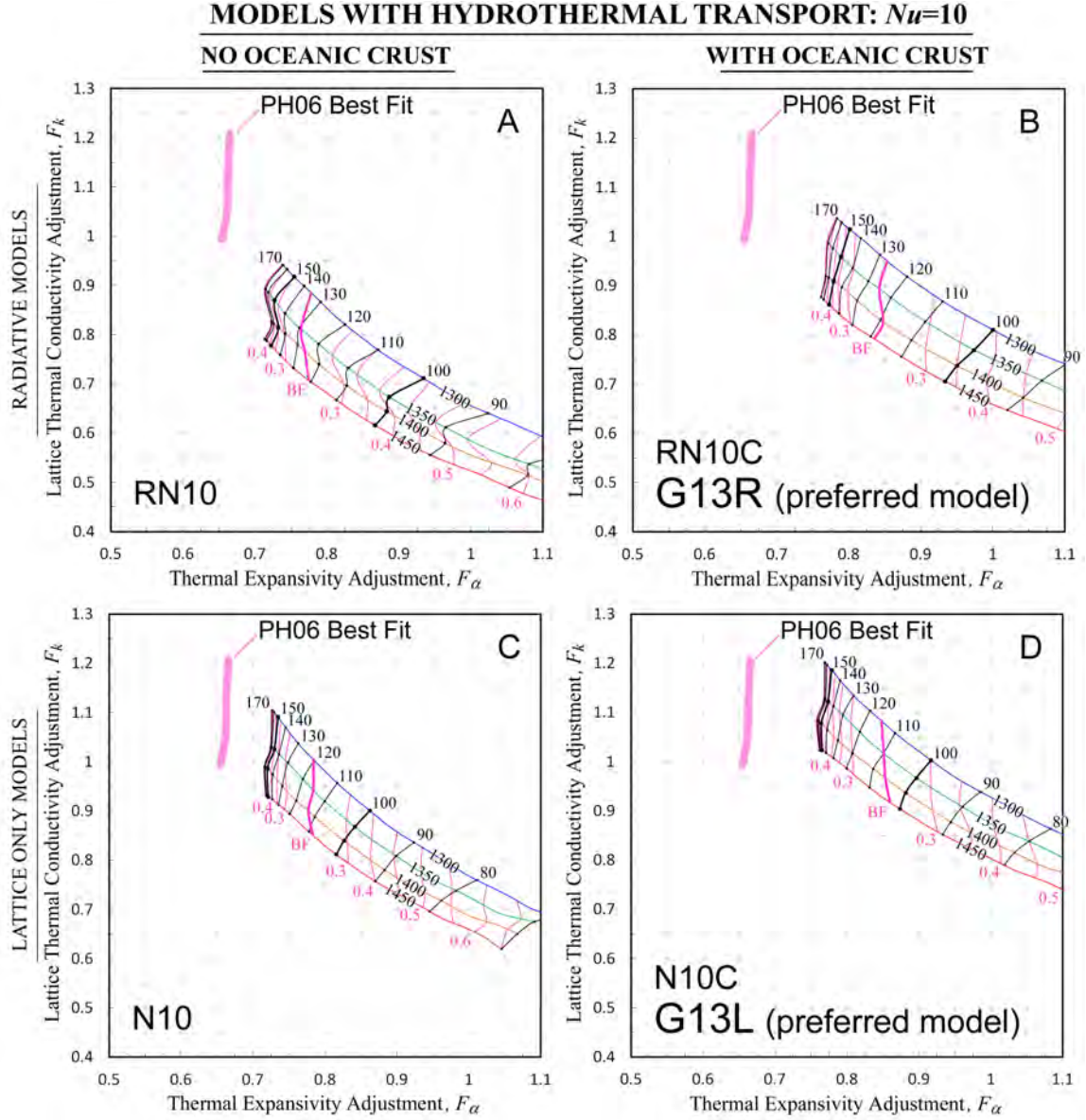


FIGURE 3.7: Same representation as in Fig. 3.10 for 2D 'comprehensive' models with hydrothermal circulation ( $Nu=10$ ). Top panels show models with a high radiative contribution to thermal conductivity, bottom panels show models with no radiative thermal conductivity, left panels show models with no oceanic crust and right panels show models with oceanic crust. See Fig. 3.3 for the same figure describing results of models with no hydrothermal circulation ( $Nu=1$ ). Panels (b) and (d) show models G13R and G13L, respectively.



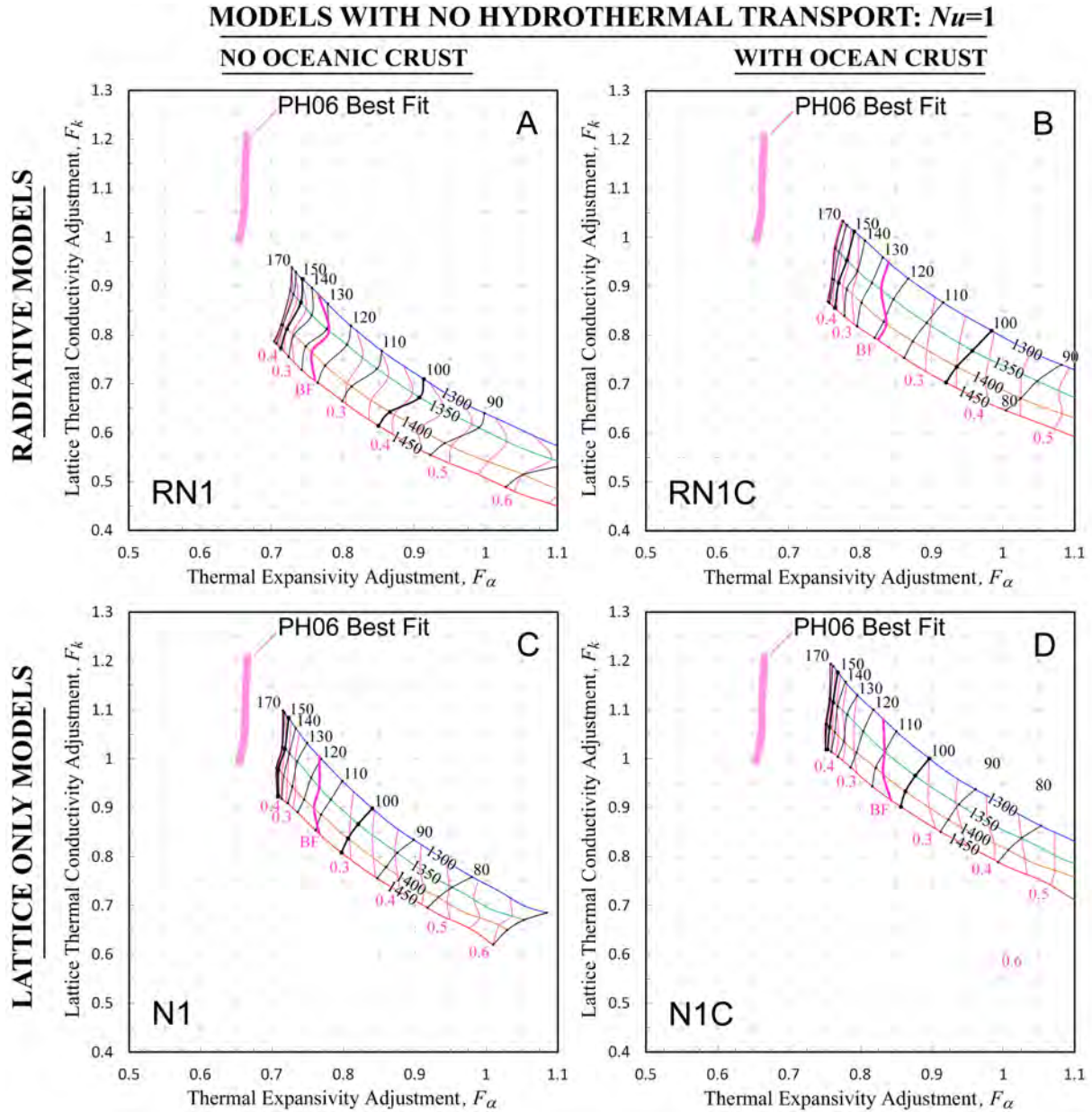


FIGURE 3.8: Same illustrations as in Fig. 3.11, except results for models without hydrothermal circulation are shown.



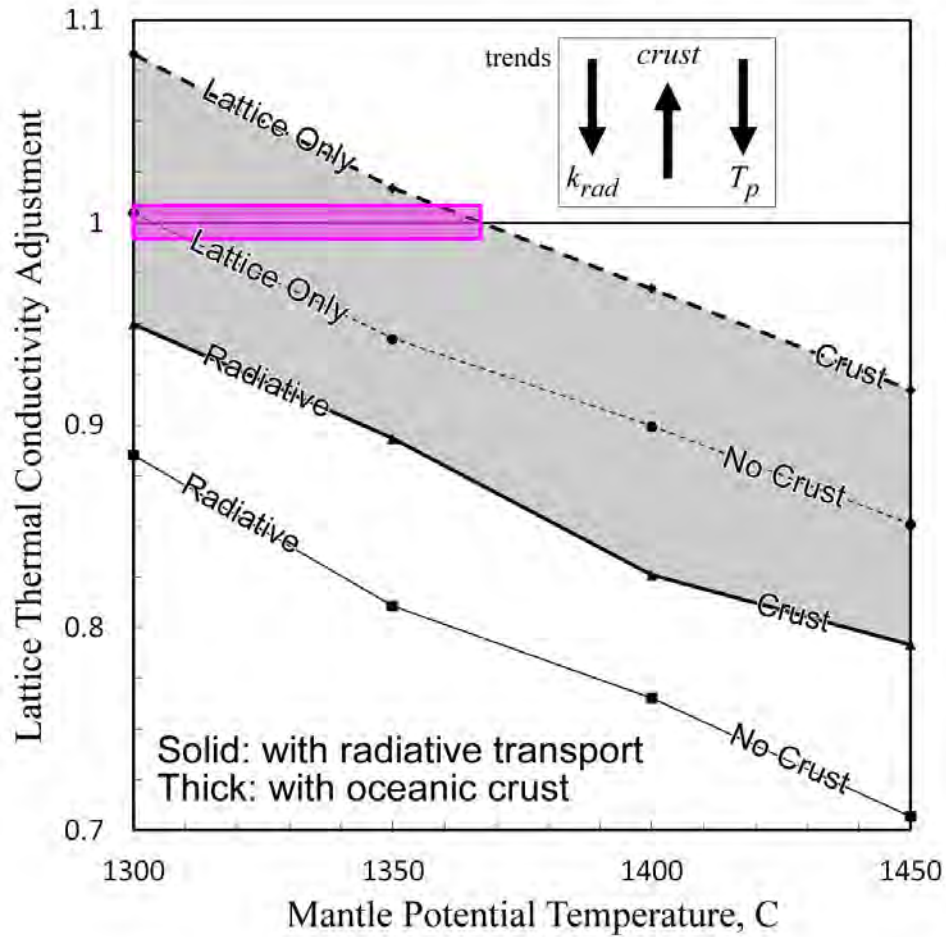


FIGURE 3.9: Thermal conductivity adjustment factor of best-fitting comprehensive models as a function of mantle potential temperature. The grey highlighted region indicates bounds for models with insulating oceanic crust with and without radiative thermal conductivity. Solid lines include radiative transport, dashed lines have no radiative transport, thick lines include insulating oceanic crust, and thin lines have no crust. The violet boxed area indicate the mantle potential temperatures where best-fitting models can be found which do not require adjustments to lattice thermal conductivity (that is, one can adjust the radiative contribution without changing lattice thermal conductivity). Compare to Fig. 3.7.

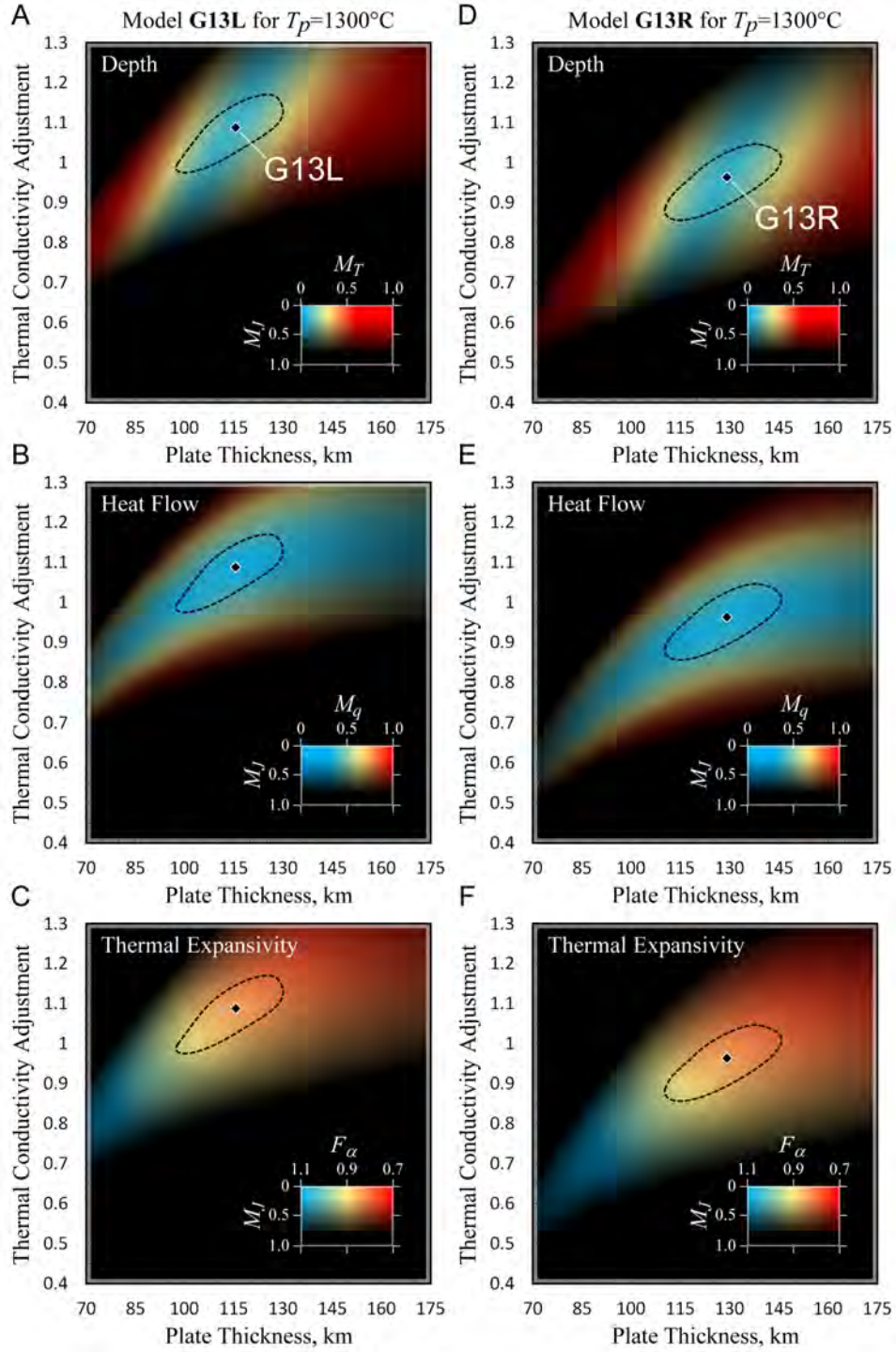


FIGURE 3.10: Properties of models G13R and G13L at  $T_p = 1300^\circ\text{C}$ . Colors show the misfit for depth (a,d), misfit for heat flow (b,e), and thermal expansivity adjustment factor  $F_\alpha$  (c,f) as a function of the thermal conductivity adjustment  $F_k$  versus plate thickness  $L$ . The shading is an 'alpha transparency' of the joint misfit in  $F_k$  versus  $L$ . This means that the field of joint misfit is everywhere black with transparency changing with magnitude, and this is overlain on the other fields in color (Fig. 3.19). The diamond is the point of minimum joint misfit (for  $T_p = 1300^\circ\text{C}$ ) and the dotted line shows where joint misfit  $M^J=0.3$ . See Fig. 3.19 for more about the construction of this figure.

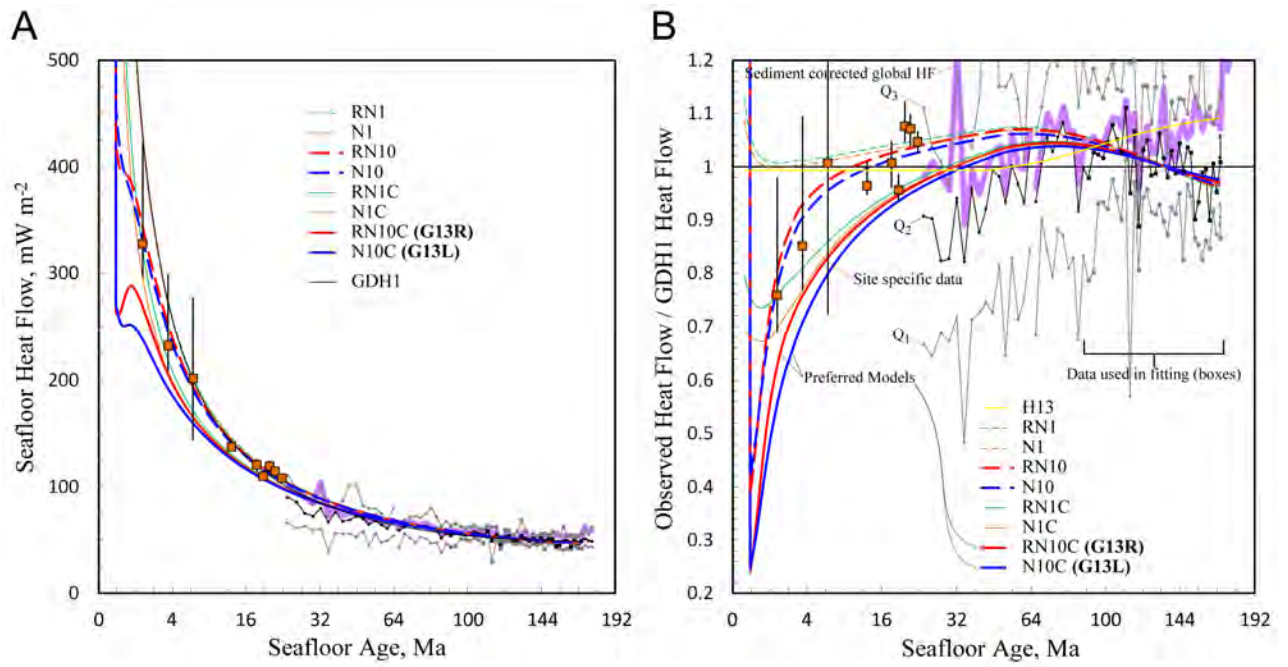


FIGURE 3.11: (a) Comparison of measured seafloor heat flow with predictions of comprehensive models, GDH1 (Stein and Stein, 1992), and global heat flow as a function of age. (b) Ratio of observed heat flow against predictions of GDH1 as a function of  $t^{1/2}$ . The grey and black thin lines with markers are 1st, 2nd (median) and 3rd quartiles for sediment uncorrected heat flow, and the thick violet line is the median sediment corrected heat flow from Hasterok (2013). The boxed markers are the heat flow points used in our calculation of misfit to heat flow. The orange boxes with error bars are median heat flow and interquartile distributions for specific sites of well resolved heat flow from Hasterok (2013).

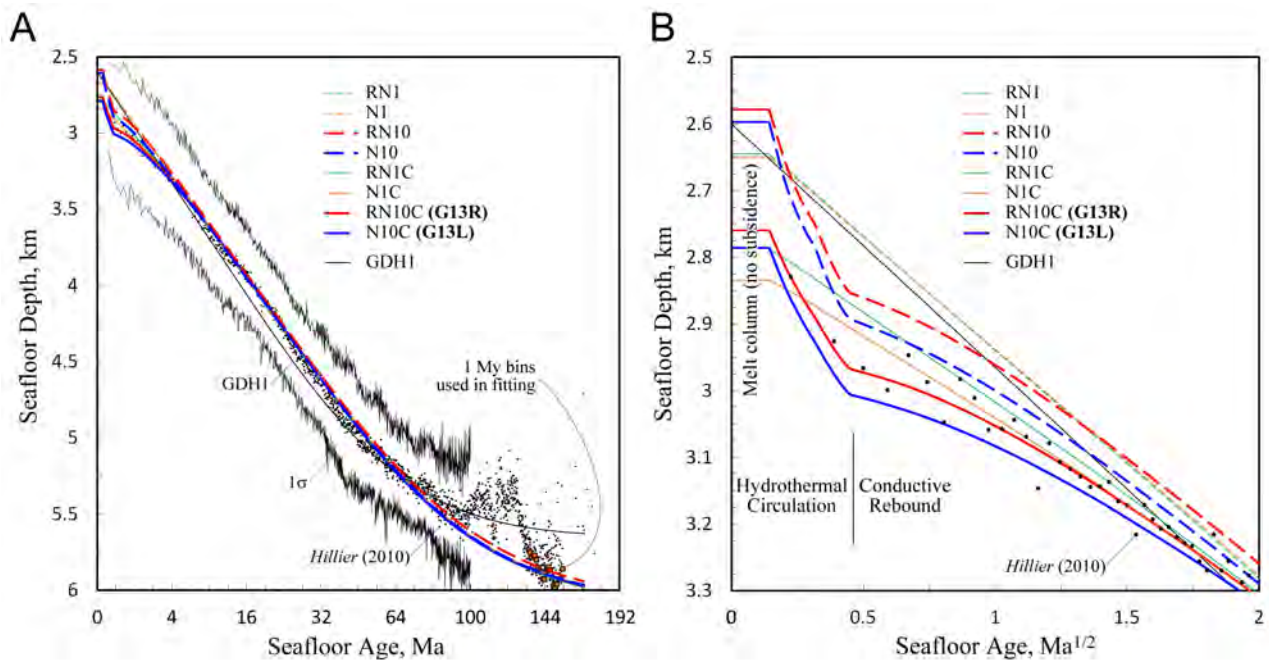


FIGURE 3.12: Predictions and observations of seafloor topography and subsidence. (a) Seafloor topography of our best-fitting 2D comprehensive models compared with model GDH1 (Stein and Stein, 1992) and 0.1 Myr binned mean global depth with  $1\sigma$  standard deviation from Hillier (2010). The orange boxes are the 1.0 Myr bins used in our formal analysis of misfit. (b) Close-up of model predictions on ridge flanks.



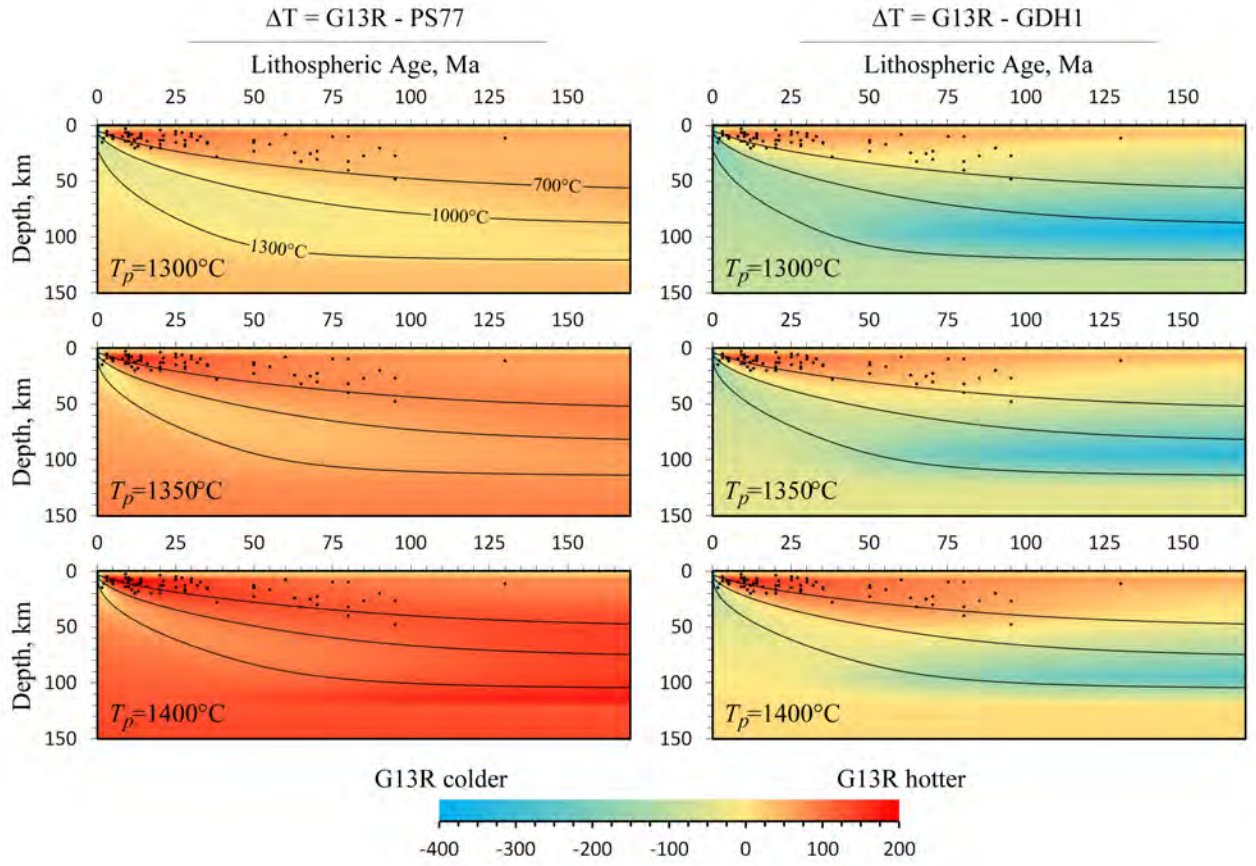


FIGURE 3.13: Thermal structure of our model G13R as compared to PS77 and GDH1. Colors indicate the difference between models with the mantle potential temperature of G13R varied between 1300 and 1400°C. Lines are isotherms for G13R. Dots are intraplate earthquake hypocenters from McKenzie et al. (2005) and Geli and Sclater (2008).

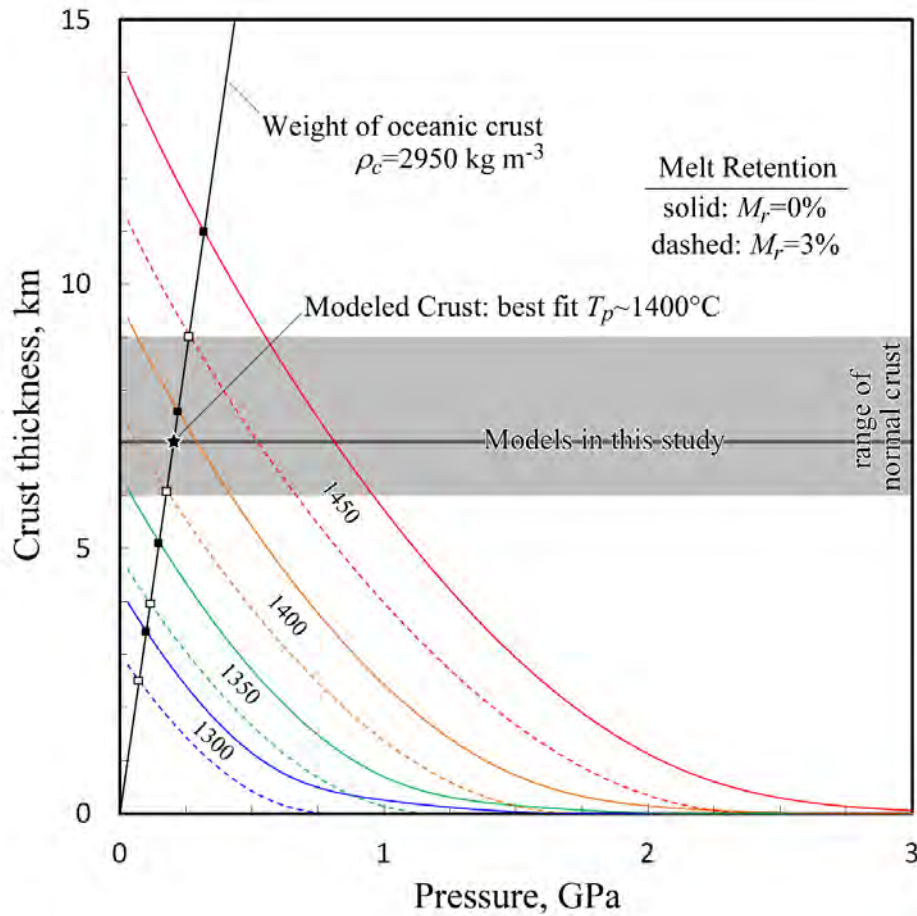


FIGURE 3.14: Thickness of oceanic crust predicted from the melting model of Asimow et al. (2001) by integrating the melt column from infinite depth to Moho depth. Predictions for mantle temperature  $1300\text{--}1450^\circ\text{C}$  are shown (color), solid lines assume that all melt produced is incorporated into the crust and dashed lines assume that the first 3% of melt residues remains unextracted. The highlighted area indicates the range for most normal oceanic crust ( $6.5 \pm 1.5 \text{ km}$ ) which can be compared to our assumption that oceanic crust is always  $7 \text{ km}$  thick.

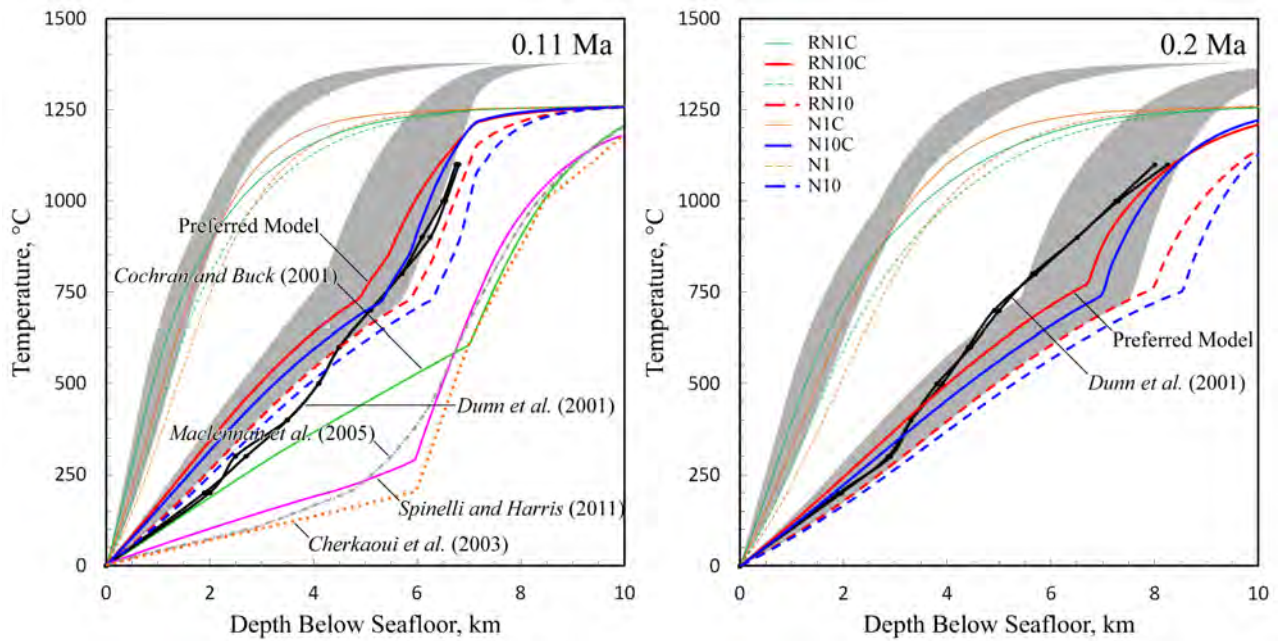


FIGURE 3.15: Geotherms for comprehensive models at 5.5 km (0.11 Ma) and 10 km (0.2 Ma) from the ridge axis. The lines for our models show predictions for models with a potential temperature of 1300°C and the highlighted regions outline the predictions for 1450°C. The thick black lines with circle markers give geotherms on either side of the East Pacific Rise from seismic tomography by Dunn et al. (2000). Models with no axial hydrothermal circulation ( $Nu=1$ ) significantly overestimate temperature at depth while models with  $Nu=10$  show good agreement. The best-fitting models have both hydrothermal circulation and crustal insulation. The case of  $t=0.11$  Ma is compared with model predictions of Cochran and Buck (2001), Cherkaoui et al. (2003), MacLennan et al. (2005), and Spinelli and Harris (2011). Cochran and Buck’s geotherm is actually for 0.1 Ma.

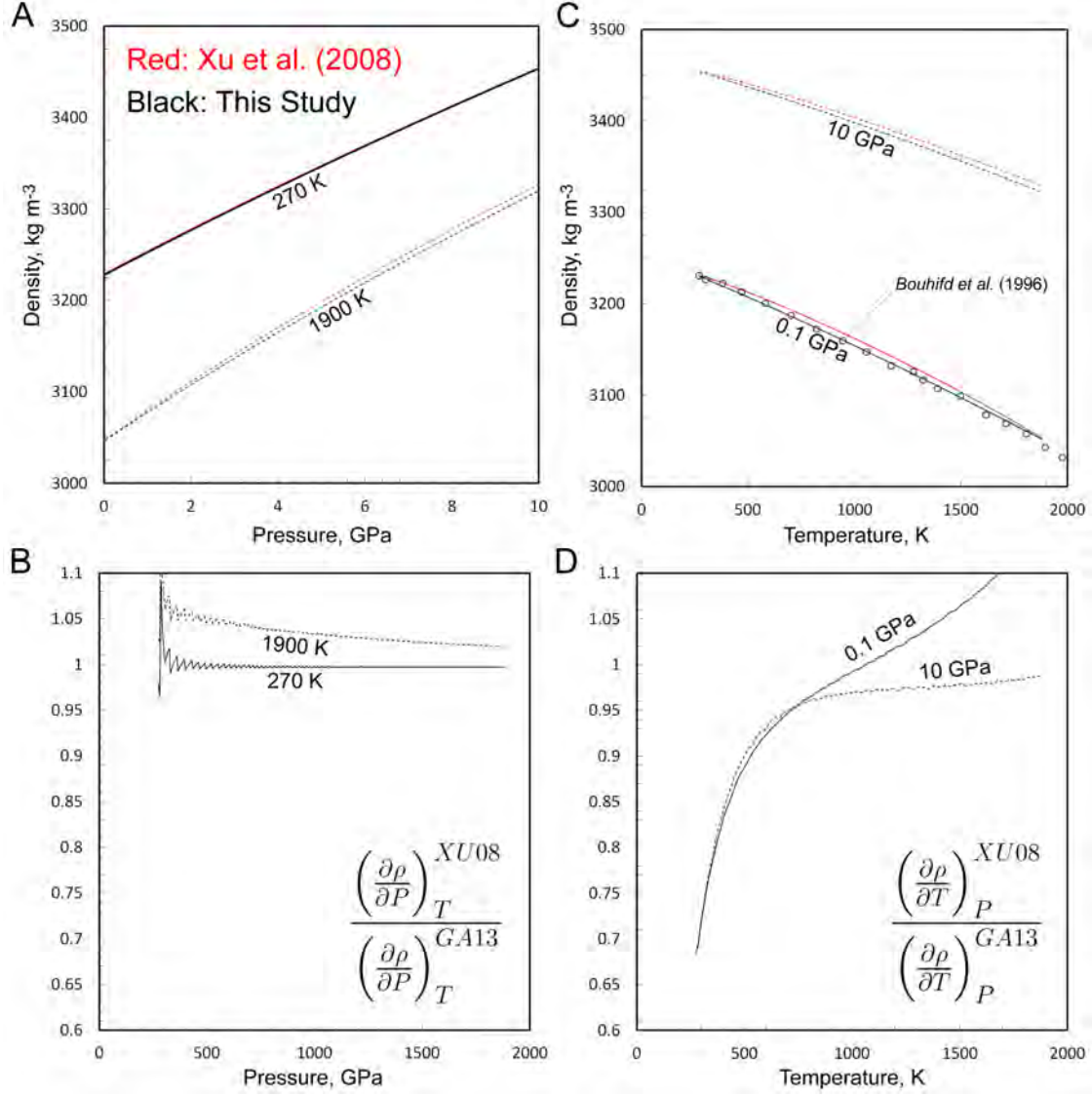


FIGURE 3.16: Predictions of forsterite density for our study compared to the self-consistent thermodynamic approach of Xu et al. (2008) as calculated using PerpleX (Connolly, 2009). (a) Density as a function of pressure at 270 K and 1900 K. (b) Ratio of volume compression predicted by the thermodynamic model over our approximation. (c) Density as a function of temperature at 0.1 GPa and 10 GPa. The open circles are volume measurements from Bouhifd et al. (1996) assuming  $\rho_0=3230 \text{ kg m}^{-3}$  at 270 K (this reference density is used to match the reference density in the PerpleX calculation). (d) Ratio of volume expansion predicted by Xu et al. (2008) over our EOS as a function of temperature at 0.1 GPa and 10 GPa. Both models predict the same compression at 270 K (Fig. 3.18a-b). The difference in predictions at temperature are similar at 0.1 GPa and 10 GPa (Fig. 3.18c-d). These observations indicate that most of the difference between these predictions is simply due to our use of a linear temperature-dependent thermal expansivity versus the thermal pressure formulation of Xu et al. (2008).



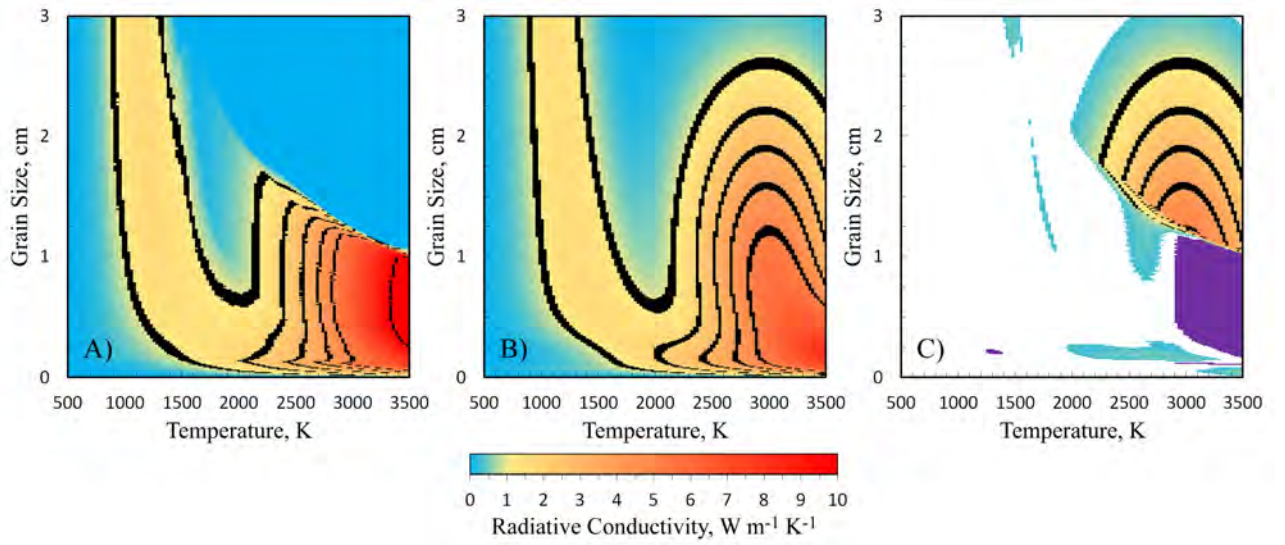


FIGURE 3.17: Radiative thermal conductivity in olivine, applied in our modeling analysis to the entire lithosphere. (a) Predictions of Eq. 3.8 using the crystallographic assumptions of Hofmeister (2005), although we have evaluated  $\sim\text{Fo}_{90}\text{Fa}_{10}$  spectra continuously with temperature using a cubic interpolation scheme. (b) Prediction of Eq. 3.17 (Appendix A), our approximation of Hofmeister's (2005) model. (c) Difference of Eq. 3.8 and 3.17. The parameter space where the difference is less than  $\pm 0.25$  W m<sup>-1</sup> K<sup>-1</sup> is white, overestimates are colored using the same scale as in Fig. 3.5a-b, and underpredicted values are purple. The fit is good for  $T < 3000$  K except for a region at high temperature and grain-size where Hofmeister's (2005) model predicts that  $k_{\text{rad}} \rightarrow 0$ . This feature could be accounted for with an additional term in Eq. 3.17, but we ignore it since our models only experience  $T < 1900$  K.

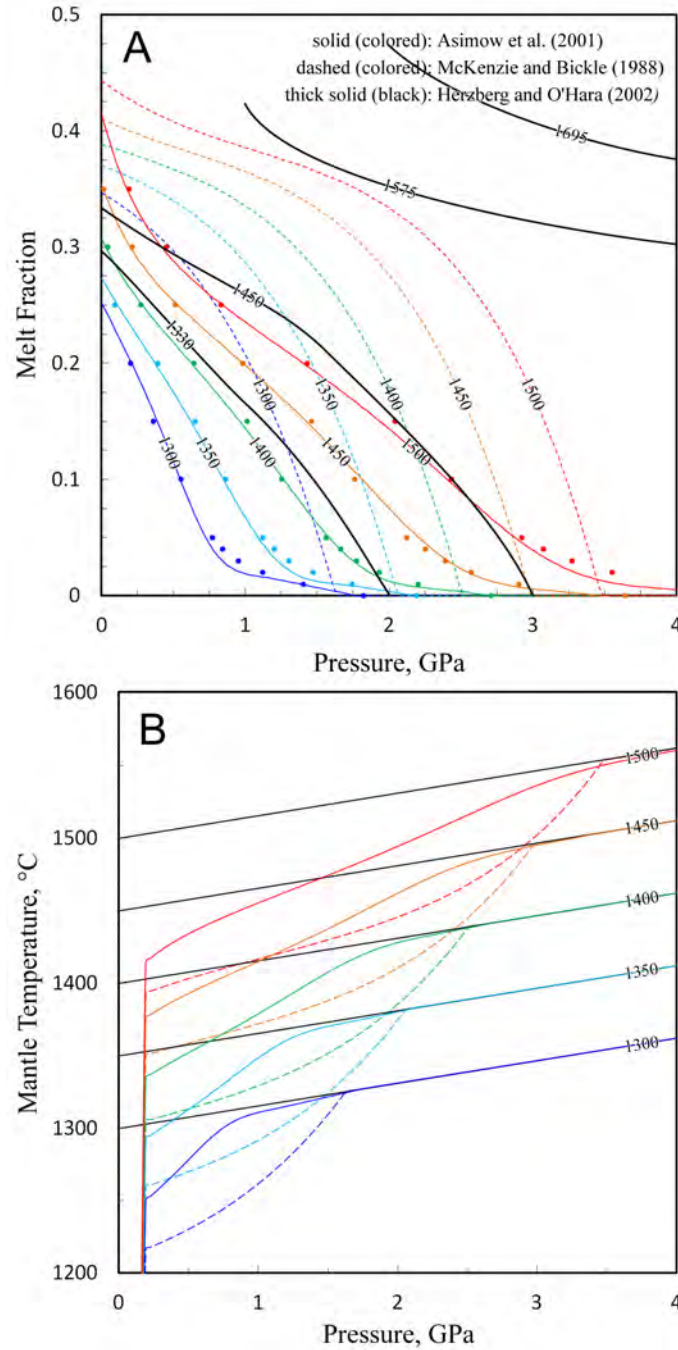


FIGURE 3.18: (a) Melt mass fraction predicted by the melting models of Asimow et al. (2001), McKenzie and Bickle (1988), and Herzberg and O'Hara (2002). Data points are graphically approximated from Asimow et al. (2001), which we have used to derive our fit (Appendix B). (b) Geotherms for potential temperatures between 1300-1500°C using the melting models of Asimow et al. (2001) and McKenzie and Bickle (1988), and an adiabatic gradient of  $0.5^{\circ}\text{C km}^{-1}$ .

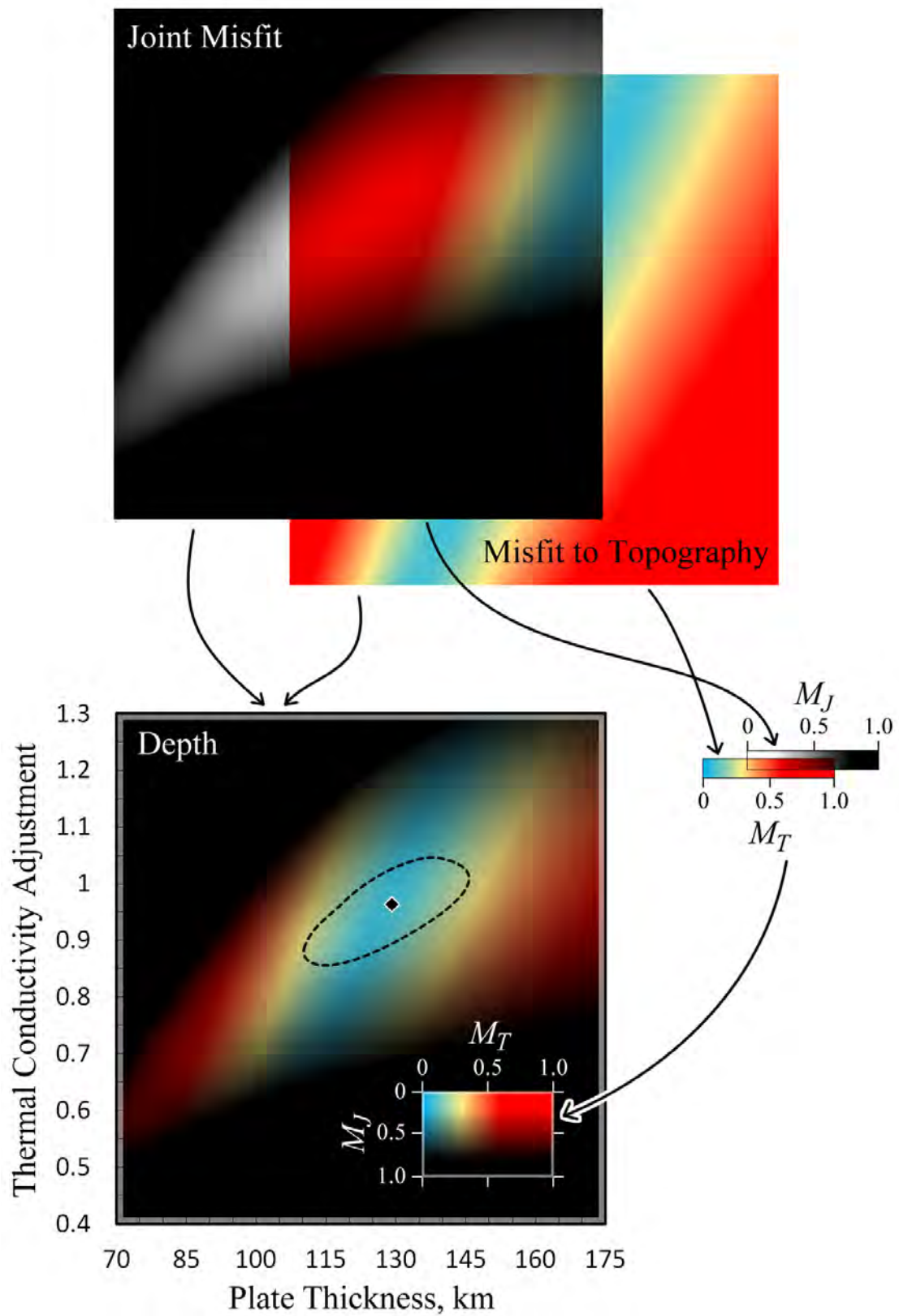


FIGURE 3.19: This figure is an attempt at illustrating the use of an alpha composite to construct Fig. 3.10. The joint misfit  $M_J$  uses a partial transparency to illustrate magnitude, whereas the misfit to topography  $M_T$  simply uses color.



# 4

## The Hydrothermal Power of Oceanic Lithosphere

### 4.1 INTRODUCTION

The cooling of oceanic lithosphere over time and distance from ridges is a key constraint on plate tectonics. A predicted consequence of this cooling is that surface heat flux over young seafloor is relatively high and gradually diminishes with age. Although elevated heat flow on average has long been recognized over ridges (Bullard, 1952; Von Herzen, 1959; Von Herzen and Uyeda, 1963; Sclater, 2004), it was also found that measurements are highly scattered. Much subsequent work attempted to explain geophysical observations with models of lithospheric cooling and subsidence, and models were gradually refined by improved constraints on the geophysical properties of the upper mantle (e.g. Langseth et al., 1966; McKenzie, 1967; McKenzie and Parker, 1967; Le Pichon, 1968; Sleep, 1969; Sclater and Francheteau, 1970; Sclater et al., 1971). Eventually, it was recognized that measured heat flow close to ridge axes was far too low to be explained by a model that also explained seafloor subsidence accurately (Sclater and Francheteau, 1970). Following the work of Lister (1972; 1974) and Bodvarsson and Lowell (1972), it became understood that the deficit between measured and predicted heat flow (as well as its scatter) originated in advective hydrothermal ventilation of heat between crustal basement and the oceans. This difference between model and measurement is therefore a proxy to estimating the lithospheric thermal power removed by hydrothermal circulation in oceanic lithosphere. Such constraints on the heat deficit are critically important for the understanding of numerous chemical and physical processes in the Earth. In addition to providing a direct constraint on the thermal budget of cooling oceanic crust and lithosphere (Mottl, 2003; Hasterok, 2013a), this is also the power available to drive chemical exchange between the crust and oceans (e.g., Seyfried et al., 1984; Spivack and Edmont, 1987; Nicolas et al., 2003; Staudigel, 2014), and pass

nutrients to sub-seafloor microbial communities (e.g. Jannasch, 1983; 1995; Hessler et al., 1988; Tunnicliffe, 1991). In addition, the alteration of oceanic crust regulating the chemical budgets of subducting slabs (Schmidt and Poli, 2013; Ryan and Chauvel, 2013). Moreover, volatile cycling between the mantle and hydrosphere may impart a major control on secular changes in the efficiency of mantle convection over Earth history (Crowley et al., 2011).

Although the mentioned heat flow deficit exists in the 'unfiltered' global database, Hasterok et al. (2011) and Hasterok (2013a;b) have demonstrated that the deficit is markedly reduced when only marine environments known to have thick sediment cover are considered. Such environments are expected to restrict advective heat transport because hydrothermal ventilation is generally confined to sites of outcropping basement, and thick sediments reduce the prevalence of outcrops. Moreover, these authors found that a compilation of heat flow estimates from young (<30 Ma) seafloor with thick sediment cover and extensive geophysical characterization agreed well with conventional lithospheric cooling models (e.g. model GDH1 of Stein and Stein, 1992).

Recently, models of the oceanic lithosphere have been developed that include constraints on the properties of the mantle and crust from mineral physics experiments (Hasterok, 2010; Grose and Afonso, 2013; Chapter 3). These models predict that lithospheric heat flow over young seafloor may be significantly lower than that estimated with conventional models. Hasterok (2010) investigated lithospheric cooling models which account for differing properties of crust and mantle. Since the crust is relatively insulating, the effective heat transport properties of the lithosphere are 'crust dominated' near ridge axes (a thermal blanketing effect yielding lower heat flow), and gradually approach mantle values over time. Also, based on work characterizing crustal accretion and cooling, and hydrothermal heat transport (e.g. Chen and Phipps Morgan, 1996; Cherkaoui et al., 2003), Cochran and Buck (2001) and Spinelli and Harris (2011) showed that hydrothermal transport near ridge axes also results in low heat flow on ridge flanks away from the axis because, after the cessation of hydrothermal advection, the crustal geotherm rebounds from the effects of advective cooling. Finally, in Chapter 3 we showed that axial hydrothermal circulation and crustal insulation together result in a compounded reduction of predicted heat flow in proximity to ridge axes. Since the most robust estimates of net ventilated hydrothermal power come from the difference of predicted and measured seafloor heat flow (Mottl, 2003), lower predicted conductive seafloor heat flow suggests that ventilated hydrothermal power in oceanic lithosphere must also decrease. The purpose of this paper is to examine these modified predictions of total ventilated hydrothermal power, and its spatial distribution, using recent models of lithospheric cooling. We will show that total ventilated hydrothermal power may be significantly less than conventional estimates, and that the fraction of hydrothermal power extracted on axis may be up to 50% of the total. Thus, the extent of off-axis hydrothermal circulation may be less than previously thought. Finally, as the resulting predictions of ventilated hydrothermal power (and its implications) depend on the accuracy of cooling models, we discuss constraints from global seafloor topography and several regions of young and geophysically well-characterized seafloor which are thought to constrain the lithospheric heat budget.

## 4.2 Methods

### 4.2.1 The Power Deficit

Heat lost from the cooling of oceanic crust and upper mantle must ultimately be transported through upper crustal layers and through (or around) sediment cover. If hydrothermal circulation occurs in the crust, and especially if hydrothermal fluids are exchanged between crust and oceans, measured heat flow can be substantially affected. Fig. 4.1 shows an illustration summarizing perturbations of seafloor heat flow by hydrothermal circulation processes. We depict three possible thermal states in which oceanic crust may be regionally characterized. Firstly, if circulation in the crust is sluggish or is not unable to occur due to crustal impermeability, then lithospheric heat loss is largely conductive and measured heat flow at the surface should match the predictions of a conductive reference model. Secondly, if circulation does occur in the crust but fluids are not vented to the oceans, all heat removed from the surface occurs conductively, but closed circuit circulation will act as a high-conductivity layer, elevating surface heat flow above that expected by a model which does not include such a high-conductivity layer. This effect can be increased by increasing the thickness of the convective layer, or by hydrothermal exchange with deeper crust by advection along faults. We may call such a state super-conductive. Finally, and most important, if vigorous hydrothermal circulation occurs in the crust and fluids are exchanged between the crust and oceans, the conductive heat flux above such an aquifer will be less than the average heat flux below it. This occurs because as heat is discharged to the oceans it is replaced by a recharge of cool water which is advected through a permeable aquifer. This reduces the temperature of aquifer as well as crust and sediment above it, lowering surface heat flow. This is the sub-conductive state in Fig. 4.1. Because measured heat flow over young seafloor is known to be systematically lower than that predicted by lithospheric models, it is believed that seafloor is dominantly in such a 'sub-conductive' state. Also, as this deficit between measured and modeled heat flow is a consequence of fluid discharge and recharge, we can use it as a proxy to estimating the power lost to the oceans by ventilated hydrothermal circulation (e.g. Wolery and Sleep, 1976; Sleep and Wolery, 1978; Stein and Stein, 1994; Davis and Elderfield, 2004).

Following much prior work on this issue (see above references), we estimate the total power deficit by finding this deficit for each age and integrating over all ages as

$$Q_H = \int_0^{t_m} (q_m - q_o) \frac{dA}{dt} dt, \quad (4.1)$$

where  $Q_H$  is the net power deficit,  $q_m$  is the modeled heat flow,  $q_o$  is the observed heat flow,  $A$  is the seafloor area,  $t$  is age, and  $t_m$  is a maximum integration age. The three key variables which must be known are thus the measured and modeled heat flow, and the seafloor area-age distribution. We take the area-age distribution from the empirical model of Müller et al. (2008). The observed heat flow is based on the raw global heat flow database updated by Hasterok (2010).

As shown in Fig. 4.1, in sub-conductive regions there are locations of discharge and recharge. The value  $q_o$  is an estimation of the average heat flow over all seafloor area. Thus, we would ideally wish to integrate over all seafloor area to approximate  $q_o$ , including

near sites of ventilated heat flow. However, because characterizing heat flow around sites of discharge has been a major interest of marine heat flow surveys, there exist biases in the databases toward the sampling of such regions. Such biases must be removed in order for the data to represent an average conductive heat flux from oceanic lithosphere. In fact, due to the comparatively minuscule area of regions with very high heat flow, we remove all measurements which are  $> 3000 \text{ W m}^{-2}$ . We also remove high-resolution heat flow surveys with dense sampling over young seafloor with regionally extensive and thick sediment cover (e.g. Hobart et al., 1985; Davis et al., 1997; 1999) and an anomalous sampling of a mud volcano in the Barents sea (Kaul et al., 2006). Also, all points for which seafloor age cannot be determined are removed.

Hasterok (2013b) employed additional filters, including a thermal correction for thickening sediment (i.e., recently deposited sediment is initially at ocean-bottom temperature and must be gradually heated by conduction of lithospheric heat), and the removal of seafloor area with large igneous provinces. We do not include these filters for reasons of simplicity, our uncertainty in the accuracy of the thermal correction (which increases measured heat flow) and the possibility of other unaccounted corrections which would decrease measured heat flow or systematically increase predicted heat flow (e.g. thermal properties of sediment cover, internal heating sources, or non-plate-like reheating phenomena). Moreover, the thermal correction for sedimentation more strongly impacts observations over old seafloor, where hydrothermal ventilation is probably unimportant. Nevertheless, we will compare our results with those of Hasterok (2013b) to highlight the differences which ought to originate in our respective methodological choices.

It is notable that in our models, we do not include passive hydrothermal circulation (cf. Spinelli and Harris, 2011). This means that our reference model is exactly a normal 'conductive' reference model. In contrast, a more accurate reference model would produce a super-conductive heat flux (Fig. 4.1). This additional heat flux originates in the fact that a crustal aquifer acts as a high conductivity layer. However, because this layer is thought to be only a few hundred meters thick (e.g. Spinelli and Harris, 2011) it has not been included in our models and thus should not substantially affect our results.

## 4.2.2 Statistical Analysis

Similar to Hasterok (2013b), we perform a Monte-Carlo statistical analysis to estimate uncertainties in heat flow and the power deficit. The heat flow database (with our filters as described above) is divided into 1 Ma bins and we construct cumulative distribution functions (CDF's) of heat flow for each bin. The fraction of observations (heat flow measurements) within the bin  $\Delta t$  having heat flow less than  $Q$  is given by the (discontinuous) CDF:

$$f_{\Delta t}^{CDF}(R) = \frac{1}{N_o} \sum_{o_1}^{o_{max}} o_i(q \leq Q) \quad (4.2)$$

where  $\Delta t$  is the bin interval (1 Ma),  $o_i(q \leq Q)$  is a measurement with heat flux  $q$  less than  $Q$ , and  $N_o$  is the total number of observations in the bin  $\Delta t$ . Figures illustrating the cumulative distribution functions of heat flow for each 1 Ma bin are shown in Fig. 4.2. By randomly sampling the CDF (which is characterized by values between 0 and 1) we obtain



samples of heat flow consistent with the frequency (or probability) of its occurrence in the data. Therefore, to estimate the power deficit via. Eq. 4.1 and 4.2, a) the CDF is randomly sampled once for each and every bin, up to a maximum age  $t_m$  of 100 Ma, b) we take the difference of the resulting statistical sample of the heat flow observations and the mean model heat flow in the bin, and c) multiply the difference by the total seafloor area which exists for the age bin. The resulting equation for the cumulative power deficit is the sum of the heat flow deficits for each bin multiplied by their respective seafloor areas, or

$$Q_H = \sum_{t=\Delta t}^{\Delta t/t_m} (q_m - \hat{q}_o) A_{\Delta t}, \quad (4.3)$$

where  $\hat{q}_o$  is the statistically sampled heat flow in the bin, and  $A_{\Delta t}$  is the total seafloor area in the bin. We note that in our analysis we use the mean over the time interval to estimate  $q_m$  for the bin. Hasterok (2013b) argued that the median is more appropriate, leading to different results (lower heat flow deficits). Finally, the statistics of the power deficit can be represented by probability density functions (PDFs) by repeating the integration of Eq. 4.3  $10^6$  times. These results are shown in Fig. 4.3 and will be discussed later in Sec. ???. Also, to illustrate how the cumulative heat flow deficit changes as the age of integration increases from 1 Ma to 60 Ma, we record PDFs for each age bin. Again, note that these PDF's represent probabilities for the cumulative (Eq. 4.3) heat flow deficit, not the deficit in individual bins.

### 4.2.3 Reference Models for Seafloor Heat Flow

For plate and half-space models, the relationship between thermal properties of the lithosphere and seafloor heat flux may be given as

$$q_{sf}(t) = [\rho C_p]_{ei}(t) \Delta T_{ei}(t) \sqrt{\frac{D_{ei}(t)}{\pi t}} + q_a, \quad (4.4)$$

where  $[\rho C_p]$  is the volume heat capacity,  $\Delta T$  is the difference of mantle and surface temperature,  $D$  the thermal diffusivity, and  $q_a$  is the adiabatic part of the heat flux. The subscript *ei* denotes that the properties are "transient effective" properties: They are "effective" properties because they are weighted in terms of the depth-integrated change in temperature of the mantle, and they are "transient" because they are in terms of the instantaneous change in the depth-integrated temperature of the mantle (see Appendices at the end of this chapter). Moving the time  $t$  to the left hand side, we can define the coefficient

$$g(t) = [q_{sf}(t) - q_a] \sqrt{t} = [\rho C_p]_{ei}(t) \Delta T_{ei}(t) \sqrt{\frac{D_{ei}(t)}{\pi}}, \quad (4.5)$$

which may be referred to as a rate of heat flow diminution over time. This coefficient has been useful to characterize simple lithospheric cooling models (e.g.  $g(t < 20 \text{ Ma}) = 510 \text{ mW m}^{-2} \text{ My}^{1/2}$  for model GDH1, Stein and Stein (1992)) as it is basically a term isolating the thermal coefficients. In addition, this coefficient is particularly useful for analysis of lithospheric models with complicated heat transport properties. In such cases, the effective

thermal properties have a characteristic time-dependence, thus yielding a time dependent  $g(t)$  coefficient. Subtle variations in these properties is much easier to discern in  $g(t)$  than in  $q_{sf}$ . Cooling half-space models with no properties that depend on depth will have a constant  $g$  value, whereas  $g(t)$  for plate models will increase when the plate boundary is sensed, and  $g(t)$  will be a continuous function of time for any thermal model with depth-dependent properties.

We test three models of predicted heat flow, from which we calculate the heat flow deficit. The first plate model we use is from Hasterok (2013a), referred to here as H13. H13 has constant thermal properties and is thus taken as an optimal model prediction when the effects of thermal insulation and hydrothermal circulation are not considered. Model H13 has been constrained based on heat flow data only, and predicts heat flow nearly equal to GDH1 (Stein and Stein, 1992) for ages  $< 50$  Ma and slightly higher heat flow at older ages. Since H13 has constant thermal properties it has a diminution coefficient which is constant over young ( $< 50$  Ma) seafloor. The second and third models we consider are from our previous work (Chapter 3), here referred to as GH and GHC. An illustration of initial and boundary conditions for these models is shown in Fig. 4.4. Both model GH and GHC have complicated thermal properties, including temperature- and pressure-dependent heat transport properties and thermal expansivity, thermal radiation heat transport, an initial geotherm calculated with an adiabat and latent heat of melting, and 2D conductive heat transport. The physical details of the models are discussed in Chapter 3. The properties of particular importance to models GH and GHC are the axial hydrothermal circulation and insulating properties of oceanic crust. The model name GHC indicates that this model includes both axial hydrothermal circulation and crustal insulation, while model GH only has axial hydrothermal circulation (in addition to the other properties noted above).

Axial hydrothermal circulation is modeled using a Nusselt ( $Nu$ ) number approximation (e.g. Cochran and Buck, 2001; Spinelli and Harris, 2011), so that the effective thermal conductivity is  $Nu$  times the lattice value (Chapter 3). High- $Nu$  ( $Nu=10$ ) occurs in lithosphere where the temperature is  $< 800^\circ\text{C}$  and the crustal age is  $< 0.2$  Ma (Fig. 4.4). These values are consistent with the 'cracking front' limit for fast-spreading ridges estimated by Manning et al. (2000), and produces a thermal structure near ridge axes which is in good agreement with predictions from seismic models for the East Pacific Rise (Dunn et al., 2000; Chapter 3). Values which produce greater cooling rates (e.g. Spinelli and Harris, 2011; MacLennan et al., 2005; Cochran and Buck, 2001; Cherkaoui et al., 2003) have been shown to predict an excessively cool ridge axis (Chapter 3).

Crustal insulation is a consequence of the low thermal conductivity of crustal rocks. Models GH and GHC use recent measurements of thermal properties (Chapter 3), but we note that the resulting thermal conductivity is nearly equal to that estimated for basalts and gabbros by Zoth et al. (1988).

Models H13, GH, and GHC are investigated here for their predictions of ventilated hydrothermal power by means of the heat flow deficit. For additional clarifications when discussing seafloor subsidence we will also consider the predictions of the additional models G and GC, which have all the properties of GHC except that model GC does not have axial hydrothermal circulation and model G has neither hydrothermal circulation nor crustal insulation. Specifically, model G, Gh, GC, and GHC are models RN1, RN10, RN1C, and

RN10C from Chapter 3, respectively.

The key features of models GH and GHC (as well as model GC) are their strongly variable  $g(t)$  coefficients, shown in Fig. 4.5. All models have been constrained with old-age seafloor heat flow. However, due to the effects of axial hydrothermal circulation and crustal insulation,  $g(t)$  (and thus heat flow) deviates significantly over young ages. Thus, comparing predictions of models H13, GH, and GHC should illustrate the consequences of axial hydrothermal circulation and crustal insulation on total ventilated hydrothermal power, and its spatial distribution.

#### 4.2.4 Spatial Power Distribution

We refer to the deficit integrated to 1 Ma as the near-axial deficit. This deficit may be further divided into active and ridge flank fluxes. The active flux is the hydrothermal power vented over the ridge axis which is driven primarily by the emplacement and cooling of melts in the crust (Lister, 1982). After 0.2 Ma, active hydrothermal circulation ceases and the geotherm is in a state of conductive rebound (Cochran and Buck, 2001; Spinelli and Harris, 2011). While model H13 is a simple conductive plate model without hydrothermal circulation, we use 0.2 Ma as a cutoff value to estimate the active flux for this model also.

To obtain the active deficit we calculate the fraction of heat loss in the 0-0.2 Ma bin as

$$N_A = \int_0^{0.2} q_m dt / \int_0^{1.0} q_m dt \quad (4.6)$$

where the integral bounds are ages in Ma. From here the active flux  $Q_A$  is simply  $Q_A = N_A Q_H(t = 1 \text{ Ma})$ , and the ridge flank flux is  $Q_F = (1 - N_A) Q_H(t = 1 \text{ Ma})$ .  $N_A$  values for models H13, GH, and GHC are 0.435, 0.852, and 0.829, respectively.  $N_A$  values are higher for model GH and GHC due to high  $q_m$  from hydrothermal circulation. Because heat loss from the lithosphere decreases with age, it may be suspected that a correction is needed for the change in observed heat flow between 0-0.2 Ma and 0.2-1.0 Ma. However, inspection of the data (not shown) indicates that the heat flow distribution does not change significantly, and is a small fraction of that predicted even if a difference could be estimated. Thus our calculations assume that observed heat flow is the same over the entire width of the 1 Ma bin (as it is for all bins).

Finally, the 'passive' power deficit is ventilated hydrothermal transport driven by heat conducted into an upper crustal aquifer (Lister, 1982), resulting in long term convective fluid exchange between the crust and oceans. The passive power deficit is the total power deficit after subtraction of the near-axial deficit:  $Q_P = Q_H(60 \text{ Ma}) - Q_H(1 \text{ Ma})$ .

### 4.3 Results and Discussion

Fig. 4.3 shows the main results of our analysis of the heat flow deficit for different cooling models. PDF's of the time-integrated power deficit are plotted (Fig. 4.3a-c) for maximum integration times between 1 and 60 Ma. Since the heat flow sampling is divided into 1 Ma bins, the PDF for the power deficit at 1 Ma is essentially the derivative of a single CDF and thus appears rough. Nevertheless, the modes (probability maxima) are well defined for all

ages. For comparison, the means and medians of the PDF's are also calculated for each age. The resulting PDF's have non-normal distributions, as the low probability realizations are skewed to low power estimates. For a different visualization, the mean, median, mode, and half-maximum bounds (HMB) of the power deficit are also plotted as a function of age up to 100 Ma in Fig. 4.3d-f. This shows that the net deficit plateaus around 50 Ma for all models, where predicted and observed heat flow converge (Fig. 4.2 and 4.5).

### 4.3.1 The Net Power Deficit

#### Model H13

For model H13, our analysis predicts that the net power deficit is 7.8 TW, with half-maximum realizations falling between 3.8 and 10.1 TW. Compared to most previous studies (e.g. Sclater et al., 1980; Stein and Stein, 1994; Stein et al., 1995; Mottl, 2003; Spinelli and Harris, 2011) this is a low estimate. The estimates of 10.3 and 11.5 TW by Sclater et al. (1980) and Stein and Stein (1994), respectively, are even outside of the HMB for this cooling model. As model H13 is nearly equivalent to GDH1 (Stein and Stein 1992), the difference is related to differences between heat flow databases, seafloor area-age distribution, and statistical treatment. In addition, our mean (6 TW) and median (6.6 TW) net power deficit estimates are even lower than the mode (Fig. 4.3a). Although they are within the HMB, they are substantially lower than previous estimates.

It is notable that our estimate of 7.8 TW for H13 is equal to that estimated by Hasterok's (2013b) analysis using his filtered heat flow database. However, this is only coincidental as his filtered database removes seafloor with sediment thickness  $>400$  m, whereas we do not include such a filter. Moreover, even the more comparable 'unfiltered' database of Hasterok (2013b) incorporates additional corrections not employed here including 1) a thermal correction for thickening sediment, 2) removal of seafloor area with large igneous provinces, and 3) median reference model heat flow  $q_m$  was used (we use means). With these additional corrections, Hasterok's (2013a) preferred methods predicted a net power deficit of 6.2 TW (using his unfiltered database). As such, our method predicts a roughly 25% greater net power deficit. Therefore, if Hasterok's (2013b) database and analytical techniques are preferred, our net deficit estimates should be reduced by 20%, or slightly less than our median estimates.

#### Models GH and GHC

The power deficits for thermal plate models GH and GHC are shown in Fig. 4.3b-c. Model GH predicts a power deficit of 10 TW, with half-maximum realizations falling between 6.1 and 12.3 TW. This value is in good agreement with many previous estimates of the power deficit as discussed above. Inspection of Fig. 4.5 shows that predicted heat flow for GH and H13 is similar except near the ridge where GH heat flow becomes lower than H13. Thus the high heat flow deficit for model GH originates in active hydrothermal transport on ridge axes. For instance, model GH predicts  $4\text{--}14\text{ W m}^{-2}$  for  $<0.2$  Ma.

Model GHC has similar properties to GH, except that GHC has an insulating oceanic crust, and all heat transport properties are allowed to vary from their experimental values in order to fit basin-scale geophysical observations (Chapter 3). The predicted net power deficit

of model GHC is substantially lower than GH. We estimate 6.6 TW, with half-maximum bounds of 2.9 and 8.8 TW (Fig. 4.3c). Thus, if normal lithospheric cooling is better modeled by GHC, then the net power deficit is about 35% lower than expected by model GH. Note, however, that this does not mean that the effect of crustal insulation is a 35% decrease. This is because, again, the differences between model GH and GHC are both crustal insulation and a re-adjustment of all mineral physics properties to best fit geophysical observations. Since the effective thermal conductivity of model GHC was adjusted to be  $\sim 10\%$  higher than GH (Chapter 3), the real effect of crustal insulation on the heat flow deficit is closer to a 45% reduction.

### 4.3.2 Spatial Distribution of the Power Deficit

#### Model H13

The spatial distribution of ventilated hydrothermal power predicted by models H13, GH, and GHC are highlighted at the top of their respective panels in Fig. 4.3a-c, and are tabulated in Table 4.1. For H13, the power deficit at 1 Ma has a probability maximum at 2.5 TW with HMB between 1.9 and 2.8 TW (approximated after smoothing due to PDF roughness). The cumulative near-axial deficit is 32% of the total. This may be divided into power on the ridge axis (0-0.2 Ma) at 14% of the total, and 18% of the total on ridge flanks (0.2-1.0 Ma). The remaining deficit of 5.3 TW (68% of the total) is due to passive ventilated hydrothermal circulation away from ridges. This prediction of 32% of total ventilated hydrothermal power occurring over  $< 1$  Ma crust is only slightly higher than most previous estimates. Stein and Stein (1994) predict a 28% near-axial deficit, Pelayo et al. (1994) predict about 23%, and Mottl (2003) predicts 29% occurring near the axis (Table 4.1). In addition to the use of an updated heat flow database, our slightly higher value may be attributed to our preference to modes of the power deficit rather than the means (Table 4.1). Using mean values, we calculate a near-axial power deficit closer to 20% of the total. This is slightly lower than Spinelli and Harris's (2011) prediction that 25% of the deficit occurs over near-axial seafloor (using Eq. 4.1 on a conduction-only model).

#### Models GH and GHC

As shown in Fig. 4.3b-c and Table 4.1, both models GH and GHC predict that about 50% of total hydrothermal power is extracted near ridge axes ( $< 1$  Ma). To our knowledge, this is a higher fraction than all previous estimates, including Spinelli and Harris' (2011) near-axial estimate of 40%. Moreover, about 85% of the axial deficit (40-45% of the total) is active circulation on  $< 0.2$  Ma seafloor. For model GH, the near-axial deficit (5.2 TW) and the active deficit (4.4 TW) are high, leaving about 4.8 TW of heat removed by passive circulation. On the other hand, because the net power estimate of model GHC is significantly lower than GH, the near-axial power estimate ( $< 1$  Ma) and the passive regime estimate are both only 3.3 TW. For the near-axial environment, this estimate is in good agreement with some previous investigations (e.g. Stein and Stein, 1994; Mottl, 2003; Spinelli and Harris, 2011; Table 4.1), but our passive estimate is much lower than all previous estimates (Table 4.1). Some passive power estimates are more than twice our value (e.g. Stein and Stein, 1994; Pelayo

et al. 1994; Mottl, 2003). The low passive power estimate for GHC originates primarily in the compounding effects of thermal rebound from active hydrothermal circulation and thermal insulation of oceanic crust. The hydrothermal model from Spinelli and Harris (2011) predicted a passive power budget of 5.4 TW, about 60% higher than our estimate for model GHC (Table 4.1). Hasterok's (2013b) passive estimate of 3.9 TW is closest to our result. However, this value is for his 'unfiltered' database which predicted a total deficit of 6.2 TW (Table 4.1). If we used similar methods, we estimate that predictions for model GHC would be about 20% lower, with a passive deficit of  $\sim 2.6$  TW and total deficit of  $\sim 5.3$  TW (80% of 6.6 TW). Thus, while the purpose of this work is to demonstrate the relative importance of crustal properties on seafloor heat flow, methodological assumptions in data analysis are important for absolute estimates of ventilated hydrothermal power.

## 4.4 Heat Flow Constrained by Topography

Our analysis has shown that insulating oceanic crust and hydrothermal circulation jointly impact estimates of hydrothermally mined energy in oceanic lithosphere, as well as its spatial distribution. This occurs because both effects result in the prediction of significantly lower heat flux over young ( $<30$  Ma) seafloor compared to conventional models (Fig. 4.5), and active hydrothermal circulation elevates net heat flow on ridge axes.

Clearly, an important question is whether or not geophysical observations actually support lower heat flow over young seafloor. Although measured seafloor heat flow is contaminated by ventilated hydrothermal circulation processes resulting in a sub-conductive heat flow (Fig. 4.1), other geophysical observations such as seafloor subsidence are thought to be robust alternative constraints on lithospheric heat loss (Parsons and McKenzie, 1978; Sandwell and Poehls, 1980; Wei and Sandwell, 2006).

Hofmeister and Criss (2005), based on the assumption that classical lithospheric cooling models do not fit the Earth, and that hydrothermal circulation cannot lead to what we have called a sub-conductive heat flow (Fig. 4.1), suggested that true heat loss from oceanic lithosphere is that actually measured ( $\sim 20$  TW, versus  $\sim 30$  TW, Von Herzen et al., 2005). Wei and Sandwell (2006) attempted to show that although measured heat flow does not match lithospheric heat loss as predicted by plate models, it is reflected in the rate of seafloor subsidence. As seafloor subsidence is related to the change in the integrated temperature of the upper mantle, subsidence may be linked to heat loss. Wei and Sandwell (2006) calculated seafloor heat flow based on a spatial integration of heat flows estimated by local subsidence rates found with the global seafloor depth grid of Smith and Sandwell (1997) and age grid of Müller et al. (1997). They calculated local seafloor heat flow by employing the equation

$$q_{sf} - q_a = \frac{\rho C_p}{\alpha \varrho} \frac{\nabla t(x, y) \cdot \nabla w}{\nabla t(x, y) \cdot \nabla t(x, y)} \quad (4.7)$$

where  $\rho$  is the lithospheric density,  $C_p$  is the lithospheric specific heat,  $\alpha$  is the lithospheric thermal expansivity,  $t(x, y)$  is the age as a function of spatial coordinates,  $q_a$  is an additional heat flux which is extracted from sub-lithospheric mantle rather than the lithosphere (e.g.

the adiabat),  $w$  is seafloor depth, and

$$\varrho = \frac{\rho_b}{\rho_b - \rho_w} \quad (4.8)$$

is the isostatic correction for seawater load, with mantle density  $\rho_b$  and seawater density  $\rho_w$ .

Although they found that their heat flux calculations were in good agreement with a simple half-space cooling model (where  $g=480 \text{ mW m}^{-2} \text{ My}^{1/2}$ ) and conventional net seafloor heat flux estimates, this agreement only occurred upon addition of a hidden lithospheric heat flux,  $q_a$ , of  $38 \text{ mW m}^{-2}$ , or about 11 TW. Consequently, by removing this additional heat flux over global seafloor we see that the analysis of Wei and Sandwell (2006) suggested that an empirical subsidence-based estimate of net seafloor heat flux is actually on the order of 20 TW, in agreement with Hofmeister and Criss (2005).

We suggest that the solution to this dilemma lay in the age-dependence of the effective thermal properties of the lithosphere, especially the consequence of thermally insulating oceanic crust (Appendix 4.A). For example, Goutorbe (2010) and our analysis in Chapter 2 found that simple thermal plate models with temperature-dependent thermal properties (i.e., no dependence on age), optimally fitted to geophysical observations, required an effective thermal expansivity about 30-40% lower than the experimental value for olivine. Since Wei and Sandwell (2006) perform no *ad hoc* adjustments to thermal properties, their use of the high experimental thermal expansivity for forsterite resulted in a low seafloor heat flux and an 11 TW addition of heat was necessary for a reasonable result. On the other hand, our model GHC has two characteristics which result in different predictions. Firstly, the mineral physics thermal expansivity only needed to be reduced by 15% to fit geophysical observations for model GHC. Secondly, the effective thermal expansivity is significantly lower near ridge axes compared to old seafloor since the properties of the lithosphere are crust dominated, rather than mantle dominated at old ages. This second item is relevant because it means that seafloor heat flow at old age represents the cooling of lithosphere having a much higher effective thermal expansivity than over young lithosphere. Consequently, a given rate of subsidence over old seafloor indicates higher heat flux than the same subsidence rate over young seafloor. Fitting a model which has different properties over young versus old lithosphere results in a different view of general lithospheric behavior.

Consider that, similar to Eq. 4.7, seafloor heat flow and subsidence may be related by the equation (Appendix 4.B)

$$\frac{b_{ei}(t)}{2\varrho(t)\alpha_{ei}(t)} = \frac{g(t)}{[\rho C_p]_{ei}(t)} \quad (4.9)$$

where  $b_{ei} = dw/d\sqrt{t}$  is the transient subsidence rate with  $w$  the seafloor depth, and  $\alpha_{ei}$  the transient effective thermal expansivity. The age-dependence in the rate of heat flow diminution  $g(t)$  is shown for our models GHC and GH, and Hasterok's (2013) model H13, in Fig. 4.5b. While the heat flow predictions of model GHC are not as low as that measured, as expected by Hofmeister and Criss (2005), the difference between model and measurement is significantly lower than that estimated with simple plate models. Since this decrease is only partially compensated by high heat flow on ridge axes, the power transported by hydrothermal circulation is also markedly reduced. Accordingly, the problem of the heat flow deficit can be attributed to both complex thermal properties and ventilated heat loss.

#### 4.4.1 The subsidence rate

Age-dependence of the subsidence rate, as predicted by models GDH1 (Stein and Stein, 1993), H13 (Hasterok, 2013a), and our models GH and GHC are shown in Fig. 4.6a compared to empirical estimates based on the global database of Hillier (2010). The empirical estimates are obtained from fitting a line (least squares fit) through the data (0.1 My bins) in a sliding window of width  $\delta t^{1/2}$ . Fig. 4.7 shows the predictions of several lithospheric models compared to the data of Hillier (2010) as well as ridge flank topography of the East Pacific Rise (EPR) from Cochran and Buck (2001). To explore the sensitivity of estimates to the sampling window size we show estimates for  $\delta t^{1/2}$  between 0.2 and 2.0 My<sup>1/2</sup>. Due to the roughness of the data in small bins, the variance is high when the window is small and decreases as the window becomes larger.

Comparison of model predictions and empirical estimates shows that model GH and GHC both fit the general trends in almost all of the data well, while models H13 and GDH1 substantially over-predict subsidence rates for the youngest lithosphere ( $< 5$  Ma). Model H13 does not fit the data well because it was fit to the depth curve predicted by the model of McKenzie et al. (2005), but we include it for completeness. The empirical subsidence rate clearly has a rising trend between near-zero age and about 30 Ma, then decreases gradually in accordance with seafloor flattening. It is notable that empirical subsidence rates using large  $\delta t^{1/2}$  tends to rise near zero age and thus appears to be in better agreement with model GH rather than GHC. However, this is due to the loss of resolution due to binning. Model GHC is a superior fit to ridge flank subsidence. The estimates with  $\delta t^{1/2} \sim 0.2$  My<sup>-1/2</sup> indicate that the subsidence rate is  $\sim 150$  m My<sup>-1/2</sup> near the ridge axis ( $\sim 0.5$  Ma), increases to  $\sim 350$  m My<sup>-1/2</sup> around 30 Ma, and finally decreases gradually from the effects of seafloor 'flattening' to great age. To explain the contributions of axial hydrothermal circulation and crustal insulation, we compare subsidence rates from three models in Fig. 4.6b. Along with model GHC, we include previously unmentioned models G and GC. As indicated by their names, model G has neither crustal insulation or hydrothermal circulation, and model GC has crustal insulation but no axial hydrothermal circulation. Subsidence rates for model G are similar to GDH1 (Stein and Stein, 1992) over young seafloor, with a roughly constant subsidence rate of  $\sim 340$  m Ma<sup>-1/2</sup>. Model GC decreases the subsidence rate to about  $\sim 270$  m Ma<sup>-1/2</sup> near ridge axes, rising gradually over about 20-30 Ma until flattening. Model GHC further decreases the subsidence rate near the ridge axis to about 110 m Ma<sup>-1/2</sup>. An important observation to consider is that while the effect of axial hydrothermal circulation on the ridge flank subsidence rate is markedly greater than that for crustal insulation, the hydrothermal circulation effect is confined to the youngest ages while crustal insulation is more persistent.

An important question is whether or not the decreasing subsidence rate in proximity to ridge axes, and the corresponding misfit of model GDH1, is a real reflection of isostatic balance, or if other contributions, such as flexural effects, are important. If other processes are important, this could indicate that observation and model prediction of a low subsidence rate on ridge flanks is not actually related to crustal insulation and hydrothermal circulation. Cochran (1979) showed that gravity anomalies are present over ridge axes. However, while the anomalies appear somewhat significant over Atlantic ridges, they are small and confined to the immediate vicinity of ridge axes over the EPR. Consequently, while elastic sources



of deviation from isostasy may be present on the ridge axis, to our knowledge there is no compelling evidence to believe that non-isostatic effects are responsible for the low subsidence rate on ridge flanks ( $>0.2$  Ma).

Fig. 4.7b shows a closeup of predicted topography for several lithospheric models compared to the data of Hillier (2010) and EPR data from Cochran and Buck (2001). Models with no crustal insulation or axial hydrothermal circulation do not fit the low subsidence rates of ridge flanks, nor the axial rise for ages  $< 0.5 \text{ Ma}^{1/2}$ . Models with only hydrothermal circulation or only crustal insulation improve the fit near ridge axes, but still fail to provide a satisfactory fit to the data. On the other hand, model GHC provides a satisfactory fit to seafloor topography. A remaining misfit occurs at zero-age, where axis depth of model GHC is about 150 m greater than that in the data of Cochran and Buck (2001). This can be explained by the buoyancy of melt. The depth change of the seafloor due to solidification of melt, with isostatic correction and using an exponential solidification rate, can be given as

$$\Delta w_m = \varrho(t) \exp\left(-\frac{t}{n}\right) \left(\frac{\rho_m}{\rho_s} - 1\right) \int_0^L \phi_m dz, \quad (4.10)$$

where  $n=0.04 \text{ Ma}$  is a time coefficient for the solidification rate,  $\rho_m=2750 \text{ kg m}^{-3}$  (Stolper and Walker, 1980; Stolper et al., 1981; Hooft and Detrick, 1993) is the density of melt,  $\rho_s=2950 \text{ kg m}^{-3}$  is the density of solidified melt (ocean crust),  $\phi_m$  is the melt volume, and other terms are defined previously. The volume of melt beneath ridges (depth integrated  $\phi_m$  in Eq. 4.10) can be estimated based on the seismic tomography study of a segment of the EPR by Dunn et al. (2000). Their seismic inversion models are consistent with a depth integrated melt column of either  $\sim 0.8 \text{ km}$  or  $1.9 \text{ km}$ , depending on whether the pore texture consists of thin films or spheres, respectively. From Eq. 4.10 this predicts  $\Delta w_m = -80 \text{ m}$  and  $-190 \text{ m}$ , respectively, at  $t=0$ , in good agreement with the difference with model GHC (Fig. 2b).  $\Delta w_m$  predicted by Eq. 4.10 are shown in Fig. 4.7b. Although Cochran and Buck (2001) argued that the axial rise and low subsidence rate over ridge flanks can be explained by axial hydrothermal circulation, our models indicate that axial circulation alone may not be able to explain these features. On the other hand, all major topographic features characteristic of normal fast-spreading seafloor are explained by model GHC.

It may be suggested that model GH can be made to better fit ridge flank topography by increasing the rate of hydrothermal heat removal (e.g.  $Nu > 10$ ). This may improve the topographic fit, although we have already noted (Sec. 4.2.4) that a consequence of this (as Cochran and Buck (2001) and Spinelli and Harris (2010) used  $Nu=20$ ) is a significantly colder near-axial environment which we earlier showed (Chapter 3) is not consistent with evidence from seismic models of the EPR by Dunn et al. (2000). Moreover, in Sec. 4.5 we will show that model GH (let alone such a model with additional axial hydrothermal cooling power) is not consistent with estimates of heat available for release in the process of crustal accretion.

#### 4.4.2 Note on Old-Age Topography and Seafloor Flattening

Although the old-age behavior of the lithosphere does not affect our calculations of ventilated hydrothermal power extraction since the heat flow deficit only exists over young seafloor,

the fit of models to old-age seafloor is a major constraint on general lithospheric properties. Consequently, the better fit of model GDH1 to the old-age ( $>50$  Ma) subsidence rate in Fig. 4.6 and Fig. 4.7a might seem to indicate the superior explanatory powers of GDH1, or at least a problem with the properties of model GHC. However, if the model of lithospheric cooling is meant to represent the normal cooling behavior of the lithosphere, this superior fit may be treated as a flaw rather than a success. Following Crosby et al. (2006) and Hillier and Watts (2005), we consider it likely that seafloor around 100-130 Ma ( $10\text{-}11.5 \text{ Ma}^{1/2}$ ) is anomalous. Of particular note, the subsidence rate becomes negative around these ages, which cannot be accomplished by passive cooling processes and is not known to occur by means of small scale convection beneath old seafloor (Zlotnik et al., 2008; Afonso et al., 2008). Thus, we consider models GH and GHC to better reflect the normal behavior of oceanic lithosphere.

## 4.5 Constraints from the Thermal Budget of Crustal Cooling

Based only on the fit to the global data, we cannot discount the possibility that crustal insulation is an unimportant contribution. On the other hand, we may cast doubt on the feasibility of model GH for a thermodynamic reason, thus requiring a contribution from crustal insulation.

It is notable that the estimate of near-axial circulation for model GH is so high (5.2 TW, Table 4.1). Based on the limited heat budget for ocean crust formation and cooling, Mottl (2003) argued that axial cooling cannot be more than about 3.1 TW. This indicates that model GH, due to high effective thermal conductivity and axial boundary conditions around the shallow axial magma chamber (Chapter 3), may be extracting more heat than can realistically be released by advection and crystallization of magmas. Model GHC, on the other hand, only transports about 3.3 TW of heat, consistent with Mottl's arguments. In addition, we previously showed (Chapter 3) that model GHC predicts ridge thermal structure that is in good agreement with a seismic model over the East Pacific Rise by Dunn et al. (2000). As this fit to a seismic model reflects the  $Nu$  number, the seismic model supports the choice of  $Nu \approx 10$  rather than significantly higher values suggested elsewhere (e.g. Cochran and Buck, 2001; Spinelli and Harris, 2011). On the other hand, Han et al. (2014), based on the observation of off-axis magma lenses in regions Dunn et al. (2000) expected to be cool, suggested that Dunn's model may be inaccurate. However, it is not clear what ambient thermal structure is consistent with the presence of off-axis magma lenses, as these may be anomalous, even if frequent, features. We stress that models GH and GHC use a simple  $Nu$ -number approximation of hydrothermal transport, and therefore can only represent the average behavior of ridges both along and across axes. Moreover, if the thermal structure of Dunn et al. (2000) is too cold, the necessary adjustments to model GHC may be small, except in direct proximity to the axial magma lens. Such corrections may also be applied to model GH, but they will be larger, and may be at the cost of good fit to seafloor subsidence.

In summary, if there is no effect of crustal insulation, the fit to seafloor subsidence is slightly compromised and unrealistic amounts of heat are extracted on axis. Thus, we

suggest that both insulating oceanic crust and a moderate amount of axial hydrothermal circulation are important for estimates of ventilated hydrothermal power.

## 4.6 Constraints from High-Resolution Heat Flow Surveys

A primary goal of this work is to show that crustal insulation strongly affects lithospheric cooling as well as the amount and distribution of hydrothermal power loss. Precise constraints on any of these three items is impossible without knowledge of the conductive lithospheric heat loss over young seafloor.

Hasterok et al. (2011) and Hasterok (2013b) attempted to use the global heat flow dataset to constrain deep lithospheric heat flow over young seafloor by applying special filters to the data. These authors showed that by removing seafloor regions with thin sediment the residual heat flow over young seafloor markedly increased. Because extensive thick sediment cover acts as an impermeable boundary over the crust, fluid exchange between the crust and oceans should become less effective with sediment thickness and heat transfer by conduction becomes dominant (Lister, 1972). Specifically, by removing oceanic regions with sediment cover  $>400$  m, measured heat flow is in good agreement with model H13 (and GDH1) for ages  $>25$  Ma. However, for younger ages a significant deficit remained (Fig. 4.5). Interestingly, while the deficit between filtered measurements and model H13 is large, the deficit with model GHC is substantially less pronounced (Fig. 4.5). As the main result of our paper shows, this implies a lower net power deficit. Nevertheless, the remaining deficit indicates that a filtered global database still fails to remove the effects of ventilated hydrothermal circulation on the seafloor heat flow. Consequently, the conductive heat flow still cannot be constrained over young seafloor with global heat flow data.

An alternative approach is to examine specific regions which have been studied extensively enough to demonstrate that the effects of ventilated hydrothermal circulation are small in certain areas. Among the global data, Hasterok et al. (2011) recognized four sites on young seafloor which have thick sediment cover and have been extensively surveyed. These include the Juan de Fuca ridge flank (Davis et al., 1997; 1999), the Costa Rica Rift flank (Davis et al., 2004; Hobart et al., 1985; Langseth et al., 1988), the Gulf of Aden (Cochran, 1981; Lucazeau et al., 2008; 2010), and the Cocos plate (Hutnak et al., 2008). Our analysis of the heat flow data for these sites is discussed in the following section and the resulting estimates are shown in Fig. 4.5. Subsequently, we discuss interpretations of the data in relation to the different estimates of young-age lithospheric heat flow by models H13, GH, and GHC.

### 4.6.1 Heat Flow at High-Resolution Sites

#### Gulf of Aden

The Gulf of Aden is a rifted margin between Africa and the Arabian plate which separated at 34 Ma with the onset of seafloor spreading around 18 Ma (Leroy et al., 2012). Lucazeau et al. (2010) reported high quality heat flow measurements along 8 seismic profiles near the margin of the Arabian plate (near Dhofar), 7 of which are aligned with the direction of

spreading. They correct their heat flow measurements for sedimentation rate (we use the average of their two cases), topography, and heat refraction. These profiles extend from the continental domain, through the ocean-continent transition, and onto oceanic lithosphere. The small variance in heat flow along profiles led Lucazeau et al. (2008) to conclude that effects of hydrothermal circulation are not important. Of their 162 measurements along 8 profiles, we use 40 points from 6 profiles located on seafloor with ages known from magnetic anomalies (d'Acremont et al., 2010). Comparison of the model age grid of Müller et al. (2008) and magnetic anomaly isochrons suggests that ages are overestimated by 5-10 Ma near the continental margin. Therefore, we neglect two profiles from seafloor on the East side of the Socotra Hadbeen fracture zone, since we cannot confidently determine precise ages. The 40 measurements are on seafloor 16-17.6 Ma and are plotted in Fig. 4.5 along with their mean and standard deviation ( $114 \pm 10 \text{ mW m}^{-2}$ ).

It is likely that this survey examines anomalous seafloor. The site characterizes the early stages of rifting margins, the onset of seafloor spreading, and any thermal consequences of abutting a continental margin. Moreover, based on an examination of heat flow and thermomechanical modeling, Lucazeau et al. (2008) suggested that an intense ( $300^\circ \text{ C}$ ) thermal anomaly below the ocean-continent transition may be likely. If this is the case, then the reported heat flow values may be elevated above that of normal seafloor.

## Cocos Plate

Hutnak et al. (2008) performed a regional survey of heat flow over Cocos Plate seafloor with ages 18-24 Ma. The region is blanketed with thick (400-500 m) sediments except for unevenly spaced sites of outcropping basement. Distributed throughout the region are colocated heat flow and seismic-reflection profiles, some of which extend from outcrop sites and others interspersed about. This heat flow survey revealed a bimodal areal variation in surface heat flow for low ( $\sim 30 \text{ mW m}^{-2}$ ) and high ( $\sim 110 \text{ mW m}^{-2}$ ) heat flow areas, a pattern which the authors explain by low-temperature hydrothermal discharge and recharge among outcrops in the low-heat flow areas, and 'warm' hydrothermally inactive crust for the high heat flow areas. Their estimate of  $97\text{-}120 \text{ mW m}^{-2}$  is plotted in Fig. 4.5 with the age range 18-24 Ma.

## Juan de Fuca Ridge

The Endeavor segment of the Juan de Fuca plate is heavily sedimented and has been extensively studied with colocated heat flow (Davis et al. 1997; 1999), seismic reflection profiles (Rosenberger et al., 2000), and geochemical study from nine ODP boreholes (Elderfield et al., 1999) over a 80 km transect in the direction of spreading. Heat flow measurements are shown in Fig. 4.5. Note that measurements cluster around 1 Ma and 3.6 Ma. The scattered black line is an empirical calculation based on the relationship between sediment thickness, basement temperature, and surface heat flow (Davis et al., 1999). Davis et al. (1999) estimated that a sediment correction of +15%, was necessary to estimate basement heat flow. However, we use the +6% correction from Pribnow et al. (2000) which accounts for thermal anisotropy of sediment. As the data are scattered we calculate distance-weighted averages of heat flow from the measurements for ages (A) 1.0-1.56 Ma and (B) 3.34-3.6 Ma.

### Costa Rica Rift

The geophysical environment of  $\sim 6.5$  Ma seafloor around ODP Hole 504B on the Costa Rica Rift (CRR) has been characterized with a high resolution ( $\sim 1$  km spacing) gridded survey of heat flow (Davis et al., 2004; Hobart et al., 1985; Langseth et al., 1988) and seismic reflection profiles (Swift et al., 1998). Fig. 4.8a shows a sediment thickness map produced from the seismic reflection profiles (12545 points) and a bicubic spline. Fig. 4.8b shows a bicubic spline of heat flow. Inspection of Fig. 4.8a and 4.8b shows that there is some correlation between sediment thickness and heat flow, although the relationship is rough (Swift et al., 1998). Using only the measurements, heat flow for the region has a mean of  $229 \pm 46$  ( $1\sigma$  uncertainty) and median of 218 (194, 250)  $\text{mW m}^{-2}$  (interquartile range uncertainty). However, since measurement coverage has a greater density around sites of elevated heat flow and thin sediment cover the statistics are biased to elevated values. The statistics for the bicubic spline are shown as a probability density function in Fig. 4.8c, which are also compared to a more coarse PDF for the measurements alone. The mean of the spline is  $211 \pm 35$   $\text{mW m}^{-2}$ , the median is 203 (186, 229)  $\text{mW m}^{-2}$ , and the mode is 190  $\text{mW m}^{-2}$  (173, 217) (half-maximum uncertainty). If we consider that sampling coverage is extensive enough to cover spatial heterogeneity, the mean of the spline may be preferred. However, we note that there are many areas where closely spaced points reveal exceptional lateral gradients, even away from areas of thin sediment or evidence of anomalies in basement topography (Fig. 4.8). Moreover, recall that measurements on the Juan de Fuca flank have a much smaller spacing ( $\sim 250$  m) and show substantial scatter. A similar scatter may be normal for the CRR site, so that the mean of the spline may not accurately characterize the true mean. We thus take the mode of the spline as the lowest reasonable statistical tendency.

## 4.6.2 Comparison of Surveys and Models

### Gulf of Aden and Cocos Plate

The goal of the examination of high resolution heat flow surveys is to evaluate whether or not the deeper (sub-crustal) lithospheric heat flux can be constrained by close regional inspection. Heat flow surveys of the Cocos Plate and Gulf of Aden regions are in best agreement with model GHC, although the statistical bounds (standard deviations or half-maximum bounds) are spread over all models. Thus, while these surveys indicate that the conductive models are a better indication of lithospheric heat flow compared to the global heat flow data (with or without a filter for sediment thickness), predicted heat flows for models over seafloor aged 16-24 Ma are too similar to clearly differentiate models. On the other hand, because the Gulf of Aden might be anomalously warm (Lucazeau et al., 2008), normal lithospheric heat flow for this age may be somewhat lower, which can improve the agreement with model GHC, but worsen the agreement with H13 and GH.

### Juan de Fuca

Comparison of the Juan de Fuca (Endeavor segment) heat flow to the models generally suggests best agreement with model GH. Ignoring the tail to low heat flow for ages  $< 1$  Ma (Fig. 4.5), the young-age end of the data is in best agreement with model GH, while the bin

of data around 3.5 Ma is in between model GHC and GH. The conventional hydrogeological interpretation of heat flow along the Endeavor flank includes recharge over the young ( $<0.66$  Ma) unsedimented seafloor and discharge at a basement high around 1.3 Ma, about 20 km from the recharge site (Davis et al., 1997; Davis et al., 1999; Newman et al., 2011). Borehole measurements and correlations of surface heat flux and sediment column thickness indicate that the temperature of crustal basement is roughly constant over this region.

Elevated heat flow in this region may be explained by 1) spatial sampling bias, 2) a source of additional heat flow, or 3) different properties of the lithosphere than expected by model GHC. Possible sources of elevated heat flow are 1) continued deep hydrothermal circulation, perhaps associated with faulting as suggested by Nedimovic et al. (2009), 2) heat release from hydration of the crust (Lowell and Rona, 2002), 3) heat transported from younger seafloor and discharged, consistent with models (Davis et al., 1997; Davis et al., 1999; Newman et al., 2011), or 4) microbial thermogenesis, which is difficult to quantify, but could be significant if nutrient supplies are adequate (Douglas LaRowe, personal communication). Davis et al. (1989; 1997; 1999) suggested that advective heat loss around 3.5 Ma seafloor is large enough to depress regional heat flow below that of basement heat flux. This would mean that heat flow predicted by model GHC is too low for this region. However, if additional heat has been introduced into the upper crustal aquifer by exchange with the deeper crust, perhaps driven by faults in this rough basement region (Davis et al., 1997), then measured heat flow may be greater than that conducted through the deeper crust, not less. If model GHC is correct for this region, measured heat flow suggests that measurements are elevated due to advective heat exchange between the upper and lower (or deeper) crust. In other words, this region may be super-conductive (Fig. 4.1), albeit with moderate ventilated discharge.

### Costa Rica Rift

The mode of  $190 \text{ mW m}^{-2}$  (173, 217; half-maximum bounds) calculated for the bicubic spline over the extensive 2D Costa Rica Rift survey is in good agreement with models GH and H13, but is significantly higher than the  $\sim 170 \text{ mW m}^{-2}$  estimate from model GHC at 6 Ma. At least part of the reason for this is that the CRR does not consist of 'normal' seafloor. In this region, the thickness of oceanic crust has been constrained to be  $\sim 5$  km thick, significantly thinner than other examples of seismically normal oceanic crust (Becker et al., 1989). Thus, the crustal insulation effect in this region should be lower. We have tested this by performing a sensitivity analysis with model GHC wherein which the thickness of the insulating layer is varied between 0 and 10 km (Fig. 4.9). Model GHC with a 5 km thick crust, or GHC-CRR, predicts heat flow  $\sim 182 \text{ mW m}^{-2}$ . This is better agreement, although it remains barely within the lower bound of uncertainty using a somewhat generous statistical technique. An additional contribution may be related to the reduced vigor of axial hydrothermal circulation due to a thinner crust. As an end-member case, we test predictions of model GHC with no hydrothermal circulation and variable crust thickness (red line). The resulting model is in good agreement with the mode, although this is a maximum. Lastly, the dashed line is a test of GHC-like models in which the crust thickness is varied and the Moho is treated as a maximum depth limit for axial hydrothermal penetration. Therefore, realistic models for the CRR likely occur between the dashed line and the red line for 5 km thick crust, or about  $182\text{--}189 \text{ mW m}^{-2}$ . While this is a remarkable agreement with our statistical

analysis, the completeness of sediment cover and apparent absence of basement outcrops and ventilated circulation in the region (Davis et al., 2004) may suggest that the median or mean, which is about  $200\text{--}210 \text{ mW m}^{-2}$ , may precisely capture lithospheric heat flux. Under this interpretation, CRR heat flow remains significantly elevated above the predictions of model GHC. We suggest that this is in fact the case, such that lithospheric heat loss in this region is noticeably higher than predicted by model GHC. Specifically, we suggest that this region is characteristically super-conductive due to deep hydrothermal circulation as depicted in Fig. 4.1. Davis et al. (2004) found that deep borehole thermal gradients decrease from apparently near-conductive values in the upper crust ( $\sim 200 \text{ mW m}^{-2}$ ) to much lower values ( $< 100 \text{ mW m}^{-2}$ ) at depths greater than  $\sim 700 \text{ m}$  from the basement surface. Davis et al. (2004) suggested that this is due to hydrothermal convection in deeper layers of the crust. If hydrothermal redistribution of heat occurs on such a scale in the crust, this will essentially result in the appearance of a higher effective thermal conductivity of the crust by raising its  $Nu$  number. Consequently, GHC may predict low heat flow because it does not use a high  $Nu$  number in crust older than  $0.2 \text{ Ma}$ .

### 4.6.3 Summary of High-Resolution Sites

Overall, the four specific sites discussed above show heat flow elevated above the predictions of the sediment-filtered global database of Hasterok (2013b), and are in rough agreement with all models considered. As previously recognized (Davis et al., 1997; 1999; Lucazeau et al., 2008; Hutnak et al., 2008; Hasterok et al., 2011), this demonstrates that the low scattered heat flow over young seafloor is due to ventilated hydrothermal circulation, and that careful geophysical characterization can allow the lithospheric heat budget to be at least partially revealed on young seafloor. Heat flow estimates from the Cocos plate (Hutnak et al., 2008) and the Gulf of Aden (Lucazeau et al., 2008; 2010) are in marginally better agreement with model GHC. However, these sites are located on seafloor where predicted heat flow from all models is not significantly different (Fig. 4.5), and the Gulf of Aden might not be considered 'normal' seafloor. The Juan de Fuca ridge flank is geophysically well characterized, but there is strong evidence of ventilated discharge over much of the sampled area (Davis et al., 1997; 1999). The elevated heat flow in this area may reflect this discharge, persistent deep hydrothermal circulation along faults (Nedimovic et al., 2009), heat release from hydration (Lowell and Rona, 2002), or advection from younger seafloor. Heat flow on the Costa Rica Rift is probably the most important datapoint as it 1) samples seafloor young enough to potentially differentiate models, 2) is heavily sedimented with no evidence of thermally significant ventilated transport, and 3) is well characterized for heat flow and basement depth. CRR heat flow is higher than our preferred model GHC, which may be partly explained by thin oceanic crust. Probably, however, the mean or median of heat flow in this region, which is significantly higher than predicted by model GHC, is a good indicator of lithospheric conduction. The high heat flow in this region may be attributed to deeper hydrothermal transport as suggested by Davis et al. (2004). The Costa-Rica Rift is in super-conductive state as depicted in Fig. 4.1. An important unanswered question then regards the 'normality' of such deeper transport in the crust. Such transport may be regarded as a process of passive hydrothermal circulation (albeit, sealed from exchange

with oceans) which is not included in model GHC. If this is normal for global oceanic crust, then model GHC may ultimately overestimate the effect of crustal insulation on lithospheric cooling.

Nevertheless, because only two sites considered here are located on  $<10$  Ma lithosphere, and only the Costa-Rica Rift appears to provide a precise constraint on lithospheric heat flow, it is difficult to judge the validity of these models using any existing heat flow measurements. Ideally, detailed surveys such as that performed near the Costa-Rica Rift should be performed over several other well sedimented near-ridge regions globally. Even still, it is not clear if heat flow measurements will succeed in providing precise constraints on normal lithospheric heat loss near ridge axes. We thus expect that continued development of our understanding of the relationship between heat loss and seafloor topography may be instrumental (e.g. Parsons and McKenzie, 1978; Sandwell and Poehls, 1980; Wei and Sandwell, 2006). Since heat flux may be calculated if the effective thermal expansivity and volume heat capacity are known (Eq. 4.9), future efforts should focus on linking detailed models of near-ridge environments (e.g. Cherkaoui et al., 2003; MacLennan, 2008; Craft and Lowell, 2009; Theissen-Krah et al., 2011) with comprehensive mineral physics and hydrogeological models of the crust and lithosphere (e.g. Davis et al., 2004; Afonso et al., 2007; Afonso et al., 2008; Hasterok, 2010; Goutorbe and Hillier, 2013; Grose and Afonso, 2013, Chapter 3).

## 4.7 CONCLUSIONS

We have estimated the power of ventilated hydrothermal heat transport, and its spatial distribution, using a set of recent plate models which highlight the effects of hydrothermal circulation and crustal insulation. The most important conclusion of our study is that a model with both of these effects predicts that the difference between measured and modeled heat flow is significantly lower than most previous estimates. Consequently, the total heat vented to the oceans by hydrothermal circulation is lower, and the fraction of total heat vented on ridge axes is higher, than that predicted using other reference models.

Our estimate of ventilated hydrothermal power for a model with constant thermal properties is similar to the recent analysis of Hasterok (2013a), predicting a net power deficit of 7.8 TW, 34% of which is extracted near the ridge axis ( $<1$  Ma). The effect of axial hydrothermal circulation alone is a higher net power deficit (10 TW), and about 50% of the hydrothermal heat flux occurs near ridge axes ( $<1$  Ma). Finally, the effect of crustal insulation with hydrothermal circulation is a markedly lower net power deficit (6.6 TW), with no relative change to the heat flow distribution (50% near the axis). If median or mean estimates are preferred against probability maxima, total ventilated hydrothermal power estimates are about 10 or 20% lower than these estimates, respectively.

Many physical and chemical processes in the Earth may be affected by the above predictions. As less heat is transported by hydrothermal circulation, this may also imply that less fluid is circulated in the crust, or that such fluids have a lower average temperature. The lower off-axis advective heat flux also suggests that off-axis 'diffusive' hydrothermal circulation is not as vigorous as previously thought. These reduced energy constraints must affect chemical exchanges between the crust and oceans, including the passing of nutrients to subseafloor microbial communities and the alteration of oceanic crust. In turn, these



effects should impact chemical budgets in the subduction factory and the secular chemical evolution of the mantle. Also, the crustal insulation effect may have broader implications for the thermal evolution of the Earth. Crustal insulation reduces the present day global heat flux by about 2-3 TW. This reduction will multiply into the past as a warm mantle generates systematically thicker crust and greater insulation.

Finally, the important question remains: does our cooling model with axial hydrothermal circulation and crustal insulation represent the average behavior of oceanic lithosphere? With this question in mind, we have studied model fits to empirical estimates of seafloor subsidence and geophysically well characterized sites of heat flow measurements. While a model with both hydrothermal circulation and crustal insulation (GHC) best fits global average seafloor subsidence, site-specific heat flow can be explained with a model which does not include crustal insulation (GH). Additional detailed heat flow surveys of <10 Ma seafloor will be helpful in the choice of best models on the basis of heat flow. The heat budget of cooling oceanic crust, however, is in best agreement with model GHC, as model GH predicts a probably unrealistic extraction of energy on the ridge axis. Accordingly, we find that the cooling regime of the near-axial environment and basin-scale oceanic lithosphere is best explained by models with insulating oceanic crust and axial hydrothermal circulation.

## APPENDICES

### 4.A Effective Thermal Properties

If we have a function of many variables  $C(z_1(t), z_2(t), \dots)$ , we may find the constant value  $C_e$  which, if substituted in an equation in which  $C(z_1(t), z_2(t), \dots)$  appears, would give the same result. For example, the multi-dependent thermal expansivity  $\alpha(T, X, P)$  and an amount of temperature change  $\delta T$  in a lithospheric column is related to the displacement of its surface  $\delta w$  as:

$$\delta w = \varrho \int_0^L \alpha(T, P, X) \delta T dz. \quad (4.11)$$

where  $L$  is the base of the column,  $X$  is the composition,  $P$  is the pressure, and

$$\varrho = \frac{\rho_b}{\rho_b - \rho_{wa}} \quad (4.12)$$

is the isostatic correction for seawater overburden where  $\rho_b$  is the mean density of the mantle column at the ridge axis and  $\rho_{wa}$  is the mean density of the seawater column.

With the effective thermal expansivity  $\alpha_e$  we may rewrite the above equation as

$$\delta w = \alpha_e \varrho \int_0^L \delta T dz. \quad (4.13)$$

If the properties  $T, P$ , and  $X$  change with time, then we may find an effective value for each time such that

$$\frac{1}{\varrho} \frac{dw}{dt} = \alpha_{ei}(t) \int_0^L \frac{dT}{dt} dz \approx \int_0^L \alpha(T, P, X) \frac{dT}{dt} dz \quad (4.14)$$

can be satisfied, where  $\approx$  indicates an approximate equivalence in the limit of incompressibility,  $dV/dt \approx 0$ , where  $V$  is the volume in which we integrate over the dimension  $z$ .

The effective thermal expansivity of a cooling lithospheric column is therefore

$$\alpha_{ei}(t) = \int_0^L \alpha(T, P, X) \frac{dT}{dt} dz / \int_0^L \frac{dT}{dt} dz, \quad (4.15)$$

and the effective volume heat capacity may be found similarly as

$$[\rho C_p]_{ei}(t) = q_{sf}(t) / \int_0^L \frac{dT}{dt} dz, \quad (4.16)$$

respectively.

The effective thermal diffusivity and thermal conductivity of the lithosphere may also be calculated, but as it seems to us to be of little substance to the current work and is more involved, it is not discussed here.

## 4.B Subsidence-Heat Flux Relation

The usual definition of the (net) seafloor subsidence rate  $b_e$  is

$$b_e(t) = \frac{h(t) - r}{\sqrt{t}} = \frac{w(t)}{\sqrt{t}}, \quad (4.17)$$

where  $h(t)$  is the seafloor depth,  $r$  is the ridge height,  $w(t)$  is the net subsidence, and  $t$  is the age. A corresponding solution to Eq. 4.17 for half-space cooling models can be given as

$$b_e(t) = 2\varrho(t)\alpha_e(t)\Delta T_e \sqrt{\frac{D_e(t)}{\pi}}, \quad (4.18)$$

where  $\Delta T_e$  is the effective difference of mantle and surface temperature,  $\alpha_e$  the effective thermal expansivity, and  $D_e$  the effective thermal diffusivity. Because many of these properties change as a function of depth, the 'effective' values for the lithosphere, and thus the seafloor subsidence rate, have a complicated dependence on time. On the other hand, conventional models with constant properties (or at least no depth-dependent properties) predict a constant subsidence rate. Eq. 4.17-4.18 characterize the net subsidence rate, which is a function of the entire cooling history. It is essentially the slope of a line in  $t^{1/2}$  between depth  $r = w(t = 0)$  and  $w(t)$ . We may also describe the transient, or instantaneous, subsidence rate as

$$b_{ei}(t) = \frac{dw}{d\sqrt{t}} \quad (4.19)$$

which is simply the local slope of  $w(t)$  in  $t^{1/2}$ . The corresponding relationship to physical coefficients may be given as

$$b_{ei}(t) = 2\varrho(t)\alpha_{ei}(t)\Delta T_{ei}(t) \sqrt{\frac{D_{ei}(t)}{\pi}}, \quad (4.20)$$

which has the same form as Eq. 4.18, except that physical coefficients are also transient effective properties. In comparison, the seafloor heat flux is

$$q_{sf}(t) = k \left. \frac{dT(t)}{dz} \right|_{z=0} \quad (4.21)$$

which, for half-space cooling, may be related to properties of the lithosphere as

$$q_{sf}(t) = [\rho C_p]_{ei}(t) \Delta T_{ei}(t) \sqrt{\frac{D_{ei}(t)}{\pi t}} + q_a, \quad (4.22)$$

where  $q_a$  is the adiabatic part of the heat flux. Moving time to the left hand side, we can define the variable

$$g(t) = [q_{sf}(t) - q_a] \sqrt{t} = [\rho C_p]_{ei}(t) \Delta T_{ei} \sqrt{\frac{D_{ei}(t)}{\pi}} \quad (4.23)$$

which may be referred to as a diminution rate for surface heat flow, analogous to the transient subsidence rate  $b_{ei}(t)$ .

From the above it can be seen that the seafloor heat flux is not easily related to net seafloor subsidence or even the net subsidence rate. However, the heat flow diminution rate may be related directly to the transient subsidence rate as

$$\frac{b_{ei}(t)}{2\rho(t)\alpha_{ei}(t)} = \frac{g(t)}{[\rho C_p]_{ei}(t)}, \quad (4.24)$$

which has a similar form to previous derivations of the relationship between the heat content of the lithosphere and seafloor topography (e.g. Parsons and McKenzie, 1978; Sandwell and Poehls, 1980; Wei and Sandwell, 2006).

## 4.8 ACKNOWLEDGEMENTS

We thank Derrick Hasterok for valuable exchanges and clarifications on the details of his work, comments on the statistical analysis of heat flow, and access to his processed data. We are grateful to John Hillier for providing his database of filtered global seafloor topography. Also thanks to Stephen Swift for his sediment thickness dataset, and Eric Mittelstaedt for critical comments on the Galapagos hotspot. Bicubic splines of sediment thickness and heat flow data used the software package GMT (Wessel and Smith, 1998). Dietmar Müller and Laurent Husson provided insightful reviews of an early version of this manuscript. The work of JCA has been supported by two Australian Research Council Discovery Grants (DP120102372 and DP110104145). This is contribution XXX from the Australian Research Council Centre of Excellence for Core to Crust Fluid Systems (<http://www.cafs.mq.edu.au>) and XXX in the GEMOC Key Centre (<http://www.gemoc.mq.edu.au>).

Model	Active Deficit	Flank Deficit	Near-Axial Deficit	Passive Deficit	Total Deficit
This Study: Mode(TW(% of total))					
H13	1.1(14%)	1.4(18%)	2.5(32%)	5.3(68%)	7.8
GH	4.4(44%)	0.8(8%)	5.2(52%)	4.8(48%)	10.0
GHC	2.8(42%)	0.5(18%)	3.3(49%)	3.3(51%)	6.6
This Study: Median(TW(% of total))					
H13	0.7(11%)	0.9(14%)	1.6(24%)	5.0(76%)	6.6
GH	3.7(42%)	0.7(8%)	4.4(49%)	4.5(51%)	8.9
GHC	2.2(39%)	0.4(7%)	2.6(46%)	3.1(54%)	5.7
This Study: Mean(TW(% of total))					
H13	0.5(8%)	0.6(10%)	1.1(18%)	4.9(82%)	6.0
GH	3.3(40%)	0.6(7%)	3.9(47%)	4.4(53%)	8.3
GHC	1.7(32%)	0.3(6%)	2.0(38%)	3.3(62%)	5.3
Previous Studies (TW(% of total))*					
SS94	-	-	3.2(28%)	8.1(72%)	11.3
P94	-	-	2.2(23%)	7.2(77%)	9.4
M03	2.0(20%)	0.8 (8%)	2.8(28%)	7.1(71%)	9.9
SH11C	-	-	2.0(25%)	6.0(75%)	8.0**
SH11H	-	-	3.6(40%)	5.4(60%)	9.0
H13U	-	-	2.3(37%)***	3.9(63%)***	6.2
H13SF	-	-	2.3(29%)***	5.5(71%)***	7.8

TABLE 4.1: \*SS94 - Stein and Stein (1994), P94 - Pelayo et al. (1994), M03 - Mottl (2003), SH11C - Conduction-only model of Spinelli and Harris (2011), SH11H - Hydrothermally corrected conduction model of Spinelli and Harris (2011), H13U - Hasterok (2013b) using his unfiltered heat flow database, H13SF - Hasterok (2013b) using his sediment-filtered heat flow database. \*\*Based on Spinelli and Harris's (2011) assertion that hydrothermal circulation does not change total hydrothermal power. \*\*\*Estimated based on inspection of figures in Hasterok (2013b).

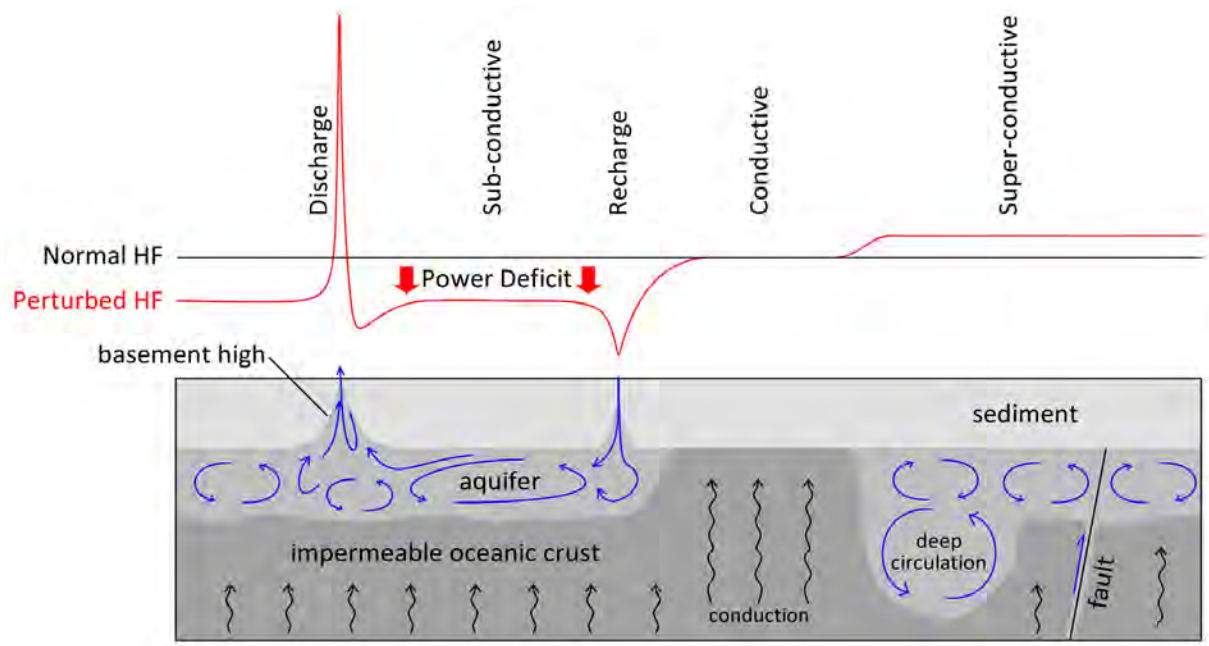


FIGURE 4.1: Cartoon showing the relationship between hydrothermal circulation patterns in the crust and resulting heat flow measured at the surface. Ventilation results in a net reduction in seafloor heat flux (sub-conductive heat flow), and vigorous hydrothermal circulation without ventilation results in a higher measured heat flux (super-conductive heat flow). The black squiggly lines indicate conductive heat transport and the blue convection lines indicate hydrothermal flow patterns. The sites of recharge and discharge are located at basement highs in these examples.

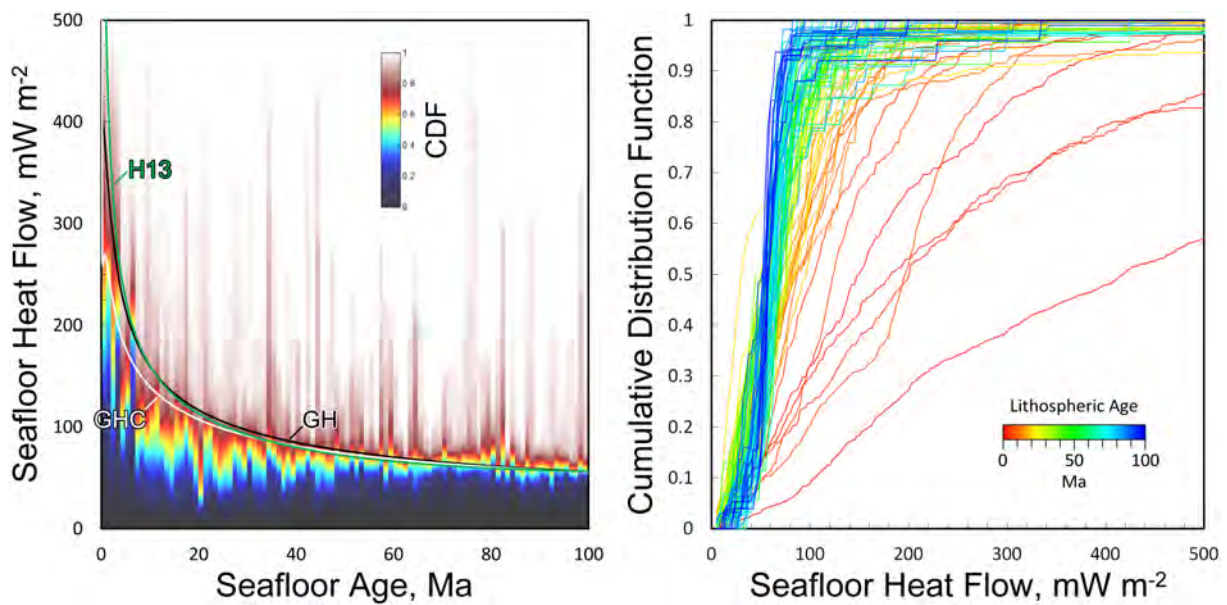


FIGURE 4.2: (a) Cumulative distribution functions of heat flow (shown by color) for 1 Ma bins to 100 Ma compared to the three thermal plate models used in this study. (b) Cumulative distribution functions of heat flow in 1 Ma bins between 1 and 100 Ma.

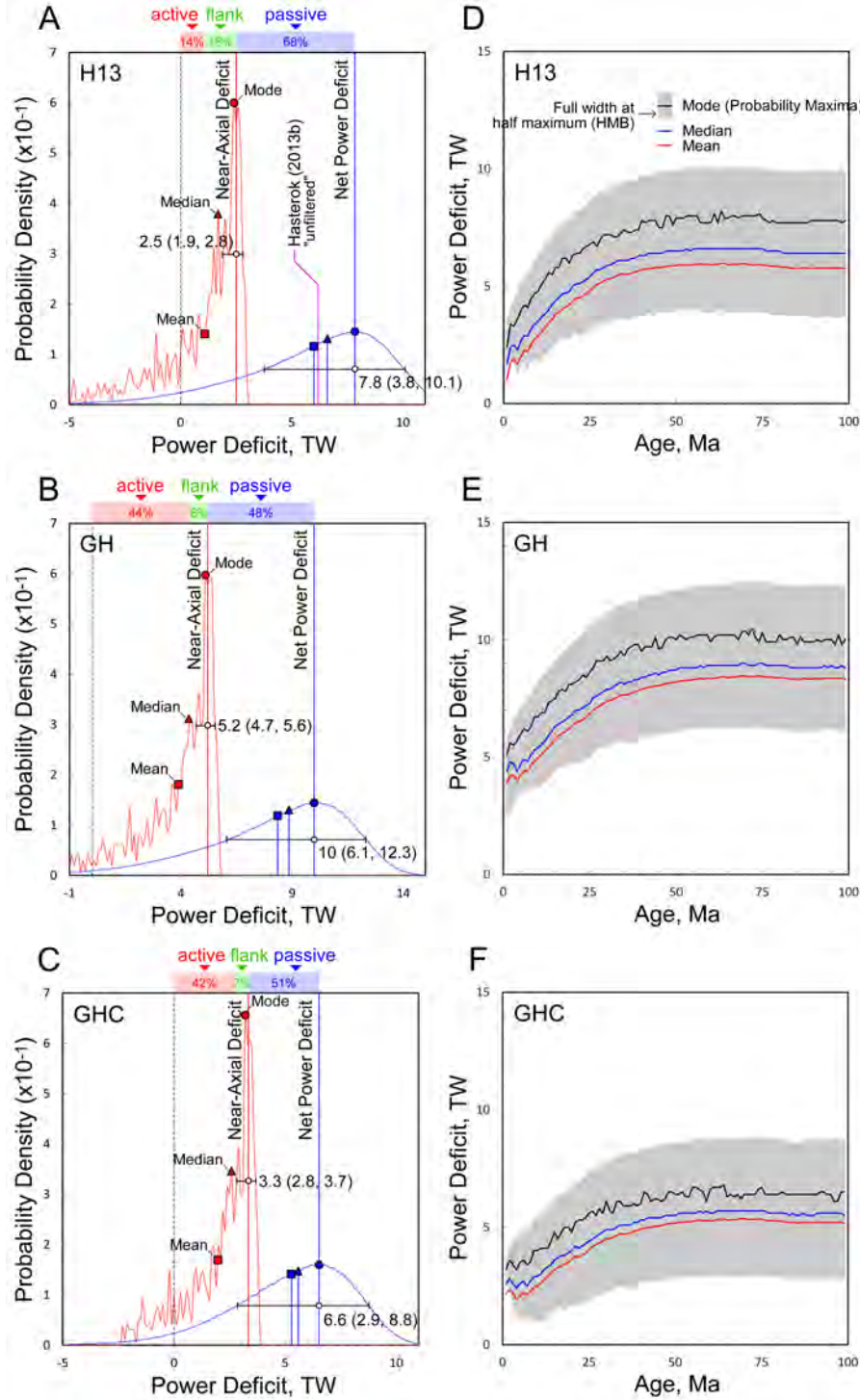


FIGURE 4.3: Probability density functions of the heat flow deficit determined from Monte-Carlo analysis for models (a) H13 (Hasterok 2013a), (b) GH, and (c) GHC (Grose and Afonso, 2013; Chapter 3). The red PDF (left panels) represents numerical integration only within the first 1 Ma bin (near-axial power deficit), and the blue PDF is the heat flow deficit integrated to 60 Ma (Net Power Deficit). The filled circles, triangles, and squares indicate the mode, median, and mean of the PDF's. The white filled circles with error bars indicate the mode and half-maximum bounds for the 1 Ma (near-axial power deficit) and 60 Ma (net power deficit) PDF's. The red, green, and blue bars above the graphs (left panels) indicate the fraction of active, flank, and passive advective power, respectively. Hasterok's (2013b) "unfiltered" estimate is indicated in panel (a). The right-side panels show the mean, median, mode, and half-maximum uncertainty of the power deficit as a function of age for each model.

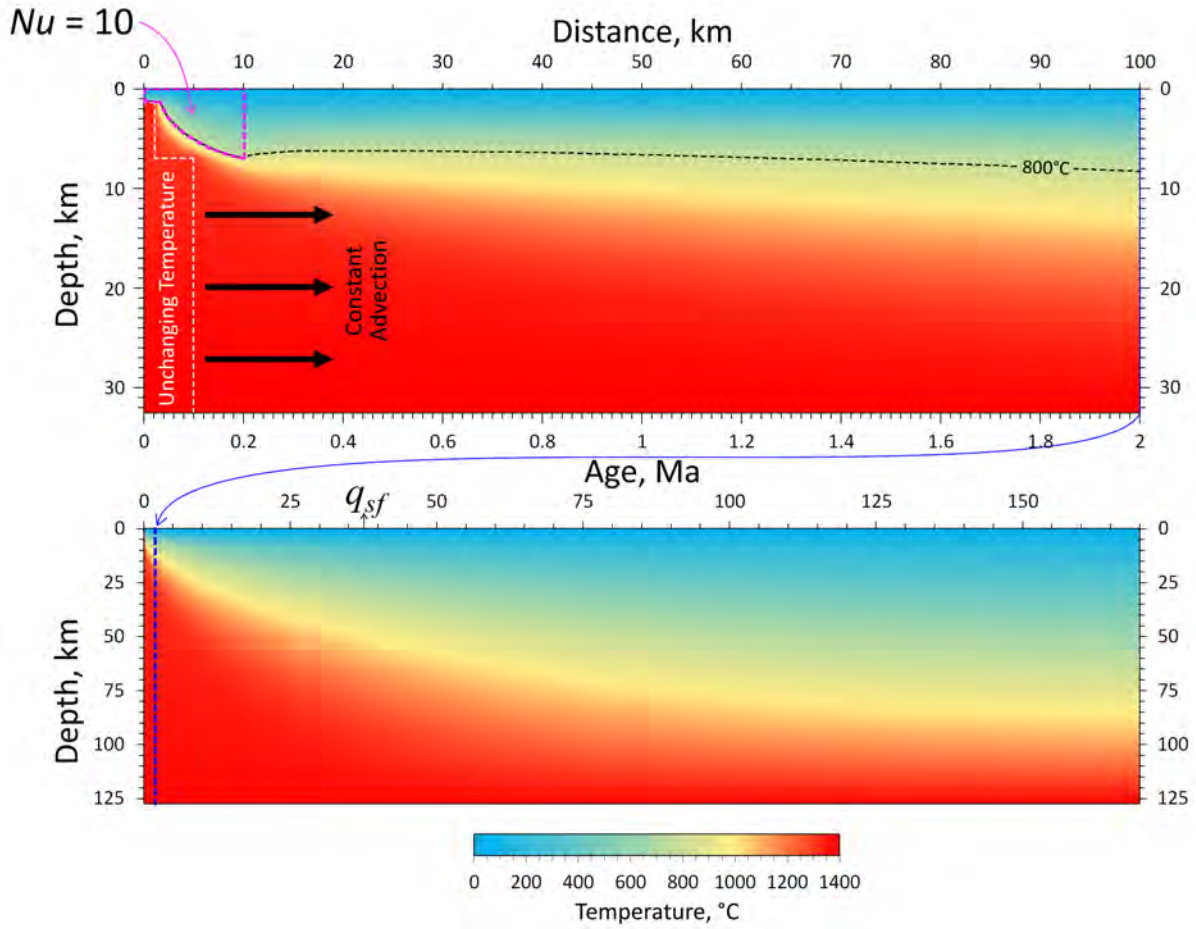


FIGURE 4.4: Boundary and initial conditions for model GH and GHC. The temperature in the region outlined in white dashes varies with depth but remains constant over horizontal distance. The distance between the surface and the top of the axial boundary condition is 1.4 km. All material around this space migrates at a constant rate away from the ridge axis. The top figure shows the boundary conditions of the 2D part of the model (0-2 Ma), and the bottom figure shows the conditions of the 1D part of the model (2-170 Ma). After figure 2 in Grose and Afonso (2013).



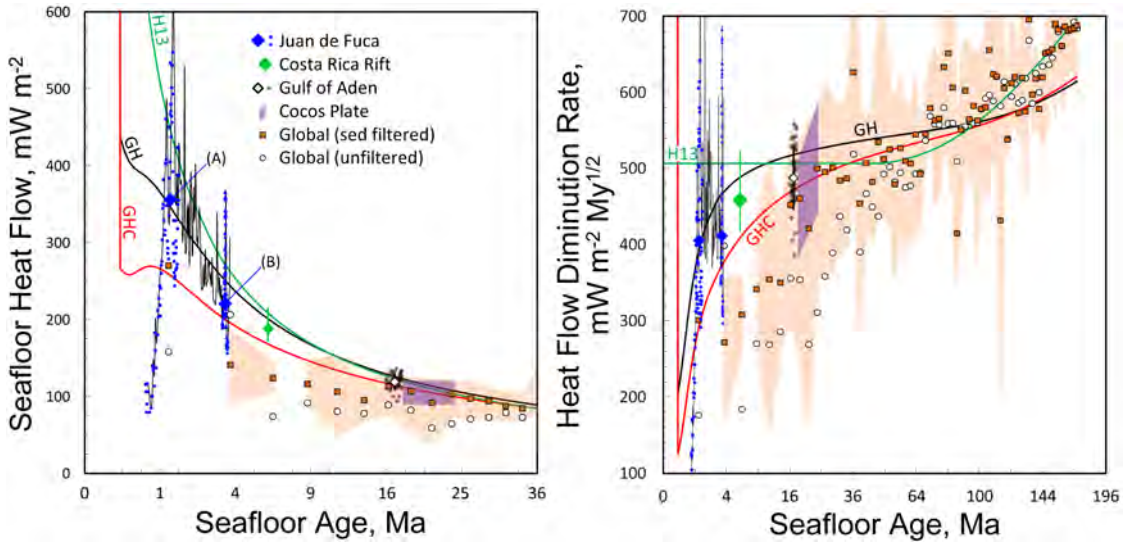


FIGURE 4.5: Predicted heat flow (a) and heat flow diminution rate (b) for models H13, GH, and GHC as a function of age compared with global and site-specific data. The site-specific data-points are discussed in the text. The global sediment filtered and unfiltered data shown here are from Hasterok (2013b). The highlighted region is the uncertainty ( $1\sigma$ ) of the sediment-filtered global dataset. Note that the misfit between models GHC and the data occurs because Grose and Afonso (2013) fitted model GHC to heat flow data which did not include a correction for continuous sedimentation.



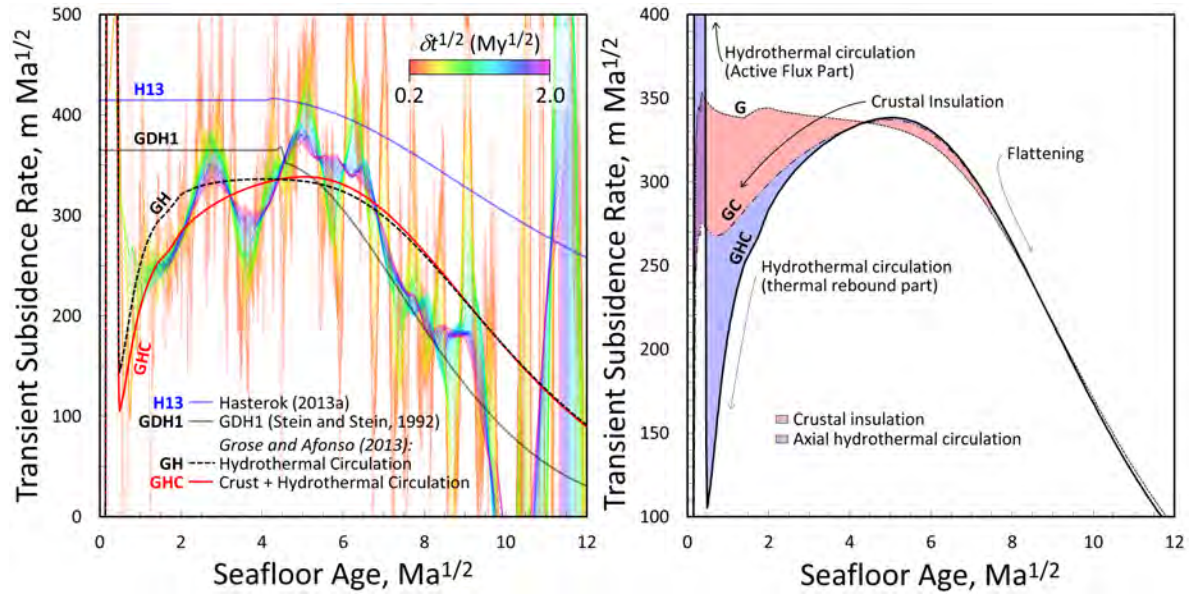


FIGURE 4.6: (a) Subsidence rates for models GH and GHC (Grose and Afonso, 2013), the classical model GDH1 (Stein and Stein, 1992), and the new plate heat-flow constrained plate model of Hasterok (2013b), compared with subsidence rates estimated from the global depth dataset of Hillier (2010). Red-yellow colors correspond to small sliding windows and blue-violet colors correspond to large sliding windows over which subsidence rates are determined using a least-squares fit. The small discontinuities around 20 Ma for GHD1 and H13 are due to the imperfect fit of their author's respective equations for seafloor depth. (b) Comparison of model predictions of model GHC, GC, and G. Models GC and G have not been used to calculate hydrothermal power loss but are included here to clarify the role of hydrothermal circulation and crustal insulation on seafloor subsidence.

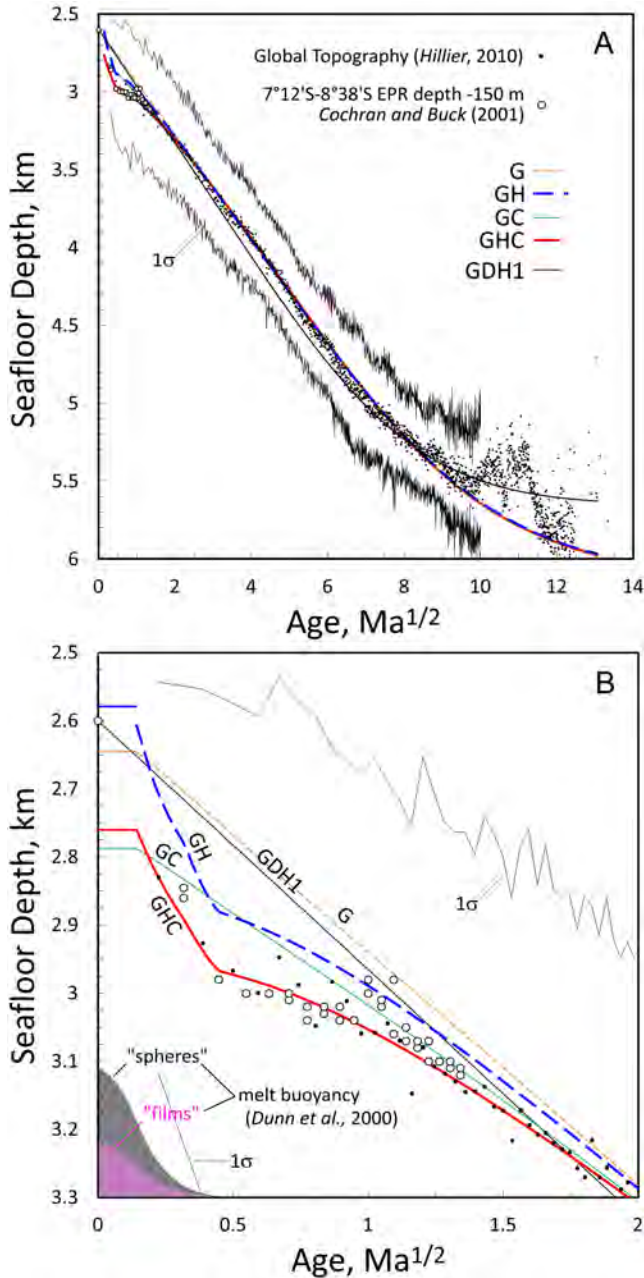


FIGURE 4.7: Predictions and observations of seafloor topography and subsidence on ridge flanks. (a) Seafloor topography of our models compared with model GDH1 (Stein and Stein, 1992), 0.1 Ma binned global 'normal' depth data with  $1\sigma$  standard deviation from Hillier (2010), and EPR ridge depth data from Cochran and Buck (2001). (b) Close-up on the model predictions and observed topography on ridge flanks. In addition, the bottom left corner shows an additional cause of ridge elevation due to the buoyancy of melt beneath the ridge based on two models of seismic tomography from Dunn et al. (2000). For ages  $<0.2 \text{ Ma}^{1/2}$  there is no subsidence in our models since energy transfer is supported by latent heat release. Figure modified after Grose and Afonso (2013).

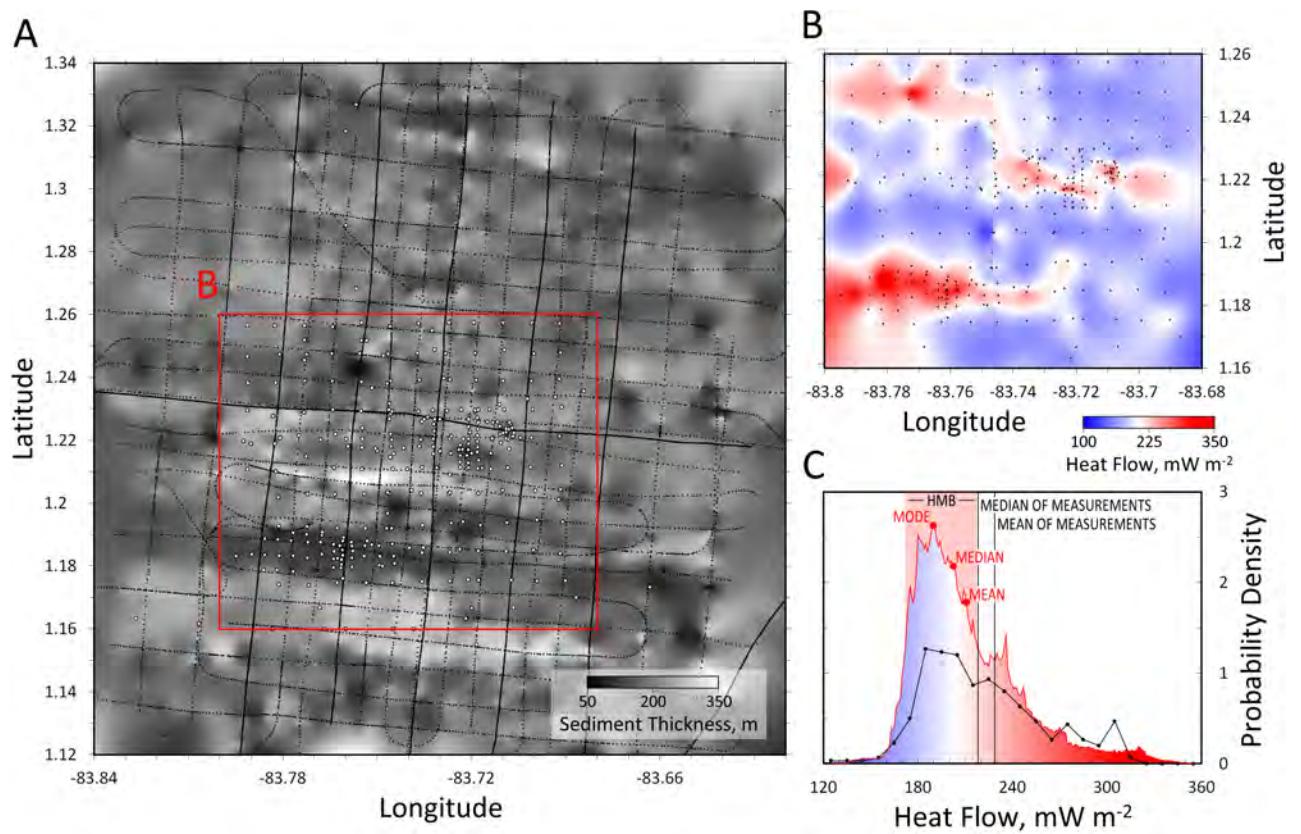


FIGURE 4.8: Sediment thickness and heat flow for the Costa Rica Rift. (a) Sediment thickness map constructed from a bicubic spline of seismic reflection profiles (dotted line, where dots are datapoints; Swift et al., 1998). Open circles are sites of heat flow measurement. (b) Heat flow map constructed from a bicubic spline of measurements (black dots). (c) Non-normalized Probability density functions (PDF) of heat flow. The red PDF is from the bicubic spline in panel (b), whereas the black line is the PDF using only measurements.

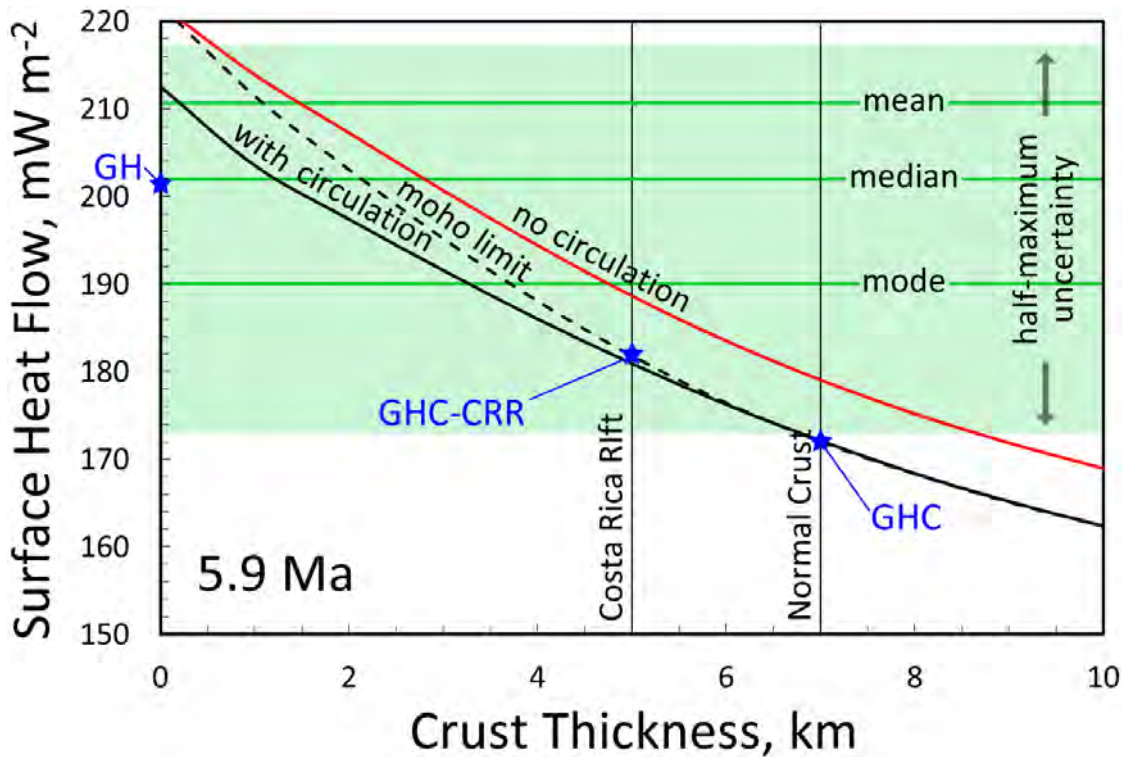


FIGURE 4.9: Predicted seafloor heat flow for model GHC with varied crust thickness and parameters affecting hydrothermal circulation are varied, compared to measured heat flow (mean, median, mode, and half-maximum bounds) for the Costa Rica Rift (Fig. 4.8). The black line is model GHC with oceanic crust varied between 0 and 10 km. The black dashed line is the same model, except hydrothermal circulation is not allowed to occur below the insulating layer. The red line is model GHC with the thickness of oceanic crust varied and no hydrothermal circulation on the ridge axis. All predictions are for 5.9 Ma seafloor.

# 5

## Microchemical Disequilibria in OIB Source Melting

### 5.1 INTRODUCTION

The exposed surface of convective mantle is the oceanic lithosphere, the upper part of which, the oceanic crust, roughly consists of geochemically and geophysically distinct regions: a roughly uniform surface of mid-ocean ridge basalts (MORB), pockmarked by ocean-island basalts (OIB). As MORB originates from passive accretion of oceanic lithosphere from continuously upwelling mantle at mid-ocean ridges, and OIB are thought to originate from deeper mantle sources by an active process impinging on the lithosphere (Morgan, 1972; McKenzie and Bickle, 1988), the characteristics of both settings must provide important constraints on the operations of mantle convection and the composition of the mantle. Among the observations, a central geochemical interest includes the progressive enrichment of incompatible elements in OIB compared to MORB (Sun and McDonough, 1989; Hofmann, 2006; Niu et al., 2012) and trends in ratios of radiogenic over non-radiogenic isotopes in the Pb, Nd, Hf, and Sr radioisotopic systems in OIB lavas (e.g. Hofmann, 2006). Although it is known that elevated incompatible elements can be attributed to low extents of melting, it is widely believed that melting phenomena cannot adequately explain the data (Hirschmann et al., 2003; Hofmann, 2006; Armienti and Gasperini, 2007; Humphreys and Niu, 2009; Niu et al., 2012). Thus, some enrichment must be attributed to the composition of the source or mixing with an enriched member. However, because the composition of the source is not observed in situ, it is largely estimated based on models of mantle melting, and is thus limited by the capabilities of the model to represent the evolution of the system. Consequently, if physical details are important, we can expect that "successful" models may lead to inaccurate conclusions about the Earth.

The purpose of this chapter is two-fold. Firstly, we develop a generalized two-dimensional

model of multi-phase coarsening, diffusive partitioning, and near-fractional melting during phase transformations in order to compute the microchemical details of disequilibrium trace element transport during mantle decompression. Secondly, we apply this model to the explanation of OIB trace element systematics and arrive at constraints on the geochemical and geophysical properties of the Earth required to explain the data.

## 5.2 The LID effect and OIB Compositions

The thermal structure of oceanic lithosphere is a classic geophysical problem which has been addressed by modeling studies of varying complexity (e.g. Sclater and Francheteau, 1970; Davis and Lister, 1974; Stein and Stein, 1992; Doin and Fleitout, 1996; McKenzie et al., 2005; Afonso et al., 2008a; 2008b; Sleep, 2011; Grose and Afonso, 2013; Chapter 3) and various approaches to the interpretation and analysis of global and regional data (e.g., Parsons and Sclater, 1977; Carlson and Johnson, 1994; Marty and Cazenave, 1989; Hillier and Watts, 2005; Crosby et al., 2006; Zhong, et al., 2007; Crosby and McKenzie, 2009; Korenaga and Korenaga, 2010; Goutorbe and Hillier, 2013; Grose, 2012; Hasterok, 2013; Chapter 2). Although the details of geophysical models and data analysis are critical to the project of linking geophysical observations to the state of oceanic lithosphere, it seems that the fundamental thermal character of the oceanic lithosphere has been largely resolved. As seafloor is created at ocean ridges and migrates away, the column of mantle below loses heat to the oceans and this cooling region of the mantle increases in thickness over time. This thickness as a function of age is well constrained by the data, and the most recent models of lithospheric cooling, while adding to our understanding of the properties and behavior of the upper mantle, do not fundamentally change this paradigm (e.g. Afonso et al., 2008a; 2008b; Chapter 3).

As the OIB source ascends through the asthenosphere it must eventually intercept and interact (thermally as well as mechanically) with the base of this cool lithosphere (or LID). This interception of a rising plume-like source by oceanic lithosphere is shown in Fig. 5.1. Although the motion or high temperature of the source may erode or deform the base of the lithosphere, the source will ultimately be prevented from further ascent. Melt generated may percolate upwards, but the source is prevented because it is solid. Prior to this encounter, the source undergoes continuous microchemical evolution, changes in the reacting assemblage, and the production of melt, such that the prediction of erupted compositions originating from this source depends on its final depth of ascent. This limit to melting, and the consequent geochemical signatures in erupted lavas, have been referred to as the LID effect (Humphreys and Niu, 2009; Niu et al., 2011). Since this final melting depth is determined by the interaction with the base of the lithosphere, it seems reasonable to associate this depth with the so-called lithosphere-asthenosphere boundary (or LAB). The LAB depth is thought to be mainly controlled by the thermal structure of the upper mantle, and the LAB is generally thought to exist around the depth where the mantle reaches a temperature of 1300°C (O'Reilly and Griffin, 2010). On the other hand, the physical origin of the LAB and its relationship to temperature is a subject of much ongoing debate (Fisher et al., 2010; Olugboji et al., 2013; above references). The nature of the LAB, both in continents and in the oceans, has become a major focus of geophysical interest due to its apparent detection



in remote sensing studies (Fischer et al., 2010) and probable relationship to important, yet poorly known, properties of the upper mantle, such as grain size (Jackson et al., 2002; Faul and Jackson, 2005), chemical layering (Hirth et al. 2000; Karato, 2004; Rychert et al., 2005; Baba et al., 2006; Eaton et al., 2009), the existence of small degrees of pooled melt (Hammond and Humphreys, 2000; Kawakatsu et al., 2009; Takei and Holtzman, 2009), or lattice preferred orientation (Gaherty et al., 1999; Levin and Park, 2000). Moreover, although the origin of the LAB is central to the interpretation of remote sensing studies, the boundary of importance to the process of deflecting an ascending OIB source is largely mechanical. Consequently, a high temperature lithospheric isotherm should be a reasonable approximation of the boundary between asthenosphere which can be displaced by a buoyant source, and lithosphere which cannot be (Afonso et al., 2008b; Ballmer et al., 2011). We will therefore refer to such an isotherm as a Lithosphere-Asthenosphere Boundary (LAB), even though it may not correlate exactly with that detected by remote sensing.

Consistent with a LID effect, it has been recognized that chemical signatures in OIB vary with the age of the seafloor on which they erupt (Park, 1990; Ellam, 1992; McKenzie and O’Nions, 1991; Haase, 1996; Humphreys and Niu, 2009; Dasgupta et al., 2010; Niu et al., 2011). Haase (1996) and Humphreys and Niu (2009) plotted light over heavy REE ratios (e.g. Tb/Yb, Ce/Yb, Nd/Yb, La/Sm, Sm/Yb) as a function of lithospheric age at the time of eruption, observing an apparent variation with age. In the analysis of Humphreys and Niu (2009) the variation is a gradual increase in La/Sm and Sm/Yb, while in the dataset of Haase (1995) there is an apparent step-like increase in Tb/Yb, Ce/Yb, and Nd/Yb distinguishing eruptions on young (<20-40 Ma) lithosphere from older lithosphere not seen by Humphreys and Niu (2009). Nevertheless, both authors study the statistical significance of the variation with linear regressions and discuss implications for the properties of the Earth with conceptual melting relationships or otherwise simple melting models.

Because Humphreys and Niu (2009) provide a more complete database of REE ratios in OIB, our analyses in this work are based on their data. However, because the final depth of melting of a source depends on an accurate determination of the age of seafloor on which eruption occurs, we have reassessed their reported seafloor ages using the global seafloor area-age grids of Müller et al. (2008). Fig. 5.2 shows a comparison of the La/Sm and Sm/Yb data using their seafloor ages, versus our age estimates. The difference is non-trivial, particularly in the case of Sm/Yb. Differences between our estimates of seafloor age and those from Humphreys and Niu (2009) are shown in Fig 5.3. The error in the ages of Humphreys and Niu (2009) probably originates in their use of present-day seafloor spreading rate and distance to ridge axes to calculate seafloor ages. Instead, variations in spreading rate over time and along the ridge axis (among other problems) results in large errors which conceal important details of the LID effect. Using our age estimates (Fig. 5.2), lavas erupted on thin lithosphere exhibit low La/Sm and Sm/Yb until a critical age (or thickness) is reached, where values step up by a factor of 2-3 over a narrow age interval. This critical age is around 15 Ma, roughly consistent with the data reported by Haase (1996). We will show that the primary cause of this step-like feature is the depth of dry melting, with a minor contribution from the garnet (or garnet-out or garnet-spinel) transition depth.

The step-like variation in La/Sm and Sm/Yb with age suggests that gradual thickening of the lithosphere must be strongly correlated with OIB chemistry. If the composition of melts

is unchanging prior to the dry solidus and then rapidly evolves toward a new composition in a narrow depth window, then this will translate to a step-like feature in the empirical data only if the seafloor age is well known and the final depth of melting is a consistent function of lithospheric age (Fig. 5.1). Accordingly, we can expect that, on a statistical basis, the variation in the OIB data as a function of age is a constraint on the evolution of OIB melt composition as a function of depth, not only the final depth of melting.

Although it is likely that the final depth of melting will change with the age of the lithosphere according to its thickness as approximated by an isotherm, it is not certain what precise temperature isotherm is most reasonable. The result of this uncertainty is shown in Fig. 5.4. The top figures show the data where seafloor ages have been converted to depths using the 1300°C isotherm, and the bottom figures use the 1100°C isotherm. For this 200°C range of LAB temperature, the corresponding uncertainty in the inferred depth of the chemical step in the OIB data (which occurs at 15-20 Ma) is about 25-30 km. Although this may seem to be an unfortunate measure of uncertainty, we will show that this is fortunate indeed. Since the depth of the chemical step can be identified with the depth of the dry solidus, and the effects of the dry solidus on chemical evolution are pronounced in models, the final melting depth at the dry solidus, and therefore the LAB temperature, can be precisely estimated. Nevertheless, the estimate of final melting depth depends on the model of melt production, and the estimate of LAB temperature depends on the model of upper mantle thermal structure, so while a particular combination of models makes precise estimates, uncertainties remain.

### 5.3 Modeling Mantle Melting: New Horizons

The Earth presents us with an interesting problem of apparent simplicity, easily explained by a conceptual picture in which thick-plate OIB represents low degree melts generated in the presence of garnet, and thin-plate OIB exemplify high-degree melts which dilute these signatures (e.g. Humphreys and Niu, 2009; Niu et al., 2011). Nevertheless, simple models cannot reproduce the observations. As an example, we perform equilibrium batch and near-fractional models using partition coefficients from Salters et al. (2002) and Adam and Green (2006) and a thermodynamic model of phase equilibria in the FCMA system (as explained later), and show predictions of La/Sm and Sm/Yb as a function of depth in Fig. 5.5. In these models the petrological description of the source is rather detailed, but the model of chemical evolution during melting is simple. Although the step-like feature in Sm/Yb is apparent, and occurs at about the right depth (~60 km), the ratios between compositions at depth (which will erupt on thick plates), versus those at shallow depth (which will erupt on thin plates) are far higher than seen in the data (Fig. 5.4). Near-fractional melting, in which only a maximum of 0.05-1.0% melt remains in contact with the solid, increases erupted values further. In addition, the low bulk partition coefficient of La in the solid results in a strong sensitivity to low degrees of melt production, which is not reflected in the data.

In this chapter, we attempt to explain the data by employing a new model of microchemical evolution during decompression melting. In our model, diffusive partitioning of trace elements occurs in a microstructure containing multiple solid phases which undergo



solid-state phase transformations and melting. A schematic picture of the LID effect and our basic model output is shown in fig. 5.1. In an ascending OIB source, the assemblage is initially melt free and it may or may not be near chemical equilibrium. With ascent, the equilibrium abundance of phases, including melt, will significantly change. Consequently, the assemblage will undergo solid-state phase transformations, followed by wet melting, dry melting, and pass the garnet-out transition until the source encounters the lithosphere and releases its final melts to the surface. Throughout these stages of evolution, both the microstructural character and the microchemical redistribution of trace elements in the source are continuously evolving in non-equilibrium processes, and it is not immediately clear how the details of such processes will impact melt compositions.

In addition, the development of a model of microchemical evolution during melting is part of a larger goal of formulating new approaches to modeling the fundamental processes relevant to chemical geodynamics in the mantle. The overarching question is the importance of microchemical disequilibria. While we only model diffusive partitioning of trace elements, diffusive partitioning of major elements is necessary to consistently model non-equilibrium thermodynamic behaviors of phase transformations and multi-phase coarsening. A better understanding of non-equilibrium effects in grain-scale evolution is likely to improve our understanding of grain size, phase transformation, bulk transport properties, and the distribution of chemical components and isotopes in the mantle over Earth history.

## METHODS

### 5.4 Microstructural Simulation

Isotropic coarsening in a multi-phase 2D model domain is simulated using a numerical technique based on the Monte-Carlo Potts model. The Potts model is a computational approach to simulate microstructural phenomena in solids and liquids. The method has been widely used in computational metallurgy, ceramics, and foam physics (c.f., Janssens et al., 2007), and has occasionally been used in the context of geological systems (e.g. Solomatov et al., 2002; Piazzolo and Jessell, 2008). Forward evolution in the Potts model is governed by the minimization of interfacial energy. Using an energy function to describe the energy density of a digitized microstructure and a probabilistic determination of local changes of state, forward microstructural evolution can be simulated. The following Potts model schemes are basically similar to previously developed models (e.g. Tikare, 1995; Tikare et al., 1998; Janssens et al., 2007), albeit heavily modified for multiple phases, phase transformation, and accuracy.

The model begins by defining an  $N \times M$  matrix where the volume elements represent a spatial distribution of lattice sites. All sites are then populated with properties such as the stable phase,  $P$ , and the "spin",  $S$ . The phases are initially distributed randomly, although with known modal abundances (e.g. 50% olivine, 10% opx, 5% melt, etc.). The model must be configured such that it can be determined if a phase is liquid or solid. The lattice spin numerically differentiates individual grains and their boundaries, and may be taken to physically represent the crystal orientation. Typically, the range of possible spin states,  $Q$ , is a finite set of integers numbering on the order of  $10^2$  for crystalline materials. Significantly

fewer  $Q$ -states can affect model results since independent grains with the same  $Q$ -state will be treated as a single grain. Moreover, for a multi-phase model in which only the  $Q$ -state is used to differentiate crystals, a model failure will occur if two lattice sites of differing phase adopt the same spin. While there are other obvious remedies, we find that treating the  $Q$ -state as a 64-bit number effectively eliminates this possibility while also being more realistic.

The energy density  $E_\alpha$  is computed from the energy function

$$E_\alpha = \frac{1}{2} \sum_{\beta}^{n=36} e_{\alpha\beta}, \quad (5.1)$$

where the subscripts  $\alpha$  and  $\beta$  refer to the site and its neighbors, respectively,  $n$  is the number of interacting neighbors, and  $e_{\alpha\beta}$  is the energy of the interaction. The interaction energies depend on the spins and phases of the interacting sites such that

$$\begin{aligned} e_{\alpha\beta} &= 0 \text{ if } S(\alpha) = S(\beta) \\ e_{\alpha\beta} &= \gamma_{ss} \text{ if } S(\alpha_s) \neq S(\beta_s) \\ e_{\alpha\beta} &= \gamma_{sl} \text{ if } S(\alpha_l) \neq S(\beta_s) \\ e_{\alpha\beta} &= \gamma_{sl} \text{ if } S(\alpha_s) \neq S(\beta_l) \end{aligned}$$

where  $S(\alpha)$  is the spin of site  $\alpha$ , subscripts  $s$  and  $l$  indicate that the sites are solid and liquid, respectively, subscripts  $ss$  and  $sl$  indicate solid-solid and solid-liquid interactions,  $\gamma_{ss}$  is the solid-solid interaction energy, and  $\gamma_{sl}$  is the solid-liquid interaction energy. The interaction energy employed in the Potts model is conceptually analogous to the extensive thermodynamic quantity of interfacial free energy, which is also related to the concept of surface tension (c.f., Porter and Easterling, 1981). In the presence of  $\geq 2$  phases whose boundaries are characterized by different free energies per unit area (or length in our 2D models), the interfacial configuration of the system will evolve toward a structure which preferentially minimizes the surface area of interfaces with high free energy. Due to the low free energy of liquid-solid interfaces compared to solid-solid interfaces ( $\gamma_{ss}/\gamma_{sl}=2.5$  in our models), the system will attempt to increase the area of solid-liquid interfaces by drawing excess liquid away from triple junctions and into inter-crystalline boundaries. The resulting migration of liquid sites is a type of capillary action which causes wetting of grain boundaries by the liquid. Although it is known that interfacial energy depends on misorientation angle, due to limited data and model simplicity we assume that interfacial energy depends only on the interacting phases.

The energy of the entire system is

$$E = \frac{1}{2} \sum_{\alpha_{ij}}^N \left( \sum_{\beta}^{n=36} e_{\alpha\beta} \right), \quad (5.2)$$

where  $N$  is the total number of lattice sites.

### 5.4.1 Large Energy Stencil

We use a large 37 point stencil with 36 nearest neighboring elements (7th nearest neighbors), whereas typical Potts models use 5 or 9 point stencils (1st and 2nd nearest neighbors). The main reasons for the large stencil are to inhibit lattice pinning effects (e.g. Holm et al. 1991) and to allow greater sensitivity to boundary geometry, thus promoting the occurrence of boundary curvature and Zener pinning effects around interstitial grains. While Potts model microstructures normally generate jagged grain edges, a large energy stencil results in rounded features which appear similar to predictions of phase-field models (compare our results to Tikare et al., 1998).

Moreover, we expect a large stencil approach to be more realistic. The Potts model, ideally, simulates the behavior of atoms on about the scale of the primitive unit cell. As the statistics of large groups of atoms are expected to behave similar to individual atoms, lattice interactions should provide realistic results at grain scales. On the other hand, the dimensions of the unit cell are much smaller than the distances over which long range electrostatic and van der Waals forces occur. For example, the properties and structure of materials calculated in molecular dynamics simulations are known to be strongly determined by the maximum distances over which atoms are allowed to interact (Huang et al., 2010). Although the details involved in the behavior of a molecular dynamic system are quite different from those involved in the Potts model, since interactions occur over distances of several unit-cells (0.5-2 nm), we should expect that self-similar behavior requires that Potts model interactions occur over several lattice spaces.

### 5.4.2 Forward Scheme

Coarsening and grain boundary migration is modeled as a statistical energy minimization process. The Monte-Carlo procedure is as follows:

1. Calculate energy density configuration using periodic boundary conditions.
2. Randomly (or non-randomly) select a lattice site in the matrix. Also, randomly (or non-randomly) select a neighboring site from 8 nearest neighbors.
3. If the spin of the site and its selected neighbor are equal, go back to step 2. Otherwise, continue.
4. If the phase of the site and its neighbor are unequal, continue to step 5. Otherwise, the site adopts the spin of the neighbor and continue to step 7. This step facilitates grain boundary migration processes.
5. If the site is a solid phase, it adopts a new random spin (all liquid sites have equal and unchanging spin). This step facilitates Ostwald ripening processes.
6. The site and its neighbor exchange places. Spin, phase, and trace element concentrations are exchanged.
7. The new energy configuration is calculated.
8. Use a probability transition function to determine whether to accept or reject the change. We use the common Metropolis function where the probability  $h$  of accepting a change is (Jannsens et al., 2007)

$$h = 1 \text{ if } \Delta E \leq 0$$

$$h = \exp(-\Delta E/K_T) \text{ if } \Delta E > 0$$

where  $\Delta E$  is the energy change and  $K_T$  is the thermal energy, or noise, of the system.

The above algorithm is repeated once for all lattice sites. Once all lattice sites have been tested for state changes, 1 Monte-Carlo step (MCS) has passed. Note that we have stated that the selection of the lattice site and its neighbor (step 2) may be random or non-random. Normally, both selections are random, such that for a single MCS a single site may be sampled many times while others are not selected at all. However, both selections may take place in a definite order. In fact, such Potts models are attractive due to their ease of parallization (e.g. Janssens et al, 2007).

For our models, the normal value of  $K_T$  is taken to be 1.0, and the normal value for time scaling is 1 MCS = 1 year.

### 5.4.3 Accelerated Coarsening

To obtain an initial condition for our models that is not substantially more computationally expensive than the model itself, while also being unique, we start models with a stage of accelerated coarsening. After the initial lattice is populated with modal abundances appropriate for the initial model conditions, we run the cellular interaction model with an elevated temperature. This introduces excess noise into the system and accelerates Ostwald ripening. We use

$$K_T = K_{Ti} + K_B \sqrt{1 - i/y} \quad (5.3)$$

where  $K_{Ti}$  is the normal thermal coefficient,  $K_B$  is a boost to the normal coefficient,  $i$  is the current MCS, and  $y$  is the number of MCS's in the accelerated coarsening phase. In our models  $y = 10^5$ .

## 5.5 The Equilibrium Assemblage and Restite Composition

The principal controls on the chemical evolution of decompressing mantle are the abundances of phases, their distribution in the microstructure, and the character of their transformation into other phases. In the previous section we laid out the aspect of our model which accounts for the phase distribution using the Potts model of microstructural evolution. Now, we concern ourselves with accounting for phase abundance, and subsequently we will deal with phase transformations.

Our approach to estimating the abundances of solid phases is based on equilibrium thermodynamics calculations. Using a model of the composition of the solid residue, combined with estimates of pressure and temperature, we calculate phase equilibria using the equilibrium thermodynamic software of Connolly (2009), the compositions in the restite of a melting fertile peridotite (Appendix 5.A-5.B), and the internally-consistent thermodynamic database of Xu et al. (2008). As we stated earlier, we will not only deal with thermodynamically consistent estimates of phase equilibria, but we will incorporate the changing modal abundances of these phases in our model. Phase transformations occur continuously with changing  $P, T, X$  conditions at all depths in the mantle column. From great depth

in the upper mantle, garnet gradually decomposes during decompression producing pyroxene phases which eventually begin to dissolve into melt at a slow rate after the wet solidus depth is exceeded, and rapidly after the dry solidus (e.g. Solomatov and Reese, 2008). To capture this continuous behavior in our model, we calculate the equilibrium assemblage in the solid (having a composition dependent on its potential temperature and total degree of melting) at 1 km intervals in the mantle column. Combining this with a microstructurally realistic approximation of phase transformation (see Sec.5.6), we may model the continuous microstructural and melting dynamics of a decompressing mantle volume.

### 5.5.1 Melt fraction and Restite Composition Model

Herzberg (2004) summarized component mass fractions in the melt residue for  $\text{SiO}_2$ ,  $\text{Al}_2\text{O}_3$ ,  $\text{FeO}$ , and  $\text{MgO}$  in the case of decompression melting of a fertile peridotite from solidus pressures of 2, 3, 5, 7, and 10 GPa, corresponding to potential temperatures  $T_p$  of 1330, 1450, 1575, 1695, and 1770°C (assuming  $dT/dz=0.5 \text{ K km}^{-1}$ ). To obtain a smooth functional relation describing melting at potential temperatures in the range  $1550 \pm 250^\circ\text{C}$  we parameterize the extent of melting as a function of potential temperature  $T_p$  and pressure  $p$  (Appendix 5.A), and parameterize component mass fractions as a function of  $F$  and  $T_p$  (Appendix 5.B). An additional  $\text{CaO}$  component is estimated using a relationship to  $\text{Al}_2\text{O}_3$  composition from Afonso and Schutt (2012).

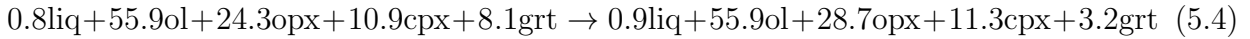
Computed modal abundances of olivine, orthopyroxene, clinopyroxene, and garnet as a function of total melt fraction and depth are shown in Fig. 5.6 for  $T_p = 1400 \pm 100^\circ\text{C}$ . Our calculations are compared with estimates of mantle petrology based on abyssal peridotite data from Niu (2004), showing good agreement.

A caveat of our implementation (and of unclear importance to our microchemical calculations for trace elements) is that the restite compositions calculated by Herzberg (2004) represent a case of equilibrium fractional melting only, wherein which a drop of residual melt is always in equilibrium with the solid. However, in the case of non-equilibrium fractional melting, a melt residue is more likely to be far from equilibrium, with the distance from equilibrium increasing with a decreasing volume of melt residue (since the residence time of melt decreases as the residual melt volume  $\phi_r \rightarrow 0$ ). While a future avenue of research may consist of the incorporation of internally consistent thermodynamic models of phase equilibria in the presence of melt (e.g. Asimow and Ghiorso, 1998; Asimow et al., 2001), a further step must be the improvement of such models for non-equilibrium thermodynamics of multi-phase, multi-component media. Nevertheless, we have taken the present route for simplicity.

## 5.6 Phase Transformations

Solid-state phase transformations and melting/precipitation reactions are based on equilibrium thermodynamic calculations. For a given bulk rock composition, the abundance of phases at chemical equilibrium may be calculated (Sec. 5.5). During melting, chemical components are unequally extracted from the solid, resulting in a bulk restite (or solid residue) composition which has changed. Thus, a recalculation of the abundance of phases with

the new composition will result in a new assemblage. Similarly, even before melting occurs changes in pressure and temperature will result in a different equilibrium assemblage. While the equilibrium modes can be calculated at different times as the pressure, temperature, and composition change, the question is how to simulate transformations which must occur to adopt the new configuration in the microstructure. Two main problems occur. Firstly, while the new equilibrium assemblage is known, the non-equilibrium path of transformation is not. For example, consider the following bulk reaction, which occurs in one of our models around 2.2 GPa:



which may be rearranged to remove non-participating phase fractions as



Although we know the bulk products and reactants, the path of reaction cannot be determined from this data alone. It may be misleading to assume that garnet directly exsolves liquid, opx, and cpx. Instead, for example, garnet may exsolve 4.4 units of opx and 0.5 units of cpx, followed by the dissolution of 0.1 unit of cpx. Similarly, if we assumed that  $\text{grt} \rightarrow \text{cpx}$  transformations cannot occur while  $\text{opx} \rightarrow \text{cpx}$  can, we might interpret the reaction such that 4.8 units of opx are exsolved, of which 0.4 units transform into cpx. Moreover, in these two cases the production of liquid or cpx may come from previously existing cpx or opx, respectively, which had not taken part in the prior reactions at all. This problem is dealt with using a matrix of coefficients which determines which phases may transform into other phases.

Secondly, a basic limitation of our model is that we treat phases as chemically indivisible identities. Consider the incongruent melting reaction of enstatite producing forsterite and liquid:



In this case the path of reaction is also not straightforward without additional information, since one may interpret it as a transformation of enstatite into melt, which then precipitates forsterite, or a transformation into forsterite, from which an excess  $\text{SiO}_2$  component dissolves. Nevertheless, because each lattice site in our model can only be a single phase, a site of opx can only transform into olivine or melt, not both. In our model, this problem is accounted for statistically. Although a phase A may only transform into one product phase B or C, the transformation of a group of lattice sites of phase A, such as those which compose an entire grain, may transform partly into phase B and partly into phase C. The above reaction would therefore be accomplished by transforming, on average, 2 lattice sites of opx into 1.4 lattice sites of olivine and 0.6 lattice sites of melt.

The spatial and temporal statistics of transformation are simulated by calculating fields of probability for the production of each product phase  $q$ , everywhere in the  $M \times N$  model domain, as

$$(n_q)_{ij} = \tau \mathbf{A}(P_{ij}, q) E_{ij} \Delta \psi_q \quad (5.7)$$

where  $\tau$  is a rate (or time) constant,  $P_{ij}$  is an index matrix of the phase matrix  $P$ ,  $q$  is one of 5 transformation products,  $E_{ij}$  is a matrix of interfacial energy,  $\mathbf{A}(P_{ij}, q)$  is the  $q \times q$

'path matrix' of transformation coefficients defining the possible source (rows) and product (columns) phases, and  $\psi_q$  is the vector of thermodynamic forces here estimated from the difference of the current and equilibrium modal abundances as

$$\Delta\psi_q = \psi_q^{eq} - \frac{1}{N} \sum \{P_{ij} = q\}, \quad (5.8)$$

where  $\psi_q^{eq}$  is the equilibrium abundance of mode  $q$  and  $N$  is the number of lattice points or control volumes. The last term in the above equation gives the fraction of lattice sites in the phase matrix  $P$  where the condition  $P_{ij} = q$  is satisfied. Note that  $\Delta\psi_q$  is a simple number for each  $q$ , such that the thermodynamic force is a global average, as opposed to a force related to local intensive variables.

Eq. 5.7 predicts that the rate at which a reaction occurs is proportional to the surface area of the source phase (i.e., we assume all transformations occur by heterogeneous nucleation processes) and the difference of the modeled and equilibrium abundance of the phases. While more robust thermodynamically consistent approaches to modeling reaction paths can undoubtedly be formulated, we forgo this labor for our method's simplicity. Since the dominant phase transformations are the transformation of garnet into orthopyroxene and the melting of cpx and opx, our model should adequately characterize the basic behavior of phase transformations during decompression melting. In the future, the details of major element microchemical controls on phase transformations will be investigated with an improved model which is more consistent with a framework of non-equilibrium thermodynamics.

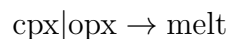
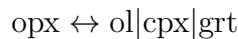
We give the transformation path matrix (assumed to be constant for all  $p, T, X$  conditions encountered) as

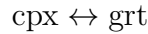
$$\mathbf{A} = \begin{pmatrix} q_{1,1} & q_{1,2} & q_{1,3} & q_{1,4} & q_{1,5} \\ q_{2,1} & q_{2,2} & q_{2,3} & q_{2,4} & q_{2,5} \\ q_{3,1} & q_{3,2} & q_{3,3} & q_{3,4} & q_{3,5} \\ q_{4,1} & q_{4,2} & q_{4,3} & q_{4,4} & q_{4,5} \\ q_{5,1} & q_{5,2} & q_{5,3} & q_{5,4} & q_{5,5} \end{pmatrix} = \begin{pmatrix} 0 & 0 & 0 & 0 & 0 \\ 0 & 0 & 1 & 0 & 0 \\ 1 & 1 & 0 & 1 & 1 \\ 1 & 0 & 1 & 0 & 1 \\ 0 & 0 & 1 & 1 & 0 \end{pmatrix} \quad (5.9)$$

where each matrix element  $q_{A,B}$  represents the part of a reaction in which there occurs a transformation of phase  $A$  into a phase  $B$ . In our models, the order of phases is: 1) melt, 2) olivine, 3) orthopyroxene, 4) clinopyroxene, and 5) garnet, or for straightforwardness:

$$\mathbf{A} = \begin{pmatrix} q_{liq \rightarrow liq} & q_{liq \rightarrow ol} & q_{liq \rightarrow opx} & q_{liq \rightarrow cpx} & q_{liq \rightarrow grt} \\ q_{ol \rightarrow liq} & q_{ol \rightarrow ol} & q_{ol \rightarrow opx} & q_{ol \rightarrow cpx} & q_{ol \rightarrow grt} \\ q_{opx \rightarrow liq} & q_{opx \rightarrow ol} & q_{opx \rightarrow opx} & q_{opx \rightarrow cpx} & q_{opx \rightarrow grt} \\ q_{cpx \rightarrow liq} & q_{cpx \rightarrow ol} & q_{cpx \rightarrow opx} & q_{cpx \rightarrow cpx} & q_{cpx \rightarrow grt} \\ q_{grt \rightarrow liq} & q_{grt \rightarrow ol} & q_{grt \rightarrow opx} & q_{grt \rightarrow cpx} & q_{grt \rightarrow grt} \end{pmatrix} = \begin{pmatrix} 0 & 0 & 0 & 0 & 0 \\ 0 & 0 & 1 & 0 & 0 \\ 1 & 1 & 0 & 1 & 1 \\ 1 & 0 & 1 & 0 & 1 \\ 0 & 0 & 1 & 1 & 0 \end{pmatrix} \quad (5.10)$$

The path matrix with the above coefficients predicts that the following types of transformations may occur on the digitized grid:





where  $|$  is an 'or' operator, and other reactions such as  $\text{ol} \leftrightarrow \text{cpx}$  and  $\text{grt} \leftrightarrow \text{melt}$  are assumed to be impossible or negligible. It is important to realize that these equations are not meant to represent chemically balanced reaction equations. The above transformation paths simply dictate what immediate phase transformations (nucleations) are possible. In the example reaction above (Eq. 5.6), enstatite transforms into forsterite and melt. In our model, this will be accounted for by increasing the abundance of olivine (forsterite) while decreasing the abundance of opx (enstatite). The amount of opx which transforms into olivine and melt depends on the phase equilibria, which is in turn dependent on the chemical solution models incorporated into the thermodynamic model. The reaction path further dictates that if a thermodynamic model predicts that forsterite and melt are produced, it must come from opx, unless cpx is present.

Notice that path coefficients for transformations are usually symmetric, except for transformations involving melt. Specifically, the transformations  $\text{opx} \rightarrow \text{melt}$  and  $\text{cpx} \rightarrow \text{melt}$  are allowed, while the complementary  $\text{melt} \rightarrow \text{opx}$  and  $\text{melt} \rightarrow \text{cpx}$  transformations are not. The reason for this is simply one of convenience in our formulation, as while  $\text{melt} \rightarrow \text{solid}$  transformations are rare if allowed, they complicate the requirements of mass conservation for trace element partitioning during fractional melting. More specifically, this complication arises due to our treatment of the 'volume density' of melt in the case of near fractional melting (Sec. 5.7.2 and 5.7.3). If a melt site with a low volume density transforms into a solid, there must be a contraction of the solid volume. Dealing with such transformations is complicated and unnecessary since melt production is almost always positive during decompression (Fig. 5.9).

Our thermodynamic calculations of phase equilibria are shown in Fig. 5.6. Prior to the onset of dry melting, the major reaction is the transformation of garnet into opx. Meanwhile, cpx fluctuates in abundance until the dry solidus, and olivine increases by a fraction of a percent due to 1% wet melting. At the onset of dry melting, olivine and melt are produced at the expense of opx and cpx. For higher mantle potential temperature we see another possible reaction. At the onset of dry melting, the abundance of garnet is affected by the production of melt. A straightforward explanation is that garnet melts. However, because of the high melting point of garnet, we expect another path will be taken (thus we set the  $\text{grt} \leftrightarrow \text{melt}$  path coefficient to zero in Eq. 5.10). Instead, garnet first transforms partly into opx, which may then partly transform into melt.

These phase equilibria calculations may be compared to the actual phase abundances which occur in our Potts model in Fig. 5.7. Basically, Fig. 5.6 shows the thermodynamic input values in our Potts model, and Fig. 5.7 shows the output of our model, in which the thermodynamic calculations are implemented. The differences between the phase equilibria calculations and our model predictions constitute the non-equilibrium characteristics of our microstructural model. However, the thermodynamic calculations and our model results are nearly identical, indicating that the rate of phase transformation is fast compared to the change in equilibrium modal abundances. The main difference occurs when the equilibrium abundance of a phase goes to zero. When this occurs  $\Delta\psi_q \rightarrow 0$  and the probability and thus rate of phase transformation goes toward zero. This is largely an unrealistic aspect of our model since  $\Delta\psi_q$  is phenomenologically related to the free energy change due to a phase



transformation, which is not actually a linear function of the equilibrium modal abundance. However, the effect of this on our predictions of trace element melt chemistry is minor due to the low abundances of these lingering phases.

## 5.7 Diffusive Partitioning

Diffusive partitioning of trace elements is described with the following advection-diffusion equation:

$$\frac{\partial C_k}{\partial t} + \mathbf{v} \cdot \nabla C_k = \nabla \cdot (D_k \nabla \hat{C}_k) \quad (5.11)$$

where  $C_k$  is the concentration of the trace component  $k$ , and  $D_k$  is the diffusivity of the component, and the hat on  $\hat{C}_k$  indicates that the concentration gradients require a special treatment when there exists a discontinuous variation in the partition coefficients. Note that although we show an advection term, advection is treated exclusively by lattice site motions in the potts model (Sec. 5.4.2).

Diffusion across phase boundaries (grain boundaries of unequal phase) is described by implementing one simple operation. For diffusion between two boundary nodes with different partition coefficients, the concentration of the node with the lower partition coefficient is changed by the amount

$$\delta K = \frac{K_n}{K} \quad (5.12)$$

where  $K$  is the partition coefficient and  $K_n$  is the partition coefficient of the neighboring node. This procedure is explained and illustrated in Fig. 5.8.

We may give a difference equation for volume diffusion throughout the domain as:

$$\nabla \cdot (D_k \nabla \hat{C}_k) \Rightarrow \sum_n^4 \left[ \frac{D_n + D}{2\Delta x^2} (C_n \theta_i - C \theta) \right]_k \quad (5.13)$$

where subscript  $n$  indicates one of four orthogonal neighboring nodes,  $\Delta x$  is the spacing, and  $\theta$  is a concentration modifier of the central node and  $\theta_i$  for the neighboring node (with respect to the self node), which depends on the partition coefficients. Specifically,

$$\text{If } \delta K < 1 \text{ then } \theta_i = \delta K^{-1} \text{ and } \theta = 1$$

otherwise  $\theta_i = \theta = 1$ . Finally, we note that in Eq. 5.13,  $\theta_i$  has been used and not  $\theta_n$  to denote that  $\theta_i$  is not a property of the neighboring node. Instead, it is a property of the central site in relation to the neighboring node.

Benchmarks of numerical accuracy in our diffusive partitioning simulations are discussed in Appendix 5.C.

### 5.7.1 Comparison to non-equilibrium thermodynamics

Our equation (Eq. 5.13) can be compared to the non-equilibrium thermodynamic equation for isothermal mass diffusion in the absence of advection (de Groot and Mazur, 1984):

$$\frac{\partial C_k}{\partial t} = \nabla \cdot \left[ \sum_{i=1}^m L_{ki} \nabla \mu_i \right], \quad (5.14)$$

where  $C_k$  is the concentration of component  $k$  (which is one component  $i$  of  $m$  total components),  $L_{ki}$  is a matrix of phenomenological coefficients (related to the mass diffusivity) of component  $k$  with respect to  $i$ , and  $\mu_i$  is the chemical potential:

$$\mu_i = \frac{\partial G}{\partial C_i} \quad (5.15)$$

where  $G$  is the Gibbs free energy. In non-equilibrium thermodynamics, isothermal mass diffusion occurs down a gradient of chemical potential, which is a continuous function of the concentration in a single phase. Across a phase boundary, however, the chemical potential at a given concentration may differ between the two media. Similarly, across a phase boundary, the apparent concentration  $C_n\theta_i$  may differ, even if the concentrations are equal. Therefore, our modified concentrations  $C_n\theta_i$  and  $C\theta$  are analogous to the chemical potential. An important difference for our model is the absence of a concentration dependence for diffusion in a given phase, whereas the chemical potential may be an arbitrary function of composition and phase.

### 5.7.2 2D near-fractional melting

Because we model diffusive partitioning of trace elements in a 2D domain at the sub-grain scale, and melt may be continuously expelled as it is produced in the case of near-fractional melting, an important problem arises. How do we model the expulsion of melt? It may seem straightforward to remove a melt site by having it migrate toward an edge and then removing it, or by transforming it into a 'void space' and allowing the surrounding media to compact. However, such implementations are not simple. The total amount of melt removed is on the order of 25%, or larger for  $T_p > 1300^\circ\text{C}$ , resulting in substantial compaction. This compaction will result in the motion of grains with respect to each other, but our Potts model is not capable of transporting grains as solid units. The consequences are not realistic. For simplicity, we therefore ignore the details of compaction. Instead, to model melt extraction we treat all 'melt' as retained in the model domain, but that the representative volume of melt decreases with extraction. This means that the Potts model behaves as a batch melting domain, whereas the transport behavior of trace components is consistent with near fractional melting. So, if a total of 4% melt is produced, but near-fractional melting predicts that residual melt is  $\phi_r=1\%$ , then 4% of the model domain sites will be melt, but the 'volume density' of each melt site is  $1/4$ , while the volume density of solid sites is always 1.

This may be introduced into the equations for mass diffusion as

$$\nabla \cdot (D_k \nabla \hat{C}_k) = \frac{1}{V_\rho} \sum_n^4 \left[ \frac{D_n + D}{2\Delta x^2} (C_n\theta_i - C\theta) \right]_k \quad (5.16)$$

where  $V_\rho$  is the volume density (1 for solid,  $\leq 1$  for liquid).

### 5.7.3 Mass conservation during melt production

When melting occurs, some melt may be extracted in order to hold the volume of residual melt below some threshold. We assume that when lattice sites melt, the site volume becomes

melt and expands in proportion to  $V_\rho^{-1}$ . The extracted melt volume is equal to the volume of this expansion, and has the composition of the previously existing melt at each new site. The composition of the new melt site is the same as the site prior to melting, and the composition of all previously existing melt sites is calculated by mixing the fraction of unreplaced mass in the previously existing melt sites with the mass replacing it from the generation of new melt.

Prior to the production of new melt, the volume density of melt, per melt site, is

$$V_\rho^m = \frac{V_{max}^m}{V_{total}^m}, \quad (5.17)$$

where  $V_{max}^m = \phi_r$  is the maximum allowed melt volume and  $V_{total}^m$  is the total melt volume produced.

The volume of new melt is simply

$$V_n^m = N_n^m \frac{N_{total}}{V_{total}}, \quad (5.18)$$

where  $N_n^m = N_1^m - N_0^m$  is the number of new melt sites,  $N_0^m$  is the number of melt sites in the previous timestep,  $N_1^m$  is the new number of melt sites,  $N_{total}$  is the total number of sites, and  $V_{total}$  is the total volume. The volume of new melt mixed into old melt sites is

$$V_d^m = N_n^m (1 - V_{\rho,1}), \quad (5.19)$$

where  $V_{\rho,1}$  is the volume density of melt after melting and extraction. The residual volume of previously existing melt is

$$V_r^m = N_0^m V_{\rho,1}. \quad (5.20)$$

The extracted volume is

$$V_e^m = \sum_{N_0^m} \left[ N_0^m + N_n^m \frac{1 - V_{\rho,1}}{N_0^m} \right]. \quad (5.21)$$

The extracted melt has the composition of previously existing melt. Our equations assume that new melt volume  $V_n^m$  is not greater than maximum residual melt volume  $V_{max}^m$ . Thus, to maintain accuracy, we ensure that the timestep is not too large for a given melting rate and maximum residual melt volume. After extraction, the concentration of the residual melt in each previously existing melt site is

$$C_e^m = C_i^m \left( 1 - \frac{V_d^m}{V_r^m} \right) + \frac{1}{N_n^m} \sum C_n^m \frac{V_d^m}{V_r^m}, \quad (5.22)$$

where  $C_i$  is the initial concentration of previously existing melt sites and  $C_n^m$  is the average concentration of new melt sites.

Note that with the exception of the fictitious variable 'volume density' of melt,  $V_{\rho,1}$ , the above formulation is essentially a volume conservation approach, which becomes mass conservative due to our assumption that solid and liquid phases have equal densities ( $\rho_f = \rho_s$ ).

### 5.7.4 Conservation equations for two-phase compaction

Dynamic evolution depends on the kinematics of melt migration. Modeling batch melting is straightforward. During ascent, no mass is gained or lost from the model domain, ascent velocity of melt and solid are equal, and the compositions of erupted volcanics are assumed to be that predicted for the melt when the mantle parcel ascends to LAB depth. Further interaction with the lithosphere is assumed to be inhibited by low temperature and additional fractionation due to shallow crystallization is assumed to be unimportant.

On the other hand, near-fractional melting assumes that most melt is extracted, and a small volume of remaining melt  $\phi_r$  is left to interact with the solid residue. We assume that residual melt is equal to the total melt produced, up to a maximum, with all additional melt extracted:

$$\phi_r = \min[F, \phi_{r,max}]. \quad (5.23)$$

Since all fluid produced is assumed to participate in migration (i.e., there are no islands of residual fluid stationary with respect to the solid), ascent velocities of solid and melt are modeled using conventional equations. The mass conservation equations used here are (Spiegelman, 1993)

$$\nabla \cdot (\rho_f \phi_r \mathbf{v}_f) = \Gamma \quad (5.24)$$

and

$$\nabla \cdot [\rho_s(1 - \phi_r) \mathbf{v}_s] = -\Gamma, \quad (5.25)$$

where  $\rho_f$  is the density of liquid,  $\rho_s$  is the density of the solid assemblage,  $\phi_r$  is the volume of residual liquid,  $\mathbf{v}_f$  is the velocity of liquid,  $\mathbf{v}_s$  is the velocity of solid, and  $\Gamma$  describes melt production as a function of  $\mathbf{v}_s$  and the extent of melting  $F$  (Appendix 5.A):

$$\Gamma = \mathbf{v}_s \rho_s \frac{\rho_s}{\rho_f} \frac{\partial F}{\partial z}. \quad (5.26)$$

The above equations essentially allow us to calculate the changing velocity of the solid due to compaction from the expulsion of melt. Velocities of fluid  $\mathbf{v}_f$  and solid  $\mathbf{v}_s$  are calculated given that their initial velocities at depth are known.

Also, often additional momentum equations are solved to obtain a more physically constrained view into the motion of the solid and the relative motion of liquid and solid phases, but we forgo this complication since grain-scale microchemical dynamics are the primary interest of the current work. In addition, we solve the above equations with the simplification  $\rho_f = \rho_s$ .

### Erupted Compositions

If the instantaneously extracted melt volume is

$$F_e = \frac{dF}{dz} - \frac{d\phi_r}{dz}, \quad (5.27)$$

erupted compositions are assumed to be an accumulation of the extracted melt:

$$[C_{erupt}]_k = \int_{z_b}^{z_{LAB}} F_e [C_f]_k dz / \int_{z_b}^{z_{LAB}} F_e dz. \quad (5.28)$$

where  $z_b$  is the initial depth at the start of the model,  $z_{LAB}$  is the depth of final extraction (or LAB depth), and  $[C_f]_k$  is the average melt concentration of component  $k$  at the time of extraction.

Note that the above formulation is applicable to upward 1D transport of melt only. It is believed that the production of MORB beneath spreading ridges has a more complicated 2D character, in which melts generated off axis migrate horizontally in the direction of younger lithosphere to produce axial crust (e.g., Canales et al., 2012). Such a melt focusing should enrich the erupted composition with lower-degree melts from off-axis. However, we ignore this effect because it is unlikely to contribute significantly to ratios of incompatible over compatible elements. For example, we saw in Fig. 5.5 that La/Sm and Sm/Yb decreases only slightly after a depth of 25-40 km has been exceeded, and this will not change in the case of disequilibrium melting. The case will be different for the major rock-forming oxides, and perhaps absolute concentrations of incompatible elements, but for incompatible trace element ratios off-axis enrichment should not be important.

## 5.8 Model Summary

Our model is an attempt to simulate microchemical, microstructural, and petrological evolution during decompression melting of a fertile peridotite. This melting source is meant to represent the OIB source as shown in Fig. 5.1. Multi-phase microstructural evolution is modeled using a Potts model, in which a 2D rectangular grid is populated with discrete lattice elements (or sites). Each lattice site has an identifying phase and crystallographic orientation (or spin). Grain boundary migration is simulated by allowing neighboring like-phase sites change their spin to match the neighboring phase, and Ostwald ripening is simulated by randomly diffusing lattice sites around the grid. Both processes are governed by a statistical process favoring changes which minimize interfacial energy. As the microstructure evolves to produce larger grains (i.e., the microstructure coarsens), solid-state transformations and melting occur. These processes are informed by thermodynamic calculations of phase equilibria. The resulting phase abundances, coupled with constraints on which phases may transform into other phases, allows us to crudely, albeit effectively, model both what phases will change in abundance, and where those transformations will occur in the microstructure. On top of this dynamically evolving microstructure, diffusive partitioning of trace elements is simulated. As the partition and diffusion coefficients for different phases are markedly different from one another (see following sections) and the microstructure coarsens over time and responds to the rapid transformation of phases during decompression, a highly complex microchemical structure can arise. During fractional melting, melts are continuously expelled while some melt is left behind to react with the solid residue. Because the kinematics of a compacting medium are beyond the capabilities of our models we perform a simplification in which the melt is not removed from the Potts model, but that each melt site represents a diminishing amount of real volume. Benchmarks of our models are shown in Appendix 5.C.

The resulting model allows us to predict the trace element concentrations in melt produced in an ascending OIB source. Although all models are computed as if there was no overridding lithosphere, eventually the source must intercept the lithosphere. At this point

the source stops releasing melt to the surface. Consequently, the same model may be used to predict the composition of erupted melts for any lithospheric age, as long as the depth to the lithosphere-asthenosphere boundary is known.

## 5.9 Partition Coefficients

We have considered the experimental datasets of Salters et al. (2002) and Adam and Green (2006; 2010). The coefficients are listed in Table 5.1. Salters et al. (2002) reported experimental partitioning data for anhydrous spinel and garnet lherzolites (doped synthetic samples) from 1 to 3.4 GPa and 1350-1660°C. Adam and Green (2006) reported trace element partition coefficients between hydrous (5 – 10 wt% H<sub>2</sub>O) basanite melts and mica- and amphibole-bearing garnet lherzolite (doped natural samples). The experimental conditions are low temperature (1000-1200°C) with high volatile contents (5-10 wt. % H<sub>2</sub>O), for pressures of 1-3.5 GPa. The main differences are thus the volatile contents and melting temperature. In addition, Salters et al. (2002) did not report values for La. In lieu of these values, we estimate them based on regular dependence of partition coefficients on ionic radius and inspection of trends in Adam and Green’s (2006) database. Although these investigators attempted to constrain dependences on pressure, temperature, and composition, we assume constants for simplicity. We have preferred the values of Salters et al. (2002) in our default models due to their higher temperature, less hydrated runs, although basic results of the Adam and Green (2006;2010) database are also investigated.

## 5.10 Diffusion Coefficients

A database of diffusion coefficients for La, Sm, and Yb, has been compiled from the literature. Among the data for each phase, only REE diffusion in cpx is reported to be significantly different for each ion (Van Orman et al., 2001). Coefficients for clinopyroxene are based on diffusion in diopside reported by Van Orman et al. (2001). As these authors do not report an estimate for Sm diffusion in cpx, we estimate  $D_{Sm}^{cpx}$  by a linear interpolation between values for La and Yb using ionic radius. For the other phases, REE diffusion in garnet is based on Van Orman (2002), diffusion in opx is based on Sano et al. (2011), and olivine uses values from Cherniak (2010). We use an activation volume of 10 cm<sup>3</sup> mol<sup>-1</sup> (Van Orman et al., 2001) for all phases except garnet, which Carlson (2012) estimated as closer to 20 cm<sup>3</sup> mol<sup>-1</sup>. Diffusion rates in melt are known to be orders of magnitude faster than in solids (Hofman and Hart, 1978). However, the implementation of high diffusion coefficients can dramatically increase the computational expense of our models. Therefore, we assume that diffusion in melt for all species is 10<sup>2</sup> times faster than the value in olivine. Although this rate of diffusion is not as high as that in melt (Koepeke and Behrens, 2001; Sec. 5.23.4), it is much greater than that in solids.

The Arrhenius dependence of chemical diffusivity on temperature is given by

$$D_k^P = C_k^P \exp \left( -\frac{A_e + A_v p}{RT} \right) \quad (5.29)$$

where  $k$  is the diffusing element,  $P$  is the phase,  $C_k^P$  is a pre-exponential coefficient,  $A_e$  is the activation energy,  $A_v$  is the activation volume,  $p$  is pressure,  $R$  is the gas constant, and  $T$  is temperature. A tabulation of coefficients for each ion and phase is provided in Table 5.2, and Fig. 5.10 illustrates the predictions as a function of temperature.

## RESULTS

### 5.11 Multi-Phase Grain Growth

To test the basic behavior of our Potts model, we show the results of several coarsening experiments in Fig. 5.11. We illustrate rates of grain growth in terms of the usual power-law function in which the grain size  $d$  as a function of time is

$$d \sim t^{1/n}. \quad (5.30)$$

The exponent in the above equation is thought to adopt specific values depending on the mechanisms responsible for coarsening. For example, the value  $n$  for ceramics, pure metals, and alloys is considered to be 2 (Beck et al., 1948; Burke, 1949; Burke and Turnbull, 1952; Anderson et al., 1984; Grest et al., 1988), where the grain boundary velocity is uninhibited by impurities and has a linear proportionality to the inverse grain size. However, experimental values for grain growth exponents is often larger in pure metals and alloys (e.g. Hu and Rath, 1970; Higgins, 1974). In two-phase systems, theories regarding the mechanisms of coarsening and their rates is more complicated, with values of  $n$  around 3-5 (Solomatov et al. 2002), which is consistent with estimates for olivine and orthopyroxene (Skemer and Karato, 2007; Evans et al., 2001), but lower than experiments on a magnesiowüstite and Ca-perovskite polycrystalline assemblage (Yamazaki et al., 1996), where  $n \sim 11$  has been measured.

Fig. 5.11a shows the effect of varying the noise level, or temperature,  $K_T$ , on the coarsening exponent in two solid phase coarsening. These experiments show that higher temperature results in a higher coarsening exponent (low  $n$ ), consistent with observations of aluminum crystals (Hu and Rath, 1970). Moreover, as our default noise coefficient is  $K_T \sim 1$  in all of our other models, our coarsening exponent is  $n \sim 10$ , consistent with Yamazaki et al. (1996). Solomatov et al. (2002) was particularly interested in explaining the low coarsening exponent measured by Yamazaki et al. (1996), performing two-phase Monte-Carlo Potts modeling to show that Ostwald ripening of a two-phase system should proceed with  $n \sim 4$ . Solomatov et al. (2002) then entertained the possibility that Yamazaki's low coarsening exponent may be caused by impurities, diffusion limited Si transport, elastic stress effects, or scaling problems in experiments. However, it seems that the difference may simply be due to the activity or noise in the model, which is related to the effects of temperature and pressure in the mantle assemblage. In fact, consider that the noise coefficient  $K_T$  was set at 0.7 in the models of Solomatov et al. (2002). We use  $K_T \sim 1$ , but our value must be decreased by a factor 8/36 to account for the size of our energy stencil (Sec. 4.1) versus that in Solomatov et al. (2002). Therefore, our results would be consistent with Solomatov if they used  $K_T \sim 0.22$ , or if we had used  $K_T \sim 0.7(36/8) = 3.15$ . Fig. 5.12 shows a

more detailed look at the predictions of our models with  $K_T$  varied between 0.5 and 4.5. Indeed, we predict that the growth exponent  $n$  is about 0.23 with a higher noise coefficient, although our models also show that the exponent increases with time from a lower value. In addition, these results show that the temperature dependence of the coarsening exponent is only apparent for  $K_T < 2.5$ . With this in mind, it should be noted that the coarsening rates in our models are relatively low ( $K_T \sim 1$ ,  $n \sim 10$ ).

Fig. 5.11b illustrates coarsening exponents predicted by our models for 2, 3, and 4 phase systems where all models consist of solid phases (solid lines) or one of these phases is liquid (dashed lines), and each phase is equally abundant. In the case where all phases are solid, increasing the number of phases decreases the coarsening exponent. This likely reflects a Zener pinning effect among an increasing number of interacting phases. However, when one phase is liquid, the behavior is more complicated. The 1:1 solid-liquid experiment shows the lowest coarsening exponent. Adding second and third solid phases in the presence of liquid increases the coarsening exponent to values higher than observed in all pure solid systems.

Fig. 5.11c and 5.11d shows a study of two-phase systems where the modal abundance of the second phase between 10 and 50%. Although there is a clear decrease in coarsening rate with second phase abundance, the effect is only present for early times, consistent with the models of Solomatin et al. (2002). Although it is not shown, as the second-phase abundance decreases to zero the coarsening exponent approaches  $n \sim 2$ , consistent with grain boundary migration theory in pure single phase systems (Anderson et al., 1984).

Fig. 5.11e shows the effect of phase proportion as in Fig. 5.11c-d, except that the second phase is liquid. Unlike the case of solid two-phase systems, the presence of liquid impacts the coarsening exponent significantly. The presence of a large amount of liquid dampens grain growth, while the presence of smaller amounts has a progressively smaller effect. The presence of a 10% solid second phase has only a small effect on the coarsening exponent, while the presence of a 10% liquid second phase predicts that  $n \sim 0.15$ .

## 5.12 Petrology and Microstructural Evolution

Continuous pictures of modal evolution in the equilibrium restite (with up to 1% total wet melting prior to the dry solidus) as a function of melt fraction and depth are shown in Fig. 5.6. Cpx abundance is roughly constant at around 10%, with small fluctuations due to mass exchanges with opx and garnet, until cpx begins to preferentially dissolve into melt. The major solid-state phase transformation is the transformation of garnet into (dominantly) opx. For low- $T_p$  geotherms at thermodynamic equilibrium, the decomposition of garnet during decompression is complete prior to the onset of dry melting. For  $T_p > 1320^\circ\text{C}$ , dry melting occurs in the presence of garnet. However, due to the high melting point of garnet, we assume that melting of garnet is not possible (Eq. 5.10). Instead, garnet undergoes solid-state transformation into opx, which may then melt.

The top row of Fig. 5.13 shows snapshots of microstructural evolution for a mantle potential temperature of  $1300^\circ\text{C}$  and 1% wet melting. Similarly, the top of Fig. 5.14 illustrates microstructural evolution for the case of  $T_p = 1500^\circ\text{C}$ . Because of space limitations we take snapshots which illustrate the state of the system at different stages of melting. Since the evolution is partly driven by changes in modal abundance with decompression, these frames



may be compared to the thermodynamic calculations in Fig. 5.6. Also, for simplicity, and our demonstration later that the OIB source is probably not significantly warmer than ambient mantle (Sec. 5.15.1), we primarily discuss the results of  $T_p = 1300^\circ\text{C}$ .

The first panel (Fig. 5.13, Panel A1) shows the system at 300 km, which is the initial condition of the model. Crystal sizes are roughly proportional to the modes of the phases such that olivine grains (green) are largest, followed by garnet (red), opx (grey), and cpx (blue) with relatively small crystals. The observation that grain edges show no tendency to adopt particular orientations indicates that lattice pinning effects (Janssens et al., 2007) are avoided in our models, and grain boundaries show smooth curvatures toward triple junctions.

The next panel (Fig. 5.13, Panel B1) shows the system after solid-state transformations have produced abundant interstitial crystals aggregating primarily at triple junctions. Although the increasing stability of orthopyroxene energetically favors that previously existing grains grow (versus the formation of new interstitial grains), phase transformation in our models occurs too fast for Ostwald ripening of opx. Thus, many transformations from the decomposition of garnet result in growth of interstitial grains, and the microstructure is in a state of strong disequilibrium. While most interstitial grains of opx occur at triple junctions involving garnet since these are the closest available sites of low energy potential (growth of second phase prefers to aggregate at triple junctions where interfacial energy is high), an exception occurs in the growth of grain Oa in center of Fig. 5.13 (Panel B1), where an opx grows away from a cpx toward the decomposing garnet source. Also, growth of grain Og (Fig. 5.13, Panel B1-C1) doesn't even occur at a triple junction, instead it is set along a olivine-garnet boundary.

Between Fig. 5.13 Panels B1 and C1, the system continues to decompress from 150 km to 75 km, nearing the garnet transition. Garnet is now breaking down rapidly while wet melting occurs. Although the generated melt prefers to gather at solid-phase triple junctions the melt is continually migrating along grain boundaries. Boundary sites of solid phases also migrate continuously along boundaries, but the rate of melt migration is much higher. This transient behavior is not clear in the snapshots, and so we direct the reader to observe the supplementary movies from which these snapshots are taken. Fast migration of melt along boundaries is due to the lower energy of solid-liquid interaction ( $\gamma_{sl} = 1$  vs.  $\gamma_{ss} = 2.5$ ) and the zero energy of liquid-liquid interaction. The lower energy of aggregated liquids causes it to more freely spread out and be squeezed into thin channels by the greater energy of solid-solid interactions. Simultaneously, we can observe the effects of continued decomposition of garnet and growth of orthopyroxene. Because most possible sites of interstitial opx grains are now occupied and decomposition of garnet is accelerating, most grains, large and small, prefer to grow, although some are absorbed by larger orthopyroxenes in close proximity. Some initially small garnets have now disappeared. At this point, and continuing through the decomposition of garnet, there is the development of elongate opx grains. Because the transformation of garnet occurs rapidly, neighboring orthopyroxenes large enough to be pinned by solid-solid interactions at their opposite ends tend to grow in the direction of the vacating garnet. This causes growth in the direction of the garnet as the opx takes over the mass of the garnet. This elongation often results in concave orthopyroxenes which could not otherwise exist during steady state isotropic coarsening (e.g. grain Oe in Panel C1 and grain Ob in Panel D1).

The next panel (Fig. 5.13, Panel D1) shows the system state after the garnet transition and the production of more melt. Although some of this melt has pooled at triple junctions, unlike solid phases much of the melt continues to exist along the edges of two solid phases. All phases which had disequilibrium features (such as concavity) have started to round, although orthopyroxenes remain elongated in the directions of previously existing garnets. It is also interesting to find that some young clinopyroxene grains (e.g. grains Ce, Cf, Ch) have grown at the expense of some large ones (e.g. grains Cb, Cg). This is probably due to a combination of fluctuating cpx stability prior to the dry solidus (Fig. 5.6) and microstructural destabilization of some cpx grains after absorption of garnet by an adjacent opx grain. A strong example of this is grain Cb, which loses significant mass to smaller grains, the production of melt, and cpx→opx transformation. This rapid loss is partly related to the high energy of its tapered configuration (Panel C1), which originated from surface tension with grains Ob and Gc during decomposition of grain Gc.

Also, it may be important to notice that a small garnet crystal still persists at a depth of 50 km even though garnet has not been stable for 10 km of decompression (Fig. 5.6). In fact, while this garnet is gradually dissolved, it still remains even at 25 km (Fig. 5.13, Panel E1). This behavior is due to our formalism for phase transformations (Eq. 5.7). The thermodynamic force governing the rate of (heterogeneous) phase transformation is the interfacial energy, multiplied by the difference of the total phase abundance and the equilibrium phase abundance, per unit volume. Thus as the volume of the phase decreases, the total volume of garnet that can breakdown decreases. Also, more importantly, when the equilibrium abundance approaches zero, the thermodynamic force decreases asymptotically, becoming very small as the modeled abundance goes toward zero. This latter part, the thermodynamic force  $\Delta\psi_k$ , is undoubtedly the unrealistic function in our equations. This is because destabilization of a phase is actually governed (in part) by the energy minimized by a phase change, which will continue to increase outside of the environment where garnet is stable. Nevertheless, in this work we do not improve our analysis with a more consistent thermodynamic treatment because we expect that it will not significantly impact the behavior of trace element partitioning. On the other hand, a thermodynamically consistent formalism will be necessary to properly model the behavior of major elements and additional details of microstructural behavior. This research direction will be pursued in the future.

In the final snapshot (Fig. 5.13, Panel E1), the system has decompressed to 25 km. Nearly half of the cpx and some opx has dissolved into melt, decreasing their grain sizes. Some opx has been incorporated into olivine, resulting in larger grains. Total melt fraction has increased significantly, and melt has formed a thick film on the edges of all grains. The pooling of melt around grains and at triple junctions has resulted in rounding to all grains. It is important to note, however, that our models of microstructural evolution are most appropriate for the case of batch melting. In a more realistic case of near-fractional melting, melt is extracted and the solid compacts (McKenzie, 1984). Compaction will result in significantly more solid-solid interaction. These interactions will decrease the rounding effect observed in Fig. 5.13 (Panel E) and could result in the promotion of grain boundary migration among residual olivine and orthopyroxene grains. Such behavior may have implications for slowly diffusing ions such as Yb.

### 5.12.1 Exsolution Lamellae

In our models, all phase transformations occur through heterogeneous nucleation. That is, phase transformations occur at the edges of grains consistent with precipitation-dissolution reactions. Although heterogeneous nucleation tends to be thermodynamically favorable due to the larger interfacial energy production of homogeneous nucleations, some polymorphic phase transformations in the olivine subsystem (Solomатов and Reese, 2008) and the production of exsolution lamellae in the pyroxene subsystem demonstrate that homogeneous nucleation may be widespread in decompressing mantle. Such behaviors are not easily treated in our model framework. Although we can allow nucleation to occur homogeneously by removing the boundary energy term from the transformation equation (Eq. 5.7), transformed sites will quickly migrate away and aggregate at interfaces. Occasionally, during rapid homogeneous transformations, exsolved sites will aggregate inside the host crystal away from boundaries, but this cannot occur frequently in space. The reason for this is a problem of scaling. We are modeling a process which actually occurs in small groups of atoms on the scale of the unit cell. Our model behavior reasonably represents coarsening behavior at large scales because of the self-similarity of boundary migration and Ostwald ripening processes on small and large scales. However, the lamellae microstructure has dimensional characteristics which are uniquely microscopic (e.g. Spengler et al., 2013). We might expect such features to be accessible to our models if our spatial discretization was many orders of magnitude larger, however this would make simulation unfeasible. There are probably many solutions to this problem of varying complexity and computational efficacy, but we do not attempt to solve them here.

## 5.13 Model Grain Size Distributions

Above, we discussed the microstructural state of the system in our simulations, with results of an example model shown in Fig. 5.13a-e. These Potts model results, however, are strictly non-dimensional. The ability to impose a given scale of length and time takes advantage of the fact that coarsening behavior tends to be self-similar from scales of nanometers to meters. A dimensionalized microstructure is necessary for coupling with diffusive partitioning, but such dimensional attributes may be defined arbitrarily for the purpose of testing the effects of variable grain sizes or the rate of coarsening. In other words, if the length scale of the model domain is defined to be large, the physical size of grains will be modeled as large, resulting in slow diffusion, for example. In our default model configuration, we have assumed that the model area is  $1 \text{ cm}^2$ . Because the grain size imparts a major control on the disequilibrium state of the system (see next section), we have characterized predictions of grain radius in our microstructural simulations of the ascending OIB source in Fig. 5.15. Since only a few dozen grains of each solid phase are present in a given simulation, we have accumulated the results of 100 different models in order to characterize the grain size distributions, for each phase, with relatively smooth density functions.

The area (as our simulations are 2D only) distributed in grains having a radius less than

$R$  is given by the cumulative distribution function (CDF)

$$f_q^{CDF}(R) = \frac{1}{A_d} \int_0^R A_q(r \leq R) dR, \quad (5.31)$$

where  $A_q(r \leq R)$  is a unit area belonging to a grain of phase  $q$  and radius  $r \leq R$ , and  $A_d$  is the total model area. The corresponding probability density function (PDF) is

$$f_q^{PDF}(R) = \frac{\partial f_q^{CDF}}{\partial R}. \quad (5.32)$$

Density functions for microstructures predicted by our models are shown at depths between 10 and 300 km at 5 km intervals in Fig. 5.15. The red curves are the deepest, with the 300 km curve corresponding to the initial condition. The roughness of the density function increases with the abundance of the phase because the total number of grains decreases with their size. Thus, olivine has the roughest PDF and the PDF for cpx is comparatively smooth. The integral of each PDF gives the area of the phase, so the olivine curve is much larger than the cpx distribution and the grain size is a function of the phase abundance.

At the initial condition (300 km), grain sizes are characterized by a bimodal distribution, where the primary mode represents the population of large grains with low probability samples skewed to small radii, and the secondary mode peaking over small radii represents a population of small interstitial grains. As phase transformations change phase abundances, the grain size distribution responds in a manner that reflects coarsening behavior. The distribution of olivine grains is virtually unchanged with ascent until the dry solidus ( $\sim 55$  km), excepting an elevation in the area of small interstitial grains. After the dry solidus, the primary olivine peak shifts to larger radii while the secondary peak (interstitial grains) diminishes and broadens. This reflects the monotonous growth of large olivine grains with olivine precipitation during dry melting and the eventual absorption of most interstitial grains as the removal of other phases increases contact among residual olivines.

As garnet decomposes to opx both populations of primary and interstitial opx crystals independently grow until garnet is exhausted around 60 km depth. Although both populations then begin to lose area to the production of melt, it is interesting that the bimodal distribution blends together until the distribution is mostly flat at 10 km depth.

The initial size distribution of clinopyroxenes consist of almost no population of interstitial grains. However, during solid-state transformations a population of interstitial grains appears and grows at the expense of large grains. This process continues gradually for decompression from 300 to 100 km, thereafter accelerating. The population of interstitial grains continues to grow at the expense of large grains until the populations blend to form a unimodal distribution skewed to a medium radii ( $\sim 40$  km) that gradually diminishes and shifts to smaller radii. The growth of interstitial grains at the expense of large cpx grains is probably driven by fluctuations in cpx equilibrium abundance with decompression, resulting in cpx $\rightarrow$ opx and grt $\rightarrow$ cpx transformations. The precipitation of cpx from garnet tends to aggregate at interstitial sites due to a high ratio of cpx-absent triple junctions versus the number of cpx grains in the system. This combined with the low area of cpx grains results in large distances in between same phase grains. Consequently, it is energetically favorable

to form a more homogeneous distribution of small grains from the decomposition of garnet. Over time, Ostwald ripening would favor the growth of larger grains, returning the size distribution to higher radii (as seen for the initial condition).

In the case of garnet, an initially small population of interstitial grains increases slightly in area until about 150 km, after which it disappears. The primary population of garnet crystals gradually diminishes and the peak shifts to lower radii. This behavior is a straightforward consequence of the gradual loss of total garnet area and the absence of significant garnet precipitation from other phases.

We note again that these density functions are those predicted for the given dimensions of our microstructural model. As such, the relative values of these distributions are more important than their absolute values. For example, we will later see that the results of our chemical disequilibrium models suggest that an optimal model can be found with a grain size about 3-5 times greater than our default model dimensions. Thus, while the present model dimensions are consistent with the radius of garnet grains being about 1 mm (Fig. 5.15d), the optimal model would be consistent with a garnet grain size distribution having a modal radius of 3-5 mm.

## 5.14 Microchemical Disequilibria

Snapshots of trace element disequilibria for La, Sm, Yb, La/Sm, and Sm/Yb are illustrated in Fig. 5.13. The microchemical results corresponding to the microstructure in the first row of panels as discussed previously (Sec. 5.12). The illustrated results are for  $T_p = 1300^\circ\text{C}$ , default partition and diffusion coefficients, fractional melting with a 0.5% melt residue, a  $1\text{ m yr}^{-1}$  ascent rate, and the 2D model domain represents an area of  $1\text{ cm}^2$ . The microchemical structures arising in the solids are considerably complicated due to the stages encountered in the evolution of the assemblage and the extreme state of disequilibrium. Nevertheless, we summarize some of the more apparent microchemical features which characterize our model predictions of diffusive partitioning in a decompressing volume of fertile mantle.

At the start of the simulation (300 km), we assume that trace elements are distributed at equilibrium according to their partition coefficients. Concentrations are given relative to the initial bulk composition (e.g.  $[\text{La}/\text{Sm}]/[\text{La}/\text{Sm}]_{bsrc}$  and  $[\text{La}/\text{La}]_{bsrc}$ , where the subscript *bsrc* denotes bulk source composition). Thus, if the bulk source composition is 1 ppm, then results are in units of ppm and no scaling is required. With the assumption of chemical equilibrium, each phase has a single concentration everywhere. Subsequently, solid-state phase transformations take place, which dominantly consists of the transformation of garnet into orthopyroxene. When a solid-state phase transformation occurs, the new phase inherits the trace element composition of the old phase. Since the partition coefficient of the daughter phase is different from the parent phase, the site will no longer be in equilibrium, and a flux of mass will occur throughout the whole system until a new equilibrium distribution is achieved. However, because the chemical diffusivities are low, mass transport is limited by time and the system state is far from equilibrium.

Most additional disequilibrium features that arise in the model can be linked to the inheritance of chemical signatures, diffusive interaction with a gradually increasing volume of melt, interaction with neighboring grains in states of disequilibrium, rates of diffusion

varying among phases and with pressure, dilution of the solid residue by melt extraction, and complex convolutions of these effects over time. In the following three sections we discuss some of these behaviors for each ion.

### 5.14.1 Lanthanum

Clinopyroxene is the dominant solid reservoir of La. Initially, since  $K_{grt/opx}^{La} > 1$ , opx inherits a rim of high-La overgrowth from the decomposition of garnet (e.g. Fig. 5.13, Panel B2, Grain Od). However, upon the production of melt, La strongly partitions out of all solid phases, causing the rims of all crystals to lose La by diffusive exchange with melt at grain boundaries. Consequently, additional opx growth from the transformation of garnet results in the inheritance of the low-La signature. Because REE diffusion is slow in opx, this can result in a core of medium La concentration surrounded by a ring of elevated La in the shape of the original crystal, and an outer zone of low La (Fig. 5.13, Panel C2, Grains Oc and Oe). Or, if opx growth occurs in the direction of decomposing garnet, producing elongate crystals, the outer low-La zone will only occur in the new extended portion (Fig. 5.13, Panel D2, Grain Od). Similarly, a combination of grt→cpx transformation and boundary migration in the direction of the decomposing garnet has resulted in one cpx grain (Grain Ca) acquiring a limb with low-La. Interstitial cpx grains formed in the course of the simulation always have lower La than original grains due to the low concentrations in their parent phases and the absorption of La in melt. This, together with the low diffusivity of La in cpx, means that old cpx grains tend to carry elevated La until they fully dissolve. For example, Grain Cc (Fig. 5.13, Panel E2) contains a core which has remained largely unaffected by diffusion over 275 km of ascent.

### 5.14.2 Samarium

Garnet, followed by cpx, are the primary hosts of Sm. As in the case of Lanthanum, the growth of opx at the expense of garnet results in the rims of opx taking on elevated Sm followed by additional rims depleted in Sm due to Sm absorption by melt. It is interesting to observe the absorption of Sm in cpx by diffusive re-equilibration with newly exsolved high-Sm opx. Prior to dry melting, cpx in the vicinity of decomposing garnet acquires rims of elevated Sm which gradually diffuses through the whole grain due to the moderately high diffusivity of Sm in cpx. For example, the cpx grain Cc (Fig. 5.13, Panels B3-B4) has acquired high-Sm at all of its boundaries except at the lower left contact with a portion of the opx grain which is far from a neighboring garnet grain. As seen in Panel C3 (Fig. 5.13), garnet acquires a thin rim of elevated concentration in response to elevated Sm in neighboring pyroxenes (induced by its own decomposition). After the onset of dry melting, the concentration in melt begins to be strongly diluted. This results in all phases, most notably cpx and garnet, acquiring low-Sm rims. The moderate diffusivity of Sm in cpx allows some diffusive re-equilibration during cpx dissolution, although significant disequilibrium remains (e.g. see grains Ca and Cc in Fig. 5.13, Panels C3-E3). The low diffusivity in opx results in persistent disequilibrium features throughout the simulation, such as the high-Sm sub-grain regions inherited from garnet (Fig. 5.13, Panels D3-E3, grains Of, Oc, and Ob).

### 5.14.3 Ytterbium

By far the dominant reservoir of Yb is garnet. The next abundant host of Yb is clinopyroxene with equilibrium distributions about an order of magnitude lower than garnet (Table 5.1). The dynamics of Yb disequilibria are arguably the most interesting. Opx inherits elevated Yb from the decomposition of garnet and maintains this disequilibrium structure due to low diffusivity in opx. Simultaneously, due to higher diffusivity in cpx, the cpx phase is sensitive to contact with elevated Yb in neighboring garnet and opx and transmits such mass changes relatively rapidly through the crystal. With decomposition, garnet acquires high-Yb rims which equilibrate rapidly with neighboring cpx and slowly with neighboring opx. Meanwhile, opx continues to inherit the composition of garnet, which gradually becomes more enriched in Yb. This interaction between cpx and opx/grt during phase change is well illustrated in Fig. 5.13 (Panels B4-D4) for the group of local grains Od, Of, Ga, and Ca, as well as the group Oc, Cc, and Gc. The clinopyroxene crystals in these groups acquire high Yb. Other more distant cpx grains also become enriched in the Yb released by garnet, but the elevation is more slight. Because of the high diffusivity of Yb in cpx (further increased with decreasing pressure), cpx is somewhat close to equilibrium at 25 km depth and no longer exhibits high Yb.

It is also interesting to note that olivine also takes on large positive disequilibrium anomalies. The decomposition of the garnet grain 'Gb' results in a locus of elevated Yb inherited by surrounding cpx. Although these concentrations are not directly inherited by olivine since our model assumes that cpx→ol transformations do not occur, the elevated concentrations increase the concentration of opx, which are then inherited by opx→ol transformations. In fact, careful inspection shows that this olivine inheritance is also present for La and Sm (Fig. 5.13, Panels D2-D3).

## 5.15 Melt Concentrations of Default Model

Fig. 5.16 shows results for our default model runs. Illustrated are predicted erupted compositions of La/Sm and Sm/Yb as a function of final melting depth for models with  $T_p = 1400 \pm 100^\circ\text{C}$ ,  $\phi_r = 0.05\%$ , and  $v_z = 1.0\text{myr}^{-1}$ . All compositions are normalized to the bulk source composition such that if the bulk source composition is 1 ppm, then results are in units of ppm and no scaling is required. Fig. 5.16c-d show the same models with source compositions adjusted until the curve fits the data (assuming  $T_{LAB} = 1300^\circ\text{C}$ ). Also, the colored circles and squares show the onset of dry melting and garnet transition, respectively. Because a small fraction of garnet remains in the residue long after the equilibrium value approaches zero (compare Fig. 5.7 and Fig. 5.6), the 'garnet transition' is here designated as the point where garnet fraction decreases below 1%.

Overall, the predictions of our default models (at least for  $T_p = 1300^\circ\text{C}$ ) fit the basic structure of the observed chemical systematics (Fig. 5.4). La/Sm and Sm/Yb are initially high when only small amounts of melt are accumulated from the deep upper mantle. In Fig. 5.5 we found that the predictions of equilibrium melting also fit this basic structure, but that La/Sm and Sm/Yb of deep low-degree melts were far higher than that observed for OIB erupted on old seafloor. Here (Fig. 5.16) we see that this problem is mitigated by

source disequilibrium. Consistent with this, it can be seen that because REE diffusion rates increase with temperature, old seafloor OIB values increase with  $T_p$  for both La/Sm and Sm/Yb. Differences in phase equilibria with  $T_p$  negligibly contribute to this observation. As the source continues to ascend, the mantle eventually passes the dry solidus (colored circles), after which melt productivity is dramatically increased. With this elevated rate of melt production, both La/Sm and Sm/Yb rapidly decrease until they plateau at a minimum. A remarkable feature of both the data and our models is the excellent agreement on where it occurs. The predicted depth of this step depends on the model of melt productivity, and the seafloor age at which it occurs additionally depends on the thermal structure of oceanic lithosphere. Consequently, we will later see that this feature provides a constraint on LAB temperature.

Because olivine and opx hold very little REE mass, REE ratios of the erupted products are about equal to that in the source by the time that cpx is completely dissolved. On the other hand, as shown in Fig. 5.17, elemental concentrations in erupted melts are always higher than in the source. Since olivine and opx remain in the residue and hold comparatively little REE mass, the absolute concentrations of OIB  $C_{k,morib}$ , when erupting on a ridge axis (Mid-Ocean Ridge Island Basalt, or 'MORIB' value), are approximately related to the bulk concentration of the source  $C_{k,bsrc}$  by

$$\left[ \frac{C_{k,morib}}{C_{k,bsrc}} \right]_{z=0} \approx \left[ \frac{1}{F_{grt} + F_{cpx}} \right]_{bsrc}$$

where  $F_{grt}$  and  $F_{cpx}$  are the mass fractions of garnet and cpx in the source, and  $C_{k,bsrc}$  is the bulk composition of the source. As  $(F_{grt} + F_{cpx})_{bsrc}^{-1} \sim 3$ , lavas erupted on ridge axes have concentrations approximately 3 times that in the source.

In addition to a control from the extent of melting via the change in melt productivity with depth, in the case of Sm/Yb there is a minor control from the decreasing abundance and eventual disappearance of garnet with decompression. Consistent with basic interpretations of REE behavior during melting (e.g. Salters and Hart, 1989; Niu et al., 1999; Humphreys and Niu, 2009; Niu et al., 2011), both La/Sm and Sm/Yb show a relatively simple gradual dilution with total melt fraction (Fig. 5.19c-d). This is related to the bulk incompatibility of La compared to Sm and Sm compared to Yb. However, due to the compatibility of Sm and Yb in garnet, the rate of Sm/Yb dilution with melt fraction is slower than for La/Sm. This behavior is related to the familiar concept of a 'garnet signature'. The garnet signature is usually described as a chemical indication that garnet is a residual phase during melting, and that this signature can be diluted by melting in the spinel field or higher pressure of melting (Salters and Hart, 1989; Hirschmann and Stolper, 1996; Putirka, 1999; Niu et al., 1999). In the case of Sm/Yb, an erupted value  $> 1$  is considered such a signature (Salters and Hart, 1989; Humphreys and Niu, 2009). As melting always starts in the garnet field in our models, initial concentrations in melt are always characterized by Sm/Yb  $> 1$ . A test of the importance of melting in the garnet field is shown in Fig. 5.20. These figures illustrate the effect of changing the amount and depth of melt generated below the dry solidus due to the presence of volatiles. When no melt is generated below the dry solidus for  $T_p = 1300^\circ\text{C}$ , no melting occurs in the garnet field and both La/Sm and Sm/Yb are always  $\sim 1$  in melt. This shows that high values of both La/Sm and Sm/Yb are signatures of



melting in the garnet field, although Sm/Yb imparts a stronger signal on the melt. As high Sm/Yb originates in the high value of  $K_{grt/melt}^{Yb}/K_{grt/melt}^{Sm}$ , high La/Sm originates in the high value of  $K_{grt/melt}^{Sm}/K_{grt/melt}^{La}$ . Also, while it is usually thought that dilution requires melting outside of the garnet field, our models show that melting in the garnet field significantly dilutes Sm/Yb. In addition, the rate of Sm/Yb dilution in the garnet field depends on the depth of melting. This is probably associated with the volume of residual garnet (Fig. 5.19b) which, for a given extent of melting, increases with  $T_p$ .

### 5.15.1 OIB source temperature is not high

Among the most straightforward and noteworthy observations in our results is that chemical predictions for high ( $T_p > 1350^\circ\text{C}$ ) OIB source temperature cannot fit the data (Fig. 5.16c-d). This occurs because the dry solidus and the garnet transition occur deeper in the mantle with higher  $T_p$ , thus shifting the step feature to greater depth (and older seafloor). Fig. 5.21 shows the conversion of seafloor ages in the data into final depths of melting using LAB isotherms between 1000 and 1300°C, as pictured in Fig. 5.1. Fitting data to predictions where OIB source temperature is high requires that the step feature occurs at older age (thicker lithosphere), but a lower LAB temperature shifts the step to younger age (thinner lithosphere). At least two reasons for this misfit may be suggested: 1) OIB sources are approximately ambient temperature or 2) the model of melt productivity or thermal structure of oceanic lithosphere is in error. We consider the former to be most probable. This is in part due to the impressiveness of the fit at lower  $T_p$ , and partly due to geophysical inconsistencies implied by the second option. We consider the plate model presented in Chapter 3 (with ambient mantle  $T_p = 1300^\circ\text{C}$ ) to be an optimal model. Although we also presented satisfactory models with higher ambient mantle  $T_p$ , this would only increase the LAB temperature, not the thickness of the lithosphere. Because large changes to the thermal structure of oceanic upper mantle are not consistent with geophysical observations, our results indicate that OIB sources are approximately ambient. However, later (Sec. 5.22) we will discuss interpretations which allow a hot OIB source. In particular, we show that it is likely that while most OIBs originate from ambient-temperature sources, some OIB volcanism may still be associated with thermal plumes.

### 5.15.2 Default models fail to fit Sm/Yb

It is notable that while predicted La/Sm appears to fit the data reasonably well for OIB  $T_p \sim 1300^\circ\text{C}$  (Fig. 5.16c), the fit for Sm/Yb is not as good. This is particularly concerning because the Sm/Yb data appears less scattered than La/Sm (fig. 5.16c). This good behavior should be treated as a delicate constraint on models. Specifically, our melting models predict that erupted Sm/Yb is 2-3 times higher than that observed in OIB erupted on old seafloor (Fig. 5.16d), even for  $T_p \sim 1300^\circ\text{C}$ . Clearly, while the models produce the basic structure of the data, they fail to produce some basic quantitative details. The explanation of such details is important. In addition to the location of the chemical step in the data, the relative values of OIB chemistry on young and old seafloor are the principal quantities to which models will be fit. Moreover, since only the second of these items is influenced by the details

of our disequilibrium melting model, chemical disequilibria can only be constrained by fitting both quantities.

In our assessment, the failure of our default models to fit the data can be most likely attributed to one of two sources. Either the extent of disequilibrium in the melting system has been underestimated, or the effective partition coefficient constants employed in our models are inappropriate.

In Fig. 5.17 we showed the evolution of cumulative La, Sm, and Yb concentration in erupted lavas. These predictions are compared to OIB concentrations from Sun and McDonough (1989) and our estimates of thick-plate OIB. Our estimates are an average of island-group-average compositions from 11615 samples in the GEOROC database (discounting select island groups on young seafloor: Amsterdam-St. Paul, Ascension, Azores, Easter and Salas Y Gomez Ridge, Galapagos, and Iceland). The highlighted regions assume that the range of uncertainty for Yb is  $\sim 2.5 \pm 0.5$  ppm. Since average La/Sm and Sm/Yb of thick-plate OIB is  $\sim 4.6$  and  $\sim 3.9$ , respectively, we estimate that  $\text{Sm} \sim 10 \pm 2$  ppm, which is also consistent with Sun and McDonough (1989), our estimate of mean thick-plate OIB composition, and the data from Niu (2011) discussed later (Sec. 5.20). We can see that elemental values for La and Yb at depth are similar to that in thick-plate OIB lavas (for  $T_p = 1300^\circ\text{C}$ ), but Sm values are significantly higher. To improve the fit, we should desire that the concentration of Sm in melt prior to the dry solidus is significantly lower, while the concentration at shallower depth is unchanged. Alternatively, Sm must be higher in melt at shallow depth, while values prior to the dry solidus remain unchanged. The most straightforward way of changing these values is to modify the experimental partition coefficients, particularly those in cpx and garnet. However, we will find that disequilibrium effects alone can easily improve the fit of predicted chemistry.

### 5.15.3 A minor observation

Although a minor anomaly, it is curious that REE concentrations and ratios begin to drop (or elevate, in the case of Yb) several kilometers below the depth of dry melting. The likely reason for this is shown in Fig. 5.18. The non-equilibrium (modeled) total melt fraction closely follows the 'equilibrium' value, except for significant deviations prior to the depth of dry melting. In the case of  $T_p = 1300^\circ\text{C}$ , melt production completely stops for about 10 km around a depth of 60 km. This behavior is probably due to our numerical method reacting to the decomposition of garnet. In our numerics, the term  $\mathbf{A}(P_{i,j}, q)E_{ij}\psi_q$  (Eq. 5.7) produces  $Q=\max(q)$  matrices of size  $N \times M$  consisting of probabilities that any lattice site transforms into each phase  $q$ . However, the order in which phase transformations are checked ascends with  $q$ , such that if a site  $ij$  attempts to transform into phase  $q_1$ , it will only succeed if the site does not also attempt to transform into phases  $q_2, q_3, \dots, q_Q$ . As the equilibrium abundance of garnet goes to zero and the existing abundance in the model remains high, the probability that an opx  $\rightarrow$  garnet transformation occurs begins to overwhelm the probability of opx  $\rightarrow$  melt transformations. When the rate of garnet decomposition diminishes, melt production quickly catches up to the equilibrium value. Since this higher rate of productivity begins before the onset of dry melting, significant chemical changes occur before this point. Although this is likely an unphysical behavior, it only produces minor anomalies of the kind just discussed.

## 5.16 Analysis of Some Model Sensitivities

### 5.16.1 Choice of partition coefficient database

The modeling results previously discussed used the partition coefficients of Salters et al. (2002). In addition, we have noted that these authors did not report values for Lanthanum, and so we have estimated them based on patterns in the dependence on ionic radius as well as inspection of the coefficient database of Adam and Green (2006). Fig. 5.22 shows a comparison of predictions using Salters et al. (2002) database (with our estimate of La consistent with their values) and the coefficients of Adam and Green (2006). These results suggest that the choice of another database does not substantially affect the results. Moreover, predicted Sm and Yb are nearly the same. Predicted La, and therefore La/Sm, differs but it is not clear if this is a meaningful difference since, again, we have estimated an appropriate value of La for the Salters et al. (2002) database.

### 5.16.2 Residual melt fraction

Fig. 5.23 shows predicted cumulative melt concentrations of La, Sm, and Yb as a function of final melting depth for near-fractional melting with residual melt fractions between 0.05 and 1.0%. Clearly, while melt fraction affects our results, there are no substantial changes to partitioning behavior. Moreover, Fig. 5.24 shows the fit of such models for  $T_p \sim 1400 \pm 100^\circ\text{C}$ , showing that residual melt fraction does not significantly impact our predictions.

### 5.16.3 Extent of hydrous melting

Fig. 5.20 shows results for tests of the impact of kinematic changes to the extent of hydrous melting on La/Sm and Sm/Yb in cumulative fractional melts ( $\phi_r=0.5\%$ ). In these models two parameters are adjusted: the total additional melt produced due to the presence of volatiles,  $F_{w,max}$ , and the distance between the dry and wet solidus,  $z_{dw}$  (Appendix 5.A). The 5 case models show predictions for  $F_{w,max}$  between 0 and 2%, and  $z_{dw}$  between 0 and 100 km. Our default models assume that  $F_{w,max}=1\%$  and  $z_{dw}=100$  km.

As discussed previously (Sec. 5.15), the most important observation in these models is that for anhydrous melting La/Sm and Sm/Yb are both always  $\sim 1$ . In addition, it can also be seen that a shorter hydrous tail ( $z_{dw} < 100$  km) leads to lower La/Sm and Sm/Yb at depth. Also, a greater extent of hydrous melting ( $F_{w,max} > 1\%$ ) further decreases La/Sm and Sm/Yb. Thus, in general, higher extents of melting and faster melting rates at shallower depth result in lower REE ratios.

### 5.16.4 Disequilibrium kinematics

We have seen from studying Figures 5.13 and 5.14, that the microchemical state of the system exists far from equilibrium at all stages of melting. Microchemical heterogeneities at the sub-grain scale persist due to low diffusivity compared to the size of grains and the ascent rate. The microchemical structure previously discussed is that predicted for a  $1 \text{ m yr}^{-1}$  ascent rate, experimental diffusion coefficients, and a  $1 \text{ cm}^2$  model area. In the following

sections, by varying these properties we show that the state of disequilibrium is a critical factor in the prediction of REE signatures in melts.

### Chemical diffusivity

The consequences of varying the chemical diffusion coefficients in our models are illustrated in Fig. 5.25. We vary the diffusion coefficients of all ions in all phases between 2% and 1000% of the experimental value. This adjustment is referred to as a diffusivity factor in Fig. 5.25. The top figures show the predicted ratios and elemental concentrations as a function of final melting depth, and the bottom figures show the same predictions for given depths as a function of the diffusivity factor. Note the colored bars in each figure denote the depths and diffusivity factors for comparison between these different visualizations of the same data. The thick black lines show the predictions of our default model.

The basic consequences of higher or lower diffusivity on La/Sm and Sm/Yb are clear from Fig. 5.25f-g. Higher diffusivity (diffusivity factor  $> 1$ ) yields higher La/Sm and Sm/Yb values below the dry solidus. Above the dry solidus all ratios and elemental concentrations approach the same values primarily due to the strong control of cpx and garnet abundance on melt concentration. Lower diffusivity results in low Sm/Yb below the dry solidus, but interestingly La/Sm stays about the same, or increases slightly.

We noted earlier (Sec. 13.2) that the fit to Sm/Yb in our default models is poor, with values below the dry solidus predicted to be too high. As seen in Fig. 5.25b (black line), the default model predicts that values prior to the dry solidus are about 6.5. The desirable value for good fit, however, is about 2.5-4. From Fig. 5.25g we see that if diffusion rates are less than 10% (diffusivity factor  $< 0.1$ ) of the default experimental values, Sm/Yb will approach an excellent agreement with the data. Simultaneously, low diffusivity does not substantially affect predicted La/Sm, although deep melts develop an anomalously high La/Sm signature. This is a remarkable coincidence supporting the possibility of fitting the data simply by increasing the extent of disequilibrium in the source.

Despite this excellent recovery of good fit to the geochemical patterns in OIB, a systematic error of an order of magnitude in measurements of REE diffusivity is difficult to believe. However, in the following we will find that the kinematic properties of grain size and ascent velocity can also accomplish the same task. Such properties are clearly more amenable sources of uncertainty, since their true values in the mantle, and the OIB source in particular, are poorly understood.

### Grain size

The effect of grain size on chemical disequilibria is strongly analogous to the effect of varying diffusivity coefficients (Sec. 15.3.1). We tested grain size factors,  $G_r$ , between 0.1 and 5, meaning that the size of the model area is between  $0.1^2$  and  $5^2$  cm<sup>2</sup>. Larger grain sizes cause greater disequilibrium, analogous to the effect of lower diffusivity. Therefore, large grains predict that melts in the wet solidus have low Sm/Yb and slightly higher La/Sm, and small grain sizes bring the system closer to equilibrium with higher Sm/Yb as well as La/Sm (Fig. 5.26a-b and Fig. 5.26f-g). Also, as in the case of low diffusivity (Fig. 5.25a), La/Sm shows a more exaggerated tail toward high values of La/Sm when the grain size is

large. However, since the depth to the LAB is less than about 100 km, these high values do not affect our fits to the data. On the other hand, if such a variation with depth is real, it may partly explain the scatter in the La/Sm data. The volatile composition of the mantle is likely not homogeneous, resulting in slightly different extents of wet melting. Sm/Yb may not be sensitive to this since predicted values in the wet melting field do not vary much, but La/Sm would be.

As the total relief (difference of the old seafloor and young seafloor OIB ratios) of Sm/Yb in the data is 2.5-4, Sm/Yb will fit the data if the grain size is more than three times greater than in our default models. An estimate for the grain size distribution in the OIB source may thus be inferred by taking the results of our grain size analyses in Fig. 5.15, and multiplying the grain radii by the factor 3. From this we can see that olivine, opx, cpx, and garnet are expected to have modal radii of at least 5, 2.4, 2.2, and 3 mm, respectively.

### Ascent rate

The results of testing the effect of the ascent rate of OIB source mantle are shown in Fig. 5.27. The ascent rate essentially controls the time available to achieve equilibrium for a given volume of extracted melt. Thus, as the ascent rate decreases, the system is closer to equilibrium and behaves similar to that predicted by a higher diffusivity (Fig. 5.25) or smaller grain size (Fig. 5.26).

We have chosen to illustrate model results for the range 0.025-1.0 m yr<sup>-1</sup>, where the high end is our default model value of 1 m yr<sup>-1</sup>. This default model value reflects our assumption that the OIB source ascends actively. In contrast, the ascent of MORB source mantle is thought to be a passive response to the divergence of oceanic plates, in which case the appropriate ascent rate would be on the order of 0.05 m yr<sup>-1</sup>. Consequently, these results can also be considered to illustrate our predictions of the differences between MORB and OIB melts in the course of their ascent and eruption (assuming that the properties of their sources are chemically and microstructurally similar). Melt concentrations in the MORB source, compared to OIB, are heavily enriched in La, slightly enriched in Sm, and depleted in Yb at depths below the pressure of dry melting. It is notable that decreasing the ascent rate increases La/Sm and Sm/Yb at depth, which will worsen the fit to both La/Sm and Sm/Yb OIB data. Therefore, the ascent rate would need to be *increased* by several factors in order to fit the data. Due to the absence of evidence for such ascent rates (e.g. Bourdon et al., 2006) we find it more likely that grain size is the primary control on the extent of disequilibria.

It is also notable that although we had investigated a large variation in the diffusivity coefficient (Fig. 5.25), lower ascent rates are associated with much more extreme near-equilibrium values than that predicted from high diffusivity. Specifically, a 10x increase in diffusivity is correlated with about a 65% decrease in ascent rate. This indicates that the behavior of the microstructural model imparts a control on the extent of disequilibrium. Probably what occurs is an increase in grain boundary diffusion, which is modeled in the microstructural Potts model by having migrating lattice sites transport their trace element concentrations (Sec. 4.2). If this is the case, this behavior will have to be investigated in more detail in the future since such transport has not been constrained by thermodynamic arguments.

Lastly, we have so-far seen that La/Sm and Sm/Yb are high at depth and then converge on a value of about 1 when the final depth of melting goes toward zero. However, for low ascent rates, La/Sm becomes noticeably elevated for shallow final melting depths. Although such a pursuit is beyond the scope of the current work, we suspect that this may be related to the explanation of features in MORB data. For example, the distribution functions for La in MORB samples are highly skewed to elevated La (Fig. 5.28). Although this may not be directly related to ascent rates, it may be related to variable extents of disequilibria. In other words, there may be a mixing between a highly equilibrated source and a source far from equilibrium.

### Grain size vs. ascent rate

We showed that predicted La/Sm values in erupted melts for our default model are in good agreement with the data, while predicted Sm/Yb values are too high at depth (Sec. 5.15.2). Later (Sec. 5.16.4), we found that increasing the extent of disequilibrium by increasing the grain size by about a factor of  $> 3$  can bring predicted Sm/Yb into good agreement with the data, apparently without significantly damaging the fit to La/Sm. Furthermore, we found in Sec. 5.16.4 that a lower ascent rate worsens the fit to the data, and that the ascent rate would have to be  $\gg 1 \text{ m yr}^{-1}$  to fit.

So-far, our studies of 'fitness' have only consisted of informal comparisons of models and the data. We will now formalize the analysis of fitness and specifically study the fitness when grain size is jointly varied along with the ascent rate. With other properties equal to our default models, we vary the grain size factor,  $G_r$ , between 0.5 and 10, and the ascent rate between 0.05 and  $2.0 \text{ m yr}^{-1}$ , resulting in 3840 models. For each of these models, we then find the best fitting bulk source concentration ratio ( $[\text{La}/\text{Sm}]_{\text{bsrc}}$  or  $[\text{Sm}/\text{Yb}]_{\text{bsrc}}$ ) and LAB temperature. The source concentration is fitted by a second-order linear regression from sampling the misfit at concentration ratio samples of 0.2, 1.0, and 3.0. Since the change in fitness from a change in LAB temperature is non-linear, we obtain misfit for all LAB temperatures between 1000 and  $1300^\circ\text{C}$  at intervals of  $5^\circ\text{C}$ . For simplicity and due to scatter in the data, we bin the empirical data into  $1 \text{ Ma}^{1/2}$  bins up to  $12 \text{ Ma}^{1/2}$  (144 Ma), so that compositions for only 12 melting depths are needed to represent each model. Since the depth corresponding to seafloor age depends on the LAB depth, this sampling is repeated for each LAB isotherm. The result is  $3840 \cdot 61 \approx 2.3 \times 10^5$  models for La/Sm and Sm/Yb each, from which the model sensitivity to grain size and ascent rate, together with the dependence on LAB temperature and source composition, can be illustrated.

It is also possible for us to estimate the absolute concentrations of La, Sm, and Yb in the source if we can constrain the absolute concentration of one element at some final depth of melting. To do this, we will use the average concentration of Sm over thick lithosphere, which is about 10 ppm. Because predicted Sm over thick lithosphere does not vary significantly, we use predictions at 64 Ma to represent all thick-plate OIB. Thus, for each model curve of elemental concentration versus depth, we adjust the concentrations by the factor

$$\text{Sm}_{\text{bsrc}} = \left( \frac{\text{Sm}_o}{\text{Sm}_m} \right)_{t=64}, \quad (5.33)$$

such that

$$\text{La}_{adj}(t) = \text{La}_m(t)\text{Sm}_{bsrc},$$

$$\text{Sm}_{adj}(t) = \text{Sm}_m(t)\text{Sm}_{bsrc},$$

and

$$\text{Yb}_{adj}(t) = \text{Yb}_m(t)\text{Sm}_{bsrc},$$

where subscripts indicate: empirical values at 64 Ma (*o*), model values normalized to 1 ppm source concentration (*m*), values adjusted to fit data at  $t=64$  Ma (*adj*), age (*t*), and the bulk concentration in the melt source (*bsrc*). Since all concentrations are adjusted equally, this procedure does not affect misfits or the predicted source concentration ratio. However, with this procedure and an analysis of La/Sm and Sm/Yb misfit, we may constrain the absolute values of La, Sm, and Yb (and therefore also the concentration ratios) in the bulk source as well as for OIB erupted on seafloor of any age. Note that because we treat the LAB isotherm as a free parameter, and the LAB isotherm changes the depth of final melting, the above adjustment to melt concentrations must be repeated for each isotherm.

For each model the misfit  $m$  is calculated as

$$m_{\frac{\text{La}}{\text{Sm}}_{L_T,bsrc}} = \frac{1}{N_t} \sum_t^{t_{max}} \left[ \frac{\text{La}_o}{\text{Sm}_o} - C_{bsrc}^{\frac{\text{La}}{\text{Sm}}} \left( \frac{\text{La}_{L_T}}{\text{Sm}_{L_T}} \right)_{adj} \right]_t^2, \quad (5.34)$$

and

$$m_{\frac{\text{Sm}}{\text{Yb}}_{L_T,bsrc}} = \frac{1}{N_t} \sum_t^{t_{max}} \left[ \frac{\text{Sm}_o}{\text{Yb}_o} - C_{bsrc}^{\frac{\text{Sm}}{\text{Yb}}} \left( \frac{\text{Sm}_{L_T}}{\text{Yb}_{L_T}} \right)_{adj} \right]_t^2. \quad (5.35)$$

where  $t$  is an age bin,  $N_t$  is the number of age bins,  $t_{max}$  is the maximum age bin (12 Ma<sup>1/2</sup>),  $C_{bsrc}$  is a bulk source ratio of La/Sm or Sm/Yb, and the subscript  $L_T$  indicates a dependence on LAB temperature. Although standard deviations in the original data are available, they are ignored as the relative changes to misfits are not useful. Due to the volume of data, for each choice of ascent rate and grain size we find the best joint fitting LAB temperature  $L_T$  and source composition ratio  $C_{bsrc}$  and discard the remaining models.

All model properties resulting from our inversions are illustrated in Fig. 5.29. The first row of panels shows the misfit to La/Sm and Sm/Yb, as well as the  $T_{LAB}$  predicted by the fit to La/Sm and Sm/Yb. The pattern of misfit to La/Sm and to Sm/Yb are somewhat different. For the fit to La/Sm, best fitting models occur at small grain size and  $v_z > 0.25$  m yr<sup>-1</sup>. On the other hand, misfit to Sm/Yb is best within a curving band extending from low  $v_z$  ( $\sim 0.25$  m yr<sup>-1</sup>) and high grain size factor ( $\sim 7$ ), over to high  $v_z$  ( $\sim 1$  m yr<sup>-1</sup>) and lower grain size factor ( $\sim 3$ ). It is notable that the models with the kinematic parameters which best fit La/Sm are characterized by exceptionally low misfits ( $\sim 0.02$ ), whereas the models which best fit Sm/Yb have comparatively high misfits ( $\sim 0.08$ ). The reason for this can be ascertained by inspection of the actual predictions of melt concentration, as a function of final melting depth, predicted by our models in Fig. 5.30. Shown are all of the melt concentration curves for the fit to La/Sm (top panels) and for the fit to Sm/Yb (bottom panels), compared to the data (black diamonds) and the binned points (connected white diamonds) used in our actual fits. In the left panels, the curves have been colored according

to their misfit, and in the right panels they have been colored according to their  $T_{LAB}$ . The method of illustration for these results is explained in Appendix 5.D. We can see that the models which best fit La/Sm consistently match the binned data points for all ages, whereas the models which best fit Sm/Yb predict slightly low values over thin lithosphere and slightly high values over thick lithosphere. This is reminiscent of the original problem seen in Fig. 5.16, indicating that while optimizing parameters which affect the state of disequilibrium can improve the fit to Sm/Yb, it does not completely solve the problem of misfit. Nevertheless, the improvement in fit is indicative that the state of disequilibrium is a major contributor to the trace element chemistry of OIB.

The manner of variation in the best fitting  $T_{LAB}$  is also notable because the best fitting value varies gradually around the parameter space, punctuated by large discontinuous changes to higher or lower  $T_{LAB}$ . For example, for  $v_z = 1 \text{ m yr}^{-1}$  and  $G_r < 1$ , the best fit  $T_{LAB}$  to Sm/Yb is about  $1300^\circ\text{C}$ , rapidly changing to about  $1240^\circ\text{C}$  for higher  $G_r$ , and then changing again to about  $1140^\circ\text{C}$  around  $G_r \sim 6$ . This discontinuous behavior is related to the trade-offs in fitness from the joint variation in source concentrations and  $T_{LAB}$ . Essentially, as the fitness of models to the data degrades with a change in  $v_z$  and  $G_r$ , the fitness can be improved by forcing either the young-age data or the old-age data to adopt excellent fits to the data, at the cost of adopting poor fits in the other part of the data. Accordingly, we may consider the models with  $T_{LAB} \sim 1275^\circ\text{C}$  to be optimal in the fit to La/Sm, and the models with  $T_{LAB} \sim 1225^\circ\text{C}$  are optimal in the fit to Sm/Yb, because such a trade-off was not necessary in producing them. For the case of the fit to Sm/Yb in particular, a significantly different  $T_{LAB}$  is an indicator of an inadequate model.

The models which achieve reasonably good fits to Sm/Yb are circled in Fig. 5.29. As noted in the figure, the best joint fitting models (good fit to both La/Sm and Sm/Yb) occur in a region where the grain size factor is about 4-5 (i.e., 4-5 times higher than in our default model, and such that cpx, opx, and grt grain sizes of 3-5 mm are predicted in the unmelted source (Fig. 5.15)) and the ascent velocity is about  $0.5\text{-}0.75 \text{ m yr}^{-1}$ . Higher grain sizes and lower ascent velocity can improve the fit to Sm/Yb, but the fit to La/Sm then becomes poor. The remaining illustrations in Fig. 5.29 show predictions of the composition of the source (second row panels), MORIB (Mid-Ocean Ridge Island Basalt, third row panels), and OIB erupted on thick lithosphere (deep final depths of melting, fourth row panels). Note that strictly, the properties found in the region of 'best joint fit', are not entirely consistent because the model properties from the fit to La/Sm use a different  $T_{LAB}$  from the models fit to Sm/Yb. Nevertheless, we do not perform a true joint fitting analysis because we believe that the predictions for the fit to Sm/Yb are more robust due to the consistency of the data, versus the scatter in La/Sm. Simultaneously, the composition for La depends on the integrity of the fit to La/Sm which may be compromised by using a  $T_{LAB}$  which only best fits Sm/Yb. We thus expect that the  $T_{LAB}$  predicted by the fit to La/Sm is less accurate, but that other model properties may be reasonably well constrained by the data. Consequently, we show results of independent fits to La/Sm and Sm/Yb. Because of this, there are also two predictions of Sm composition, one from the fit to La/Sm and another from the fit to Sm/Yb. The differences between these two predictions might be considered a proxy to the error in our predictions for La. Alternatively, if it is believed that the La/Sm data is not compromised by scatter, this difference may be considered to exemplify a problem with our



approach in general.

Although the predictions at all regions of the parameter space are available for inspection, we focus on properties obtained by the best fitting models. Such a summary is shown in Fig. 5.31. Also, we will later find in our upcoming analysis of partition coefficient sensitivity that the predicted compositions of best fit models are, therein, generally the same. Because this upcoming analysis is also much more voluminous, we withhold discussion of compositional predictions until Sec. 5.17.2 and 5.19.

## 5.17 Partition Coefficient Sensitivity

Previously (Sec. 5.15), we showed that our default models predict good fitting La/Sm, and that values of Sm/Yb prior to the dry solidus are too high to fit the data (Sec. 5.15.2). We then showed that varying kinematic parameters which increase the extent of disequilibria (lower diffusivity, larger grains, or faster ascent rate) preserved the good fit to La/Sm and significantly improved the fit to Sm/Yb (Sec. 5.16.4). Although this is a satisfying outcome, we caution that due to the crudity of our models, some caveats of which we will discuss later (Sec. 5.23), the success of our models, and with it the apparent consistency of our models with data, may be misleading. Undoubtedly, future efforts must involve the development of more thermodynamically consistent models with improved numerical techniques in order to test whether or not various simplifications result in errors in the relationship between system properties and geochemical predictions. As such, we continue our study by investigating the consequences of varying the partition coefficients.

There are at least three reasons that our direct application of experimental partition coefficients may result in a model which does not represent the Earth. Firstly, the standard deviations in their calculation from experimental measurements can be large, even several factors away from the means (Adam et al., 2014). Second, although we have used constant values, partition coefficients vary with pressure and compositional changes in the melt and solid phases. Consequently, the partition constants used in our models are 'effective' values. That a best fit effective value is different from that inferred from experiments may imply a difference in the environmental conditions of melting, rather than experimental uncertainty. Lastly, straightforward experimental determination of equilibrium partition coefficients requires that the system is at equilibrium, which may be difficult to account for in a system where diffusion rates are slow and crystals may grow rapidly (e.g. Schneider and Eggler, 1986; Adam et al., 1993; 1997). The diffusion rates in solids (Table 5.2) suggest that trace element diffusion in crystals is negligible over the timescales of experiments (a few days) unless cross effects with major elements are significant. Experimental estimates of trace element diffusion rates in silicate melts suggest that diffusivities are on the order of  $10^{-8}$ - $10^{-6}$  cm s<sup>-1</sup>, depending significantly on temperature and H<sub>2</sub>O content (e.g., see Koepke and Behrens (2001) and references therein). The low end of this range will result in a system which is far from equilibrium for typical experiments (distance scales of  $\sim 1$  mm and timescales of several days). The high end of this range is about that necessary for significant diffusion to occur over distances of 500-1000  $\mu$ m and timescales of a few hours. However, because crystal growth is a continuous process which decelerates over time (as expected from the form of Eq. 5.11), equilibrium requires diffusive interactions to occur over timescales which are negligible

compare to the rate of crystal growth. Therefore, it seems likely that fast diffusive interactions may only occur in a local environment about the crystal, with diffusive interactions occurring over longer ranges resulting in disequilibrium features in experiments. In addition, even if diffusion rates in liquids are effectively infinite, the bulk partition coefficient must be  $\approx 1$  throughout the precipitation and growth of crystals, or zoning will occur with the changing compositions of the fluid. Consequently, only a rim on the order of  $< 0.1\mu\text{m}$  in thickness will be in equilibrium with the fluid (for a chemical diffusivity of  $\sim 10^{-15} \text{ cm s}^{-1}$ ). Although it is beyond the scope of our current study, modeling the experimental environment in much the same way as we have investigated here for the mantle assemblage may be useful for linking experimental observations to theories of non-equilibrium thermodynamic processes, and for constraints on coefficients.

For these reasons, we entertain the possibility that the partition coefficients in our default models do not fit the system, and determine how different these coefficients must be for model results to fit the data.

### 5.17.1 Analysis of partition coefficient sensitivity

Performing a meaningful test of the sensitivity of models to partition coefficients is difficult for several reasons. Firstly, We have already found that the system is likely in a state of disequilibrium. However, the extent of disequilibrium cannot be constrained unless all kinematic parameters or partition coefficients are known. If it was the case that partition coefficients were precisely known, we might simply constrain the optimal grain size or the ascent rate, as before. Thus, for the extent of disequilibrium to remain a free parameter, an entire suite of models must be run for each state of disequilibrium. Secondly, for our system of 5 phases and 3 elements, there are 12 partition coefficients which determine the chemical evolution of all elements in the system (all partition coefficients are normalized to melt). Thus, including the grain size, ascent rate, bulk source concentration ratios ( $[\text{La}/\text{Sm}]_{\text{bsrc}}$  and  $[\text{Sm}/\text{Yb}]_{\text{bsrc}}$ ), and the LAB depth (which controls the relationship between seafloor age and the depth of final melting), there are 17 free parameters which may be fit to La/Sm and Sm/Yb.

Since the partition coefficients in olivine and orthopyroxene are much lower than in clinopyroxene and garnet (Table 5.1), we will assume they are known from experiments. An additional simplification is allowed because we assume that there are no diffusive cross effects, such that diffusion of one ion has no effect on diffusion of another ion. Therefore, for a given extent of disequilibrium (grain size and ascent rate parameters), there are only two coupled parameters for each element: the partition coefficients in garnet and clinopyroxene. Since the other parameters are uncoupled, they may be adjusted *a posteriori*, and the number of simulation results required are not overwhelming.

Because of the computational expense of jointly inverting partition coefficients and disequilibrium parameters (grain size and ascent rate), we only test the sensitivity of partition coefficients with the default grain size and ascent rate. This will at least provide us with a test of the sensitivity of our models to changes in partition coefficients. We obtain results for models in which the partition coefficients in garnet and clinopyroxene are varied by a factor  $Z$  between 0.2-3.0 times the experimental values, at intervals of 0.05. The result is a set of  $57 \times 57 = 3249$  separate simulations, each of which calculate La, Sm, and Yb concentrations

in melt for each possible combination of partition coefficients.

Because cumulative melt concentration is strongly affected by the stochastic details of microstructural evolution, each model is different, having predictions which vary about a mean (Fig. 5.32). This results in a large amount of noise in calculations of misfit even if properties are not varied. In our sensitivity analysis we attempt to average out this noise to clarify the dependence on input parameters. This smoothing step is described in Appendix 5.E. Next, as in the analysis of grain size and ascent rate before (Sec. 5.16.4), we assume that the average value of Sm occurring in thick-plate OIB (approximated by a seafloor age of 64 Ma) is 10 ppm (Eq. 5.33). This alteration allows us to obtain estimates of absolute La, Sm, and Yb concentration in the source, as well as at any depth.

Using the adjusted model melt concentrations, La/Sm is found at selected final melting depths for all combinations of  $Z_{La,cpx}$ ,  $Z_{La,grt}$ ,  $Z_{Sm,cpx}$ , and  $Z_{Sm,grt}$ , resulting in  $57^2 \cdot 57^2$  models with compositions for each selected depth. For each of these models we find the best fitting  $T_{LAB}$  and source La/Sm composition, as in our previous analysis (Sec. 5.16.4).

The above is repeated for Sm/Yb, finding model compositions for all combinations of  $Z_{Sm,cpx}$ ,  $Z_{Sm,grt}$ ,  $Z_{Yb,cpx}$ , and  $Z_{Yb,grt}$ , with the best fitting LAB isotherm and source composition. Thus, we obtain a total of  $57^2 \cdot 57^2 \cdot 61 \approx 6.4 \cdot 10^8$  models for La/Sm and Sm/Yb each, from which the sensitivity of melt concentration to independent variations in partition coefficients of La, Sm, and Yb in garnet and clinopyroxene, together with dependence on LAB depth and source composition, can be illustrated. For each model the misfit is calculated from Eq. 5.34. Also, due to the volume of data, for each combination of partition coefficients we find the best joint fitting LAB temperature  $T_T$  and source composition ratio  $C_{bsrc}$  and discard the remaining models. Consequently, our analysis produces  $57^2 \cdot 57^2$  model results for La/Sm and Sm/Yb each.

### 5.17.2 Results of partition coefficient sensitivity

Visualization of the results may be treated in the following way. In the case of La/Sm, for each combined choice of  $Z_{La,cpx}$  and  $Z_{La,grt}$ , the misfit from adjusting the additional parameters  $Z_{Sm,cpx}$  and  $Z_{Sm,grt}$  may be visualized as a map. Illustrating all of the data in this way would result in  $57 \times 57$  maps of misfit. Since a figure of such size is overwhelming, we reduce the sampling to  $6 \times 6$  by only showing results where  $Z_{La,cpx}$  and  $Z_{La,grt}$  are equal to 0.5, 1.0, 1.5, 2.0, 2.5, or 3.0. The resulting figure (Fig. 5.33) thus illustrates how the misfit changes as a function of 4 free parameters. The same type of illustration for the fit to Sm/Yb is shown in Fig. 5.34. These suites of models are characterized by corresponding properties and predictions which are presented in additional independent figures. These predictions include the LAB temperature (Fig. 5.35-5.36), bulk source concentrations (Fig. 5.37-5.42), erupted OIB concentrations on thick plates (Fig. 5.43-5.46), and MORIB (Mid-Ocean Ridge Island Basalt) concentrations (Fig. 5.47-5.52) for La, Sm, Yb, La/Sm, and Sm/Yb.

Also, Fig. 5.53 compares a sampling of our melt concentration curves for La/Sm (where  $Z_{La,cpx}=Z_{La,grt}=3.0$ ) and Sm/Yb (where  $Z_{Sm,cpx}=Z_{Sm,grt}=3.0$ ) with the data and our binned points (to which models are actually fit). In the left panels, the curves have been colored according to their misfit, and in the right panels they have been colored according to their  $T_{LAB}$ . This graphical illustration of melt concentration curves is biased toward best fit

models such that models with low misfit appear in the foreground (see Appendix 5.D). For completeness, this illustration of the melt concentration as a function of final depth of melting is also shown for a more complete sampling of our models in Figs. 5.54-5.57.

We previously showed in our investigation of the effect of grain size and ascent rate (Sec. 5.16.4) that the fit to Sm/Yb can be improved with a larger grain size and slightly lower ascent rate. However, the fit to La/Sm degrades slightly when these kinematic parameters are adopted. When partition coefficients are treated as slightly free parameters, the fit to the data can also be dramatically improved, although the interpretation of these results is not straightforward. For example, in Fig. 5.53 we see that models with the associated partition coefficients ( $Z_{La,cpx}=Z_{La,grt}=3.0$  for the fit to La/Sm and  $Z_{Sm,cpx}=Z_{Sm,grt}=3.0$  for the fit to Sm/Yb) contain excellent fitting models, but these models are not sampling a consistent region of the parameter space. The models for the fit to La/Sm are shown in the bottom right-hand corner of Fig. 5.33. Here we see that for  $Z_{La,cpx}=Z_{La,grt}=3.0$ , good fitting models occur when  $Z_{Sm,cpx} > 2$  and  $Z_{Sm,grt} < 1$ . The models consistent with this region of parameter space are in the bottom left-hand corner of Fig. 5.34. Comparing this to the models in the bottom right-hand corner of 5.34 we see that some models with  $Z_{Yb,grt} > 1$  are poorly fit to Sm/Yb when  $Z_{Sm,grt} = 0.5$ , but the fit is improved when  $Z_{Sm,grt} \gg 1$ . To figure out the consistencies among the predictions, one may take a single panel from Fig. 5.33 and stretch it approximately to the size of all the panels in Fig. 5.34. For example, if we do this to the top left panel in Fig. 5.33, we can see that models which fit La/Sm well only cover the models near the left-hand side of Fig. 5.34. This is because in this plot only models with  $Z_{Sm,grt} < 1.5$  have reasonable fits to La/Sm. One may then further consider the region of  $Z_{Yb}$  parameter space in Fig. 5.34 to find the partition coefficients of Yb which result in good fits to Sm/Yb, in addition to La/Sm.

Surveying the data, some generalities may be noted. As previously discussed, the default partition coefficients result in a good fit to La/Sm (noted in the second column, second row panel in Fig. 5.33), but these default La and Sm partition coefficients, coupled with default partition coefficients for Yb results in a poor fit (also noted in the second column, second row panel in Fig. 5.34). It is not necessary to adjust partition coefficients for La since the fit is already good. However, since the fit to Sm/Yb can be improved by increasing the partition coefficient of Sm (in cpx, garnet, or both), it must be kept in mind that the fit to La/Sm may suffer. For example, by increasing  $Z_{Sm,grt}$  to 2.5-3.0, the fit to Sm/Yb significantly improves. However, the fit to La/Sm becomes very poor with this adjustment. Adjusting  $Z_{La,cpx}$  cannot compensate for this change, but increasing  $Z_{La,grt}$  can partially compensate for this adjustment. Nevertheless, the fit to both La/Sm is not optimal unless  $Z_{La,grt} > 3.0$ . Increasing  $Z_{Sm,cpx}$  improves the fit to Sm/Yb without damaging the fit to La/Sm. Other possible adjustments may also be proposed.

Our semi-qualitative inspection of the results indicates that an optimal case of minimal adjustment to achieve the maximum improvement must consist of a decrease in the partition coefficient of Yb in garnet ( $Z_{Yb,grt}$ ). If we allow that  $Z_{Yb,grt}$  is 60% lower than the experimental value, then no adjustment is needed to partition coefficients for La and Sm, and La/Sm and Sm/Yb achieve good fits ( $m \sim 0.05$ ). Alternatively, one may achieve a good fit by reducing  $Z_{Yb,grt}$  by only 30%, increasing  $Z_{Sm,cpx}$  and  $Z_{Sm,grt}$  by 50%, and increasing  $Z_{La,grt}$  by 100% to obtain a model which has excellent fits ( $m \sim 0.07$ ) to La/Sm and

Sm/Yb. Inasmuch as the partition coefficients are uncertain, other such combinations may be entertained.

Recall that a small but noticeable misfit to Sm/Yb remained after optimal grain size and ascent rate were constrained. Although we do not show it here, our investigations of variable partition coefficients suggests that this remaining misfit can be eliminated by very modest changes in partition coefficients, on the order of 5-20%, depending on which coefficients are adjusted. These observations are consistent with the use of experimental partition coefficients as effective values in decompression melting systems. On the other hand, since the extent of chemical disequilibrium is not known, we can only confidently offer a view into the sensitivity of the problem to the physical coefficients, rather than conclusions regarding the precise thermodynamic properties responsible for the observations.

The many remaining figures (5.35-5.52) illustrate the corresponding predictions for compositions in the bulk source, OIB erupted on thick lithosphere, and OIB erupted on ridges (MORB). These results are available to study in greater detail. However, because the fitness of each model underlies our assessment of its viability, we can be more succinct by focusing exclusively on the relationship between the chemistry predicted and the misfits of the models which predict them. Therefore, we illustrate 2D density functions for the properties of all models as a function of misfit in Fig. 5.58. While this shows the frequency of the model predictions for different misfits, an understanding of the partition coefficients which produce them requires a survey of Figs. 5.35-5.52. For example, consider the model predictions of bulk source Ytterbium ( $\text{Yb}_{\text{bsrc}}$ ; Fig. 5.58: 4th column, 2nd row), we can see that models with misfit of  $\sim 0.2$  predict  $\text{Yb}_{\text{bsrc}} \sim 1.6$  ppm, however as the misfit decreases the mean value of  $\text{Yb}_{\text{bsrc}}$  approaches  $\sim 0.7$ , which we would consider a more robust value since no good fitting models predict higher bulk source concentration. Lastly, using the density functions for models with misfit  $< 0.05$  we find the mean and use the bounds at half-maximum as an approximation of uncertainty. These final isolated values are tabulated in Table 5.3, and the main features of our data are discussed in the following sections.

## DISCUSSION

### 5.18 LAB Temperature

Figures 5.35 and 5.36 shows how the prediction of LAB temperature varies with the choice of partition coefficients, and Fig. 5.29 showed how the LAB temperature varies with the choice of disequilibrium parameters (grain size and ascent rate). As noted earlier (Sec. 5.16.4), the best fitting models are characterized by a particular narrow range of LAB temperatures. Both in our experiments with partition coefficients and disequilibrium parameters, for fits to the La/Sm OIB data our models predict that  $T_{\text{LAB}} \sim 1275^\circ\text{C}$ , whereas in fits to Sm/Yb data the models predict that  $T_{\text{LAB}} \sim 1225^\circ\text{C}$ . This is also visualized in our PDF's of model properties in Fig. 5.31 and Fig. 5.58 (top panels). We consider the LAB temperature predicted by the fit to Sm/Yb to be more robust, primarily due to the consistency of the data compared to La/Sm.

As noted earlier (Sec. 5.2), the LAB constrained here is a thermomechanical boundary separating the region of the upper mantle which may readily yield to stresses experienced at the base of the lithosphere. These stresses may originate from the positive buoyancy of a

plume-like source (e.g. Ballmer et al., 2011) or negative buoyancy of cool basal lithosphere (e.g. Afonso et al. 2008). Although a precise determination of the thermomechanical LAB has not been a primary focus of geodynamic modeling, we may estimate the temperature of this boundary by identifying the isotherms which have been deformed by convective erosion processes. For example, inspection of the results of Ballmer et al. (2011) indicates that this isotherm is about 1250°C, which is also consistent with the results of Afonso et al. (2008; see their supplementary information) in which this temperature occurs between 1200 and 1300°C. It is remarkable that the geochemical data, through the LID effect and our models of melting and the thermal structure of oceanic lithosphere (Chapter 3), predicts an LAB temperature which is so consistent with the geodynamic models.

## 5.19 REE Composition of the OIB Source

We have used a model of mantle melting to predict the cumulative compositions of fractional melts erupted at the surface. We have constrained the La/Sm and Sm/Yb concentration in the source by fitting models to La/Sm and Sm/Yb in global OIB as a function of the seafloor age on which eruptions occur. In addition, by also employing a constraint on the absolute concentration of Sm in OIB erupted on seafloor of a given age, we have been able to estimate the absolute concentrations of La, Sm, and Yb in the OIB source and in OIB erupted on seafloor of any age. Summaries of these compositional predictions are shown in Fig. 5.31 for our analysis of disequilibrium parameters (grain size and ascent velocity) and Fig. 5.58 shows these predictions from our sensitivity analysis of model results to varying partition coefficients. The best fit models from both of these analyses make similar predictions, but the results of the analysis of disequilibrium parameters is sparse so we will focus on the more complete analysis of partition coefficients.

Overall, the predictions for OIB erupted on thick plates (third row panels) is the most consistent due to the fact that the  $\text{Sm}_{\text{oib}}$  value is assumed to be 10 ppm for all models, and no deviation from this value has been allowed. Consequently,  $\text{La}_{\text{oib}}$ ,  $\text{Sm}_{\text{oib}}$  (both from fits to La/Sm and Sm/Yb),  $\text{Yb}_{\text{oib}}$  and thus also  $\text{La}/\text{Sm}_{\text{oib}}$  and  $\text{Sm}/\text{Yb}_{\text{oib}}$  are well constrained. Even models which generate poor fits to the data do not make much different predictions. Bulk source and MORIB compositions have a larger (but still well behaved) variance for models with low misfit, although  $\text{Sm}_{\text{bsrc}}$  from the fit to La/Sm is particularly invariable.

In the following two sections (5.19.1-5.19.2), we discuss two important and related implications of our compositional predictions for the properties of the OIB source and the Earth.

### 5.19.1 Compositional similarity of MORB and OIB sources

Firstly, both the empirical data and our models show that melts produced by decompression melting of the OIB source will erupt with nearly MORB-like composition if allowed to ascend to the surface uninhibited by thick oceanic lithosphere (generating MORIB, or Mid-Ocean Ridge Island Basalt). In other words,  $\text{OIB}_{\text{bsrc}} = \text{MORIB}_{\text{bsrc}} \approx \text{MORB}_{\text{bsrc}}$ , in terms of REE. Although we have not used the composition of MORB to constrain our models, our best fitting models predict MORIB compositions which are remarkably close to (albeit

slightly elevated in comparison to) MORB. Models with excellent fits to Sm/Yb and which are characterized by MORIB Sm/Yb compositions equal to MORB can be found without difficulty (e.g. Fig. 5.53). On the other hand, models with MORIB La/Sm values which fit the MORB composition ( $\sim 1.5$ ) have larger misfit ( $m > 0.05$ ). Our predictions of REE ratios and absolute concentrations of erupted MORIB (half-maximum ranges and means of models with excellent  $< 0.05$  misfit) are compared to the MORB database (Gale et al., 2013) in Fig. 5.28. The MORB value of Yb is well within the HMB (half-maximum bounds) of our predictions for MORIB. The MORB value for Sm is within our HMB for Sm in MORIB, but it lay near the low end. Our HMB for La in MORIB, however, is markedly higher than La observed in MORB. This progressive increase in the difference between model MORIB and observed MORB also results in the HMB for La/Sm and Sm/Yb in MORIB being about 30% higher than mean MORB values.

Although this misfit is consistent with a small degree of enrichment in the MORIB source, we should note that MORIB should only be consistent with MORB if the microstructural properties of the source (e.g., grain size) and the ascent rate are the same, which will not be the case if OIB ascends actively. Although predicting MORB (not MORIB) concentration is not straightforward in the work discussed here since we do not perform a thorough investigation of models with low ( $< 0.1 \text{ m yr}^{-1}$ ) ascent rates, our observations provide evidence that the OIB and MORB source may be compositionally indistinguishable. This is because the differences between MORB and MORIB composition may be related to different extent of disequilibrium in MORB and OIB source melting, rather than reflect a difference in source composition. Consider La/Sm and Sm/Yb evolution as a function of ascent rate in Fig. 5.27. The value of La/Sm for a final depth of melting near zero (MORIB value) increases by about 25% between  $1 \text{ m yr}^{-1}$  and  $0.025 \text{ m yr}^{-1}$ , where the latter value may be a reasonable estimate of passive mantle ascent beneath ridges. Therefore,  $[\text{La/Sm}]_{\text{morib}}$  is about 25% greater than  $[\text{La/Sm}]_{\text{morb}}$  due to disequilibrium effects, thus explaining (at least in greater part) our elevated values in MORIB. Also, we caution that our models of absolute concentrations are dependent on our choice of an average concentration of Sm in thick-plate (alkaline) OIB lavas ( $\text{Sm}_{\text{oib}} = 10 \text{ ppm}$ ). A slightly lower value of Sm in OIB should increase the similarity of our MORIB predictions to that in MORB. Later, we will see that a value closer to 9 ppm may be a more appropriate average (Sec. 5.20). This coupled with disequilibrium features in La should strengthen the similarity between MORIB and MORB. In addition, the scatter in La/Sm may be compromising the integrity of our bins over young seafloor. If additional data demonstrated that La/Sm over thin lithosphere is lower than that represented by our bins, models would predict lower MORIB values for La/Sm. Moreover, a reactive open system melt migration regime may result in slightly different chemical predictions at shallow melting depths.

### 5.19.2 REE concentration of primitive mantle

The second implication of our compositional predictions is related to the composition of the Earth. Our estimates of absolute concentration in the OIB source are much higher than previous estimates of depleted MORB mantle (DMM), which is the reservoir from which present-day MORB is extracted, and also higher than the primitive mantle (PM), which

is the bulk silicate Earth (BSE) composition (mantle and crust). Treating our OIB source concentrations as representative of DMM composition, we may calculate PM composition using bulk compositions in continental crust from Rudnick and Gao (2003). Our results are shown in Table 5.4. Since our OIB source composition is assumed to sample a uniform DMM reservoir, and the compositions are high, our estimates for DMM are much higher than those from Workman and Hart (2005). Specifically, La, Sm, and Yb are about 7.3, 3.8, and 2.2 times higher than Workman and Hart (2005). The higher values for progressively more incompatible elements also results in higher La/Sm and Sm/Yb in DMM. Also, because we assume a uniform mantle reservoir, the mass of continental crust is a small fraction of BSE, and our DMM estimates are high, our resulting estimates of PM are only fractionally higher than DMM. In contrast, previous estimates of PM composition have tended to be significantly higher than DMM (Sun and McDonough, 1989; Lyubetskaya and Korenaga, 2007).

Probably, the most important assumption in the above brief analysis is that of a uniform reservoir, in which the MORB source is compositionally indistinguishable from the OIB source. As argued above, this inference is related to our observation that modeled MORIB composition is nearly equal to observed MORB composition, meaning that their respective source compositions are largely indifferent. As we did not find it difficult to argue that moderately enriched MORIB values obtained here may be related to a combination of OIB source disequilibria, uncertainty in the Sm composition of thick-plate OIB, and the statistical robustness of the La/Sm data, we find no diagnostic evidence that the OIB source is enriched in REE. Our results suggest that the view in which OIB sample chemically enriched and isolated reservoirs (whether in the form of meso-scale marble cake compositional heterogeneity or a compositionally layered mantle structure) is not compatible with advanced theories of melting dynamics.

Within the view that the sources of MORB and OIB are compositionally different, it was natural to hypothesize models which characterize the distributions of compositional heterogeneity in the mantle, and to relate the features of such models to the nature of mantle convection in the Earth (e.g. Zindler and Hart, 1986; McKenzie and O’Nions, 1995; Armienti and Gasperini, 2007). If we are now confronted by a compositionally uniform mantle, the heuristic powers of mixing mantle component models may have to be partially replaced or adjoined by largely new heuristics wherein which chemical heterogeneity originates in the non-equilibrium thermodynamic evolution of the source, rather than its bulk composition.

## 5.20 The Chemical Step and Major Element Systematics

A critically important interpretation in our analysis of OIB systematics is the existence of the chemical step demarcating eruptions on seafloor greater than about 15 Ma from eruptions on younger seafloor. Values observed in eruptions on old seafloor indicate low extents of melting at high pressure while eruptions on young seafloor indicate high extents of melting during dry melting. If the chemical step does not exist, then chemical constraints on source potential temperature, LAB temperature, and other properties of the source cannot be well



established. Nevertheless, we have shown that the data for La/Sm and especially Sm/Yb show strong evidence for the step-like trend. In addition, in Fig. 5.60-5.61 we further employ the database of Humphreys and Niu (2009) and Niu et al. (2011) by illustrating variations in major element chemistry versus seafloor age, using our corrected ages. The figure shows SiO<sub>2</sub>, TiO<sub>2</sub>, Al<sub>2</sub>O<sub>3</sub>, FeO, MnO, MgO, CaO, NaO, K<sub>2</sub>O, and P<sub>2</sub>O<sub>5</sub>, which Humphreys and Niu (2009) corrected for fractionation effects to an Mg-number of 0.72. Two types of trends occur. Firstly, we see gradual and nearly linear variation between zero age and about 70 Ma in Si, Al, Fe, Mn, and Mg. Such a variation is observed strongly in SiO<sub>2</sub> and MgO, noticeably in Al<sub>2</sub>O<sub>3</sub> and FeO, and weakly in MnO. Secondly, in several major oxides we find the familiar kink or step-like chemical discontinuity at much younger age (10-20 Ma). This variation is observed strongly in K<sub>2</sub>O and P<sub>2</sub>O<sub>5</sub>, and noticeably in TiO<sub>2</sub>, NaO and CaO. A linear variation with age to at least 70 Ma is consistent with a control on chemistry from the melting pressure, whereas the oxides with step-like features indicate strong incompatibility and thus similar behavior to the light Rare-Earth Elements. In Sec. 5.21 we will also show that some isotopic systems exhibit this behavior as well.

## 5.21 Isotopic Variations

So far we have primarily discussed observations and predictions of trace element compositions in melts, and have shown that the trace element chemistry of OIB are consistent with a source composition which is not markedly enriched compared to MORB. However, while trace elements have been used to argue for an enriched OIB source, arguments for enrichment are mainly based on evidence from isotopic systems. Following the explanation of Hofmann (2006), we use the decay  $^{87}\text{Rb} \rightarrow ^{87}\text{Sr}$  as an example. The decay occurs with a half life of  $t_{hl} = 48.8 \times 10^9$  yr, and  $\lambda = \ln(2)/t_{hl} = 1.42 \times 10^{-11}$  is a decay constant such that the abundance of  $^{87}\text{Sr}$  over time can be given by

$$^{87}\text{Sr} = ^{87}\text{Sr}_i + ^{87}\text{Rb} \times [\exp(\lambda t) - 1],$$

where the subscript  $i$  indicates the initial abundance. If we divide both sides by the non-radiogenic isotope  $^{86}\text{Sr}$ , we find that the isotope ratio  $^{87}\text{Sr}/^{86}\text{Sr}$  of a source depends on the time and the Rb/Sr ratio in the source as

$$\frac{^{87}\text{Sr}}{^{86}\text{Sr}} = \left( \frac{^{87}\text{Sr}}{^{86}\text{Sr}} \right)_i + \frac{^{87}\text{Rb}}{^{86}\text{Sr}} \times [\exp(\lambda t) - 1].$$

If the source undergoes equilibrium partial melting, the generated melt will inherit the  $^{87}\text{Sr}/^{86}\text{Sr}$  ratio of the source. The inclusion of other isotopic systems such as Sm-Nd, Lu-Hf, U-Pb, and Th-Pb has shown that various island groups cluster around particular regions of parameter space within these systems (Hofmann, 2006). Moreover, due to the consistency of isotopic characteristics in MORB compared to OIB, and the assumption that isotopic heterogeneity is an unaltered reflection of source composition, isotopic compositions have been considered to come from different places in the mantle (Hofmann and Hart, 1978). On the other hand, it has become widely believed that isotopic heterogeneity in the mantle occurs on the smaller scale of a 'marble-cake' mantle (Allegre and Turcotte, 1986; Hirschmann et

al., 2003; Hofmann, 2006; Hirschmann and Stolper, 1996; Armienti and Gasperini, 2007; Niu et al., 2012).

Central to these models is the long recognized, albeit dubiously justified, assumption that significant fractionation of parent and daughter isotopes cannot occur in the mantle during melting due to fast diffusion rates (Hofmann and Hart, 1978). However, based on Van Orman et al. (1998), van Orman et al. (2002), Remmert et al. (2008), and Sano et al. (2011), it is apparent that diffusion rates in major mantle minerals of all radioactive and radiogenic elements for which measurements are available, are not far higher than those for REE. Hofmann and Hart (1978) recognized that volume diffusion in minerals was much higher than in melt, but nevertheless believed that fast diffusion in melt might be sufficient for the assumption of equilibrium. In our view volume diffusion rates in solids is the limiting factor. Therefore, it is unlikely that the system is near equilibrium and the consequences of disequilibrium partitioning and preferential melting of phases (as examined here for REEs) must affect isotopic signals in erupted melts. Disequilibria as a caveat to conventional interpretations of isotopic trends has long been known. Indeed, the work of Hofmann and Hart (1978) was a response to earlier work by O'Nions and Pankurst (1974) and Vollmer (1976), who invoked disequilibrium and the preferential melting of accessory phases such as phlogopite (which has high Rb/Sr and thus higher  $^{87}\text{Sr}/^{86}\text{Sr}$  than the bulk assemblage) to explain high  $^{87}\text{Sr}/^{86}\text{Sr}$  in OIB. However, this particular accessory mineral in the melting process may not be necessary for the generation of observed structures in isotopic systematics.

As we have shown that correlations of REE (and incompatible major elements) in OIB with seafloor age may be related to melting processes without enrichment, an important question is whether or not melting processes may also be responsible for isotopic variations. This first requires that isotopes correlate with seafloor age. In general, such correlations have indeed been reported by previous authors. Park et al. (1990) noted a correlation in Pb isotopes with seafloor age. Also, Haase (1996) recognized age correlations in REE ratios (Ce/Yb, Tb/Yb, and Nd/Sm) with step-like patterns much like that observed here (Fig. 5.62). However, Haase (1996) claimed to "find no correlation of Nd isotopes, implying that the age of the plate has no influence on  $^{143}\text{Nd}/^{144}\text{Nd}$  except for the near-ridge regions (lithospheric age <15 Ma)". This view was apparently influenced by the belief that isotopic variation must originate in source composition and was supported by the observation that Ce/Yb and Tb/Yb exhibits a larger scatter, making the age correlation appear more linear in REEs. Consequently, a step-like feature in the isotopic data appeared to disagree with an expected linear or continuous variation with seafloor age. In our view, it is clear from their report that  $^{143}\text{Nd}/^{144}\text{Nd}$  has a strong dependence on age reflecting the step-like features in REE ratios. More recently, Niu et al. (2011) found weak correlations in all major isotopic systems with seafloor age. However, as we found that faulty seafloor ages appear to have compromised observed correlations in the REE data, we can expect that the isotopic data is similarly compromised. Therefore, we illustrate the isotopic data (personal communication, Yaoling Niu, 2015) as a function of age using our new seafloor ages in Fig. 5.63. As in the Rare-Earth and major element data examined previously,  $^{143}\text{Nd}/^{144}\text{Nd}$ ,  $^{176}\text{Hf}/^{177}\text{Hf}$ , and  $^{87}\text{Sr}/^{86}\text{Sr}$  exhibit impressive correlations with age.  $^{143}\text{Nd}/^{144}\text{Nd}$  and  $^{176}\text{Hf}/^{177}\text{Hf}$  gradually approach highest values near zero age and, perhaps most importantly, a kink or discontinuity in the data occurs at around 20 Ma.  $^{87}\text{Sr}/^{86}\text{Sr}$  values converge on low values over the youngest

seafloor and a step-like feature is observed around 20 Ma. On the other hand, we note that low values of  $^{87}\text{Sr}/^{86}\text{Sr}$  are found over  $> 65$  Ma seafloor as well, although high values are absent over young seafloor. Similarly,  $^{176}\text{Hf}/^{177}\text{Hf}$  shows high values over old seafloor, and  $^{143}\text{Nd}/^{144}\text{Nd}$  also bends to higher values at older ages. Without isotopic modeling, we cannot explain this zig-zag type behavior in all of the isotopic systems. However, we suspect that it is related to the gradual decomposition of garnet which occurs over much greater depths than the transition between wet and dry melting (which we have interpreted as the main cause of the step feature). Unfortunately, we cannot confirm the correlations observed by Park (1990). In our figures we find no noticeable correlations in any Pb system with age.

We hypothesize that, as in the case of Rare-Earth elements, isotopic systematics may be largely controlled by disequilibrium melting processes. Moreover, we have argued that OIB may simply be the high-pressure end-member of near-MORB source composition. Consequently, the principal variations in isotopic characteristics do not represent the mixing of 'mantle components'. This also means that MORIB erupted compositions must be about equal to MORB composition. Ascent kinematics and perhaps thermochemical differences between MORB versus MORIB sources will impart different signatures, but if melting processes are primarily responsible for isotopic variations, then  $\text{MORIB} \approx \text{MORB}$  and it should be found that OIB trends toward MORB as erupted lithospheric age goes to zero. This is precisely that seen in Fig. 5.63 for  $^{143}\text{Nd}/^{144}\text{Nd}$ ,  $^{176}\text{Hf}/^{177}\text{Hf}$ , and  $^{87}\text{Sr}/^{86}\text{Sr}$ . In contrast, Hofmann and Hart (1978) noted that OIB erupted on ocean ridges exhibits isotopic signatures ( $^{87}\text{Sr}/^{86}\text{Sr}$ ) which differ significantly from MORB.

Although a phenomenological cause of the greater part of isotopic variation seems viable, we do not establish it here. We must investigate this explanation by incorporating radioisotopic decay and assumptions regarding the secular  $PT$  history of the mantle source. The major questions are: a) is diffusive fractionation among major phases sufficient, or are accessory minerals such as phlogopite (e.g., O'Nions and Pankhurst, 1974; Vollmer, 1976; Hofmann and Hart, 1978) necessary to produce observed variations, b) can grain-scale isotopic heterogeneities originating in the abundances of parent isotopes in minerals be maintained over timescales of  $10^8 - 10^9$  years in the mantle, c) can melting processes explain the continuous variation in isotopic systems with final melting depth, and d) what are the roles of additional phenomenological complexities in melting, such as open-system melt migration, in the production of MORIB, MORB, and OIB signatures?

## 5.22 Viability of Thermal Plumes

The major feature in the chemical data is the chemical step distinguishing large extents of melting on young seafloor from low extents of melting on older seafloor. This step occurs around 20 Ma, which is consistent with the intersection of the LAB with the depth of dry melting. However, this interpretation only works for a mantle potential temperature of  $< 1400^\circ \text{C}$  in the source. If the source temperature is significantly higher, the depth of dry melting occurs deeper and the chemical step will be predicted to occur at a significantly older age. A straightforward interpretation of the data is that OIB sources are not hot ( $> 1400^\circ \text{C}$ ). However, we can conceive of at least two alternative interpretations of the data which are consistent with thermal plumes as a source for OIB volcanism. The first

explanation is that most OIB sources are composed primarily of petite spots which are not associated with a hot source. In this interpretation, only the most voluminous sites of localized volcanism (e.g. Iceland, Galapagos, Reunion, Hawaii-Emperor, and West Africa) originate from thermal plumes. This interpretation is supported by the chemical data in Fig. 5.60-5.63, where the suspected hot spots are green while the remaining 'petite' spots are red. As discussed earlier (Sec. 5.20), OIB erupted on young seafloor are anomalous due to low-pressure melting, but Reunion, Hawaii, and West Africa are low in incompatible elements (La, Sm, P, K, La/Sm, Sm/Yb). This is expected from high-degree melting beneath the ridge in these sources. Similarly, high-degree melts beneath old lithosphere are consistent with anomalously elevated extents of melting, which may be attributed to high temperature, but may also be due to compositional heterogeneity.

The second explanation is that many or all OIB sources are hot, but that the chemical signatures originate from melting of surrounding ambient mantle gradually heated by the thermal plume. This seems possible in principle, but it is not clear how such a process can produce values consistent with the observations. The hypothesis requires that the fraction of melt produced and transported from within the thermal plume is small enough to be overwhelmed by the signal of ambient mantle melt. Also, the extent of melting within ambient mantle must either be small, or should not be reheated to more than  $\sim 1400^\circ\text{C}$ . In this interpretation, mixing may be able to account for the values observed in the following way. It is likely that ambient mantle is moving passively at rates consistent with plate tectonics, and the vertical component of this ascent may be very small or zero. Thus, ambient mantle is close to equilibrium. The associated values of La/Sm and Sm/Yb expected for melting near equilibrium are much higher than observed in the data (Fig. 5.27). Mixing between an equilibrium and OIB source of melt may result in erupted compositions like those seen, if mixing occurs in the correct proportions. To understand the efficacy of such a hypothesis it will be helpful to perform a coupled model of thermomechanical ascent, plume-lithosphere interaction, and microchemical evolution of both plume and ambient asthenosphere.

## 5.23 Some Caveats and Future Efforts

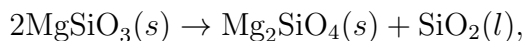
### 5.23.1 Microstructural evolution

Some properties which may change the behavior of our microstructural simulations are the following. First, there is the choice of time scaling, both as it appears in the equation governing phase transformations (Eq. 5.7) and in the definition of the Monte-Carlo step (MCS). Changing the time scaling essentially modifies how close the system is to microstructural equilibrium. If our assumption of  $1 \text{ MCS} = 1 \text{ year}$  is too slow, a significantly lower physical time represented by the MCS will result in faster coarsening. In turn, this will tend to reduce the abundance and area of interstitial grains from Ostwald ripening processes, resulting in grain size distributions for all depths shifted to larger radii (Fig. 5.15). Second, our models assume that there are no stresses other than to those related to interfacial energy. However, the application of large external shear stresses can cause dislocations inside grains, slowing or even reversing coarsening rates (Solomatov and Reese, 2008). If the OIB source ascends actively then such deformation effects may impact grain sizes in regions where shear stresses

are high. Thirdly, the fact that we do not model compaction related to the extraction of the melt volume may affect microstructural evolution in shallow depths. Since our microstructural models assume that melt is not extracted and that there is no gravity to compact grains, individual crystals lose contact with each other. In reality, such contacts will be preserved which will accommodate further grain boundary migration.

### 5.23.2 Major element non-equilibrium thermodynamics

Our assumption that phases have indivisible homogeneous identities is a substantial simplification which does not allow us to consistently model non-equilibrium thermodynamic controls on coarsening and microstructural development. For example, to model Ostwald ripening processes, a lattice site of some phase can break off of a host crystal and migrate around the assemblage until it is absorbed by a different crystal of like phase. In reality, such transport will take place by diffusion of chemical components which are released from a dissolving phase and may be absorbed by multiple neighboring phases. Similarly, when a lattice site of some phase transforms into another phase, there is no redistribution of major components in our model. Instead, the chemical balances of phase transformations are accomplished statistically, depending on the phase equilibrium calculations, which themselves depend on chemical mass balance solutions. For example, consider again the melting reaction of enstatite producing forsterite and liquid



which can be accomplished by transforming, on average, 2 lattice sites of opx into 1.4 lattice sites of olivine and 0.6 lattice sites of melt. In real thermodynamic systems additional reactions may be preferred, resulting in a more complicated mass balance and different phase equilibria.

The necessary coupling of major component diffusion and microstructural evolution may be accomplished with an approach similar to the recent work of Homer et al. (2013), whom developed a hybrid Potts-phase field model. In their model, a Potts model controls grain boundary evolution while a phase-field model controlled the diffusive 'partitioning' of components using chemical potentials. In the future, we plan to develop our models in this direction, although we suspect that the incorporation of the phase-field technique may be more complicated than is necessary. Our method of diffusive partitioning should be easily converted to a thermodynamically consistent formulation by using chemical potentials  $\mu_k$  instead of 'apparent' concentration gradients  $C_k\theta$ .

Although our approach of diffusing 'phases' rather than diffusion of components is known to fit much of the behavior of multi-phase coarsening (Homer et al. 2013; Solomatov et al., 2002), problems may arise when phase transformations are diffusion limited. Consider the compositions of pyroxenes and garnets during equilibrium decomposition of garnet shown in Fig. 5.65. All major chemical components (in wt. %) are shown for completeness, but we will only discuss  $\text{Al}_2\text{O}_3$  and  $\text{SiO}_2$ . During the decomposition of garnet, abundances of cpx and olivine remain mostly constant while opx mass increases in proportion with the loss of mass in garnet (Fig. 5.6). The most straightforward explanation of this is that garnet transforms directly into opx and other reaction paths are not important, but equilibrium

compositions in pyroxenes indicate that diffusion plays a role in (and may impart kinetic limitations to) phase transformations.

As garnet exsolves pyroxene, equilibrium thermodynamics predicts that garnet composition changes, losing  $\text{SiO}_2$  and gaining  $\text{Al}_2\text{O}_3$ . Simultaneously, both opx and cpx lose  $\text{SiO}_2$  and gain  $\text{Al}_2\text{O}_3$ . If only orthopyroxene exsolves from garnet, then opx will initially have a high Al content, which must then re-equilibrate by losing  $\text{Al}_2\text{O}_3$  to (and gaining  $\text{SiO}_2$  from) cpx and garnet. It is also possible that clinopyroxene exsolves from garnet, at the expense of low-Al cpx, if high-Al cpx is more stable than low-Al cpx. In either case, the new pyroxene phases must re-equilibrate with garnet and previously existing pyroxenes. Moreover, although we do not show it here, higher bulk system  $\text{Al}_2\text{O}_3$  results in a greater abundance of garnet. From the above, we may predict that pyroxenes exsolved from garnet, since they remain in contact with each other, will result in a diffusion-limited metastability of garnet. The lower-energy state of decreased garnet volume with decompression requires that diffusion redistributes  $\text{Al}_2\text{O}_3$  and  $\text{SiO}_2$  among phases. If such an effect significantly changes the abundances of solid phases during decompression of an OIB source, then predictions of trace element abundances in melt may change.

More generally, if non-equilibrium processes such as diffusion of major components significantly impact the stability of phases on the sub-grain scale, then it will be found that applications of equilibrium thermodynamics to many problems in chemical and physical geodynamics produce misleading results. For this reason, it will be important to further develop thermodynamically consistent models which couple microstructural and microchemical phenomena.

### 5.23.3 The 3D versus 2D polycrystal

We have so far only investigated the predictions of microstructural and chemical evolution models in two-dimensional (2D) domains. Clearly, an important question is whether or not the behavior of a real 3D system is accurately approximated by a 2D model. There are two avenues of possible inconsistency.

#### 3D Potts model

Firstly, we may question the possibility of different behavior in the Monte-Carlo Potts model in 2D versus 3D. Although we have not thoroughly critiqued the behavior of the Monte-Carlo Potts model in 3D, we do provide a basic examination of 3D Potts model output. The extension of the 2D Potts model to 3D is relatively straightforward. The two-dimensional stencil for the energy density functional  $E_\alpha$  (Eq. 5.1) is extended to 3D by increasing the number of neighbors from 36 to 170 as

$$E_\alpha = \frac{1}{2} \sum_{\beta}^{n=170} e_{\alpha\beta}, \quad (5.36)$$

and the equation is employed in a  $N \times M \times W$  matrix. The dramatic increase in computational expense moving from a 2D model to a 3D model (especially given the size of our energy functional discretization) is the main reason for not obtaining our results in 3D. Fig. 5.64a

shows the results of a 3D simulation of size  $288 \times 288 \times 288$  using the properties of our default model at 300 km depth. Also, Fig 5.64b shows the microstructure of the same model except that 5% melt has been artificially introduced. Note that grains the size of that shown would require substantial computational expense to grow using normal stochastic forward evolution. Instead we have achieved such a microstructure using a trick of accelerated development. Unfortunately, this also means that a detailed study of grain growth evolution is not warranted. Nevertheless, it is notable that the 3D microstructure is not fundamentally different from that observed in the 2D results. The reliability of the 2D Potts model to represent 3D polycrystalline behavior has been studied rather extensively (e.g. Anderson et al., 1989; Hui et al., 2003; Yu and Esche, 2003; Huang et al., 2006; Yang et al., 2000; Zollner and Streitenberger, 2008; Kim et al., 2006). From these investigations it seems that while the description of grain boundary migration, interactions, and statistics in the 3D setting are more complicated, the 2D approximation does not suffer from inaccuracy in the production of grain size distributions or growth rates. On the other hand, it is known that a cross-sectional analysis of grain sizes which develop in a 3D model can be markedly different from those observed in the 2D model (Yu and Esche, 2003; Zollner and Streitenberger, 2008). This is because a given cross-section in a 3D model can slice across the far edges of a crystal, shifting naive 2D grain size distributions to small sizes. However, this is simply a result a dimensional limitation in cross-sectional analysis which can be corrected for. More importantly, when anisotropic forces are imposed on the 3D microstructure (e.g. Yang et al., 2000) a 2D model may fail to describe characteristics which evolve in the microstructure. Since we only attempt to describe isotropic microstructural phenomena, we do not believe that new microstructural features of great importance will arise in a 3D simulation of isotropic coarsening.

### 3D diffusive partitioning

On the other hand, the second inconsistency which may arise in our models is in regards to 3D effects in diffusive partitioning. We suspect that 3D effects in diffusion are likely to impact our results. The expected overall difference is a higher rate of diffusive equilibration due to chemical gradients in the third dimension and the closer proximity among phases of different diffusivity. The higher rate of equilibration decreases the amount of disequilibrium for a given microstructure, shifting our predictions of grain size and ascent velocity to higher and lower values, respectively. Benchmarks of the importance of this behavior on our assessments must be performed in future work, and ultimately it will be necessary to fully extend our models to 3D. Nevertheless, we must note the importance of obtaining reliable 2D results due to the great computational expense of 3D simulations. If coupled microchemical-microstructural models are to be eventually incorporated into large-scale thermochemical simulations of the mantle, such simulations may only be viable with 2D grain-scale models even with massive parallelization. Simple scaling adjustments may then be imposed on the 2D thermodynamic equations to approximate 3D effects.

#### 5.23.4 Diffusion rates in melt

It is known that diffusion coefficients in silicate melts are much higher than those in silicate minerals (Koepke and Behrens, 2001). However, the coefficients of diffusion impart difficult

constraints on numerical stability in our models. We initially considered it reasonable to approximate the large difference between diffusion in solids and liquids by assigning the diffusion rate in liquids to be about a factor of  $10^2$  greater than the rate of Yb in cpx, which features the highest diffusion rate among the solid phases. In this case, the diffusion rate of melt at 300 km for  $T_p = 1300^\circ\text{C}$  is about  $10^{-12} \text{ cm s}^{-1}$ . This is a factor of about  $10^4$ – $10^6$  lower than some estimates for trace elements in silicate melts (e.g. Koepke and Behrens, 2001). Admittedly, our implementation of a straightforward explicit finite-difference scheme is a bow to simplicity in this development of, to our knowledge, the first coupled microstructural-microchemical mantle melting model. However, as our models (for  $T_p = 1300^\circ\text{C}$ ,  $\phi_r = 0.5\%$ ,  $v_z = 1.0 \text{ m yr}^{-1}$ , and a grain size factor of 1) require a few hours to compute on a single core of a modern Intel CPU (i7 4960X at 4.0 GHz), solving the diffusion equation with such large diffusion coefficients will require an intelligent revision to the numerical approach. The avenues of numerical speed-up techniques are many and may include implementation of implicit formulations, stiff algorithms, meshing techniques, and special consideration of the fact that melt is volumetrically small and contains the expensive properties. In addition, one may simply employ more computational power through parallelization, GPU architecture, and hardware budgets.

It may be tempting to assume infinite diffusivity by, for example, averaging melt concentrations at each timestep. For our default grain sizes (domain size of  $1 \text{ cm}^2$ ) and a high melt diffusion coefficient of about  $10^{-6} \text{ cm s}^{-1}$ , diffusion on timescales of years is effectively infinite. However, since the grain size may be several factors larger and the appropriate diffusion coefficients may be  $< 10^{-7} \text{ cm s}^{-1}$ , disequilibrium in the melt will occur for timescales of years to decades or more. Moreover, because melt is not everywhere connected, the implementation of an infinite diffusivity approximation is not strictly trivial.

### 5.23.5 Open-system melting and melt migration dynamics

Our models assume that extracted melt is transported to the surface without reacting with intervening mantle. As such, the framework of migration represented by our models is one in which residual melt reacts with residual solids and is subsequently expelled into a conduit or vein which rapidly transports melt to the surface with negligible reactive exchange with the walls of such conduits. In typical theories of trace element partitioning in magmas, this is known as a closed-system model (Shaw, 2006). On the other hand, we may consider that the volume of residual melt is part of a larger network of interconnected porous melt channels. In this case, the system is open and melt continuously migrates through the system along grain boundaries, transporting melt from below and reacting with the residue in which it is injected. Spurred by difficulties explaining the origin of geochemical features in oceanic basalts (e.g. Kelemen et al., 1995; Hirschmann and Stolper, 1996; Lundstrom et al., 2000; Stracke et al., 2006), and the progressively increasing complexity of solutions to these problems, understanding this style of reactive melt migration has long been a central interest of geochemical modeling (e.g., McKenzie, 1984; Scott and Stevenson, 1986; Spiegelman, 1993; 1996; Spiegelman et al., 2001; Spiegelman and Kelemen, 2003; Liang et al., 2010; Katz and Weatherley, 2012). In our models, open-system behavior may buffer melt concentrations, effectively dragging the high compositions below the solidus to shallower depths. Such an



effect may result in MORIB La/Sm and Sm/Yb which are higher than our current models predict.

The coupling of a model of microchemical evolution and open-system melt migration, although not without numerical and computational difficulties, may fortunately minimize the problem of the high diffusivity in melt discussed previously (Sec. 5.23.4). This is because compositional heterogeneities in melt must become thoroughly mixed by advection. Consequently, an infinite-diffusivity assumption in melt at the grain-scale might be justified, and low chemical diffusivities in solids may allow the implementation of algorithms which substantially reduce computational expense.

### 5.23.6 Melting lithologies

Our models have assumed that the source of OIB is a chemically homogeneous fertile peridotite with major element compositions consistent with Herzberg (2004). However, it has become widely accepted that the compositional consistency of the mantle is that of a 'marble cake', with an enriched pyroxenite component interspersed about (Allegre and Turcotte, 1986; Hirschmann et al., 2003; Hofmann, 2006; Hirschmann and Stolper, 1996; Armienti and Gasperini, 2007; Niu et al., 2012; Ricard and Coltice, 2013). According to this view, the marble cake mantle is thought to account for variability in OIB and MORB chemistry due to different degrees of partial melting in a source that is heterogeneous in composition and age (Armienti and Gasperini, 2007; Ricard and Coltice, 2013). The differences between melt compositions generated in a pyroxenite-peridotite mixture, compared to the fertile peridotite investigated here, are not straightforward. However, we first note that our analysis has shown that, without regard to variance in the data, the average compositions of erupted lavas can be accounted for by melting of largely homogeneous fertile peridotite. On the other hand, compositional (and thus lithological) heterogeneity may account for the variance in both MORB and OIB data. The similarity in the density functions of OIB and MORB composition suggests that the extent of disequilibria might not be able to account for the scatter. Changing the final depth of melting by eroding the base of the lithosphere may impact melt concentrations erupted over 10-30 Ma seafloor, but the lack of a reduction in scatter with seafloor age indicates that the source of scatter occurs for any age. The most straightforward explanation is a compositional heterogeneity which results in a variation in the extent of melting. This may be related to major element compositional heterogeneity, such as the preferential melting of pyroxenite blocks or veins (Hirschmann and Stolper, 1996), however it is not clear how pyroxenite melting, specifically, can explain the data. For example, the pyroxenite solidus was estimated to be 35-50 km deeper than that for peridotite by Pertermann and Hirschmann (2003). If pyroxenite contributes significant mass to the production of melt, and such heterogeneities exist in all or most OIB sources, then the location of the chemical step should be shifted to greater age to correspond with a deeper solidus. It may be argued (as in Sec. 5.22) that the chemical step occurs due to mixing with ambient upper mantle, but if this is the case then ambient upper mantle should not contain significant pyroxenite. Alternatively, large variations in the extent of melting, without producing more than a few percent melt before the dry solidus of fertile peridotite, may be generated by volatile heterogeneity (Asimow and Langmuir, 2003).

Ultimately, the contribution of pyroxenite to melt signatures will have to be investigated later. Moreover, since the inference of a marble cake mantle is often based on observations in isotopic systems, the investigation of pyroxenite contributions and our hypothesis that isotopic variations may be explained by normal melting of fertile peridotite (Sec. 5.21) may be investigated jointly.

## 5.24 CONCLUSIONS

**New Melting Model.** We have developed a new model of decompression melting in the mantle, consisting of a joint simulation of microstructural and trace element microchemical evolution during solid-state phase transformations and near-fractional melting. In this model, solid-state phase transformations and melting reactions result in microstructural evolution of the source in which interstitial grains grow and melt progressively wets the boundaries of solid crystals. Due to slow rates of volume diffusion, we find that the system is likely in a state of extreme disequilibrium. The 2D microstructure and distribution of phases results in the observation of many interesting and complex microchemical disequilibrium features in the trace element distribution. The dominant solid-state phase transformation consists of the transformation of garnet into opx, resulting in inheritance of garnet signatures by opx and zoning in all phases as trace elements attempt to slowly diffuse toward new equilibrium distributions. Later, as the production of melt increases, trace elements partition into liquid and concentrations are diluted by fractional extraction, and all phases adopt REE depleted rims.

**We Explain REE in Global OIB via the LID Effect.** We find that our model effectively explains the major compositional trends of REE in all OIB, and relates them to the LID effect. The effect of seafloor age on which OIB are erupted (and thus lithospheric thickness) is strongly correlated with OIB composition. Specifically, La/Sm and Sm/Yb are low in lavas erupted on young (<15 Ma) seafloor, and step up by a factor of 2-3 on all older seafloor. Comparison to our model results indicates that this chemical step feature originates in the depth to the dry solidus. Both La/Sm and Sm/Yb are primarily affected by the extent of melting, and variation in Sm/Yb has a comparatively minor sensitivity to the presence of garnet. The relatively precise age of the chemical step and the association with the dry solidus results in a strong constraint on the temperature at the thermo-mechanical lithosphere-asthenosphere boundary (LAB). Our fits to La/Sm suggest that  $T_{LAB} \sim 1275^\circ\text{C}$ , whereas the fit to Sm/Yb suggests  $T_{LAB} \sim 1225^\circ\text{C}$ . The latter is preferred due to scatter in the La/Sm data compromising the age position of the chemical step.

**Extreme Chemical Disequilibria.** Although our default models fit the general structure of the data, Sm/Yb in our default models is predicted to be much too high over thick lithosphere compared to thin lithosphere. We have therefore examined the impact of varying the many important parameters which occur in the equations of our models. We find that the most likely causes of misfit between modeled and measured Sm/Yb include properties which affect the degree of disequilibrium (e.g., grain size), and/or the partition coefficients employed in the model. We can achieve reasonably good fits to all of the data if the grain radii (for opx, cpx, and garnet) are on the order of 2.5-5 mm. Alternatively, modifying the partition coefficients (justified based on our crude implementation of constants or the

possibility of experimental inaccuracy) can also improve the fit if some coefficients in nature are different from experiments by on the order of 50%. It is likely that a joint optimization of grain size and effective partition coefficients would require an even smaller difference.

**Properties of the OIB Source.** In addition to a strong constraint on LAB temperature, our analysis suggests that the OIB source temperature must be  $< 1400^\circ\text{C}$ , meaning that the OIB source is not significantly warmer than ambient mantle. Alternatively, if OIB sources are warm, it is necessary that erupted OIB mix with a lower temperature source, or that hot OIB sources are rare. The latter cannot be ruled out, but the first seems unlikely since it requires a fractionally large melt contribution from ambient mantle versus the OIB source. We also obtain uniquely high estimates of absolute concentration in the OIB source. Although REE ratios are similar to previous reports, the absolute bulk source concentrations of La, Sm and Yb are 2.3-2.8 times higher than previous estimates of primitive mantle (PM) and 2-7 times higher than estimates of depleted MORB mantle (DMM). Predictions of the OIB source erupting on ocean ridges, producing a Mid-Ocean Ridge Island Basalt (MORIB) composition, are within a few tens of percent of observed MORB compositions, although our prediction of La in MORIB is somewhat higher than that observed in MORB (largely due to a disequilibrium effect). Absolute MORB compositions cannot be produced in our model with previous reports of DMM composition. This simultaneous prediction of MORB-like lavas and the MOR end-member of OIB composition indicates that the sources of oceanic basalts are compositionally similar and much more enriched in REEs than previously thought.

## APPENDICES

### 5.A MELT FRACTION

Melt mass fraction is calculated for dry melting as

$$F_d = \text{if}[F_1 < F_2, \text{if}(F_1 < 0, 0, F_1), F_2] \quad (5.37)$$

with

$$\begin{aligned} F_1 &= C + DP, \\ F_2 &= E(P + 0.5)^{-1/3}, \\ C &= aT_p^5 + bT_p^4 + cT_p^3 + dT_p^2 + eT_p + f, \end{aligned} \quad (5.38)$$

where  $a=6.2961615 \cdot 10^{-13}$ ,  $b=-4.80539528654 \cdot 10^{-9}$ ,  $c=0.0000146123041228641$ ,  $d=-0.0221277679681786$ ,  $e=16.688659160847$ , and  $f=-5015.32649568478$ .

$$D = aT_p^4 + bT_p^3 + cT_p^2 + dT_p + e, \quad (5.39)$$

where  $a=-2.37952415 \cdot 10^{-12}$ ,  $b=1.515094358784 \cdot 10^{-8}$ ,  $c=-0.000035700039669403$ ,  $d=0.037002595533383$ , and  $e=-14.4077741343854$ ,

and

$$E = aT_p^5 + bT_p^4 + cT_p^3 + dT_p^2 + eT_p + f, \quad (5.40)$$

where  $a=0.000000000000275932$ ,  $b=-0.000000002078214327$ ,  $c=0.0000062338200851$ ,  $d=-0.00930716444515817$ ,  $e=6.91618606938352$ , and  $f=-2046.33137198094$ .

With an additional contribution from wet melting, the total melt fraction as a function of depth is

$$F(z) = \max [F_d, F_w, 0],$$

where  $F_d$  is the dry extent of melting and  $F_w$  is a wet melting contribution given by

$$F_w = (z_d(T_p) - z) \frac{F_{w,max}}{\Delta z_{dw}} + F_{w,max}$$

where  $z_d$  is the dry solidus depth,  $z$  is depth,  $F_{w,max}$  is the extent of wet melting at the dry solidus depth, and  $\Delta z_{dw}$  is the distance between the dry and wet solidus.

Note that we expect some errors to arise due to our assumption that residual compositions are a function of  $T_p$  and extent of melting only. Thus, our wet fractional melting models at 1% melting will have removed the same chemical components as dry fractional melting, even though wet melting will occur at greater depths.

## 5.B RESIDUAL COMPONENTS

Mass fractions of components  $\text{SiO}_2$ ,  $\text{Al}_2\text{O}_3$ ,  $\text{FeO}$ , and  $\text{MgO}$  in residues are based on fits to compositional data from polybaric perfect fractional melting of the peridotite KR-4003 (Herzberg, 2004). We obtain the following fits to compositions as a function of melt mass fraction  $F$  and mantle potential temperature  $T_p$ .

$$M_{\text{SiO}_2} = \exp \left( -\frac{F^A}{fT_p + g} \right) h + (iT_p^3 + jT_p^2 + kT_p + l)F, \quad (5.41)$$

where

$$A = (aT_p^4 + bT_p^3 + cT_p^2 + dT_p + e),$$

and where  $a=-0.00000000026008$ ,  $b=0.0000014628$ ,  $c=-0.003054044$ ,  $d=2.80959$ ,  $e=-958.644$ ,  $f=-0.00008196171$ ,  $g=0.25897$ ,  $h=44.9$ ,  $i=-0.000000036156929$ ,  $j=0.000148755940732$ ,  $k=-0.190501612151735$ , and  $l=72.2968884540246$ .

$$M_{\text{Al}_2\text{O}_3} = \exp \left( -\frac{F^{(aT_p+b)}}{c} \right) (d + BF) \quad (5.42)$$

where  $B = eT_p^5 + fT_p^4 + gT_p^3 + hT_p^2 + iT_p + j$  and  $a=0.0049177$ ,  $b=-2.3380249$ ,  $c=0.0035$ ,  $d=4.3$ ,  $e=1.856068303 \cdot 10^{-11}$ ,  $f=-1.4007815610868 \cdot 10^{-7}$ ,  $g=0.00042138319547678$ ,  $h=-0.631525301009316$ ,  $i=471.539287680339$ , and  $j=-140354.043752457$ .

$$M_{\text{FeO}} = a + (bT_p^3 + cT_p^2 + dT_p + e)F + \exp(F/f) \quad (5.43)$$

where  $a=7$ ,  $b=0.000000121222$ ,  $c=-0.000535114228$ ,  $d=0.761892997052$ ,  $e=-352.243373301817$ , and  $f=0.5$ .

$$M_{\text{MgO}} = a + (bT_p + c)F + \exp\left(\frac{F}{dT_p + e}\right) \quad (5.44)$$

where  $a=37$ ,  $b=-0.043920053745$ ,  $c=84.804081289889$ ,  $d=0.000054988$ , and  $e=0.11658$ .

The component CaO is estimated following Afonso and Schutt (2012) as

$$M_{\text{CaO}} = a + bM_{\text{Al}} \quad (5.45)$$

where  $a=-0.164$  and  $b=0.906$ .

After all components are estimated for a given  $F - T_p$  condition the sum is recast to 100% and mineral modes are calculated from the equilibrium thermodynamic model of Connolly (2009).

## 5.C Model Validations

### 5.C.1 Diffusive partitioning

The primary source of error in our simulations is the grid spacing. This error is particularly important to quantify in our models because our simulations are performed at a somewhat low resolution (120-by-120) due to the nature of our exploratory analyses, high diffusion rates for the simulated time, and an expensive stability criterion due to the properties of melt. Benchmarks of error due to grid resolution are shown in Fig. 5.66, 5.67, and 5.68. The problem solved is one of 1D diffusive partitioning with insulating boundaries, a crystal interface at the center, and a different partition coefficient for each side of the model (i.e., each crystal). The high-resolution model uses  $x_{\text{num}}=1000$  nodes, such that 500 are phase A and 500 are phase B. Low-resolution models test the value of  $x_{\text{num}}$  at 250, 100, and 50. Also, the partition coefficients are varied. The partition coefficient on the right-hand side of the model is always unity, whereas the left-hand side is  $\delta K = 0$ , 0.1, or 4. For each of the 9 resulting test models, we quantify the error by computing the difference to the high resolution model. The panels on the left are the concentrations in the model, and the panel on the right is the error. Since our models are comparable to the case of  $x_{\text{num}}=50$ , the error in our models is expected to be on the order of at least a few percent. On the other hand, it is good that the error is significantly reduced for the model with  $x_{\text{num}}=250$ . This is because we expect future modeling efforts to be accelerated by shifting Ostwald ripening behavior from being controlled by the Potts model, to being controlled by a solution to thermodynamic partial differential equations, which are more easily accelerated by advanced methods.

### 5.C.2 Potts model resolution

An additional source of error related to the grid resolution is the operation of the Potts model. The model domain uses periodic boundary conditions both for ostwald ripening and diffusive partitioning. As the grid resolution decreases, the grain size becomes a larger fraction of the domain area, which can cause an artificial sensitivity to boundaries in coarsening, disrupting the development of grain textures and chemical exchanges in the neighborhood of all points.

The effect that this behavior has on our model results is shown in terms of predicted Sm/Yb in Fig. 5.69. We compute as many models sufficient to represent approximately a  $536 \times 536$  area which represents about a  $20 \text{ cm}^2$  area. Thus we compute 320 models of  $30 \times 30$  resolution, 80 models of  $60 \times 60$  resolution, 20 models of  $120 \times 120$  resolution, etc. Subsequently, all models of the same type are averaged together. The results in Fig. 5.69 are for each  $N \times N$  model. These results suggest that the  $120 \times 120$  resolution of our models is adequate, but the results of a significantly lower resolution model will be compromised by its low resolution.

### 5.C.3 Mass conservation

During the transformation of melt from solid and the extraction of melt in our models, masses are moved around, or removed from, the model. It is important to ensure that mass is conserved throughout these transport processes. Therefore, we show the mass conservation error for Lanthanum in a typical model in Fig. 5.70. The top panel shows the La mass residing in the residue (melt+solid), the extracted mass, and the total. The bottom panel shows the error in total mass fraction (black line in top panel, minus 1).

## 5.D Curve Mapping

To help establish a link between the values of misfit and the actual predictions for melt concentration evolution, we have illustrated melt concentration curves predicted by our models in Fig. 5.30 and Fig. 5.53. This graphical illustration of melt concentration curves is biased toward low-misfitting models such that the curve represented at each pixel is a strongly non-linear weighted average:

$$\epsilon_m = \frac{\sum w(1 - m)^{200}m}{\sum w(1 - m)^{200}}$$

where  $\epsilon_m$  is the misfit value at the pixel,  $w$  is a weight of linear interpolation to the pixel, and  $m$  is the misfit of each model (represented by a curve). This essentially forces best fitting models to be shown in the foreground. Less well fitting models are still observed since their poor fits result in their occurrence in space where good fitting models do not. Based on our inspection of these figures, we consider that the demarcation between good and inadequately fitting models is about 0.12. It should be noted that the representation of the data in these figures, compared to the model predictions, is not exactly correct. This is because the final depth of melting of each volcanic center is not known, only the age is known. Thus we have used an LAB isotherm from a model of oceanic lithosphere (Chapter 3) to estimate the final melting depth. However, the LAB temperature has been fitted for each individual model. As seen in the top right panel in Fig. 5.53, for all models  $T_{LAB} \sim 1230 - 1300^\circ\text{C}$ , so we have chosen to compare the model predictions to the data using  $T_{LAB} \sim 1275^\circ\text{C}$  as a reasonable average. On the other hand, the best fit  $T_{LAB}$  for Sm/Yb varies through the whole range considered ( $1000\text{-}1300^\circ\text{C}$ ). However, we chose to illustrate the data using  $T_{LAB} = 1225^\circ\text{C}$  since this is where the best fitting models occur. This results in a slightly misleading mismatch between models with low  $T_{LAB}$  and the data. For example, the models

with  $T_{LAB} \sim 1000^\circ\text{C}$  occur at shallower depths because the data would also be shifted to such a shallower depth if this isotherm had been used (see Fig. 5.21).

## 5.E SMOOTHING

Because of microstructural complexity and small digitized grid (120x120), melt concentration curves tend to vary about a mean (Fig. 5.32). Initially, to obtain a more consistent picture of the predictions of a particular parametric model configuration, we resolved to simply run a number of the same models having the same properties, and averaging the curves of melt concentration. The number of models needed to obtain a repeatable result within a few percent variation is on the order of 10-20. Of course, the size of the model may simply be increased by this amount, but running separate models has obvious parallelization benefits. While this approach is ideal for obtaining consistent and repeatable predictions of a particular model configuration, it is needlessly exhaustive for parametric sensitivity analysis. Instead, as the density of models sampling the parameter space of  $Z_{grt}$  and  $Z_{cpx}$ , as described above, is reasonably large, we smooth the noise using a finite-difference solution to a diffusion equation:

$$\Delta C_k(z, Z_{grt}, Z_{cpx}) = L \sum_n^4 [C_k^n(z, Z_{grt}, Z_{cpx}) - C_k(z, Z_{grt}, Z_{cpx})] \quad (5.46)$$

where  $z$  is the final depth of melting,  $Z_{grt}$  and  $Z_{cpx}$  are the partition coefficient adjustment factors for the chemical element  $k$ ,  $L$  is a smoothing coefficient, and  $n$  indicates a neighboring element. The equation is solved for 10 steps with  $L=0.1$ , using 'insulating' boundaries, and where  $Z_{grt}$  and  $Z_{cpx}$  are the dimensions over which diffusion is performed.

	Olivine/Melt	Opx/Melt	Cpx/Melt	Grt/Melt	Melt/Melt	Reference
La	0.00015	0.0033	0.0328	0.007625	1.0	Salters et al. (2002)
Sm	0.0013	0.0188	0.1352	0.22125	1.0	Salters et al. (2002)
Yb	0.0305	0.0988	0.3432	3.95425	1.0	Salters et al. (2002)
La	0.000001	0.0006	0.03	0.005	1.0	Adam and Green (2010)
Sm	0.0001	0.011	0.25	0.164	1.0	Adam and Green (2010)
Yb	0.017	0.077	0.43	4.54	1.0	Adam and Green (2010)

TABLE 5.1: Partition coefficients used in this study.

	Melt	Olivine	Opx	Cpx	Grt
$C_e(\text{La})$	-7	-9.097	-11.6	-4.22	-8.47
$C_e(\text{Sm})$	-7	-9.097	-11.6	-4.453	-8.47
$C_e(\text{Yb})$	-7	-9.097	-11.6	-4.64	-8.47
$A_e(\text{La})$	289	289	233	466	322
$A_e(\text{Sm})$	289	289	233	435	322
$A_e(\text{Yb})$	289	289	233	411	322
$A_V(\text{La})$	10	10	10	10	20
$A_V(\text{Sm})$	10	10	10	10	20
$A_V(\text{Yb})$	10	10	10	10	20

TABLE 5.2: Chemical diffusivity coefficients used in this study.



	Mean( $m < 0.05$ )	HMB
$T_{LAB}(\text{La/Sm}), ^\circ\text{C}$	1274.2	15
$T_{LAB}(\text{Sm/Yb}), ^\circ\text{C}$	1230.2	15
$\text{La}_{bsrc}, \text{ ppm}$	1.4	0.35
$\text{Sm}_{bsrc}(\text{La/Sm}), \text{ ppm}$	0.8	0.21
$\text{Sm}_{bsrc}(\text{Sm/Yb}), \text{ ppm}$	1.0	0.54
$\text{Yb}_{bsrc}, \text{ ppm}$	0.8	0.41
$[\text{La/Sm}]_{bsrc}$	1.8	0.27
$[\text{Sm/Yb}]_{bsrc}$	1.3	0.33
$\text{La}_{oib}, \text{ ppm}$	46.4	1.0
$\text{Sm}_{oib}(\text{La/Sm}), \text{ ppm}$	10	0.0
$\text{Sm}_{oib}(\text{Sm/Yb}), \text{ ppm}$	10	0.0
$\text{Yb}_{oib}, \text{ ppm}$	2.4	0.05
$[\text{La/Sm}]_{oib}$	4.6	0.12
$[\text{Sm/Yb}]_{oib}$	4.3	0.1
$\text{La}_{morib}, \text{ ppm}$	8.3	1.65
$\text{Sm}_{morib}(\text{La/Sm}), \text{ ppm}$	4.4	0.85
$\text{Sm}_{morib}(\text{Sm/Yb}), \text{ ppm}$	5.2	2.9
$\text{Yb}_{morib}, \text{ ppm}$	3.6	2.05
$[\text{La/Sm}]_{morib}$	1.9	0.27
$[\text{Sm/Yb}]_{morib}$	1.5	0.32

TABLE 5.3: Properties obtained from inversions with variable partition coefficients. Note that while these values are precise, the HMB are not indicators of accuracy. Precise values are obtained due to the assumption that  $\text{Sm}_{oib}=10$  ppm is exact, whereas it actually has a standard deviation of  $\sim 20\%$  (Fig. 5.62)

	WH05	SM89	LK07	This Study
La (DMM), ppm	0.192			1.4
Sm (DMM), ppm	0.239			0.9
Yb (DMM), ppm	0.365			0.8
La/Sm (DMM)	0.8			1.56
Sm/Yb (DMM)	0.66			1.13
La (PM), ppm		0.689	0.508	1.52
Sm (PM), ppm		0.444	0.324	0.92
Yb (PM), ppm		0.493	0.346	0.81
La/Sm (PM)		1.55	1.57	1.65
Sm/Yb (PM)		0.9	0.94	1.14

TABLE 5.4: Comparison of previous estimates of the REE compositions of Depleted MORB Mantle (DMM) and Primitive Mantle (PM) with our calculations using OIB source composition as a proxy to the composition of a uniform depleted mantle reservoir.

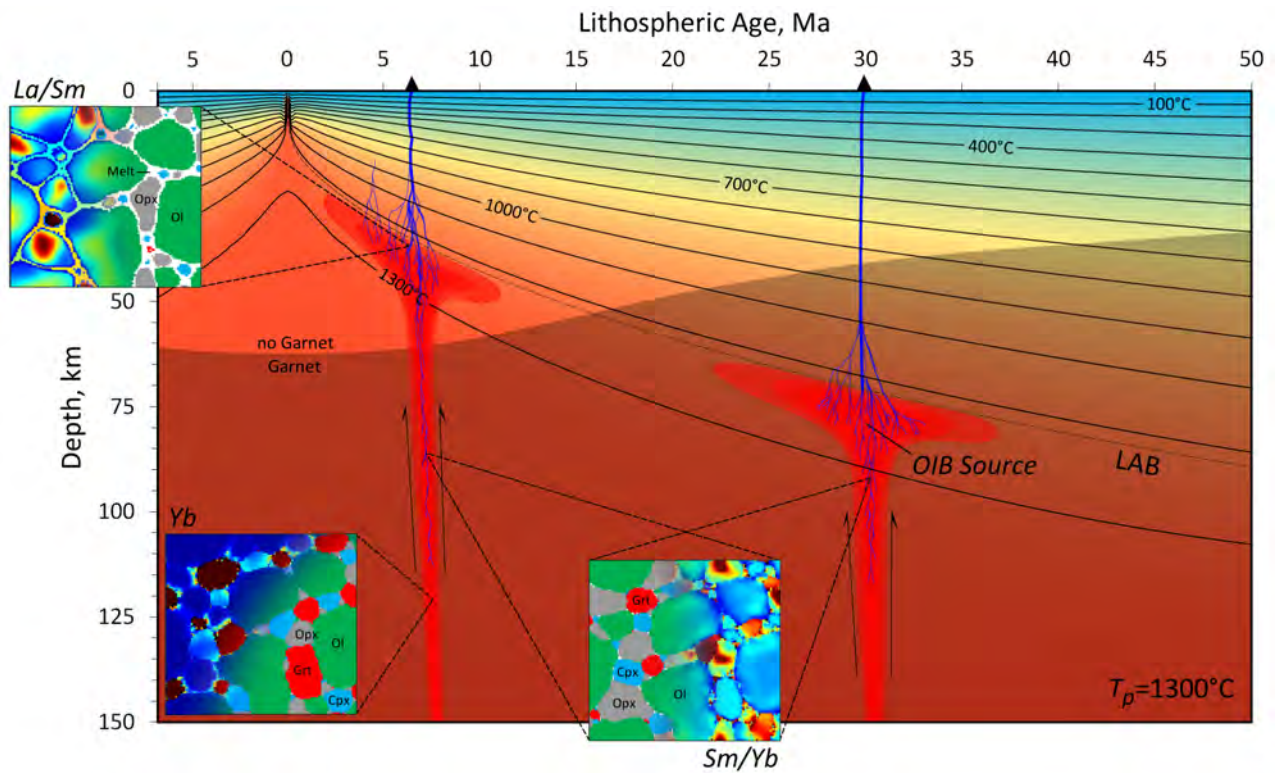


FIGURE 5.1: Illustration of the oceanic lithosphere cooling and thickening with distance and age from the ridge axis. Isotherms are to scale based on the model developed in Chapter 3 for  $T_p = 1300^\circ\text{C}$ . Also shown are plume-like conduits which ascend in the mantle until interrupted by mechanical interaction with the base of the lithosphere (LAB). The three small images illustrate examples of microstructure and microchemistry which our melting model predicts to exist in the ascending OIB source.

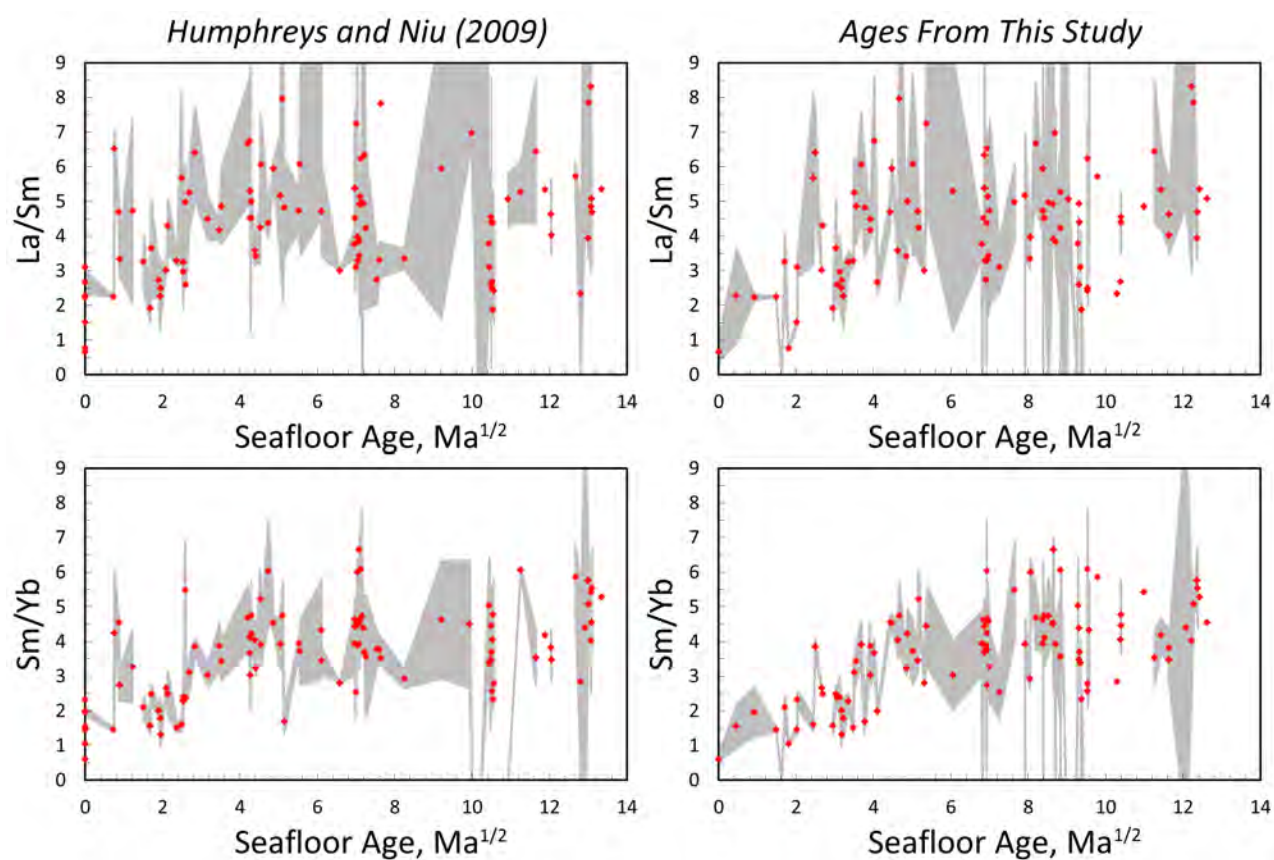


FIGURE 5.2: Graphs of OIB geochemical data for La/Sm and Sm/Yb (with no normalizations) from Humphreys and Niu (2009) on the left, compared to our reconstructions using the same chemical data with our estimates of seafloor age. The grey areas are standard deviations from Humphreys and Niu's (2009) dataset.

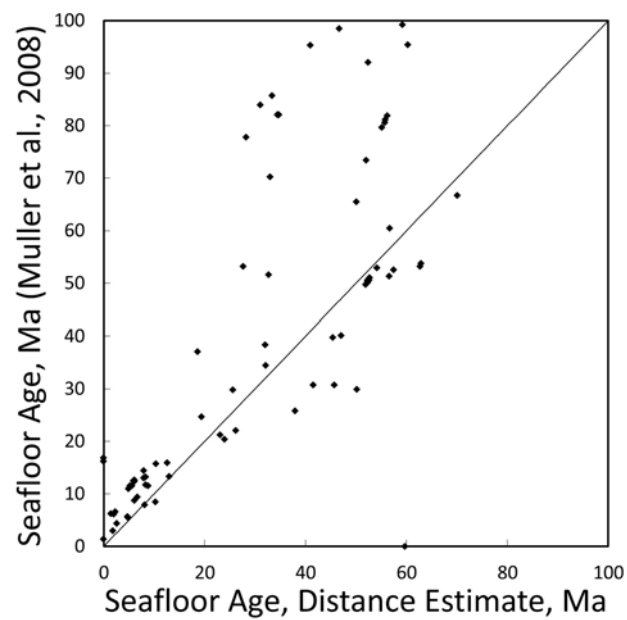


FIGURE 5.3: Difference in ages using the distance to ocean ridges estimate in Humphreys and Niu (2009) compared to our estimates using the global database of Müller et al. (2008).

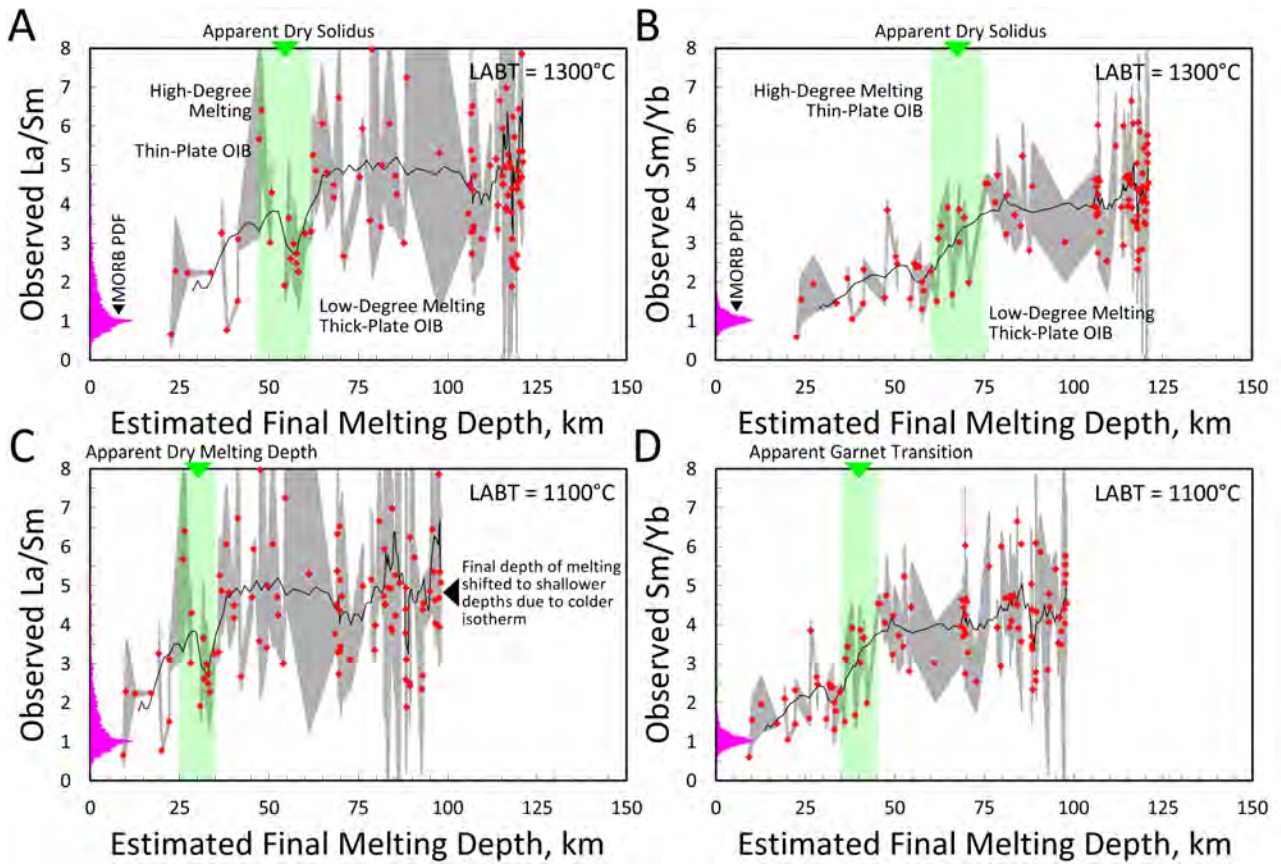


FIGURE 5.4: La/Sm and Sm/Yb systematics as a function of the final depth of melting. In the top figures the final depth of melting is based on the 1300°C isotherm from the model we developed in Chapter 3 (for  $T_p = 1300^\circ\text{C}$ ). The bottom figures are the same, except using the 1100°C isotherm. The green bar highlights the region where the step-like feature occurs in the data, which we associate with the dry solidus.

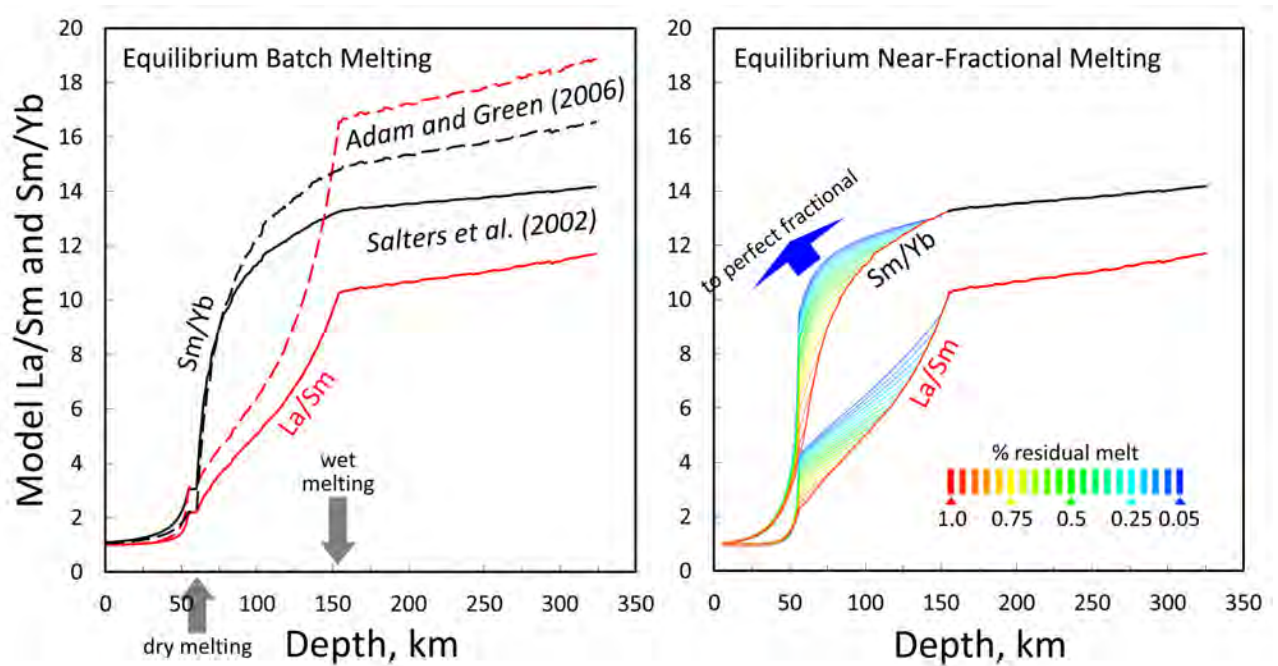


FIGURE 5.5: Equilibrium batch melting (left) and near-fractional melting (right) models using our thermodynamically constrained equilibrium restite assemblage ( $T_p = 1300^\circ \text{C}$ ) and partition coefficient databases of Adam and Green (2006) as dashed lines, and Salters et al. (2002) as solid lines. The red lines are predictions of La/Sm and black lines are for Sm/Yb. Near-fractional melting models use Salters et al. (2002) database only. Results for 20 near-fractional melting models are shown with the amount of residual melt varied between 0.05 and 1.0%. The depths at which wet melting and dry melting occur in our models are indicated.



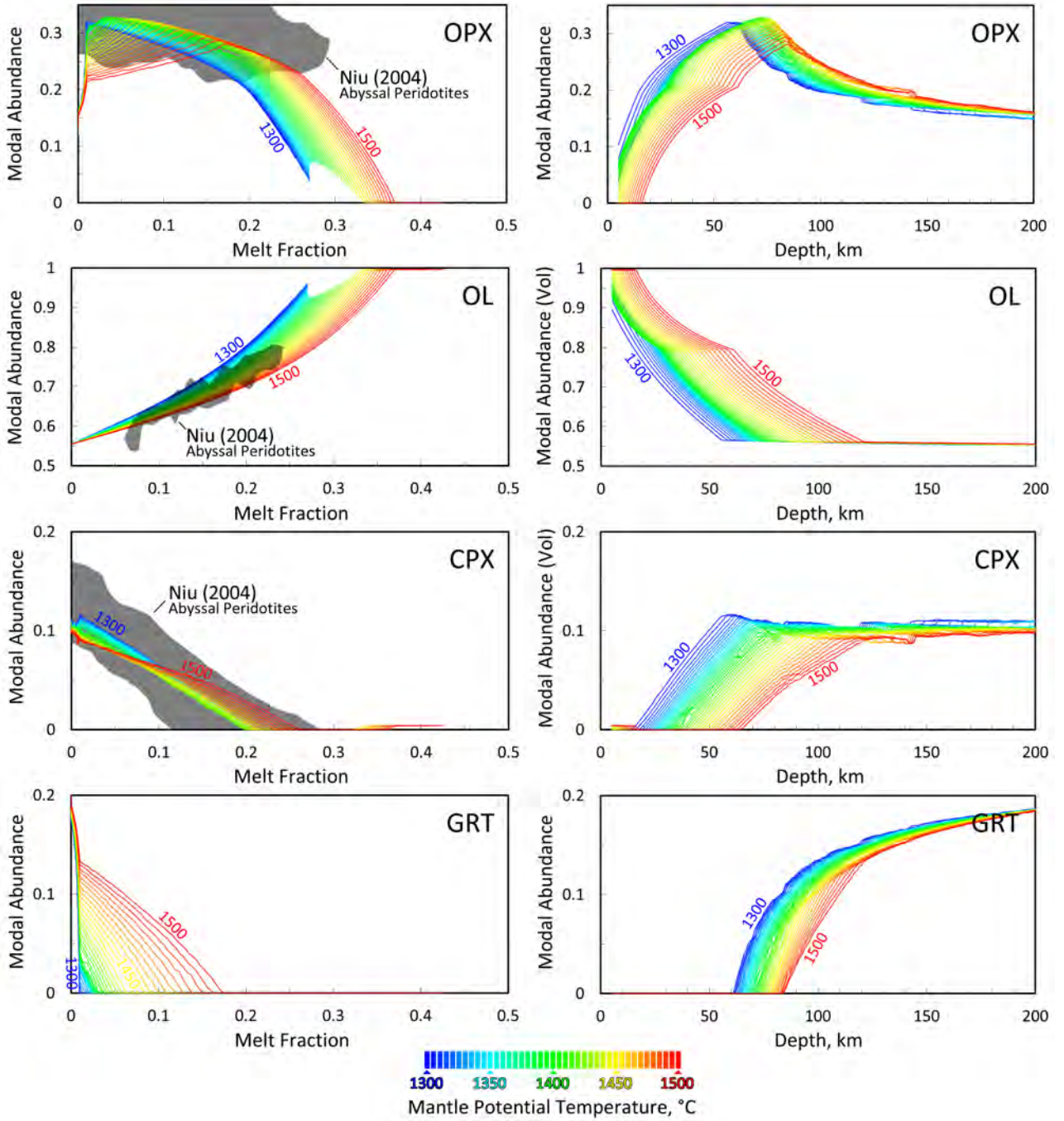
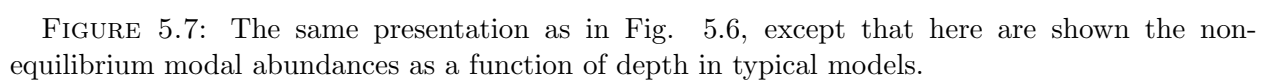


FIGURE 5.6: Restite phase equilibria for  $T_p = 1400 \pm 100^\circ\text{C}$  as a function of total melt fraction (left panels) and depth (right panels) calculated as described in Sec. 5.5. The grey highlighted regions are modal abundances of abyssal peridotites as a function of melt fraction from Niu (2004).





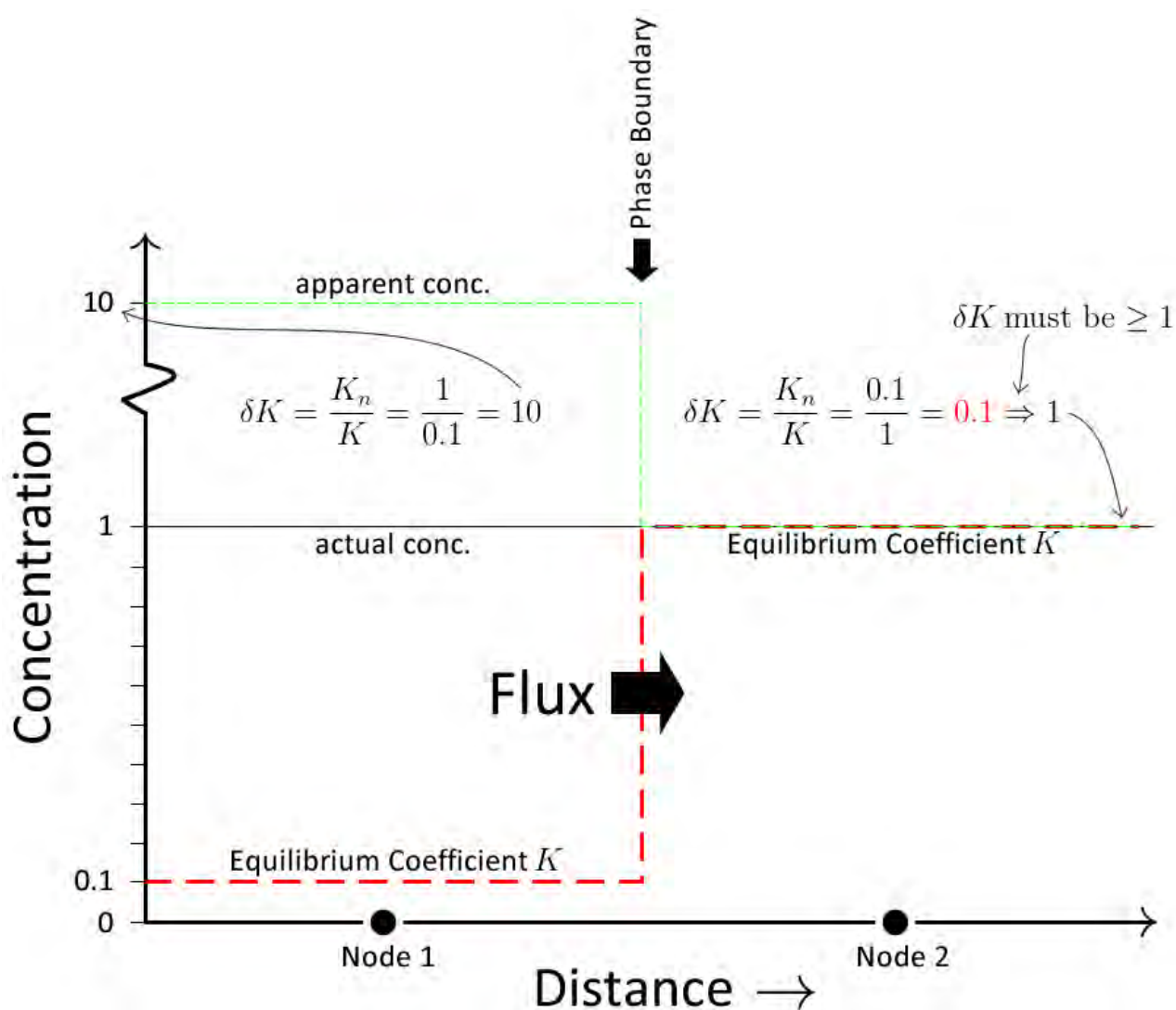


FIGURE 5.8: Adjustment of concentrations for flux determination across phase boundaries. For each calculation of flux between neighboring elements (or nodes), the neighbor with the lower partition coefficient has its concentration multiplied by the factor  $\delta K$ , while the concentration of the other node is unchanged. In the case illustrated here, since the apparent concentration of Node 1 is greater than Node 2, a flux will occur in the direction of Node 2.

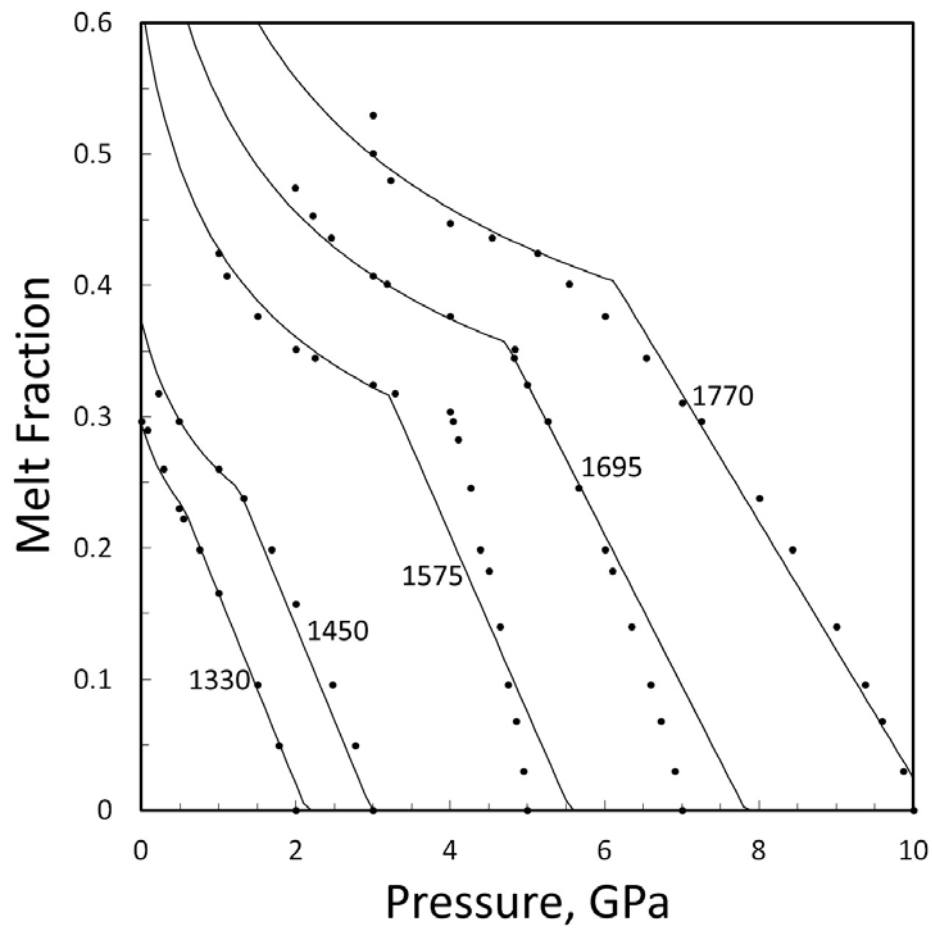


FIGURE 5.9: Total melt fraction for dry fertile peridotite as a function of pressure. The dots are predictions of Herzberg (2004) and the lines are our 'fits'. The large misfit for some temperatures is due to our attempt to fit a single function to all of the data. It is not clear to us if the changes in the slope of melt production observed in the experiments is real or if our approximation does not capture complex variations in the melting process.

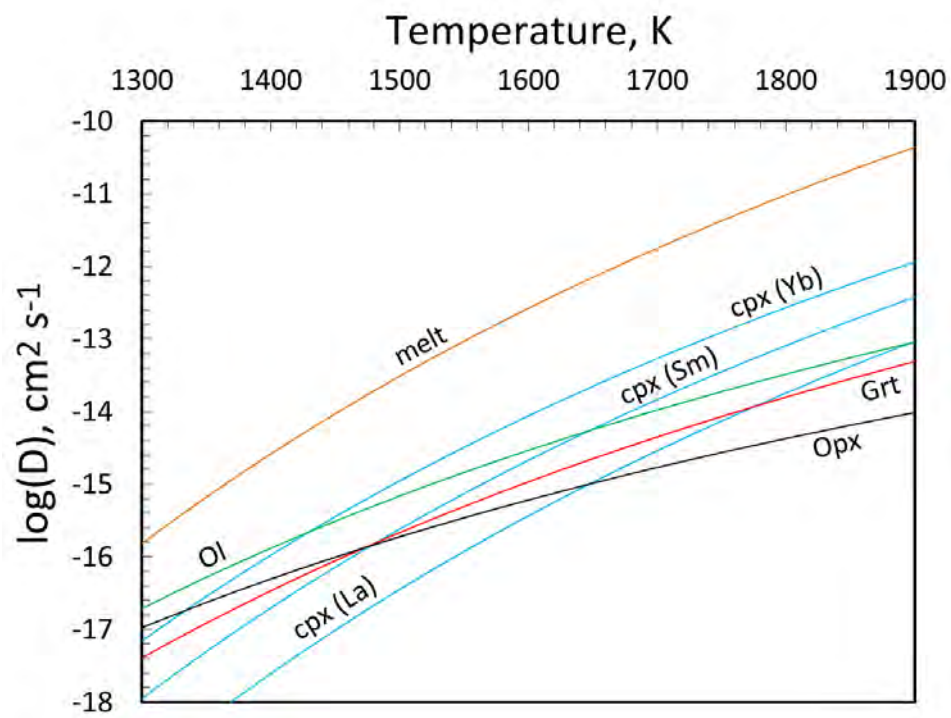


FIGURE 5.10: Chemical diffusivities as a function of temperature used in this study. Note that mineral diffusivities are taken from the literature, but melt diffusivity is estimated. See Table 5.24 for diffusion coefficient parameters.

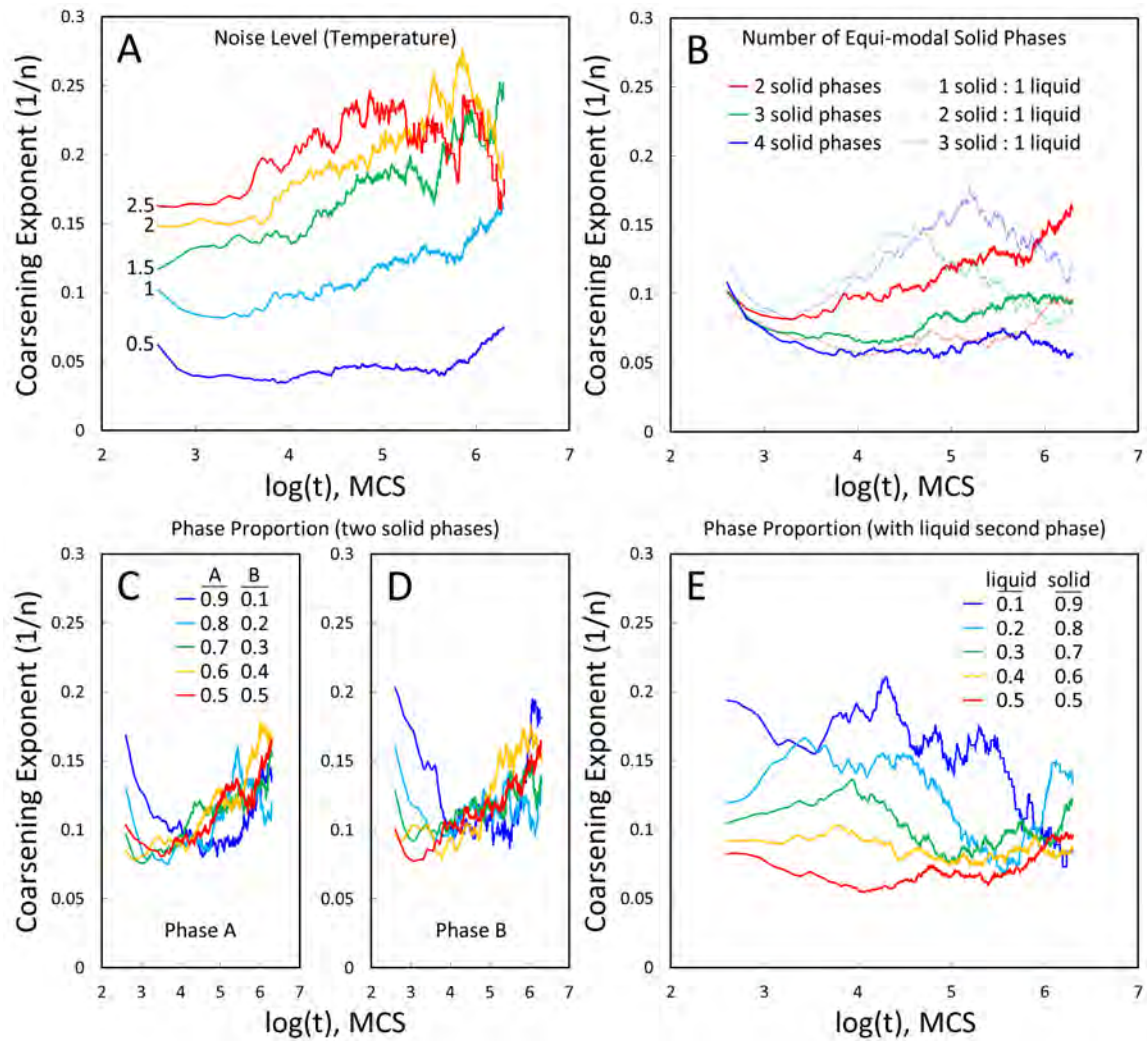


FIGURE 5.11: Results of coarsening experiments shown in terms of the coarsening exponent  $1/n$  as it changes over time (or Monte-Carlo step). See text for discussion.



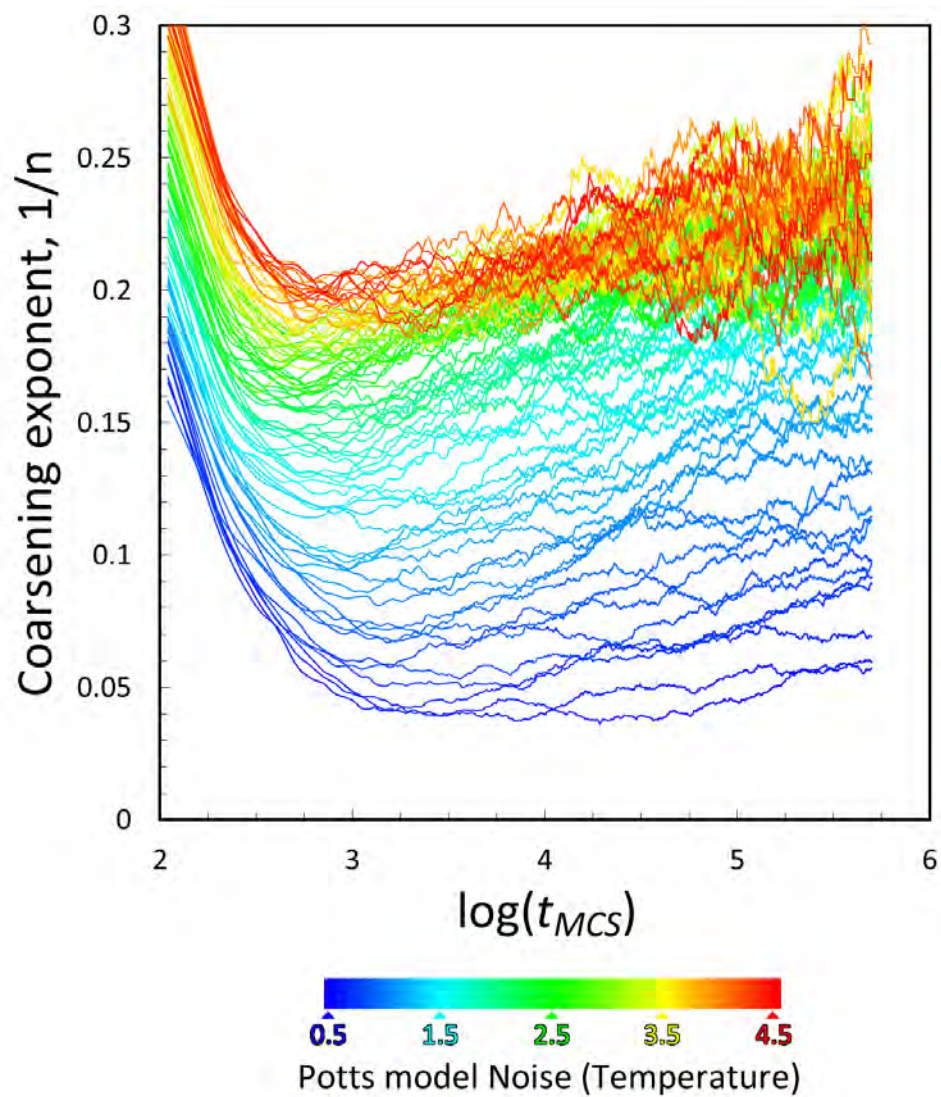


FIGURE 5.12: A dense survey of coarsening exponents fitted to the predictions of our Potts models as a function of model noise (or temperature),  $K_T$ .

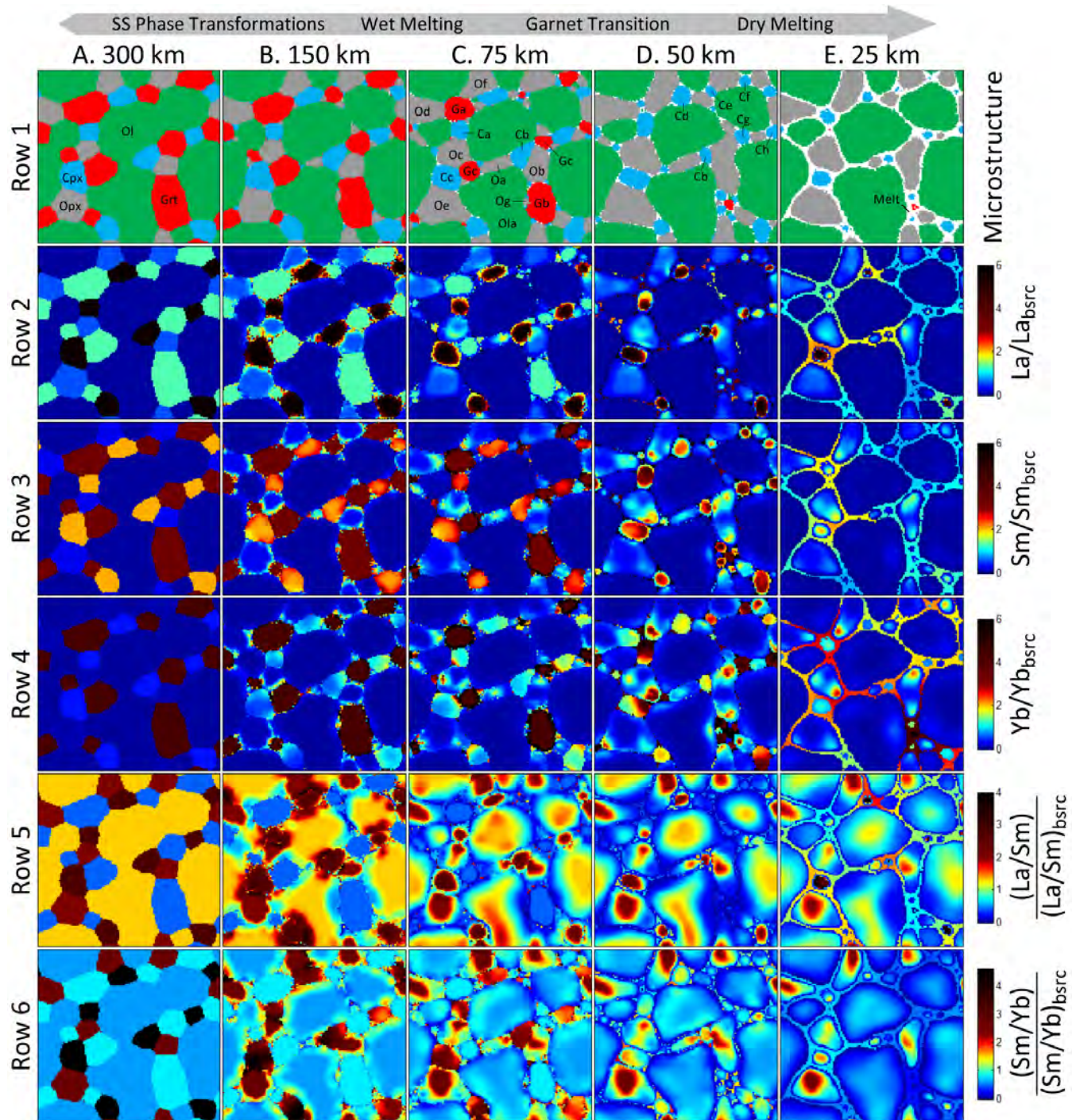


FIGURE 5.13: Results of a typical model with default properties ( $v_z=1$  m yr $^{-1}$ ,  $G_r=1$ ,  $T_p = 1300^\circ\text{C}$ ,  $\phi_r=0.05\%$ ). The top panels (row 1) show the microstructure with colors corresponding to phases as labeled in the first panel. The labeling of individual crystals shown in panel C1 and D1 are for the purposes of discussion in the text. The remaining panels in Rows 2-6 show microchemical predictions with concentrations given relative to bulk source concentration (i.e., the average concentrations found in column 1).



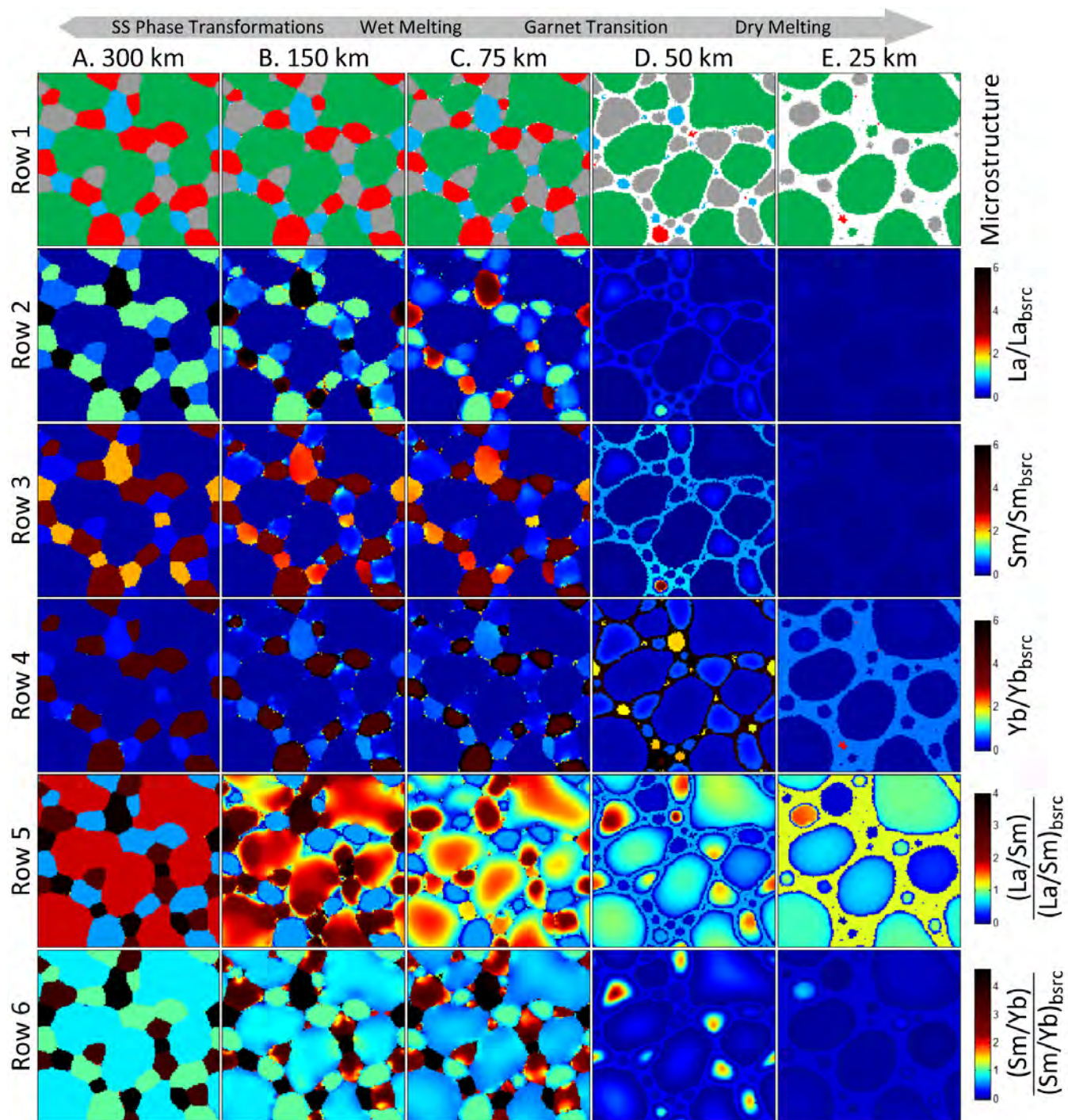


FIGURE 5.14: Same visualization as in Fig. 5.13, except that the mantle potential temperature  $T_p = 1500^\circ\text{C}$  is used.



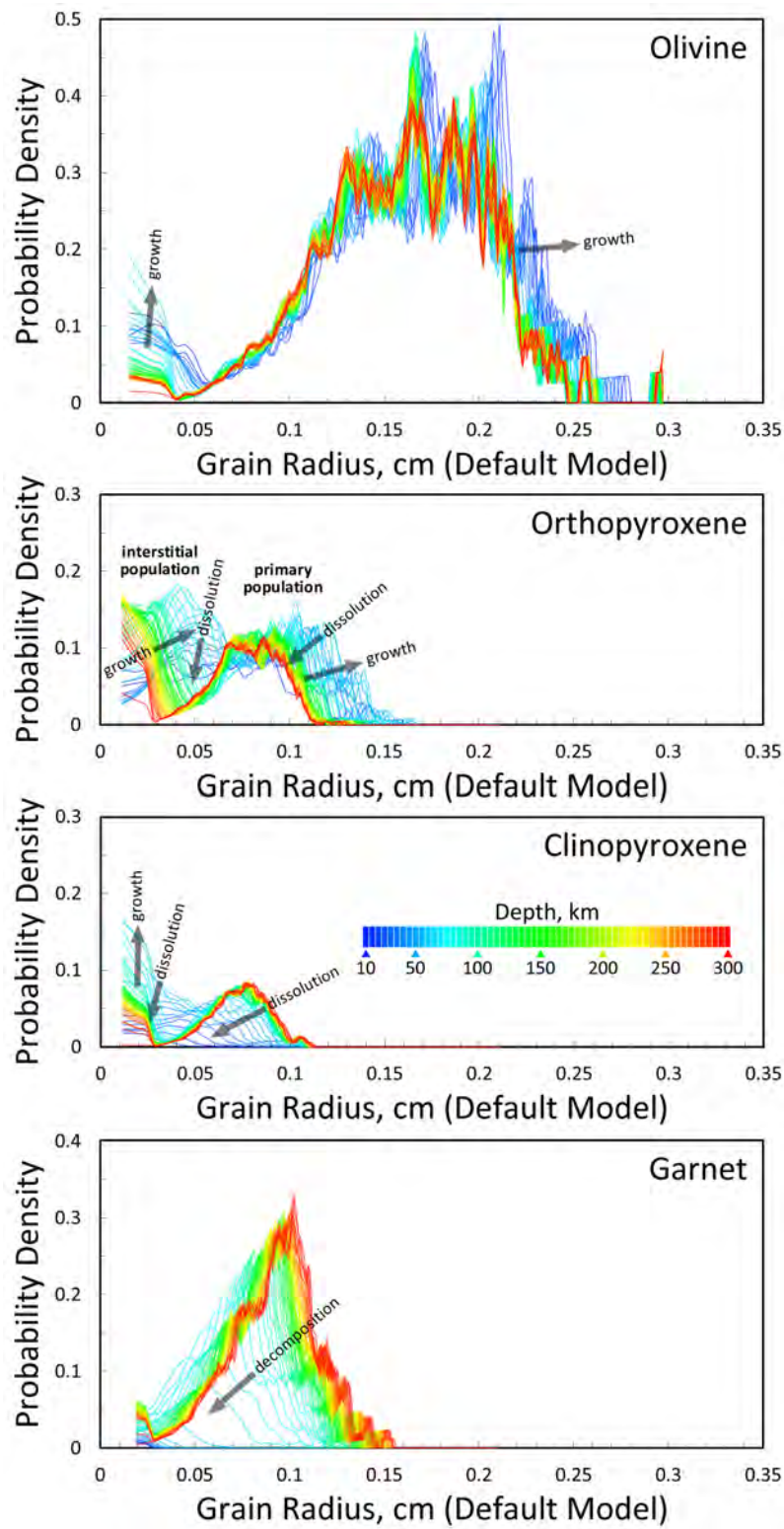


FIGURE 5.15: Probability density functions for the grain size in the OIB source as a function of depth for mineral modes olivine, orthopyroxene, clinopyroxene, and garnet. All results here are for our default model where the model domain size is  $1 \text{ cm}^2$ .

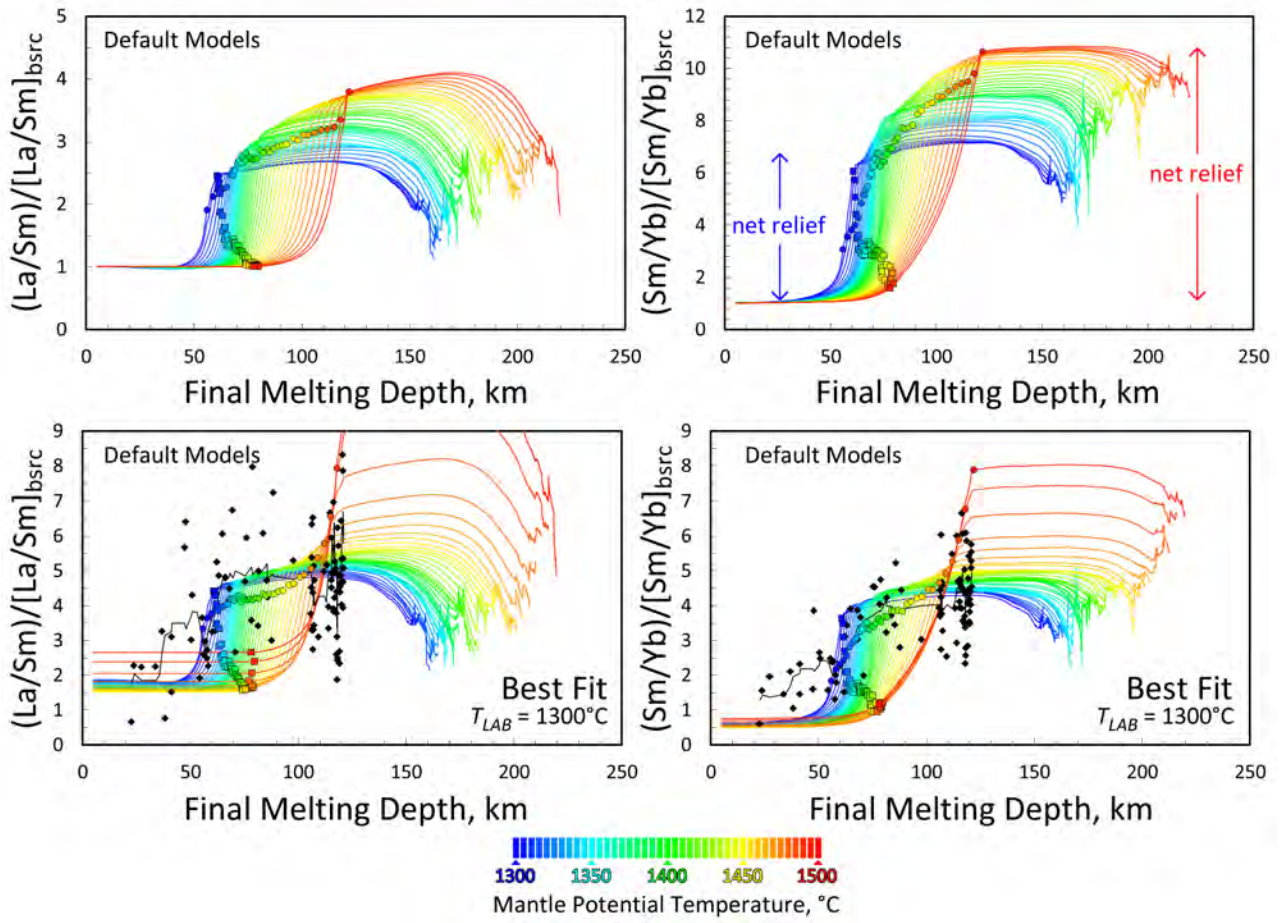


FIGURE 5.16: Predicted La/Sm (left) and Sm/Yb (right) as a function of final melting depth in our default models with  $T_p$  varied between 1300 and 1500°C. The top figures show model results normalized to bulk source concentration. Bottom figures show the same models with source concentration adjusted to best fit the data (black dots). The colored open circles and squares are the depth of dry melting and garnet transition, respectively.

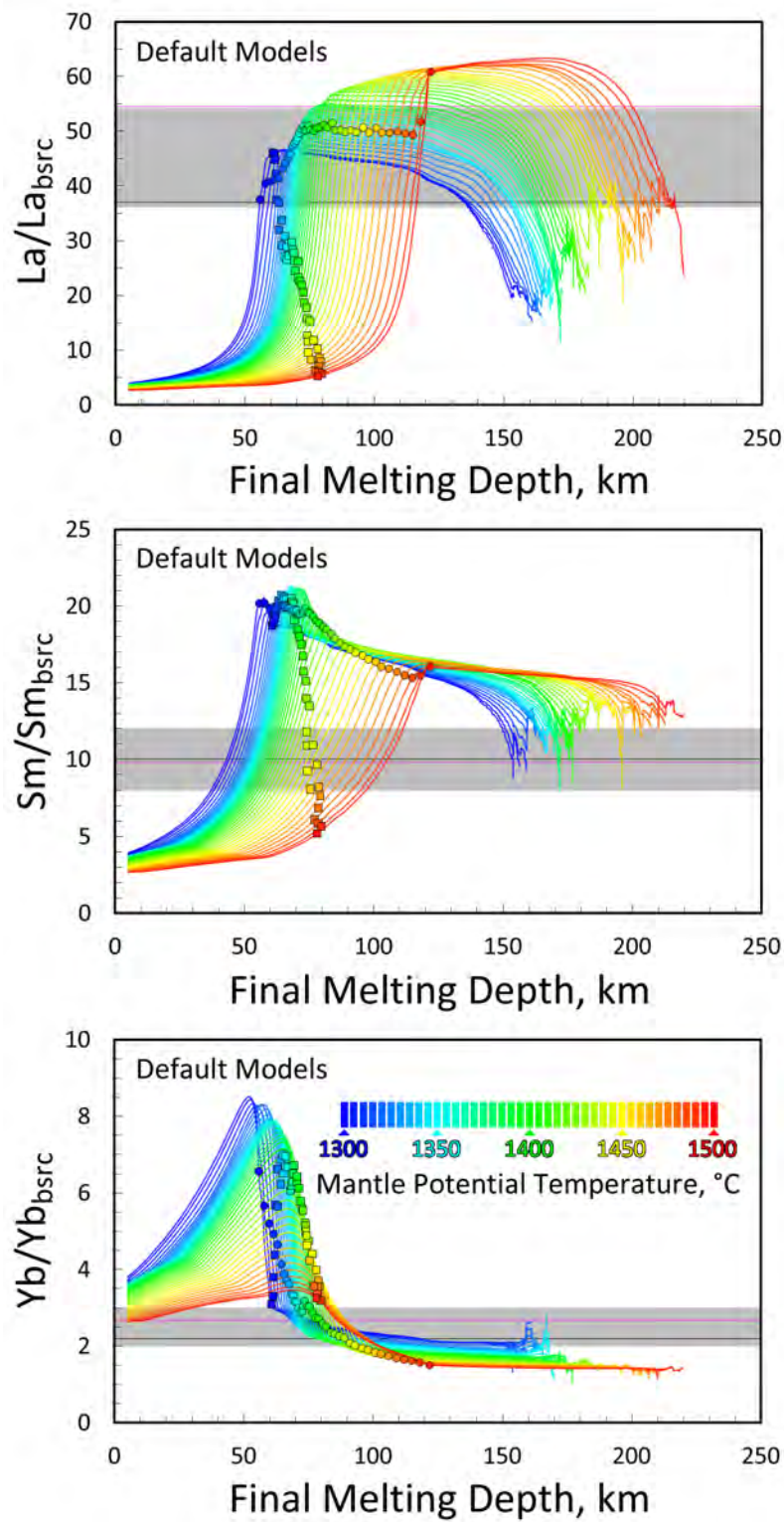


FIGURE 5.17: Predicted La, Sm, and Yb concentrations in erupted OIB, normalized to bulk source concentration, in our default models with  $T_p$  varied between 1300 and 1500°C. Horizontal bars are ranges of possible thick-plate OIB concentration, the horizontal black line are OIB concentrations from Sun and McDonough (1989), and pink horizontal lines are our estimates of thick-plate OIB from the GEOROC database.

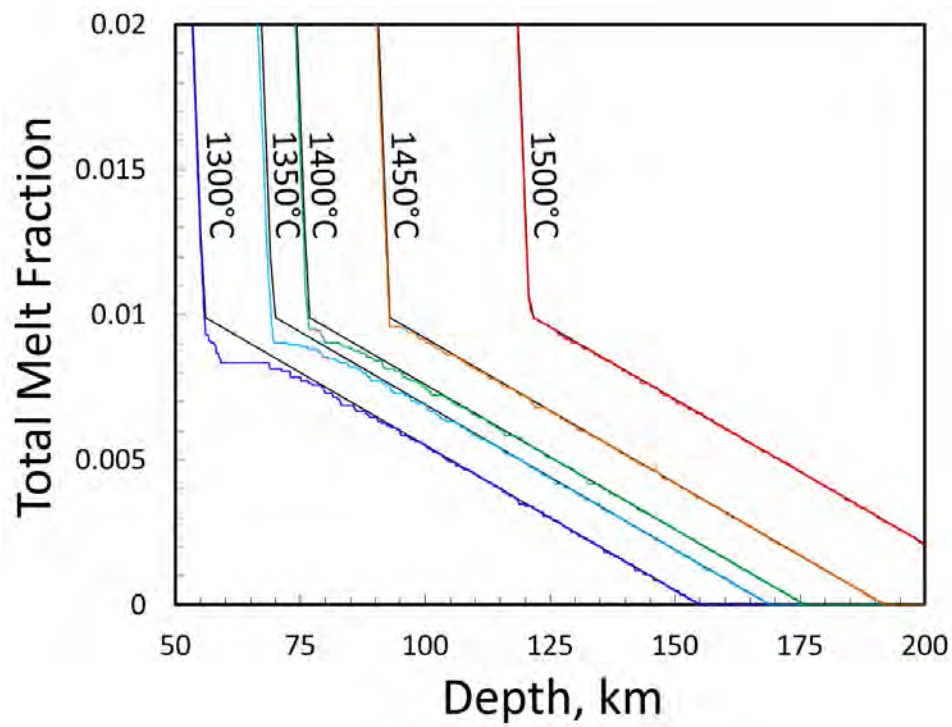


FIGURE 5.18: Comparison of the input model total melt fraction as a function of depth (black) with the non-equilibrium output model result (colored lines) for mantle potential temperatures between 1300 and 1500°C



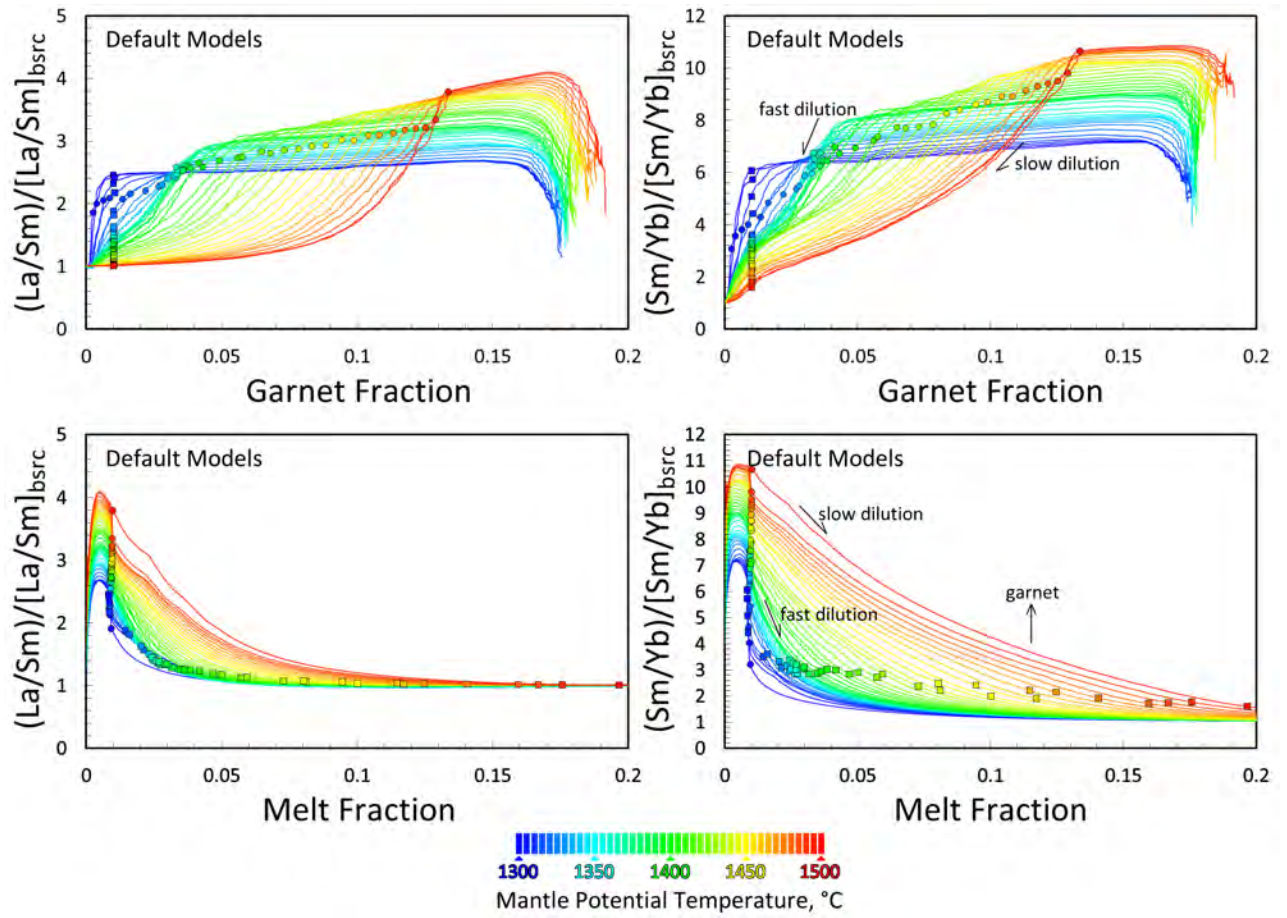


FIGURE 5.19: Predicted La/Sm and Sm/Yb, normalized to bulk source concentration, for default models with  $T_p = 1300\text{--}1500^{\circ}\text{C}$ , as a function of garnet fraction (top panels) and total melt fraction (bottom panels). The color of lines corresponds to potential temperatures indicated in the scale.

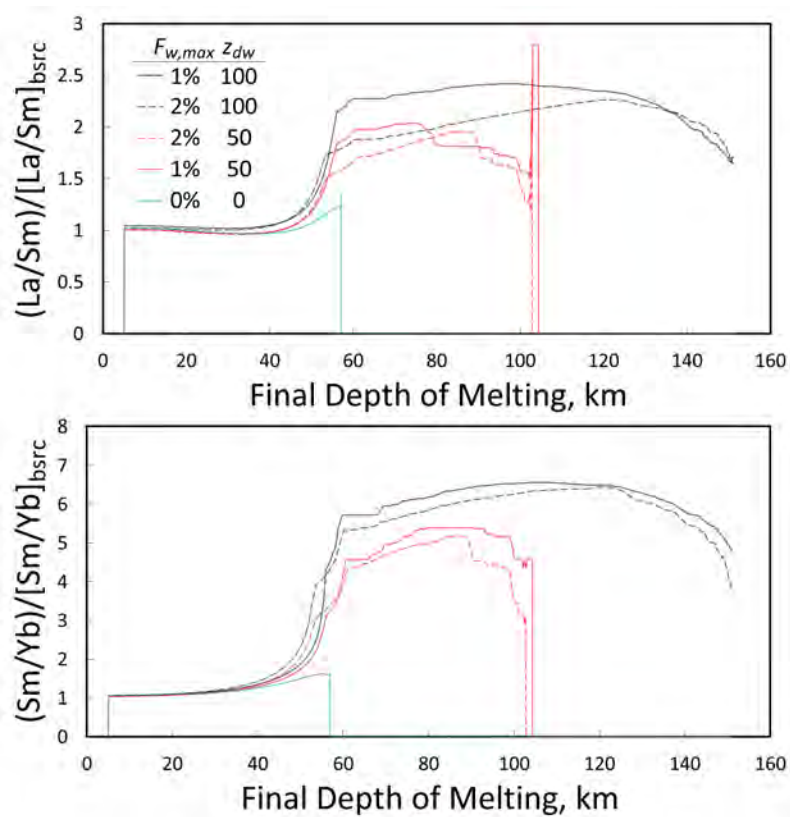


FIGURE 5.20: Depiction of the difference in predicted La/Sm and Sm/Yb, normalized to bulk source concentration, for models with different parameters controlling the depth and extent of melting occurring between the dry and wet solidi.

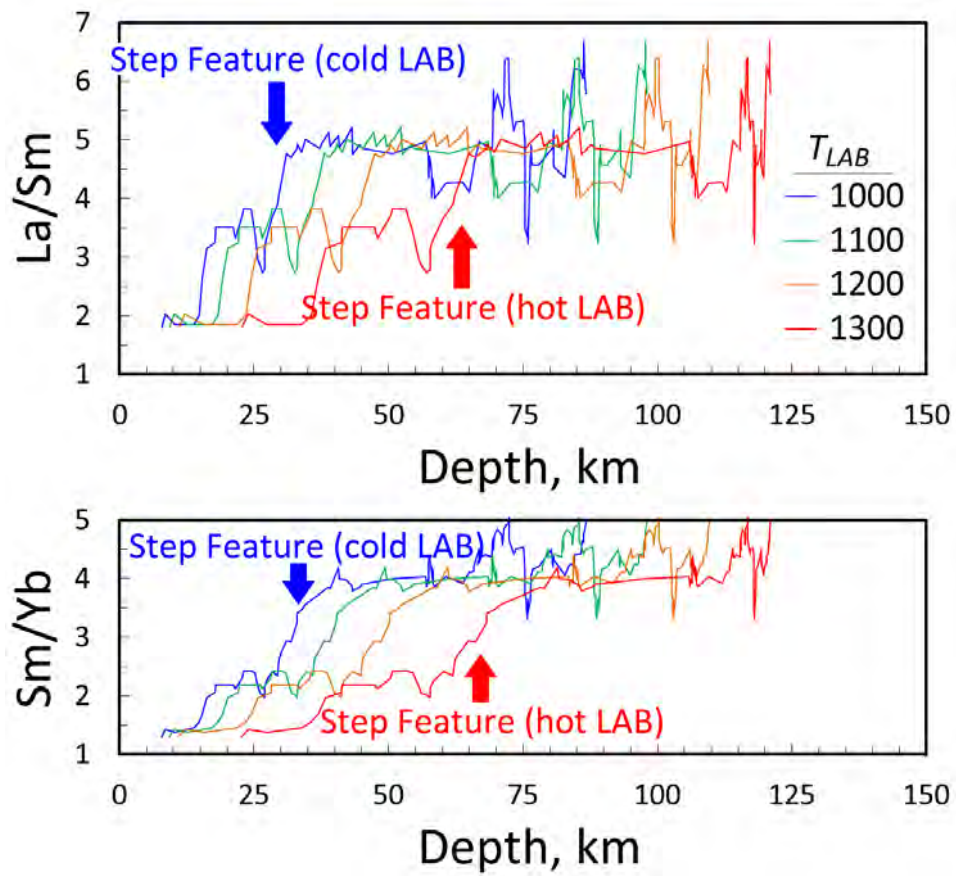


FIGURE 5.21: Illustration of a moving average of the empirical data for La/Sm and Sm/Yb as a function of the final depth of melting for different choices of LAB temperature. Depths of final melting increase with the choice of higher LAB temperature since the higher temperature isotherms occur at greater depth for any given seafloor age.

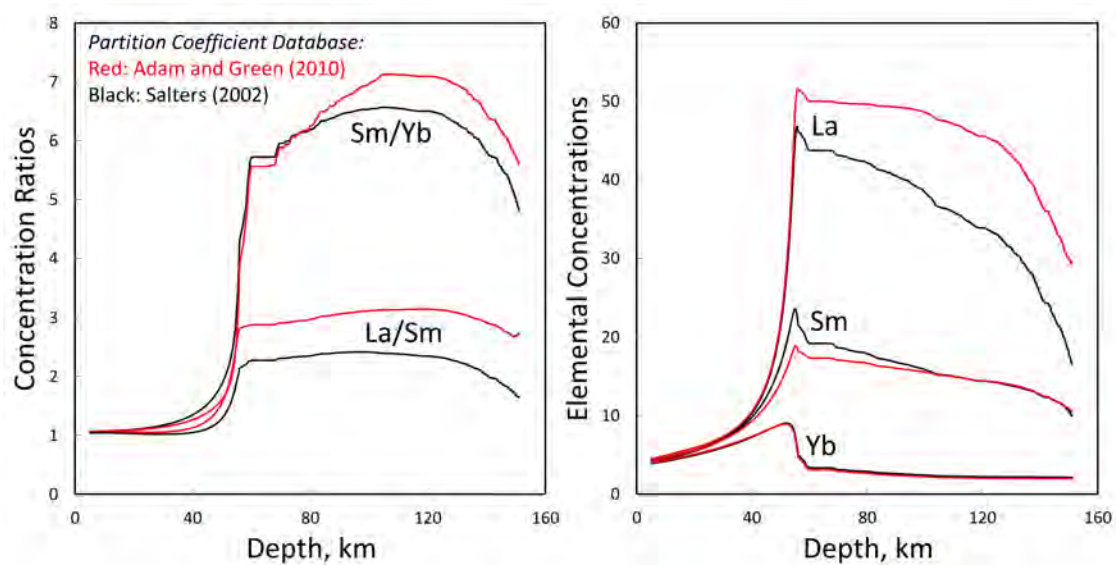


FIGURE 5.22: Predicted cumulative melt La/Sm and Sm/Yb (left panel) and La, Sm, and Yb (right panel) as a function of final melting depth for a default model and choice of partition coefficient databases from either Salters et al. (2002, black lines) or Adam and Green (2010, red lines).



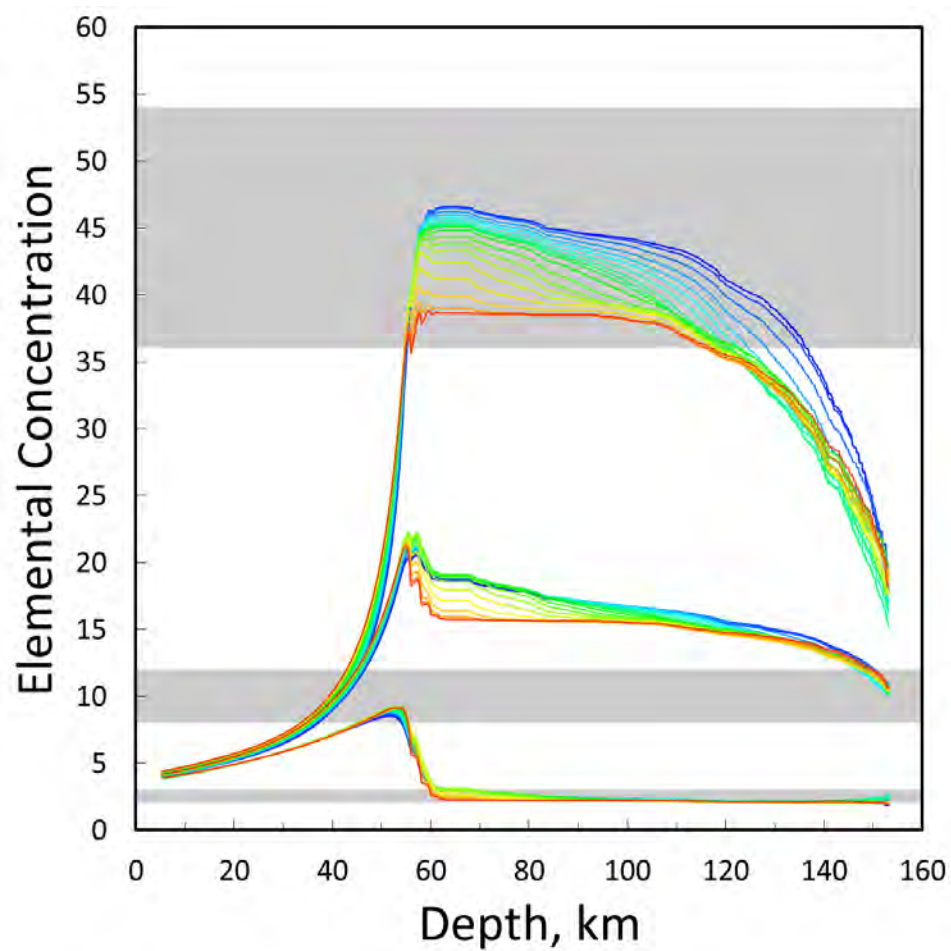


FIGURE 5.23: Elemental concentrations (ppm) of La (high concentration lines), Sm (medium concentration lines), and Yb (low concentration lines) as a function of final melting depth. The different curves for each element, characterized by colors red to blue, indicate predictions with residual melt fraction changed from 0.1% (blue) to 1.0% (red).

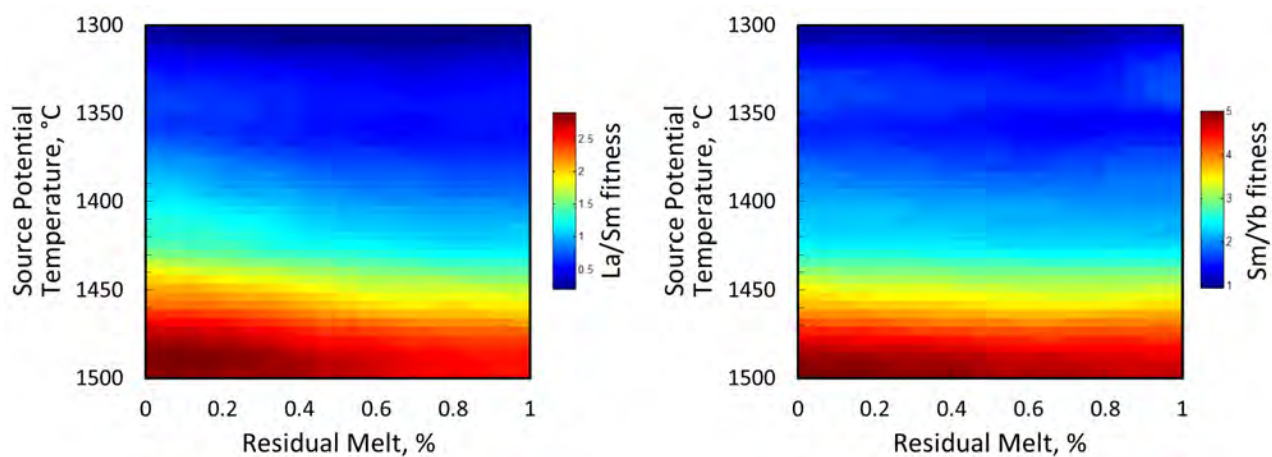


FIGURE 5.24: Misfit of default models to observed OIB La/Sm (left panel) and Sm/Yb (right panel) as a function of residual melt fraction and the mantle potential temperature of the source.

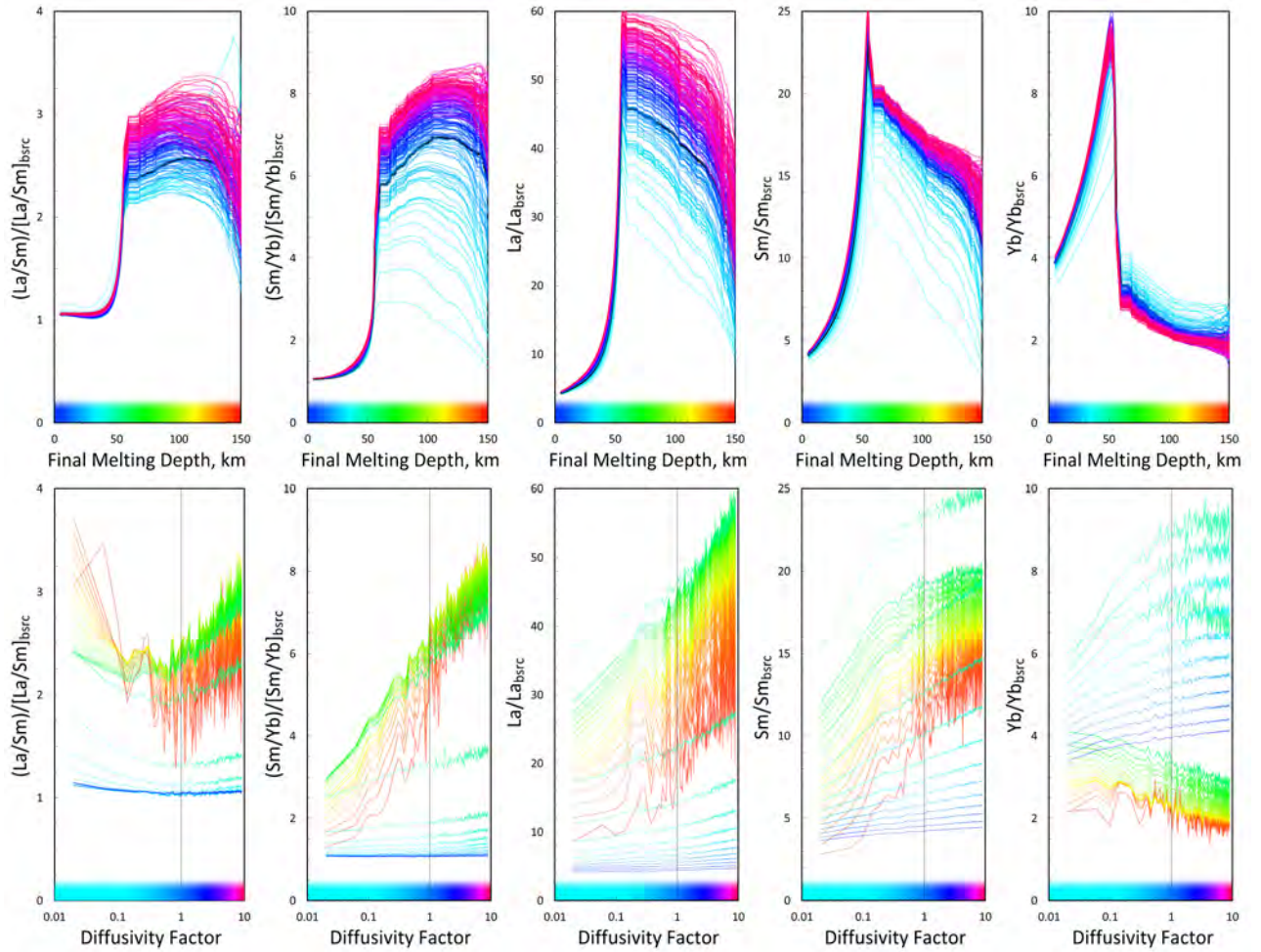


FIGURE 5.25: Sensitivity analysis of our models to changes in diffusion rates. The diffusivity factor is a scaling factor multiplied by the diffusivities of all phases to obtain higher or lower case diffusivities. Concentrations for La/Sm, Sm/Yb, La, Sm, and Yb, all normalized to bulk source concentration are shown. The top panels show the cumulative melt concentrations as a function of final melting depth. The bottom panels show lines of cumulative melt concentrations for a constant depth as a function of the varied diffusivity factor. The colors of the lines on the top panels correspond to slices in the bottom panel, and vice versa. These results have been slightly smoothed. The black curve in the top panels is the default model of this work, for comparison.

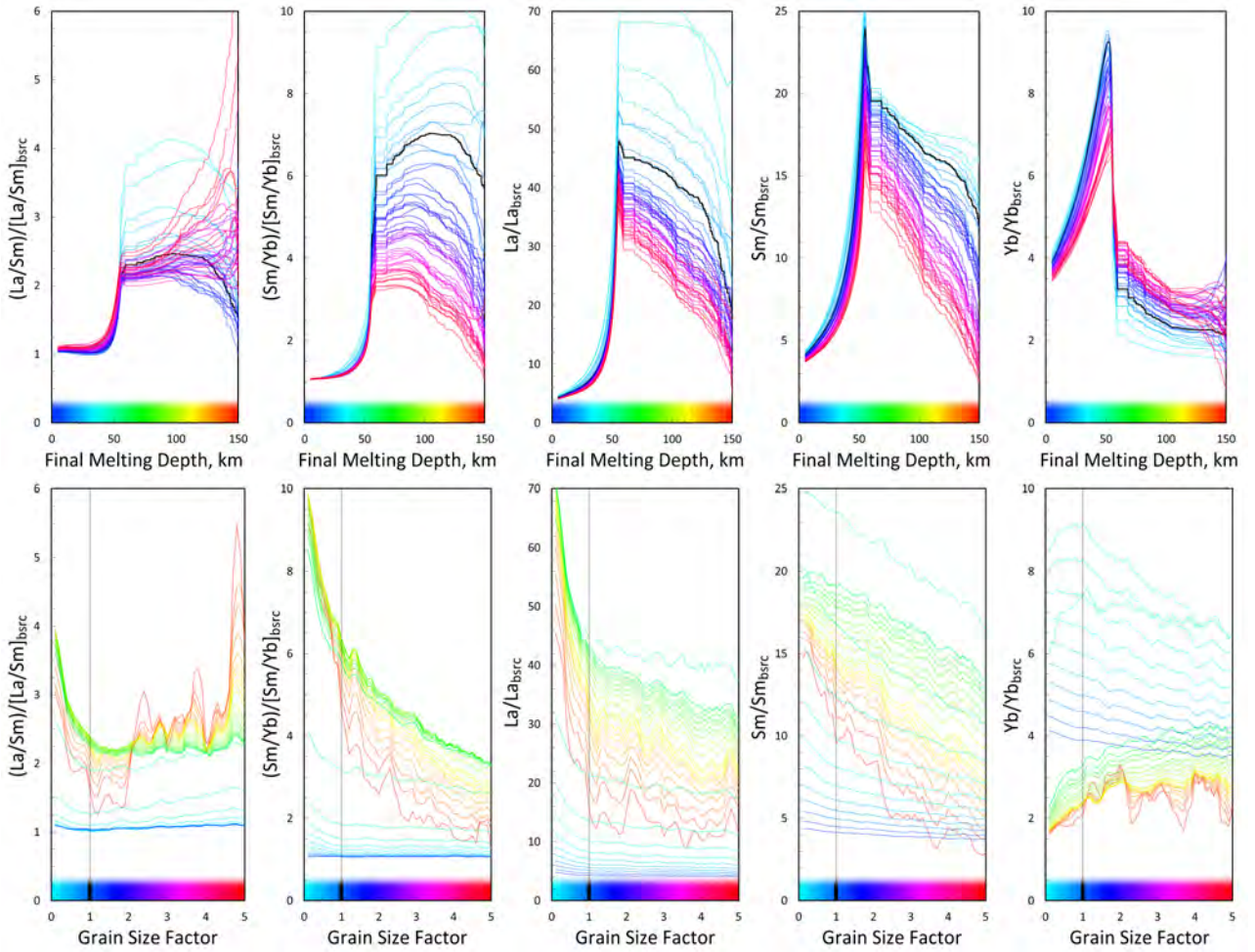


FIGURE 5.26: Sensitivity analysis of our model results of cumulative melt concentration to changes in the grain size (or grain size factor). The presentation of the model results is the same as in fig. 5.25. Models with low grain size are closer to equilibrium, and models with greater grain size are farther from equilibrium, compared to the default model (black lines).



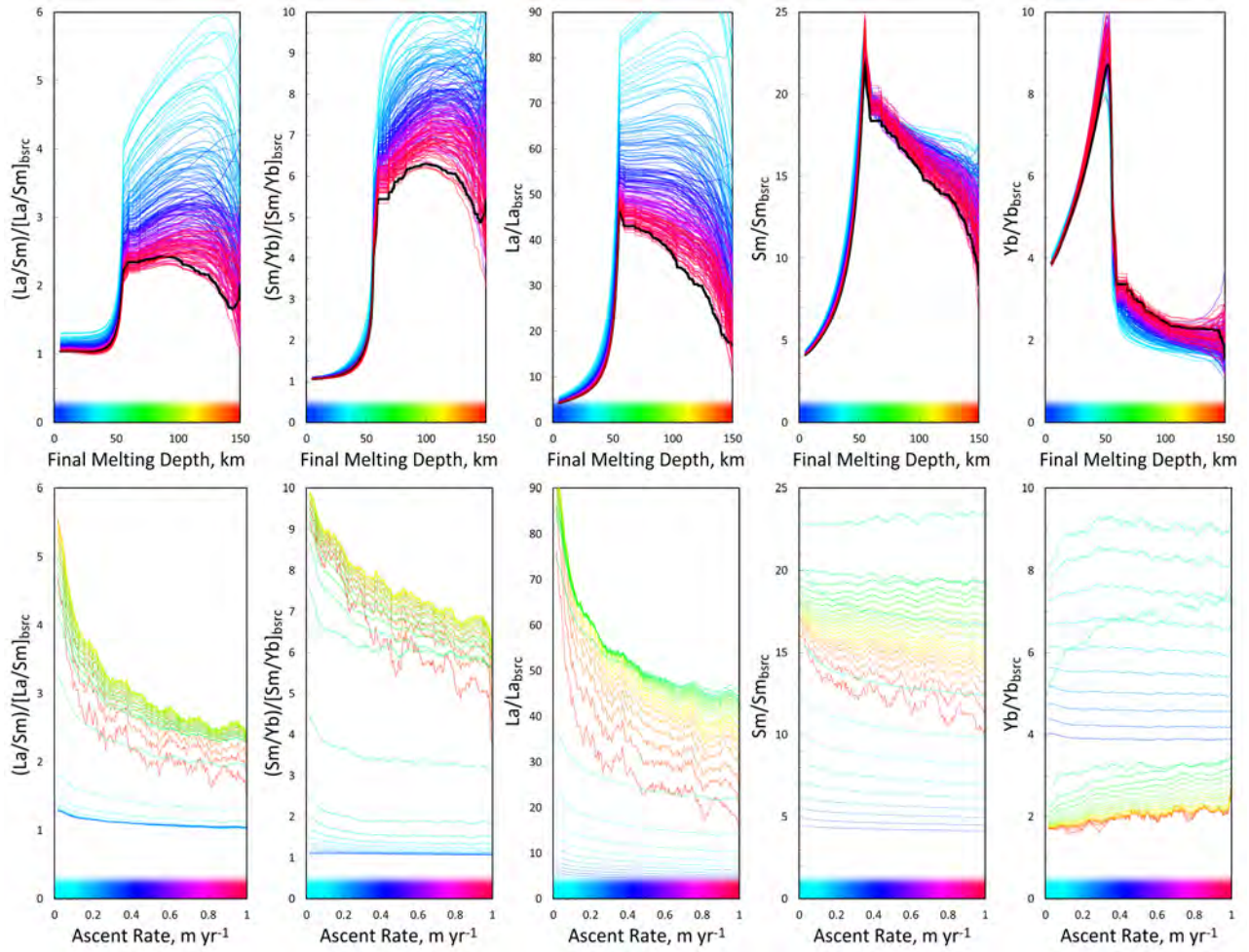


FIGURE 5.27: Model predictions of cumulative melt composition for models in which the ascent rate is varied between  $0.025\ m\ yr^{-1}$  and  $1.0\ m\ yr^{-1}$ . All other parameters are those in our default model, represented by the thick black lines. The top figures show melt composition as a function of final melting depth and the bottom figures show isobaric compositions for models in the range of ascent rates. The color bar in the top figures correspond to the curves in the bottom figures, and vice versa.

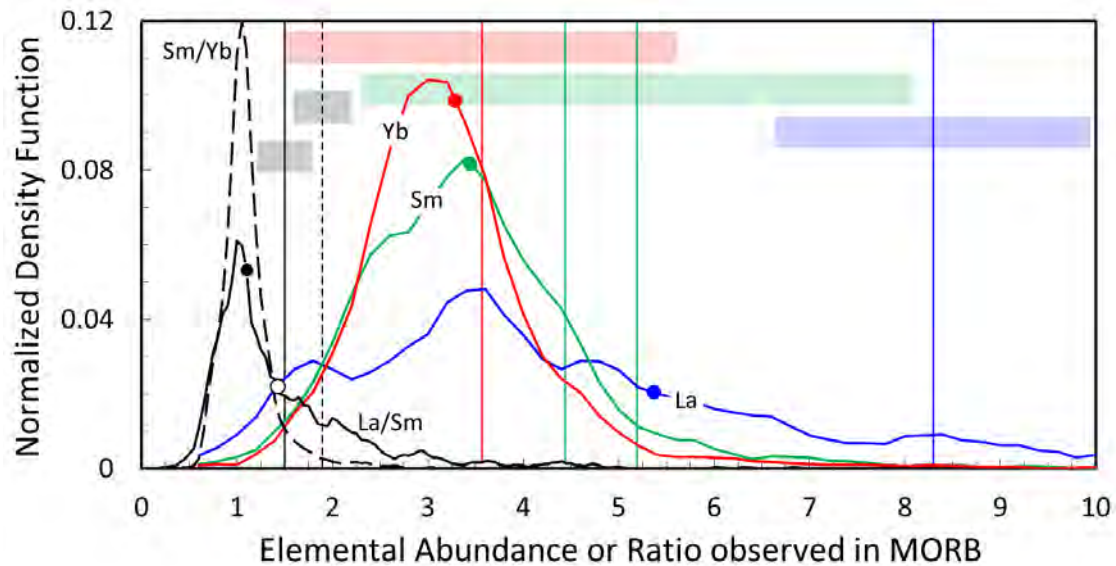


FIGURE 5.28: Density functions for La/Sm, Sm/Yb, La, Sm, and Yb in MORB from the database of Gale et al. (2013). Absolute values are in ppm. Horizontal highlighted bars are the HMB from our analysis of best fitting models in our tests of sensitivity to partition coefficients. The vertical position of these bars is meaningless. The large dots on the curves for ratios and elemental concentrations indicate the means of each distribution function.

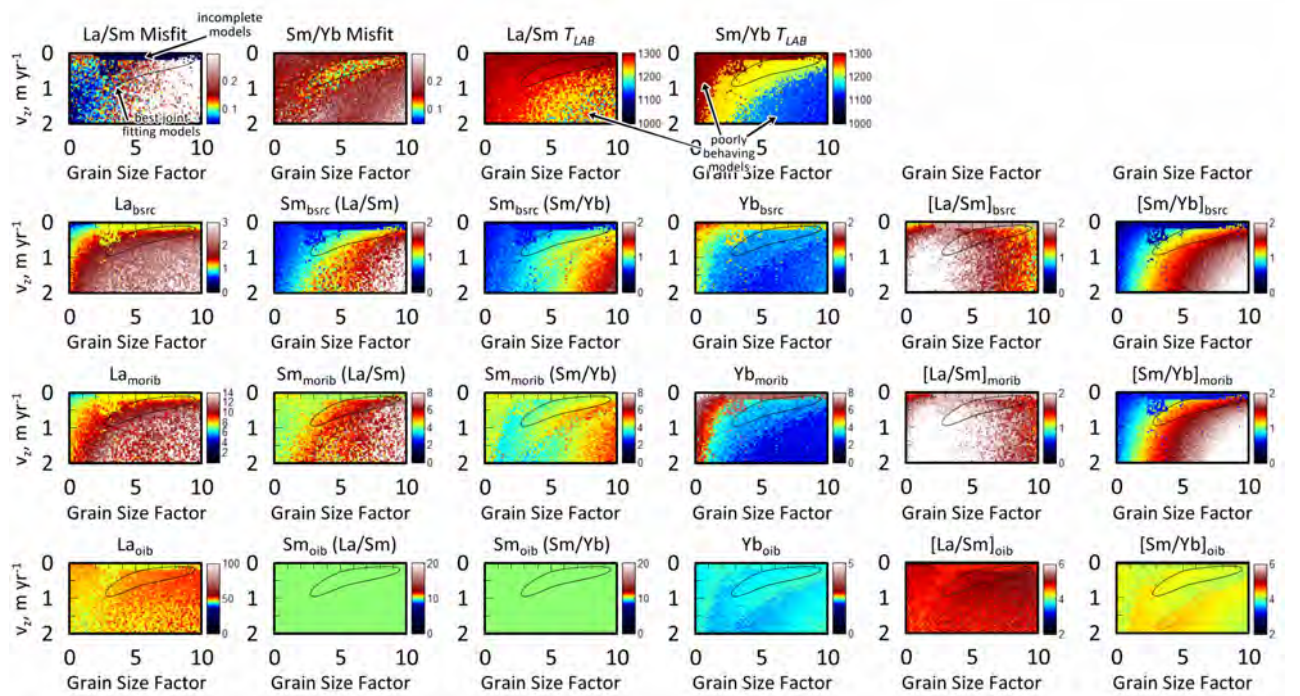


FIGURE 5.29: Results of our analysis of our model sensitivity to joint variation in the ascent rate and grain size factor. Top panels show the misfits to La/Sm and Sm/Yb, and the corresponding  $T_{LAB}$  for each fit. The remaining figures show predictions of bulk source concentrations (second row), Mid-Ocean Ridge Island Basalt (MORIB) concentrations (third row), and thick-plate OIB concentrations (fourth row) corresponding to the fit to La/Sm and Sm/Yb. The predictions of La, Sm(La/Sm), and [La/Sm] indicate predictions from the fit to La/Sm, whereas Sm(Sm/Yb), Yb, and [Sm/Yb] are obtained from the fit to Sm/Yb.



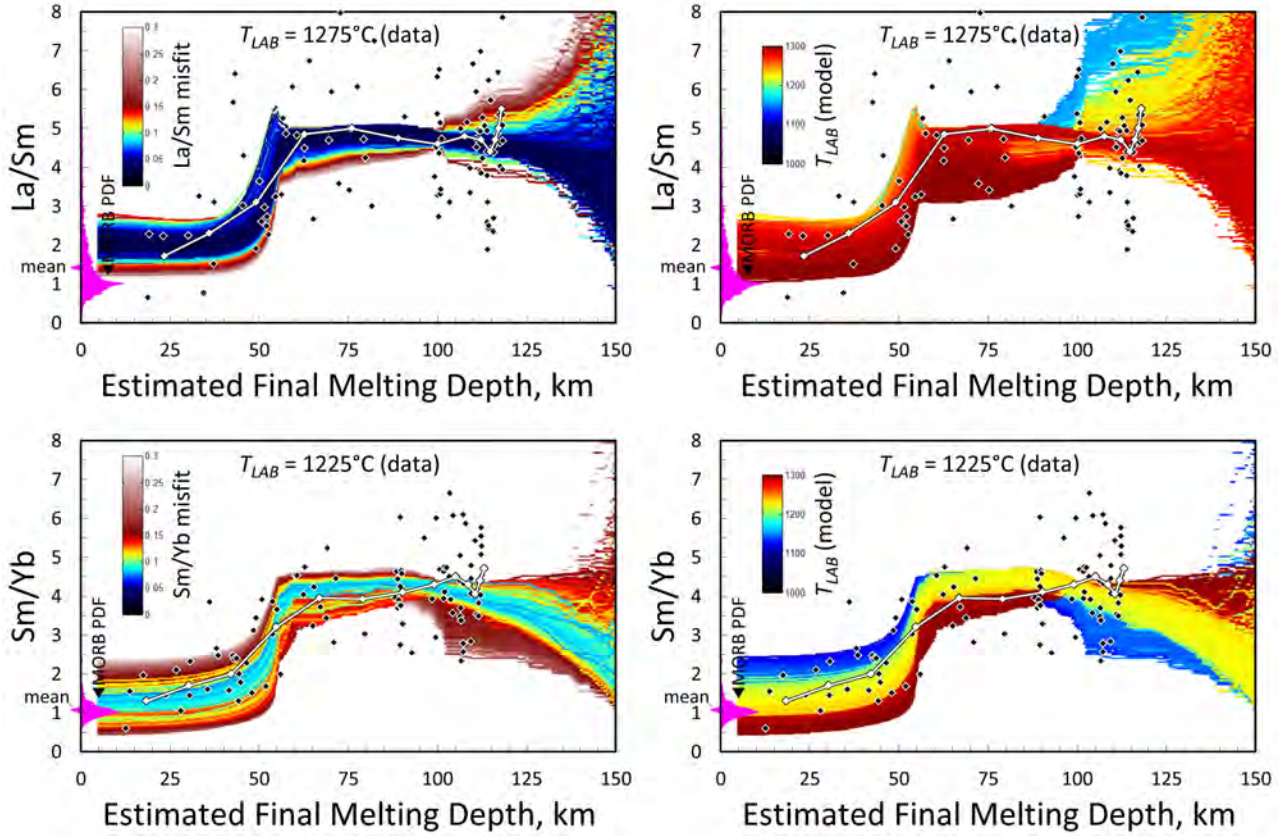


FIGURE 5.30: Comparison of the empirical data (black diamonds with white borders), our bins to which we fit models (white connected diamonds with black borders), and the predictions of all models in Fig. 5.29. The top figures show data and model results for La/Sm, and the bottom figures show data and models for Sm/Yb. The curves in the left panels are colored according to their misfit, whereas the curves in the right panels are colored according to the  $T_{LAB}$  of each model. The data in the bottom plots has used  $T_{LAB} = 1225^\circ \text{C}$ , and in the top plots have used  $T_{LAB} = 1275^\circ \text{C}$ . In addition, the pink data on the left hand side of each figure shows a density function for La/Sm and Sm/Yb in MORB from the data of Gale et al. (2013).



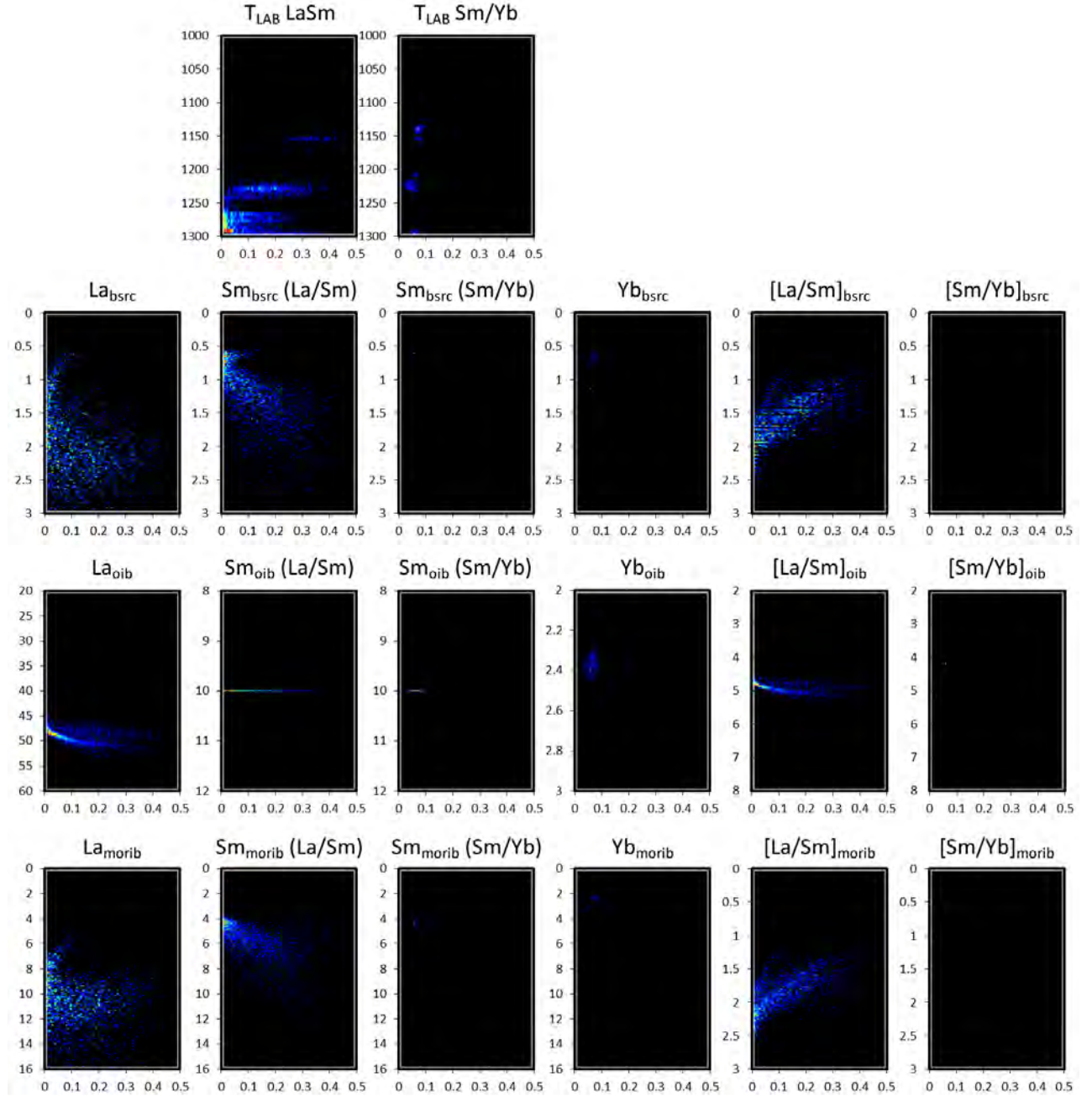


FIGURE 5.31: Probability density fields constructed from the predicted model properties in Fig. 5.29. The horizontal scales in each of these figures is the misfit  $m$ . Values of La, Sm, and Yb for bulk source (bsrc), thick-plate OIB (oib), and Mid-Ocean Ridge Island Basalt (morib) concentrations are in units of ppm. Values of  $T_{LAB}$  are in units of °C.

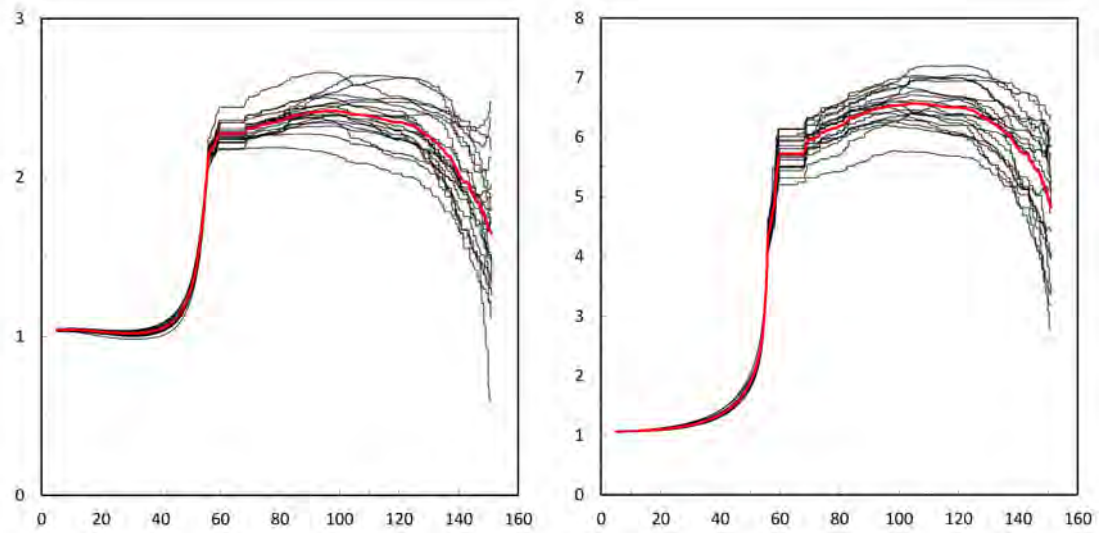


FIGURE 5.32: Predicted cumulative melt concentrations of La/Sm (left panel) and Sm/Yb (right panel) as a function of depth (in km), for 20 runs of our default model. Repeated model runs show variation about a mean. The thick red line is the mean of the models shown.

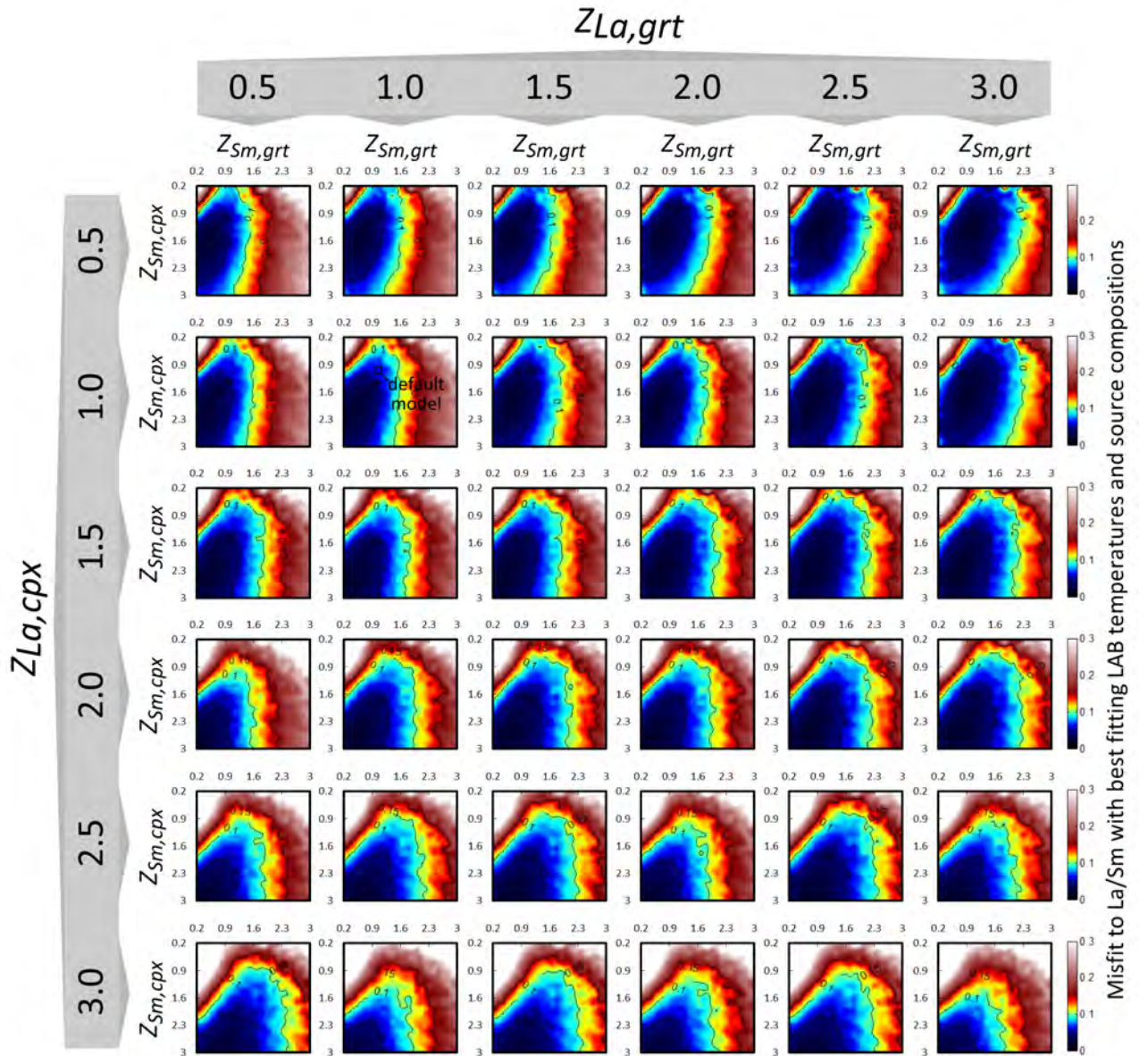


FIGURE 5.33: Predicted misfit to La/Sm for models in which the partition coefficients of Sm and La in cpx and garnet are varied. The position of our default model is indicated in the second row, second column panel. See text for discussion.



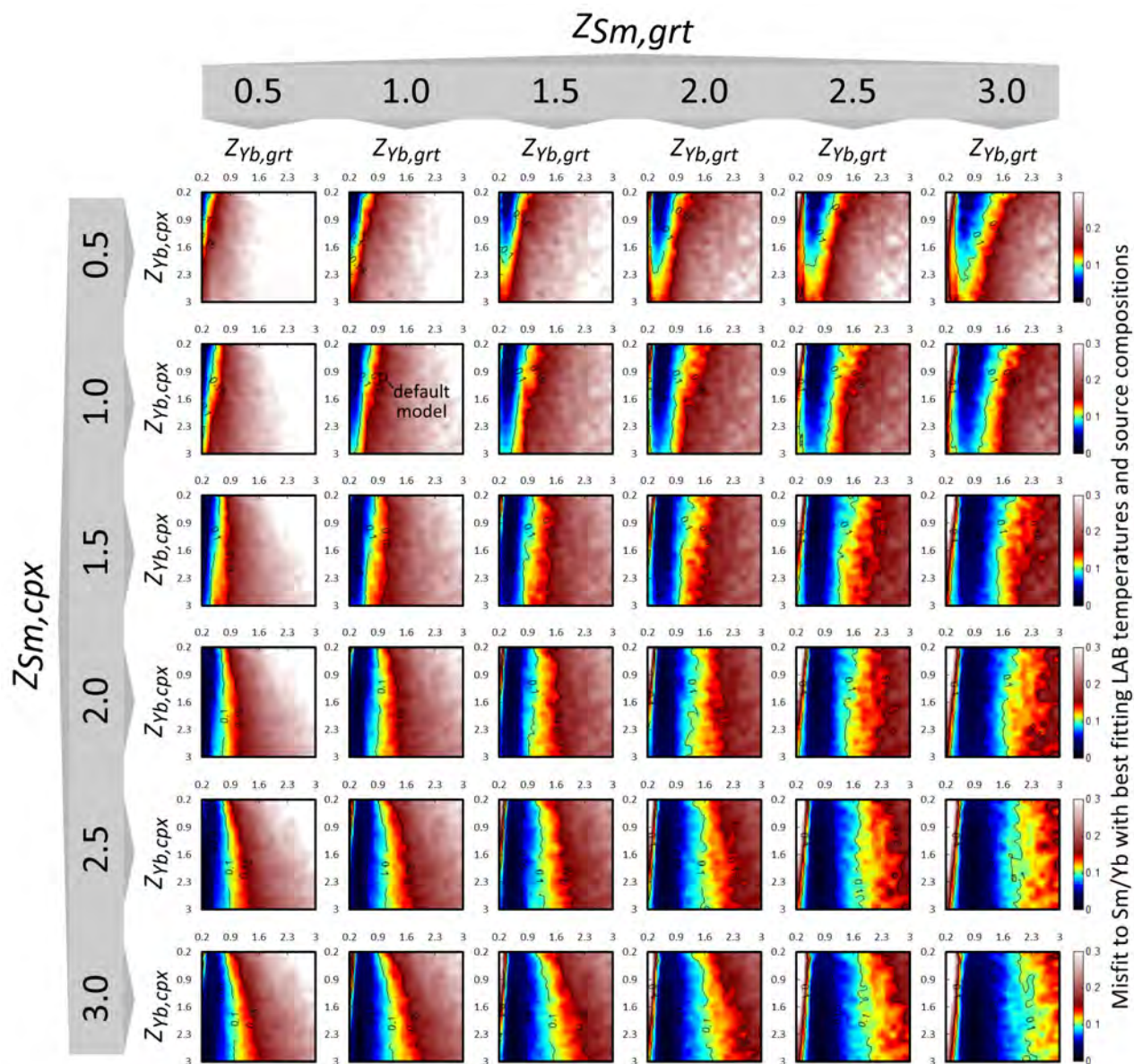


FIGURE 5.34: Predicted misfit to Sm/Yb for models in which the partition coefficients of Yb and Sm in cpx and garnet are varied. The position of our default model is indicated in the second row, second column panel. See text for discussion.

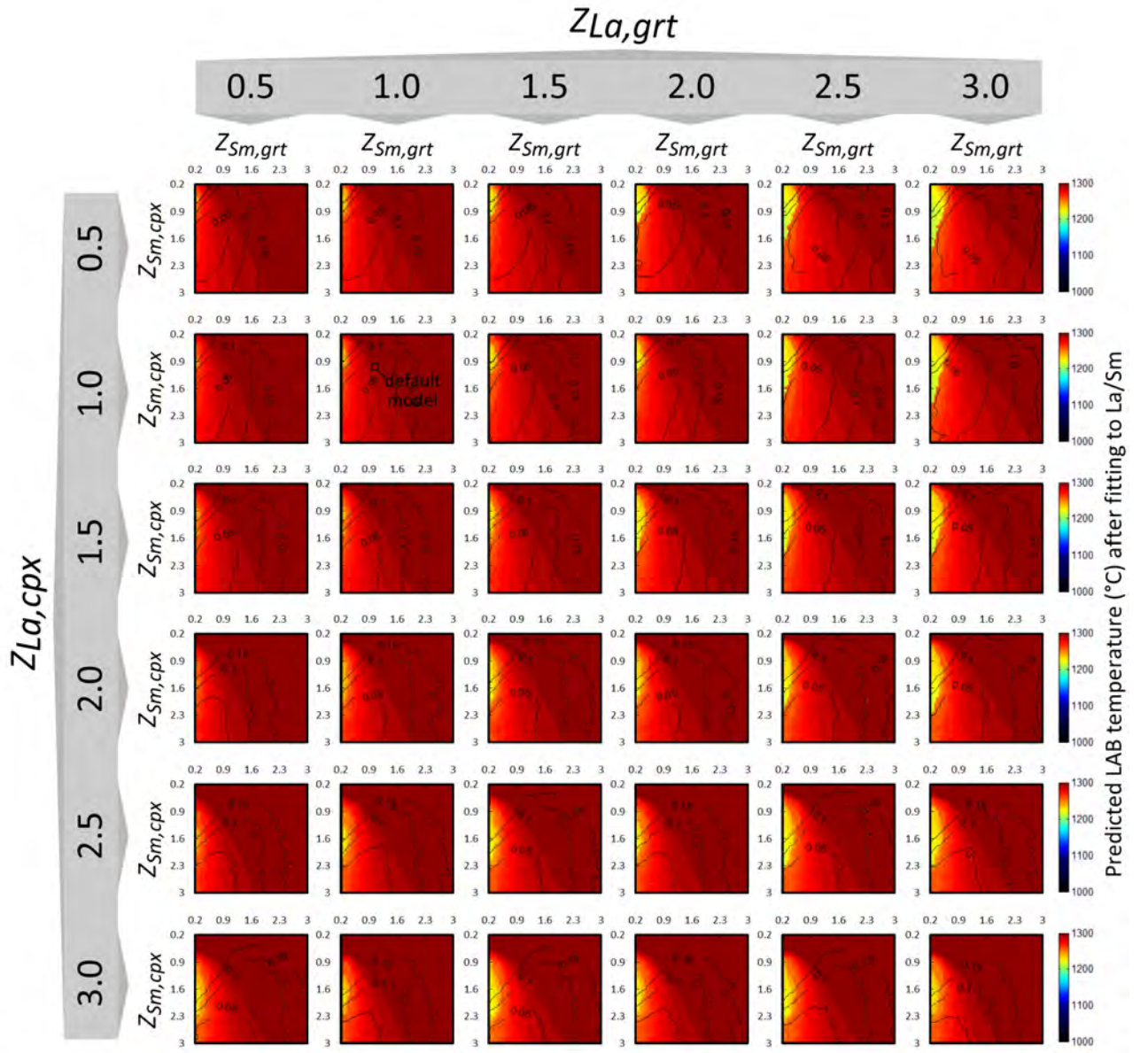
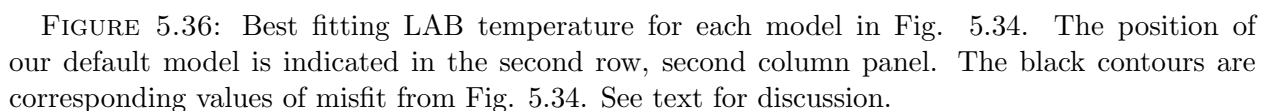


FIGURE 5.35: Best fitting LAB temperature for each model in Fig. 5.33. The position of our default model is indicated in the second row, second column panel. The black contours are corresponding values of misfit from Fig. 5.33. See text for discussion.





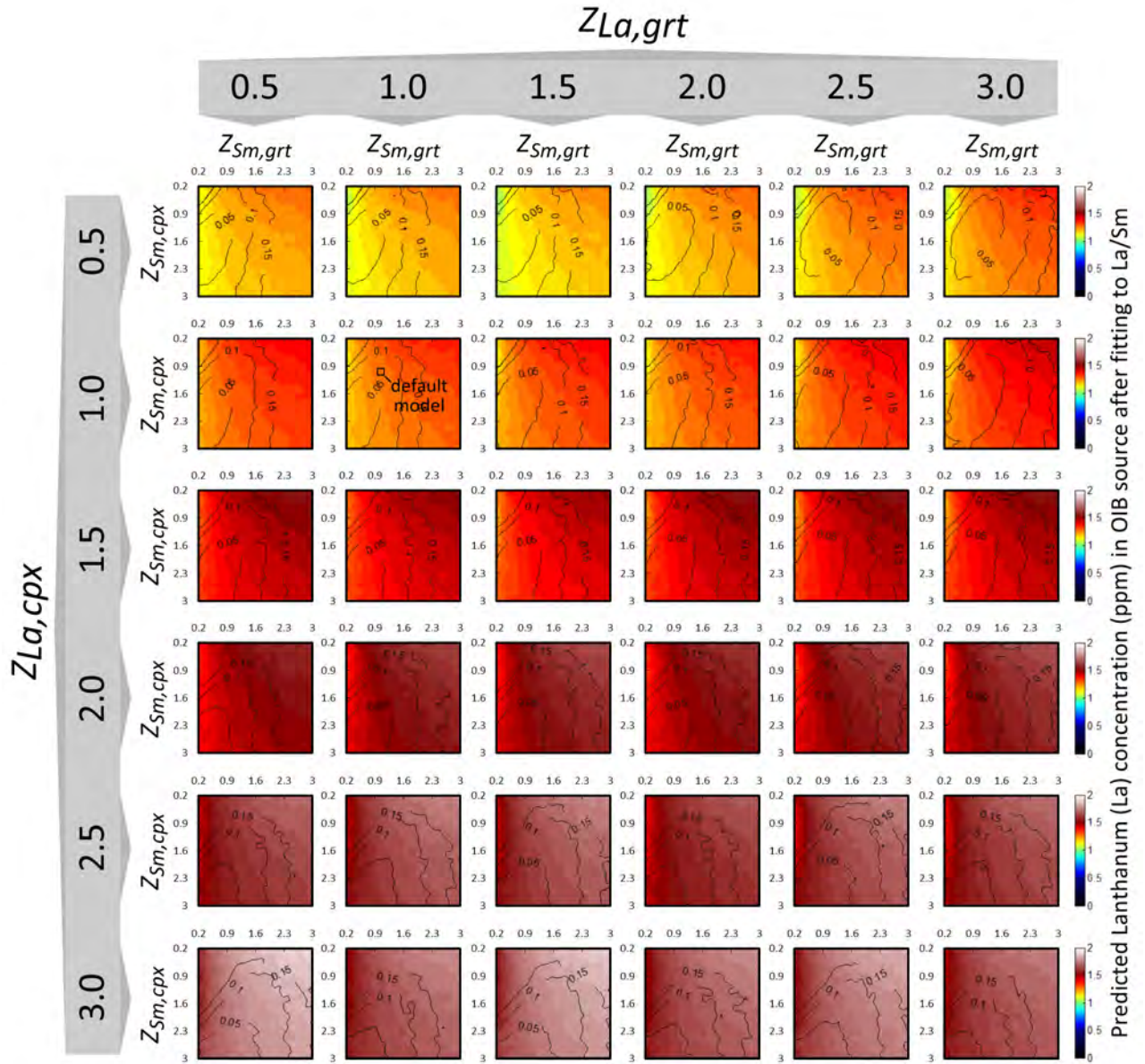


FIGURE 5.37: Predicted absolute La concentration in the OIB source obtained from the fit to La/Sm and an estimate of Sm concentration in thick-plate OIB. The position of our default model is indicated in the second row, second column panel. The black contours are corresponding values of misfit from Fig. 5.33. See text for discussion.



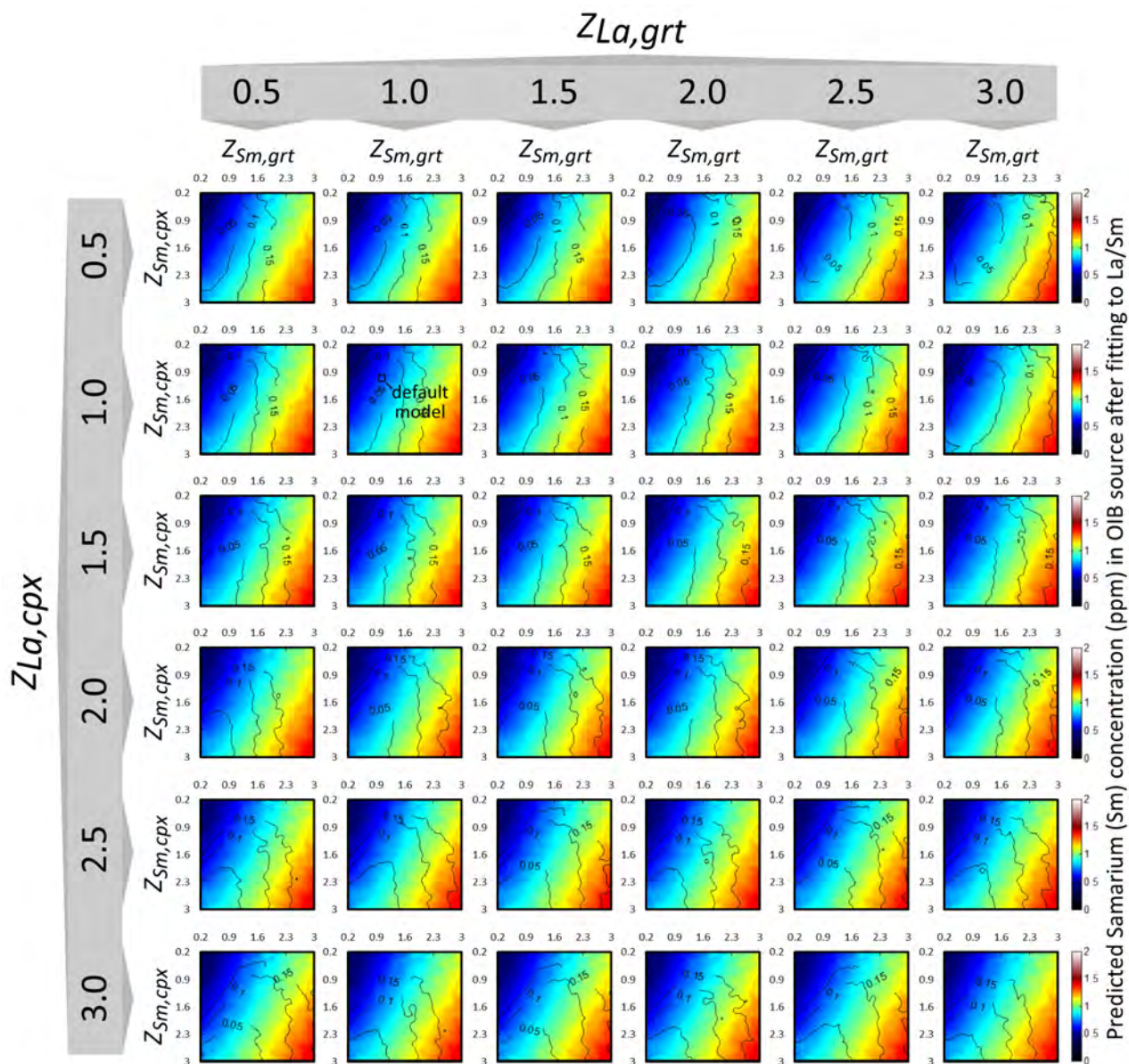


FIGURE 5.38: Predicted absolute Sm concentration in the OIB source obtained from the fit to La/Sm and an estimate of Sm concentration in thick-plate OIB. The position of our default model is indicated in the second row, second column panel. The black contours are corresponding values of misfit from Fig. 5.33. Note that all of these models have different source concentrations while predicting that Sm in thick plate OIB = 10 ppm.



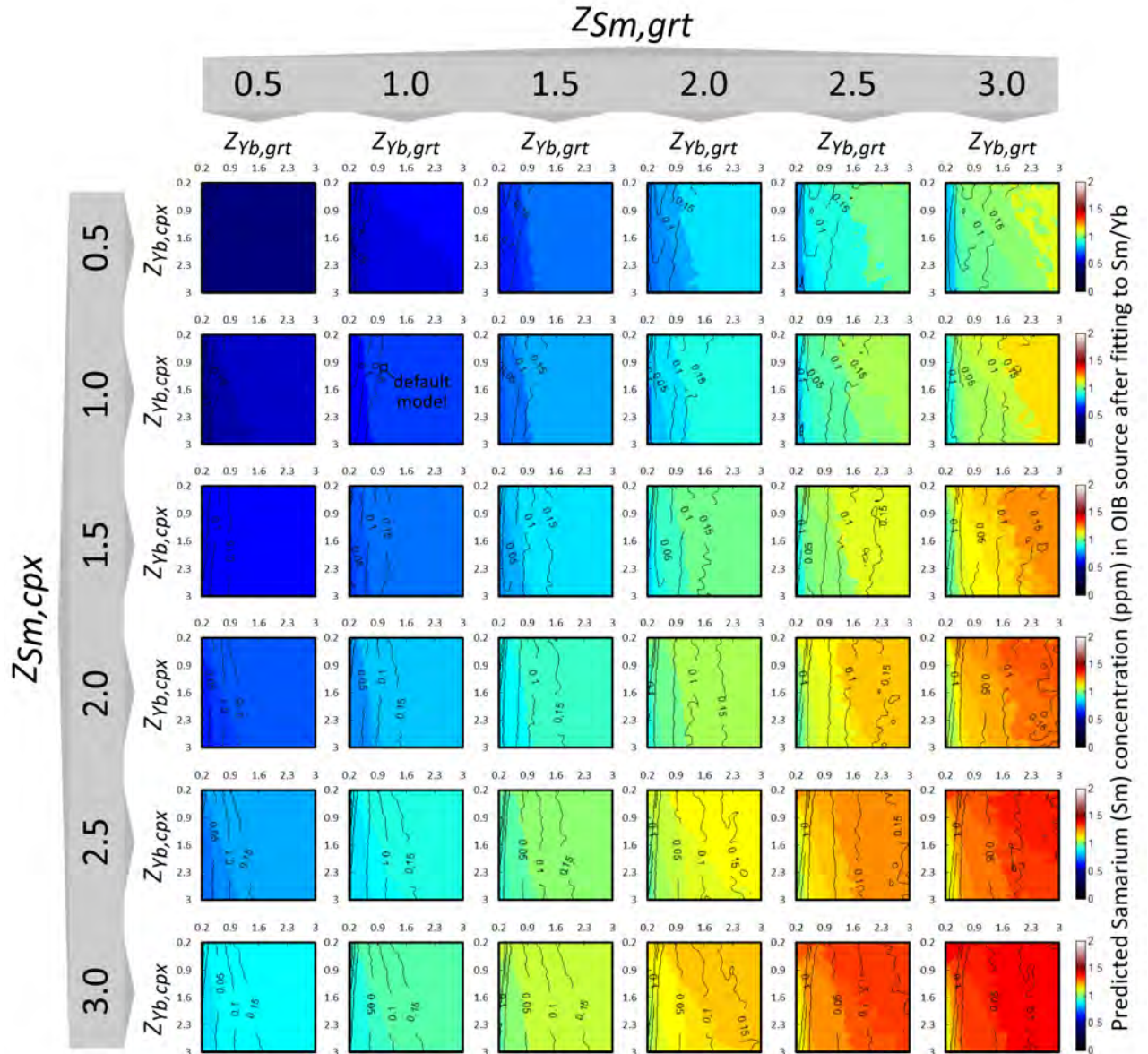


FIGURE 5.39: Predicted absolute Sm concentration in the OIB source obtained from the fit to Sm/Yb and an estimate of Sm concentration in thick-plate OIB. The position of our default model is indicated in the second row, second column panel. The black contours are corresponding values of misfit from Fig. 5.34. Note that all of these models have different source concentrations while predicting that Sm in thick plate OIB = 10 ppm.

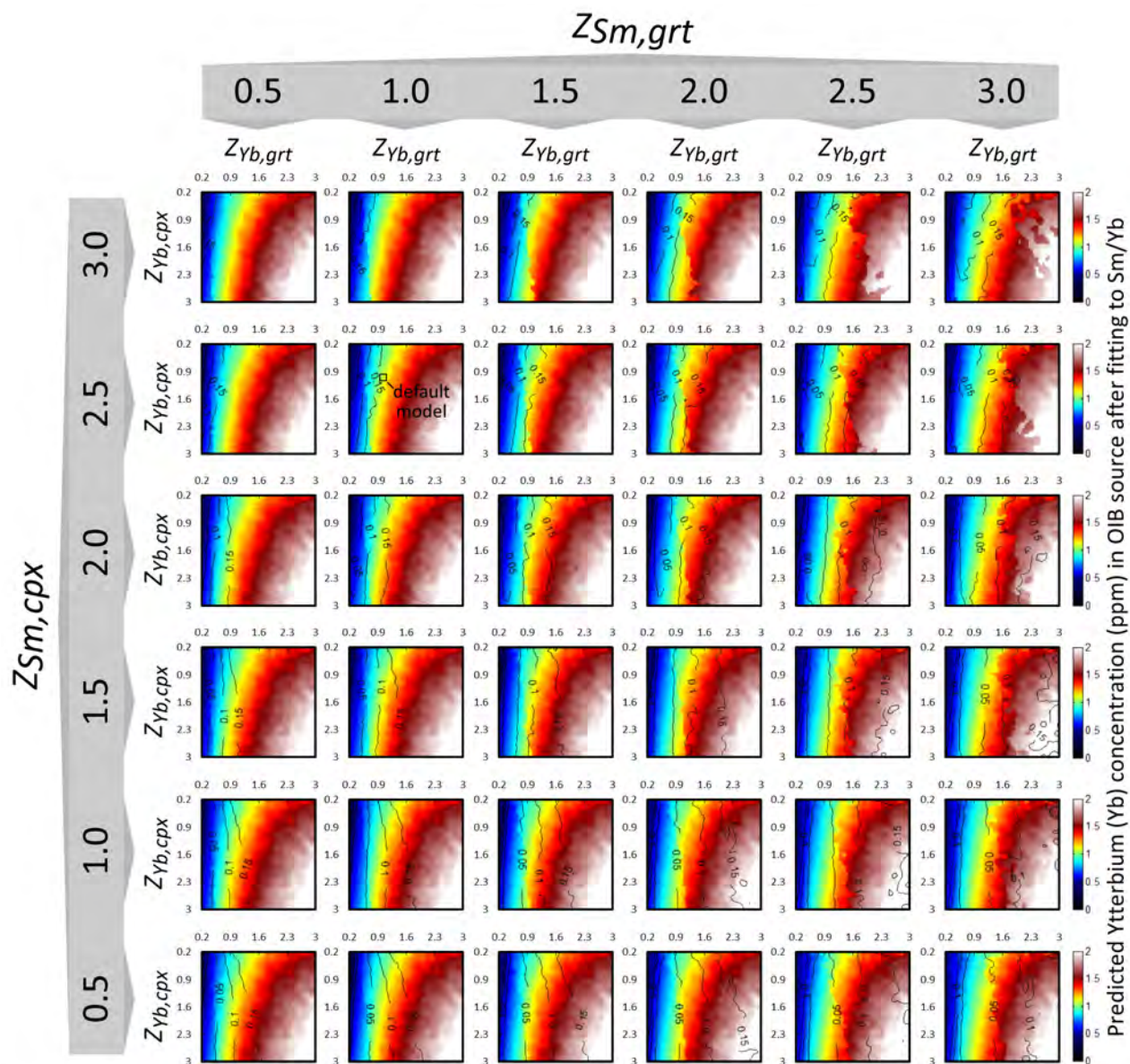


FIGURE 5.40: Predicted absolute Yb concentration in the OIB source obtained from the fit to  $Sm/Yb$  and an estimate of  $Sm$  concentration in thick-plate OIB. The position of our default model is indicated in the second row, second column panel. The black contours are corresponding values of misfit from Fig. 5.34.



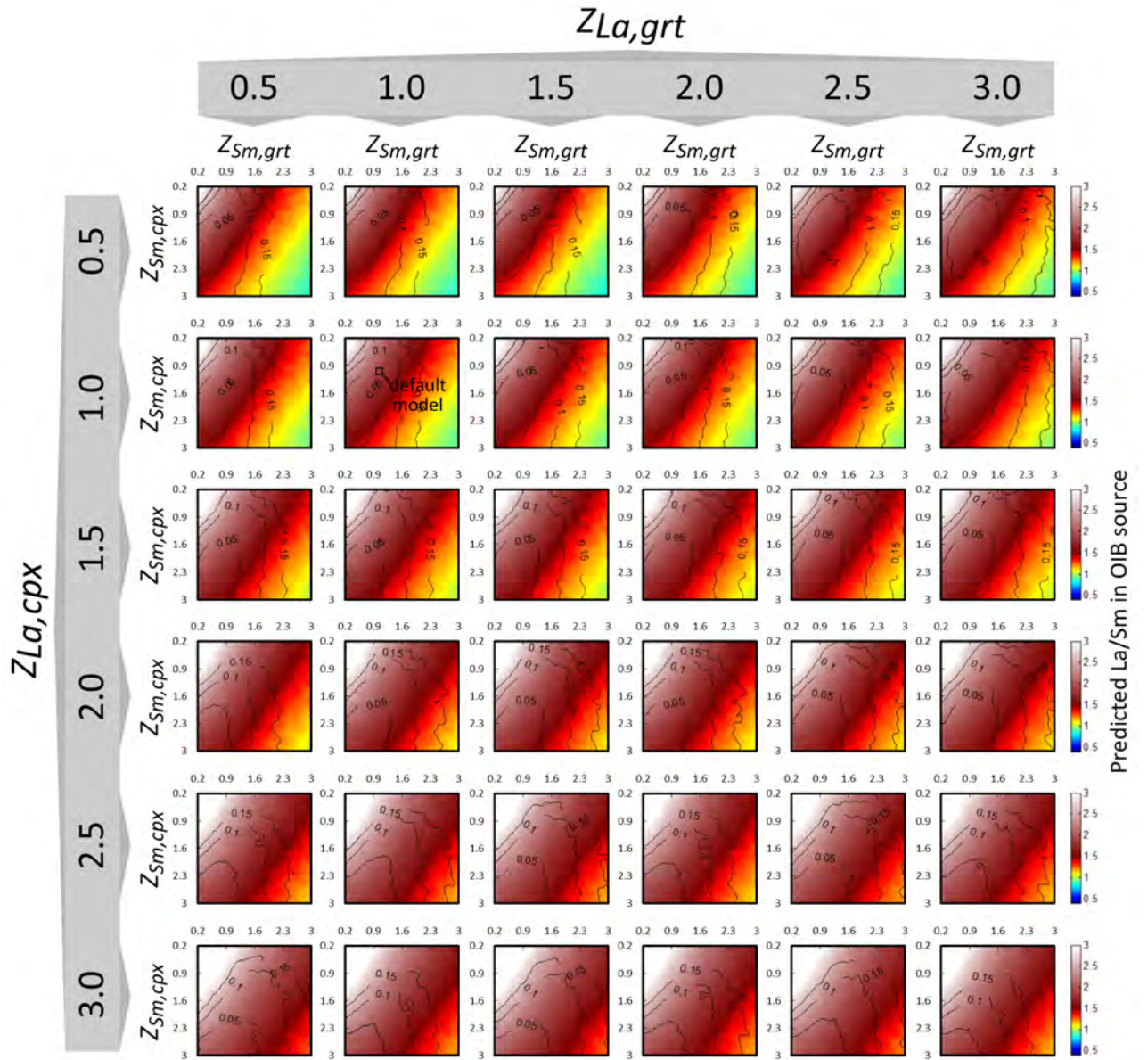


FIGURE 5.41: Predicted La/Sm concentration in the OIB source obtained from the fit to La/Sm. The position of our default model is indicated in the second row, second column panel. The black contours are corresponding values of misfit from Fig. 5.33.

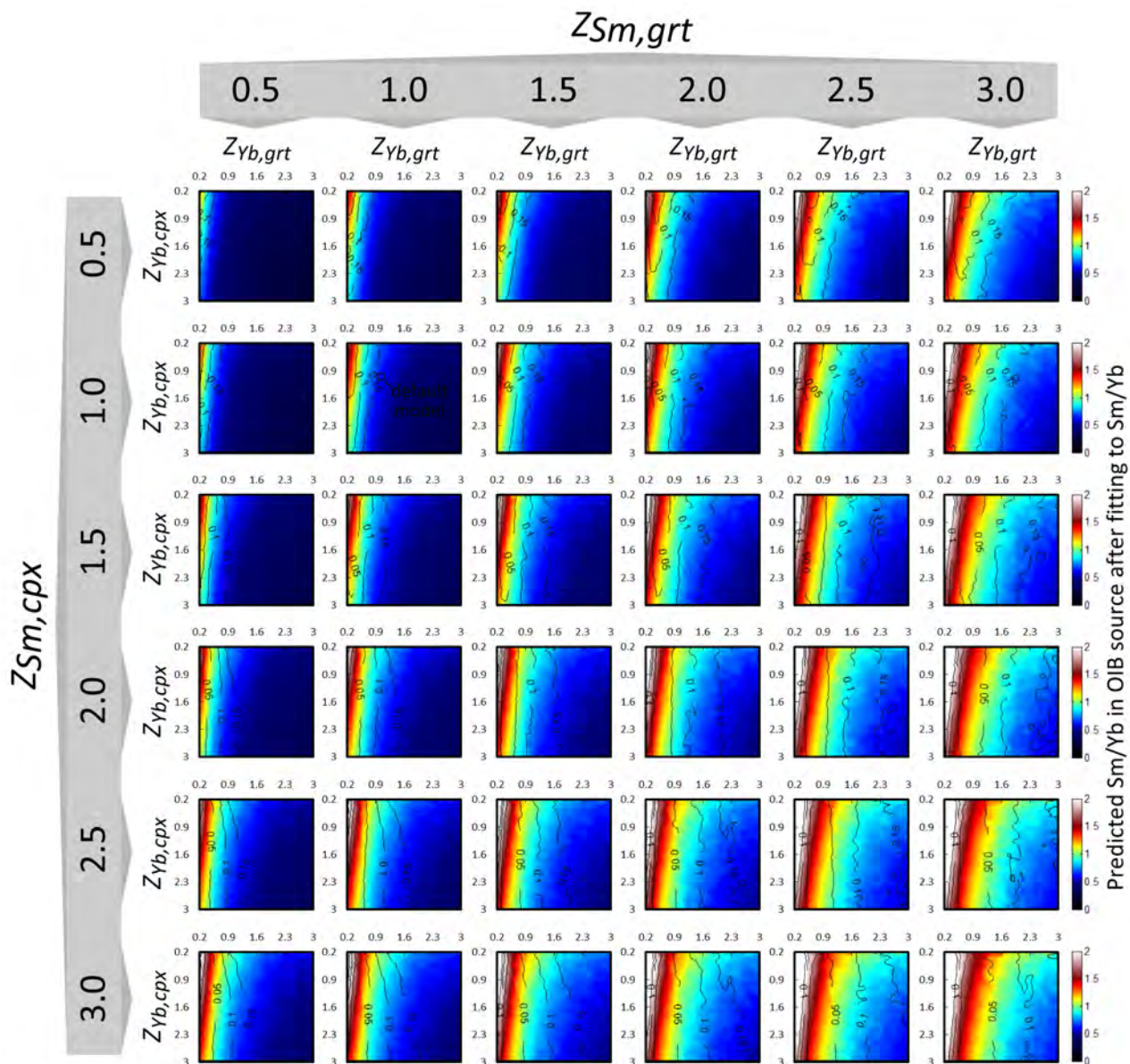


FIGURE 5.42: Predicted Sm/Yb concentration in the OIB source obtained from the fit to Sm/Yb. The position of our default model is indicated in the second row, second column panel. The black contours are corresponding values of misfit from Fig. 5.34.



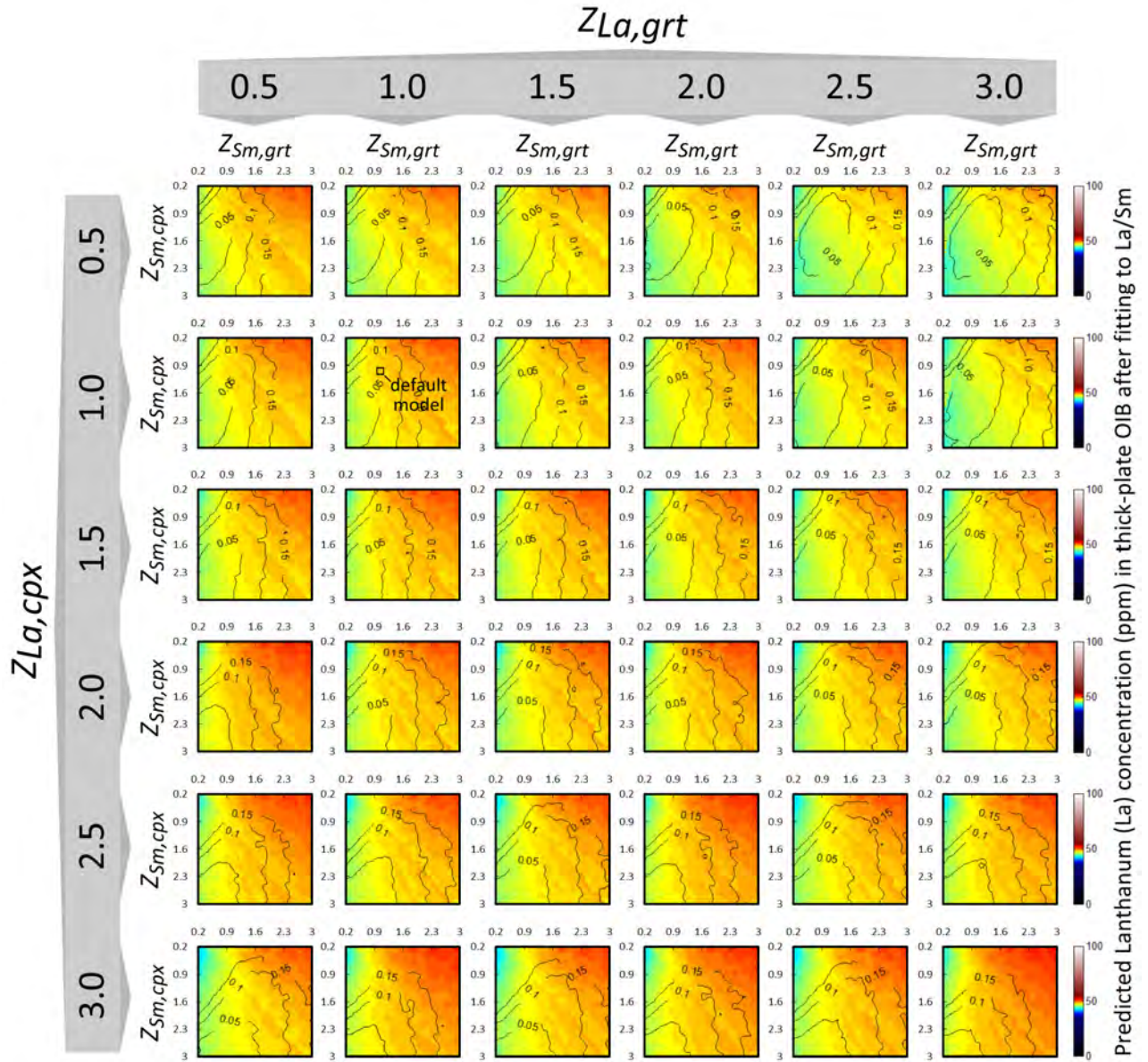


FIGURE 5.43: Predicted absolute La concentration in thick-plate OIB (approximated by eruptions on seafloor age of 64 Ma) obtained from the fit to La/Sm and an estimate of Sm concentration in thick-plate OIB. The position of our default model is indicated in the second row, second column panel. The black contours are corresponding values of misfit from Fig. 5.33.

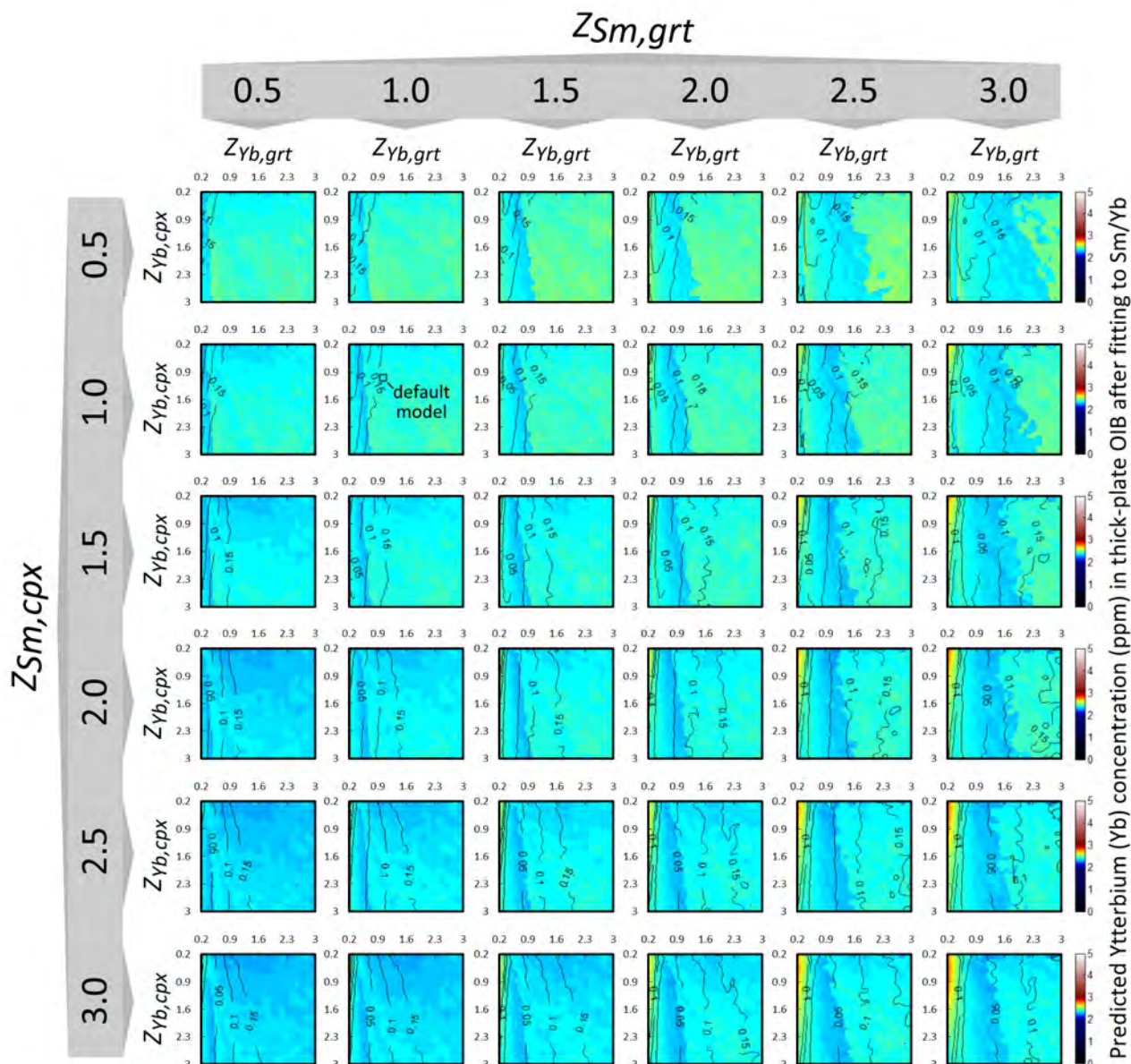


FIGURE 5.44: Predicted absolute Yb concentration in thick-plate OIB (approximated by eruptions on seafloor age of 64 Ma) obtained from the fit to Sm/Yb and an estimate of Sm concentration in thick-plate OIB. The position of our default model is indicated in the second row, second column panel. The black contours are corresponding values of misfit from Fig. 5.34.



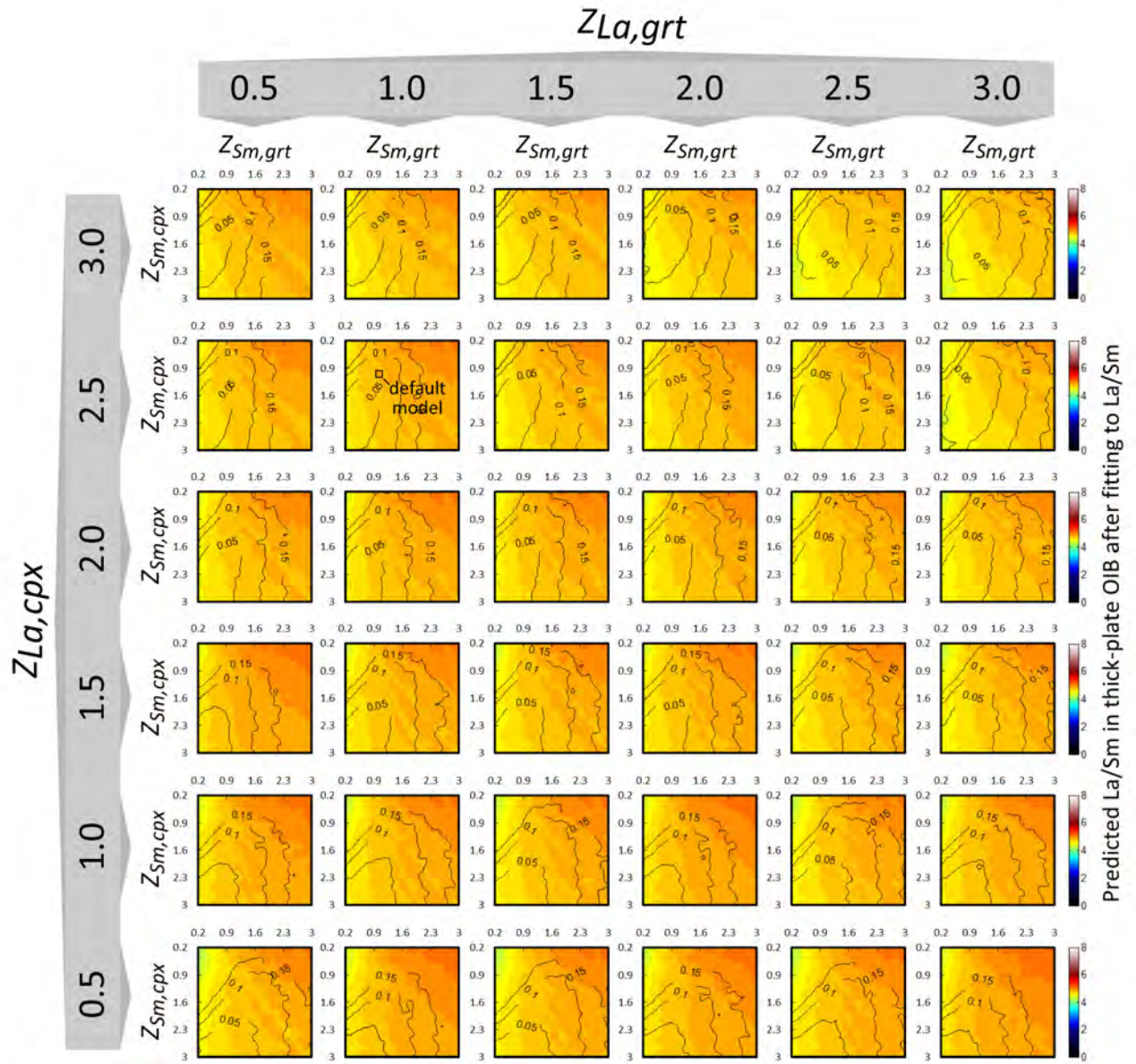


FIGURE 5.45: Predicted La/Sm concentration in thick-plate OIB (approximated by eruptions on seafloor age of 64 Ma) obtained from the fit to La/Sm. The position of our default model is indicated in the second row, second column panel. The black contours are corresponding values of misfit from Fig. 5.33.

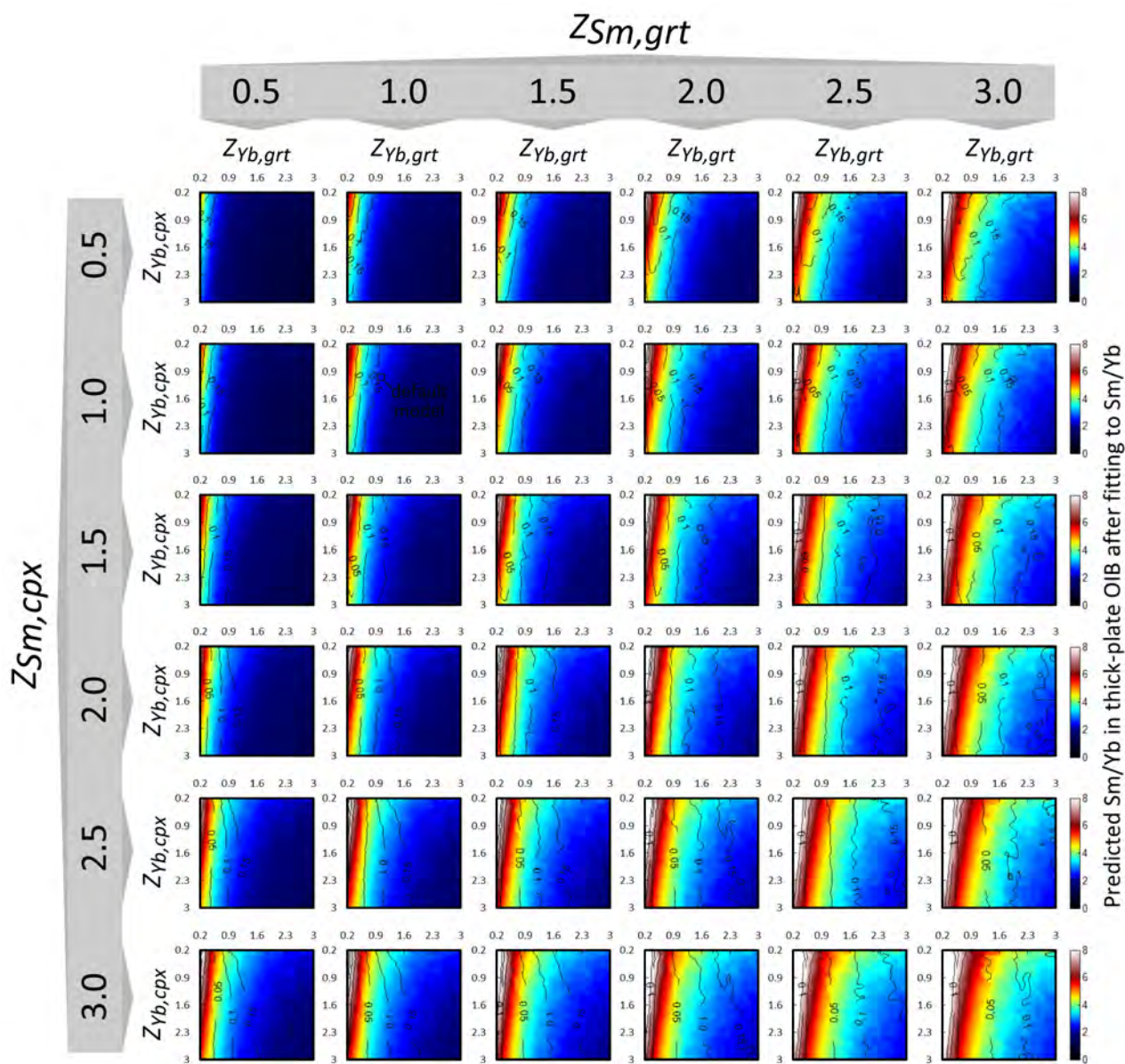


FIGURE 5.46: Predicted Sm/Yb concentration in thick-plate OIB (approximated by eruptions on seafloor age of 64 Ma) obtained from the fit to Sm/Yb. The position of our default model is indicated in the second row, second column panel. The black contours are corresponding values of misfit from Fig. 5.34.



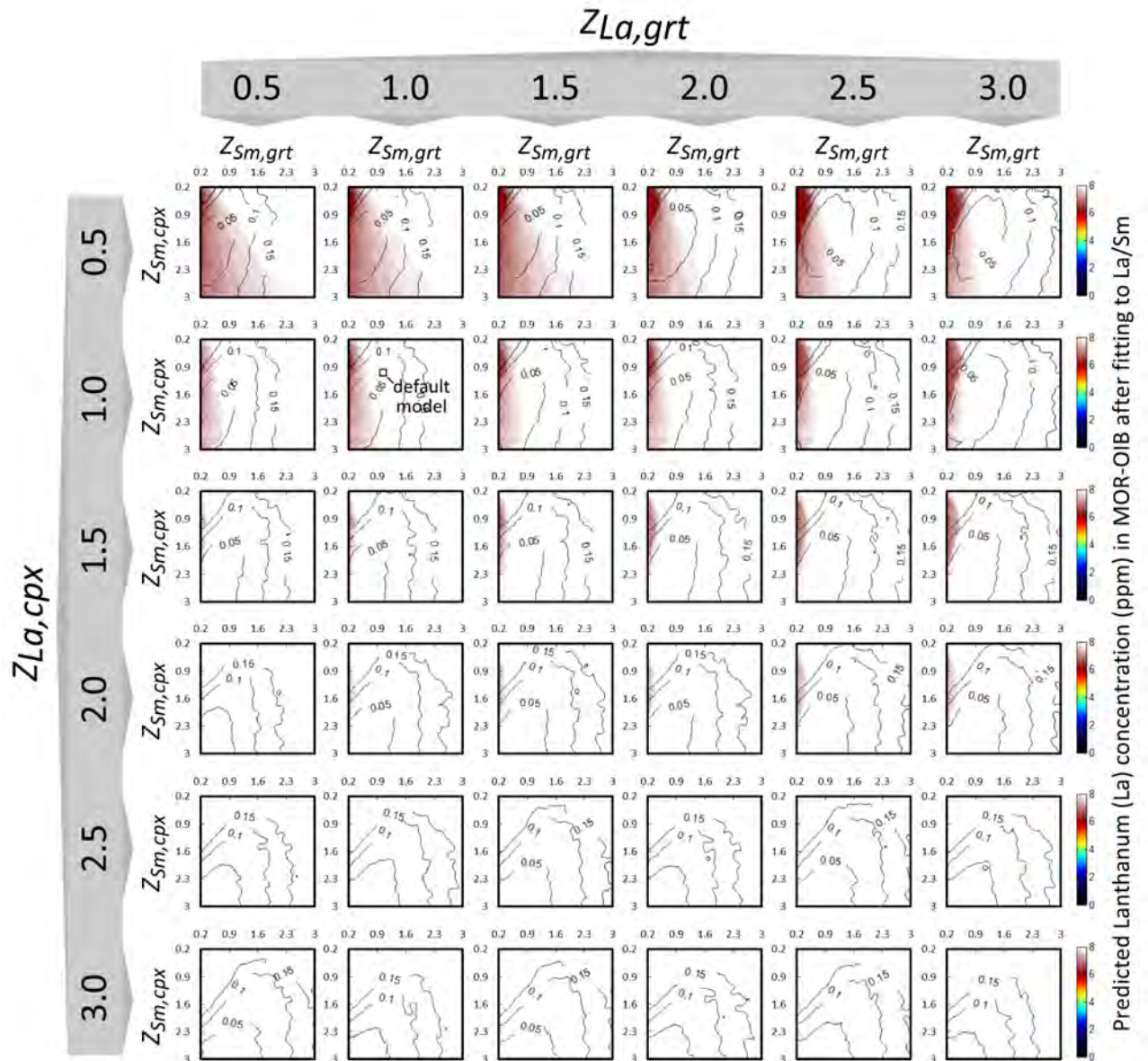


FIGURE 5.47: Predicted absolute La concentration over ridge axes (approximated by eruptions on seafloor age of 1 Ma) obtained from the fit to La/Sm and an estimate of Sm concentration in thick-plate OIB. The position of our default model is indicated in the second row, second column panel. The black contours are corresponding values of misfit from Fig. 5.33.

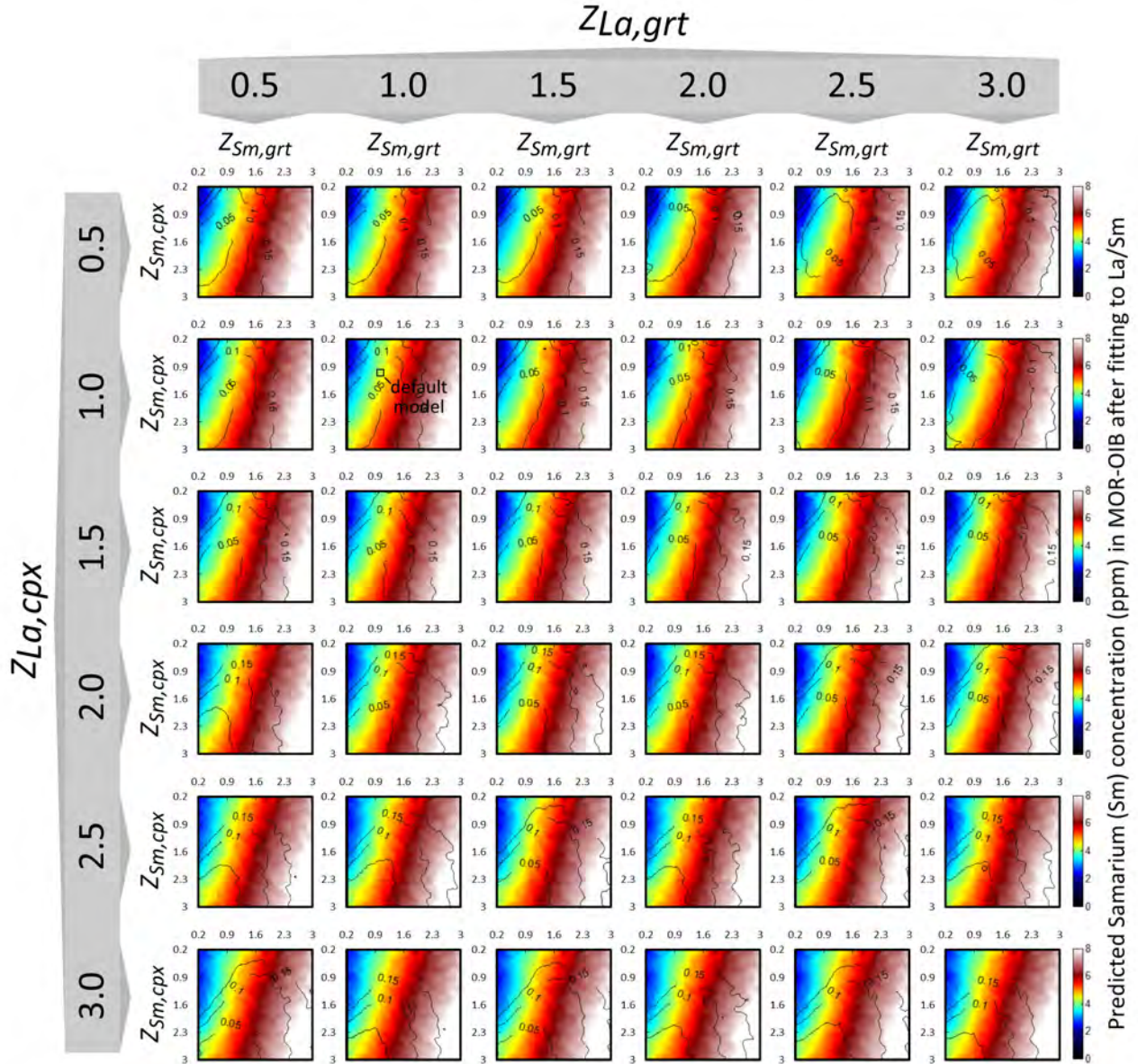


FIGURE 5.48: Predicted absolute Sm concentration over ridge axes (approximated by eruptions on seafloor age of 1 Ma) obtained from the fit to La/Sm and an estimate of Sm concentration in thick-plate OIB. The position of our default model is indicated in the second row, second column panel. The black contours are corresponding values of misfit from Fig. 5.33.



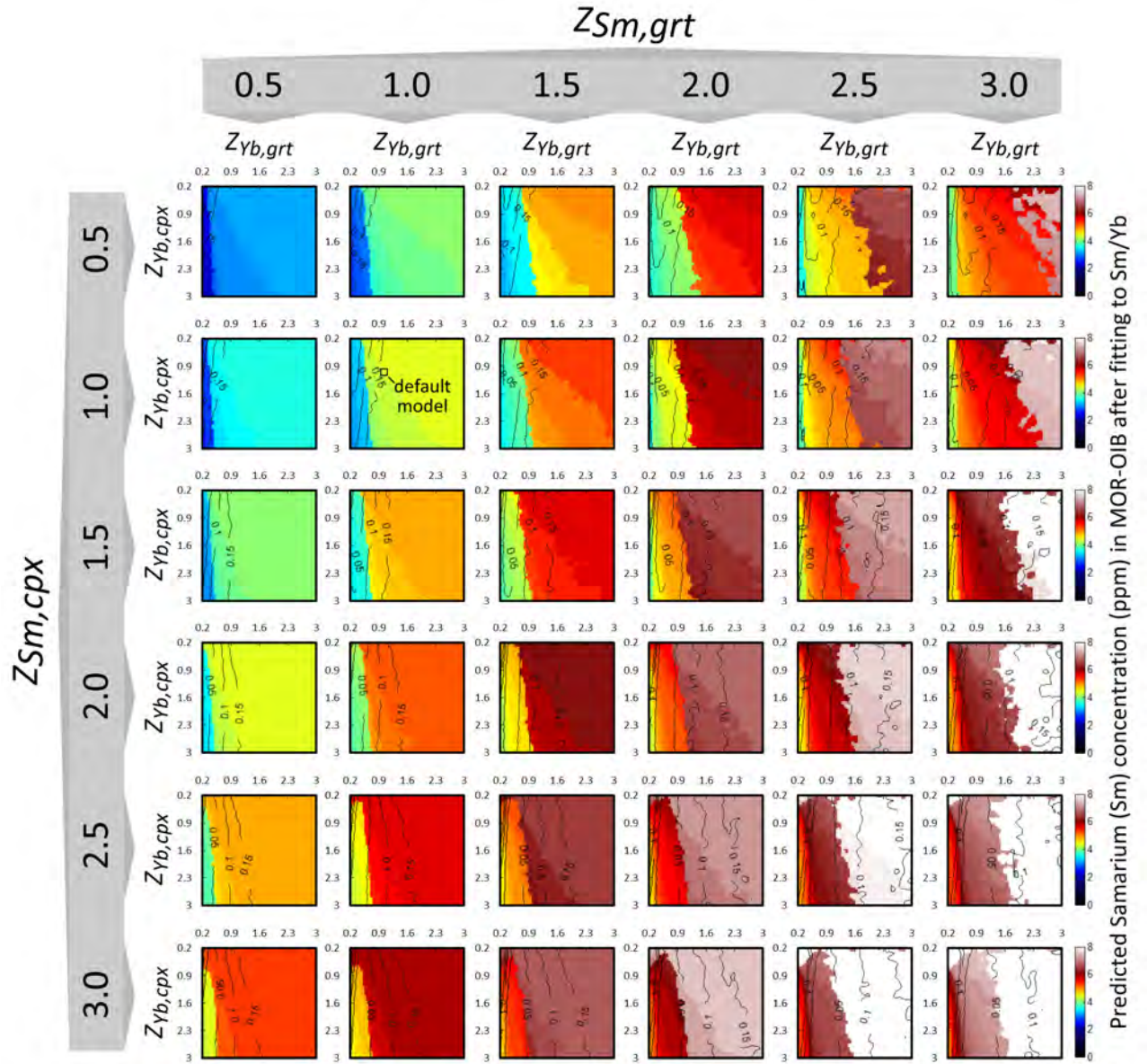


FIGURE 5.49: Predicted absolute Sm concentration over ridge axes (approximated by eruptions on seafloor age of 1 Ma) obtained from the fit to Sm/Yb and an estimate of Sm concentration in thick-plate OIB. The position of our default model is indicated in the second row, second column panel. The black contours are corresponding values of misfit from Fig. 5.34.

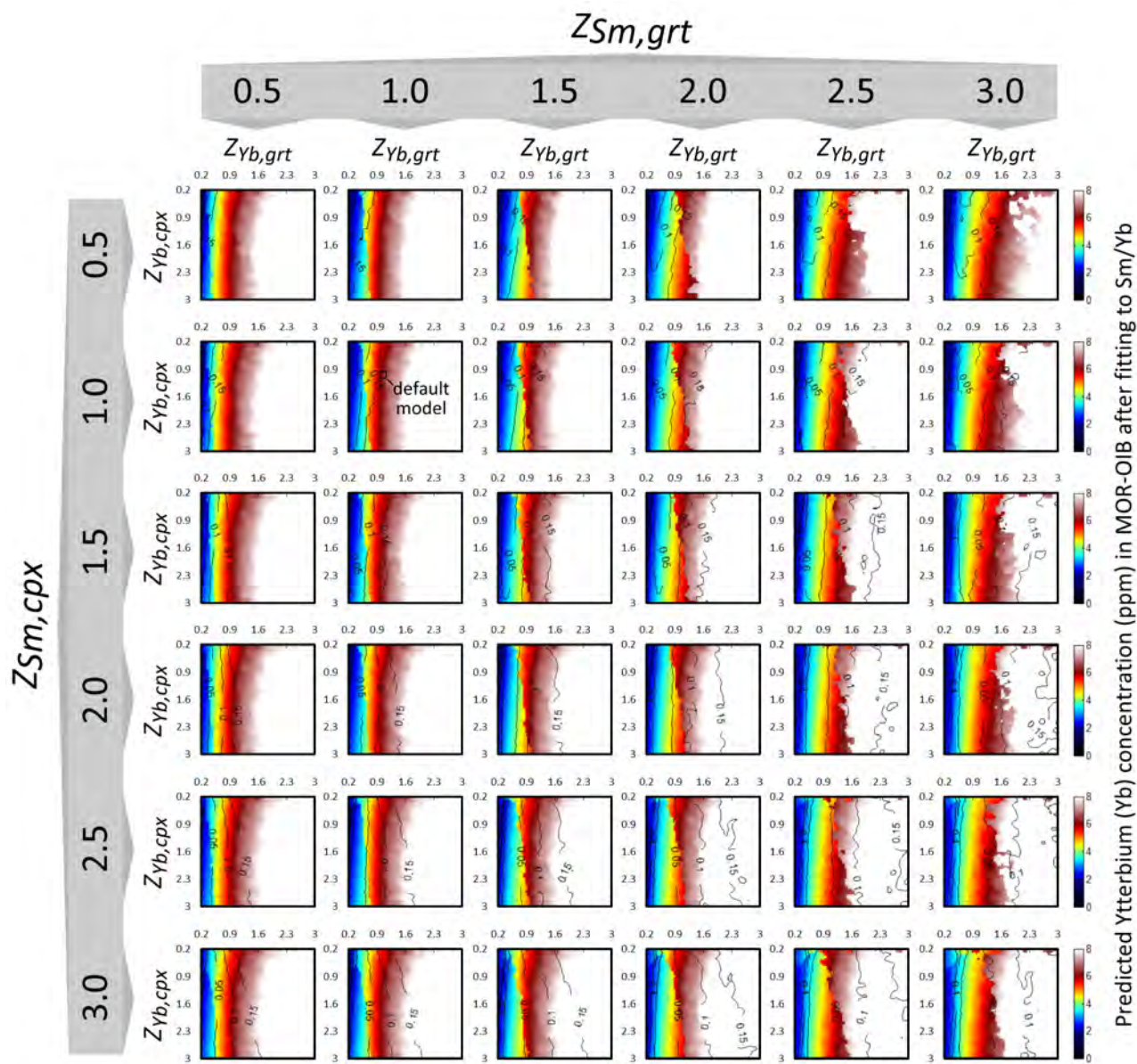


FIGURE 5.50: Predicted absolute Yb concentration over ridge axes (approximated by eruptions on seafloor age of 1 Ma) obtained from the fit to Sm/Yb and an estimate of Sm concentration in thick-plate OIB. The position of our default model is indicated in the second row, second column panel. The black contours are corresponding values of misfit from Fig. 5.34.



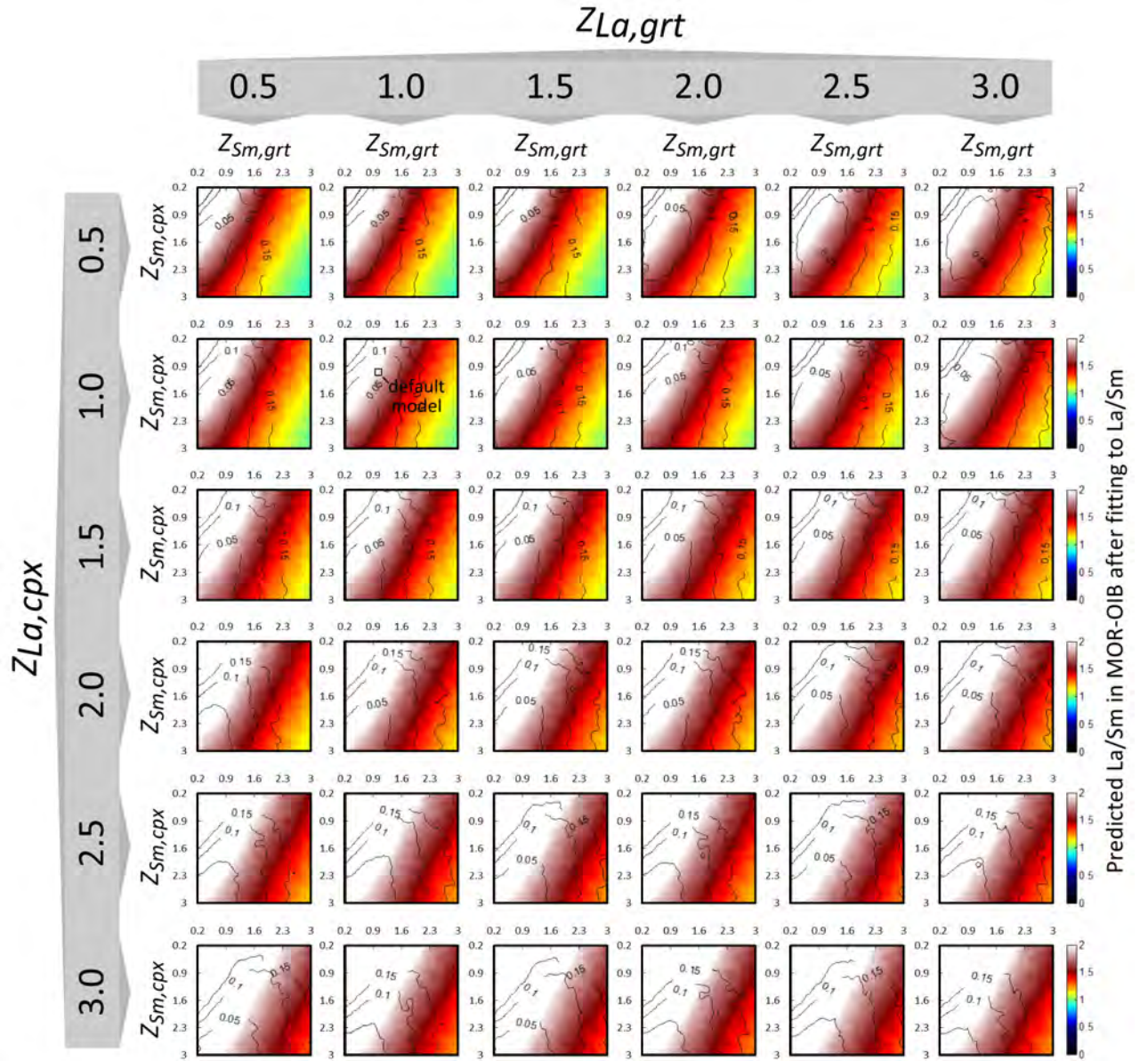


FIGURE 5.51: Predicted La/Sm concentration over ridge axes (approximated by eruptions on seafloor age of 1 Ma) obtained from the fit to La/Sm. The position of our default model is indicated in the second row, second column panel. The black contours are corresponding values of misfit from Fig. 5.33.

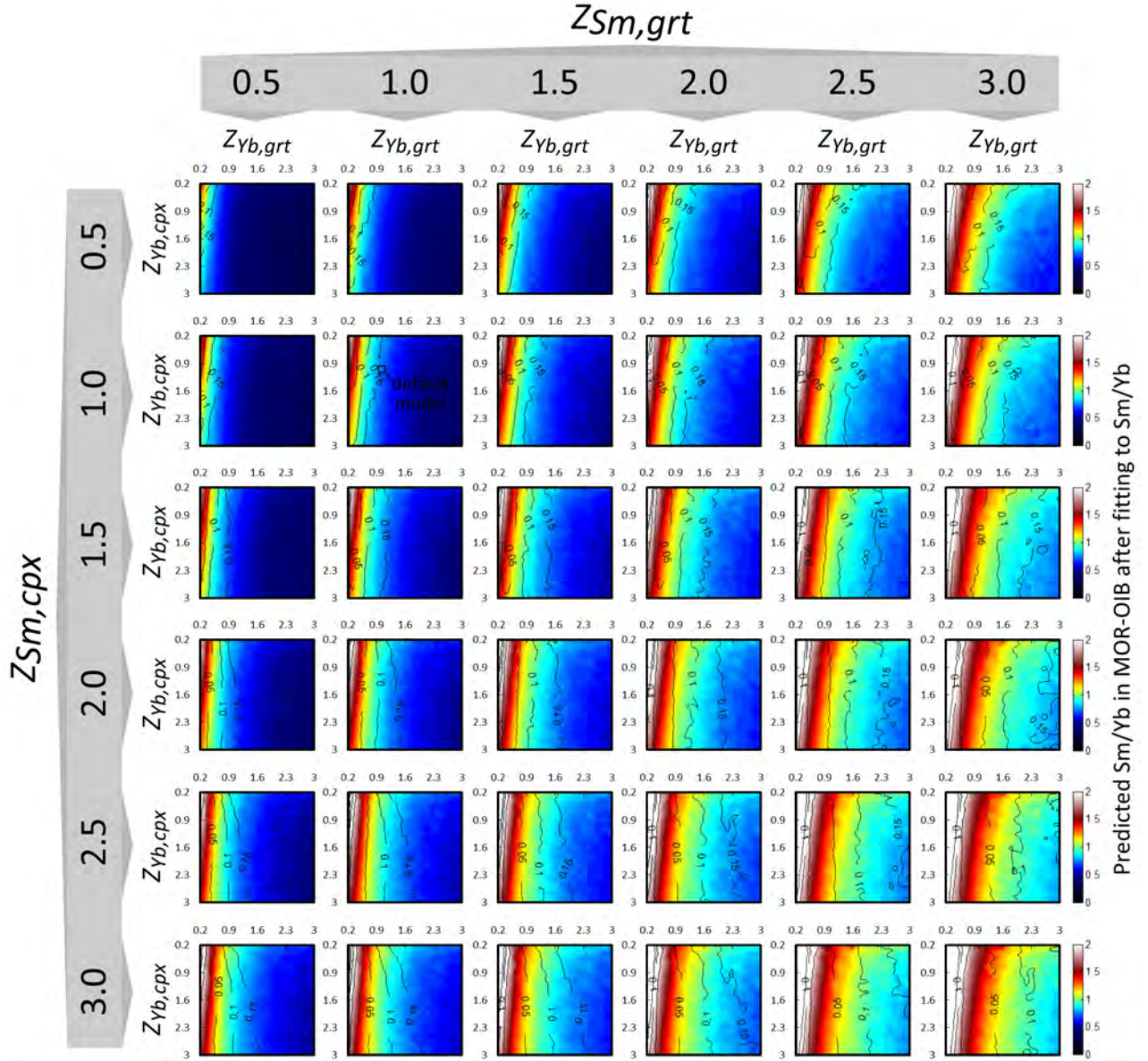


FIGURE 5.52: Predicted Sm/Yb concentration over ridge axes (approximated by eruptions on seafloor age of 1 Ma) obtained from the fit to Sm/Yb. The position of our default model is indicated in the second row, second column panel. The black contours are corresponding values of misfit from Fig. 5.33.



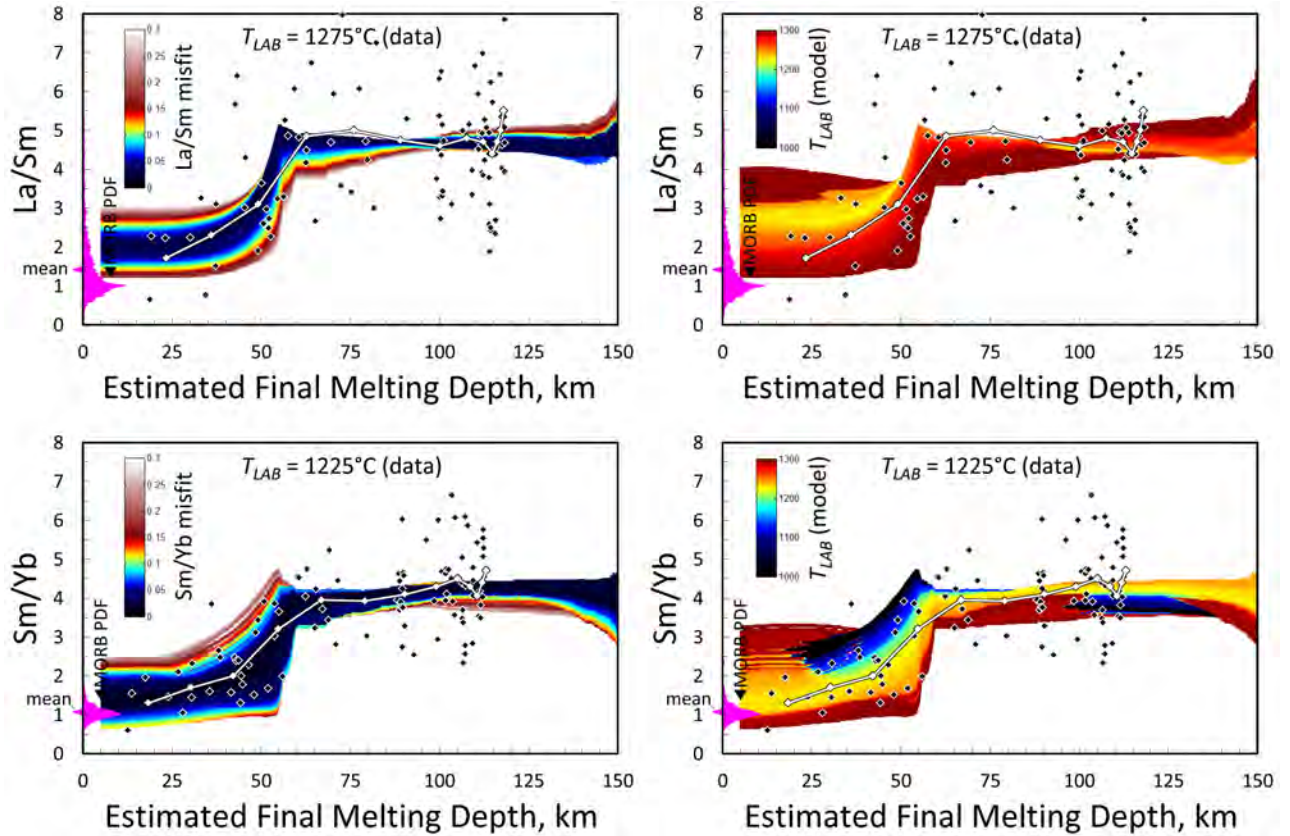


FIGURE 5.53: Comparison of the empirical data (black diamonds with white borders), our bins to which we fit models (white connected diamonds with black borders), and the predictions of all models from our sensitivity analysis of partition coefficients (Fig. 5.33-5.36). The top figures show data and model results for La/Sm, and the bottom figures show data and models for Sm/Yb. The curves in the left panels are colored according to their misfit, whereas the curves in the right panels are colored according to the  $T_{LAB}$  of each model. The data in the bottom plots has used  $T_{LAB} = 1225^\circ \text{C}$ , and in the top plots have used  $T_{LAB} = 1275^\circ \text{C}$ . In addition, the pink data on the left hand side of each figure shows a density function for La/Sm and Sm/Yb in MORB from the data of Gale et al. (2013).



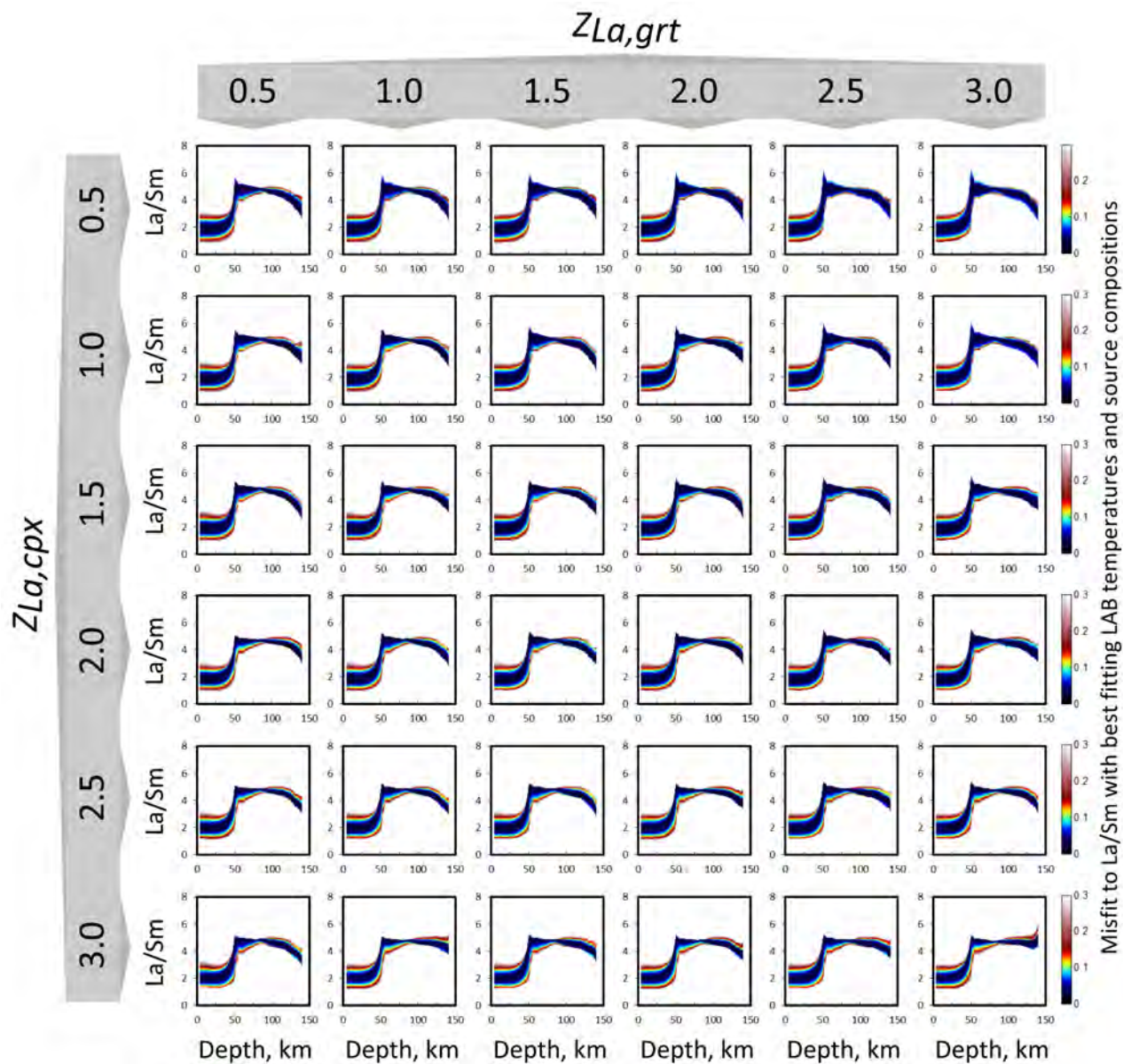


FIGURE 5.54: Predictions of cumulative melt concentration, as in Fig. 5.53, except all combinations of  $Z_{La,cpx}$  and  $Z_{La,grt}$  are shown, corresponding to the panels in Fig. 5.33. Curves are colored according to the misfit of each model.

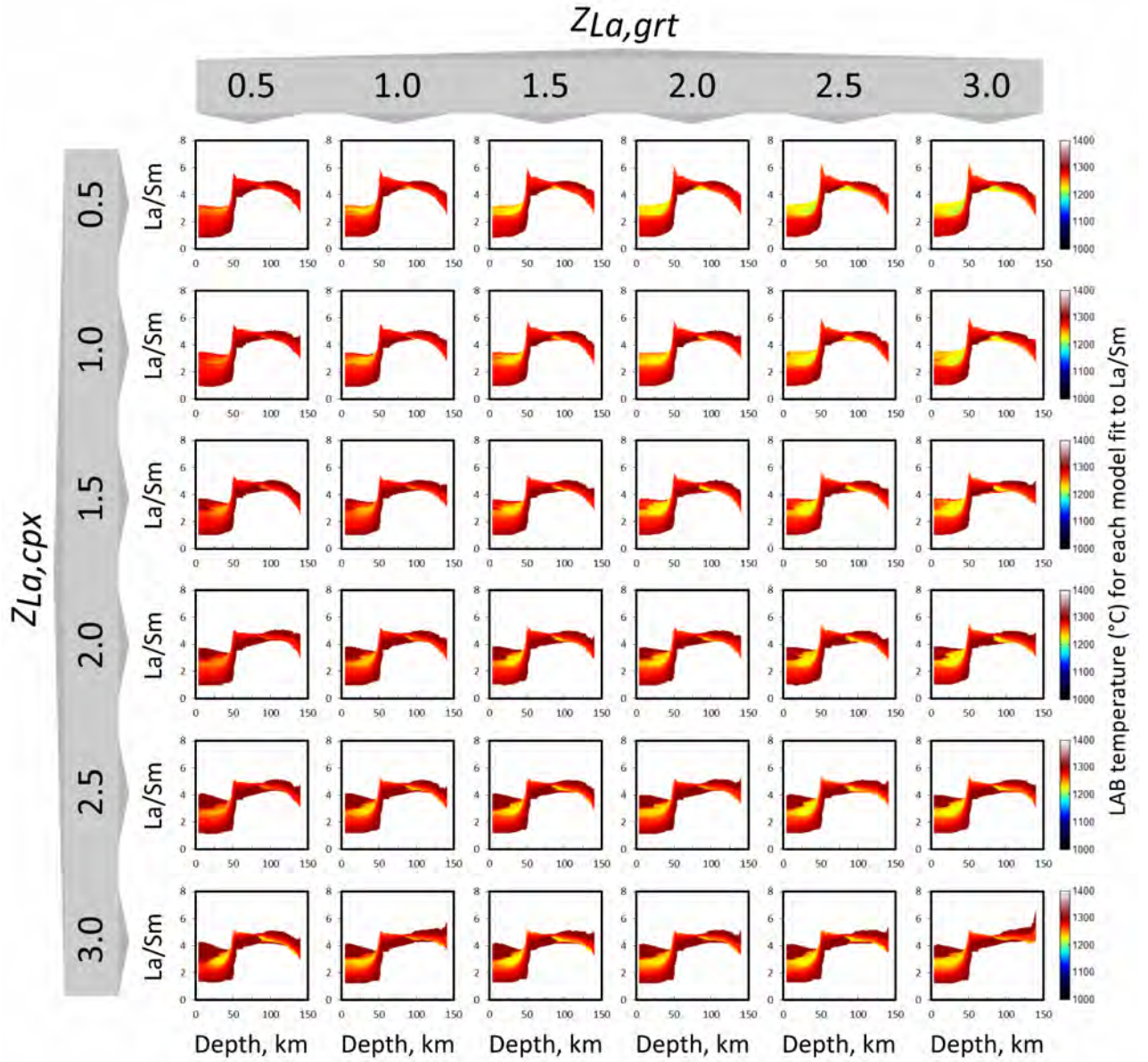


FIGURE 5.55: Predictions of cumulative melt concentration, as in Fig. 5.53, except all combinations of  $Z_{La,cpx}$  and  $Z_{La,grt}$  are shown, corresponding to the panels in Fig. 5.33. Curves are colored according to the LAB temperatures of each model.



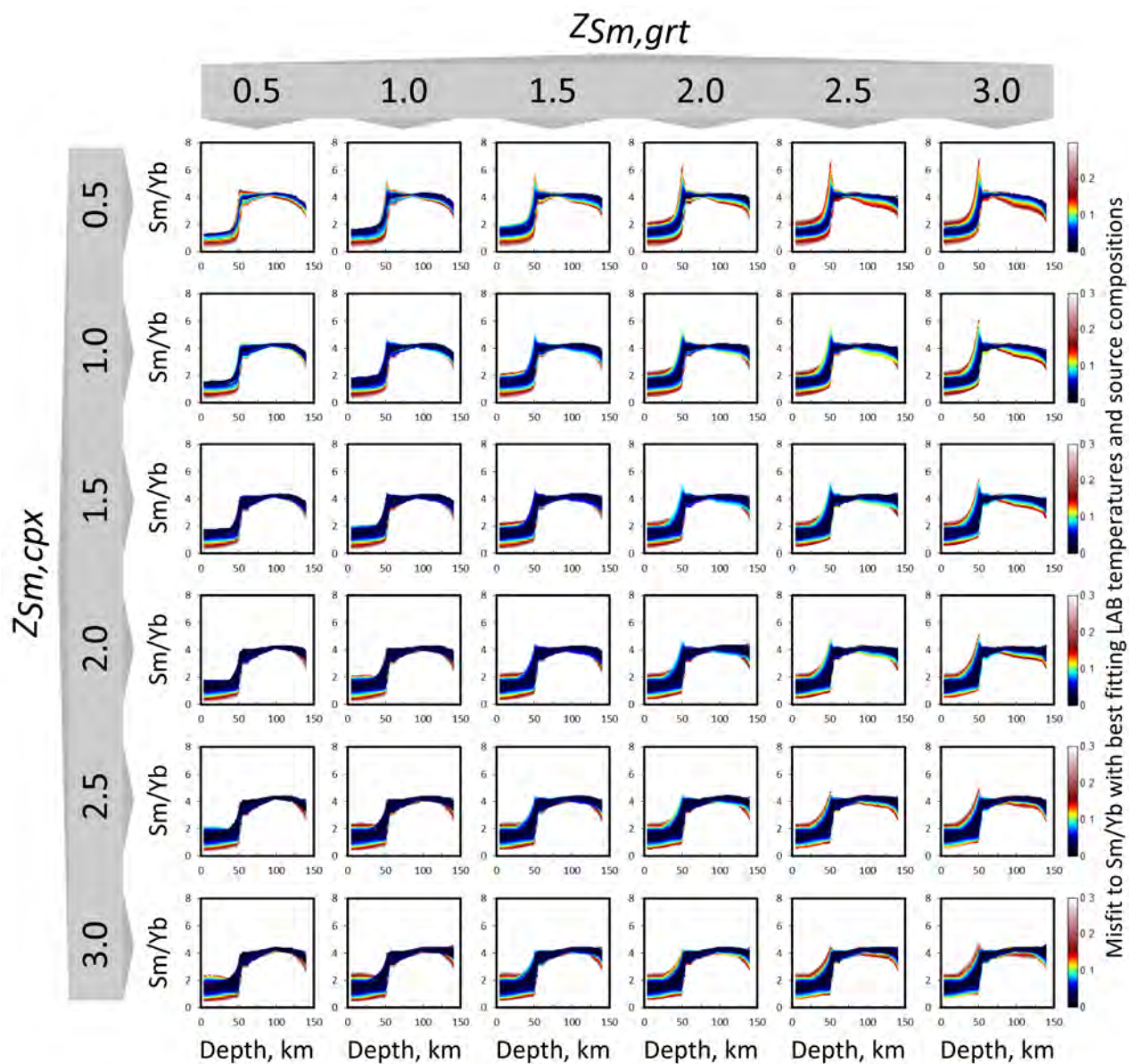


FIGURE 5.56: Predictions of cumulative melt concentration, as in Fig. 5.53, except all combinations of  $Z_{Sm,cpx}$  and  $Z_{Sm,grt}$  are shown, corresponding to the panels in Fig. 5.34. Curves are colored according to the misfit of each model.

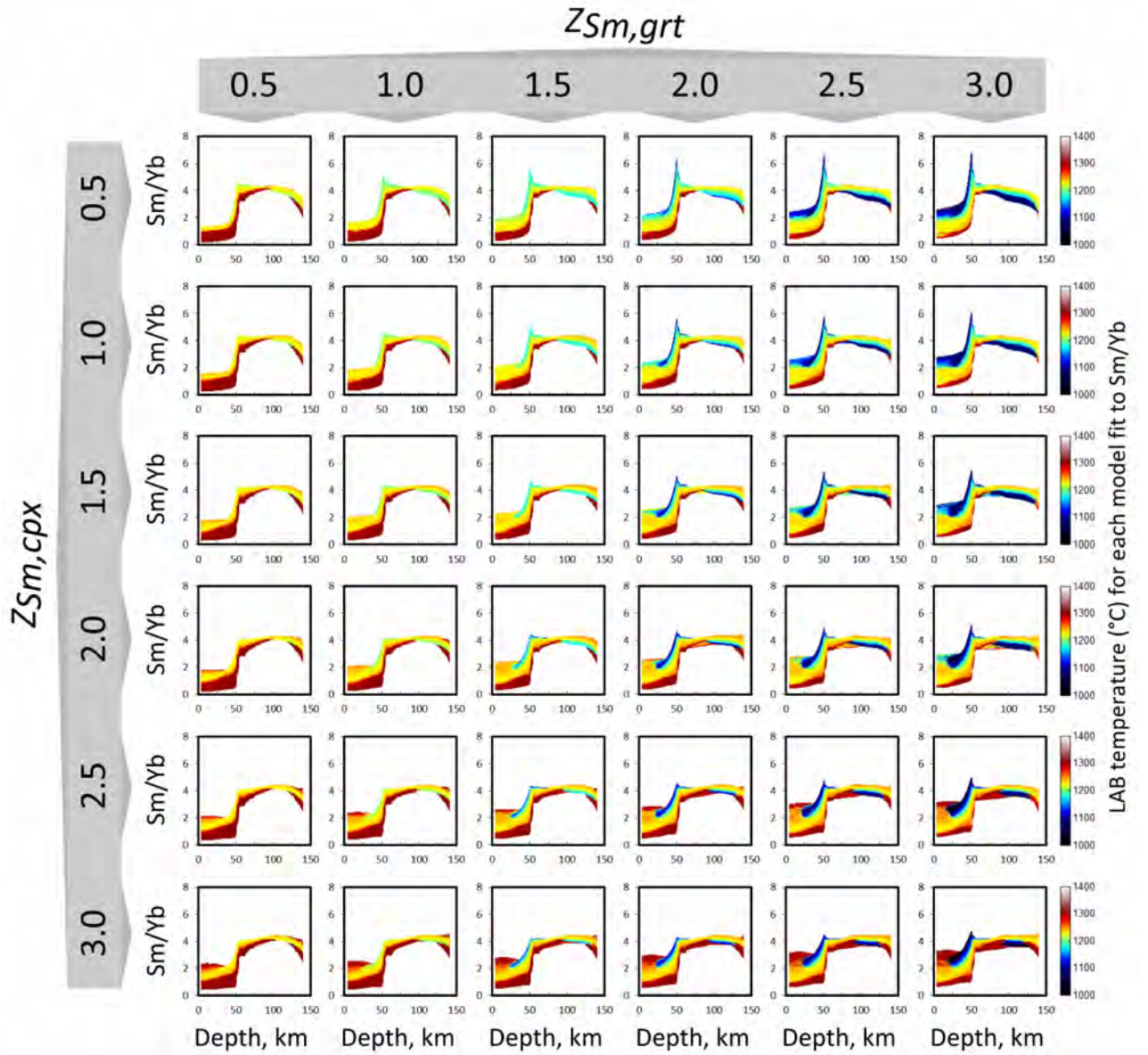


FIGURE 5.57: predictions of cumulative melt concentration, as in Fig. 5.53, except all combinations of  $Z_{Sm,cpx}$  and  $Z_{Sm,grt}$  are shown, corresponding to the panels in Fig. 5.34. Curves are colored according to the LAB temperatures of each model.

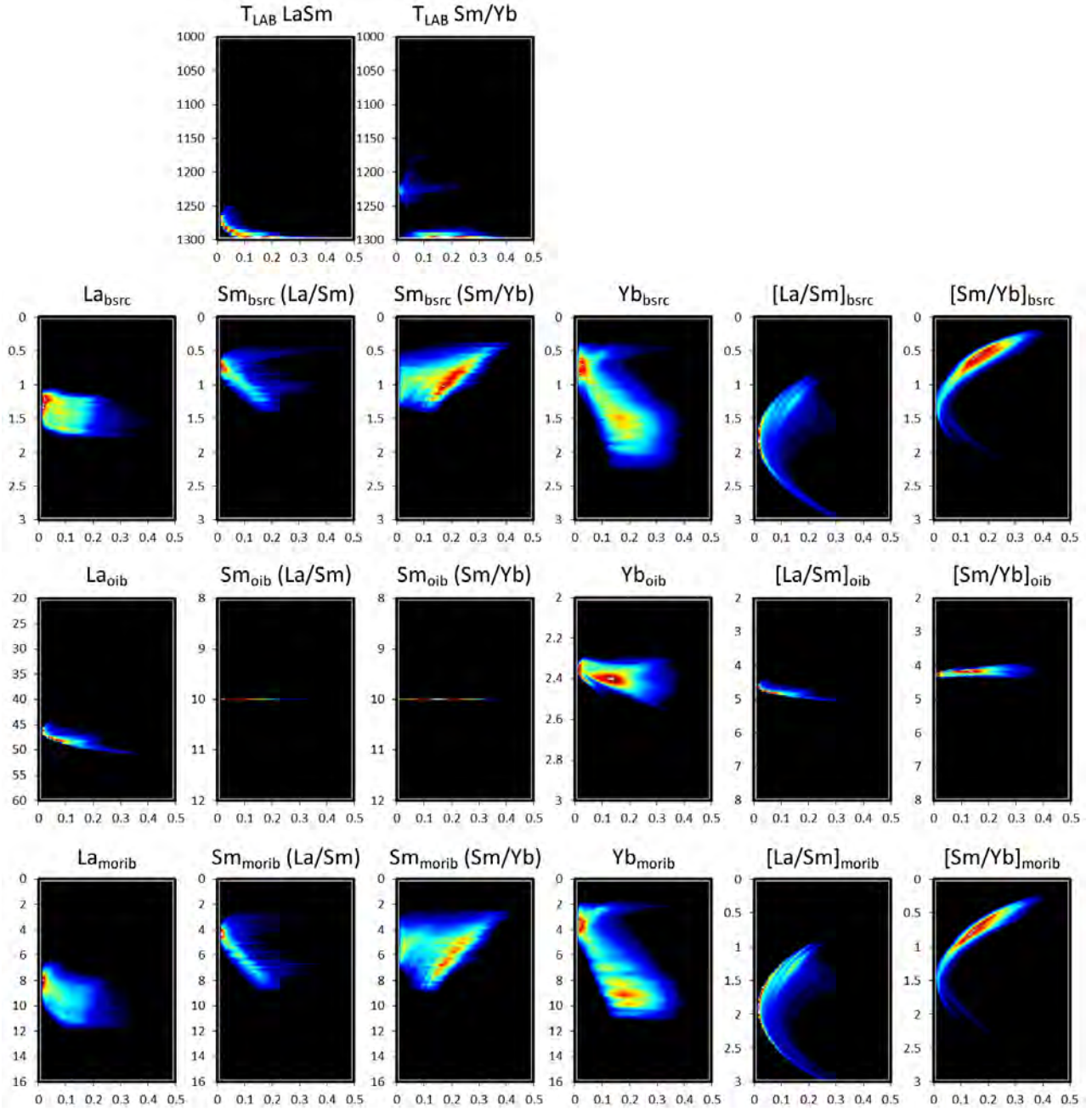


FIGURE 5.58: Probability density fields constructed from the predicted model properties in Fig. (5.33 and Fig. 5.34). The horizontal scales in each of these figures is the misfit  $m$ . Values of La, Sm, and Yb for bulk source (bsrc), thick-plate OIB (oib), and Mid-Ocean Ridge Island Basalt (morib) concentrations are in units of ppm. Values of  $T_{LAB}$  are in units of °C. The means and half-maximum bounds of the data for misfit  $< 0.05$  are tabulated in Table 5.24.



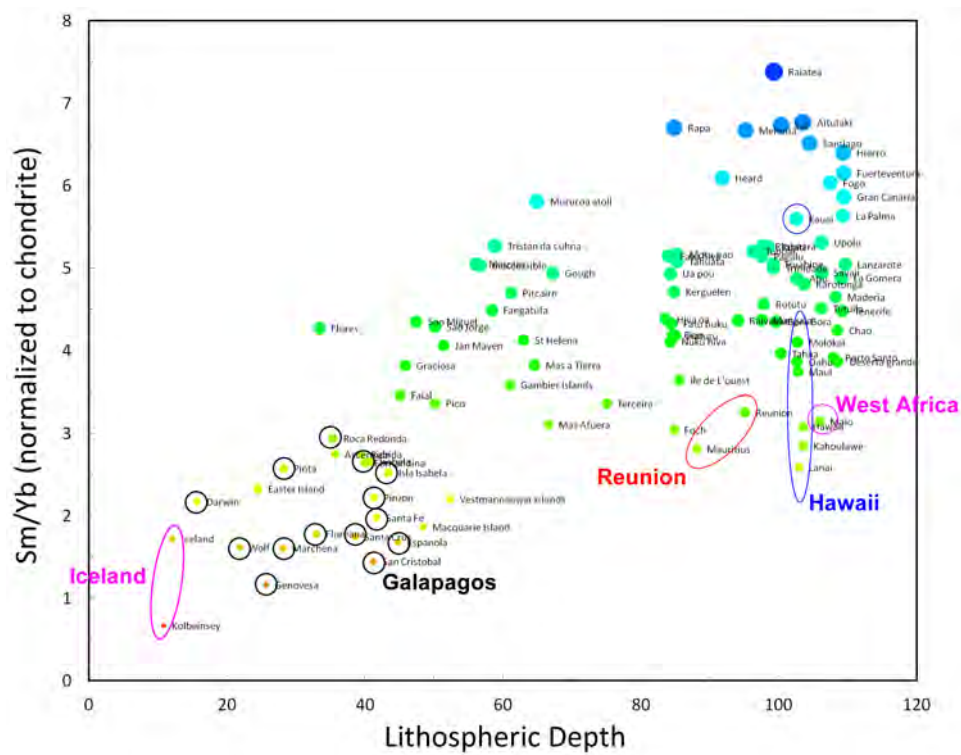


FIGURE 5.59: The empirical Sm/Yb data (normalized to Chondrite) from Humphreys and Niu (2009) with islands, and some island groups, labeled.

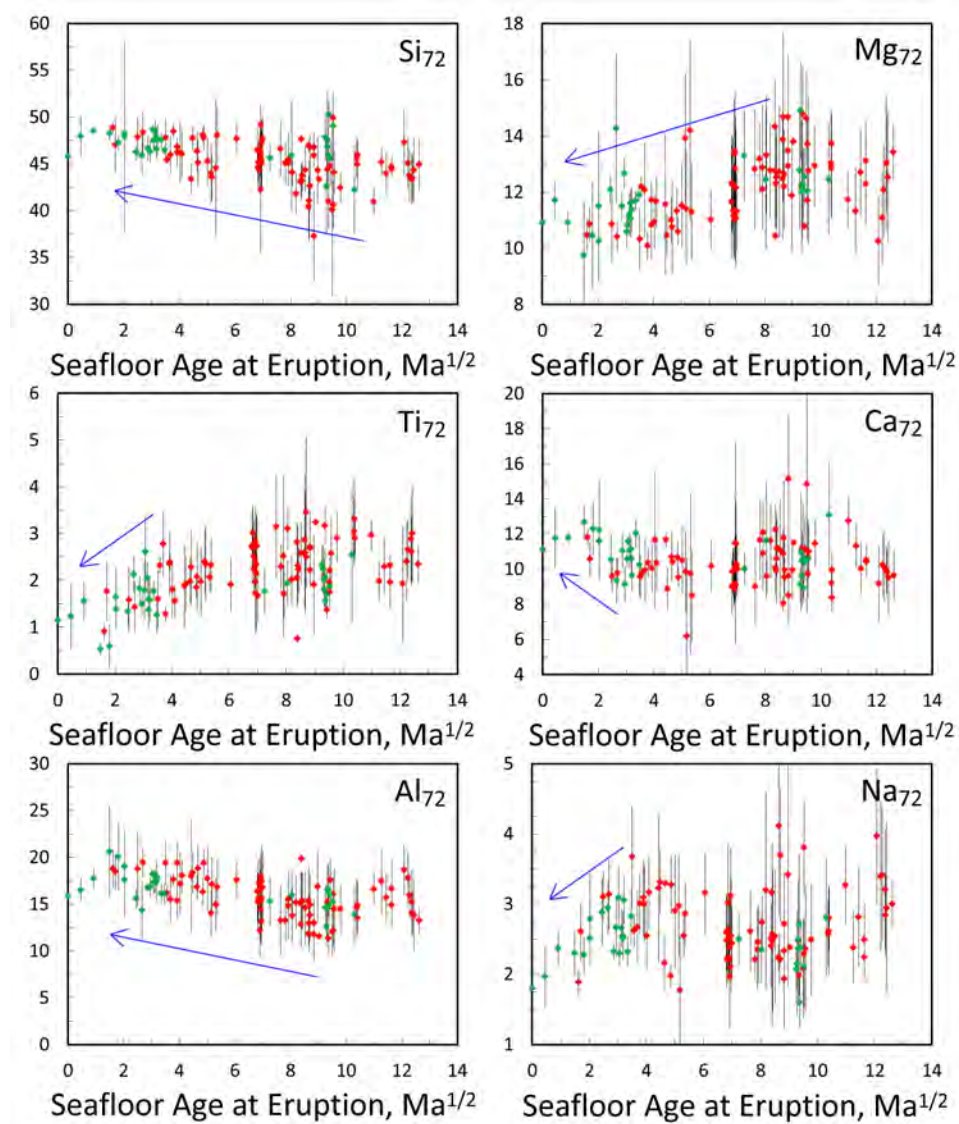


FIGURE 5.60: Major element systematics for oxides corrected to Mg-number 0.72 by Humphreys and Niu (2009) and Niu (2011). Values are given in wt. %. Error bars are  $1\sigma$  standard deviations of the intra-island dataset. Green symbols indicate islands associated with classical hotspots (Fig. 5.59) and red values indicate all other islands.



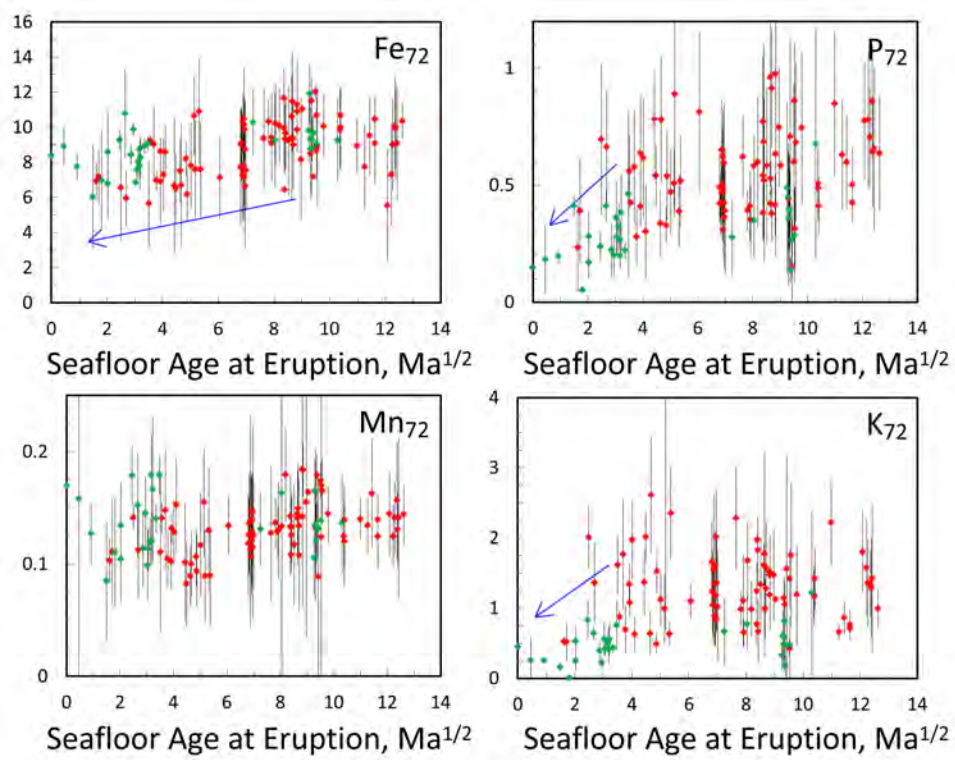


FIGURE 5.61: Continued from previous panels.

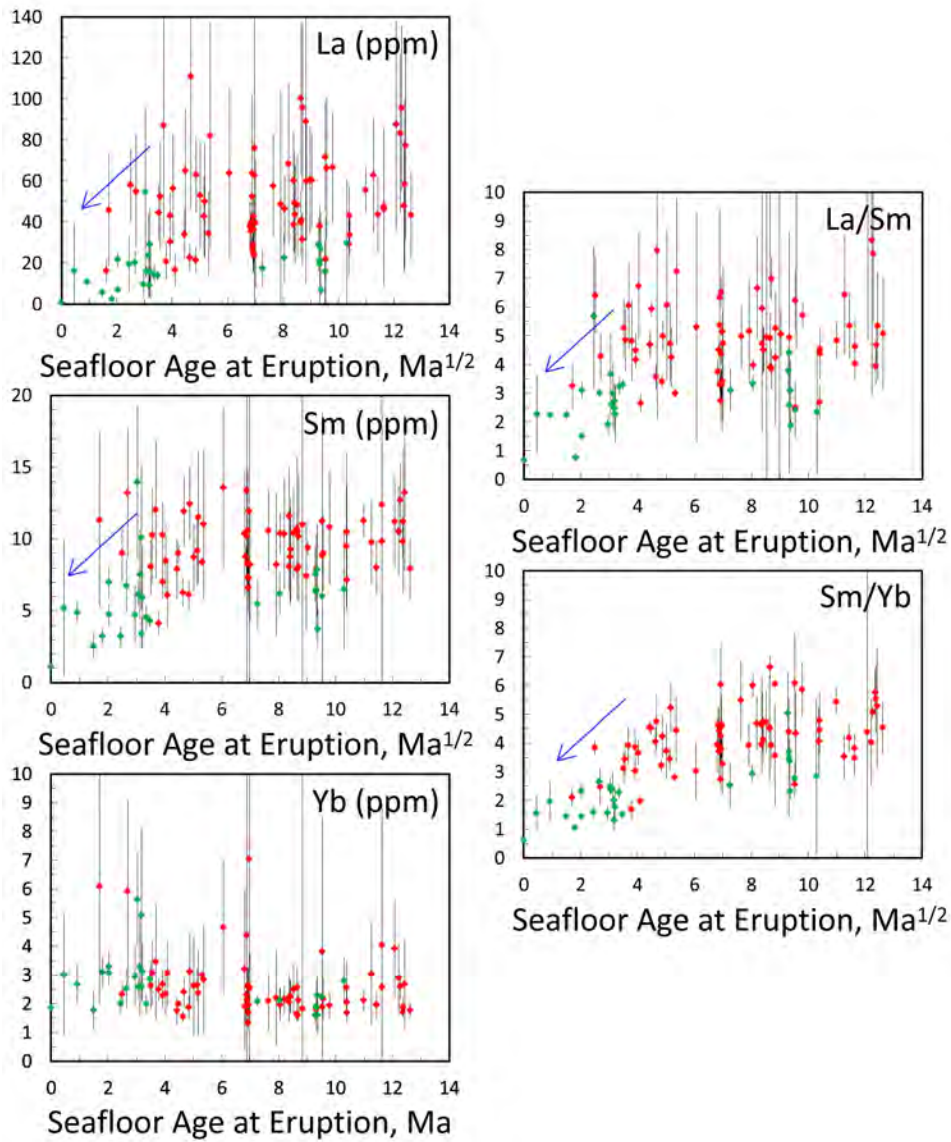


FIGURE 5.62: Absolute values of La, Sm, Yb, and ratios La/Sm and Sm/Yb of all OIB sources considered in this work. Data from Humphreys and Niu (2009). Error bars are  $1\sigma$  standard deviations of the intra-islandic dataset. Green symbols indicate islands associated with classical hotspots (Fig. 5.59) and red values indicate all other islands.

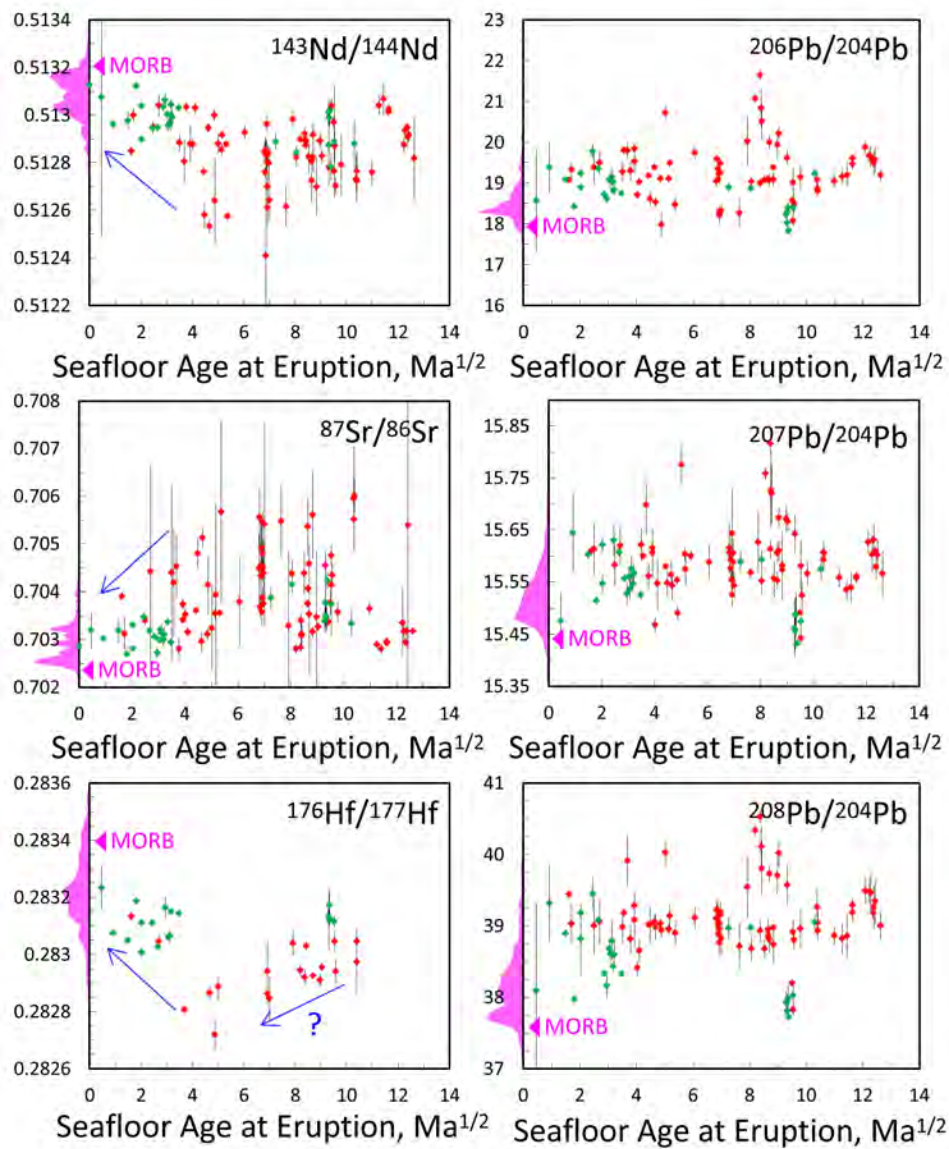


FIGURE 5.63: Isotopic ratios for all islands in the dataset of Niu (2011). Error bars are  $1\sigma$  standard deviations of the intra-islandic dataset. The pink density function projecting to the left of each panel represents values observed in MORB from Gale et al. (2013). Green symbols indicate islands associated with classical hotspots (Fig. 5.59) and red values indicate all other islands.

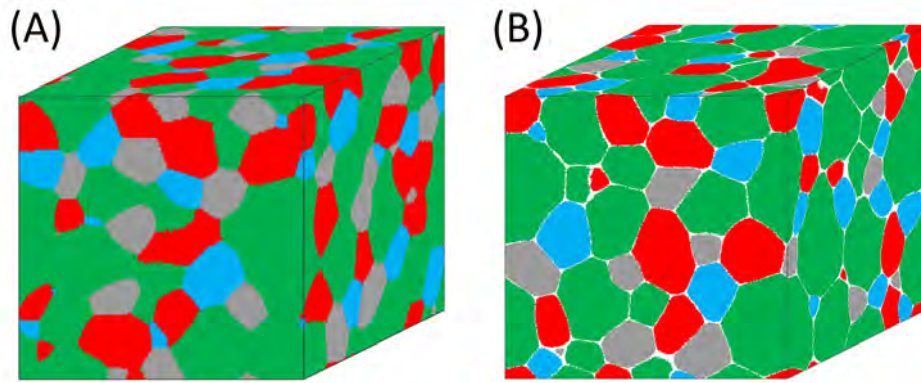


FIGURE 5.64: Three-dimensional microstructures produced from our 3D Potts models. a) model without melt present, b) model with 5% melt. Green is olivine, grey is opx, blue is cpx, red is garnet, and white is melt.

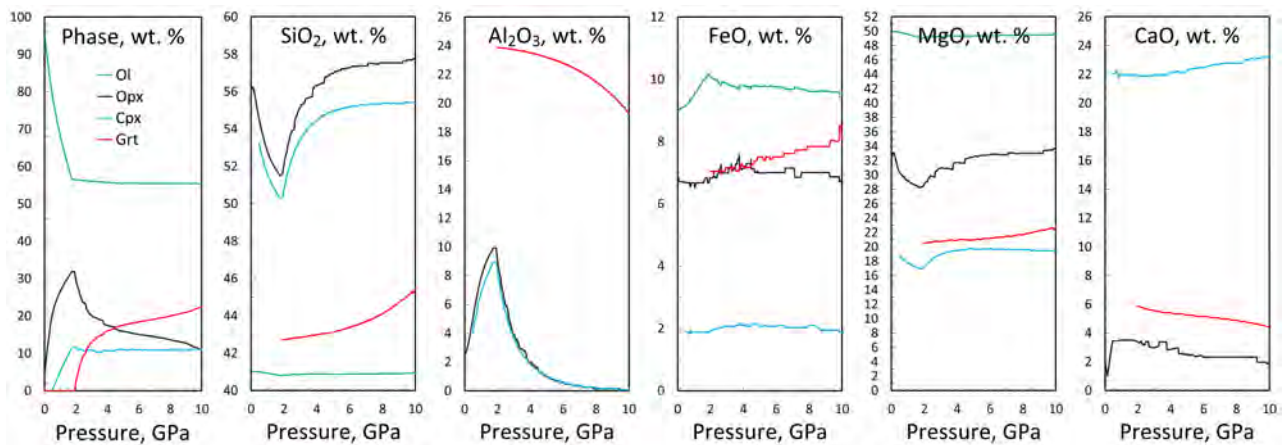


FIGURE 5.65: Compositions of phases at equilibrium as a function of pressure, calculated as described in Sec. 5.5.



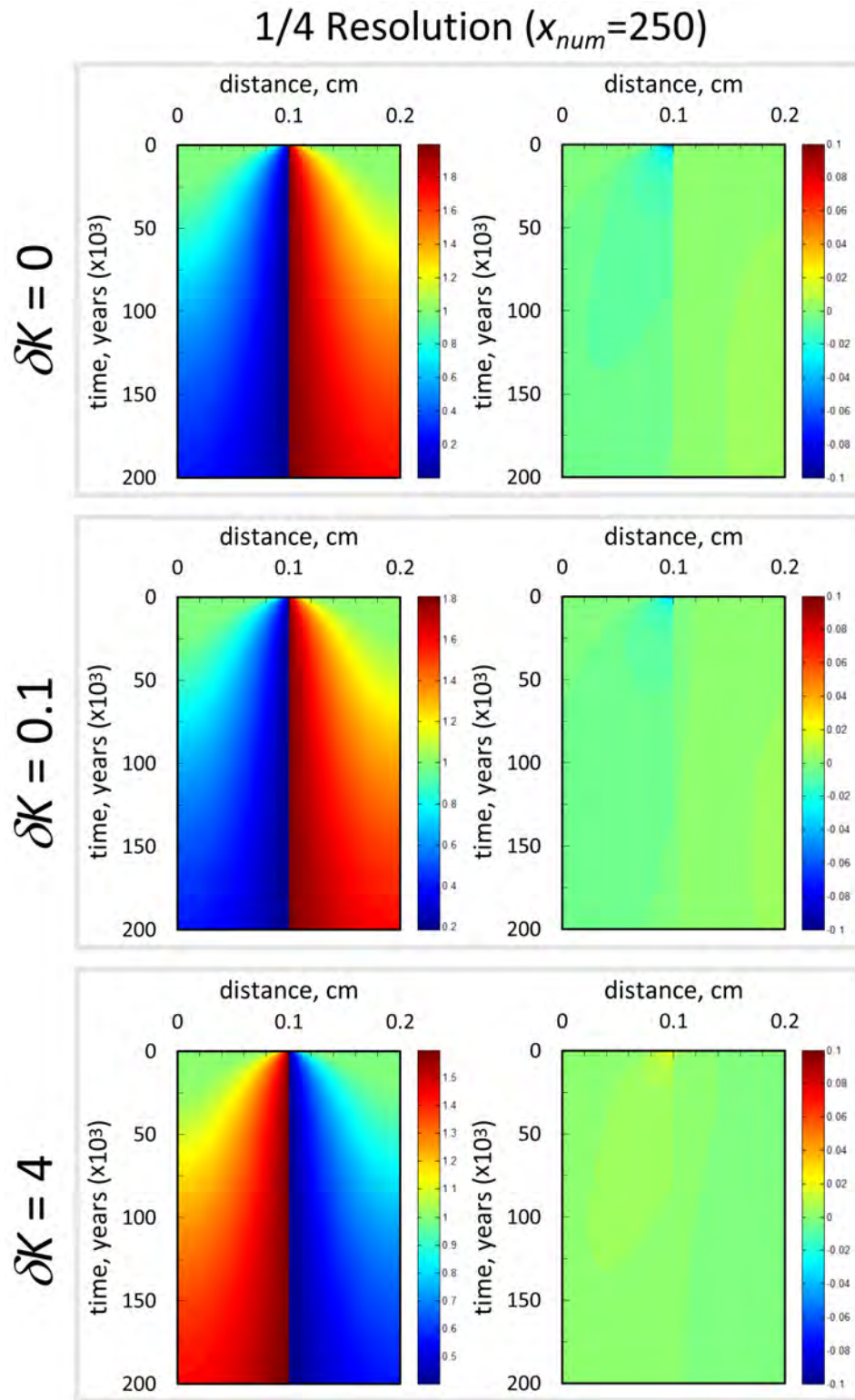


FIGURE 5.66: Benchmark of model resolution, here results are shown for 250 finite difference nodes. See Appendix 5.C.1 for discussion.

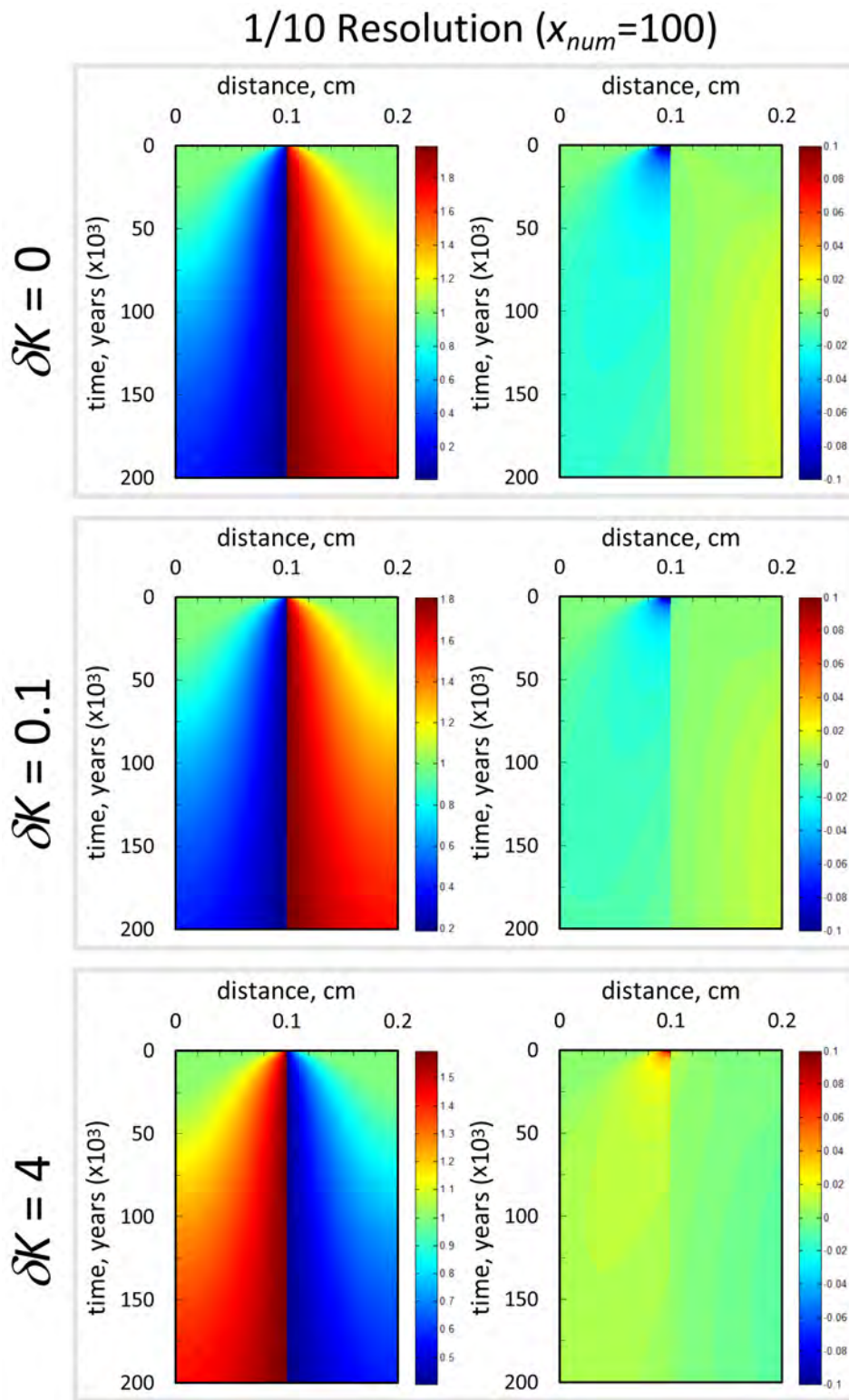


FIGURE 5.67: Benchmark of model resolution, here results are shown for 100 finite difference nodes. See Appendix 5.C.1 for discussion.

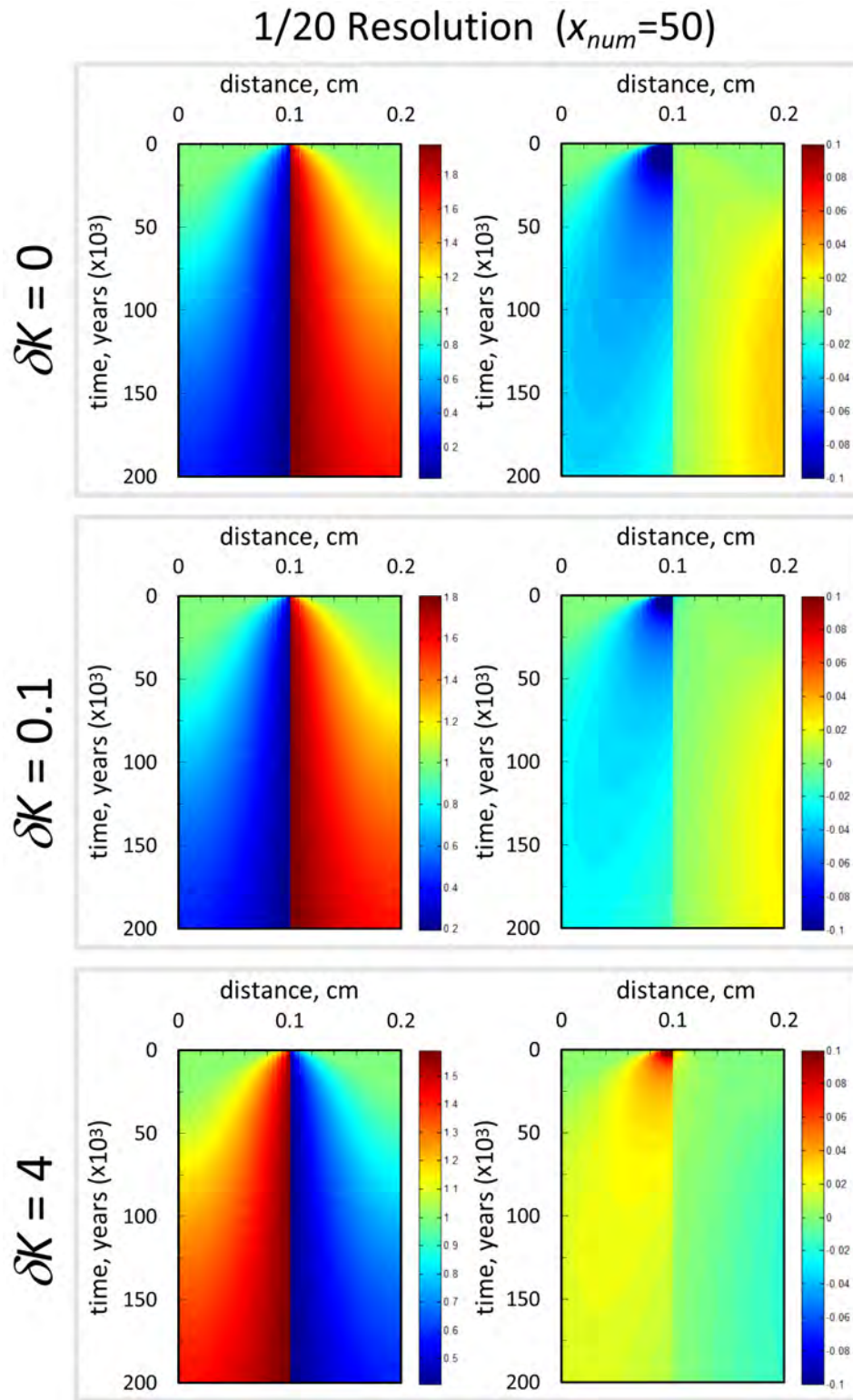


FIGURE 5.68: Benchmark of model resolution, here results are shown for 50 finite difference nodes. See Appendix 5.C.1 for discussion.



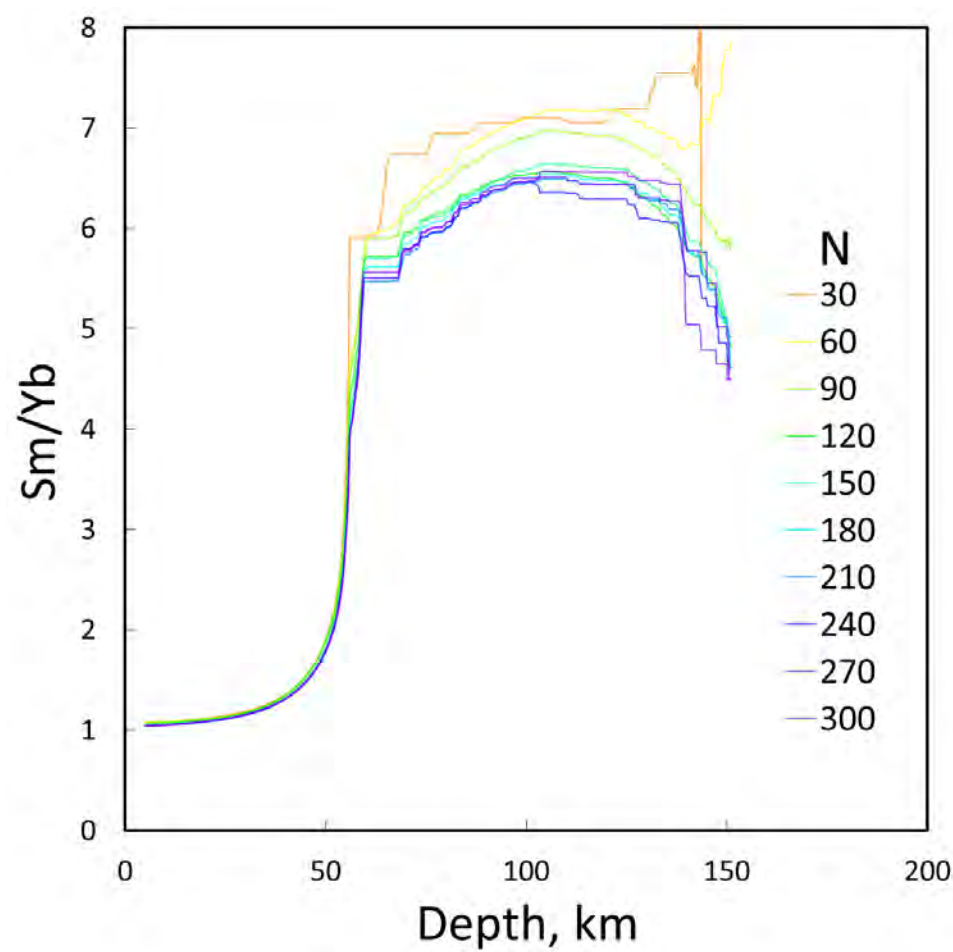


FIGURE 5.69: Sm/Yb predicted by models with different grid sizes. See Appendix 5.C.2 for discussion.

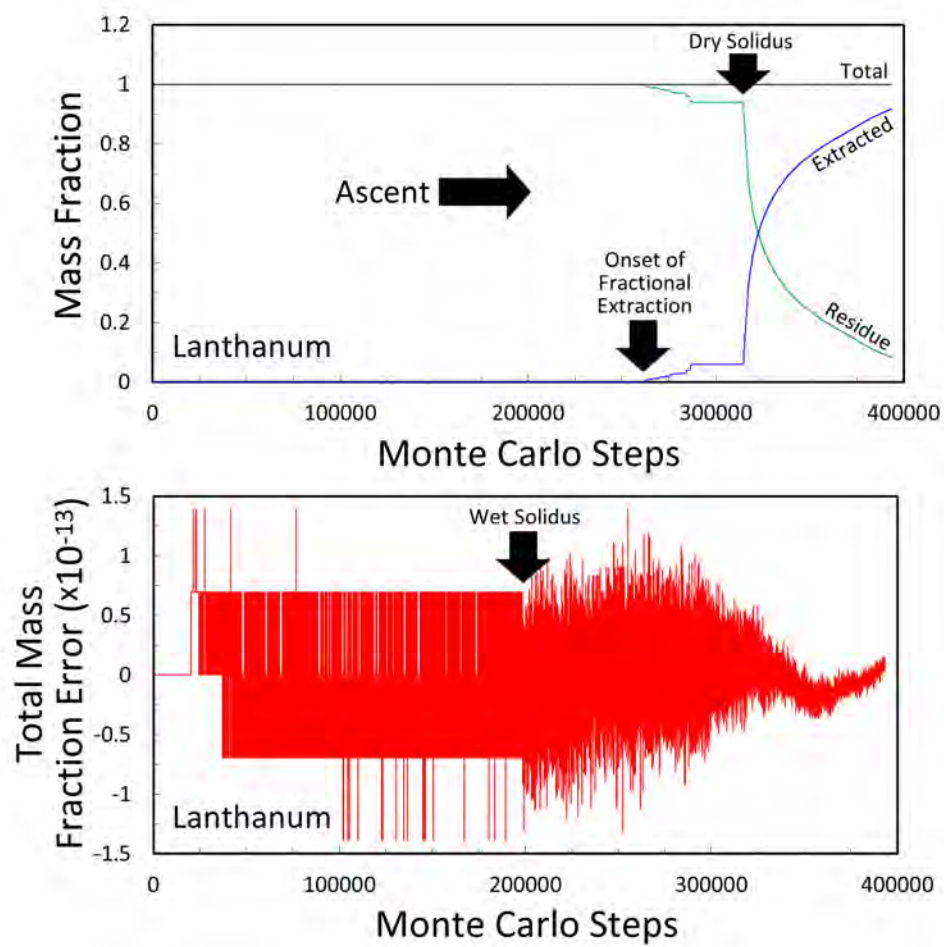


FIGURE 5.70: Benchmark of mass conservation in a typical model. See Appendix 5.C.3 for discussion.



## References

- Adam, J. T. H. Green, S. H. Sie, C. G. Ryan (1997), Trace element partitioning between aqueous fluids, silicate melts and minerals. *Eur. J. Mineral.*, 9, 569-584.
- Adam, J., and T. Green (2006), Trace element partitioning between mica- and amphibole-bearing garnet lherzolite and hydrous basanitic melt: 1. Experimental results and the investigation of controls on partitioning behavior. *Contrib. Mineral. Petrol.*, 152:1-17.
- Adam, J., and T. Green (2010), Trace element partitioning between mica- and amphibole-bearing garnet lherzolite and hydrous basanitic melt: 2. Tasmanian Cainozoic basalts and the origins of intraplate basaltic magmas. *Contrib. Mineral. Petrol.*, DOI 10.1007/s00410-010-0570-7
- Adam, J., M. Locmelis, J. C. Afonso, T. Rushmer, M. L. Fiorentini (2014), The capacity of hydrous fluids to transport and fractionate incompatible elements and metals within the Earths mantle. *Geochem. Geophys. Geosyst.*, 15, doi:10.1002/2013GC005199.
- Adam, J., T. H. Green, and S. H. Sie (1993), Proton microprobe determined partitioning of Rb, Sr, Ba, Y, Zr, Nb, and Ta between experimentally produced amphiboles and silicate melts with variable F content. *Chem. Geol.*, 109, 29-49.
- Afonso, J. C., and Zlotnik S. (2011), The subductability of the continental lithosphere: the before and after story, in *Arc-continent collision*, D. Brown and P.D. Ryan (eds.), *Frontiers in Earth Sciences*, 53-86.
- Afonso, J. C., and D. L. Schutt (2012), The effects of polybaric partial melting on density and seismic velocities of mantle restites. *Lithos*, 134-135, 289-303.
- Afonso, J. C., G. Ranalli, and M. Fernandez (2005), Thermal expansivity and elastic properties of the lithospheric mantle: results from mineral physics of composites. *Phys. Earth Planet. Int.*, 149, 279-306.
- Afonso, J.C., G. Ranalli, and M. Fernandez (2007), Density structure and buoyancy of the oceanic lithosphere revisited, *Geophys. Res. Lett.*, 34, L10302.
- Afonso, J.C., M. Fernandez, G. Ranalli, W. L. Griffin, and J. A. D. Connolly (2008a), Integrated geophysical-petrological modeling of the lithosphere and sublithospheric upper mantle: Methodology and applications, *Geochem. Geophys. Geosys.*, 9, 5.

- Afonso, J.C., Zlotnik, S., M. Fernandez (2008b), Effects of compositional and rheological stratifications on small-scale convection under the oceans: implications for the thickness of oceanic lithosphere and seafloor flattening. *Geophys. Res. Lett.*, 35, DOI: 10.1029/2008GL035419.
- Aichlmayr, H.T., and Kulacki, F. A. (2006), "The Effective Thermal Conductivity of Saturated Porous Media", *Advances in Heat Transfer*, Green, G. et al., Eds., 39, pp. 377-460.
- Allegre, C. J., and D. L. Turcotte (1986), Implications of a two-component marble-cake mantle. *Nature*, 232, 123-127.
- Anderson, M. P., D. J. Srolovitz, G. S. Grest, P. S. Sahni (1984), Computer simulation of grain growth. I. Kinetics. *Acta Metall.* 32 (5), 783-791.
- Anderson, M. P., G. S. Grest, and D. J. Srolovitz (1989), Computer simulation of normal grain growth in three dimensions, *Philosophical Magazine Part B*, 59:3, 293-329.
- Anderson, O. L (1967), Equation for thermal expansivity in planetary interiors, *J. Geophys. Res.*, 72, 3661.
- Anderson, O. L. and D. G. Isaak (1995), Elastic constants of mantle minerals at high temperature, in *Mineral Physics and Crystallography: A Handbook of Physical Constants*, edited by J. T. Ahrens, pp. 64-97, American Geophysical Union, Washington, DC.
- Anderson, O.L. (1974), The determination of the volume dependence of the Gruneisen parameter, *J. Geophys. Res.*, 79, 8, 1153-1155.
- Anderson, O.L., and D.G. Isaak (1993), The dependence of the Anderson-Gruneisen parameter  $T$  upon compression at extreme conditions, *J. Phys. Chem. Solids*, 54, 221.
- Anderson, O.L., D.G. Isaak, and H. Oda (1992), A model for the computation of thermal expansivity at high compression and high temperatures: MgO as an example, *Geophys. Res. Lett.*, 19, 1987-1990.
- Armienti, P., and D. Gasperini (2007), Do we really need mantle components to define mantle composition? *J. Petrol.*, 48, 4, 693-709.
- Asimow, P. D., and C. H. Langmuir (2003), The importance of water to oceanic mantle melting regimes. *Nature*, vol. 421, 815-820.
- Asimow, P. D., and M. S. Ghiorso (1998), Algorithmic modifications extending MELTS to calculate subsolidus phase relations, *Am. Mineral.*, 83, 1127-1132.
- Asimow, P. D., M. M. Hirschmann, and E. M. Stopler (2001), Calculation of peridotite partial melting from thermodynamic models of minerals and melts, IV. Adiabatic decompression and the composition and mean properties of mid-ocean ridge basalts, *J. Petrology*, 42, 5, 963-998.

- Baba, K., A. D. Chave, R. L. Evans, G. Hirth, R.L. Mackie (2006), Mantle dynamics beneath the East Pacific Rise at 17°S: insights from the Mantle Electromagnetic and Tomography (MELT) experiment. *J. Geophys. Res.* 111:B02101.
- Ballmer, M. D., G. Ito, J. van Hunen, and P. J. Tackley (2011), Spatial and temporal variability in Hawaiian hotspot volcanism induced by small-scale convection, *Nature Geosciences*, 4, 457-460. doi:10.1038/ngeo1187
- Beck, P. A., J. C. Kremer, L. J. Demer, M. L. Holzworth (1948), Grain growth in high-purity aluminum and in an aluminum-magnesium alloy. *Trans. AIME* 175,372-394.
- Beck, P., A. F. Goncharov, V. V. Struzhkin, B. Militzer, H. Mao, and R. J. Hemley (2009), Response to Comment on Measurement of thermal diffusivity at high pressure using a transient heating technique, *Appl. Phys. Lett.*, 95, 096102.
- Becker, K., et al. (1989), Drilling deep into young oceanic crust, hole 504b, Costa Rica rift, *Reviews of Geophysics*, 27, 1, pp. 79-102.
- Becker, T. W., S. Chevrot, V. Schulte-Pelkum, and D. K. Blackman (2006), Statistical properties of seismic anisotropy predicted by upper mantle geodynamic models. *J. Geophys. Res.*, 111, B08309.
- Berman, R. G., and L. Y. Aranovich (1996), Optimized standard state and solution properties of minerals: 1. Model calibration for olivine, orthopyroxene, cordierite, garnet and ilmenite in the system FeO-MgO-CaO-Al<sub>2</sub>O<sub>3</sub>-TiO<sub>2</sub>-SiO<sub>2</sub>, *Contrib. Mineral. Petrol.*, 126, 1-24.
- Bodvarsson, G., and R. P. Lowell (1972), Ocean-floor heat flow and circulation of interstitial waters, *J. Geophys. Res.*, 77, 23, pp. 4472-4475.
- Bottinga, Y. and L. Steinmetz (1979), A geophysical, geochemical, petrological model of the sub-marine lithosphere, *Tectonophysics*, 55, 311-347.
- Bouhifd, M. A., D. Andraut, G. Fiquet, P. Richet (1996), Thermal expansion of forsterite up to the melting point, *Geophys. Res. Lett.*, 23, 1143-1146.
- Bourdon, B., N. M. Ribe, A. Stracke, A. E. Saal., and S. P. Turner (2006), Insights into the dynamics of mantle plumes from uranium-series geochemistry. *Nature*, 444, 713-717.
- Branlund, J. M., and A. M. Hofmeister (2012), Heat transfer in plagioclase feldspars, *Am. Mineral.*, 97, 1145-1154.
- Brown, J. W., and R. S. White (1994), Variation with spreading rate of oceanic crustal thickness and geochemistry, *Earth. Planet. Sci. Lett.*, 121, 435-449.
- Bullard, E. C. (1952), Discussion of a paper by R. Revelle and A. E. Maxwell, heat flow through the floor of the eastern North Pacific Ocean. *Nature*, 170, 200.



- Burke, J. E. (1949), Some factors affecting the rate of grain growth in metals. *Trans. Metall. Soc. AIME* 180, 73-91.
- Burke, J. E., and D. Turnbull (1952), Recrystallization and grain growth. *Prog. Metal. Phys.* 3, 220-292.
- Calcagno, P., and A. Cazenave (1994), Subsidence of the seafloor in the Atlantic and Pacific oceans: Regional and large-scale variations. *Earth. Planet. Sci. Lett.*, 126, 473-492.
- Canales, J. P., H. Carton, S. M. Carbotte, J. C. Mutter, M. R. Nedimovic, M. Xu, O. Aghaei, M. Marjanovic, and K. Newman (2012), *Nature Geoscience*, 5, 279-283.
- Carlson, R. L., and H. P. Johnson (1994), On modeling the thermal evolution of the oceanic upper mantle: An assessment of the cooling plate model, *J. Geophys. Res.*, 99, pp. 3201-3214.
- Carlson, W. D. (2012), Rates and mechanism of Y, REE, and Cr diffusion in garnet. *Am. Mineral.*, 97, 1598-1618.
- Cazenave, A., B. Lago, and K. Dominh (1983), Thermal parameters of the oceanic lithosphere estimated from geoid height data. *J. Geophys. Res.*, 88, B2, 1105-1118.
- Chen, Y. J. (1992), Oceanic crustal thickness versus spreading rate, *Geophys. Res. Lett.*, 19, 753-756.
- Chen, Y. J., and J. P. Morgan (1996), The effects of spreading rate, the magma budget, and the geometry of magma emplacement on the axial heat flux at mid-ocean ridges, *J. Geophys. Res.*, 101, B5, 11475-11482.
- Cherkaoui, A. S. M., W. S. D. Wilcock, R. A. Dunn, and D. R. Toomey (2003), A numerical model of hydrothermal cooling and crustal accretion at fast spreading mid-ocean ridges, *J. Geophys. Res.*, 101, 11,475-11,482.
- Cherniak, D. J. (2010), REE diffusion in olivine, *Am. Mineral.*, 95, 362-368.
- Cochran, J. R. (1979), An analysis of isostasy in the worlds oceans: 2. Midocean ridge crests. *J. Geophys. Res.*, 84, B9, 4713.
- Cochran, J. R. (1981), Simple models of diffuse extension and pre-seafloor spreading development of the continental margin of the Northeastern Gulf of Aden. *Oceanologica Acta* sp., 155-165.
- Cochran, J. R., and W. R. Buck (2001), Near-axis subsidence rates, hydrothermal circulation, and thermal structure of mid-ocean ridge crests, *J. Geophys. Res.*, 106, 19233-19258.
- Connolly, J. A. D. (2005), Computation of phase equilibria by linear programming: A tool for geodynamic modeling and its application to subduction zone decarbonation, *Earth. Planet. Sci. Lett.*, 236, 524-541.

- Connolly, J. A. D. (2009), The geodynamic equation of state: What and how, *Geochem. Geophys. Geosyst.*, 10, Q10014, doi:10.1029/2009GC002540.
- Craft, K. L., R. P. Lowell (2009), A boundary layer model for submarine hydrothermal heat flows at on-axis and near-axis regions, *Geochem. Geophys. Geosyst.*, 10, 12, pp. 14.
- Crosby, A. G., and D. McKenzie (2009), An analysis of young ocean depth, gravity and global residual topography. *Geophys. J. Int.*, 178, 1198-1219.
- Crosby, A., D. McKenzie, and J.G. Sclater (2006), The relationship between depth, age, and gravity in the oceans, *Geophys. J. Int.*, 166, pp. 553-573.
- Crowley, J. W., M. Gerault, R. J.. O'Connell (2011), On the relative influence of heat and water transport on planetary dynamics, *Earth. Planet. Sci. Lett.*, 310, 380-388.
- d'Acremont, E., S. Leroy, M. Maia, P. Gente, J. Autin (2010), Volcanism, jump and propagation on the Sheba ridge, eastern Gulf of Aden: Segmentation evolution and implications for oceanic accretion processes. *Geophys. J. Int.*, 180, 535-551.
- Dasgupta, R., M. G. Jackson, C. A. Lee (2010), Major element chemistry of ocean island basalts conditions of mantle melting and heterogeneity of mantle source. *Earth Planet. Sci. Lett.*, 289, 377-392.
- Davies, G. F. (1980), Review of oceanic and global heat flow estimates, *Rev. Geophys. Space Phys.*, 18, 718-722.
- Davies, J. H., and D. R. Davies (2010), Earths surface heat flux, *Solid Earth*, 1, 5-24.
- Davis, E. E., D. S. Chapman, C. B. Forster, and H. Villinger (1989), Heat-flow variations correlated with buried basement topography on the Juan de Fuca Ridge flank. *Nature*, 342, 533-537.
- Davis, e. E., A. T. Fisher, Firth, J. V., et al. (1997), Introduction and Summary: hydrothermal circulation in the oceanic crust and its consequences on the eastern flank of the Juan de Fuca ridge. *Proceedings of the Ocean Drilling Program, Initial Reports*, 168, 7-21.
- Davis, E. E., and C. R. B. Lister (1974), Fundamentals of ridge crest topography, *Earth. Planet. Sci. Lett.*, 21, 405-413.
- Davis, E. E., and H. Elderfield (2004), *Hydrogeology of oceanic lithosphere*. Cambridge University Press, Cambridge, 706 pp.
- Davis, E. E., D. S. Chapman, K. Wang, H. Villinger, A. T. Fisher, S. W. Robinson, J. Grigel, D. Pribnow, J. Stein, and K. Becker (1999), Regional heat flow variations across the sedimented Juan de Fuca Ridge eastern flank: Constraints on lithospheric cooling and lateral hydrothermal heat transport, *J. Geophys. Res.*, 104, 17675-17688.
- Davis, E. E., Becker, K., and He, J. (2004), Costa Rica Rift revisited: constraints on shallow and deep hydrothermal circulation in young oceanic crust. *Earth Planet. Sci. Lett.*, 222: 863-879.

- de Groot, S. R., and P. Mazur (1984), *Non-equilibrium thermodynamics*. Dover Publications, Inc., New York. 510 pg.
- Denlinger, R. P. (1992), A revised estimate for the temperature structure of the oceanic lithosphere, *J. Geophys. Res.*, 97, 7219-7222.
- Denlinger, R. P., and W. Z. Savage (1989), Thermal stresses due to cooling of a viscoelastic oceanic lithosphere, *J. Geophys. Res.*, 94, 744-752.
- Divins, D. L., (retrieved) (2011), NGDC total sediment thickness of the worlds oceans and marginal seas, <http://www.ngdc.noaa.gov/mgg/sedthick/sedthick.html>
- Doin M. P., and L. Fleitout (1996), Thermal evolution of the oceanic lithosphere: an alternative view, *Earth Planet. Sci. Lett.*, 142, 121-136.
- Driscoll, M. L., and B. Parsons (1988), Cooling of the oceanic lithosphere: evidence from geoid anomalies across the Udintsev and Eltanin fracture zones. *Earth. Planet Sci. Lett.*, 88, 289-307.
- Dunn, R. A., D. R. Toomey, and S. C. Solomon (2000), Three-dimensional seismic structure and physical properties of the crust and shallow mantle beneath the East Pacific Rise at 9°30'N, *J. Geophys. Res.*, 105, 23537-23555.
- Eaton, D. W., F. Darbyshire, R. L. Evans, H. Grutter, A. G. Jones, X. Yuan (2009), The elusive lithosphere-asthenosphere boundary (LAB) beneath cratons. *Lithos*, 109:1-22.
- Elderfield, H., C. G. Wheat, M. J. Mottl, C. Monnin, B. Spiro (1999), Fluid and geochemical transport through oceanic crust: a transect across the eastern flank of the Juan de Fuca ridge. *Earth Planet. Sci. Lett.*, 172, 151-165.
- Ellam, R. M. (1992), Lithosphere thickness as a control on basalt chemistry. *Geology*, 20, 153-156.
- Evans, B. W. (2004), The serpentinite multisystem revisited: chrysotile is metastable, in *Serpentine and Serpentinites: Mineralogy, Petrology, Geochemistry, Ecology, Geophysics, and Tectonics* A tribute to Robert G. Coleman, ed. W. G. Ernst, GSA International Book Series (IBS008).
- Evans, B., J. Renner, and G. Hirth (2001), A few remarks on the kinetics of static grain growth in rocks, *Int. J. Earth Sci.*, 90, 88-103.
- Faul, U. H., and I. Jackson (2005), The seismological signature of temperature and grain size variations in the upper mantle, *Earth Planet. Sci. Lett.*, 234, 119-134.
- Fisher, K. M., H. A. Ford, D. L. Abt, C. A. Rychert (2010), The Lithosphere-Asthenosphere Boundary. *Ann. Rev. Earth Planet. Sci.*, vol. 38, 551-575. doi: 10.1146/annurev-earth-040809-152438.

- Fisher, A., and Von Herzen, R. (2005), Models of hydrothermal circulation within 106 Ma seafloor: Constraints on the vigor of fluid circulation and crustal properties, below the Madeira abyssal plain, *Geochem. Geophys. Geosyst.*, 6, Q11001.
- Forsyth D. W., and F. Press (1971), Geophysical tests of petrological models of the spreading lithosphere, *J. Geophys. Res.*, 76, 7963-7979.
- Forsyth D. W., Harmon N., Scheirer D.S., and Duncan R.A. (2006), Distribution of recent volcanism and the morphology of seamounts and ridges in the GLIMPSE study area: Implications for the lithospheric cracking hypothesis for the origin of intraplate, non-hot spot volcanic chains, *J. Geophys. Res.*, 111, B11407.
- Freedman, A. P., and B. Parsons (1990), Geoid anomalies over two South Atlantic fracture zones. *Earth. Planet. Sci. Lett.*, 100, 18-41.
- Gaherty, J. B., M. Kato, T. H. Jordan (1999), Seismological structure of the upper mantle: a regional comparison of seismic layering. *Phys. Earth. Planet. Inter.* 110:21-41.
- Geli, L., and J. Sclater (2008), On the depth of oceanic earthquakes: Brief comments on The thermal structure of oceanic and continental lithosphere, by McKenzie, D., Jackson, J. and Priestley, K., *Earth Planet. Sci. Lett.*, 233, [2005], 337-349., *Earth Planet. Sci. Lett.*, 265, 766-772.
- Ghiorso, M. S., and R. O. Sack (1995), Chemical mass transfer in magmatic processes IV. A revised and internally consistent thermodynamic model for the interpolation and extrapolation of liquid-solid equilibria in magmatic systems at elevated temperatures and pressures. *Contrib. Mineral. Petrol.*, 119, 197-212.
- Goutorbe, B. (2010), Combining seismically derived temperature with heat flow and bathymetry to constrain the thermal structure of oceanic lithosphere, *Earth Planet. Sci. Lett.*, 295, pp. 390-400.
- Goutorbe, B. and J. K. Hillier (2013), An integration to optimally constrain the thermal structure of oceanic lithosphere. *J. Geophys. Res.*, 118, 432-446. doi:10.1029/2012JB009527
- Grest, G. S., M. P. Anderson, D. J. Srolovitz (1988), Domain-growth kinetics for the Q-state Potts model in two and three dimensions. *Phys. Rev.* 38B, 4752-4760.
- Grose, C. J. (2012), Properties of oceanic lithosphere: revised plate model predictions, *Earth Planet. Sci. Lett.*, 333-334, 250-264.
- Grose, C. J., Afonso, J.C. (2013), Comprehensive plate models for the thermal evolution of oceanic lithosphere, *Geochem. Geophys. Geosyst.*, 14, 3751-3778.
- Haase, K. M. (1996), The relationship between the age of the lithosphere and the composition of the oceanic magmas: Constraints on partial melting, mantle sources and the thermal structure of plates. *Earth Planet. Sci. Lett.*, 144, 75-92.

- Hammond, W.C., and E. D. Humphreys (2000), Upper mantle seismic wave velocity: effects of realistic partial melt geometries. *J. Geophys. Res.* 105(B5):1097586.
- Han, S., S. M. Carbotte, H. Carton, J. C. Mutter, O. Aghaei, M. R. Nedimovic, J. P. Canales (2014), Architecture of on- and off-axis magma bodies at EPR 9°37-40'N and implications for oceanic crustal accretion. *Earth. Planet. Sci. Lett.*, 390, 31-44.
- Hasterok, D. (2010), Thermal regime of the continental and oceanic lithosphere, Ph.D. Dissertation. University of Utah, 156 pp.
- Hasterok, D. (2013a), A heat flow based cooling model for tectonic plates, *Earth. Planet. Sci. Lett.*, 311, 386-395.
- Hasterok, D. (2013b), Global patterns and vigor of ventilated hydrothermal circulation through young seafloor, *Earth. Planet. Sci. Lett.*, 12-20.
- Hasterok, D., D. S. Chapman, and E. E. Davis (2011), Oceanic Heat Flow: Implications for Global Heat Loss, *Earth. Planet. Sci. Lett.*, 311, 386-395.
- Haxby, W. F., and D. L. Turcotte (1978), On isostatic geoid anomalies. *J. Geophys. Res.*, 83, B11, 5473-5478.
- Haxby, W. F., and E. M. Parmentier (1988), Thermal Contraction and the State of Stress in the Oceanic Lithosphere, *J. Geophys. Res.*, 93, 6419-6429.
- Hearn, E. H., E. D. Humphreys, M. Chai, and J. M. Brown (1997), Effect of anisotropy on oceanic upper mantle temperatures, structure, and dynamics, *J. Geophys. Res.*, 102, 11943-11956.
- Heestand, R. L., and S. T. Crough (1981), The effect of hot spots on the oceanic age-depth relation, *J. Geophys. Res.* 86. B7, 6107-6114.
- Hertogen, J., R. Emmermann, P. T. Robinson, and J. Erzinger (2002), Lithology, mineralogy, and geochemistry of the lower ocean crust, ODP Hole 735B, Southwest Indian Ridge. In Natland, J.H., H.J.B. Dick, D.J. Miller, and R.P. Von Herzen (Eds.), *Proc. ODP, Sci. Results*, 176, 182.
- Herzberg, C. (2004), Geodynamic information in peridotite petrology, *J. Petrol.*, 45(12), 2507-2530.
- Herzberg, C. (2004), Geodynamic Information in Peridotite, *J. Petrol.*, 45, 12, 2507-2530.
- Herzberg, C., and P. D. Asimow (2008), Petrology of some oceanic island basalts: PRIMELT2.XLS software for primary magma calculation, *Geochem. Geophys. Geosyst.*, 9, Q09001.
- Herzberg, C., P. Asimow, N. Arndt, Y. Niu, C. Leshner, J. Fitton, M. Cheadle, and A. Saunders (2007), Temperatures in ambient mantle and plumes: constraints from basalts, picrites, and komatiites, *Geochem. Geophys. Geosyst.* 8 (2), Q02006.

- Hessler, R. R., W. M. Smithey, M. A. Boudrias, C. H. Keller, R. A. Lutz, and J. J. Childress (1988), Spatial and temporal variation of giant clams, tube worms, and mussels at deep-sea hydrothermal vents, *Bull. Biol. Soc. Wash.*, 6, 411-428.
- Higgins, G.T. (1974), Grain-boundary migration and grain growth. *Metal Sci.* 8, 143150
- Hillier, J. K, and A. B. Watts (2005), Relationship between depth and age in the North Pacific Ocean, *J. Geophys. Res.*, 110, B02405.
- Hillier, J. K. (2010), Subsidence of normal seafloor: Observations do indicate flattening, *J. Geophys. Res.*, 115, B03102.
- Hirschmann, M. M., and E. M. Stolper (1996), A possible role for garnet pyroxenite in the origin of the garnet signature in MORB. *Contrib. Mineral. Petrol.*, 124:185-208.
- Hirschmann, M. M., T. Kogiso, M. B. Baker, E. M. Stolper (2003), Alkalic magmas generated by partial melting of garnet pyroxenite. *Geology*. 31, 6, 481-484.
- Hirth, G., R. L. Evans, A. D. Chave (2000), Comparison of continental and oceanic mantle electrical conductivity: Is the Archean lithosphere dry? *Geochem. Geophys. Geosyst.* 1(12):1030.
- Hobart, M., M. Langseth, R. Anderson (1985), A geothermal and geophysical survey of the south flank of the Costa Rica Rift: Site 504 and 505, Initial Rep. Deep Sea Drill. Proj., 83, 379-404.
- Hofman, A. W., and S. R. Hart (1978), An assessment of local and regional isotopic equilibrium in the mantle. *Earth Planet. Sci. Lett.*, 38, 44-62.
- Hofmann, A. W. (2006), Sampling Mantle Heterogeneity through Oceanic Basalts: Isotopes and Trace Elements. In: *Treatise on Geochemistry*, Elsevier Ltd. Vol. 2; (ISBN: 0-08-044337-0); pp. 61-101.
- Hofmeister, A. M. (1999), Mantle values of thermal conductivity and the geotherm from phonon lifetimes, *Science*, 283, 1699.
- Hofmeister, A. M. (2005), Dependence of diffusive radiative transfer on grain-size, temperature, and Fe-content: Implications for mantle processes, *J. Geodynamics*, 40, pp. 51-72.
- Hofmeister, A. M. (2006), Thermal diffusivity of garnets at high temperature. *Phys.Chem. Mineral.*, 33, 45-61.
- Hofmeister, A. M. (2007), Pressure dependence of thermal diffusivity, *Proc. National Acad. Sci.* 104, 9192-9197.
- Hofmeister, A. M. (2009), Comment on "Measurement of thermal diffusivity at high pressure using a transient heating technique". *Appl. Phys. Lett.*, 91, 181914.
- Hofmeister, A. M. and D. A. Yuen (2007), Critical phenomena in thermal conductivity: Implications for lower mantle dynamics. *J. Geodynamics*, 44, 186-199.

- Hofmeister, A. M., and M. Pertermann (2008), Thermal diffusivity of clinopyroxenes at elevated temperature, *Eur. J. Mineral.*, 20, 537-549.
- Hofmeister, A. M., R. E. Criss (2005), Earth's heat flux revisited and linked to chemistry. *Tectonophysics*, 395, 159-177.
- Hofmesiter, A. M., Pertermann, M., Branlund, J. M., Whittington, A. G. (2006), Geophysical implications of reduction in thermal conductivity due to hydration, *Geophys. Res. Lett.*, 33, L11310.
- Holm, E. A., J. A. Glazier, D. J. Srolovitz, G. S. Grest (1991), Effects of lattice anisotropy and temperature on domain growth in the two-dimensional Potts model. *Phys. Rev. A*. vo. 43, 6, 2662-2668.
- Homer, E. R., V. Tikare, E. A. Holm (2013), Hybrid Potts-phase field model for coupled microstructural-compositional evolution. *Comp. Mat. Sci.*, 69, 414-423.
- Honda, S., and D. A. Yuen (2001), Interplay of variable thermal conductivity and expansivity on the thermal structure of oceanic lithosphere. *Geophys. Res. Lett.*, 28, 351-354.
- Honda, S., and D. A. Yuen (2004), Interplay of variable thermal conductivity and expansivity on the thermal structure of oceanic lithosphere II, *Earth Planets Space*, 56, e1-e4.
- Hooft, E. E., and R. S. Detrick (1993), The role of density in the accumulation of basaltic melts at mid-ocean ridges. *Geophys. Res. Lett.*, 20, 6, 423-426.
- Hostetler, P. B., R. G. Coleman, and B. W. Evans (1966), Brucite in Alpine serpentinites, *Am. Mineral.*, 51, Jan-Feb.
- Houseman, G., and D. McKenzie (1982), Numerical experiments on the onset of convective instability in the Earths mantle. *Geophys. J. R. astr. Soc.*, 68, 133-164.
- Hu, H., B.B. Rath (1970), On the time exponent in isothermal grain growth. *Metall. Trans.* 1, 31813184.
- Huang, C., C. Li, P. Y. K. Choi, K. Nandakumar, and L. W. Kostiuik (2010), Effect of cut-off distance used in molecular dynamics simulations on fluid properties, *Molecular Simulation*, Vol. 36, 11, 856-864, DOI: 10.1080/08927022.2010.489556
- Huang, C. M., C. L. Joanne, B. S. V. Patnaik, R. Jayaganthan (2000), Monte Carlo simulation of grain growth in polycrystalline materials, *App. Surf. Sci.*, 252, 3997-4002.
- Hui, Li, W. Guanghou, D. Feng, B. Xiufang, F. Pederiva (2003), Monte Carlo simulation of three-dimensional polycrystalline material, *Mat. Sci. and Engineer.* A357, 153-158.
- Humphreys, E. R., and Y. Niu (2009), On the composition of ocean island basalts (OIB): The effects of lithospheric thickness variation and mantle metasomatism. *Lithos*, 112, 118-136.
- Hutchison, I. (1985), The effects of sedimentation and compaction on oceanic heat flow, *Geophys. J. R. astr. Soc.*, 82, 439-459.



- Hutnak, M., A. T. Fisher, R. Harris, C. Stein, K. Wang, G. Spinelli, M. Schindler, H. Villinger, and E. Silver (2008), Large heat and fluid fluxes driven through mid-plate outcrops on ocean crust. *Nature Geoscience*, 1, 611-614.
- Hutnak, M., and A. T. Fisher (2007), Influence of sedimentation, local and regional hydrothermal circulation, and thermal rebound on measurements on seafloor heat flux. *J. Geophys. Res.*, 112, B12101.
- Ito, K. (1974), Petrological models of the oceanic lithosphere: Geophysical and geochemical tests, *Earth Planet. Sci. Lett.*, 21, 169-180.
- Jackson, I., J. D. Fitz Gerald, U. H. Faul, B. H. Tan (2002), Grain-size-sensitive seismic wave attenuation in polycrystalline olivine. *J. Geophys. Res.*, 107(B12):2360.
- Jannasch, H. W., (1983), Microbial processes at deep-sea hydrothermal vents, in *Hydrothermal processes at sea floor spreading centers*, edited by P. A. Rona, K. bostrom, L. Laubier, and K. L. Smith, pp. 677-709, Plenum Press, New York.
- Jannasch, H. W., (1995), Microbial interactions with hydrothermal fluids, in *Seafloor hydrothermal systems*, *Geophys. Monograph*, vol. 91, edited by S. E. Humphreis, R. A. Zierenberg, L. S. Mullineaux, and R. E. Thomson, pp. 273-296, Am. Geophys. Union, Washington, D. C.
- Janssens, K. G. F., D. Raabe, E. Kozeschnik, M. A. Miodownik, B. Nestler (2007), *Computational Materials Engineering: An Introduction to Microstructure Evolution*. Elsevier Academic Press.
- Jaupart, C., S. Labrosse, J.-C. Mareschal (2007), Temperature, Heat, and Energy in the Mantle of the Earth, in *Treatise on Geophysics*, Schubert G. (ed.), vol.7, pp. 253-304, Oxford :Elsevier Ltd.
- Karato, S., (2004), Mapping water content in the upper mantle. In *Inside the Subduction Factory*, ed. J Eiler, *Geophys. Monogr. Ser.* 138:13552. Washington, DC: AGU
- Katz, R. F., and S. M. Weatherley (2012), Consequences of mantle heterogeneity for melt extraction at mid-ocean ridges., *Earth Planet. Sci. Lett.*, 335-336, 226-237.
- Kaul, N., J.-P. Foucher, M. Heesemann (2006), Estimating mud expulsion rates from temperature measurements on Hakon Mosby Mud Volcano, SW Barents Sea, *Marine Geology*, 229, 1-14.
- Kaus, B.J.P., J.A.D. Connolly, Y.Y. Podladchikov, S.M. Schmalholz (2005), Effect of mineral phase transitions on sedimentary basin subsidence and uplift, *Earth Planet. Sci. Lett.*, 233, 1-2, 213-228.
- Kawakatsu, H., P. Kumar, Y. Takei, M. Shinohara, T. Kanazawa, et al. (2009), Seismic evidence for sharp lithosphere-asthenosphere boundaries of oceanic plates. *Science*, 324:499-502.

- Kelemen, P., N. Shimizu, V. Salters (1995), Extraction of mid-ocean-ridge basalt from the upwelling mantle by focused flow of melt in dunite channels. *Nature*, 375 (6534), 747-753.
- Kim, S. G., D. I. Kim, W. T. Kim, and Y. B. Park (2006), Computer simulations of two-dimensional and three-dimensional ideal grain growth, *Phys. Rev. E*, 74, 061605.
- Koepke, J., and H. Behrens (2001), Trace element diffusion in andesitic melts: An application of synchrotron X-ray fluorescence analysis. *Geochimica et. Cosmochim. Acta*, 65, 9, 1481-1498.
- Korenaga J. (2007a), Effective thermal expansivity of Maxwellian oceanic lithosphere, *Earth Planet. Sci. Lett.*, 257, 343-349.
- Korenaga, J. (2007b), Thermal cracking and the deep hydration of oceanic lithosphere: A key to the generation of plate tectonics? *J. Geophys. Res.*, 112, B05408.
- Korenaga, J., and S.-I. Karato (2008), A new analysis of experimental data on olivine rheology. *J. Geophys. Res.*, 113, B02403.
- Korenaga, T., and J. Korenaga (2008), Subsidence of normal oceanic lithosphere, apparent thermal expansivity, and seafloor flattening, *Earth Planet. Sci. Lett.*, 268, pp. 41-51.
- Kumar, M., and S. S., Bedi (1998), Analysis of the pressure dependence of thermal expansivity, *Phys. State. Sol. (b)*, 207, 75-80.
- Kumar, R. R., and R. G. Gordon (2009), Horizontal thermal contraction of oceanic lithosphere: The ultimate limit to the rigid plate approximation, *J. Geophys. Res.*, 114, B01403.
- Kusznir, N. J. (1991), The distribution of stress with depth in the lithosphere: Thermo-rheological and geodynamic constraints, *Phil. Trans. R. Soc. Lond. A*, 337, 95-110.
- Langmuir, C. H., E. M. Klein, and T. Plank (1992), Petrological systematic of mid-ocean ridge basalts: Constraints on melt generation beneath ocean ridges, in *Mantle Flow and Melt Generation at Mid-Ocean Ridges*, (eds.) J. P. Morgan, D. K. Blackman, and J. M. Sinton, AGU, Washington, D.C.
- Langseth M. G., X. Le Pichon, and M. Ewing (1966), Crustal structure of the mid-ocean ridges, 5, Heat flow through the Atlantic Ocean floor and convection currents, *J. Geophys. Res.*, 71, 5321.
- Langseth, M. G., M. J. Mottl, M. A. Hobart, and A. T. Fisher (1988), The distribution of geothermal and geochemical gradients near Site 501/504: implications for hydrothermal circulation in the oceanic crust, *Proc. Ocean Drill. Prog., Sci. Results* 111, 23-32.
- Le Pichon, X. (1968), Sea-floor spreading and continental drift, *J. Geophys. Res.*, 73, 12, 3661-3697.

- Lee, C.-T., P. Luffi, T. Plank, H. Dalton, and W. P. Leeman (2009), Constraints on the depths and temperatures of basaltic magma generation on Earth and other terrestrial planets using new thermobarometers for mafic magmas, *Earth Planet. Sci. Lett.*, 279, 20-33.
- Leroy, S., et al. (2012), From rifting to oceanic spreading in the Gulf of Aden: A synthesis. In K. Al Hosani et al. (eds.) *Lithosphere Dynamics and Sedimentary Basins: The Arabian Plate and Analogues*, *Frontiers in Earth Sciences*, 385-427.
- Levin, V., and J. Park (2000), Shear zones in the Proterozoic lithosphere of the Arabian Shield and the nature of the Hales discontinuity. *Tectonophysics* 323:13148
- Li Li, R. M. Wentzcovitch, D. J. Weidner, and C. R. S. Da Silva (2007), Vibrational and thermodynamic properties of forsterite at mantle conditions. *J. Geophys. Res.*, 112, B05206.
- Liang, Y., a. Schiemenz, M. A. Hesse, E. M. Parmentier, J. S. Hesthaven (2010), High-porosity channels for melt migration in the mantle: Top is the dunite and bottom is the harzburgite and lherzolite, *Geophys. Res. Lett.*, 37, L15306. doi:10.1029/2010GL044162
- Lister, C. R. B. (1972), On the thermal balance of a mid-ocean ridge. *Geophys. J. R. Astron. Soc.*, 26, 515.
- Lister, C. R. B. (1974), On the penetration of water into hot rock. *Geophys. J. Roy. Astron. Soc.*, 39, 465-509.
- Lister, C. R. B. (1977), Estimators for heat flow and deep rock properties based on boundary layer theory, *Tectonophysics*, 41, 157-171.
- Lister, C. R. B. (1982), "Active" and "Passive" hydrothermal systems in the ocean crust. Predicted physical conditions. In *The dynamic Environment of the Ocean Floor*, eds. K. A. Fanning and F. T. Manheim. Lexington, MA: Heath. pp. 441-470.
- Lowell, R. P., and P. A. Rona (2002), Seafloor hydrothermal systems driven by the serpentinization of peridotite. *Geophys. Res. Lett.*, 29, 11, 1531.
- Lucazeau, F. et al. (2008), Persistent thermal activity at the Eastern Gulf of Aden after continental break-up. *Nature Geoscience*, 1.
- Lucazeau, F., S. Leroy, F. Rolandone, E. d'Acremont, L. Watremez, A. Bonneville, B. Goutorbe, D. Dusunur (2010), Heat-flow and hydrothermal circulation at the ocean-continent transition of the eastern gulf of Aden. *Earth. Planet. Sci. Lett.*, 554-570.
- Lundstrom, C., J. Gill, Q. Williams (2000), A geochemically consistent hypothesis for MORB generation. *Chem. Geol.* 162 (2), 105126.
- Lynch M.A. (1999), Linear ridge groups: Evidence for tensional cracking in the Pacific Plate: *J. Geophys. Res.*, 104, 29,321-29,334.

- Lyubetskaya, T., and J. Korenaga (2007), Chemical composition of Earth's primitive mantle and its variance: Method and results. *J. Geophys. Res.*, 112, B03211.
- MacLennan, J. T. (2008), The supply of heat to mid-ocean ridges by crystallization and cooling of mantle melts, in *Magma to Microbe: Modeling hydrothermal processes at oceanic spreading centers*, R. P. Lowell, J. S. Seewald, A. Metaxas, M. R. Perfit (eds.), *Geophysical Monograph 178*, American Geophysical Union, Washington, DC.
- MacLennan, J., T. Hulme, and S. C. Singh (2005), Cooling of the lower oceanic crust. *Geology*, 33, 357-360.
- Maggi, A., E. Debayle, K. Priestley, and B. Guilhem (2006), Multimode surface waveform tomography of the Pacific Ocean: a closer look at the lithospheric cooling signature. *Geophys. J. Int.*, 166, 1384-1397.
- Manning, C. E., C. J. MacLeod, P. E. Weston (2000), Lower-crustal cracking front at fast-spreading ridges: Evidence from the East Pacific Rise and the Oman ophiolite. In: *Geological Society of America Special Papers*, 349, 261-272.
- Marty, J. C., and A. Cazenave (1989), Regional variations in subsidence rate of oceanic plates: a global analysis, *Earth Planet. Sci. Lett.*, 94, 301-315.
- McClain, J. S., and C. A. Atallah (1986), Thickening of the oceanic crust with age, *Geology*, 14, 574-576.
- McKenzie, D. (1967), Some remarks on heat flow and gravity anomalies. *J. Geophys. Res.*, 72, 24, 6261-6273.
- McKenzie, D. (1984), The generation and compaction of partially molten rock, *J. Petrol.*, 25(3), 713-765.
- McKenzie, D. and R. K. O'Nions (1991), Partial Melt distributions from Inversion of Rare Earth Element Concentrations. *J. Petrol.*, Vol. 32, Part 5, pp. 1021-1091.
- McKenzie, D. and R. K. O'Nions (1995), The Source Regions of Ocean Island Basalts, *J. Petrol.*, 36, 1, 133-159.
- McKenzie, D., and M. J. Bickle (1988), The volume and composition of melt generated by extension of the lithosphere, *J. Petrol.*, 29, 625-679.
- McKenzie, D., and R. L. Parker (1967), The North Pacific: An example of tectonics on a sphere, *Nature*, 216, p. 1276-1280.
- McKenzie, D., J. Jackson, and K. Priestley (2005), Thermal structure of oceanic and continental lithosphere, *Earth. Planet. Sci. Lett.*, 233, 337-349.
- Mooney, W. D., G. Laske, and T. G. Masters (1998), CRUST 5.1: A global crustal model at  $5^\circ \times 5^\circ$ . *J. Geophys. Res.*, 103, B1, 727-747.

- Morgan, W.J. (1972), Deep mantle convection plumes and plate motions. *Am. Assoc. Pet. Geol. Bull.* 56, 203213.
- Mottl, M. J. (2003), Partitioning of Energy and Mass Fluxes between mid-ocean ridge axes and flanks at high and low temperature. In *Energy and mass transfer in marine hydrothermal systems*, P.E. Halbach, V. Tunncliffe, and J. R. Hein (eds), 271-286.
- Muller, R. D., et al. (1997), Digital isochrones of the world's ocean floor, *J. Geophys. Res.*, 102, 3211-3214.
- Muller, R. D., M. Sdrolias, C. Gaina, and W.R. Roest (2008), Age, spreading rates and spreading symmetry of the world's ocean crust, *Geochem. Geophys. Geosyst.*, 9, Q04006.
- Nedimovic, M. R., D. R. Bohnenstiehl, s. M. Carbotte, J. P. Canales, R. P. Dziak (2009), Faulting and hydration of the Juan de Fuca plate system, *Earth. Planet. Sci. Lett.*, 284, 94-102.
- Newman, K. R., M. R. Nedimovic, J. P. Canales, S. M. Carbotte (2011), Evolution of seismic layer 2B across the Juan de Fuca ridge from hydrophone streamer 2-D traveltime tomography. *Geochem. Geophys. Geosyst.*, 12. Q05009.
- Nicolas, A., D. Mainprice, F. Boudier (2003), High-temperature seawater circulation throughout crust of oceanic ridges: A model derived from the Oman ophiolites. *J. Geophys. Res.*, 108, B8, 2371.
- Nikolaeva, K., Gerya, T.V., Connolly, J.A.D. (2008), Numerical modelling of crustal growth in intraoceanic volcanic arcs. *Phys. Earth Planet. Int.*, 171, 336-356.
- Niu, Y., K. D. Collerson, R. Batiza, J. I. Wendt, and M. Regelous (1999), The origin of E-type MORB at ridges far from mantle plumes: the East Pacific Rise at 11°20N. *J. Geophys. Res.*, 104, 7067-7087.
- Niu, Y., M. Wilson, E. R. Humphreys, M. J. OHara (2011), The origin of intra-plate Ocean Island Basalts (OIB): the Lid Effect and its Geodynamic Implications. *J. Petrol.*, 52, 7-8,1443-1468.
- Niu, Y., M. Wilson, E. R. Humphreys, M. J. OHara (2012), A trace element perspective on the source of ocean island basalts (OIB) and fate of subducted ocean crust (SOC) and mantle lithosphere (SML). *Episodes*, Vol. 35, no. 2. 310-327.
- OHanley, D. S. (1992), Solution to the volume problem in serpentinization, *Geology*, 20, 705-708.
- Olugboji, T. M., S. Karato, and J. Park (2013), Structures of the oceanic lithosphere-asthenosphere boundary: Mineral-physics modeling and seismological signatures. *Geochem. Geophys. Geosyst.*, Vol. 14, 4, doi:10.1002/ggge.20086
- O'Nions, R. K., and R. J. Pankurst (1974), Petrogenetic significance of isotope and trace element variations in volcanic rocks from the Mid-Atlantic. *J. Petrol.* 15, 603-634.

- O'Reilly, S. Y., and W. L. Griffin (2010), The continental lithosphere-asthenosphere boundary: Can we sample it? *Lithos*, 120, 1-13.
- Osako, M., A. Yoneda, and E. Ito (2010), Thermal diffusivity, thermal conductivity and heat capacity of serpentinite (antigorite) under high pressure, *Phys. Earth Planet. Int.*, 183, 229-233.
- Page, N. J. (1967), Serpentinization considered as a constant volume metasomatic process: a discussion, *Am. Mineral.*, 52, 545-549.
- Park, K.-H. (1990), Sr, Nd and Pb isotope studies of ocean island basalts: Constraints on their origin and evolution, PhD thesis, Columbia University, New York
- Parmentier, E. M., and W. F. Haxby (1986), Thermal stress in the oceanic lithosphere: Evidence from geoid anomalies at fracture zones, *J. Geophys. Res.*, 91, 7193-7204.
- Parsons, B. and J. G. Sclater (1977), An analysis of the variation of ocean floor bathymetry and heat flow with age, *J. Geophys. Res.*, 82, 803-827.
- Parsons, B., D. McKenzie, (1978), Mantle convection and the thermal structure of the plates, *J. Geophys. Res.*, 83, 4485-4496.
- Pelayo, A. M., S. Stein, C. A. Stein (1994), Estimation of oceanic hydrothermal heat flux from heat flow and depths of midocean ridge seismicity and magma chambers, *Geophys. Res. Lett.*, 21, 8, 713-716.
- Pertermann, M., and A. M. Hofmeister (2006), Thermal diffusivity of olivine-group minerals, *Am. Mineral.*, 91, 1747-1760.
- Pertermann, M., and M. M. Hirschmann (2003), Partial melting experiments on a MORB-like pyroxenite between 2 and 3 GPa: constraints on the presence of pyroxenite in basalt source regions from solidus location and melting rate. *J. Geophys. Res.*, 108, B2, 2125.
- Piazolo, S., and M. W. Jessell (2008), Subgrain growth Potts model. In: *Microdynamics Simulation. Lecture Notes in Earth Sciences*, vol. 106. (eds) P. D. Bons, D. Koehn, and M. W. Jessell. 97-103.
- Pollack, H. N. (1980), On the use of the volumetric thermal expansion coefficient in models of ocean floor topography, *Tectonophysics*, 64, T45-T47.
- Pollack, H. N., S. J., Hurter, J. R. Johnson (1993), Heat flow from the Earth's interior: analysis of the global data set, *Rev. Geophys.*, 31, 267-280.
- Porter, D. A., and K. E. Easterling (1981), *Phase Transformations in Metals and Alloys*. Van Nostrand Reinhold (UK) Co. Ltd. 445 pg.
- Pribnow, D. F. C., E. E. Davis, A. T. Fisher (2000), Borehole heat flow along the eastern flank of the Juan de Fuca ridge, including effects of anisotropy and temperature dependence of sediment thermal conductivity, *J. Geophys. Res.*, 105, B6, 13449-13456.

- Priestley K., and D. McKenzie (2006), The thermal structure of the lithosphere from shear wave velocities, *Earth Planet. Sci. Lett.*, 244, 285-301.
- Putirka, K. D. (1999), Melting depths and mantle heterogeneity beneath Hawaii and the East Pacific Rise: constraints from Na/Ti and rare earth element ratios. *J. Geophys. Res.*, 104, 2817-2829.
- Putirka, K. D. (2008), Excess temperatures at ocean islands: implications for mantle layering and convection, *Geology*, 36, 283-286.
- Remmert, P., R., Dohmen, and S. Chakraborty (2008), Diffusion of REE, Hf and Sr in olivine. *Eos Transactions, AGU*, 89(53) Fall Meeting Supplement, Abstract MR33A-1844.
- Reynard, B., and G.D. Price, (1990), Thermal expansion of mantle minerals at high pressures: a theoretical study, *Geophys. Res. Lett.*, 17, 6, 689-692.
- Ricard, Y., and N. Coltice (2013), Geophysical and geochemical models of mantle convection: successes and future challenges. In: *The State of the Planet: Frontiers and Challenges in Geophysics*. DOI: 10.1029/150GM06
- Ritzwoller, M. H., N. M. Shapiro, S. Zhong (2004), Cooling history of the Pacific lithosphere. *Earth Planet. Sci. Lett.*, 226, 69-84.
- Robie, R. A., Hemingway, B. S. (1995), Thermodynamic properties of minerals and related substances at 298.15 K and 1 bar (105 pascals) pressure and at higher temperatures U.S. Geological Survey Bulletin 2131.
- Rosenberger, A., E. E. Davis, H. Villinger (2000), Data Report: Hydrocell-95 and -96 single-channel seismic data on the eastern Juan de Fuca ridge flank, in Fisher, A., Davis, E. E., and Escutia, C. (eds.), *Proceedings of the Ocean Drilling Program, Scientific Results*, 168, pp. 9-19.
- Rudnick, R. L., and S. Gao (2003), Composition of the Continental Crust, *Treatise on Geochemistry*, Vol. 3. pp. 1-64.
- Ryan, J. G., and C. C. Chauvel (2013), The subduction zone conveyor and the impact of recycled materials on the evolution of the mantle, Chapter 2.11 The mantle and core (Carlson, R. Ed.), *Treatise on Geochemistry*, Second Edition.
- Rychert, C. A., K. M. Fisher, S. Rondenay (2005), A sharp lithosphere-asthenosphere boundary imaged beneath eastern North America. *Nature*, 436:542-545.
- Salters, V. J. M., and S. R. Hart (1989), The hafnium paradox and the role of garnet in the source of mid-ocean-ridge basalts. *Nature*, vol. 342. 420-422.
- Salters, V. J. M., J. E. Longhi, and M. Bizimis (2002), Near mantle solidus trace element partitioning at pressures up to 3.4 GPa. *Geochem. Geophys. Geosyst.*, vol. 3, 7, doi: 10.1029/2001GC000148



- Sandwell D.T., Winterer E.L., Mammerrickx J., Duncan R.A., Lynch M.A., Levitt D.A., Johnson C.L. (1995), Evidence for diffuse extension of the Pacific plate from Pukapuka ridges and cross-grain gravity lineations. *J. Geophys. Res.*, 100, 15,087-15,100.
- Sandwell, D. T. (1986), Thermal stress and the spacings of transform faults, *J. Geophys. Res.*, 91, 6405-6417.
- Sandwell, D. T., and G. Schubert (1982), Geoid height-age relation from SEASAT altimeter profiles across the Mendocino fracture zone. *J. Geophys. Res.*, 87, B5, 3949-3958.
- Sandwell, D. T., K.A. Poehls, (1980), A compensation mechanism for the central Pacific, *J. Geophys. Res.*, 85, 3751-3758.
- Sano, J., J. Ganguly, R. Hervig, R. Dohmen, X. Zhang (2011), Neodymium diffusion in orthopyroxene: Experimental studies and applications to geological and planetary problems. *Geochim. Cosmochim. Acta*, 75, 4684-4698.
- Saxena S.K., Chatterjee N., Fei Y., Shen G. (1993), Thermodynamic data on oxides and silicates. Springer, Berlin Heidelberg New York, pp. 168-169.
- Schatz, J. F., and G. Simmons (1972), Thermal conductivity of Earth materials at High Temperatures, *J. Geophys. Res.*, 77, 6966-6983.
- Schmidt, M. W., and S. Poli (2013), Devolitization during subduction, in *Treatise of Geochemistry, The crust*, p. 669-701, Second Edition.
- Schneider, M. E., and D. H. Eggler (1986), Fluids in equilibrium with peridotite minerals: implications for mantle metasomatism. *Geochim. Cosmochim. Acta*, 50, 711-724.
- Schroeder, W. (1984), The empirical age-depth relation and depth anomalies in the Pacific ocean basin, *J. Geophys. Res.*, 89, 9873-9883.
- Sclater, J. G. (2004), Variability of heat flux through the seafloor: discovery of hydrothermal circulation in the oceanic crust, in *Hydrogeology of the Oceanic Lithosphere*, E. E. Davis and H. Elderfield (eds.), Cambridge University Press.
- Sclater, J. G., and J. Francheteau (1970), The implications of terrestrial heat flow observations on current tectonic and geochemical models of the crust and upper mantle of the Earth, *Geophys. J. R. astr. Soc.*, 20, 509-542.
- Sclater, J. G., Anderson, R. N., and Bell, M. L. (1971), Elevation of ridges and evolution of the central eastern Pacific, *J. Geophys. Res.*, 76, 7888-7915.
- Sclater, J. G., C. Jaupart, D. Galson (1980), The heat flow through oceanic and continental crust and the heat loss of the Earth. *Rev. Geophys. Space Phys.*, 18, 269-311.
- Scott, D., and D. Stevenson (1986), Magma ascent by porous flow. *J. Geophys. Res.*, 91:9283-9296.

- Seipold, U., and F. R. Schilling (2003), Heat transport in serpentinites, *Tectonophysics*, 370, 147-162.
- Seyfried, W. E., D. R. Janecky, M. J. Mottl (1984), Alteration of the oceanic crust: implications for geochemical cycles of lithium and boron, *Geochim. Cosmochim. Acta*, 48, pp. 557-569.
- Shankland, T. J., U. Nitsan, and A. G. Duba (1979), Optical absorption and radiative heat transport in olivine at high temperature, *J. Geophys. Res.*, 84, 1603-1610.
- Shaw, D. M. (2006), *Trace elements in magmas: A theoretical treatment*. Cambridge University Press.
- Silver, P. G., and M. D. Behn (2008), Intermittent Plate Tectonics?, *Science*, 319, 85-88.
- Simon N.S.C., and Podladchikov Y.Y. (2008), The effect of mantle composition on density in the extending lithosphere, *Earth Planet. Sci. Lett.*, 272 (1-2), 148-157.
- Skemer, P., and S.-I. Karato (2007), Effects of solute segregation on the grain-growth kinetics of orthopyroxene with implications for the deformation of the upper mantle. *Phys. Earth Planet. Inter.*, 164, 186-196.
- Sleep, N. H. (1969), Sensitivity of heat flow and gravity to the mechanism of sea-floor spreading. *J. Geophys. Res.*, 74, 542-549.
- Sleep, N. S. (1975), Formation of oceanic crust: some thermal constraints, *J. Geophys. Res.*, 80, 4037-4042.
- Sleep, N. S. (2011a), Small-scale convection beneath oceans and continents. *Chinese Sci. Bull.*, 56, 1292-1317.
- Sleep, N. S. (2011b), Seismically observable features of mature stagnant-lid convection at the base of the lithosphere: Some scaling relationships. *Geochem. Geophys. Geosys.*, 12, Q10018.
- Sleep, N. H., and T. J. Wolery (1978), Egress of hot water from mid-ocean ridge hydrothermal systems: Some thermal constraints, *J. Geophys. Res.*, 83, 5913-5922.
- Smith, W. H. F., and D. T. Sandwell (1997), Global sea floor topography from satellite altimetry and ship depth soundings. *Science*, 277, 1956-1962.
- Solomatov, V. S., and C. C. Reese (2008), Grain size variations in the Earth's mantle and the evolution of primordial chemical heterogeneities. *J. Geophys. Res.*, 113, B07408, doi:10.1029/2007JB005319.
- Solomatov, V.S., R. El-Khozondar, V. Tikare (2002), Grain size in the lower mantle: constraints from numerical modeling of grain growth in two-phase systems. *Phys. Earth Planet. Int.*, 129, 265-282.

- Spengler, D., Y. Nishihara, K. Fujino (2013), Super-Si garnet exsolution kinetics denotes multistage mantle exhumation. *Geophysical Research Abstracts*. Vo. 15, EGU2013-4377.
- Spiegelman, M. (1996), Geochemical consequences of melt transport in 2D: The sensitivity of trace elements to mantle dynamics. *Earth Planet. Sci. Lett.*, 139, 115-132.
- Spiegelman, M., (1993), Physics of melt extraction: theory, implications, and applications. *Philos. Trans. R. Soc. London A* 342, 2341.
- Spiegelman, M., and P. B. Kelemen (2003), Extreme chemical variability as a consequence of channelized melt transport. *Geochem. Geophys. Geosyst.*, 4, 7, 1055, doi:10.1029/2002GC000336
- Spiegelman, M., P. B. Kelemen, and E. Aharonov (2001), Causes and consequences of flow organization during melt transport: The reaction infiltration instability in compactible media, *J. Geophys. Res.*, 106, 2061–2077.
- Spinelli, G. A., and R. N. Harris (2011), Effects of the legacy of axial cooling on partitioning of hydrothermal heat extraction from oceanic lithosphere, *J. Geophys. Res.*, 116, B09102.
- Spivack, A. J., and J. M. Edmond (1987), Boron isotopic exchange between seawater and the oceanic crust. *Geochim. Cosmochim. Acta*, 51, 1033-1043.
- Staudigel, H. (2014), Chemical fluxes from hydrothermal alteration of oceanic crust, Chapter 4.16, The crust, *Treatise on Geochemistry*, Second edition.
- Stein, C. A., and S. Stein (1992), A model for the global variation in oceanic depth and heat flow with lithospheric age, *Nature*, 359, 123-129.
- Stein, C. A., and S. Stein (1993), Constraints on Pacific midplate swells from global depth-age and heat flow-age models. In *The Mesozoic Pacific: Geology, Tectonics, Volcanism*. American Geophysical Union Geophysical Monograph 77.
- Stein, C. A., S. Stein (1994), Constraints on hydrothermal heat flux through the oceanic lithosphere from global heat flow, *J. Geophys. Res.*, 99, B2, 3081-3095.
- Stein, C. A., S. Stein, and A. M. Pelayo (1995), Heat flow and hydrothermal circulation, in *Seafloor Hydrothermal Systems: Physical, Chemical, Biological and Geological Interactions*, edited by S. E. Humphris, et al., pp. 425-445, American Geophysical Union, Washington, D. C.
- Stixrude, L. and C. Lithgow-Bertelloni (2005), Mineralogy and elasticity of the oceanic upper mantle: Origin of the low velocity zone, *J. Geophys. Res.*, 110, B03204.
- Stolper, E., and D. Walker (1980), Melt density and the average composition of basalt. *Contrib. Mineral. Petrol*, 74, 7-12.
- Stolper, E., D. Walker, B. H. Hager, J. F. Hays (1981), Melt segregation from partially molten source regions: The importance of melt density and source region size. *J. Geophys. Res.*, 86, B7, 6261-6271.

- Stracke, A., B. Bourdon, D. McKenzie, (2006), Melt extraction in the Earth's mantle: constraints from UThPaRa studies in oceanic basalts. *Earth Planet. Sci. Lett.*, 244, 97112.
- Sun, S.-S. and W. F. McDonough, (1989), Chemical and isotopic systematics of oceanic basalts: implications for mantle composition and processes. Geological Society, London, Special Publications, v. 42; p. 313-345.
- Swift, S. A., G. M. Kent, R. S. Detrick, J. A. Collins, R. A. Stephen (1998), Oceanic basement structure, sediment thickness, and heat flow near Hole 504B, *J. Geophys. Res.*, 103, B7, 15377-15391.
- Takei, Y., and B. K. Holtzman (2009), Viscous constitutive relations of solid-liquid composites in terms of grain boundary contiguity: 1. Grain boundary diffusion control model. *J. Geophys. Res.*, 114:B06205.
- Thayer, T. P. (1966), Serpentinization considered as a constant-volume metasomatic process, *Am Mineral.*, 51, 685-710.
- Theissen-Krah, S., K. Lyr, L. H. Rupke, J. P. Morgan (2011), Coupled mechanical and hydrothermal modeling of crustal accretion at intermediate to fast spreading ridges, *Earth Planet. Sci. Lett.*, 311, 275-286.
- Thieblot, L., J. Roux, and P. Richet (1998), High-temperature thermal expansion and decomposition of garnets. *Eur. J. Mineral.*, 10, 7-15.
- Tikare, V. (1995), Numerical simulation of grain growth in liquid phase sintered materials. PhD Thesis. Case Western Reserve University.
- Tikare, V., E. A. Holm, D. Fan, L. Q. Chen (1998), Comparison of phase-field and Potts models for coarsening processes. *Acta Mater.* 47, 363-371.
- Tommasi, A., B. Gibert, U. Seipold, and D. Mainprice (2001), Anisotropy of thermal diffusivity in the upper mantle, *Nature*, 411.
- Tribaudino M., R.J. Angel, F. Camara, F. Nestola, D. Pasqual, I. Margiolaki (2010), Thermal expansion of plagioclase feldspars, *Contrib. Mineral. Petrol.*, 160, 899-908.
- Tunnicliffe, V. (1991), The biology of hydrothermal vents: Ecology and evolution, *Oceanogr. Mar. Biol. Annu. Rev.*, 29, 319-407.
- Turcotte, D. L. (1974), Are transform faults thermal contraction cracks? *J. Geophys. Res.*, 79, 47, 2573-2577.
- Turcotte, D. L., and G. Schubert (2002), *Geodynamics*, 2nd Ed. Cambridge, New York. 456 pp.
- Van Hunen, J., J. Huang, and S. Zhong (2003), The effect of shearing on the onset and vigour of small-scale convection in a Newtonian rheology. *Geophys. Res. Lett.*, 30, 19, 6.

- Van Orman, J. A., T. L. Grove, N. Shimizu (1998), Uranium and thorium diffusion in diopside. *Earth Planet. Sci. Lett.*, 160, 505-519.
- Van Orman, J. A., T. L. Grove, N. Shimizu (2001), Rare earth element diffusion in diopside: influence of temperature, pressure, and ionic radius, and an elastic diffusion model for diffusion in silicates. *Contrib. Mineral. Petrol.*, 141, 687-703.
- Van Orman, J. A., T. L. Grove, N. Shimizu (2002), Diffusive fractionation of trace elements during production and transport of melting in the Earth's upper mantle. *Earth Planet. Sci. Lett.*, 198, 93-112.
- Van Orman, J. A., T. L. Grove, N. Shimizu, G. D. Layne (2002), Rare earth element diffusion in a natural pyrope single crystal at 2.8 GPa. *Contrib. Mineral. Petrol.*, 142-416-424.
- Vollmer, R. (1976), Rb-Sr and U-Th-Pb systematics of alkaline rocks: the alkaline rocks from Italy. *Geochim. Cosmochim. Acta* 40, 283-295.
- Von Herzen, E. E. Davis, A. T. Fisher, C. A. Stein, H. N. Pollack (2005), Comments on "Earth's heat flux revisited and linked to chemistry" by A. M. Hofmeister and R. E. Criss, *Tectonophysics*, 409, 193-198.
- Von Herzen, R. (2004), Geothermal evidence for continuing hydrothermal circulation in older (>60 M.y.) ocean crust, in *Hydrogeology of the Oceanic Lithosphere*, E. E. Davis and H. Elderfield (eds.), Cambridge University Press.
- Von Herzen, R. P. (1959), Heat flow values from the South-Eastern Pacific. *Nature*, 183, 882-883.
- Von Herzen, R., Uyeda, S. (1963), Heat flow through the eastern Pacific ocean floor, *J. Geophys. Res.*, 68, 4219-4250.
- Wei, M., D.T. Sandwell, (2006), Estimates of heat flow from Cenozoic seafloor using global depth and age data, *Tectonophysics*, 417, 325-335.
- Wessel, P. and W. H. F. Smith (1998), New, improved version of the Generic Mapping Tools released, *EOS Trans. AGU*, 79, 579.
- Wheat, C. G., M. J. Mottl, A. T. Fisher, D. Kadko, E. E. Davis, E. Baker (2004), Heat flow through a basaltic outcrop on a sedimented young ridge flank. *Geochem. Geophys. Geosyst.*, 5, Q12006.
- Whittington, A. G., A. M. Hofmeister, P. I. Nabelek (2009), Temperature-dependent thermal diffusivity of the Earth's crust and implications for magmatism. *Nature*, 458, 319-321.
- Wilson, D. S., and R. N. Hey (1995), History of rift propagation and magnetization intensity for the Cocos-Nazca spreading center, *J. Geophys. Res.*, 100, B7, 10041-10056.
- Winterbourne, J., A. Crosby, and N. White (2009), Depth, age and dynamic topography of oceanic lithosphere beneath heavily sedimented Atlantic margins. *Earth. Planet. Sci. Lett.*, 287, 137-151.

- Wolery, T. J., and N. H. Sleep (1976), Hydrothermal circulation and geochemical flux at mid-ocean ridges, *J. Geol.*, 84, 249-275.
- Wood, B. J., and D. A. Yuen (1983), The role of lithospheric phase transitions on seafloor flattening at old ages, *Earth Planet. Sci. Lett.*, 66, 303-314.
- Workman, R. K., and S. R. Hart (2005), Major and trace element composition of the depleted MORB mantle (DMM), *Earth Planet. Sci. Lett.*, 231, 53-72.
- Xu, W., C. Lithgow-Bertelloni, L. Stixrude, J. Ritsema (2008), The effect of bulk composition and temperature on mantle seismic structure, *Earth Planet. Sci. Lett.*, 275, 70-79.
- Yamazaki, D., T. Kato, E. Ohtani, M. Toriumi (1996), Grain grow rates of MgSiO<sub>3</sub>-perovskite and periclase under lower mantle conditions. *Science*, 274, 2052-2054.
- Yang, Z., S. Sista, J. W. Elmer, T. Debroy (2000), Three dimensional Monte Carlo simulation of grain growth during GTA welding of titanium, *Acta Mater.*, 48, 4813-4825.
- Yu, Q., S. K. Esche (2003), Three-dimensional grain growth modeling with a Monte Carlo algorithm, *Materials Letters*, 57, 4622-4626.
- Zhong, S., M. Ritzwoller, N. Shapiro, W. Landuyt, J. Huang, and P. Wessel (2007), Bathymetry of the pacific plate and its implications for thermal evolution of the lithosphere and mantle dynamics, *J. Geophys. Res.*, 112, B06412.
- Zindler, A., and S. Hart (1986), Chemical Geodynamics, *Ann. Rev. Earth Planet. Sci.* 14:493-571.
- Zlotnik, S., J.C. Afonso, P. Diez, and M. Fernandez (2008), Small-scale gravitational instabilities under the oceans: Implications for the evolution of oceanic lithosphere and its expression in geophysical observables, *Phil. Mag.*, 88, 28-29, 1-11, 3197-3217.
- Zollner, D., and P. Streitenberger (2008), Normal grain growth: Monte Carlo Potts model simulation and mean-field theory. In: *Micr-Macro-Interactions in Strutured Media and Particle Systems*, A. Bertram and J. Tomas, (Eds.), Springer-Verlag Berlin Heidelberg, 3-18.
- Zoth, G., R. Haenel (1988), Chapter 10, in *Handbook of terrestrial Heat Flow Density determination*, Haenel, R., L. Rybach, L. Stegena (eds.), Kluwer Academic Publishing, Dordrecht, 449-466.